PHYSICAL CHEMISTRY 2012

[11th] International Conference
on Fundamental and Applied Aspects of
Physical Chemistry

Under the auspices of the
University of Belgrade

Proceedings

The Conference is dedicated to
Professor Ivan Draganić

September 24-28, 2012
Belgrade, Serbia

ISBN 978-86-82475-27-9 ***Volume*** **1**
ISBN 978-86-82475-28-6 ***Volume*** **II**

Title: PHYSICAL CHEMISTRY 2012 (Proceedings)
Editors: S. Anić and Ž. Čupić
Published by: Society of Physical Chemists of Serbia, Studenski trg 12-16, 11158, Belgrade, Serbia
Publisher: Society of Physical Chemists of Serbia
For Publisher: S. Anić, President of Society of Physical Chemists of Serbia
Printed by: "Jovan" Priting and Publishing Company; 200 Copies;
Number of pages: 6+ 497; **Format**: B5; Printing finished in September 2012.

Text and Layout: "Jovan"

200- *Coppy printing*

CONTENTS

H-03-SL

CHARACTERIZATION OF Sm^{3+} DOPED TiO_2 AND Ni^{2+} DOPED TiO_2 NANOCRYSTALS

M. Vranješ[1], J. Kuljanin-Jakovljević[1], I. Zeković[1], Z. Konstantinović[2], M. Stoiljković[1], J. Nedeljković[1], Z. Šaponjić[1]

[1]*University of Belgrade, Vinča Institute of Nuclear Sciences, Belgrade, Serbia;*
[2]*Institut de Ciencia de Materials de Barcelona, CSIC,Campus UAB, 08193 Bellaterra, Spain*

Abstract

We report on a new approach toward synthesis of Sm^{3+} doped TiO_2 and Ni^{2+} doped TiO_2 nanocrystals by shape transformation of hydrothermally treated titania nanotubes in the presence of Sm^{3+} or Ni^{2+} ions. The percentage ratio of Sm^{3+} (or Ni^{2+}) to Ti^{4+} ions in doped nanocrystals was determined using ICP atomic emission spectroscopy. The XRD patterns revealed the homogeneous anatase crystal phase of both 0.4 at% Sm^{3+} doped TiO_2 and 0.12 at% Ni^{2+} doped TiO_2 nanoparticles. An average size of polyhedral Sm^{3+} doped TiO_2 nanocrystals was between 12 and 14 nm. In the orange-red spectral region, room temperature photoluminescence signals associated with $^4G_{5/2} \rightarrow {}^6H_J$ (J = 5/2, 7/2 and 9/2) transitions of Sm^{3+} was observed in Sm^{3+} doped TiO_2 nanocrystals. Optically transparent film made of 0.12 at% Ni^{2+} doped TiO_2 nanoparticles showed room temperature ferromagnetic ordering. The coercive field was found to be $H_C \sim 80$ Oe.

Introduction

Doping semiconductors with rare earth ions (Eu^{3+}, Sm^{3+}) opens the possibility of controlling the optical properties by the band gap structure of the semiconductor host [1]. This type of luminescent material can find applications for visible and infrared light emitting diodes and optical amplifiers. Compared with other host materials, TiO_2 is very effective in light confinement for an optical waveguide amplifier structure because of its high refractive index of about 2.5 and high transparency in visible and infrared wavelength region. On the other hand, wide band metal oxide semiconductors, e.g. TiO_2, after doping with transition metal ions (Co^{2+}, Mn^{2+}, Ni^{2+}), as a diluted magnetic semiconductor which support room temperature ferromagnetism, can be used for the development of the spin-based electronic devices.

Experimental

Scrolled titania nanotubes were synthesized according to Kassuga et al. using TiO_2 powder (Fluka) as a precursor [2]. Sm^{3+} or Ni^{2+} doped TiO_2 nanoparticles were synthesized by hydrothermal treatment (60 min/250 ^oC) of a suspension containing 25 mg of titania nanotubes (pH 3) as the starting materials in the presence of 5 ×

10^{-3} M $Sm(NO_3)_3$ for the synthesis of Sm^{3+} doped TiO_2 or 6.2×10^{-4} M $Ni(NO_3)_2$ for the synthesis of Ni^{2+} doped TiO_2 nanoparticles. In order to remove excess dopant ions, the dispersions of Sm^{3+} doped TiO_2 nanoparticles and Ni^{2+} doped TiO_2 nanoparticles were dialyzed against acidified water (pH 3) at 4 ^oC for three days. Morphology of titania nanotubes and doped TiO_2 nanoparticles was studied by transmission electron microscopy (TEM) technique. Crystallographic properties were studied by X-ray diffraction (XRD) measurements. Photoluminescence measurements were performed at room temperature on Fluorolog-3 Model FL3-221 spectroflurometer system (Horiba Jobin-Yvon). The magnetization of the films made of Ni^{2+} doped TiO_2 nanoparticles, as a function of magnetic field strength (*H*), was measured at room temperature with superconducting quantum interference device magnetometer (Quantum Design).

Results and Discussion

Sm^{3+} doped TiO_2 nanoparticles

Hydrothermal treatment of scrolled titania nanotubes in the presence of Sm^{3+} ions results in the formation of polyhedral 0.4 at% Sm^{3+} doped TiO_2 nanoparticles mainly of square/rectangular shape with average dimension between 12 and 14 nm, inset in Figure 1. The powder X-ray diffraction analysis of Sm^{3+} doped TiO_2 nanoparticles showed the existence of a homogeneous anatase (tetragonal, JCPDS 84-1286) crystal phase. The presence of all the characteristic anatase diffraction peaks with preserved intensity ratios implies random orientation of the nanoparticles. Emission spectrum of the 0.4 at.% Sm^{3+} doped TiO_2 nanocrystals observed after band-to-band excitations (λ_{exc} = 365 nm) is shown in Figure 1. Due to large exciton binding energy in the TiO_2, indirect excitation of Sm^{3+} by energy transfer from electron-hole pair in the TiO_2 was confirmed by characteristic orange-red emission observed by room temperature photoluminescence measurements. It consists of three emission bands peaking at 582, 612 and 662 nm originating from of $^4G_{5/2} \rightarrow {}^6H_J$ (J = 5/2, 7/2 and 9/2) *f–f* transitions of the Sm^{3+} in the $4f^5$ configuration. The transitions corresponding to $^4G_{5/2} \rightarrow {}^6H_{7/2}$ are most pronounced in accordance to the selection rule $\Delta_J = \pm 1$. The line positions of the Sm^{3+}-related emissions are in good agreement with those of Sm^{3+}-doped wide band gap semiconductors and Sm^{3+}-doped glasses. Nonexponential luminescence decay curve of Sm^{3+} (not shown) obtained by monitoring the $^4G_{5/2} \rightarrow {}^6H_{7/2}$ ransition at λ = 612 nm under the excitation at λ_{exc} = 365 nm, is due to the nonradiative

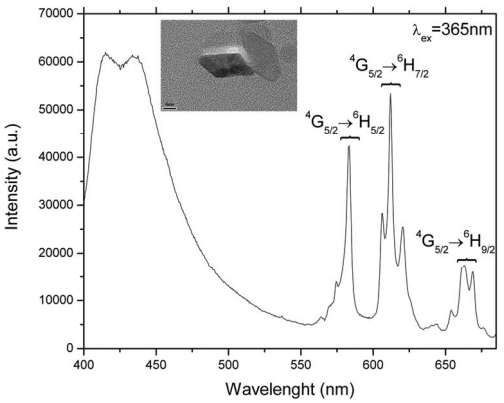

Figure 1. Emission spectrum of Sm^{3+} doped TiO_2 nanocrystals.

energy transfer process from Sm^{3+} to their neighboring defects. The luminescence lifetime of $^4G_{5/2}$ was determined to be 970 μs.

Ni^{2+} doped TiO_2 nanoparticles

Ni^{2+} ions were incorporated into TiO_2 nanoparticles through shape transformation of hydrothermally treated scrolled titania nanotubes in the presence of $Ni(NO_3)_2$. In the XRD spectrum of 0.12 at% Ni^{2+} doped TiO_2 nanoparticles, there are no peaks that indicate the presence of any other crystal phases except anatase TiO_2. For the optically transparent film made of 0.12 at% Ni^{2+} doped TiO_2 nanocrystals, the magnetic response was measured at room temperature. The in plane hysteresis loop, Figure 2, represents distinct evidence, although response is weak, of the ferromagnetic ordering at room temperature. The coercive field was found to be $H_C \sim 80$ Oe. We can conclude that the observed ferromagnetism of the film is an intrinsic property of Ni^{2+} doped TiO_2 nanoparticles taking into account that XRD analysis showed the absence of any peaks that would indicate segregation of Ni in metalic form. The explanation for the observed room temperature ferromagnetic response in of 0.12 at% Ni^{2+} doped TiO_2 nanocrystals, can be found in the simultaneous existence of Ni^{2+} ions in the nanoparticles core and donor type defects such are oxygen vacancies.

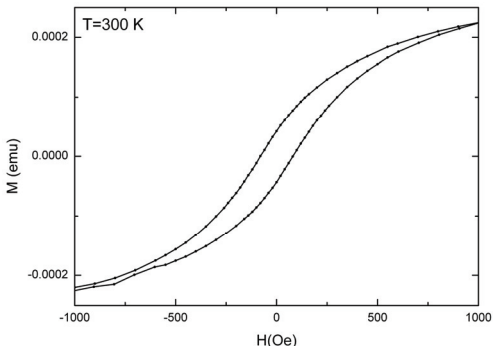

Figure 2. Isothermal magnetization of the film made of 0.12 at% Ni^{2+} doped TiO_2 nanoparticles recorded at 300 K.

Conclusion

XRD confirmed anatase crystal structure of both types of doped TiO_2 nanocrystals. In the orange-red spectral region, room temperature photoluminescence signals associated with $^4G_{5/2} \rightarrow {}^6H_J$ (J = 5/2, 7/2 and 9/2) transitions of the Sm^{3+} after band-to-band excitation were observed in Sm^{3+} doped TiO_2 nanocrystals. The Ni^{2+} doped TiO_2 nanocrystals enabled synthesis of optically transparent film that shows room temperature ferromagnetic ordering based probably on the presence of critical amount of oxygen vacancies that mediate interaction between Ni^{2+} spins trapped in the lattice structure of TiO_2 nanoparticles.

References

[1] Q. Xiao, Y. Liu, L. Liu, R. Li, W. Luo, X. Chen, J. Phys. Chem. C, 2010, 114 9314–9321.

[2] T. Kasuga, M. Hiramatsu, A. Hoson, T. Sekino, K. Niihara, Adv.Mater., 1999, 11, 1307–1311.

H-04-P

CONTROLLED HYDROTHERMAL PROCESSING OF ZnO POWDERS IN THE PRESENCE OF PVP

A. Stanković, Z. Stojanović, Lj. Veselinović, S. Marković, D. Uskoković

Institute of Technical Sciences of the Serbian Academy of Sciences and Arts, Knez Mihailova 35/IV, Belgrade 11001, Serbia (ana.stankovic@itn.sanu.ac.rs)

Abstract

In this study low-temperature hydrothermal processing was used for synthesis of ZnO powders with controlled morphology, from micro-rods *via* hexagonal prism like to nano-spheres, by the varying of $[Zn^{2+}]/[OH^-]$ molar ratio. The synthesized powders were characterized using XRPD, FE-SEM, UV-Vis diffuse reflectance and Raman spectroscopy. It is noticed that the modification of the particle size and morphology from nanospheres to micro-rods resulted in increased visible light absorption. Besides, the band gap energy of the synthesized ZnO powders showed the red shift (~0.20 eV) compared to bulk ZnO. The enhanced visible light absorption of the ZnO powders is related to the existence of lattice defects and the particle surface sensitization by PVP.

Introduction

Since the functionality of materials are determined by the phase purity, homogeneity, particle size, morphology, as well as crystallinity, the possibility to control the synthesis process is of utmost importance. Several techniques such as precipitation, sol–gel process, spray pyrolysis, hydrothermal synthesis, and mechanochemical processing are used for the preparation of ZnO materials with controlled properties. Among them, hydrothermal synthesis is the most attractive due to the fact that it allows perfect control of purity, crystallinity, composition, size and morphology by simple tuning of the experimental variables: reaction temperature, time, reactant molar ratio and/or addition of the appropriate polymer surfactants [1,2]. Moreover, hydrothermal synthesis is environmentally safe and economical for large-scale production.

Here, we propose a low-temperature hydrothermal method for the synthesis of phase-pure ZnO powders with a controlled morphology and narrow particle size distribution. This simple and low-cost method allows to tailor the shape and size of ZnO particles, from micro-rods *via* hexagonal prism like to nano-spheres, by the varying of $[Zn^{2+}]/[OH^-]$ molar ratio. The synthesized powders were characterized by XRPD, FE-SEM, UV-Vis diffuse reflectance and Raman spectroscopy.

Experimental

ZnO powders were prepared by low-temperature hydrothermal processing. The reaction temperature and time were kept constant, while the $[Zn^{2+}]/[OH^-]$ molar ratio in the starting solution was changed in order to tailor the particle size and shape. The $[Zn^{2+}]/[OH^-]$ molar ratio was varied from 1:1, 1:3, 1:3.5, to 1:5,

resulting in the pH values of the reaction solution: 8, 10, 11, and 13, respectively. The starting materials were zinc acetate ($Zn(CH_3COO)_2 \cdot 2H_2O$), sodium hydroxide (NaOH) and polyvinylpyrrolidone (PVP), as a polymer surfactant. After the dissolution of zinc acetate dihydrate and PVP, an adequate amount of the aqueous solution of NaOH was added dropwise, resulting in a white precipitate. The as-prepared suspension was thermally treated in 2 l *Parr* stainless steel reactor up to 120 °C under constant stirring of 400 rpm. The reaction time was 72 h. The synthesized ZnO powders were designated as ZnO8, ZnO10, ZnO11 and ZnO13, where the number signifies the pH value of the reaction solution.

The crystal phases of synthesized powders were identified by XRPD analysis (Philips PW-1050). The morphology of ZnO particles was observed by FE-SEM (SUPRA 35 VP Carl Zeiss). The UV-Vis diffuse reflectance spectra were recorded in the wavelength range 300–800 nm (Evolution 600 UV-Vis spectrophotometer, Thermo Scientific). The μ-Raman spectra were recorded in the frequency interval of 50–3500 cm^{-1} (DXR Raman microscope, Thermo Scientific).

Results and Discussion

The results of XRPD analysis show that the synthesized ZnO powders are pure, highly crystalline, a wurtzite-type hexagonal structure with nanosized crystallites.

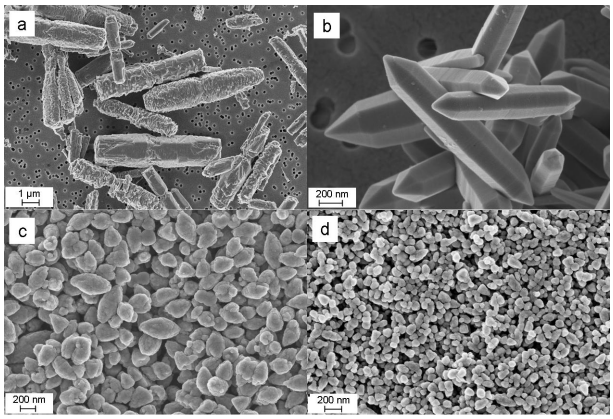

Figure 1. FE-SEM micrographs of: (a) ZnO8; (b) ZnO10; (c) ZnO11, and (d) ZnO13.

The morphologies of the synthesized ZnO powders, examined by FE-SEM, are shown in Fig. 1. The ZnO8 powder is consisted of the micro-rods with a rough particle surface and partially cracked edges with non-uniform particles size distribution; the particle lengths are between 1.4 and 7.1 μm, while the diameters are between 0.3 and 1.7 μm (Fig. 1a). ZnO10 powder, Fig 1b, is composed of the particles with a smooth hexagonal-faceted prismatic morphology with hexagonal pyramidal ends. The most of the rods have rather uniform diameters of about 200 nm and lengths of 1-2 μm. Powder ZnO11, Fig. 1c, is composed of ellipsoidal particles with an average diameter and length of about 200 nm and 500 nm,

respectively. Finally, ZnO13 powder consists of spherical nano-sized particles with uniform size distribution and average diameters of ~ 50 nm, Fig. 1d.

Influence of particles size and morphology on optical properties of ZnO was examined by UV-Vis diffuse reflectance spectroscopy (DRS). Using the recorded UV-Vis DRS and the Kubelka-Munk transformation method, the band gap energies (E_{bg}) were determined, and they are: ZnO8 — 3.16 eV, ZnO10 — 3.18 eV, ZnO11 — 3.19 eV, and ZnO13 — 3.22 eV. It is noticed that all the synthesized ZnO powders show increased absorption in the visible region at room temperature.

Raman spectroscopy was used to explain the improved optical properties of the synthesized ZnO powders (red shift of band gap). The modes that appear in the Raman spectra were assigned to wurtzite crystal structure, to the structural defects (impurities, oxygen vacancies and zinc interstitials) as well as to PVP. According to the Raman spectroscopy study, the red shift of the band gap (~ 0.20 eV) for the synthesized ZnO powders compared to bulk ZnO (E_{bg} = 3.37 eV) could be related to two phenomena: the introduction of lattice defects and surface sensitization by PVP, because PVP can improve visible light absorption. Detailed analysis of Raman spectra yields that nano-sized powder ZnO13 and ZnO11 has ordered wurtzite crystal structure with very few defects, while in micro-sized powders, ZnO10 and ZnO8, number of defects and impurities, as well as absorption of PVP at the surface increase.

Conclusion

The effect of the $[Zn^{2+}]/[OH^-]$ molar ratio i.e. pH of the reaction solution on the sizes and morphology of ZnO particles synthesized *via* low-temperature hydrothermal processing was examined. Varying the pH from almost neutral, pH=8, to a strong base solution, pH=13, ZnO particles from non-ordered micro-rods, hexagonal-faceted prismatic morphology with hexagonal pyramidal ends, sub-micron elipsoids to the nano-spheres were prepared. Therefore, it is possible to control morphology and sizes of the ZnO particles by adjusting the pH value of the reaction solution. The synthesized ZnO powders exhibit enhanced visible light absorption in comparison to bulk ZnO. Improved optical properties are related to two phenomena: introduction of lattice defects (impurities, oxygen vacancies and zinc interstitials), also, surface sensitization by PVP.

Proposed synthesis method provides simple, economic and low-temperature approach for a growth of ZnO particles with the different morphology and improved optical properties.

Acknowledgments

This study was supported by the Ministry of Education and Science of the Republic of Serbia under grant no III45004.

References

[1] Y, Zhang, J. Mu, Nanotechnology 2007, 18, 075606 (6 pp).
[2] H. Zhang, D. Yang, D. Li, X. Ma, S. Li, D. Que, Crystal Growth & Design 2005, 5, 547-50.

H-05-P

SYNTHESIS OF NEW TYPE OF CORDIERITE COATINGS

A. Prstić[1], Z. Aćimović-Pavlović[2], A. Terzić[3], L. Pavlović[4]
[1]AMI-Beograd, Beograd, Serbia;[2]Faculty of Technology and Metallurgy, University of Belgrade, Belgrade, Serbia; [3]Institute for Materials Testing, Belgrade, Serbia; [4]Institute ITNMS, Belgrade, Serbia

Abstract
New refractory coatings based on synthesized cordierite for the casting applications were investigated. The investigation included synthesis of the cordierite and design of the refractory coating as final product. Design and optimization of the coating composition, with controlled rheological properties included, were achieved by application of different coating components, namely different suspension agents and by alteration of the coating production procedure. Cordierite, used as filler, was obtained by means of synthesis in the solid state reaction on the basis of talc, kaolin and alumina. The investigation showed that the application of these particular types of coatings has positive influence on surface quality, structural and mechanical properties of the castings of aluminum alloys.

Introduction
The main role of coating is the creation of an efficient and unbreakable firm refractory barrier separating sandy substrate from the liquid metal flow [1]. Certain coating properties are being required [2]: good refractoriness, suitable gas permeability, simple application, good adhesion to sand mold and polymer model, easy coating layer thickness adjustment, high drying rate. This can be achieved by optimization of the coating composition and production technology [3]. The cordierite was chosen as refractory coating filler due to the following properties: (1) low thermal conductivity: 3 W/(m·K) and low coefficient of linear thermal expansion (α): 1.7 10^{-6}/°C at 25 °C [4]; (2) high thermal shock resistance (quenching/500) and high maximal use temperature (1371 °C) [5]; (3) extreme resistance on liquid metal absorption [6]; (4) no gas production when in contact with liquid metal. Different additive types and various quantities were tested in order to enable the best possible absorption between additives and the refractory filler particles and, thus, maintenance of the filler in a dispersed state and prevention of the filler building up or segregation.

Experimental
Cordierite used as refractory filler for the coating was synthesized by means of high-temperature reaction in solid state. The raw materials - talc, kaolin and alumina were milled down to the grain size of $1 \cdot 10^{-4}$ m and then mixed in the ratio $2MgO : 2Al_2O_3 : 5SiO_2$. The samples were sintered at 1300 °C during 8 hours in a laboratory furnace in the oxidation atmosphere. X-ray fluorescence technique was used to conduct chemical element analysis (XRF spectrophotometer *ED 2000* –

Oxford). Mineral phase composition was analyzed by means of X-ray powder diffraction (XRD - *Philips PW-1710* diffractometer). DTA was performed with a *Shimadzu DTA–50* apparatus. The microstructure of the samples was characterized by scanning electron microscopy method (SEM) using a *JEOL* JSM-6390 Lv microscope. Distribution of refractory filler and bonding agent in a coating suspension was conducted by means of polarized optical microscope with passing light *JENAPOL* type (*Carl Zeiss – Jena*). Analysis of the particle size and shape factor was conducted by means of the PC software *OZARIA 2.5*. Cordierite samples synthetically obtained were applied as refractory filler in three types of coatings. Compositions of refractory coatings included refractory filler, bonding agent, additive and solvent and they were as follows: *Type I* - cordierite (93-95 %) + colophonium ($C_{20}H_{30}O_2$) 2-2.5 % + Bentone 25 0.8-1 % + isopropyl alcohol; *Type II:* cordierite (93-95 %) + colophonium ($C_{20}H_{30}O_2$) 1.2-1.5%, dextrin 0.5-1 % + Bentone SD-3 1.2-1.5%, phenol formaldehyde resins 1.2-1.7 % + isopropyl alcohol; *Type III:* cordierite (92-94 %) + bentonite 1.5-2.5%; bindal H 0.5-1% + suspension maintenance agent: $Na_3P_3O_3$ 1-3%, Carboxymethyl cellulose (CMC) 0.5-1% + water.

Results and Discussion

Synthesized cordierite had following chemical composition (%): MgO 13.2, Al_2O_3 31.9, SiO_2 52.9, Fe_2O_3 1.2, CaO 1.5. The composition of synthesized cordierite is approximately the same as composition of natural cordierite, which approves the soundness of the method applied. Identified crystalline major phases present in the sample were: cordierite, spinel ($MgAl_2O_4$), cristobalite (SiO_2) and quartz (SiO_2). Spinel, cristobalite and quartz were noted in relatively negligible amounts. Their peaks on the diffractogram (Fig 1) are overlapping, thus exact corresponding peaks are hard to detect.

The processes taking place during sample thermal treatment from 20 up to 1200 ºC were identified by means of DTA method. The thermal treatment of the cordierite comprises three separate regions that are monitored by three individual peaks. First endothermic effect appearing at relatively low temperatures (up to 200°C) is a consequence of evaporation of physically bonded water. Second endothermic effect was noticed at 507 °C and it corresponds to the α-tridymite → α-quartz transformation. The third peak, which is exothermal, corresponds to the reactions between MgO and SiO_2, where magnesium methasilicate is formed at the temperature of 1121 °C. Microstructure analysis of the coating filler and suspension samples, performed with *OZARIA 2.5*, showed that filler particles are varying in size but mainly maintain more or less uniform morphology – in terms that majority of the filler particles showed coefficients from 0.5 to 0.8. Coefficient values referred to sub-oval shape as mid-solution between needle shape (0) and spherical shape (1). However, further SEM analysis (Fig.2) of the cordierite sample morphology pointed out that its grains are mostly irregularly shaped (hexagonally). Estimated mean size of the filler particles was $35x10^{-6}$ m. As seen on the microphotograph, morphology of cordierite samples points out that most of the

particles are irregularly shaped. Dimensions of the grains are significantly varying. Small, needle-like shaped particles can be seen on the microphotograph. Such shape of particles is characteristic for quartz. Cordierite grains are commonly large with elongated shapes and are surrounded by smaller quartz particles. Smaller particles are forming clusters by merging together or with bigger grains.

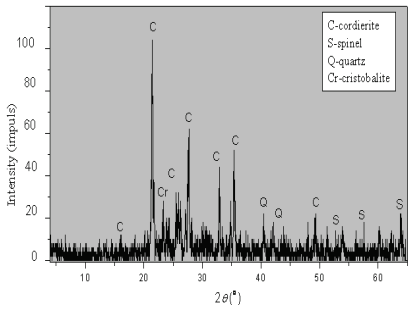

Figure 1. Diffractogram of cordierite.

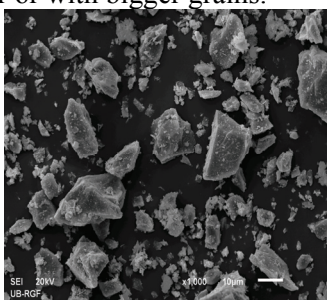

Figure 2. Microphotography of cordierite.

Conclusion

The investigation showed that synthesized cordierite met the casting application requirements. Furthermore, all investigated types of refractory coatings promoted acceptable casting surface finish; they added stiffness to the cluster and allowed the foam decomposition products to escape. The investigated coatings showed possibility of easy application on the sandy molds and polymer models; they evenly flow down during pouring and submerging. After drying, coating surfaces were smooth, coating layers had even thickness all over the surfaces of the molds and models without bubbling, cracks, peeling or taking off.

Acknowledgment

This investigation was supported by Serbian Ministry of Science and Education and it was conducted under following projects: 33007, 172057 and 45008.

References

[1] R. Monroe, Expandable Pattern Casting, p.71, AFS Inc. USA, 1994.
[2] Standard: SRPS EN 12890:2000 / CEN/TC 190.
[3] H. Gökce, D. Agaogulları, M. Lütfi Övecoglu, I. Duman, T. Boyraz,, Journal of the European Ceramic Society, 2011, 31, 2741–2747.
[4] A. Yamun, S. Honda, K. Sumita, M. Yanagihara, S. Hashimoto, H. Awaji, Microporous and Mesoporous Materials, 2005, 85, 169–175.
[5] J. Banjuraizah, H. Mohamad, Z. A. Ahmad, Journal of Alloys and Compounds 2011, 509, 1874–1879.
[6] A. Yamuna, R. Johnson, Y.R. Mahajan, M. Lalithambika, Journal of the European Ceramic Society, 2004, 24 65–73.

SYNTHESIS AND THERMAL PROPERTIES OF CHITOSAN/BENTONITE NANOCOMPOSITES

J. Pavličević[1], A. Aroguz[2], O. Bera[1], S. Sinadinović-Fišer[1], N. Lazić[3], O. Borota[1], Milovan Janković[1]

[1]*University of Novi Sad, Faculty of Technology, Republic of Serbia*
[2]*Istanbul University, Engineering Faculty, Istanbul, Turkey*
[3]*Institute of General and Physical Chemistry, Belgrade, Republic of Serbia*

Abstract
Biopolymer nanocomposites are often used as superior adsorbents in colored waste water treatment, due to their biodegradable and nontoxic nature. In this study chitosan/bentonite nanocomposites were produced by clay addition into the polymer using solution technique. Bentonite was modified before the composite preparation. The morphology of the composites was studied by scanning electron microscopy (SEM). The glass transition temperature of obtained nanobeads was investigated using differential scanning calorimetry (DSC). It was estimated that finely dispersed clay particles in the polymer matrix affects the adsorption behavior. Taking into consideration the area of application, the chitosan seems to be very promising material as the component in nanocomposites for the adsorption of dye from waste water.

Introduction
Nowadays, the significant attention is paid to resolving the problem of earth-environmental pollution and biopolymer composites are used as excellent adsorbents [1]. Chitosan, a linear polysaccharide formed from randomly distributed β-(1-4)-linked D-glucosamine and N-acetyl-D-glucosamine, is a positively charged polymer that can bind to negatively charged substances [2]. Bentonite is a member of the smectite group minerals and has a layered structure with large adsorption capacities for polymer molecules due to their unique crystal structure [3]. The aim of this applicative investigation was to study the adsorption and thermal properties of chitosan/bentonite composites for theit possible application in the industry for colored waste water treatment.

Experimental
In the first step, clay was modified in a following way: bentonite (obtained from MTA, Ankara, Turkey) was dried at 110 °C for 2 h and modified after sieved through 200 μm sieve. Then, 1g of bentonite was suspended in 100 ml distilled water at room temperature. The surfactant, cetyltrimethyl ammonium bromide (CTAB) was used to form the network structure with chitosan and thus, enhance its adsorption properties. Firstly, CTAB was dissolved in hot water (1 wt. %) and then slowly poured into the bentonite suspension and stirred for 24 h at ambient temperature. Bentonite was filtered, washed three times, dried under vacuum and,

as final product, crushed into powder and sieved again. In order to obtain chitosan solution, biopolymer was suspended in water at 121 °C for 25 minutes and then dissolved by addition of acetic acid, in a sterile medium. The homogeneous solution was obtained after stirring for 48 h. Four different chitosan/bentonite nanobeads (see Table 1) were prepared using the following procedure: modified clay was firstly swelled by 50 ml of distilled water, added to 50 ml chitosan solution and stirred at 60 °C to overnight. The chitosan droplets formed a bead shape in the solution and they were left in the solution for 12 h. The filtered nanocomposite beads were washed by deionized water and stored in distilled water for use. The mean diameter of the beads was 2.5-3.0 mm. The structure of obtained chitosan/bentonite nanocomposites was followed using scanning electron microscope JEOL JSM-6460 at magnifications from 10^3 to $2x10^6$ at 25 kV. Thermal properties of obtained nanobeads were investigated by DSC Q20 TA Instruments, from 30 °C to 300 °C, with a heating rate of 10 °C/min.

Table 1. The code and description of obtained chitosan/bentonite nanobeads (sample name, the volume of chitosan/bentonite solution, the weight content of chitosan/bentonite nanocomposites powder, the volume of NaOH solution and the molarity of NaOH solution).

sample code	Chitosan/clay solution, ml	Chitosan/clay powder, wt. %	NaOH, ml	NaOH, mol
Sample 1	3	6	10	1
Sample 2	5	4	10	1
Sample 3	3	6	10	5
Sample 4	2	5	10	5

Results and Discussion

The intercalated structure of different nanobeads is displayed in Fig. 1. On the basis of SEM results, it can be seen that the adsorption properties of chitosan/bentonite nanocomposites final structure is significantly influenced by the concentration of base (NaOH).

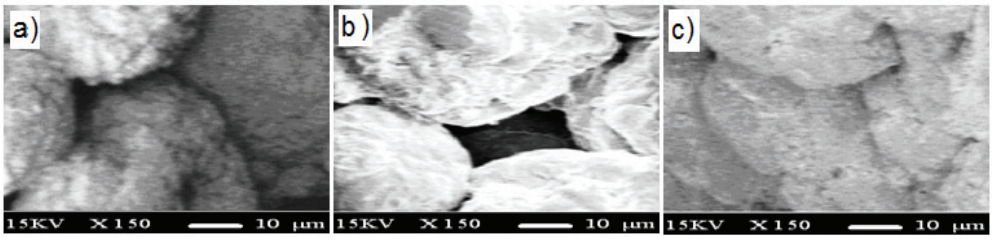

Figure 1. SEM micrographs of a) sample 1, b) sample 2 and c) sample 3.

DSC thermograms of obtained chitosan/bentonite nanocomposites are shown in Fig. 2a. The enthalpy of endothermic peak assigned to adsorbed water evaporation (detected above 100 °C) depends on molarity of NaOH solution. To

erase the effect of moisture, two heating cycles were performed. The first and second runs of chosen sample are shown in Fig. 2b. From the second scan for all investigated samples, the glass transition temperature was found at 144 °C.

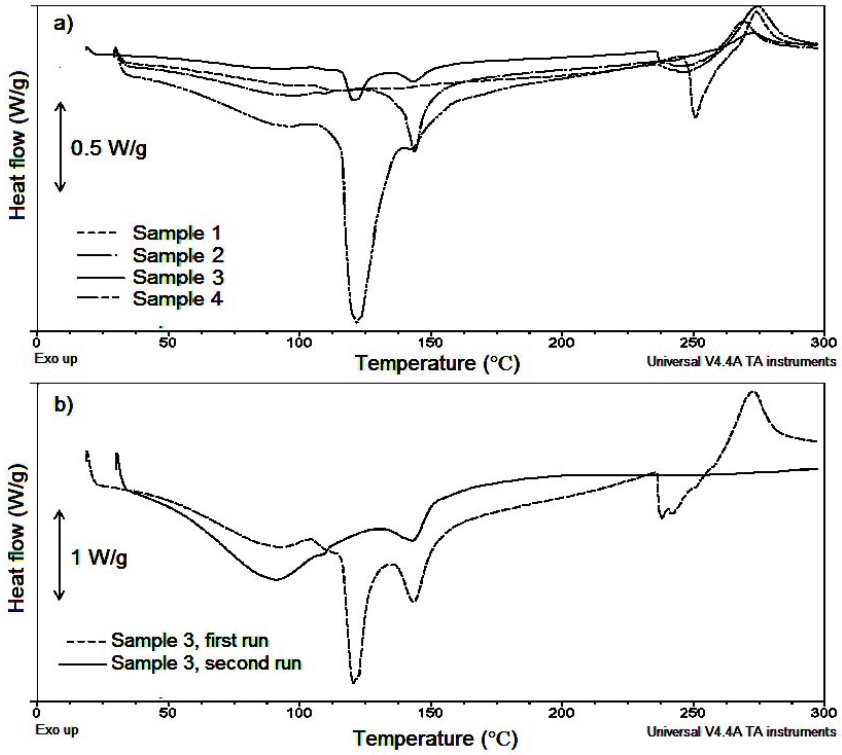

Figure 2. a) DSC curves of prepared chitosan/bentonite nanobeads and b) the first and second DSC run for sample 3.

Conclusions

In this applicative research, with a proper preparation procedure biopolymer nanobeads based on chitosan and bentonite intended for waste water purification were successfully obtained. It was shown that the preparation procedure of nanobeads affects the morphology and thermal behavior of biopolymer nanocomposites. It was found that the concentration of base for composites precipitation is very effective for the final structure of beads. Thermal properties of biopolymer hybrid materials are influenced by bentonite incorporation, thanks to a physical barrier effect of the silicate layers. The addition of bentonite improves adsorption properties of deflocculated chitosan, which is desired for the application of obtained biopolymers in colored waste water treatment.

Acknowledgement

This work is financially supported by Ministry of Education and Science of the Republic of Serbia (Project No. III45022).

References

[1] K. Sakurai, T. Maegawa, T. Takahashi, Polym., 2000, 41, 7051–7056.
[2] E. Gunister, D. Pestreli, C.H. Unlu, O. Atıcı, N. Gungo Carbohyd. Polym., 2007, 67, 358–365.
[3] Q.Y. Yue, Q. Li, B. Y. Gao, Y. Wang, Sep. Pur. Technol., 2007, 54, 279-290.

H-07-P

SYNTHESIS AND STRUCTURAL PROPERTIES OF F-DOPED $LiFePO_4$/C COMPOSITE

M. Milović[1], D. Jugović[1], M. Mitrić[2], B. Jokić[3], D. Uskoković[1]

[1]*Institute of Technical Sciences of SASA, Belgrade, Serbia*
[2]*Vinča Institute of Nuclear Sciences, University of Belgrade, Belgrade, Serbia*
[3]*Faculty of Technology and Metallurgy, University of Belgrade, Belgrade, Serbia*

Introduction

Olivine type $LiFePO_4$ is used as a cathode material for Li-ion batteries because of its high energy density (with capacity of 170 mAh/g and plateau voltage of 3.5 V vs. Li^+/Li), stability, safety, environmental friendliness and low cost. However, the low intrinsic electronic and ionic conductivity limits its application.

Effects of cation doping on improving electrochemical performance of $LiFePO_4$ has been widely studied and debated [1]. On the other hand, anion doping has not been sufficiently investigated. It is generally accepted that doping of $LiFePO_4$ with fluorine would enhance its electrochemical performance. Several papers are dealing with the influence of small quantities of fluorine dopant on the properties of $LiFePO_4$ [2, 3]. In this paper, we report on the impact of F doping on the crystal structure of $LiFePO_4$/C composite obtained through the co-precipitation in molten stearic acid, a new method established by our group [4].

Experimental

F-doped $LiFePO_4$/C was synthesized by co-precipitation in molten stearic acid [4]. In the molten stearic acid, stoichiometric amounts of aqueous solutions of $(NH_4)_2HPO_4$ and $FeSO_4 \cdot 7H_2O$ were added sequentially when precipitation occurred. Dry melt was reground and mixed with solid LiF, which served as both lithium and fluorine source. Thus obtained powder was calcined at temperature of 700°C for 3 hours in a slightly reductive atmosphere (Ar + 5%H_2), then washed in distilled water and dried under vacuum. The properties of thus obtained powder were compared with the previously published data of the undoped one obtained under the same synthesis conditions, except for lithium salt [4].

X-ray diffraction data were collected on a Philips PW 1050 diffractometer with Cu-K$\alpha_{1,2}$ radiation (Ni filter) at the room temperature. Measurements were done in 2θ range of 10-110° with scanning step width of 0.02° and 14 s times per step. Crystal structure refinement was based on the Rietveld full profile method [5] using the Koalariet computing program [6]. Chemical composition of the final compound was Li:Fe:P = 0.99:1.00:1.00 determined by inductively coupled plasma (ICP) analysis. The fluorine in the sample was detected with SA720 ion selective electrode (ISE).

Results and Discussion

X-ray powder diffraction pattern (Fig. 1) was used for phase identification and structural analysis. Olivine type $LiFePO_4$ was obtained as a major phase with FeS as an impuritiy phase. There is no evidence of a crystalline carbon, so internal carbon could be treated as a contribution to the background. The structure of F-doped $LiFePO_4$ has been refined in the space group *Pnma* (D_{2h}^{16}) in olivine type with following crystallographic positions: Li^+ ions in special crystallographic position 4*a* [0,0,0] with local symmetry $\bar{1}$; Fe^{2+} and P^{5+} ions occupy two different crystallographic 4*c* positions [x,0.25,z] with local symmetry m; O^{2-} ions occupy three different crystallographic positions: additional two 4*c* positions and one general 8*d* position [x,y,z] with local symmetry 1.

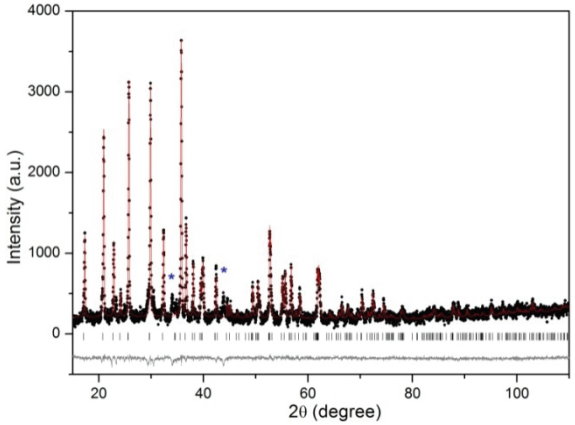

Fig. 1. The observed (•), calculated (-), and difference (bottom) X-ray diffraction data of F-doped $LiFePO_4$/C taken at room temperature; vertical markers bellow the diffraction pattern indicate positions of possible Bragg reflections; the

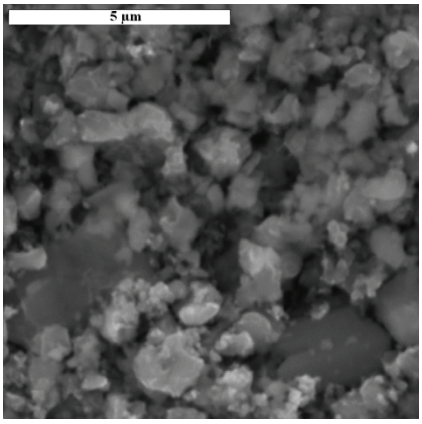

Fig. 2. Scanning electron microscopy image of F-doped $LiFePO_4$/C prepared via co-precipitation method.

The Rietveld refinement results (Table 1 and 2) indicate decreased lattice parameters and primitive cell volume compared with the undoped sample synthesized under the same conditions [4]. This finding is an evidence that F^- ions are successfully incorporated in the lattice, since F^- ions are smaller than O^{2-} ions ($r^{VI}(F^-)$ = 1.33 Å, $r^{VI}(O^{2-})$ = 1.40 Å). There are three kinds of O sites (namely O1, O2, and O3) in the lattice that may be occupied by fluorine separately or randomly. The best refinement was accomplished when O2 site was allowed to be occupied by fluorine ions. The calculated value of dopant concentration matches well with the chemical composition of the powder. Furthermore, doping with fluorine resulted in increased crystallite size. The Rietveld refinement also showed additional electron density on the lithium sites indicating so-called "anti-site" defect in which Li ion (on the M1 site) and Fe ion (on the M2 site) are interchanged.

Table 1. The final results of the structural refinement for undoped [4] and F-doped $LiFePO_4$.

	Lattice parameters [Å]	Primitive cell volume [$Å^3$]	Mean crystallite size [nm]	Li site occ. by Fe	O2 site occ. by F	R factor [%]
$LiFePO_4$	a = 10.3279(3) b = 6.0096(2) c = 4.6994(1)	V = 291.68(9)	75(10)	0.020(5)	-	Rwp = 4.49
F-doped $LiFePO_4$	a = 10.3340(2) b = 6.0086(1) c = 4.6943(3)	V = 291.49(8)	150(9)	0.027(3)	0.04(1)	Rwp = 2.07

Table 2. Fixed and refined atomic coordinates.

Fractional coordinates	$LiFePO_4$			F-doped $LiFePO_4$		
	x	y	z	x	y	z
Li (4*a*)	0	0	0	0	0	0
Fe (4*c*)	0.2820(3)	0.25	0.9749(4)	0.2820(2)	0.25	0.9724(8)
P (4*c*)	0.0924(4)	0.25	0.4140(6)	0.0939(6)	0.25	0.4155(6)
O(1) (4c)	0.1039(6)	0.25	0.7343(7)	0.1076(9)	0.25	0.7331(2)
O(2) (4c)	0.4563(6)	0.25	0.2100(7)	0.4650(9)	0.25	0.2126(6)
O(3) (8d)	0.1682(1)	0.0426(7)	0.2828(6)	0.1691(9)	0.0365(9)	0.2804(5)

The typical SEM image of as-prepared F-doped $LiFePO_4$/C composite is presented in Fig. 2. It shows wide particle size distribution, with increased particle size compared to the undoped powder. Apparently, F substitution catalyzes the growth of the primary particles. By comparing mean particle size estimated from SEM image (Fig. 2.) with mean crystallite size (Table 1) it can be concluded that particles are polycrystalline composed of a number of crystallites.

Conclusion

F-doped lithium iron phosphate powder was successfully synthesized by facile co-precipitation in molten stearic acid followed by thermal treatment. Crystal structure refinement showed that doping with fluorine ions preserves olivine structure. According to the Rietveld refinement fluorine ions occupy separately O2 oxygen site. Scanning electron microscopy showed that F substitution catalyzes the growth of the primary particles.

References

[1] J. W. Fergus, J. Power Sources, 2010, 195, 939-954.
[2] F. Lu, Y. Zhou, J. Liu, Y. Pan, Electrochim. Acta, 2011, 56, 8833-8838.
[3] M. Pan, X. Lin, Z. Zhou, J. Solid State Electrochem., 2011, 16, 1615-1621.
[4] D. Jugović et. al., J. Power Sources, 2011, 196, 4613-4618.
[5] H. M. Rietveld, J. Appl. Cryst., 1969, 2, 65-71.
[6] R. W. Cheary, A. Coelho, J. Appl. Cryst., 1992, 25, 109-121.

H-08-P

SYNTHESIS, CHARACTERIZATION AND PHOTOCATALYTIC ACTIVITY OF ANATASE NANOPARTICLES DOPED WITH GADOLINIUM IONS

N. D. Abazović, M. Radoičić, M.I. Čomor
Vinča Institute of Nuclear Sciences, University of Belgrade, P.O. Box 522, 11001 Belgrade, Serbia

Abstract
Gd^{3+}-doped anatase nanoparticles have been synthesized via acidic hydrolysis of Gd^{3+} and Ti^{4+} organic precursors. The resulting products were characterized by X-ray diffraction (XRD) and diffuse reflection spectra (DRS). Experimental results indicated that different Gd^{3+}-doping levels make great impact on the optical properties and photocatalytic activity of the obtained TiO_2 nanoparticles. All applied doping concentrations induced enhancement of photoactivity regarding degradation of Rhodamine B (RB), compared to pure TiO_2. The inter-band defect states formed as a result of incorporation of Gd^{3+} ions in the TiO_2 matrix are most probably the cause of observed improved photoacatalytic activity and optical properties of the doped TiO_2 nanoparticles.

Introduction
The photocatalytic degradation of pollutants in water and air has attracted much interest in the last several decades. A special attention is focused on the application of anatase titania for photodegradation of various organic pollutants under ultraviolet (UV) or solar light [1]. The band gap of anatase (3.2 eV) is not ideal for solar applications, which limits its wide application in visible range. The development of titania based photocatalysts that can be excited by visible light has received lately great attention. Many methods are attempted, such as dye sensitization, surface modification and transition metals doping [2].

Homogenous hydrolysis of titanium (IV) salts in acidic solution (pH about 1) is very simple preparation method, which can be easy executable in production of titania nanostructures doped with various metal ions [3]. Modification of previously described method [3] was used in preparation of series of titania photocatalysts doped with gadolinium ions. Obtained materials were characterized using XRD, UV/Vis reflectance and absorption, and their photocatalytic activity was checked. Rhodamine B dye (RB) was selected as a model reactant for photodegradation.

Experimental
Chemicals including $Ti(O\text{-}i\text{-}C_3H_7)_4$ (Sigma-Aldrich), $i\text{-}C_3H_7OH$ (Baker, HPLC grade), Gd^{3+} -acetylacetonate (Aldrich), etc. were commercial products and used as received without further purification. Water was purified by a Milli-Q system (Millipore) and had a resistivity ≥ 18 MV cm.

Routinely, 2 mL of Ti(O-*i*-C_3H_7)$_4$, dissolved in 10 mL of *i*-C_3H_7OH, was added into 250 mL of a mixture of water and *i*-C_3H_7OH (1 : 1, pH~ 1 adjusted by HNO_3) when TiO_2 was synthesized, or solution of appropriate amount of Gd^{3+} - acetylacetonate dissolved into 250 mL of a mixture of water and *i*-C_3H_7OH (1 : 1, pH~1 adjusted by HNO_3) under vigorous stirring at 0º C. After being continuously stirred at room temperature (20ºC) for two days, the reaction solution was dialyzed for purification and adjustment of the pH of the colloidal solution as formed (pH~ 2.3). Finally, the solution was vacuum evaporated at RT to yield powder samples.

The UV/vis diffuse reflectance spectra (DRS) were recorded on an Evolution 600 UV/vis spectrophotometer (Thermo Scientific), equipped with DRA-EV-600 Diffuse Reflectance Accessory.

Photocatalytic activity was obtained using whole spectrum of Xe-lamp, 150 W, as irradiation source used routinely when simulation of solar spectrum is neccesary. Experimental solutions were irradiated in cylindrical vessels (20 ml) in the stream of O_2. In certain time intervals, aliquots were taken from experimental solutions, centrifuged in order to separate powder catalyst and absorption at 552 nm (peak of RB) of the supernatant was measured. Photocatalytic activity was observed as a fraction of RB (C/C_0) still present in the reactor after certain time of irradiation.

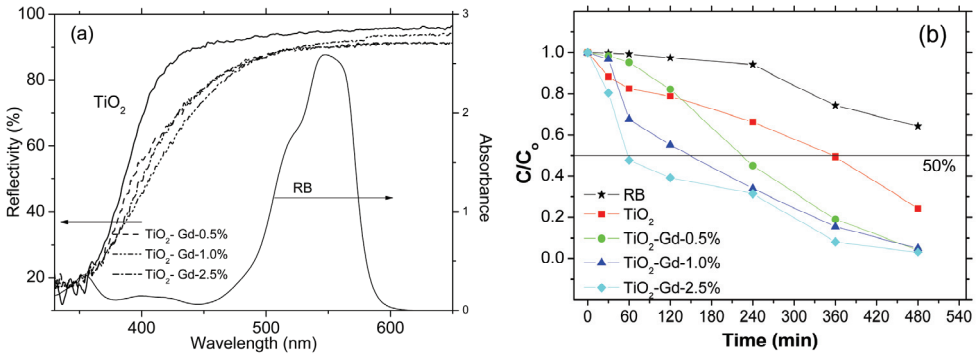

Figure 1 (a) DRS of the obtained powders and absorption spectrum of RB; (b) effect of different photocatalysts on the degradation of RB. Initial concentration of RB was 10^{-5} M; concentration of catalyst was 1 mg/ml. For comparison photolysis of RB is also presented.

Results and Discussion

The DRS spectra of synthesized samples are shown in Fig. 1 (a). The onset of the absorption spectrum of pure TiO_2 appearing at about 400 nm matches well with the intrinsic band-gap of anatase (3.2 eV). Comparing diffuse reflectance spectra of pure TiO_2 and Gd^{3+}-doped samples with Gd nominal amount of 0.5, 1.0 and 2.5 at% it can be seen that there is a significant shift in the onset absorption towards the higher wavelengths for all the Gd^{3+}-doped samples. Firstly, it may be due to appearance of a new electronic state in the TiO_2 band gap. Therefore, the distance of charge transfer between f electrons of the rare earth ions and the conduction or valence band of TiO_2 is narrowed. Accordingly, it leads to visible light absorption

response of obtained samples. Second, Gd^{3+} ions enter into the anatase structure as substitutional defects on the Ti position and act as photo-electron traps, playing an important role in the separation of electron–hole pairs, which could increase the photon efficiency. Consequently, doping with Gd^{3+} might be favorable for the separation of photo-induced electron–hole pairs, which leads to the enhancement of the photo-catalytic activity.

In order to explore this possibility, we used photocatalytic degradation of RB dye. In Fig. 1 (b) comparison of photocatalytic activity of pure, Gd^{3+}-doped TiO_2 and photolysis of RB using Xe-lamp is presented. As shown, there are great differences between photolysis and photocatalytic degradation of RB. After one hour of irradiation, 50% of RB is degraded using TiO_2 doped with 2.5 at.% of Gd^{3+} ions, while photolysis yield almost no degradation and pure TiO_2 degraded ~ 20 % of RB in applied experimental conditions. With longer irradiation times, differences between doped samples decrease, but they are all more active than pure TiO_2 obtained using the same synthetic procedure. So, as already stated the presence of Gd^{3+} ions is beneficial for photocatalytic activity because of separation of photoexcited charges and extended absorption threshold into visible spectral range. Furthermore, subsituting Ti^{4+} by Gd^{3+} creates a charge imbalance, which must be satiated [4]. Therefore more hydroxide ions would be adsorbed on the catalyst surface. The hydroxide ions act as hole traps that also inhibit electron/hole recombination and promotes degradation reactions.

Conclusions

Gd^{3+}-doped anatase nanoparticles were synthesized using room-temperature sol-gel process from organic precursors. Obtained powders had absorption thresholds moved to visible spectral range compared to pure TiO_2. Optical properties were correlated with photocatalytic activity of obtained powders. The best photocatalytic activity regarding degradation of Rhodamine B showed doped TiO_2 nanopowder with 2.5 at% nominal concentration of Gd^{3+} ions. It is shown that doping of TiO_2 with Gd^{3+} is beneficial for improvement of its photocatalytic activity regarding degradation of RB.

Acknowledgment

Financial support for this study was granted by Ministry of Education and Science of the Republic of Serbia, project 172056.

References

[1] A. Fujishima, T. N. Rao, D. A. Tryk, J. Photochem. Photobiol. C, 2000, 1, 1–21.
[2] X. Chen, S. S. Mao, Chem. Rev., 2007, 107, 2891-2959.
[3] D. V. Šojić, V.N. Despotović, N.D. Abazović, M.I. Čomor, B.F. Abramović, J. Hazard. Mater., 2010, 179, 49-56.
[4] J. Xu, Y. Ao, D. Fu, C. Yuan, Colloids and Surfaces A: Physicochem. Eng. Aspects 2009, 34, 107–111.

H-09-P

GREEN SYNTHESIS OF SILVER NANOPARTICLES USING *BACILLUS LICHENIFORMIS* STRAIN

D. Jakovljević[1] , J. Stefanović[1], D. Ilić[2], G. Gojgić-Cvijović[1], M. Vrvić[1,2]

[1]IChTM - Department of Chemistry, University of Belgrade, Njegoševa 12, P.O. Box 473, 11000 Belgrade, Serbia (djakovlj@chem.bg.ac.rs)
[2]Faculty of Chemistry, University of Belgrade, Studentski trg 12-16, P.O. Box 51, 11158 Belgrade, Serbia

Abstract

The development of eco-friendly technologies in different areas, as well as in nanotechnology, is of great importance to the expansion of the many biological applications of microrganisms. In this work, the synthesis of silver nanoparticles by the reduction of aqueous Ag^+ ions using the non-pathogenic bacterial strain *B. licheniformis*, under mild conditions, was investigated. The synthesized nanoparticles were characterized by UV–Vis spectroscopy, scanning electron microscopy (SEM), and electron diffraction spectroscopy (EDX).

Introduction

Nanoparticles usually can be synthesized by physical, chemical and biological methods. Nowadays, important segment of nanotechnology is the synthesis of nanoparticles with well-defined chemical composition, size, shape and polydispersity by different microorganisms [1]. In this way the process of obtaining the metal nanoparticles is usually a part of the defense mechanism of microorganisms from highly reactive metal ions. The synthesized nanoparticles are used in many areas, such as catalysis, biosensors or drug delivery systems. Silver nanoparticles have important applications as an antibacterial agent, and also show excellent biocompatibility which makes them suitable for use in nanoimmunology and nanomedicine [1].

The aim of the presented work was the synthesis of silver nanoparticles through a eco-friendly process, by the non-pathogenic *B. licheniformis* strain isolated from petroleum sludge sample taken from Oil Refinery Novi Sad [2].

Experimental

B. licheniformis strain was grown on nutrient broth by incubation at 200 rpm for 24 h at 28 ^oC. After 24 h, the culture was centrifuged at 15,000 rpm for 15 min. Wet biomass (2 g) was washed with phosphate buffer (pH 7.0), mixed with 1 mM $AgNO_3$ (3 ml) and incubated for 24 h at 200 rpm followed by sonication (5min, 40 KHz, 20 ^oC) and centrifugation (10,000 rpm; 30 min) [3]. The culture supernatant was used for the characterization of silver nanoparticles. UV-VIS spectra were obtained using spectrophotometer GBC Cintra 40. Further characterization of particles was performed through analysis of dried sample (obtained by evaporation

of water at 50 °C) by using scanning electron microscope (SEM), Model JEOL JSM-6610LV, that equiped with energy dispersive X-ray spectrometry (EDX).

Results and Discussion

The aqueous silver ions were reduced to metallic silver on exposure to the bacterial biomass. The UV-VIS spectrum of culture supernatant showed a strong, broad absorption maximum at 430 nm (Fig. 1.) characteristic of silver nanoparticles due to its surface plasmon resonance [4].

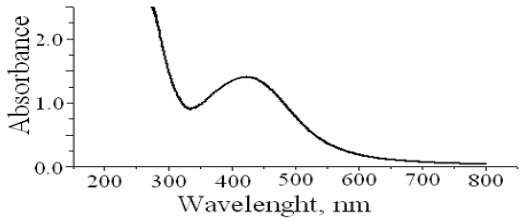

Figure1. UV-VIS spectrum of silver nanoparticles synthesized by *B. licheniformis* strain.

Their formation was confirmed visually too, by solution color change from colorless to brown. The nano particles formed were polydisperse and some of them were self-assembled into larger aggregates (Fig 2.a).

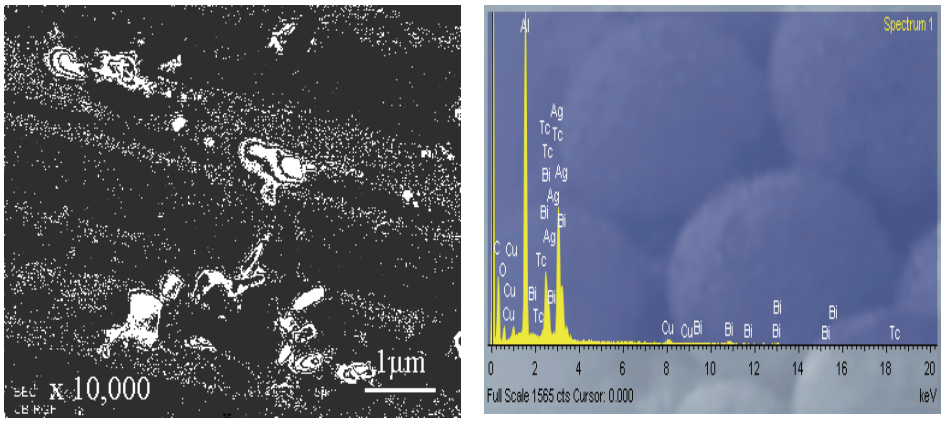

(a) (b)

Figure 2. SEM micrograph (a) and EDX spectrum (b) of the dried sample nanoparticles produced by *B. licheniformis* cells with the treatment of 1×10^{-3} M silver nitrate.

The enzyme involved in this synthesis is likely the nitrate reductase, present in *B. licheniformis*. This nitrate inducible enzyme reduces Ag^{+} ions to metallic silver [5].

Presence of silver was confirmed by EDX spectrum (Fig. 2b). Sharp signal in the silver region confirmed the formation of silver nanoparticles (Fig 2). Metallic silver nanocrystals generally show typical absorption peak approximately at 3 keV due to surface plasmon resonance.

Conclusion

The results present in this work showed a route for the production of silver nanoparticles from aqueous solution of $AgNO_3$ by *B. licheniformis* strain. The synthesis of these particles was confirmed by UV-VIS, SEM and EDX data. The production of nanoparticles by microrganisms is considered to be clean, nontoxic, and environmentally acceptable "green chemistry" procedures.

Acknowledgement

This work was supported by the Ministry of Education and Science of the Republic of Serbia, through Project III 43004.

References

[1] V. Deepak, K. *Kalishwarlal*, S. R. K. Pandian, S. Gurunathan, in M. Rai, N. *Duran* (Eds), *Metal Nanoparticles in Microbiology,* 2011, 17-37.
[2] G. D. Gojgic-Cvijovic, J. S. Milic, T. M. Solevic, V. P. Beskoski, M. V. Ilic, L. S. Djokic, T. M. Narancic, M. M. Vrvic, Biodegradation, 2012, 23, 1-14.
[3] K. Kalimuthu, R.S. Babu, D. Venkataraman, M. Bilal, S. Gurunathan, *Colloids Surf. B: Biointerface*, 2008, *65*, *150*-153.
[4] M. Sastry, K.S. Mayya, K. Bandyopadhyay, Colloids Surf. A, 1997, 127, 221-228.
[5] M. Sastry, V. Patil, S.R. Sainkar, J. Phys. Chem. B, 1998, 102, 404-1410.

H-10-P

EFFECTS OF AMBIENT AND ELEVATED DRYING TEMPERATURE ON MORPHOLOGICAL CHARACTERISTICS OF POLY(ε-CAPROLACTONE) OBTAINED WITHOUT AND WITH DIFFERENT STABILIZERS

[*]N. Filipović, [*]M. Stevanović, [*]D. Uskoković

**Institute of Technical Sciences of the Serbian Academy of Sciences and Arts, Knez Mihailova 35/IV, Belgrade 11000, Serbia*

Abstract

Biomaterials have drawn a lot of attention in recent years. In this everyday growing field the key is in synthesis procedure. Thus understanding of the effects of different processing parameters allows us to obtain the desired structure and provides insight into the directions of their further development. In this study it has been examined the influence of different drying temperature on morphology of the poly(ε-caprolactone) particles prepared without and with addition of two stabilizers. Samples were dried on ambient and elevated temperature and characterized by Fourier transform infrared spectroscopy (FTIR) and scanning electron microscopy (SEM). For some samples the results showed a big difference between obtained structures.

Introduction

Biodegradable polymers represent a class of extremely useful biomaterials that have found a wide range of application in biomedicine and pharmacology [1]. Its expansion and popularity owes mostly to synthetic polymers used for drug delivery and tissue engineering. Among them a special place belongs to the poly(ε-caprolactone) (PCL). This aliphatic polyester have been extensively investigated and considered of high interest due to its biocompatibility, non-toxicity, high permeability to many drugs, exceptional ability to form blends with other polymers, very low degradation rate and ability to avoid acidic conditions during degradation (compared to other well-known drug carriers, such as poly(d,l-lactide-*co*-glycolide)) [2,3].

Experimental

The method we used to obtain PCL micro/nanopaticles was physicochemical method with solvent/non-solvent systems. It consists of dissolving commercial polymer granules in organic solvent (chloroform) followed by abrupt addition of non-solvent (ethanol). Instantaneous formation of a white suspension-precipitation is due to the polymer deposition on the interface between the solvent and non

solvent medium. The obtained suspension was homogenized on magnetic stirrer at 500 rpm, and after that poured into a Petri dish. Three sets of probes were prepared (i) without addition of any stabilizer, (ii) with dropwise addition of polyvinylpyrrolidone **(**PVP) and (iii) dropwise addition of poly(α, γ, L-glutamic acid) (PGA). Concentration of PVP and PGA in water was 0.05%. All samples were dried at room and elevated temperature (40 °C) during the next 72 h. The morphology of obtained nano/microparticles and porous samples was evaluated by scanning electron microscope (SEM) (JEOL JSM-639OLV).

Results and discussion

The quality analysis of the samples was performed with FTIR spectroscopy. The three characteristic bands are noticeable for all samples. Those are: carbonyl (C=O) stretching band at 1720cm^{-1}, aliphatic carboxyl-hydro band at 2930 cm^{-1}, and C-O stretching band at 1190 cm^{-1}. Comparing all three spectra there has been no change in appearance or significant shifting of the bands, which was expected bearing in mind that small amounts of stabilizers were used. Only visible changes were observable for the sample prepared with addition of PGA. Bands intensity was significantly increased (probably as the result of overlapping bands from PGA adsorbed on same function groups) and a new band was noted at 1300 cm^{-1}, which could be assigned to N-H band from PGA [4]. These results led us to conclusion that PGA managed to adsorb on the surfaces of PCL particles.

For the PCL sample prepared without stabilizer irregularly shaped and strongly agglomerated particles were obtained (Fig. 1.A). When drying was performed at an elevated temperature the resulting morphology was quite different (Fig. 1.B). There were no small, individual units, but one compact structure. Reduce of the coalescence and agglomerations were achieved by the addition of stabilizers. When PVP was used as stabilizer, particles were still agglomerated and irregular in shape, but particles with spherical shape were observed (Fig. 1.C). The same sample only dried at elevated temp. showed slight changes in morphology (Fig. 1.D). Particles were bigger and more agglomerated. It is evident that PVP did not allow the coalescence of the particles and formation of structure similar to the previous sample. Fig. 1.E revealed that spherical particles with a smooth surface and size below one micron were obtained when PGA was used. This can be explained by the formation of thin protective layer of PGA around the suspended PCL particles. In contrast to room temperature condition instead of spherical particles, porous structure was obtained (Fig. 1.F). It is our opinion that increasing of drying temperature has changed the interaction between particles towards increasing tendency for agglomeration. This way the repulsion of stabilized particles was overwhelmed by its coalescence on a surface contact, leaving the pores of different sizes in all directions.

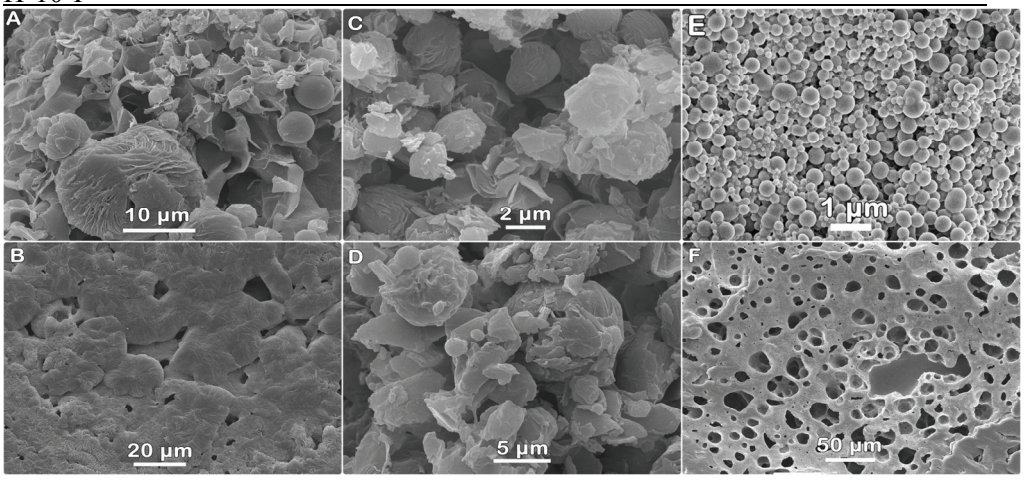

Figure 1. Representative SEM images of different PCL samples. Left column: samples prepared without addition of stabilizer, dried on room (A) and elevated temp. (B); Middle column: samples prepared with PVP, dried on room (C) and elevated temp. (D); Right column samples prepared with addition of PGA, dried on room (E) and elevated temp. (F).

Conclusion

The present study has shown that varying of drying temperature can significantly effect the morphology of obtained particles as well as that this effect is related to the composition of the system. Thus, the changes in morphology was different for all samples after drying at 40 °C: (i) when no stabilizer was used particles were completely coalesced, (ii) for the sample prepared with PVP particles were slightly more agglomerated and bigger, (iii) when PGA was used as stabilizer completely new porous structure was obtained. This highly porous structure could be further investigated as a potential scaffold material.

Acknowledgements

This study was supported by the Ministry of Education and Science of the Republic of Serbia, under Grant No. III45004. Authors would like to thank to Vladimir Pavlović for his help in SEM analysis and Aleksandra Radulović for FTIR measurements.

References

[1] O. Coulembier et al. Progr. Polym. Sci., 2006, 31, 723–747.
[2] J. L. Arias, et al. Colloids Surf. B, 2010, 75, 204-208.
[3] T.K. Dash, and V.B. Konkimalla, J. Control. Release, 2011, 158, 15-33.
[4] M. Stevanović, et al. Int. J. Nanomedicine, 2011, 6, 2837-2847.

H-11-P

THE INFLUENCE OF CALCINATION TIME ON THE ELECTROCHEMICAL BEHAVIOUR OF $Li_4Ti_5O_{12}$

M. Vujković[1], I. Stojković[1], N. Cvjetićanin[1] and S. Mentus[1,*]

[1]*University of Belgrade, Faculty of Physical Chemistry, Studentski trg 12-16, P.O. Box 137, Belgrade, Serbia, e-mail: milicavuj5@yahoo.com*

[*] *The Serbian Academy of Sciences and Arts, Knez Mihajlova 35, 11158 Belgrade, Serbia*

Abstract

Nanostructured $Li_4Ti_5O_{12}$ sample was prepared in two steps: hydrothermal reaction at 130°C and post-calcination at 400°C for either 0.5h or 6h. Even half an hour calcination was sufficient to obtain pure spinel $Li_4Ti_5O_{12}$ phase. Its fine crystallite grains enabled favorable electrochemical properties, manifesting themselves by a sharp cyclic voltammograms (CVs) and high charge/discharge capacity. Prolonged calcination made crystallites coarser what corrupted the electrochemical behavior.

Introduction

The safe, cost effective and environmentally acceptable nanostructured electrode materials attract considerable attention in the development of the next generation of Li-ion batteries for automobile industry. Regarding this, $Li_4Ti_5O_{12}$ is one of the most promising candidates. By varying the synthesis condition such as calcination time, Liu et al showed [1] that $Li_4Ti_5O_{12}$ obtained by ball milling method exhibited the best electrochemical performance when calcined for a very long time of 24h. Typical calcination time reported thus far for hydrothermally synthesized $Li_4Ti_5O_{12}$ was 2h [2] and 6h [3]. This study unveiled that much shorter time of annealing suffices for $Li_4Ti_5O_{12}$ to keep favorable electrochemical performance.

Experimental

$Li_4Ti_5O_{12}$ powder was prepared hydrothermally using as starting reactants tetra-n-butyl orthotitanate, LiOH and 30% hydrogen peroxide. After stirred for 1h, the suspension was transferred into a 32 ml Teflon-lined stainless steel autoclave and heated at 130°C for 12 h at the self-established pressure. The solid product was separated by centrifugation, washed with deionized water and dried at 80°C for 4 h. Finally, hydrothermally prepared powder was calcined at 400°C for 0.5h and 6h, in an inert argon atmosphere. For electrochemical investigations, the working electrode was made from the synthesized material (85%), carbon black (10%) and poly(vinylidenefluoride) (PVDF) binder (5%) homogeneously mixed in N-methyl 2-pyrrolidone. The slurry was treated for about 40 min in an ultrasonic bath, homogeneously deposited on a platinum foil (~ 2 cm^2), and dried under vacuum at 120-140°C for at least 4h.

The electrolyte was 1M $LiClO_4$ (Lithium Corporation of America) dissolved in PC (Fluka).

Cyclic voltammetry was performed in a three-electrode electrochemical cell, with the lithium foils as both counter and reference electrodes, using Gamry PCI4/300 Potenstiotat/ Galvanostat. The potential was cycled within the limits 2.5 and 1V.

Galvanostatic charging/discharging experiments were performed in a two-electrode arrangement, by means of the software-controlled battery testing device Arbin BT 2042.

Results and discussion

X-ray diffraction (XRD) confirmed that the powders obtained upon annealing of hydrothermally prepared powder precursor for either 0.5h or 6h are pure $Li_4Ti_5O_{12}$ spinel. The morphology of these $Li_4Ti_5O_{12}$ crystalline phases observed by SEM (Fig.1) shows two types of agglomerated spherical particles. The first type of particles, submicron in size, is flower-like spheres composed of numerous homogeneous petals, Fig1 (left). The second type of particles were larger, micron sized particles with a rough surface composed of densely packed rectangular plates, Fig1 (right). With the increase in calcination time, both type of particles became more agglomerated, while the thickness of the plates increased from about 40-60 nm (0.5h annealing) to about 50-80 nm (6h annealing). Thinner and less agglomerated $Li_4Ti_5O_{12}$ nanoparticles obtained at shorter time of annealing are expected to enable shorter diffusion distances of lithium through the solid phase.

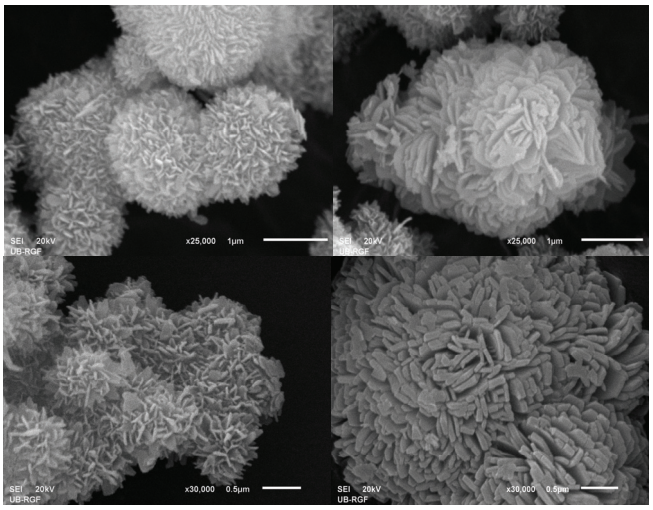

Figure 1. Nanopetals and nanoplates of $Li_4Ti_5O_{12}$ calcined at 400^{o}C for 30min (above) and for 6h (down).

The cyclic voltammograms (CVs) recorded at a common scan rate of 1 mV/s, in 1M$LiClO_4$/PC electrolyte of $Li_4Ti_5O_{12}$ samples obtained upon different annealing time intervals, are presented in Fig2a. The cathodic and anodic peaks

indicate intercalation/deintercalaton of Li ion in/from the spinel lattice, respectively. The shorter peak potential separation and higher peak current distance, which is characteristic for faster processes, is observed for the sample treated only half an hour. This may be attributed to the shorter diffusion path for Li ions thanks to the reduced particle size. The initial galvanostatic discharge curves (Fig.2b) displays also higher coulombic capacity utilization for this sample.

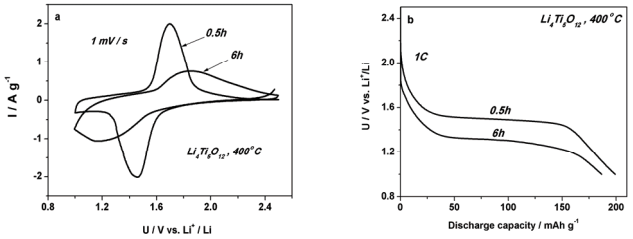

Figure 2. The electrochemical behavior of $Li_4Ti_5O_{12}$ calcined at 400°C for 0.5h and 6h a) CVs, b) Initial discharge curves at a rate of 1C.

Conclusion

The nanostructured $Li_4Ti_5O_{12}$ was successfully synthesized by hydrothermal synthesis at 130 °C followed by calcination at 400°C during two time intervals, 0.5 and 6h. Much better electrochemical behavior with respect to lithium intercalation/deintercalation was observed for the sample treated shorter time. Such improvement is attributed to the reduced particle size of this sample. This may help to save time and energy in the process of gross production of $Li_4Ti_5O_{12}$ for Li-ion batteries.

Acknowledgement: The present investigations were supported by the Ministry of Sciences and Environmental Protection of Serbia, Project No III45014.

References:

1. G. Q. Liu, L. Wen, G. Y. Liu, Q. Y. Wu, H. Z. Luo, B. Y. Ma, W. W. Tian, J. Alloys Compd, 2011, 509, 6427-6423.
2. Y. Tang, L. Yang, S. Fang, Z. Qiu, Electrochim. Acta, 2009, 54, 6244-6249.
3. J. Chen, L. Yang, S. Fang, Y. Tang, Electrochim. Acta, 2010, 50, 6596-6600.

H-12-P

ATR-FTIR MICROSPECTROSCOPIC CHARACTERIZATION OF NANOMATERIAL CALCIUM PHOSPHATE/POLY-DL-LACTIDE-*co*-GLYCOLIDE IN SIMULATED BODY FLUID

Ž. Mitić[1], M. Vukelić[1], N. Ignjatović[2], D. Uskoković[2], P. Vasiljević[3], S. Najman[1], M. Trajanović[4]

[1]*Faculty of Medicine, University of Niš, RS-18000 Niš, Serbia*
e-mail: zak_chem2001@yahoo.com
[2]*Institute of Technical Sciences of the Serbian Academy of Sciences and Arts,RS-11000 Belgrade, Serbia*
[3]*Faculty of Sciences and Mathematics, University of Niš, RS-18000 Niš, Serbia*
[4]*Faculty of Mechanical Engineering, University of Niš, RS-18000 Niš, Serbia*

Abstract
The interaction between nanomaterial containing calcium phosphate/poly-DL-lactide-*co*-glycolide (N-CP/PLGA) and simulated body fluid (SBF) was investigated by Attenuated total reflectance-Fourier transform infrared (ATR-FTIR) microspectroscopy. FTIR results indicate that the basis of morphological changes seen in the material N-CP/PLGA are dissolution of its polymer component and precipitation of the material similar to hydroxyapatite (HA) on its surface. The results obtained in this work indicate that N-CP/PLGA may be a good candidate for application in bone regeneration.

Introduction

Calcium phosphate (CP) crystals, typically a few nanometers in width, incorporated into the polymer matrix are the key components of human bone tissue [1]. Good osteoconductive characteristics of CP, as well as possibility of deriving it from synthetic or natural resources [2], have enabled the development of a wide range of CP based composite biomaterials [3], like hydroxyapatite/bioresorbable polymer composite biomaterials which can be used for the bone tissue reconstruction [4].

Many different types of polymers were used for tissue engineering. Some of the most common polymers include polylactic acid (PLA), polyglycolic acid (PGA), copolymers of PLA and PGA (PLGA), polyanhydrides, polyorthoesters, polycarbonates, etc. [5,6]. Bioresorptive polylactides (PLA) and their copolymers belong to group of nontoxic polymers, because the final products of their degradation (CO_2 and H_2O) enter without difficulty three-carboxylic acid cycle, not disturbing the metabolism of the surrounding tissue. These polymers have been known for their biocompatibility and can be easily seeded with cells and implanted into the recipient [7]. Polymer based nanocomposites will also be briefly introduced as an interesting strategy to improve the biological and mechanical performances of polymer scaffolds, especially for bone tissue engineering [8]. In this paper we compare the interaction between nanomaterial containing calcium

phosphate/poly-DL-lactide-*co*-glycolide (N-CP/PLGA) and SBF by ATR-FTIR microspectroscopy, in order to investigate whether and to what extent ionic composition of human plasma leads to the changes in N-CP/PLGA nanomaterial.

Experimental

The optimization and the entire process of the nanomaterial N-CP/PLGA synthesis, as well as the reaction mechanism of N-CP/PLGA interaction with SBF have been described in detail by Vukelić et al. [9].

FTIR microspectroscopic system, ATR-FTIR spectrometer Bruker Hyperion Tensor-27 in conjunction with a FTIR Bruker Hyperion-1000/2000 microscopy attachment equipped with a 15× objective and a 250-μm liquid nitrogen cooled a narrow-band mercury-cadmium-telluride (MCT) detector (ATR objective GMBH, Germany) with the range of the IR spectrum from 4000 to 400 cm^{-1}, was used in this work. The spectra were measured with 4 cm^{-1} resolution and 320 scans co-addition.

Results and discussion

The IR spectra of the nanomaterial before and after incubation contain following characteristic bands (Table 1).

Table 1.

$\bar{\nu}$ (cm^{-1})	Band assignation	Comment
3570 – 3440	ν(O–H)	OH
295 – 3000	ν(C–H)	CH
~1760	ν(C=O)	carbonyl
1450	δ_{as}(C–H)	CH
1380	δ_{sy}(C–H)	CH
~1420	δ(O–H)	OH
1200 – 1100	ν(P=O)	complex band
1100 – 1000	ν(P–O)	complex band
950–600	γ(C–H) and γ(O–H)	complex band

The IR spectrum shown in Fig. 1 corresponds to nanomaterial containing calcium phosphate/poly-DL-lactide-*co*-glycolide since it contains groups characteristic of N-CP/PLGA. N-CP is identified within the spectrum by a doublet with maxima at 1050 and 1087 cm^{-1}, which are the most intense and originate from phosphate groups, and by a triplet with maxima at somewhat lower frequencies of 571 and 602 cm^{-1}, arising from the PO_4^{3-} group vibrations, and at 629 cm^{-1}, assigned to OH group vibrations appearing also at 3574 cm^{-1}. PLGA is characterized by an absorption band at 1757 cm^{-1} corresponding to C=O group vibrations and a lower band at 2940 cm^{-1} ascribed to C–H group vibrations. Absorption bands at 1454 cm^{-1} and 1379 cm^{-1} originates from the CH_3 group bending vibrations. The IR bands changes in the region of OH^- and PO_4^{3-} group vibrations, were registered on the nanomaterial after incubation in SBF, correspond to hydroxyapatite similar nanomaterial. The formation of apatite on the surface of

the nanomaterial after immersion in SBF was attributed to the ionic exchange between N-CP/PLGA particles and the SBF solution.

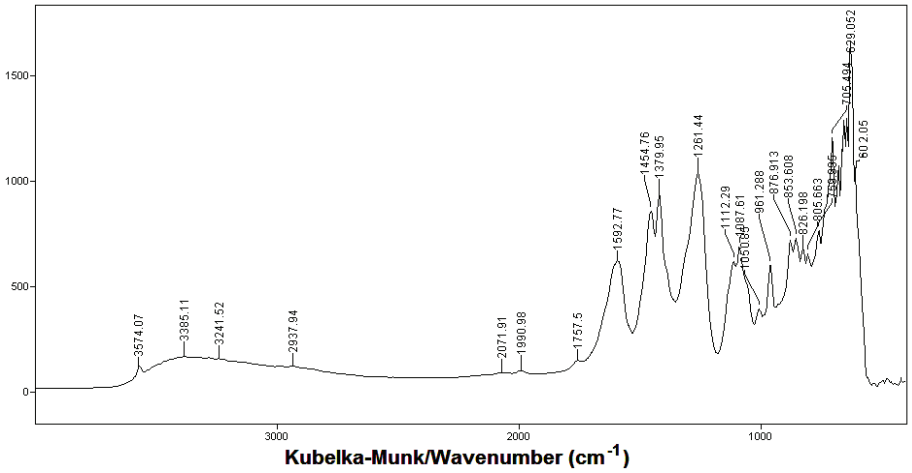

Figure 1. ATR-FTIR spectrum of nanomaterial containing N-CP/PLGA in SBF

Conclusion

The interaction between nanomaterial containing calcium phosphate/poly-DL-lactide-*co*-glycolide (N-CP/PLGA) and simulated body fluid (SBF) was studied by ATR-FTIR microspectroscopy in order to investigate whether and to what extent ionic composition of human blood plasma leads to the changes in the nanomaterial N-CP/PLGA. FTIR results indicate that in SBF nanomaterial N-CP/PLGA undergo precipitation process of the material similar to hydroxyapatite on its surface.

Acknowledgment

This work was realized within **III 41017** project, funded by the Ministry of Education and Science of the Republic of Serbia.

References

[1] M. Vallet-Regi, J. Gonzales-Calbet, Prog. Solid State Ch., 2004, 32, 1.
[2] G. Gergely, F. Wéber, I. Lukács, L. Illés, A.L. Tóth, Z.E. Horváth, J. Mihály, C. Balázsi, Cent. Eur. J. Chem., 2010, 8, 375.
[3] R. LeGeros, Clin. Orthop. Relat. Res., 2002, 395, 81.
[4] N. Ignjatović, V. Savić, S. Najman, M. Plavšić, D. Uskoković, Biomaterials, 2001, 22, 571.
[5] N. Ignjatović, E. Suljovrujić, J. Budinski-Simendić, I. Krakovsky, D. Uskoković, J. Biomed. Mater. Res. B, 2004, 71, 284.
[6] C.M. Agrawal, R.B. Ray, J. Biomed. Mater. Res., 2001, 55, 141.
[7] R.K. Kulkarni, K.C. Pani, C. Neuman, F. Leonard, Arch. Surg- Chicago, 1966, 93, 839.
[8] A. Gloria, R. De Santis, L. Ambrosio, J. Appl. Biomater. Biomech., 2010, 8, 57.
[9] M.Đ. Vukelić, Ž.J. Mitić, M.S. Miljković, J.M. Živković, N.L. Ignjatović, D.P. Uskoković, J.Ž. Živanov-Čurlis, P.J. Vasiljević, S.J. Najman, J. Appl. Biomater. Biomech., DOI 10.5301/JABB.2012.9167.

H-13-P

THERMAL PROPERTIES OF POLYCARBONATE–BASED POLYURETHANE/SILICA NANOCOMPOSITES

J. Pavličević[1], S. Petrić[2], M. Jovičić[1], O. Bera[1], R. Radičević[1], B. Pilić[1], M. Špírková[3]

[1]*University of Novi Sad, Faculty of Technology, Republic of Serbia*
[2]*Stock Company for Production of Petrochemicals, Raw Materials and Chemicals „HIP-Petrohemija" Pancevo-In Restructuring, Republic of Serbia*
[3]*Institute of Macromolecular Chemistry, Academy of Sciences of the Czech Republic, Czech Republic*

Abstract
A series of polyrethane/silica nanocomposites with different nanofiller content were prepared by one-step procedure. All starting components were aliphatic: polycarbonate diol, hexamethylene-diisocyanate (HDI) and 1,4-butanediol (BD) as chain extender. The weight fraction of silica nanoparticles of an average diameter of 150 nm was varied (1, 2, 5 and 10 wt. %). The thermal properties of elastomers were determined using differential scanning calorimetry (DSC). It was found that the melting of hard segments and recrystallization region were influenced by silica addition.

Introduction
The polycarbonate-based polyurethane elastomers are thermoplastic block copolymers consisted of hard (acting as physical crosslinks) and soft (rubbery) segments which form two phase structure on the nanometer level. The properties of polyurethane/silica nanocomposites strongly depend on the type, size and shape of filler, and also on the used preparation method [1, 2]. In our previous research, three phase transitions of polycarbonate-based polyurethanes were detected by differential scanning calorimetry [3]. It was shown that the glass transition temperature of soft segments was not significantly influenced by addition of nanoparticles. This work is aimed at the investigation of the influence of nanosilica content on the endothermic events related to the relaxation of chain segments in the diffused interface between soft and hard segment domains, and melting of hard segments. The effect of silica presence on the recrystallization region of polyurethane hybrid materials was also the subject of interest.

Experimental
The polyurethane nanocomposite films (with the constant layer thickness of 0.4 nm) were obtained by one-step technique. The isocyanate index (r = [NCO]/[OH]) was 1.05. The number of OH groups belonging to polycarbonate diol and chain extender was equal (R = [OH]diol/[OH]ext = 1). In the first step, the mixture of macrodiol and silica particles was stirred briefly for 24 h. Then, the chain extender and 20 wt. % of catalyst solution were put, and the mixture was degassed. After, as

the last component, diisocyanate was added. The mixture was stirred for 20 min and again degassed. Finally, such prepared multicomponent system was spread on polypropylene sheets using a ruler. All samples were kept in oven at 90 °C for 24 h. The unfilled polyurethane was also analyzed. The investigation of polyurethane phase transition was carried out by means of differential scanning calorimetry (Q20 TA Instruments), from 40 to 180 °C at the heating rate of 10 °C/min. The samples (masses of about 5 mg) were placed in sealed aluminum pans.

Results and Discussion

Figure 1 shows DSC curves of polyurethanes with different silica content in heating and cooling regime. The relaxation of chain segments in diffused interface between soft and hard segment is registered as endothermic event in the temperature range from 40 to 70 °C, while multiple endotherms, assigned to the melting of hard segments (the disruption of physical crosslinks), start above 100 °C (Fig. 1a). From Fig. 1b it can be seen that the recrystallization temperature decreased with the increase of silica content.

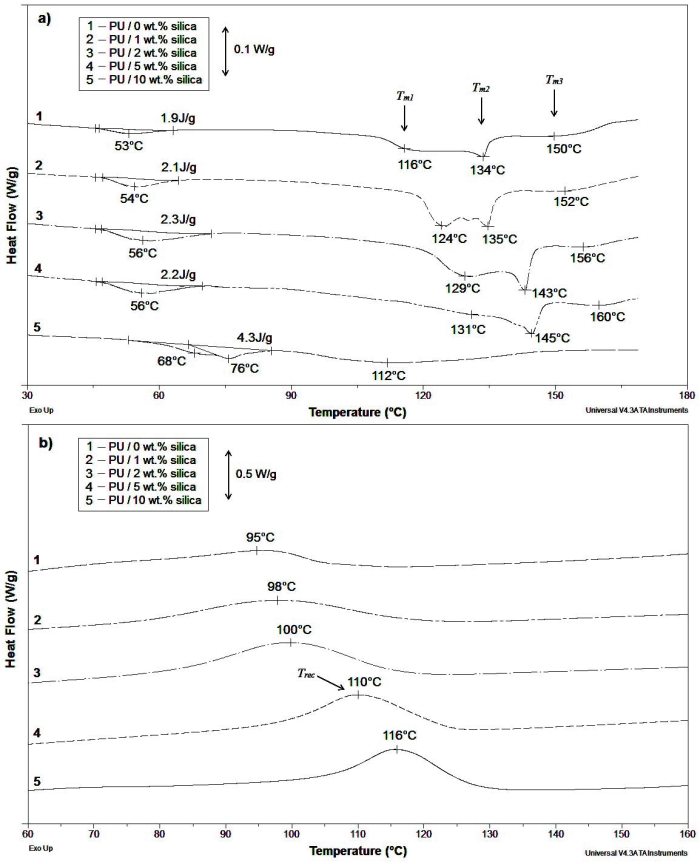

Figure 1. DSC thermograms of polycarbonate-based polyurethanes with different nanosilica content in: a) heating and b) cooling regime.

By the increase of nanofiller content, the melting temperatures (T_{m1}, T_{m2} and T_{m3},) are shifted to higher values, indicating that the silica strongly interacts with hard segments, causing the formation of hydrogen bonding and improving thermal properties of polyurethane. The addition of 1, 2 and 5 wt. % of silica did not cause the significant change of enthalpy of relaxation ΔH_{rel}, enthalpy of fusion ΔH_{fus} and recrystallization enthalpy ΔH_{rec} (Table 1), implying its very good incorporation into the PU matrix. On the other hand, the higher silica concentration (10 wt. %), caused the significant change of enthalpy values and melting mechanism of polyurethane, indicating the heterogeneous structure of obtained nanocomposite.

Table 1. Thermal properties of polycarbonate-based polyurethane with different nanosilica content (relaxation enthalpy ΔH_{rel}, fusion enthalpy ΔH_{fus} and recrystallization enthalpy ΔH_{rec}).

PU code	Silica content (% wt.)	ΔH_{rel}, J/g	ΔH_{fus}, J/g	ΔH_{rec}, J/g
PU / 0	0	1.9	18.9	8.3
PU / 1	1	2.1	18.7	8.1
PU / 2	2	2.3	18.0	7.9
PU / 5	5	2.2	12.3	6.4
PU / 10	10	4.4	11.1	6.1

Conclusions

In this work, a series of polycarbonate-based polyurethane/silica nanocomposites were successfully prepared. By increasing filler content, the melting temperatures of polyurethane nanocomposites are shifted to higher values. The addition of 1, 2 and 5 wt. % of silica negligible changed the enthalpy of relaxation (1.9-2.2 J/g) and the fusion enthalpy (18.0-18.9 J/g), indicating a good silica incorporation into the PU matrix. The higher nanofiller content (10 wt. %) caused significant decrease of ΔH_{fus}, implying the heterogeneous structure of obtained polyurethane/silica nanocomposite.

Acknowledgment

This work is financially supported by Ministry of Education and Science of the Republic of Serbia (Project No. III45022) and Grant Agency of the Czech Republic (Czech Science Foundation, project No. P108/10/0195).

References

[1] Z. S. Petrovic, I. Javni, A. Waddon, G. Banhegyi, J. App. Polym. Sci., 2000, 76, 133-151.
[2] X. Chen, L. Wu, S. Zhou, B. You, Polym. Int., 2003, 52, 993-998.
[3] M. Špírková, J. Pavličević, A. Strachota, R. Poreba, O. Bera, L. Kaprálková, J. Baldrian, M. Šlouf, N. Lazić, J. Budinski-Simendić, Eur. Polym. J., 2011, 47, 959-972.

H-14-P

TEXTURAL PROPERTIES OF MACROPOROUS ACID MODIFIED MONTMORILLONITE NANOCOMPOSITES

M. Žunić[1], Z. Vuković[1], D. Maksin[2], S. Marinović[1], A. Nastasović[3], A. Milutinović-Nikolić[1]

[1]*University of Belgrade, Institute of Chemistry, Technology and Metallurgy, Center for Catalysis and Chemical Engineering, Njegoševa 12, 11000 Belgrade, Serbia*

[2]*University of Belgrade, Vinča Institute of Nuclear Sciences, P.O. Box 522, 11001 Belgrade, Republic of Serbia*

[3]*University of Belgrade, Institute of Chemistry, Technology and Metallurgy, Center for Chemistry, Njegoševa 12, 11000 Belgrade, Serbia*

Abstract

Macroporous crosslinked copolymer, poly(glycidyl methacrylate-*co*-ethylene glycol dimethacrylate) and its nanocomposites with acid modified montmorillonite (W_A) were synthesized by radical suspension copolymerization. Nanocomposites were obtained by introducing various amounts of W_A into the reaction system. Textural properties of synthesized samples were analyzed by mercury intrusion porosimetry. The synthesized nanocomposites have significantly higher specific surface area in comparison to the copolymer. Total pore volume and the most dominant pore diameter decrease with incorporation of acid modified montmorillonite in copolymer matrix.

Introduction

The study of polymer/clay nanocomposites is currently an expanding field of research because polymer/clay nanocomposites often exhibit a wide range of improved properties over their unmodified starting polymers. The improved properties for these nanocomposites include mechanical, thermal, flammability [1], and textural properties [2,3] and are related to the dispersion and nanostructure of the layered silicate in the polymer.

To our knowledge, we were the first to report the preparation of porous polymer/clay nanocomposites of poly(GMA-*co*-EGDMA) by radical suspension copolymerization [2,3]. Porous materials have numerous applications in such areas as catalysis, chromatography and separation, where control over pore structure and pore size strongly influences the efficiency of the material [4]. Since the application of the obtained nanocomposites strongly depends on its textural properties the goal of the present work was mainly to study the effect of acid modified montmorillonite incorporation on the porous structure of poly(GMA-*co*-EGDMA) based nanocomposites.

The influence of the amount of acid modified montmorillonite introduced into the reaction mixture on the tailoring of textural properties of poly(GMA-*co*-EGDMA) based nanocomposites was investigated.

Experimental

Starting material for acid modification was Wyoming type Na-montmorillonite (Clay Minerals Society Source Clay). Acid modification was performed with 3 M HCl at 90 °C for 2 h. The liquid (acid solution)/ solid (clay) ratio was 4:1. After modification, the clay suspension was filtrated under vacuum. The filtration cake was rinsed with deionized water at 80 °C until the filtrate was Cl^- and/or Fe^{3+} free. After drying to constant mass at 110 °C acid modified clay was reground to pass through a 74 μm sieve and denoted W_A [2,3]. Macroporous crosslinked copolymer, poly(glycidyl methacrylate-*co*-ethylene glycol dimethacrylate) was synthesized by suspension copolymerization in manner that was previously reported [5] and denoted as CP. Nanocomposites were obtained in same manner as CP, only 2.5, 5, 10 mass % of acid modified montmorillonite was introduced into reaction system [2, 3]. The obtained nanocomposites in form of regular spheres (0.15 mm <d< 0.30 mm) were denoted CP-2.5W_A, CP-5W_A and CP-10W_A. The porous structure of samples was determined using Carlo Erba Porosimeter 2000 with Milestone 100 Software System. The specific surface area of samples (S_{Hg}), total pore volume (V_p) and the most dominant diameter in macroporous region (d_{max}) were determined from cumulative pore size distribution curves [6]. Pores have commonly irregular shape and the most similar geometric form is used to represent pore shape [7]. For investigated materials the cylindrical shape is assumed for calculation of textural properties [2, 5].

Results and Discussion

Results obtained by mercury intrusion porosimetry for copolymer and nanocomposites are given in Fig. 1 and Table 1.

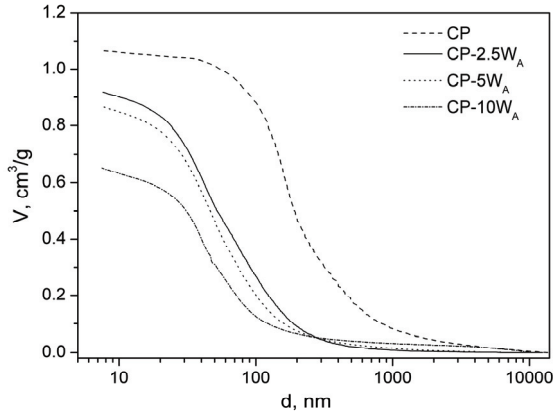

Figure 1. Cumulative pore size distribution curves of the copolymer and nanocomposites with varied amount of acid modified montmorillonite

By comparison of the results obtained for the copolymer and the nanocomposites it can be concluded that all textural properties were affected by the incorporation of the acid modified mont-morillonite. The cumulative pore size distribution curve for the copolymer has a plateau in the area of mesopores (<50 nm). On the other hand, the curves for all nanocomposites have a constant increase in the mesoporous area instead of a plateau suggesting the presence of pores <7.5 nm.

Table 1. Porosity parameters of copolymer and nanocomposites.

Sample	S_{Hg} m^2g^{-1}	V_p cm^3g^{-1}	d_{max} nm
CP	33	1.06	170
CP-2.5W_A	88	0.92	58
CP-5W_A	84	0.87	53
CP-10W_A	73	0.66	47

The pore diameter of the nanocomposites shifted toward pores with smaller pore diameters, falling entirely below 200 nm.

Also, a significant increase of specific surface area (almost three times) of the nanocomposites in comparison to the copolymer was obtained.On the other hand, difference in textural properties between nanocomposites with varied amount of incorporated acid modified montmorillonite was less expressed. The values of S_{Hg}, V_p and d_{max} of the nanocomposites slightly decreased with the increase of the amount of introduced W_A.

Conclusion

Macroporous crosslinked copolymer poly(glycidyl methacrylate-*co*-ethylene glycol dimethacrylate) and its nanocomposites with different amounts of acid modified Na-montmorillonite originated from Wyoming (W_A) were synthesized by radical suspension copolymerization. The formation of nanocomposites strongly affected all textural properties. The incorporation of clay filer into copolymer lead to materials with slightly smaller total pore volume but almost three times increased specific surface area in comparison to the copolymer. The difference in textural properties between nanocomposites with varied amount of incorporated acid modified montmorillonite was less expressed.

Acknowledgement

This work was supported by the Ministry of Education and Science of the Republic of Serbia (Projects III 45001 and III 43009).

References

[1] A. B. Morgan, J. W. Gilman, J. Appl. Polym. Sci., 2003, 87, 1329–1338.
[2] S. Marinović, Z. Vuković, A. Nastasović, A. Milutinović-Nikolić, D. Jovanović, Mater. Chem. Phys., 2011, 128, 291-297.
[3] S. Marinović, A. Milutinović-Nikolić, M. Žunić, Z. Vuković, D. Maksin, A. Nastasović, D. Jovanović, Russ. J. Phys. Chem. A, 2011, 85, 2386-2391.
[4] J. Normatov, M.S. Silverstein, Macromolecules, 2007, 40, 8329-8335.
[5] S. M. Jovanović, A. Nastasović, N. N. Jovanović, K. Jeremić, Z. Savić, Angew. Makromol. Chem., 1994, 219, 161-168.
[6] P. A. Webb, C. Orr, Analytical Methods in Fine Particle Technology, Micromeritics Instrument Corporation, Norcross, 1997.
[7] G. Leofanti, M. Padovan, G. Tozzola, B. Venturelli, Cat. Today, 1998, 41, 207-219.

H-15-P

OPTICAL PROPERTIES OF $ZnO/ZnWO_4$ COMPOSITE NANOPARTICLES

T. D. Savić, I. Lj. Validžić, M. I. Čomor
Vinča Institute of Nuclear Sciences, University of Belgrade, P.O. Box 522, 11001 Belgrade, Serbia

Abstract
$ZnO/ZnWO_4$ composite rod-like nanoparticles were synthesized by low-temperature soft solution method at 95º C with different reaction times (1-120 hours), in the presence of non-ionic copolymer surfactant Pluronic F68. Optical properties such as reflection and room temperature photoluminescence of obtained samples showed strong dependence on their crystallinity and composition.

Introduction
It is well known that ZnO shows good photocatalytic effect and high quantum activity for degradation of environmental polutants. ZnO has been characterized with its wide bandgap (3.37 eV) and relatively large exciton binding energy (60 meV) at room temperature [1]. $ZnWO_4$ has been also used for water splitting and mineralization of organic pollutants under UV irradiation [2]. Its commercial application is modest because the photocatalytic activity of $ZnWO_4$ is not high enough for the requirements of practical application. Literature data regarding band gap energy are different: ranging from 3.8 - 4.6 eV [3].

The subject of this paper is detailed correlation between structure and morphology of $ZnO/ZnWO_4$ composite nanoparticles and their optical properties. We will show that close junction between ZnO and $ZnWO_4$ and charge transfer processes define optical properties of nanocomposite

Experimental
All chemicals: Na_2WO_4 x $2H_2O$ (99% Riedel-de Haën), $ZnCl_2$ (99% Merck), non-ionic copolymer surfactant Pluronic F68 (Polyoxyethylene-polyoxypropylene block copolymer, M_n~8400 (Aldrich)), NaOH (98% Fluka) and ZnO (≥ 99% Sigma-Aldrich), were of the highest purity available and they were used without further purification. Water employed throughout the work was purified by a Milli-Q system (Millipore) and had a resistivity ≥ 18 MΩ cm^{-1}.

Synthesis of $ZnO/ZnWO_4$ nanoparticles: 0.1 M $ZnCl_2$ solution was mixed with 100 ml of copolymer solution (10 g/L). The pH of the solution was adjusted to 8 using 0.1 M NaOH. Under vigorous stirring, 0.1 M Na_2WO_4 x $2H_2O$ was added drop by drop, and the mixture was refluxed at 95 ^{0}C for 1, 5, 48 and 120 hours, assigned as samples A, B, C, D respectively. During the reflux, precipitation of ZnO and $ZnWO_4$ took place. The obtained $ZnO/ZnWO_4$ nanoparticles were separated from solvent containing copolymer immediately after synthesis by using ultra-centrifugation. Synthesized $ZnO/ZnWO_4$ nanoparticles were washed several times with ethanol and distilled water using centrifugation in every washing step

and annealed at 95 ^{0}C for 18 hours. XRD measurements of obtained powders were used for characterization: samples were mainly $ZnWO_4$ with traces of ZnO [3].

Diffuse reflectance spectra (DRS) of the ZnO/$ZnWO_4$ pellets were recorded using Perkin Elmer Lambda 9 UV-VIS-NIR Spectrophotometer. Photoluminescence (PL) spectra were obtained using Perkin Elmer LS 45 Luminescence spectrometer.

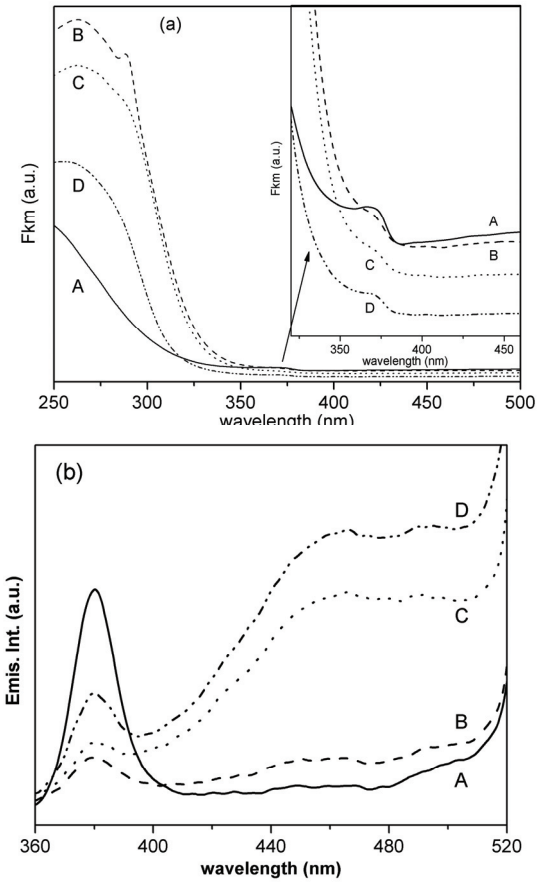

Figure 1. (a) Absorption spectra of obtained powders, calculated from DRS (Kubelka-Munk); (b) PL spectra of obtained powders, λ_{exc}= 270 nm.

Results and Discussion

Optical properties of obtained samples were investigated by diffuse reflectance spectroscopy. Obtained data were converted in absorption units (Fkm) using Kubelka-Munk equation and presented in Figure 1 (a). Two regions of the wavelengths can be observed, region which cover ZnO (~ 3.37 eV) absorption, $\lambda \geq 350$ nm, and region that corresponds to band gap of both ZnO and $ZnWO_4$ (≥ 3.8 eV), $\lambda \leq 350$ nm. The part of the spectra that corresponds to ZnO is enlarged in the inset of Figure 1 (a). As can be seen, sample A shows only one shoulder at about 370 nm, which corresponds well with band gap of ZnO. After that shoulder, absorption increases monotonically with decreasing wavelengths. Most probably in sample A $ZnWO_4$ phase was not formed yet. According to chemical reactions that lead to precipitation of ZnO/$ZnWO_4$ [3], ZnO phase is formed before $ZnWO_4$. In spectra of samples B, D and C a shoulder at the same position (Figure 1 (a), inset, ~ 370 nm) only less stressed, and broad peak at about 270 nm can be seen. This broad peak can be assigned to superposition of ZnO and $ZnWO_4$ absorptions, although its maximum corresponds well with literature data for band gap of $ZnWO_4$ (≤ 4.6 eV). Sample D showed the lowest intensity of absorption in the region of ZnO absorption, probably because ZnO phase is mostly spent on the $ZnWO_4$ synthesis. We presumed that sample A is mainly ZnO and sample D is mainly $ZnWO_4$ with traces of ZnO which can be also detected due to its PL properties.

In PL spectra of all samples, Fig. 1 (b), peak at about 380 nm can be observed with max intensity for sample A and minimum intensity for sample B. This peak can be assigned to ZnO band edge emission. Prolonging synthesis time from 5 h (B), 48 h (C) to 120 h (D) induced increase of intensity of 380 nm peak as well as green emission intensity ($\lambda \geq 400$ nm). These results indicated that prolonged reaction time gives rise to formation of near-surface oxygen vacancies in ZnO which cannot be blocked by formation of $ZnWO_4$ layer. Similar PL spectra measured Kim et al [4] when nanorod arrays of ZnO were surface covered by different oxides (TiO_2, Y_2O_3, CeO_2, and Er_2O_3). Obviously surface layer of $ZnWO_4$ favorably induced the formation of oxygen vacancies in ZnO nanoparticles responsible for green emission. Nanostructured ZnO (Fig. 1 (b) curve A) showed only band edge emission that is typical for small ZnO clusters. This effect can be explained by core/shell structure of composite nanoparticles, where ZnO is core and $ZnWO_4$ exist as a shell which partially cover the surface of ZnO. Figure 2 depicts energetic positions of the conduction and valence bands (cb, vb) of ZnO and $ZnWO_4$ [5]. So, after excitation, all photogenerated holes and electrons are transferred to ZnO part of the composite due to their band edge positions. All observed PL properties originate from ZnO part of the composite.

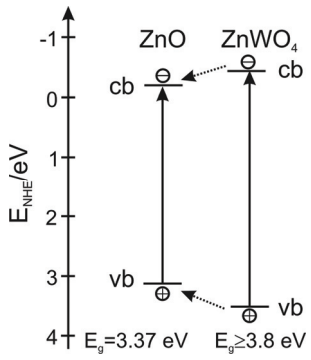

Figure 2. Electronic correlation diagram of the $ZnO/ZnWO_4$ core-shell nanoparticles.

Conclusions

A low temperature method which involves non-ionic copolymer surfactant was used for preparation of $ZnO/ZnWO_4$ composite nanoparticles. The development of ZnO and $ZnWO_4$ phases was followed by optical absorption measurements. Room-temperature PL was observed for all samples (λ_{exc}= 270nm). PL spectra were characterized by band edge emission of ZnO (380 nm) and green emission from oxygen vacancies present in ZnO. Optical properties were correlated and explained by conduction and valence band positions in our composite nanoparticles.

Acknowledgment

Financial support for this study was granted by Ministry of Education and Science of the Republic of Serbia, project 172056.

References

[1] W. I. Park, G. C. Yi, M. Kin, S. J. Pennycook, Adv. Mater. 2003, 15, 526-529.
[2] X. Zhao, Y. F. Zhu, Environ. Sci. Technol., 2006, 40, 3367-3372.
[3] I.Lj. Validžić, T. D. Savić, R. M. Krsmanović, D. J. Jovanović, M. M. Novaković, M. Č. Popović, M. I. Čomor, Mat. Sci. Eng. B, 2012, 177, 645-651.
[4] Y. Kim, Y. Kim, S. Kang, J. Phys. Chem. C, 2010, 114, 17894–17898.
[5] M. Bonnani, L. Spanhel, M. Lerch, E. Füglein, G. Müller, Chem. Mater., 1998, 10, 304-310.

H-16-P

MORPHOLOGY AND SURFACE FRACTAL DIMENSION OF TiO_2 FILMS

Lj. Rožić[1], N. Radić[1], B. Grbić[1], J. Dostanić[1], S. Petrović[1], R. Vasilić[3], S. Stojadinović[2]

[1]*University of Belgrade, IChTM-Department of Catalysis and Chemical Engineering, , Njegoševa 12, Belgrade, Republic of Serbia*

[2]*Faculty of Physics, University of Belgrade, Studentski trg 12-16, 11000 Belgrade, Serbia*

[3]*Faculty of Environmental Governance and Corporate Responsibility, Educons University, Vojvode Putnika bb, Sremska Kamenica, Serbia*

Abstract

The effect of calcinations temperature on the morphology and surface fractal dimensions of the TiO_2 films prepared via a spray pyrolysis process was investigated. The morphology and surface fractal dimensions are evaluated by image analysis methods, based on AFM (atomic force microscopy) micrographs. The results indicate that the value surface roughness of TiO_2 films increases with the increase of calcinations temperature. Also, we found that for samples calcined at temperatures in the range of 500 to 700 °C the fractal dimension is nearly constant (2.60 – 2.65). This indicates that the surfaces of TiO_2 films calcined at different temperatures are indeed irregular and may be described by fractal geometry in a certain range of length scale.

Introduction

TiO_2 is one of the most used multifunctional materials. The use of TiO_2 as photocatalyst is an important subject in a few publications [1, 2]. The versatility of preparation procedures has lead to a wide variety of structural and morphological characteristics as well as to the variety of potential applications. The morphology structure of the TiO_2 films prepared by physical methods is a crucial factor for photocatalytic processes because of its influence on heat transfer and surface reaction rate. It is know that TiO_2 films have complex surface structure. Therefore, it is hard to characterize the surface morphology objectively and factually by applying standard parameters characterizations such as specific surface area, pore size distribution and pore volume. Atomic force microscopy is considered as one of the most powerful method for surface roughness characterization, because of its accuracy, non-damage to the surface and non-vacuum condition. Fractal dimension can give some useful information about TiO_2 films physical structure [3].

In this study, the feasibility of preparing immobilized Degussa P-25 TiO_2 films on a stainless steel substrate by the spray pyrolysis technique is presented. The prepared samples were annealed at different temperatures and characterized by the AFM techniques and influence of thermal treatment on film morphology was

investigated. Surface roughness obtained by AFM analysis is correlated with surface fractal dimension in order to elucidate surface morphology.

Experimental

Material and methods

TiO_2 thin films supported on stainless steel (SS) foil have been prepared by the spray pyrolysis method. The spray pyrolysis apparatus and procedure for preparing the films immobilized on stainless steel is similar to that reported in a previously published study [4]. As prepared multilayered TiO_2 thin films were treated in a tube furnace in a range of temperature from 500 up to 700 °C. The surface morphology of the samples was investigated by atomic force microscopy (Veeco Instruments, model Dimension V). Micrographs were obtained in tapping mode under ambient conditions, using Tap300 tips (resonance frequency300 kHz, force constant 40 N/m). Roughness data were obtained using diNanoScope software (version 7.0) and reported values are calculate as mean values for a number of different samples obtained under same conditions. Fractal dimension estimation using ImageJ 1.45s Box Count Method and flooding analysis were done by FracLac 2.5 Release 1e of the images was calculating using box counting method

Results and discussion

The topographies of the TiO_2 thin films supported on stainless steel foil are first presented. Figure 1 shows the typical AFM top view surfaces and 3D images of the four samples obtained with different temperature at the same scan size.

It was found that all the TiO_2 thin films have some roughness. The both, R_a (arithmetic average of absolute value) and R_q(root mean square roughness) gradually increase with the increase of temperature (Table 1).

Table 1. Surface roughness and fractal dimension of TiO_2 thin films as prepared - 460 ^oC (a) and calcined at 500 ^oC (b), 600 ^oC (c) and 700 ^oC (d)

	Sample			
	a	*b*	*c*	*d*
Temperature (°C)	460	500	600	700
R_q (nm)	333	469	495	555
R_a (nm)	273	367	397	461
Fractal dimension	2.65	2.64	2.62	2.61

According to the fractal analysis, we found that the values of fractal dimension of thin films surface are in the range from 2.60 to 2.65, with the correlation coefficients, R^2, higher than 0.97.

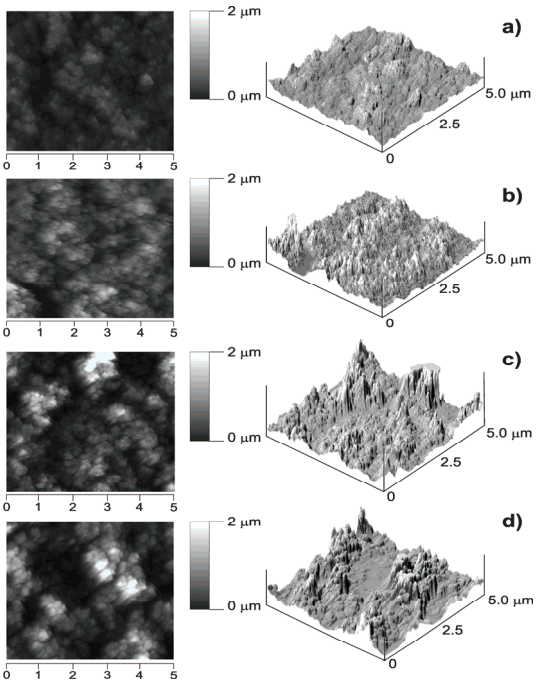

Figure 1. Two and three-dimensional AFM images of TiO_2 thin films, as prepared- 460 ^oC (a) and calcined at 500 ^oC (b), 600 ^oC (c) and 700 ^oC (d)

As can be observed, all surface exhibit a self-similar behaviour, reflecting the property that a part of the surface is similar to the whole surface. Both films, as prepared and thermally treated at 500 ^oC show almost identical morphological and structural properties, i.e. anatase phase are dominant.At higher temperatures partial phase transformation anatase to rutile was observed (XRD analysis). This changes lead to the increase of surface roughness value and slight decrease of fractal dimension. The rutile phase formed at these temperatures serves as stabilizer of structure of films.

Conclusion

Based on the obtained results, we can conclude that the Box Count Method is a reliable method for determination of the fractal dimension, and can be used for fractal analysis of AFM images of TiO_2 thin films surface. There is no one to one correspondence between the surface roughness (R_q and R_a) and fractal dimension.

Acknowledgments

This work was supported by the Ministry of Education and Science of the Republic of Serbia (Project number 172015).

References

[1]H. D. Jang, S. K. Kim, S. J. Kim, J. Nanopart. Res., 2001, 3, 141–147.
[2]J. Dostanić, B. Grbić, N. Radić, P. Stefanov, Z. Šaponjić, J. Buha, D. Mijin, Chem. Ing. J., 2012, 180, 57-65.
[3] C. Trapalis, N. Todorova, M. Anastasescu, C. Anastasescu, M. Stoica, M. Gartner, M. Zaharescu, T. Stoica, Thin Solid Films, 2009, 517, 6243 – 6247.
[4] T. Novaković, N. Radić, B. Grbić, T. Marinova, P. Stefanov, D. Stojčev, Catal. Commun., 2008, 9, 1111-1118.

H-17-P

FRACTAL APPROACH TO SURFACE ROUGHNESS OF TiO_2/WO_3 COATINGS

B. Grbić[1], R. Vasilić[3], N. Radić[1], S. Stojadinović[2], Lj. Rožić[1], S. Petrović[1]
[1]*University of Belgrade, IChTM-Department of Catalysis and Chemical Engineering, , Njegoševa 12, Belgrade, Republic of Serbia*
[2]*Faculty of Physics, University of Belgrade, Studentski trg 12-16, 11000 Belgrade, Serbia*
[3]*Faculty of Environmental Governance and Corporate Responsibility, Educons University, Vojvode Putnika bb, Sremska Kamenica, Serbia*

Abstract
The surface roughness has an effect on many physical properties so that an accurate description of the roughness parameters is of great interest. In this study, we have shown that atomic force microscopy (AFM) is powerful techniques to study the fractal parameters of TiO_2/WO_3 coatings prepared by plasma electrolytic oxidation (PEO) process. The surface roughness, described by root mean squared (R_q) and arithmetic average values (R_a), were analyzed considering the scans of an atomic force microscopy measurement. The results show that the oxide coatings exhibit lower surface roughness in initial stage of PEO process. Also, the surfaces of TiO_2/WO_3 coatings were found to be fractal during the whole process.

Introduction
Titanium dioxide coatings obtained by PEO process of titanium has been widely investigated because of its potential widespread applications, including biocompatible materials, structural ceramics, photocatalysis, sensors, optical coatings, etc. [1]. Plasma-chemical, thermal and anodic oxidation processes are induced at the discharge sites due to increased local temperature and pressure modifying the structure, composition, and morphology of such oxide coatings. Oxide coatings have controllable morphology and composition, excellent bonding strength with the metal, high micro hardness, high-quality wear and corrosion resistance.

It is well known that the optimum performance of coatings requires an exhaustive control of structural characteristics and surface morphology. Hence, the control of structure and the surface roughness are crucial aspects that largely determine the use of these materials [2]. Fractal dimension is a parameter used to quantitatively assess fractal geometry and it represents a measure of the irregularities on the surface of a solid. The value for this parameter may vary from 2 to 3, where the lowest value (2) corresponds to a perfectly smooth surface, while the upper limit (3) correspods to a totally irregular or rough surface [3]. Within this range of values, subtle variations may be considered significant.

The aim of this work is to obtain further insight into surface morphology by means of fractal geometry of the surface, as a contemporary approach to the surface analysis. Within present study the surface fractal dimension of the

TiO_2/WO_3 coatings was evaluated using high resolution AFM imaging, in order to test its sensitivity with respect to the change of surface morphology as the consequence of PEO process duration.

Experimental

Material and methods

TiO_2/WO_3 oxide coatings were formed by plasma electrolytic oxidation of titanium in 12-tungstosilicic acid ($H_4SiW_{12}O_{40}$), according to procedure, reported in a previous study [4]. Roughness of the samples was analyzed using an atomic force microscopy (Veeco Instruments, model Dimension V). Micrographs were obtained in tapping mode under ambient conditions, using Tap300 tips (resonance frequency 300 kHz, force constant 40 N/m). Roughness data were obtained using diNanoScope software (version 7.0). The box-counting method is applied and improvement is made to calculate the fractal dimensions of the morphology of coatings using ImageJ software with FracLac 2.5 plugin.

Results and Discussion

AFM images of oxidised TiO_2/WO_3 coatings recorded on (5 μm × 5μm) are shown on Figure 1. R_q and R_a values of all the AFM images were calculated and listed in Table 1. The results show that, discharge channels are well distributed and oxide coatings exhibit lower surface roughness (174 nm) in initial stage of PEO process. As the number of discharge channels decreases with time of PEO, non uniformities in the oxide coatings appear causing an increase in surface roughness (307 nm). Also, the influence of flatten order on surface roughness of TiO_2/WO_3 coatings was studied. The AFM images of oxide coatings were flattened with order 1, 2 and 3, successively, and R_q and R_a values of these samples were calculated and presented in Table 1. Obtained results shows that surface roughness decrease for all samples with increase of the flatten order.

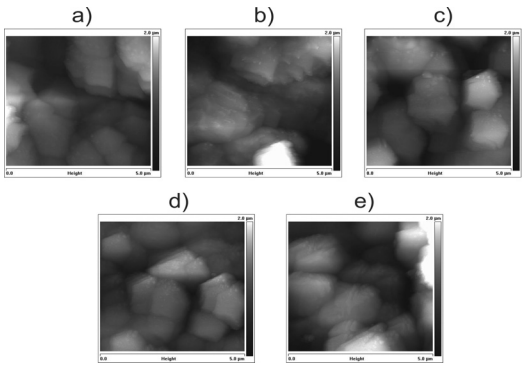

Figure 1. 2D AFM images of oxide coatings formed in various stage of PEO process: a) 30 s; (b) 60 s; (c) 90 s; (d) 180 s; (e) 300 s.

The fractal dimensions were calculated from AFM images of oxide coatings formed in various stage of process using only flattened order 2. The fractal dimension values of each samples significantly deviates from 2, consequently, surface morphology of oxide coatings possesses fractal properties. Surface fractal dimension of samples a (30 s), b (60 s) and c (90 s) increases slightly from 2.482, via 2.484, to 2.513 and then decreases to 2.504 for samples d (180 s) and to 2.492 for sample e (300 s). The fractal dimension, as a measure of surface roughness of

coatings, reflects complexity of PEO process, as well as significance of PEO process duration.

Table 1. R_q and R_a calculated from the AFM images of TiO_2/WO_3 coatings with different flatten orders expressed in nm.

Metrology	***Flatten order***	***Sample***				
		a	*b*	*c*	*d*	*e*
R_q	0	322	446	395	287	480
R_q	1	215	349	331	252	439
R_q	2	174	237	294	221	307
R_q	3	138	194	238	201	209
R_a	0	259	335	325	230	400
R_a	1	171	233	278	195	358
R_a	2	144	172	241	164	236
R_a	3	111	131	190	150	164

Conclusion

The AFM images were used to calculate fractal dimensions of TiO_2/WO_3 coatings at various stages of PEO process. Surface roughness and fractal dimension are dependent and sensitive to the time of PEO process, particularly at early stages (30, 60 and 90 s).

Acknowledgments

This work was supported by the Ministry of Education and Science of the Republic of Serbia (Project number 172015).

References

[1] P. J. Chu, S.Y. Wu, K.C. Chen, J. L. He, A. Yerokhin, A. Matthews, Thin Solid Films, 2010, 519, 1723 - 1728.
[2] J. Dostanić, B. Grbić, N. Radić, P. Stefanov, Z. Šaponjić, J. Buha, D. Mijin, Chem. Ing. J., 2012, 180, 57-65.
[3] C. Trapalis, N. Todorova, M. Anastasescu, C. Anastasescu, M. Stoica, M. Gartner, M. Zaharescu, T. Stoica, Thin Solid Films, 2009, 517, 6243 – 6247.
[4] M. Petković, S. Stojadinović, R. Vasilić, I. Belča, Z. Nedić, B. Kasalica, U.B. Mioč, Appl. Surf. Sci., 2011, 257, 9555– 9561.

H-18-P

MICROSTRUCTURE AND CRYSTAL GROWTH IN THERMALLY TREATED $Fe_{73.5}Cu_1Nb_3Si_{15.5}B_7$ ALLOY

D. M. Minić[1], S. Meseldžija[2], M. Vasić[1], V. Blagojević[1]
[1]*Faculty of Physical Chemistry, University of Belgrade, Serbia*
[2]*Institute for Nuclear Science Vinca, University of Belgrade, Belgrade, Serbia*

Abstract
Thermal treatment of $Fe_{73.5}Cu_1Nb_3Si_{15.5}B_7$ amorphous alloy induces structural changes, including crystallization of several different phases and subsequent crystal growth. X-ray diffraction combined with differential scanning calorimetry were used to investigate these, to determine kinetic parameters and mechanism of individual steps, and the dimensionality of crystal growth using Matusita-Sakka method and texture analysis. It was found that after the alloy becomes fully crystalline, crystal growth of individual phases is, in general, impeded, leading to decreased dimensionality of growth. However, this does not impact the texture, due to lack of preferred direction of crystal growth.

Introduction
Metallic glasses (amorphous metallic alloys) are materials characterized by homogenous and isotropic structure with absence of the long-range order, which possess isotropic physical and mechanical properties. Iron based amorphous alloys have attracted much attention in recent times, because of their favorable physical properties. These materials are kinetically and thermodynamically metastable, usually stable at room temperature and can be transformed to polycrystalline materials at higher temperatures. During the crystallization process, microstructure of the alloy changes from amorphous, through hybrid amorphous/crystalline, to purely crystalline structure. Since hybrid amorphous/crystalline materials often have functional properties superior to those of purely amorphous and purely crystalline materials, control of crystallization process of these materials can lead to creation of materials with targeted properties.
The goal of this work was to study influence of thermal treatment on microstructure and crystal growth in $Fe_{73.5}Cu_1Nb_3Si_{15.5}B_7$ alloy.

Results and Discussion
Amorphous alloy $Fe_{73.5}Cu_1Nb_3Si_{15.5}B_7$ was prepared in form of a ribbon by melt spinning method. The thermal stability and kinetic parameters of the alloy had been investigated in 25-800^{o}C temperature range using DSC. XRD of thermally treated alloy samples was also used, to determine phase composition and perform texture analysis. The alloy was stable up to about 500^{o}C after which two exothermic crystallization peaks are observed in DSC, at around 500^{o}C and 680^{o}C, respectively. Crystallization occurs in a multi-step process. To investigate each

individual step of these processes, complex experimental peaks were deconvoluted using Origin software package. In order to determine kinetic parameters (apparent activation energy, Ea and pre-exponential factor, A) of processes of crystallization, we used Kissinger's [1] and Ozawa's [2] methods. It was observed from Table 1 that the values for Ea and A obtained by these two methods are in good correlation.

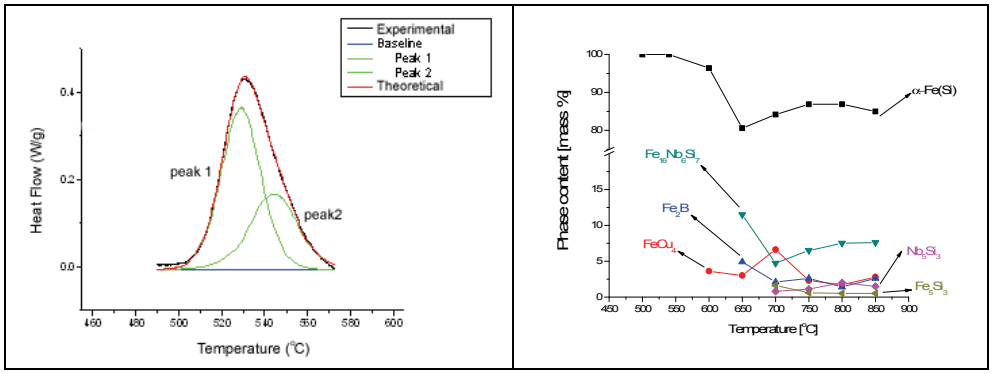

Figure 1. Deconvolution of first experimental DSC peak (left) and phase content of individual crystal phases in thermally treated alloy samples (right).

Table 1. Kinetic parameters of individual steps for the first experimental DSC peak determined by Kissinger's and Ozawa's methods.

		KISSINGER		OZAWA	
		Ea[kJ/mol]	A[min^{-1}]	Ea[kJ/mol]	A[min^{-1}]
Experimental peak 1	Peak 1	(316 ± 11)	(1.6 ± 0.1)•10^{20}	(313 ± 10)	(1.1 ± 0.1)•10^{20}
	Peak 2	(248 ± 13)	(2.5 ± 0.2)•10^{15}	(249 ± 13)	(2.8 ± 0.2)•10^{15}

Crystal growth of α-Fe(Si) phase occurs in two distinct stages: first stage includes nucleation and subsequent growth from amorphous phase, which occurs three-dimensionally (m=2.7 in Matusita-Sakka method [3]), while the second stage occurs in fully crystallized alloy, where its crystal growth is impeded by presence of other crystalline phases. This means that, in the second stage, the growth of α-Fe(Si) is prevented on interphase boundaries, which is exhibited as the value of m=1.7 in Matusita-Sakka calculation. However, since there is no preferred direction of growth, there is no significant change in texture of α-Fe(Si) phase, even though the growth is nominally not three-dimensional.

The growth of Fe_2B phase also exhibits two distinct stages, due to different sources of crystallization. Initial crystallization of Fe_2B occurs from the amorphous phase, while, later, it also crystallizes from metastable Fe_3B phase [4]. The crystal growth from amorphous phase occurs three-dimensionally, while the growth from metastable Fe_3B phase occurs two-dimensionally, as suggested by change in dimensionality of crystal growth observed using Matusita-Sakka method.

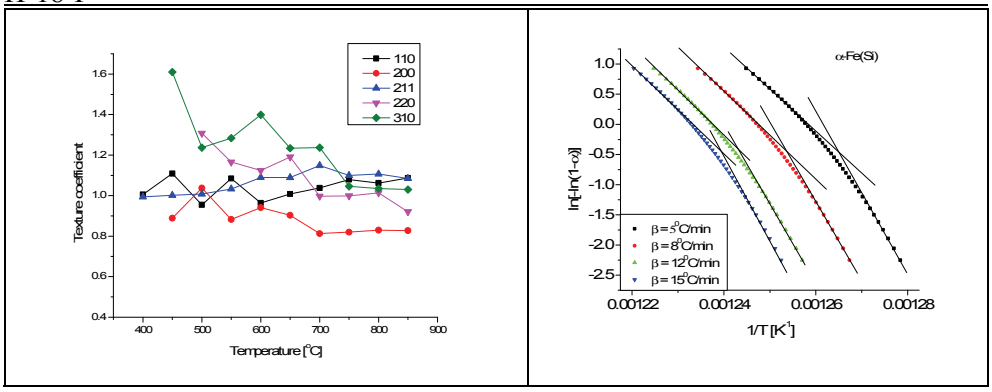

Figure 2. Texture analysis (left) and Matusita curves (right) for α-Fe(Si) phase.

Conclusion

Thermally induced crystallization and crystal growth in $Fe_{73.5}Cu_1Nb_3Si_{15.5}B_7$ amorphous alloy shows that crystallization and growth occurs in two temperature regions: around 500 and 680°C. There are multiple stable and metastable phases observed and it is shown that dimensionality of their crystal growth depends on the degree of crystallization of the alloy, with impeded growth in fully crystallized alloy.

References

[1] H. E.Kissinger, Anal. Chem., 1957, 29, 1702-1706.
[2] T. Ozawa, J. Therm. Anal., 1970, 2, 301-324
[3] K. Matusita, S. Sakka, J. Non-Cryst. Solids, 1980, 741, 38-39
[4] V. A. Blagojević, D. M. Minić, T. Žak, D. M. Minić, Intermetallics, 2011, 19, 1780-1785

CRYSTALLIZATION AND SINTERING PHENOMENA OF GLASSES IN THE SYSTEM La_2O_3-SrO-B_2O_3

S. V. Ždrale[1], S. R. Grujić [1], M. B. Tošić [2], V.D.Živanović[2], A. Z. Bjelajac[1], S. D. Matijašević[2], J. D. Nikolić [2]

[1]*Faculty of Technology and Metallurgy, University of Belgrade 4 Karnegijeva St, 11000 Belgrade, Serbia,* [2]*Institute for Technology of Nuclear and other Mineral Raw Materials, 86 Franchet d' Esperey St, 11000 Belgrade, Serbia*

Abstract

In this work crystallization and sintering phenomena of glasses in the system La_2O_3-SrO-B_2O_3 (LaSrB) were studied. Hot stage microscope (HSM) technique was used to determine characteristic temperatures for sintering processes and differential temperature analysis (DTA) to determine glass transition temperature, t_g, and onset of crystallization glass temperature, t_x. A combination of these analyses provided information about the quality of glass ceramic by determining differences in glass transition and maximum shrinkage temperatures. It has been shown that with increasing content of La_2O_3, differences of these temperatures decreased.

Introduction

In the present work sintering and crystallization processes of LaSrB system were studied. Glass ceramics showed improved properties, low thermal expansion, low dielectric constant, high abrasion resistance, chemical resistance. Sintering and crystallization behavior of this system are investigated to obtain high performance material, reduced porosity, for specific application. A combination of HSM and DTA represents a simple approach of determining the sintering and crystallization phenomena [1].

Experimental

The reagent grade mixture of H_3BO_3, $SrCO_3$, $La_2(CO_3)_3$ was used to prepare glasses by melting in electrical furnace. Mixture was placed in platinum crucible in electric furnace and melted at 1200 °C for 30 min. The melt was cast and cooled at stainless steel plate in air at room temperature. The obtained glasses were transparent, without visible bubbles in glasses. Obtained glass compositions are given in table 1.

Table 1. Compositions of studied glasses.

Glass, number	x_i (mol%)		
	La_2O_3	SrO	B_2O_3
1	5.7	22.9	71.4
2	9.5	19.1	71.4
3	14.3	14.3	71.4
4	19.1	9.5	71.4

A hot stage microscope, E. LEITZ WETZLAR, that was used, projects the image through a quartz window. The specimens of glass powders were pressed into cylinders and placed on platinum plate, then on alumina support contacted with thermocouple. The temperature was measured by (Pt/Rh/Pt) thermocouple at heating rate 10 °C min^{-1}. The obtained temperatures from photomicrographs corresponding to typical viscosity points are: first shrinkage, maximum shrinkage, deformation, sphere, half ball and flow [2-3].

The crystallization properties of the glass samples were determined by differential thermal analysis (DTA) using Netzch STA 409 EP instrument and Al_2O_3 powder as the reference material. Powder glass samples were prepared by crushing and grinding the bulk glass in agate mortar and sieving it up to grain size < 0.048 mm. Glass powder were heated at 10 °C/min rate to determine glass transition temperature, t_g, and onset of crystallization temperature, t_x.

Results and Discussion

Characteristic temperatures of the first shrinkage (t_{FS}), maximum shrinkage (t_{MS}), deformation (t_D), sphere (t_S), half ball (t_{HB}) and flow (t_F) are designated from the results obtained by HSM [3-4]. In Figure 1 are shown characteristic photomicrographs of the shape of glass 1 taken during HSM experiments [2-3].

t= 25°C t_{FS}=580°C t_{MS}=600°C t_D=680°Ct_S=700°C t_{HB}=840°C t_F=890°C

Figure 1. Photomicrographs of the shape sample during the HSM measurements.

The glass transition temperature, t_g, and onset of crystallization temperature are determined from DTA curve in figure 2. Results obtained by DTA and HSM for all samples are shown in table 2. The exothermal temperature peaks at the DTA curves correspond to the crystallization of glass.

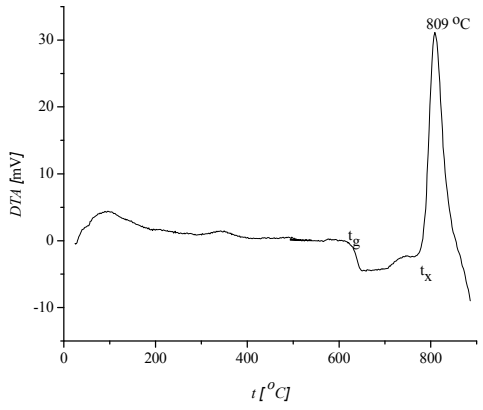

Figure 2. DTA curve obtained for glass sample 1.

It is important to determine temperature differences of onset crystallization and maximum shrinkage in attempt to predict if porous sample will be obtained [2-3]. If t_x is greater than t_{MS} glass powder samples sinter before crystallization. Glass sample number 1 with the lowest content of La_2O_3 shows the greatest difference in these temperatures. With increasing content of La_2O_3 the difference decreased because t_{MS} increased.

Table 2. Temperatures obtained by DTA and HSM.

Glass	t_g, °C	t_x, °C	t_{ms}, °C	(t_x-t_{ms}),°C
1	622	735	600	135
2	640	763	700	63
3	643	756	720	36
4	644	765	740	25

Conclusion

In this study DTA and HSM techniques provided basic information about crystallization and sintering processes in the system and showed that t_x and t_{MS} differences decreased with increasing content of La_2O_3 which is significant information to determine quality of obtained glassceramics and therefore their application.

Acknowledgment

The authors are grateful to the Ministry of Education and Science, Republic of the Serbia for financial support (Projects 172004 and 34001).

References

[1] A. R. Bocaccini, B. Hamman, J. Mater. Sci., 1999, 34, 5419–5436.
[2] C. Lara, M. J. Pascual, M. O. Pradob, A. Duran, Solid State Ionics, 2004, 170, 201- 208.
[3] M.J. Pascual, A. Duran, Phys. Chem. Glasses, 2004, 46, 512-520.

H-20-P

MESOPHASE BEHAVIOUR OF BINARY MIXTURES OF BENT-CORE AND CALAMITIC COMPOUNDS

D. Obadović[1], M. Stojanović[1], M. Cvetinov[1], A. Vajda[2], N. Eber[2], K. Fodor-Csorba[2]

[1] *Department of Physics, University of Novi Sad, Novi Sad, Serbia*

[2] *Institute for Solid State Physics and Optics, Wigner Research Centre for Physics, Hungarian Academy of Sciences, Budapest, Hungary*

Abstract

Due to their attractive properties, bent-core liquid crystalline compounds were extensively studied in the last two decades [1]. Here we present the phase diagram for binary mixtures of bent-core and calamitic liquid crystals. One mixing component is the previously prepared 4,6-dichloro-1,3-phenylene bis[4'-(10-undecen-1-yloxy)-1,1'-biphenyl-4-carboxylate] (**I**), which is a nematogenic ester-type banana-shaped compound [2]. The calamitic compound is the well known ethyl 4'-(9-decen-1-yloxy)-1,1'-biphenyl-4-carboxylate (**II**) which exhibits smectic A (SmA) phase in a wide temperature range [3]. A total number of 6 mixtures were prepared and investigated by polarising optical microscopy. Selected mixtures were studied by X-ray diffraction on non-oriented samples. General formulae of the studied compounds are:

I

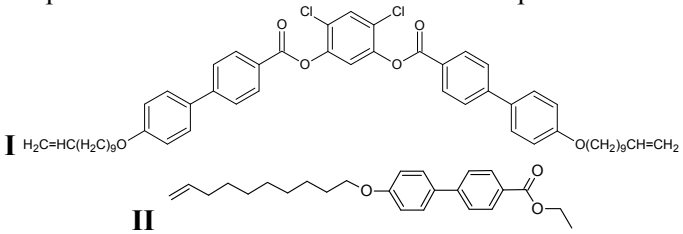

II

In the selected mixtures a nematic phase exists above the SmA phase, with the temperature range of both phases highly dependent on the concentration of the comprising compounds. Lowered melting temperatures were observed for all mixtures with respect to that of the pure compounds.

Introduction

Lowering the transition temperatures of liquid crystals and stabilizing their mesophases over wide temperature range, is always an important aim of the research. In order to respond to these demands, the required liquid crystalline properties can be rather reached by mixing compounds with different molecular structures and properties than by looking for the pure compounds with definite properties. As bent-core compounds exhibit limited miscibility even among themselves, to find mixtures especially with calamitic compounds is always a challenging problem [3].

Results and Discussion

The goal of the present study was to test the miscibility of the bent-core compound **I** with the rod-like material **II**, and to study the mesomorphic behaviour of their binary mixtures. For the detailed study, six mixtures, **Mix1** to **Mix6**, were prepared

with 18, 26, 38, 50, 63 and 80 wt% of the bent-core component **I**, respectively. The phase transition temperatures of pure compounds and their mixtures in heating were detected by polarizing optical microscopy and presented in Table 1.

Table 1. Sequence of Phases, Phase Transition Temperatures [°C]. All these Data were Obtained in Heating. (• the Phase Exists)

Code	Cr	T	Cr2	T	CrE	T	SmA	T	N	T	I
II	•	64.5	•	76.0	•	85.9	•	98.7			•
Mix1	•	53.4	•	61.0	•	79.5	•	81.7	•	99.0	•
Mix2	•	52.2	•	66.0	•	68.0	•	73.3	•	103.0	•
Mix3	•	53.5	•	65.5	•	77.0	•	86.7	•	99.7	•
Mix4	•	54.0	•	61.2	•	69.0	•	79.0	•	99.3	•
Mix5	•	62.3	•	65.9	•	77.4	•	88.0	•	100.9	•
Mix6	•	60.3	•	67.4	•	70.2	•	86.0	•	100.2	•
I	•	71.2	•	78.9					•	102.7	•

The widest temperature range for nematic (N) phase was obtained for **Mix2**. For smectic phase, the widest temperature range of 15.8°C was observed for **Mix6**. The N-I (isotropic) transition temperature reaches its minimum of 99.0°C for concentration of 18 wt% of compound **I** (**Mix1**).

X-ray diffraction studies were carried out in a transmission geometry using a conventional powder diffractometer, Seifert V-14, at CuKα radiation (λ=0.154 nm), equipped with an automatic high-temperature kit Paar HTK-10. The set-up was calibrated to the two most intense platinum lines: 2Θ = 39.76° (100%) and 2Θ = 46.23° (53%). Molecular parameters, the thickness of the smectic layers d and the average intermolecular distance D between the long axes of neighbouring molecules, could be determined from the positions of the small angle and wide-angle diffraction peaks, respectively, using Bragg's law: $n\lambda = 2d \sin\Theta$.

In Figures 1(a) and 1(b) we present typical diffraction spectra for each phase for the pure bent-core compound **I** as well as for the mixture **Mix5**. In all investigated mixtures two crystal modifications (Cr1, Cr2) and a crystalline smectic E (CrE) phase were detected. The CrE phase in **Mix5** is primarily characterized by increased scattering at large angles in proximity of 2Θ=20.5° which is due to the hexatic ordering. Yet in CrE many other peaks appear due to a long range in-plane order. In the SmA phase of **Mix5** one reflection peak appears at the small angle 2Θ=1.9°, corresponding to the thickness of the smectic layers of d=46.64Å. Starting with the minimal concentration of 18 wt% of bent-core compound **I** (**Mix1)** thickness of smectic layers increases, reaching its saturation value of 46.64Å for 50 wt% of compound **I** (**Mix4**), which might be regarded as the experimental value for the length of compound **I.**

Both the isotropic and the nematic phases are characterized by a broad diffusion peak which appears in the range of 2Θ=12–26°, whose maximum yields D values in the interval 4.22 Å < D < 4.92 Å for the isotropic phase of **Mix3** and the SmA phase of **Mix5**.

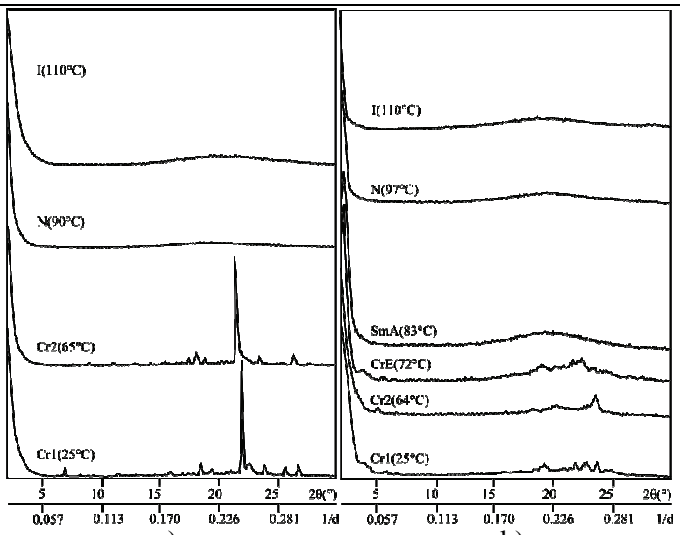

Figure 1. X ray diffractogram of compound **I** (a) and **Mix5** (b).

Conclusion

We found that the polymorphism (I–SmA–Cr phase sequence) of the pure calamitic component **II** is fully preserved in all studied mixtures with addition of nematic phase that follows SmA phase on heating. The layer spacing (d) increases when adding the bent-core compound. The monotropic smectic phase exists in the full concentration range in all studied mixtures. The nematic phase remains detectable even for the highest calamitic content **Mix1**. Therefore, mesophase behaviour existed over a broad composition range in the mixtures and could be extended close to room temperature. The results suggest that mixing conventional calamitics with bent-core mesogens with an appropriate molecular design may be a tool to tune the phase behaviour and properties of different liquid crystal mixtures.

Acknowledgments

This work was partly supported by the research Grant No. OI171015 from the Ministry of Education and Science of the Republic of Serbia, the Hungarian Research Fund OTKA K81250 and the SASA-HAS bilateral scientific exchange project #9.

References

[1] D. Ž . Obadović, A. Vajda, A Jákli, A. Menyhárd, M. Kohout, J. Svoboda, M. Stojanović, N. Eber, G. Galli and K. Fodor-Csorba, Mesophase behaviour of binary mixtures of bell-shaped and calamitic compounds, Liq. Cryst., 37, 5, 527 (2010).

[2] K. Fodor-Csorba, A. Vajda, A. Jákli, C. Slugovc, G. Trimmel, D. Demus, E. Gács-Baitz, S. Holly and G. Galli, Ester type banana-shaped liquid crystalline monomers: synthesis and physical properties, J. Mater. Chem., 14, 2499 (2004).

[3] Z.-S. Xu, R. P. Lemieux, A. Natansohn, P. Rochon and R. Shashidhar, Synthesis and characterization of novel ferroelectric liquid crystals and copolymers containing biphenyl azobenzene and /or phenyl biphenyl carboxylate mesogenic groups, Liquid Crystals, 26 (3), 351 (1999).

H-21-P

A MODEL FOR COMPUTER STUDY OF GRAIN COARSENING IN LIQUID PHASE SINTERING

Z. S. Nikolić[1], K.i Shinagawa[2]

[1]*University of Niš, Faculty of Electronic Engineering, Serbia*
[2]*Kagawa University, Faculty of Engineering, Japan*

Abstract
Computer study of grain growth by grain boundary migration based on numerical modeling of solution-precipitation during liquid phase sintering will be considered.

Introduction
Grain coarsening is a typical multibody free boundary problem in which the grains alter their morphologies in response to the diffusion field. After solution-precipitation, the grains grow in supersaturated liquid phase, and after the supersaturation becomes small, large grains start to grow at the expense of small grains. This paper describes the computer-based simulation method for simulation of a moving grain boundary on the solid/liquid interface during liquid phase sintering (LPS), where the grain boundary migration means that solid atoms that are dissolved on one side of the boundary transport across the liquid layer and deposit on the other side of the boundary.

Results and Discussion
The main characteristic of the solution-precipitation process is that the smaller solid grains dissolve at solid/liquid interface (thermodynamically unstable), diffuse through the liquid, and precipitate on the larger grains.

If a system consisting of a dispersion of spherical grains with different radii in a liquid in which the solid phase has some solubility is assumed, then the concentration of the dissolved solid, C, around a grain of radius R is given by the Gibbs-Thomson equation

$$\Delta C = C_{\mathrm{o}} \cdot \frac{2\gamma_{sl}\Omega}{kT} \cdot \frac{1}{R} \quad (\Delta C = C - C_{\mathrm{o}}), \tag{1}$$

where C_{o} is the equilibrium concentration of liquid in contact with the flat solid, γ_{sl} is the solid/liquid interfacial energy, Ω is the molecular volume of the solid, and kT has its usual meaning. It can be seen that the concentration at an interface with high curvature will be above that at an interface with low curvature, thus a higher concentration around a smaller grain gives rise to a net flux of matter from the smaller to the larger one. Mass diffusion outside the grains is assumed to be the only mass transfer process defined by the partial differential equation of the parabolic type $\partial C/\partial t = D_{\mathrm{L}}\nabla^2 C$, where D_{L} is the concentration independent

diffusivity of the solid in the liquid. The effects of the dissolution and precipitation processes can be computed by applying the flux equation $\mathbf{J} = -D_{\mathrm{L}} \nabla C$ at boundary points of solid interface.

Shinagawa *et al.* [1,2] proposed microscopic modeling for viscoplastic finite element analysis of sintering processes. Taking into account the surface tension acting on the pore surface, and assuming that the grains during sintering are viscoplastic and the flow stress is proportional to the viscosity, they calculated deformation behaviors of the grains for slightly compressible materials. This method can be also applied for definition two-dimensional finite element mesh (FEM) within (pendular) liquid bridge as a function of grain size, the contact angle, θ, the normalized liquid volume, ϕ, and the separation distance, d (Fig. 1) and applied for computer simulation of grain coarsening during LPS characterized by small amount of liquid located within liquid bridges only. To the best of our knowledge, there is no theoretical investigation of grain coarsening within liquid bridge only.

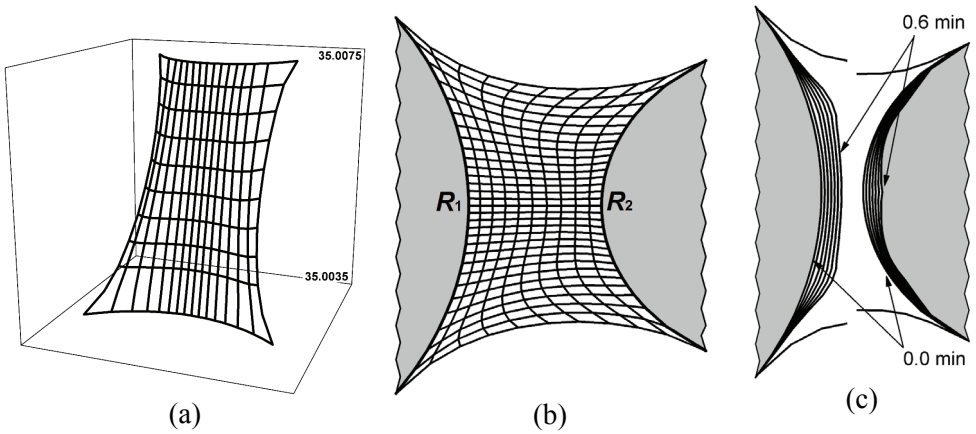

Figure 1. (a) Initial concentration profile. (b) FE mesh within liquid bridge. (c) Time dependent grain coarsening. $R_1 = 10\ \mu\mathrm{m}$, $R_2 = 5\ \mu\mathrm{m}$, $d = 3\ \mu\mathrm{m}$, $\theta = 10^\circ$, $\phi = 0.35$.

Morphological development is governed by diffusion through the liquid between grains. Assuming that solid–liquid system is held isothermally and under interfacial equilibrium condition, coarsening occurs by the exchange of solute between grains.

We will simulate grain coarsening using two unequally sized grains of tungsten connected with liquid nickel as a bridge. For the W–Ni system the next data will be used: $T = 1750\ K$, $\gamma_{sl} = 0.35\ \mathrm{J/m^2}$, $C_{\mathrm{o}} = 35\ \mathrm{at.\%W}$, $D_{\mathrm{L}} = 10^{-9}\ \mathrm{m^2/s}$, $\Omega = 9.53 \times 10^{-5}\ \mathrm{m^3/mol}$.

As was already mentioned, the concentration on solid–liquid interfaces will be computed by equation (1). The initial concentration of liquid phase within liquid bridge (Fig. 1a) and the flux of materials will be computed on changeable FE mesh

(Fig. 1b), which must be remeshed always when solid–liquid interface on larger grain reaches mesh line.

The time-dependent concentration of liquid phase in contact with the smaller grain is greater than in contact with the larger one. Therefore the smaller one dissolves in the liquid matrix and dissolved atoms flow from the matrix to the larger grain. Pure tungsten dissolved into the liquid, transports through the liquid and precipitates as W(Ni) solid solution on the larger grain (Fig. 1c). It can be seen that due to high concentration gradient in this area, dissolution and reprecipitation processes are very fast. Although the larger grain continues to grow, the separation distance remains essentially constant, but the centers of mass of both grains move to the right. It can be seen that the larger grain undergoing a larger shape distortion than the smaller one.

Conclusion

This paper outlines FE method for the simulation of coarsening of two-grain model during LPS, as a result of matter transport by diffusion from the dissolving smaller grain toward the growing larger one. The time dependent model system geometry is determined by initial topology, by size and shape of precipitates, by growth kinetics and by transport properties of a liquid phase. The numerical model consists of a few basic equations that establish concentration profiles of solid–liquid system at sintering temperature. The accuracy and efficiency of the simulation method depend only on how well the compositions of the solid phase and the diffusion coefficient in the liquid are known. The qualitative and quantitative characteristics of model system should be sound and appear to agree with the expected physical behavior of real system. Theoretical basis of this analysis is general and applicable to any binary system that satisfies three general requirements: there is a liquid phase at the sintering temperature, the solid phase is soluble in the liquid and the liquid wets the solid.

Acknowledgements

The first author was performed present study under the project (No. OI172057) supported by the Ministry of Education and Science of the Republic of Serbia. He would also like to acknowledge partial support for this study by the Japan Society for the Promotion of Science (Invitation Fellowship ID No. S-10175).

References

[1] K. Shinagawa, K. Osakada and K. Mori, Computer Aided Innovation of New Materials II, M. Doyama, J. Kihara, M. Tanaka and R. Yamamoto (Eds), 1993, 1747-1750.

[2] K. Shinagawa, JSME International Journal, Series A, 1996, 39, 565-572.

H-22-P

COMPUTER STUDY OF REARRANGEMENT DRIVEN BY CAPILLARY AND VISCOUS FORCES IN LIQUID PHASE SINTERING

Z. S. Nikolić[1], K. Shinagawa[2]

[1]*University of Niš, Faculty of Electronic Engineering, Serbia*
[2]*Kagawa University, Faculty of Engineering, Japan*

Abstract
Computer study of rearrangement driven by attractive forces (static and dynamic in nature) during liquid phase sintering will be considered.

Introduction
The rearrangement during liquid phase sintering has been generally accepted that driven by the attractive forces developed between the grains connected by the liquid bridges. Capillary forces usually dominate in cases where the liquid exists as discrete bridges, but viscous forces can become significant when the liquid viscosity is very high or at high inter-grain velocities. This paper outlines computer-based methods for simulation of time-dependent rearrangement induced by both capillary and viscous forces.

Results and Discussion
The capillary force acting normal to the solid-liquid interfaces within a liquid bridge between two grains of radius R_1 and R_2 ($R_1 \geq R_2$) is given by [1]

$$F = 2\pi\gamma x_1 \sin(\varphi_1 + \theta) + \pi\gamma x_1^2 (\frac{1}{\rho_2} - \frac{1}{\rho_1}), \quad x_1 = R_1 \sin\varphi_1, \tag{1}$$

where γ is the surface tension, ρ_1 and ρ_2 are the radii of the meniscus [1]

$$\rho_1 = R_1 \sin\varphi_1 - \rho_2[1 - \sin(\varphi_1 + \theta)], \; \rho_2 = \frac{R_1(1-\cos\varphi_1) + R_2(1-\cos\varphi_2) + D}{2\cos(\frac{\varphi_1+\varphi_2}{2} + \theta)\cos(\frac{\varphi_1-\varphi_2}{2})},$$

φ_1 and φ_2 are the angles subtended by the contact at the center of the grains, D is inter-grain distance and θ is the contact angle measured between the solid and the liquid phases.

On the other side, assuming an infinite liquid and the dynamic viscosity of the liquid, η, an expression for the viscous force acting on the spherical grains of radius R can be derived [2]

$$F_{\text{vis}} = \frac{3}{2}\pi\eta R^2 \frac{1}{D}\frac{dD}{dt}. \tag{2}$$

For simulation of time dependent rearrangement we will apply numerical method defined in [1]

$$\Delta\mathbf{D}_{kj}^{n+1} = D_{kj}^{n}\chi(\mathbf{F}_{kj}^{n+1} - \mathbf{F}_{\mathrm{vis},kj}^{n+1}), \tag{3}$$

where $\Delta\mathbf{D}_{kj}^{n+1}$ is the change of the inter-grain distance between grains *k* and *j* after time $t+\Delta t$, D_{kj}^{n} is the inter-grain distance at previous time step, χ is a constant at a given grain size, $\mathbf{F}_{kj}^{n+1}$ is the capillary force per *kj*-th contact defined by (1), and

$$\mathbf{F}_{\mathrm{vis},kj}^{n+1} = \frac{3}{2}\pi\eta R_{\mathrm{eff}}^{2}\frac{1}{D_{kj}^{n}}\frac{\Delta\mathbf{D}_{kj}^{n}}{\Delta t}, \quad R_{\mathrm{eff}} = \frac{2R_1R_2}{R_1+R_2}. \tag{4}$$

obtained from equation (2) by assuming $dD/dt \approx \Delta D/\Delta t$.

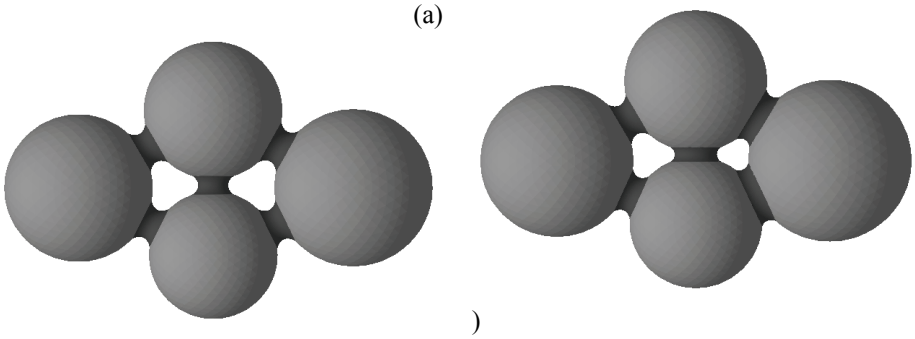

Figure 1. Four-grain model. (a) Initial ($\langle R\rangle = 145$ μm, $\langle D\rangle = 25$ μm). (b) After $t = 4.2$ μsec ($\langle D\rangle = 12.2$ μm). $\chi = 2\times10^{-3}$ N^{-1}, $\theta = 10^{\circ}$, $\eta = 5$ mPas.

For a proper description of the rearrangement, the existence of the total driving force and the relative-displacement mobile network must both be taken into account. Thus, the model system rearrangement defined by the equation (3) and based on the equations (1) and (4) which relate forces and relative displacements within liquid bridge can be applied for simulation of the relative grain displacement due to both capillary and viscous forces.

Figure 1 shows simple model of four spherical grains connected with liquid bridges, whereas the evolution of the average separation distance for three values of viscosity is plotted in Fig. 2a. As it can be seen, as the time proceeds the inter-grain distances change; the densification is very rapid for low viscosity, while for high viscosity the grain displacements are very small due to almost monotonous decreasing of separation distances, therefore similar densification corresponds to longer rearrangement time. For evaluating the total driving force, the rate-dependent term in the equation (3) defined by the equation (4)) has to be taken into account. Figure 2b compares the capillary and the viscous forces during rearrangement and approaching of grains for high viscosity. Interactions correspond to large inter-grain distances are dominated by the capillary forces

(capillary regime), whereas the viscous forces slowly increase due to slow decreasing separation distances but also followed by decreasing of the relative grain displacements. As it can be seen, after ~80 μsec both forces become approximately equal (a transitional regime) which corresponds to very small relative displacements. After intermediate separation distances, the total force becomes repulsive (viscous regime). Obtained theoretical predictions pretty well agree with the conclusion given by Pitois *et al*. [2]. They have also presented interesting result that the maximum dynamic attractive force measured was about 3 times higher than the corresponding static one.

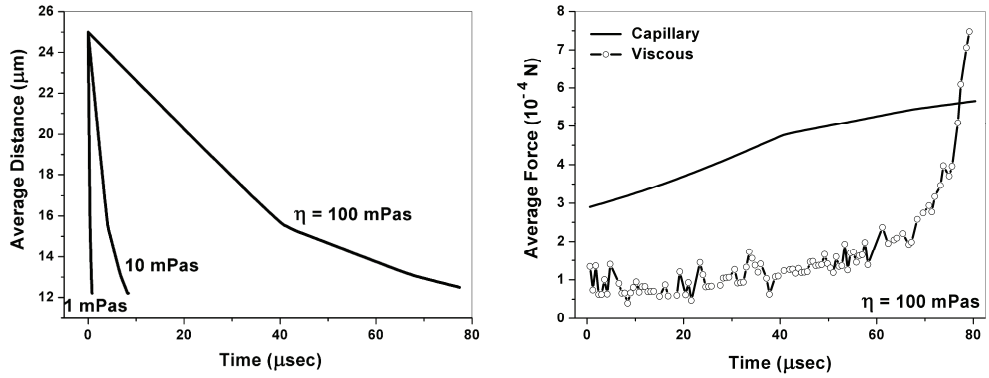

Figure 2. Rearrangement of four-grain model. (a) Time-dependent shrinkage for different values of viscosity. (b) Time dependent driving forces.

Conclusion

In this paper, the theoretical models dealing with the fundamental interaction forces that exist between grains attached by liquid bridges were outlined and the development from these pair-wise interactions to multi-grain model was described. It was shown that the rearrangement is essentially determined by dynamic viscosity and by the ratio of driving forces. However, it was also shown that the rearrangement is governed by geometrical factors (topology of liquid bridges) and nearest neighbor interaction (capillary forces between connected grains).

Acknowledgements

The first author was performed present study under the project (No. OI172057) supported by the Ministry of Education and Science of the Republic of Serbia. He would also like to acknowledge partial support for this study by the Japan Society for the Promotion of Science (Invitation Fellowship ID No. S-10175).

References

[3] Z. S. Nikolic, F. Wakai, Math. Comput. Modell., 2012, 55, 1251–1262.

[4] O. Pitois, P. Moucheront, X. Chateau, J. Colloid Interface Sci., 2000, 231, 26–31.

H-23-P

COMPUTER STUDY OF LIQUID BRIDGE RUPTURE IN LIQUID PHASE SINTERING

Z. S. Nikolić[1], K. Shinagawa[2]

[1]*University of Niš, Faculty of Electronic Engineering, Serbia*
[2]*Kagawa University, Faculty of Engineering, Japan*

Abstract
During rearrangement some liquid bridges become unstable due to elongation and their ruptures occur. In this paper a model for bridge rupture will be considered.

Introduction
The rearrangement process during liquid phase sintering has been generally recognized by remarkable approaching of some grains combined with the filling pores process, but also by the enlargement of some inter-grain distances followed by the growing of some inter-grain pores. The overall effect of separating the grains while keeping constant the liquid volume is therefore an elongation of the bridge, which becomes longer and thinner and less concave. Such liquid bridge elongation combined with rupture of some liquid bridges can reinforce grain rearrangement, but also generate non-uniform distribution of small and large pores. These phenomena will be the subject of our study. The bridge which is not stable any more will be modeled as ruptured bridge replaced by two liquid droplets on the surfaces of grains. Investigation of the model system densification combined with liquid bridge rupture will be analyzed in a simple grain arrangement.

Results and Discussion

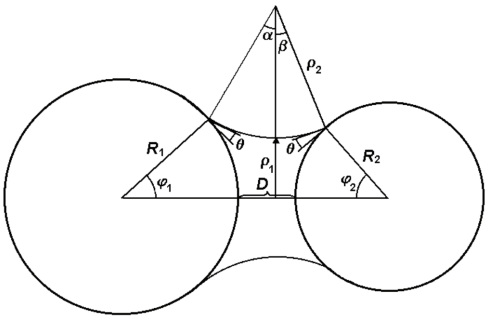

Figure 1. Topology of the liquid bridge.

Let us consider two spherical grains of radius R_1 and R_2 ($R_1 \geq R_2$) joined by a liquid bridge of constant volume (Fig. 1). The liquid meniscus can be carried out using the circle approximation [1] defined by the radii of the meniscus

$$\rho_1 = R_1 \sin\varphi_1 - \rho_2[1-\sin(\varphi_1+\theta)]$$

$$\rho_2 = \frac{R_1(1-\cos\varphi_1)+R_2(1-\cos\varphi_2)+D}{2\cos(\frac{\varphi_1+\varphi_2}{2}+\theta)\cos(\frac{\varphi_1-\varphi_2}{2})}$$

where φ_1 and φ_2 are the subtended angles, D is the inter-grain distance and θ is the contact angle measured between the solid and the liquid phases.

When two grains are pulled apart due to rearrangement, the liquid bridge and corresponding capillary force within it evolve from a static state toward a critical configuration in which, at some point, the liquid menisci first touch each other (ρ_1 approaches zero, Fig. 2) and the liquid bridge ruptures. The liquid bridge after rupture can be considered so that it breaks into two smaller liquid droplets adhere to the surface of each grain [2]. We will assume that their volumes are proportional to the grain size ratio, as well as that their shape can be approximated by a perfect sphere because gravity has negligible effects on their small liquid volumes.

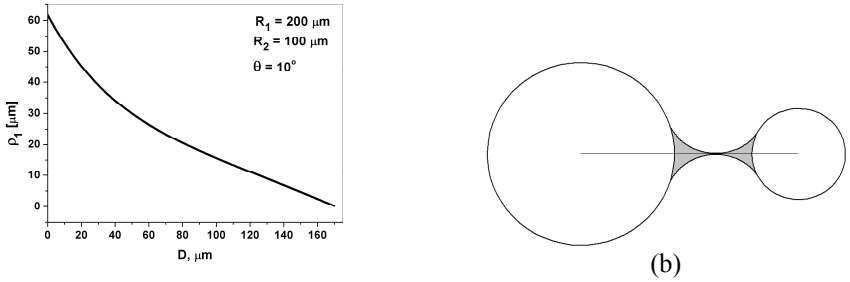

(a) (b)

Figure 2. (a) The variation of ρ_1 with D. (b) Critical configuration corresponds to $\rho_1 \approx 0$.

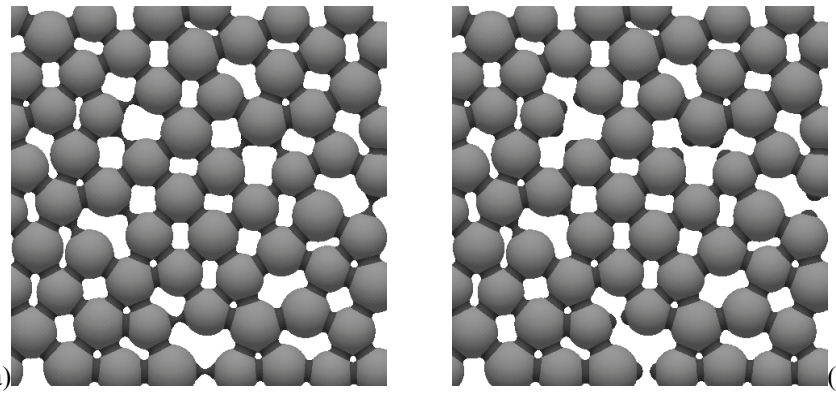

(a) (b)

Figure 3. Snapshot of microstructures (a) with no rupture and (b) with rupture.

Time dependent separation distances during rearrangement are determined by the resultant capillary forces [1]. As long as the inter-grain distance is less than the critical separation distance, the rearrangement is governed by the capillary force. Beyond the rupture distance the capillary force will be set to zero.

In order to demonstrate simulation method based on determination the critical rupture distance and the formation of two liquid droplets, the liquid bridge rupture phenomenon will be simulated on planar multi-grain model of spherical grains (W–Cu system, data given in [1]) with the average radius of ~55 μm and with the average separation distance of ~9.5 μm. The result of rearrangement [1] after 2000 rearrangement steps (RS) is shown in Fig. 3a, where the average inter-grain

distance was now ~3.33 μm with the average shrinkage of ~65%. It can be seen remarkable approaching of most grains combined with the filling pores process, but also much exaggerated enlargement of some separation distances followed by the growing of some inter-grain pores. Due to the overall effect of grain separation liquid bridge elongation occur while keeping constant their liquid volume: they become longer and thinner and less concave. Such bridges are not stable any more and formation of liquid droplets on the surfaces of grains is preferable. Therefore, the rearrangement method [1] will be replaced by new one, which takes into account the fact that at greater separation distance there is a maximum value of the separation distance corresponding to liquid bridge rupture ($\rho_l \approx 0$). Figure 3b shows obtained simulation result after 2000 RS with the average shrinkage of ~87% and the mean inter-grain distance ~1.3 μm that corresponds almost to the equilibrium configuration. It can be seen, however, that during this simulation several new unstable liquid bridges also were generated. It is expected that some of them will be most likely ruptured during next rearrangement. In practice, however, this liquid bridge elongation combined with rupture of some liquid bridges can reinforce grain rearrangement, but also generate non-uniform distribution of small and large pores.

Conclusion

It is well known that during rearrangement some liquid bridges become unstable due to elongation and their ruptures occur. In this paper a model for bridge rupture was considered. For computer study of rearrangement, two different configurations were simulated: the generic configuration characterized by liquid bridge connected grains (inter-grain distance smaller than the critical rupture distance) and the mixed state with connected and separated grains. For this reason it was carried out the calculation of the evolution of multi-grain (planar due to better visualization) system when the constituent grains are pulled apart from each other due to the rearrangement. Such system was characterized from a geometrical (noncontact geometry) and from a quasistatic viewpoint.

Acknowledgements

The first author was performed present study under the project (No. OI172057) supported by the Ministry of Education and Science of the Republic of Serbia. He would also like to acknowledge partial support for this study by the Japan Society for the Promotion of Science (Invitation Fellowship ID No. S-10175).

References

[5] Z. S. Nikolic, F. Wakai, Math. Comput. Modell., 2012, 55, 1251–1262.

[6] X. Pepin, D. Rossetti, S.M. Iveson and S.J.R. Simons, J. Colloid Interface Sci., 2000, 232, 289–297.

H-24-P

HIGH PERFORMANCE PROTON CONDUCTING MEMBRANES FOR FUEL CELLS MADE BY PHOTOPOLYMERIZATION OF HYDROLYTICALLY STABLE MONOMERS

M. Kellner[1], F. Radovanovic[3], J. Matovic[2], R.t Liska[1]
[1]*Vienna University of Technology - IAS, Getreidemarkt 9, 1060 Vienna, Austria*
[2]*Vienna University of Technology - ISAS,Floragasse 7, 1040 Vienna, Austria*
[3]*IHTM - IMTM, University of Belgrade, Njegoseva 12, 11000 Belgrade, Serbia*

Abstract
Proton conducting membranes were prepared by photopolymerization of 2-acrylamido-2-methylpropane sulfonic acid solutions within the pores of polypropylene membranes. Several commercial and novel multifunctional monomers synthesized in IAS lab were investigated as suitable crosslinking agents for this application. Some membranes made with synthesized crosslinkers at low crosslinker concentrations exceeded 2.5 times the conductivity of Nafion® 115 membrane, while exhibiting a good hydrolytical stability, in contrast to the commercial crosslinkers based on multifunctional (meth)acrylates.

Introduction
Polymer electrolyte fuel cells (PEFC) gained a lot of interest in recent years as a potential solution for an eco-friendly energy production used for automotive transportation [1]. Proton exchange membranes (PEM) for PEFCs require mechanical and chemical stability to ensure high proton conductivity and effective separation of anode and cathode under challenging conditions. Best commercial membranes made from sulfonated fluoropolymers, such as Nafion®, are quite expensive [2]. To improve fuel cell performance at a lower cost, 2-acrylamido-2-methylpropane sulfonic acid (AMPS) was investigated recently[3-4]. In this work, novel formulations based on AMPS have been polymerized by UV-initiated radical polymerization and crosslinked with commercial and multifunctional monomers synthesized in IAS lab. To facilitate conductivity measurements, formulations were constrained within a porous membrane as described by Zhou et al. [5].

Experimental
AMPS and N-methyl-2-pyrrolidone (NMP) were purchased from Sigma Aldrich and used without further purification. Biaxially stretched PP membranes with 115 □m thickness and 85% porosity were obtained from 3M [6]. N,N-bis(ω-(methacrylamido)polyoxyethylene)methacryl-amide(PEA-3MMA), tris[2-(metha-cryloylamino)ethyl]amine (3(MAAE)A) and polyethyleneimine-co-methacrylamide (PEI-MAA) were synthesized as described in reference [7].

Sheets of PP membrane were hydrophilized by coating with a 5% Triton X-100 solution in acetone. Hydrophilized membranes were dip-coated in a solution

of ionomer, crosslinker and photoinitiator, covered with a Teflon sheet and irradiated with a high intensity Intelliray 600 UVA Lamp (60 sec exposure at 90% intensity and 12 cm distance). After polymerization the membranes were stored in deionized (DI) water for several days with daily exchange of water.

Proton conductivity was measured in the plane of samples using a 4-point DC method: electrical conductivity between two gold-plated inner electrodes placed 1 cm apart ata potential difference between two gold-plated outer electrodes of 100 mV was equal to proton conductivity under these conditions.

Results and discussion

Tetraethylene glycol diacrylate (4EG-DA) and decanediol dimethacrylate (D3MA) were investigated as commercial crosslinking agents with AMPS concentrations from 40 to 83 wt% dissolved in water or NMP (Table 1).

Table 1. Compositions of different proton-conductive formulations.

Formulation no.	AMPS concentration [wt%]	Crosslinker	Solvent
1	40	D3MA	NMP
2	40	4EG-DA	NMP
3	41	4EG-DA	H2O
4	83	4EG-DA	H2O

As Figure 1 shows, membranes made with a hydrophilic crosslinker (4EG-DA) had significantly higher conductivity than membranes with a hydrophobic crosslinker (D3MA) which reduced water uptake. Proton conductivity mainly increased with higher concentrations of monomers. Conductivity of membranes made with commercial (meth)acrylate crosslinkers significantly decreased after heating for 24h in DI water, but remained unchanged when polyAMPS was converted to the sodium salt before heating. This conductivity reduction may have been related to the cleavage of crosslinker ester bonds catalyzed in strongly acidic environments.

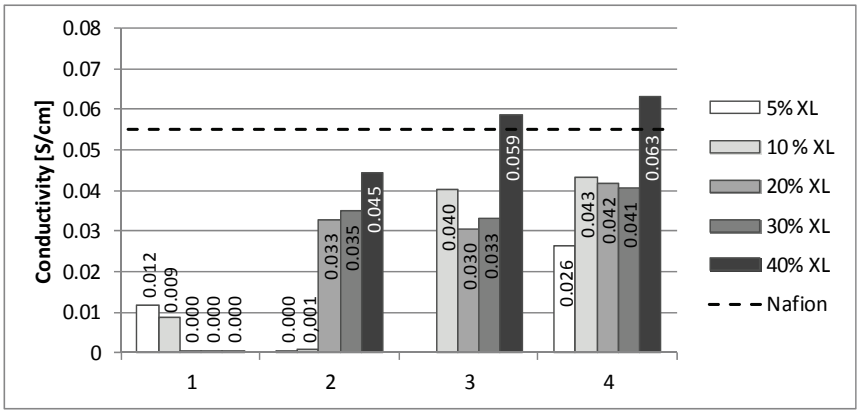

Figure 1. Conductivity as a function of the concentration of meth(acrylate) XL.

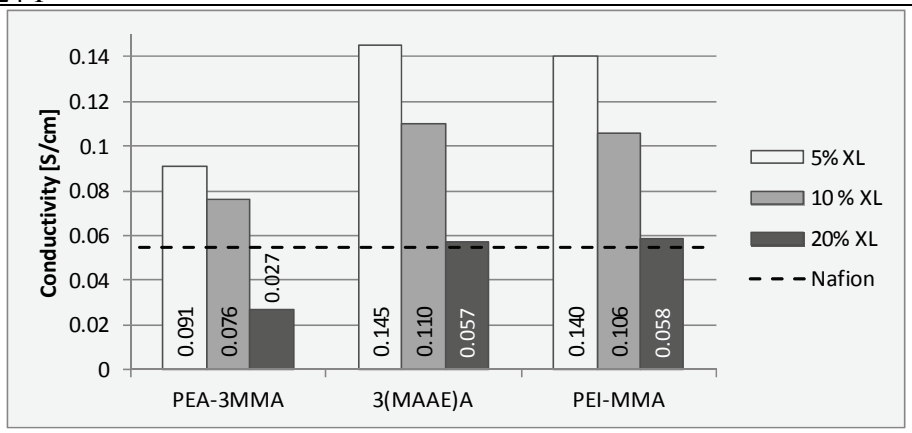

Figure 2. Conductivity as a function of the concentration of methacryamide XL.

Conductivity of membranes made with synthesized multifunctional crosslinkers is shown in Figure 2. Membranes made with 3(MAAE)A and PEI-MMA at a 5% XL level had 2.5 times higher conductivities than Nafion 115 and were significantly more stable than (meth)acrylate crosslinkers when heated in DI water.

Conclusions

The effects of newly synthesized and commercially available crosslinkers on PEM conductivity have been investigated in membrane-constrained polyAMPS gels. Best results in terms of conductivity and hydrolytic stability were obtained with multifunctional acrylamides synthesized in IAS lab.

Acknowledgements

The research leading to these results has received funding from the European Community's FP7- NMP Programme, under the Project Acronym MultiPlat, the Austrian Federal Ministry of Science and Research and the Serbian Ministry of Education and Science within the framework of the project TR 32008. The authors would like to thank 3M and Ciba SC for providing membranes and initiators.

References

[1] J. Patric, Current Opinion in Colloids and Interface Science, 2003, 8, 96-102.
[2] Fuel cells I, 1st ed. Advances in Polymer Science, 2008, NY: Springer. 268.
[3] H. Diao et al., Macromolecules, 2010, 43, 6398-6405.
[4] J. Qiao et al, J. Mater. Chem., 2005,15, 4414-4423.
[5] J. Zhou et al, J. Membr. Sci., 2005, 254, 89-99.
[6] D.R. Lloyd et al, J. Membr. Sci., 1990,52, 239-261.
[7] M. Kellner et al, Novel crosslinkers for high performance Poly-AMPS-based proton exchange membranes for fuel cells, Designed Monomers and Polymers, submitted 2012.

H-25-P

FUNCTIONALIZED POLYMER MEMBRANES FOR PLASMONIC SENSING WITH ENHANCED SELECTIVITY

Z. Jakšić[1], F. Radovanović[1], A. Nastasović[2]
[1] *IHTM – Centre of Microelectronic Technologies and Single Crystals Njegoševa 12, University of Belgrade, Serbia*
[2] *IHTM – Centre for Chemistry, Njegoševa 12, University of Belgrade, Serbia*

Abstract
We investigate theoretically and experimentally the concept of enhancing the selectivity of chemical, biochemical and biological (nano)plasmonic sensors utilizing multifunctionalized polymer membranes. Membrane nanocompositing is done by lamination and surface/pore immobilization. A separator/filter and an affinity-based adsorption enhancer are integrated into a single multifunctional membrane structure. Functionalized membrane may be transferred across platforms and even used for different types of sensing devices.

Introduction
Surface plasmon optics is the basis for a novel generation of ultra-sensitive (bio)chemical and biological sensors that are label-free and ultrafast [1]. Typically their active part is a surface composed of metal or metal-dielectric (plasmonic metamaterial) [2] with a negative real part of the relative dielectric permittivity. Two distinct types of surface plasmon resonance are used for such sensing, one of them based on propagating surface waves (surface plasmon polaritons, SPP), the other on nonpropagating (localized) SPP [3]. In both cases analyte particles adsorb on the active surface, modifying the conditions for the existence of SPP. In its basic configuration a plasmonic sensor is thus a refractive index sensor. Its sensitivity may well exceed 10^{-8} refractive index units, i.e. 1 ng/cm^2 (0.003 monolayer) [4].

A problem with plasmonic sensors in their basic form is their relatively low selectivity based solely on refractive index changes, so that different materials with similar refractive indexes cause similar outputs. An approach to overcome this problem is functionalization of the sensor surface by nanocompositing [5]. Here an interaction partner ("ligand") is immobilized to the sensor surface, serving as affinity-based binding material for the target analyte. Another way is to utilize a filter or separator to remove undesired species and allow only the target analyte to reach the sensor surface [5]. Membranes are often used for this, while the separation mechanism may be based on nanopores (e.g. molecular sieves) or nonporous (dense) structures with solution-diffusion mechanism. Built-in electrical charges within the membrane may be also utilized (e.g. ion exchangers).

In this work we investigate the possibility to integrate the separator/filter structure and the affinity-based target-specific adsorption enhancer into a single membrane structure which may further be merged with the sensitive plasmonic

structure itself. We consider both interface and pore modification of membranes towards enhanced device selectivity.

Multifunctionalization

A structure of a plasmonic sensor is schematically shown in Fig. 1a. A surface with negative effective value of relative dielectric permittivity is the sensing part. An enhanced selectivity structure may contain separator and immobilizing structure, the latter fully immersed in the SPP field. Fig. 1b shows two approaches to integration of the separator (a porous membrane) and affinity blocks: surface-based (left) and bulk-based (right).

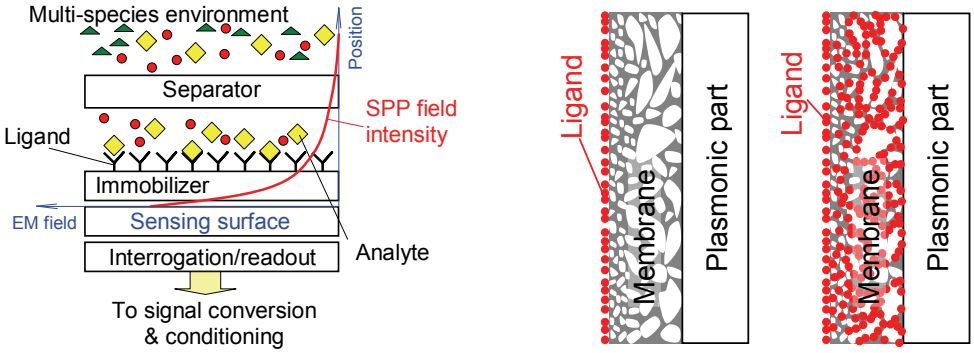

Figure 1. a) Schematic presentation of plasmonic chemical sensor; b) two approaches to integration of separator and ligand (surface and bulk immobilization)

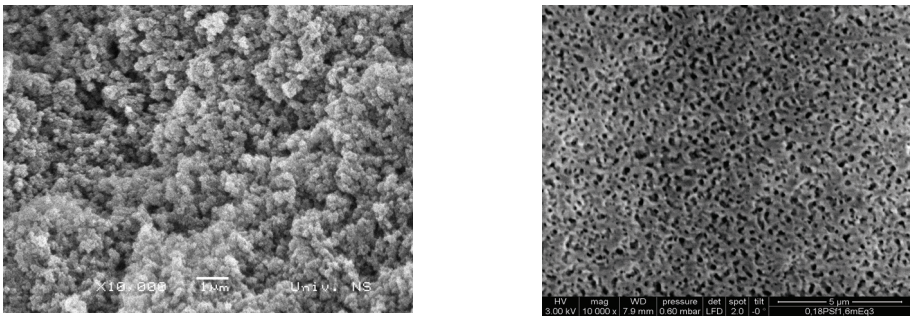

Figure 2. a) SEM picture of porous poly(GMA-*co*-EGDMA) surface. b) ESEM image of the top surface of an asymmetric membrane made by photopolymerization.

Experimental

We chose macroporous crosslinked copolymers (MCP) which are readily formed into membranes and keep a permanent well-developed porous structure. Particularly we used glycidyl methacrylate (GMA)-based MCP. The attractiveness of GMA for affinity-enhanced sensing originates from the presence of an epoxy group in GMA molecule that can easily be transformed into various functional groups, like amine, iminodiacetate, thiol, dithiocarbamate, pyridine, etc., making it a multipurpose material. GMA was already successfully used for heavy and precious metals

adsorption [6] and enzyme immobilization [7]. Fig. 2a shows a scanning electron micrograph (SEM) of the poly(GMA-*co*-EGDMA) surface.

For the formation of membranes comprising GMA as a precursor for subsequent functionalization we selected a new method recently described in literature [8-9]. It combines a traditional immersion precipitation process for making membranes with photopolymerization and crosslinking of functional monomers included in the casting solution. As the environmental SEM micrograph of the top surface in Fig. 2b shows, the resulting membranes have an integral top skin layer with fine selective channels over a coarser mechanically stable support. The top skin layer has a separation function against undesirable species present in the feed solution. Subsequent fuctionalization of the epoxy groups entrapped within the membrane provides ligand sites for enhanced plasmonic sensing.

Conclusion

Possibilities to integrate separator and ligand for plasmonic sensor into a single structure are considered. The multifunctionalization ensures a highly tailorable element that is transferable across platforms. This allows for a multiple use of a single sensor type for a larger number of different analytes or massive process parallelization using the identical plasmonic structure as the basic element. At the same one may use built-in (nano)pores to augment the effective surface for adsorption and thus vastly increase the amount of adsorbate, furnishing a further increased sensitivity. Additional reaction enhancements may also be incorporated, including but not limited to catalyst particles. The approach may be extended to other types of chemical and bio sensors.

Acknowledgment

This work has been funded by Serbian Ministry of Education and Science within the framework of the projects TR32008 and III 43009.

References

[1] W. L. Barnes, A. Dereux, T. W. Ebbesen, Nature, 2003, 424, 824-830.
[2] Z. Jakšić, O. Jakšić, Z. Djurić, C. Kment, J. Optics A, 2007, 9, S377-S384.
[3] M. E. Stewart, C. R. Anderton, L. B. Thompson, J. Maria, S. K. Gray, J. A. Rogers, R. G. Nuzzo, Chem. Rev., 2008, 108, 494-521.
[4] L. S. Jung, C. T. Campbell, T. M. Chinowsky, M. N. Mar, S. S. Yee, Langmuir, 1998, 14, 5636-5648.
[5] Z. Jakšić, J. Matovic, Materials, 2010, 1, 165-200.
[6] A. Nastasović, Z. Sandić, Lj. Suručić, D. Maksin, D. Jakovljević, A. Onjia, J. Hazard. Mater., 2009, 171, 153-159.
[7] N. Miletić, Z. Vuković, A. Nastasović, K. Loos, Macromol. Biosci., 2011, 11, 1537–1543.
[8] P. Radovanovic, M. Kellner, J. Matovic, R. Liska, T. Koch, J. Membrane Sci., 2012, 401-402, 254-261.
[9] P. Radovanovic, J. Matovic, R. Liska, M. Kellner, Austrian Patent Application, A824/2011.

H-26-P

SENSITIZED GELATIN AS AN EYE PROTECTION FILTER AGAINST DIRECT LASER RADIATION

B. Murić, D. Pantelić, D. Vasiljević, B. Jelenković
Institute of Physics, University of Belgrade, Pregrevica 118, 11080 Zemun, Serbia

Abstract
Tot'hema eosin sensitized gelatin (TESG) layer is used as an eye protection filter against 2nd harmonic Nd:YAG laser light. Compared to classical eye protection filters our material uses microlens formation to protect eye from direct laser radiation. TESG laser safety goggles were manufactured, at the same time satisfying European eye protection standard EN 207. Measurements have shown that the eye is protected from 10W of direct laser beam. Eye protection filters can be manufactured for other wavelengths too, by changing the sensitizer.

Introduction
Due to increasing of lasers use in medicine, science, industry… the laser eye protection become very important. Different parts of the eye can be damaged, depending on the laser wavelength and intensity. UV light (<400 nm) and IR light (>1400 nm) damage the cornea and eye lens. Wavelengths from 400 nm to 1400 nm are focused on the retina, which is the most sensitive part of the eye [1, 2].

Eye protection filters (absorption, reflection...) are mostly plastic materials that protect human eye from diffusely reflected laser light [3, 4]. Direct laser irradiation heats the plastics and laser beam punches a hole in the filter. Different, commercially available, laser safety glasses have a very small transmission for the laser beam, but enough for visible light. They should protect an eye against scattered laser beam, under standardized conditions defined by European laser eye protection standards EN 207 [5] and EN 208 [6]. The same standards require that a laser goggle must be able to protect the user for a minimum of 10 seconds (CW laser) or 100 pulses (pulsed laser), when exposed to direct laser radiation. Maximum permissible exposure (MPE) measured at the cornea of the human eye, is the highest laser power density or energy density that is considered safe for a given wavelength and exposure time [5, 7].

We have shown that TESG can be used as an eye protection filter against the high-power direct laser beam, by utilizing a microlens formation on the protective material.

Experimental
TESG layer is simple to prepare and use. Heated mixture of gelatin, tot'hema and eosin is poured on the polycarbonate (lexan) plate and dried. Crystallization of layer is prevented by adding a small amount of NaCl. After drying, TESG layer is very elastic and sticky, and can be easily peeled and transferred to another substrate. Medical drinkable solution of tot'hema softens gelatin layer, increasing its flexibility. Eosin is a dye used to enhance absorption at 532 nm [8]. Protection

filter was prepared by adhering 1 mm thick TESG layers on both sides of 2 mm thick transparent lexan plate (see Fig.1). Through our experiments 10 W maximum power, 532 nm Nd:YAG laser was used (Fig. 2). Laser power was measured by powermeter placed 2 cm behind 5 mm diameter diaphragm (simulating the human pupil which normally opens about 2 mm in daylight, and 7 mm in the dark [9]).

Figure 1. Cross-section of TESG filters.

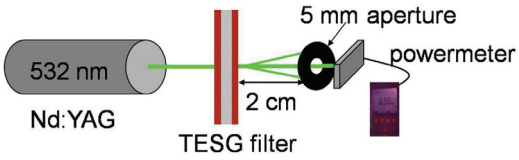

Figure 2. Experimental setup.

Results and Discussion

In our previous research transparent, diverging microlenses (focal lengths far below 1 mm) were formed quickly at TESG layer [10, 11]. As shown in Fig. 3 the protection mechanism is influenced by the laser power. Absorption of laser light dominates up to 50 mW, and it doesn't affect the protective layer. Microlenses formation starts above 50 mW. The laser beam diverges and significantly reduces the energy density on the second layer, which effectively absorbs the laser beam. Above 600 mW the protection layer starts to carbonize, producing nontransparent black area, which further blocks the laser beam.

The power density behind the TESG filter, as a function of exposure time, for various laser powers was measured (Fig. 4). Five measurements were made for each laser power and the average values are shown. As can be seen, the protection achieved by TESG filter is bellow MPE values for all incident laser powers (0.3W – 9.6W).

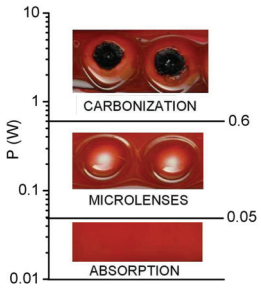

Figure. 3. TESG layer appearance as a function of laser power

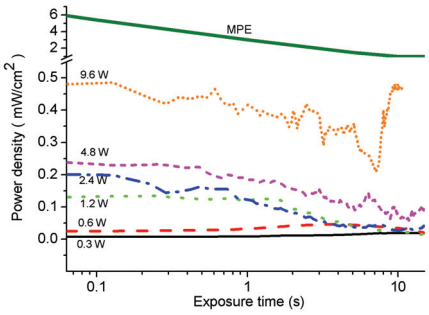

Figure 4. Power density vs. exposure time or different laser powers

We have produced laser protective eyewear by modifying welder's goggles (see Fig. 5). The protection level can be controlled by flipping, up or down, the front set of filters. If a single filter is in use (Fig. 5a), goggles offer lower protection level but allow one to see well and adjust the laser. If both filters are used (Fig. 5b) goggles efficiently protect eyes from direct laser beam. If

accidentally damaged TESG layers can be peeled and replaced. Efficiency of TESG goggles is shown in Fig. 5c. We can see that after 30 s of irradiation by 10 W direct laser beam transmitted power is still below 10 μW.

Figure 5. Photograph of TESG eye-protection goggle: (a) for laser adjustment; (b) for laser protection; (c) irradiated with 10W 532nm Nd:YAG laser for 30 s.

Conclusions

TESG material, used as a protection filter against 2nd harmonic Nd:YAG laser beam, is described. Results have shown that an eye is protected from 10 W of direct laser beam as a result of microlens formation. Effective TESG protection goggles, for laboratory use, were made and tested. Preliminary results have shown that eye protection filter can be manufactured for other wavelengths too, by changing the dye (sensitizer).

Acknowledgments

Paper was written as a part of research on the projects ON 171038 and III 45016 supported by the Ministry of education and science of the Republic of Serbia.

References

[1] A. Schirmacher, Medical Laser Application, 2010, 25, 93-98.
[2] E. Sutter, A. Schirmacher, Opt. & Laser Technol., 2001, 33, 255-258.
[3] M. Lenner, C. Spielmann, Appl. Opt., 2005, 44, 3532-3539.
[4] C. H. Lee, B. Bihari, R. Filler, B. K. Mandal, Opt. Mater., 2009, 32, 147-153.
[5] EN 207: 2009 Personal eye-protection equipment—Filters and eye-protectors against laser radiation (laser eye-protectors).
[6] EN 208: 2009 Personal eye-protection—Eye-protectors for adjustment work on lasers and laser systems (laser adjustment eye-protectors).
[7] Standard Z-136. 1, ‘‘Safe use of lasers,’’ ANSI, New York, 1986.
[8] B. Murić, D. Pantelić, D. Vasiljević, B. Panić, Opt. Mater., 2008, 30, 1217-1220.
[9] D. A. Atchinson, C. C. Girgenti, G. M. Campbell, J. P. Dodds, T. M. Byrnes, A. J. Zele, Clin. Exp. Optom., 2011, 94, 545-549.
[10] B. Murić, D. Pantelić, D. Vasiljević, B. Panić, Appl. Opt., 2007, 46, 8527-8532.
[11] B. Murić, D. Pantelić, D. Vasiljević, B. Panić, B. Jelenković, Appl. Opt., 2009, 48, 3854-3859.

ANALYSIS OF FACTORS INFLUENCING Cu(II) SORPTION BY CLINOPTIOLITE

M. Šljivić-Ivanović, I. Smičiklas, J. Marković

University of Belgrade, Vin a Institute of Nuclear Sciences, P.O. Box 522, Belgrade Serbia

Abstract

The effects of initial metal concentration and pH, as well as the sorbent mass and particle size, on Cu(II) sorption by natural clinoptilolite were evaluated and compared. Full factorial experimental design at two levels was applied. Statistically significant factors were determined considering residual Cu(II) concentrations as a system response.

Introduction

Heavy metals are major pollutants of some ground and surface waters and are often present in industrial or urban wastewaters. Among different methods for water purification, sorption processes are widely investigated using natural and synthetic materials. Clinoptilolite is naturally occurring zeolite, which sorption properties toward heavy metal cations, NH_4^+, inorganic anions and organic substances were intensively studied [1]. The effectiveness of sorption process can be significantly influenced by variation of operating conditions. The objective of this work was to analyze and compare the effects of initial solution pH, initial metal concentration, sorbent mass and particle size, on Cu(II) removal by natural clinoptilolite, using experimental design methodology [2].

Materials and Methods

The experiments were conducted in batch conditions, at 20±1°C. Variable amounts of solid phase (clinoptilolite, Vranjska Banja, Serbia) were equilibrated for 48 h on a horizontal shaker with 20 mL of Cu(II) solutions. Independent variables and their levels are given in Table 1, while Table 2 presents coded experimental conditions based on full factorial design and defined by the statistical software. After filtration, residual concentrations of Cu(II) ions were measured by Perkin Elmer Emission Spectrometer Plasma 400, at λ=222.78 nm.

Table 1. Variables and their levels.

Factor	Level	
	-1	+1
A - initial pH	3	5
B - sorbent mass (g)	0.1	0.4
C - initial Cu(II) conc. (mol/L)	0.0002	0.005
D- particle size (mm)	<100	1-3

Table 2. Experimental design matrix

Results and Discussion

The study of full factorial design consists of exploring all possible combinations of the factors considered in the experiment. Using residual Cu(II) concentrations as system response, Pareto chart (Fig. 1a) and Main effect plot (Fig. 1b) were constructed by statistical software (MINITAB).

Factor				Response(Y)
A	B	C	D	Cu (mg/L)
1	-1	-1	-1	4.01
1	1	1	1	289.71
1	1	1	-1	233.18
-1	1	1	1	286.39
1	1	-1	1	3.91
-1	1	-1	1	7.21
-1	-1	1	-1	341.47
1	-1	1	-1	328.90
-1	-1	1	1	350.82
-1	-1	-1	-1	10.97
1	-1	-1	1	8.27
-1	1	1	-1	274.16
1	1	-1	-1	1.66
-1	-1	-1	1	0.05
-1	1	-1	-1	0.04
1	-1	1	1	343.94

In Pareto chart, the absolute values of effects are compared and information about their statistical significance at a confidence interval of 95% is provided. Each bar length in Pareto chart is proportional to the standardized effect, produced by variation of a given factor between lower and higher level [2]. The change of initial metal concentration influenced process the most. The variation of sorbent mass and the interaction between initial Cu(II) concentration and sorbent mass as well produced statistically significant effects.

The Main effect plot (Fig 1b) gives information on whether the change between two variable levels decreased or increased the selected system response [2]. The horizontal line in the graph represents the overall mean response of the system, for both levels of all factors. From the Fig. 1b, it can be concluded that decrease of concentration and increase of sorbent mass caused reduction of aqueous Cu(II) concentration, while the effects of initial pH and sorbent granulation were negligible.

Finally, for the investigated range of variables, the following mathematical model can be used for process description:

$$Y = 155.3-18.26\ B+150.78C-16.95BC$$

where Y is residual Cu(II) concentration, whereas B, C and BC represent effects of sorbent mass, initial metal concentration and their interaction, respectively.

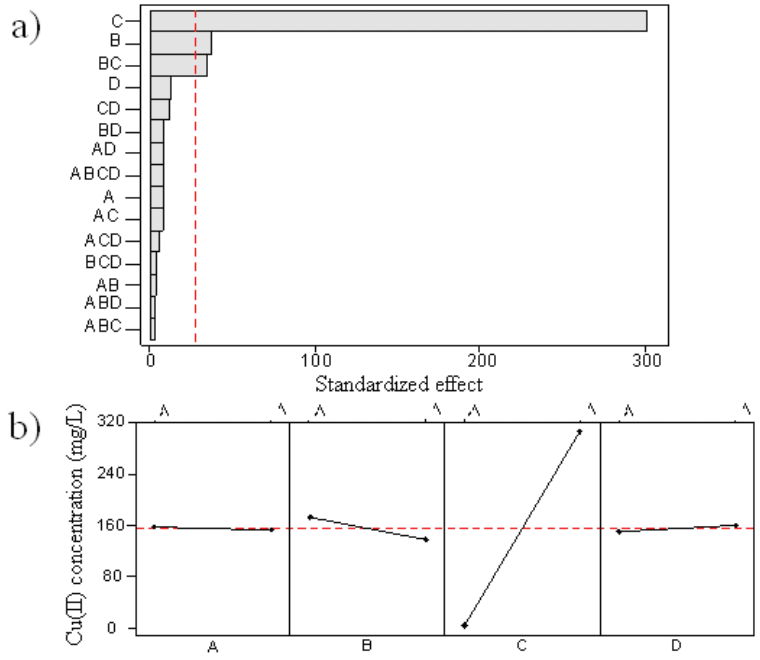

Figure1. a) Pareto chart and b) Main effect plot for residual Cu(II) concentrations

Conclusion

The influence of process variables (initial solution pH, initial metal concentration, sorbent mass and particle size) on Cu(II) removal from aqueous solutions by clinoptilolite was investigated using full factorial design. The effect of initial metal concentration was the most pronounced, followed by the effect of sorbent mass and interaction effect between sorbent mass and sorbate concentration. The empirical equation practical for process description was derived.

Ackonwledgments

The work was supported by the Ministry of Education and Science of the Republic of Serbia (Project No. III 43009).

References

[1] S. Wanga, Y. Peng, Chem.Eng. J., 2010, 156, 11–24.

[2] F. Yates, The Design and Analysis of Factorial Experiments, Imperial Bureau of Soil Science, Harpenden, 1937.

SOLID STATE
PHYSICAL CHEMISTRY

I-01-SL

PLASMAELASTIC AND THERMOELASTIC EFFECTS IN MICROMECHANICAL STRUCTURES

D. M. Todorović
Institute for Multidisciplinary Research, Beograde, Serbia

Abstract
Plasmaelastic and thermoelastic effects can be important as driven mechanisms for micromechanical structures, based on the plasma, thermal and elastic wave phenomena, generated by absorption of modulated optical power. The plasmaelastic and thermoelastic mechanisms of photoacoustic generation in a micromechanical structure, photogenerated by an intensity-modulated optical beam, were studied. The amplitude and phase of the PA elastic bending in the micromechanical structure were calculated and analysed, including the various plasma and thermal sources. The theoretical results were compared with the experimental data. Experimental data were obtained by the PA elastic bending method, based on the optical excitation of the micromechanical structure and detection of the acoustic response (PA signal) with a very sensitive PA detection system.

Introduction

A new approach for producing compact, lightweight, a highly sensitive detector is provided by micro-(opto)-electro-mechanical systems (MOEMS) technology. The photoacoustic (PA) and photothermal (PT) science and technology extensively developed new methods for study MOEMS. The PA and PT effects can be important as driven mechanisms for micromechanical structures [1].

When a micromechanical structure is exposed to periodic optical excitation, the photogenerated carrier-density (the plasma wave) causes a mechanical stress. The mechanical stress produces periodic elastic deformation in the sample, the so-called electronic deformation [2]. This mechanism of elastic wave generation - plasmaelastic (PE) effect (or the electronic deformation – ED effect) is the property of semiconductors and electronic materials. The PE mechanism is based on the fact that photogenerated plasma in the semiconductor causes a deformation of the crystal lattice, i.e. it causes the change of the potential of the conduction and valence bands in the semiconductor. On the other hand, the photogenerated carrier termalization and surface and bulk recombination, as thermal sources, cause the thermal wave generation. The thermal waves cause elastic bending in the micromechanical structure - the thermoelastic (TE) effect.

There are three mechanisms of PA generation [3]. The PA signal $S(\omega)$, can be given as a sum of plasmaelastic, $S^{PE}(\omega)$, the thermoelastic, $S^{TE}(\omega)$ and thermodiffusion $S^{TD}(\omega)$,components. The TD component of PA signal $S^{TD}(\omega)$ is a consequence of the heat diffusion processes in the sample, i.e., it depends on the periodic temperature variations at the sample surface and it can be given with well-known Rosencwaig – Gersho theory [4].

The TE mechanism can have an important influence on the PA signal, especially at higher frequencies. Jackson and Amer [5] developed a theory of piezoelectric photoacoustic detection by treating the sample as an elastic layer. They solved three-dimensional uncoupled quasi-static thermoelastic equations for elastic stress and strain. Rousset et al. [6] analyzed the effect of thermoelastic expansion and bending on PA signal related to measurements of thermal diffusivity of metals. Rosencwaig et al. [7,8] have developed a noncontact PT technique that can be used at high modulation frequencies and detected local thermoelastic deformations of its surface by a focused probe beam. Rosencwaig et al. [9] and Opsal and Rosencwaig [10] used the same method in an investigation of semiconductors. Perondi and Miranda [11] used the so-called open photoacoustic cell technique to study the effect of TE sample bending in the thermal characterization of solid materials.

The PE effect in semiconductors had been studied previously by, among others, Stearns and Kino [2]. They measured the phase of the photoacoustically generated waves and analyzed the contribution of the PE mechanism to the PA signal in silicon samples. The theory of Stearns and Kino included the electronic component of strain in the stress-strain relation in a manner analogous to elastic wave generation by local periodic thermal expansion. Dersh and Amer [12] measured the surface displacement of Si and a-Si:H samples by use of an interferometric technique. Further, Avanesyan et al [13] and Avanesyan and Gusev [14] have shown that the PE mechanism, related to changes in the equilibrium density of photoexcited electron-hole pairs, can contribute more than the TE mechanism to excited acoustic pulses. Sablikov [15] theoretically investigate photothermal surface dilatation of semiconductors including the electronic deformation mechanism. Prak and Lammerink [16] investigated the effect of electronic strain on a photothermally induced mechanical moment in a silicon microstructure.

The theory of Stearns and Kino [2] included the PE mechanism in the photoacoustic effect. Gusev [17] considered the role of free-carriers in the process of photogeneration of longitudinal acoustic waves in semiconductors. The linear theory of longitudinal acoustic wave generation in the case of interband absorption of optical radiation was given by Gusev and Petrosyan [18].

The theoretical analysis of the plasma, thermal and elastic effects in micromechanical structures consists in modeling a complex system by simultaneous analysis of the plasma and thermal wave equations. In this work the plasma, thermal and elastic waves, i.e. the plasmaelastic and thermoelastic effects in a circular plate and square membrane, photogenerated by an intensity-modulated laser beam, are presented. The theoretical PA signal was compared with experimental measured by using the PA elastic bending method [19-21]. The PA elastic bending method implies the optical generation of elastic bending in the sample and detection of this deformation over PA effect (the gas-microphone detection technique with transmission configuration).

The plasma and thermal waves, i.e. the carrier-density and temperature space and frequency distribution in a rectangular plate (3D geometry), photogenerated by a focused and intensity-modulated laser beam, were are analyzed in our previously paper [22]. The detailed analysis and relations for TD, TE and ED components of the PA signal for circular thin plate were given in our previously published papers [1,3,23,24].

Plasmaelastic and Thermoelastic Efects

The theoretical treatment enables quantitative accounts of the carrier density field, $n(\boldsymbol{r},t)$, the temperature field, $T(\boldsymbol{r},t)$, and the elastic displacement field, $\boldsymbol{u}(\boldsymbol{r},t)$. In the case of periodical excitation, with angular modulating frequency of the incident beam $\omega = 2\pi f$, can be assumed as $n(\boldsymbol{r},t) = \mathrm{Re}[N(\boldsymbol{r};\omega)\exp(i\omega t)]$, $T(\boldsymbol{r},t) = \mathrm{Re}[T(\boldsymbol{r};\omega)\exp(i\omega t)]$ and $\boldsymbol{u}(z,t) = \mathrm{Re}[\boldsymbol{U}(\boldsymbol{r};\omega)\exp(i\omega t)]$ where $N(\boldsymbol{r};\omega)$, $T(\boldsymbol{r};\omega)$ and $\boldsymbol{U}(\boldsymbol{r};\omega)$ are complex values which define the amplitude and phase of the carrier-density, temperature and dispacment fields, respectively.

The electronic elastic displacement $\boldsymbol{U}^{PE}(\boldsymbol{r};\omega)$, using the strain-stress relations, can be given vs. the $N(\boldsymbol{r};\omega)$. Also, the thermal elastic displacement $\boldsymbol{U}^{TE}(\boldsymbol{r};\omega)$, can be given vs. $T(\boldsymbol{r};\omega)$, Than, the elastic displacement $\boldsymbol{U}(\boldsymbol{r};\omega)$ can be given as the vector sum of two components: $\boldsymbol{U}^{PE}(\boldsymbol{r};\omega)$ and $\boldsymbol{U}^{TE}(\boldsymbol{r};\omega)$. In accordance with the elastic theory of thin plate, using the elastic Green function method to solve the elastic equation, $U_z^i(x,y,z;\omega) \approx W_d{}^i(x,y;\omega)$ (i = *TE, ED*; $W_d{}^i$ is the dynamic elastic bending of the thin plate) are obtained. Then, the PE and TE component of PA signal for square plate can be given vs. integral relations of $W_d{}^{PE}(x,y;\omega)$ and $W_d{}^{TE}(x,y;\omega)$, respectively [22,25].

There are three main mechanisms in thermal wave generation, i.e. there are many thermal sources in semiconductors: the thermalization heat source, $Q^T(\mathbf{r},\omega)$, the bulk recombination source, $Q^{BR}(\mathbf{r}, \omega)$ and two different heat sources at the plate surface z=0, $Q_1{}^{SR}(\omega)$ and $Q_2{}^{SR}(\omega)$ at the plate surfaces $z=L_z$. Then, the periodic temperature distribution, $T(x,y,z;\omega)$ in the plate can be given as a sum of four components: the thermalization, $T^{TZ}(x,y,z;\omega)$, surface recombination $T^{SR1}(x,y,z;\omega)$, $T^{SR2}(x,y,z;\omega)$ and bulk $T^{BR}(x,y,z;\omega)$ components of the temperature distribution, respectively [22].

For uniform optical excitation, if the lateral effects are omitted, it is possible to reduce the problem to one-dimensional, i.e. the carrier-density $N(x,y,z;\omega) \approx N(z;\omega)$ and temperature $T(x,y,z,t) \approx T(z,t)$ distribution in the thin Si plate, were calculated and use as a source term in the elastic bending equation. The carrier-density field $N(z;\omega)$ can be find by solving the appropriate plasma differential equation in the Si plate. In order to find the periodic temperature distributions $T(z;\omega)$, the heat-diffusion equations needed to be solved.

The theoretical model, derived in this work, enables to calculate the PA elastic bending signal (PE, TE, and TD components) and compare with experimental data.

Analysis and Discussion

The PE and TE effects in micromechanical structures were measured by using the PA elastic bending method. The PA elastic bending method implies the optical generation of elastic bending in the sample and detection of this deformation over PA effect. The experimental PA elastic bending signals were measured by using specially constructed PA cell [23] (the gas-microphone detection technique with transmission configuration) where the sample is mechanically supported on the edges. In the transmission PA technique, the sample is excited on one side and the PA signal is detected on the other side. The PA cell uses a miniature electrets microphone as an acoustic detector; the sample is mounted directly onto a front surface of microphone, which usually has a circular hole as the sound inlet. It uses the internal microphone air chamber, adjacent to the membrane, as a conventional measuring gas chamber of PA cell. The construction of the PA cell was optimized to get maximum acoustic protection from the surroundings, a good signal/noise ratio and a flat frequency characteristic in the range between 20 and 20000 Hz. These alterations made possible the achievement of high quality PA signals. The sample was mounted in the PA cell between two rigid annular knife-edges, which defined the case of sample mechanical supporting. This is very important for TE and PE components of the PA signal, i.e., for the PA elastic bending signal.

Circular plate The samples were Si circular plate (diameter 10 mm) with different thicknesses (~ 380 - 190 μm). Samples are prepared from 3 inch, 520 μm thick, one side polished Si wafers (n-type, 3-5 Ωcm, and 500-1000 Ωcm).The different thicknesses were obtained with mechanical dressing.

Fig. 1 shows typical experimental PA amplitude spectra for the Si circular plate (378 um thick) and the theoretically calculated components of PA amplitude vs. modulation frequency. It is possible to see that in this case, the TD component is dominant in the frequency range below ~ 1 kHz; TE component is dominant above ~ 3 kHz and PE component; above ~ 15 kHz.

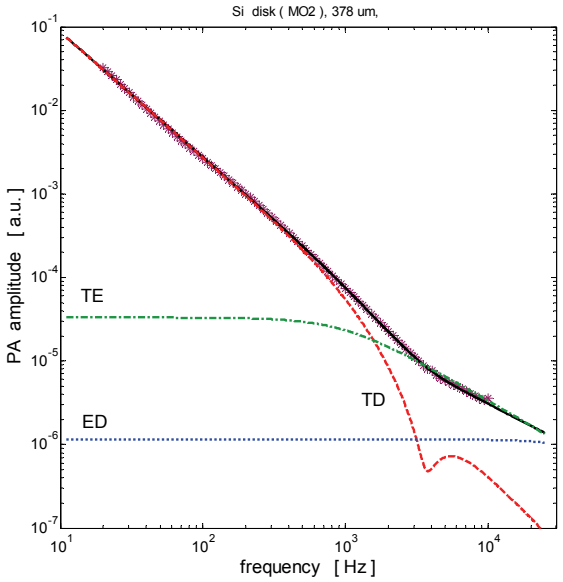

Figure 1. PA amplitude vs modulation frequency for Si circular plate (diameter 10 mm, 378 μm thick): (*) experimental ; (- -) TD componente ; (- . -) TE ; (. . .) PE ; (-) sum (TD + TE + PE).

Contribution of the PE

component (the electronic deformation– ED component) to PA signal can be in see from the previously given results by Todorović et al. [23,24]. The PA signal were measured and theoretically analyzed in the low frequency range (~60÷4000 Hz) by using the gas-microphone detection. The analysis showed that, for a typical Si sample, the ED component reaches ~10% of the total PA signal. Then it is possible to see clearly the contribution of the ED component to the normalized PA diagram.

In Fig.2 the PA phase difference of the sum of TD and TE components and the total PA signal (TD+TE+ED) are shown. It can be seen that the ED component significantly changes the slope of the PA phase difference curve for frequencies up to ~2 kHz. This shows that the ED component can be detected with a simple detection method at relatively low frequencies as a significant component of the PA signal for semiconductor materials.

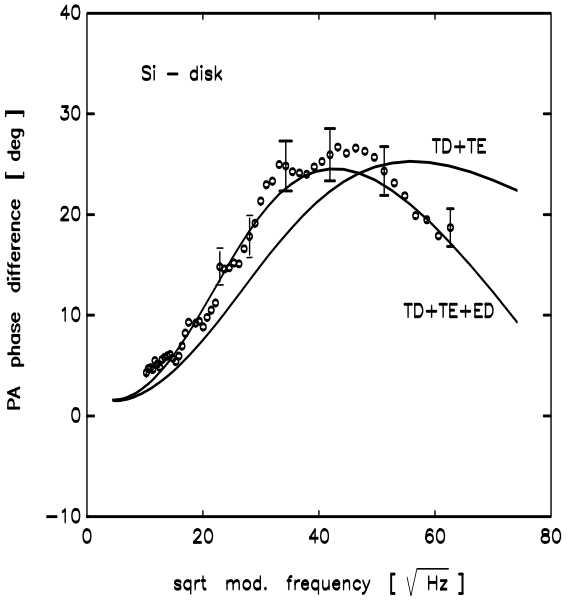

Figure 2. Influence of the ED component to the PA signal of the Si-sample: (o) normalized experimental PA data; (-) TD+TE+ED; (--) TD+TE componentes.

Square membrane Si chip with square membranes are prepared from 3 inch, 390 μm thick, double side polished, 3-5 Ω·cm n-type Si wafers. Masking material is thermally grown SiO_2. SiO_2 is grown at 1100 ^oC from oxygen saturated with water vapor. Oxide thickness is about 1 μm. Etch square windows (3200 x 3200 μm^2. Si membranes are fabricated by wet anisotropic bulk micromachining process. Potassium hydroxide (KOH) solution in water is used as enchant of Si. The micromachining is carried out at 80 ^oC using 30 wt% KOH solution. Membrane thickness is function of etching time. After membrane fabrication, and dicing single elements, remaining masking material is completely removed. These PA signals were calculated for Si chip with the square membrane for typical parameters of Si.

Typical experimental amplitude PA elastic bending spectra for different thicknesses of Si square membranes (Si chip, frame 5 x 5 mm, square membrane 3 x 3 mm) are given in Fig. 3. Experimental results show that the PA measuring system (PA cell width electrets microphone and lock-in amplifier) has S/N ~ 20000 at 100 Hz; ~ 2000 at 1000 Hz; ~ 10 at 10000 Hz and ~ 1-2 at 20000 Hz. It is clear from that analyze that for frequency above 10000 Hz, the PA signal is small and comparable width the noise (coherent electronic noise increase with increasing the

frequency; the sensitivity of the acoustic detector, i.e. the electrets microphone decrease in this frequency range).

Then, it is possible to accept the high frequency limit from our PA measuring system at 20000 Hz.

Fig.4 shows a typical example of the PA elastic bending spectra of the square Si membrane with dimensions: $L_x = L_y = L = 2788$ μm and thickness $L_z = 98.4$ μm. It is possible to see that in the case of square membrane, the TD component is dominant in the frequency range below ~ 10 kHz; TE component is dominant above ~ 20 kHz and PE component; above ~ 40 kHz.

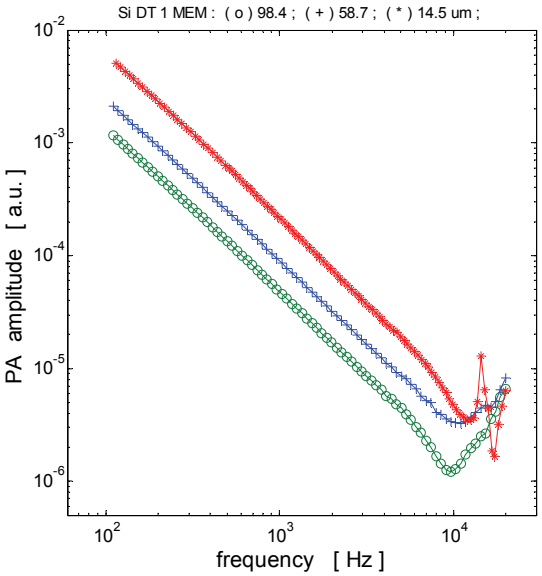

Figure 3. Experimental PA amplitude for different square membranes thicknesses (Si chip, frame 5x5 mm, square membrane 3x3 mm): (o) 98.4 μm; (+) 58.7 μm; (*) 14.5 μm;

Conclusion

The theoretical model for the frequency distribution of the PA elastic bending signals in a Si chip with square membrane, photogenerated by a uniform and intensity-modulated laser beam was given. The theoretical relations for PA signal, including the plasmaelastic and thermoelastic effects of the elastic bending were derived.

The experimental amplitude and phase were measured vs. frequency by the PA elastic bending method and compare with theoretical ones. These results showed that the PA elastic bending spectra are very

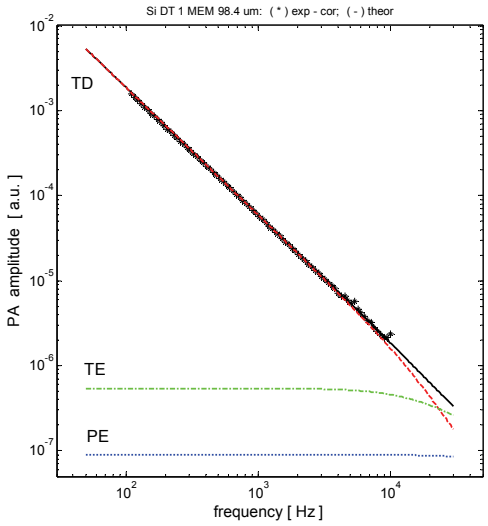

Figure 4. PA amplitude vs. frequency for square membrane (Si chip, frame 5x5 mm, membrane 3x3 mm, 98.4 μm thick): (*) experiment; (- -) TD; (-.-) TE; (...) PE component; (-) TD + TE + PE.

convenient for investigation micro- mechanical structures (the elastic natural modes – spontaneous elastic vibrations). This investigation is in progress. The PA elastic signal is the consequence of PE and TE effects in Si microstructure; these effects may have significant influence at frequencies below ~ 10 kHz.

Acknowledgement
This work was supported by the Serbian Ministry of Education and Science - the projects ON171016 and TR32008.

[1] D. M.Todorovic, P.M.Nikolic, Ch. 9 in Semiconductors and Electronic Materials, A. Mandelis, P. Hess (Eds)., SPIE Opt.Eng . Press, Belingham, Washington, 2000, 273-318.
[2] R. G. Stearns, G. S.Kino, Appl. Phys. Lett., 1985, 47, 1048-1050.
[3] D. M. Todorović, P. M. Nikolić, A. I. Bojičić, K. Radulović, Phys.Rev. B, 1997, 55(23), 15631-15642.
[4] A Rosencwaig, A. Gersho, J. Appl. Phys., 1976, 47(1), 64
[5] W. Jackson, N .M.Amer, J.Appl.Phys., 1980, 51(6), 3343.
[6] G. Rousset, F. Lepoutre, L. Bertrand, J.Appl.Phys., 1983, 54(5), 2383-2391.
[7] A.Rosencwaig, J. Opsal, D. L. Willenborg, Appl.Phys.Lett., 1983, 43(2), 166-168.
[8] J. Opsal, A. Rosencwaig, D. L.Willenborg, Appl.Opt., 1983, 22(20), 3169-3176.
[9] A.Rosencwaig, J. Opsal, W. L. Smith, D. L. Willenborg, Appl.Phys.Lett., 1985, 46(11), 1013-1015.
[10] J. Opsal, A. Rosencwaig, Appl.Phys.Lett., 1985, 47(5), 498-500.
[11] L. F. Perondi, L. C. M.Miranda, J.Appl.Phys., 1987, 62(7), 2955-2959.
[12] H. Dersh, N. M. Amer, Appl.Phys.Lett., 1985, 47(3), 292-294.
[13] S. M. Avanesyan, V. E. Gusev, N. I. Zheludov, Appl. Phys. A, 1986, 40, 163-166.
[14] S. M .Avanesyan, V. E. Gusev, Kvant. Elektron. (USSR), 1986, 13(6), 1241-1249.
[15] V. Sablikov, Soviet. Physics, Semicond., 1987, 21(12), 1319-1322.
[16] A.Prak, T. S. J.Lammerink, J.Appl.Phys., 1992, 71(10), 5242-5245.
[17] V. E. Gusev, Akust. Zhurn., (USSR), 1986, 32(6), 778-784.
[18] V. E. Gusev, E. G. Petrosyan, Akust. Zhurn., (USSR), 1987, 33(2), 223-232.
[19] D. M. Todorović, Rev. Sci.Instrum., vol. 2003, 74 (1), 578-581.
[20] Y. Song, B. Cretin, D. M. Todorović, P. Vairac, J.Phys.D: Appl Phys., 2008, 41, 155106.
[21] D. M. Todorović, B. Cretin, Y. Song, P. Vairac, J.Appl. Phys., 2010, 107, 023516(9p).
[22] D. M. Todorović, Y. Q. Song, Journal of Physics: Conference Series, 2010, 214, 012104.
[23] D. M. Todorović, P. M. Nikolić, Opt. Eng., 1997, 36(2), 432.
[24] D. M. Todorović, P. M. Nikolić, A. I.Bojicić, J.Appl.Phys., 1999, 85(11), 7716-7726.
[25] D. M. Todorović, M. D. Rabasović, D. D. Markushev, V. Jović, K. T. Radulović, Int J Thermophys, DOI 10.1007/s10765-012-1242

MACROMOLECULAR PHYSICAL CHEMISTRY

J-01-O

SYNTHESIS OF POLYANILINE-COLLAGEN COMPOSITES BY DOPANT-FREE POLYMERIZATION OF ANILINE IN AQUEOUS SOLUTION

A. A. Rakić[a], V. B. Pavlović[b], G. N. Ćirić-Marjanović[a]
[a]*Faculty of Physical Chemistry, University of Belgrade, Studentski Trg 12-16, 11158 Belgrade, Serbia*
[b]*Institute of Technical Sciences of SASA, Knez Mihailova 35/IV, 11000 Belgrade, Serbia*

Abstract
Polyaniline-collagen (PANI-collagen) composites were synthesized by the oxidation of aniline with ammonium peroxydisulfate (APS) in the presence of collagen in water without added acid. Electrical conductivity of PANI-collagen was in the range (0.7–6.8) × 10^{-3} S cm^{-1}. The increase of initial collagen amount lead to the decrease of aniline polymerization reaction rate. FTIR and Raman spectroscopies are used for resolving molecular structure of composites. The influence of collagen content on the molecular structure, morphology and physico-chemical properties of PANI-collagen composites was investigated.

Introduction
Conducting polymers that inherently conduct electricity, such as polyaniline (PANI), continue to find numerous novel applications in modern technology: rechargeable batteries, fuel and solar cells, antistatic and corrosion protection, sensors, catalysts, actuators, supercapacitors. The preparation of nanostructured conducting polymers and their composites has been the subject of intense research during the recent years owing to their significantly enhanced dispersibility and processibility, and improved performance in many applications in comparison with ordinary granular and colloidal conducting polymers [1]. Biocomposites of conducting polymers and biomacromolecules have received increasing attention during the last decade because of their potential applicability in biosensors, drug delivery, wound dressing, and scaffolds in tissue engineering. Special attention was paid to the biocomposites of PANI because of its tunable conductivity, simple and low-cost synthesis, environmental stability, and unique acid/base doping/dedoping chemistry. Composites of PANI with DNA, RNA, albumin, gelatin, cellulose, starch, chitosan, etc., have been investigated.

Our objective is to synthesize and characterize novel bionanocomposites of PANI and collagen, naturally occurring protein found in animals. The dopant-free template-free falling-pH method of the synthesis of nanostructured PANI [2] has been applied for the preparation of PANI-collagen composites. Characterization of the PANI-collagen samples by conductivity measurements, FTIR spectroscopy and scanning electron microscopy (SEM) has been performed.

Experimental

The aqueous solution (100 ml) of 0.5 M APS was poured into the solution of 0.4 M aniline (100 ml) containing defined amount of collagen, 10 g, 5 g, 1 g, 0.5 g, or 0.1 g. The precipitated product, PANI-collagen composite, was collected on a filter, rinsed, dried in vacuum and characterized by FTIR spectroscopy, SEM and conductivity measurement. As a reference sample, PANI was prepared by the same procedure, without collagen.

Results and Discussion

The temperature profiles for all the PANI-collagen syntheses have similar shape and reveal that the oxidation of aniline with APS in the aqueous solution of aniline and collagen proceeds in two rapid exothermic phases which are well separated by an athermal period (Fig.1, left). The increase of initial collagen mass leads to the significant prolongation of athermal period, i.e. to the delay of subsequent autoacceleration phase of aniline polymerization.

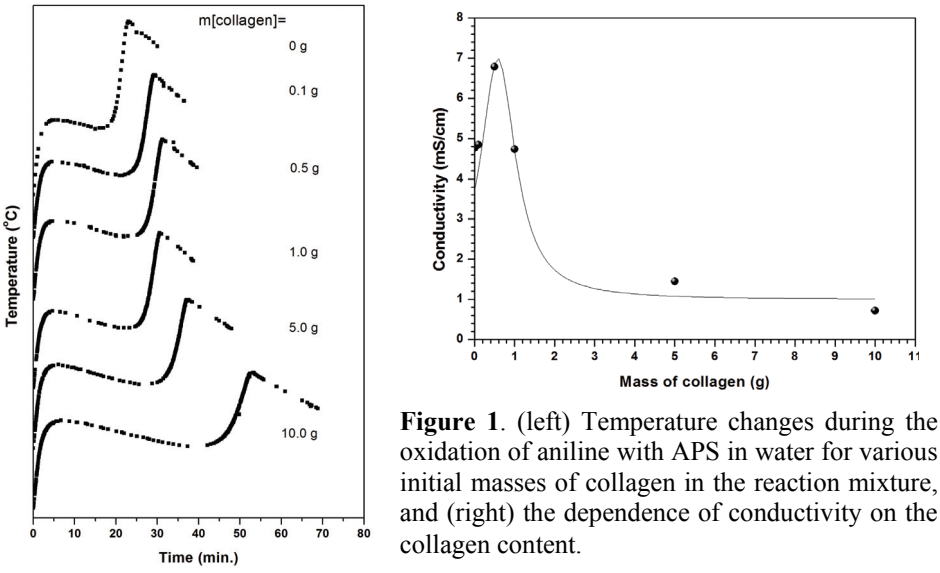

Figure 1. (left) Temperature changes during the oxidation of aniline with APS in water for various initial masses of collagen in the reaction mixture, and (right) the dependence of conductivity on the collagen content.

Electrical conductivity of PANI-collagen composites significantly depends on the content of collagen in the starting reaction mixture (Fig. 1, right). The highest conductivity (6.8×10^{-3} S cm^{-1}) exhibited the composite which was prepared with 0.5 g of collagen. The significant decrease of conductivity is observed for masses of collagen higher than 0.5 g.

SEM images (Fig. 2.) reveal the heterogeneity in the morphology of PANI-collagen samples. The content of nanorods and nanosheets decreases, while the content of hollow submicrospheres and nanogranules increases, as the initial mass of collagen increases from 0 g to 10 g. FTIR spectra of the PANI-collagen samples are very similar to the spectrum of PANI which was prepared without added collagen (Fig. 3). Characteristic PANI bands are observed at about 1579 cm^{-1},

1497 cm^{-1}, 1300 cm^{-1}, 1242 cm^{-1}, 1146 cm^{-1} and ~824 cm^{-1} [2]. The band attributable to collagen is observable at ~1660 cm^{-1} only in the spectra of the composites obtained with 5.0 and 10 g of collagen, and it corresponds to the amide I band (mainly due to the C=O stretching vibration).

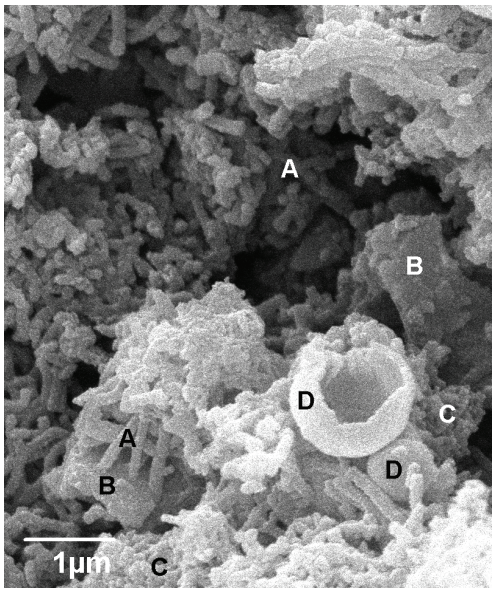

Figure 2. SEM image of the PANI-collagen sample prepared with 1.0 g of collagen: (A) nanorods, (B) nanosheets, (C) nanogranules, (D) hollow submicro- and microspheres.

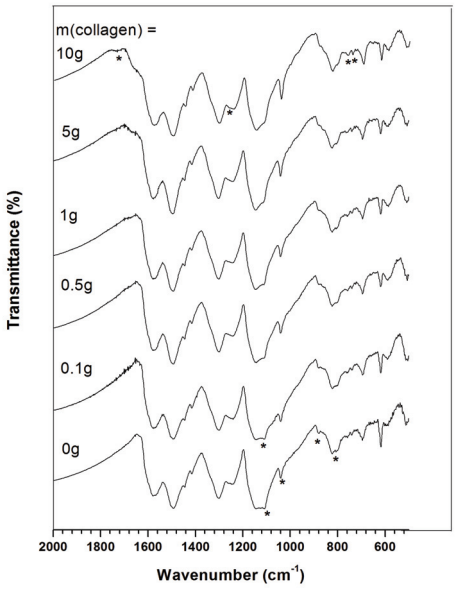

Figure 3. FTIR spectra of PANI-collagen and PANI samples.

Conclusion

Novel semiconducting bionanocomposites of polyaniline and collagen were prepared by the dopant-free template-free falling-pH method. The composites were characterized by various physico-chemical techniques.

Acknowledgement

This work was supported by the Ministry of Education and Science of the Republic of Serbia (projects OI 172043).

References

[1] G. Ćirić-Marjanović, Polyaniline Nanostructures, Chapter 2, in Nanostructured Conductive Polymers, A. Eftekhari (Ed.), London, John Wiley & Sons, 2010, 19–98.

[2] A. Rakić, D. Bajuk-Bogdanović, M. Mojović, G. Ćirić-Marjanović, M. Milojević-Rakić, S. Mentus, B. Marjanović, M. Trchová, J. Stejskal, Mater. Chem. Phys., 2011, 127, 501–510.

J-02-P

DOPANT-FREE POLYMERIZATION OF ANILINE IN THE WATER/ISOPROPANOL MIXTURE

A. A. Rakić, G. N. Ćirić-Marjanović
Faculty of Physical Chemistry, University of Belgrade,
Studentski Trg 12-16, 11158 Belgrade, Serbia

Abstract
Polyaniline (PANI) was synthesized by the oxidation of aniline with ammonium peroxydisulphate (APS) in the water-isopropanol mixture ($V_{isopropanol}/V_{water}$=1). Electrical conductivity of obtained PANI samples (~2 × 10^{-6} S cm^{-1}) was more than three magnitude lower compared to PANI (~5× 10^{-3} S cm^{-1}) synthesized in water. FTIR spectroscopy was used for resolving molecular structure, while scanning electron microscopy (SEM) was employed for observing the morphology of synthesised polymerization products. The influence of introduced isopropanol co-solvent and reaction time on molecular structure, morphology and properties of synthesized PANI was studied.

Introduction
The simple and low-cost synthesis, reversible acid/base doping/dedoping chemistry, redox activity, tunable conductivity, and environmental stability ranks PANI high among the most studied conductive polymers. The increased interest has recently been shown for efficient production of PANI nanostructures, such as nanofibers and nanotubes, due to their improved performance in many applications: sensors, catalysis, corrosion protection, data storage, actuators, membranes, solar and fuel cells, rechargeable batteries, and tissue engineering [1]. It has been recognized that the oxidation of aniline with ammonium peroxydisulfate (APS) as an oxidant in aqueous solution, starting at pH ≥ 3.5 and finishing at pH <2 (a falling-pH method), represents an efficient synthetic route to PANI nanostructures, without the use of any external template [2,3].

In order to investigate the impact of the change of solvent polarity on the morphology and physico-chemical characteristics of PANI, we have applied dopant-free template-free falling-pH method for the polymerization of aniline with APS in the mixture of water and isopropanol. Synthesized PANI samples were characterized by FTIR, SEM and conductivity measurements.

Experimental
The oxidation reaction started after pouring an aqueous solution (100 ml) of 0.5 M APS into vigorously stirred 0.4 M aniline solution (100 ml) in isopropanol. After defined time the precipitates were collected on a filter, rinsed, dried in vacuum and characterized by FTIR, SEM and electrical conductivity measurements. The conductivity of the samples pressed into pellets was measured between stainless

pistons, at room temperature, by means of an ac bridge (Waynne Kerr Universal Bridge B 224), at fixed frequency of 1.0 kHz, under pressure of 124 MPA. The samples produced at polymerization times 1.5 h and 24 h are denoted as PANI-IPA-1.5 and PANI-IPA-24, respectively. The referent PANI sample was obtained in water after 0.5 h by the same procedure and under the equivalent experimental conditions as those used for the PANI-IPA syntheses.

Results and Discussion

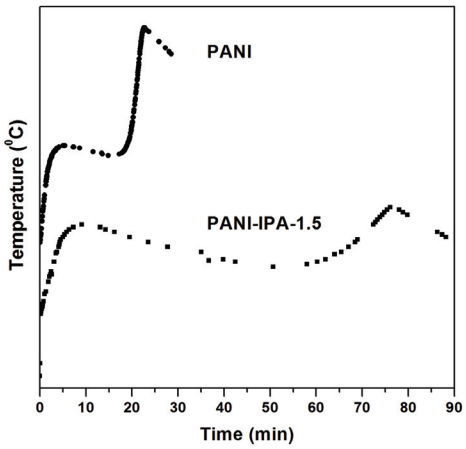

Figure 1. Temperature changes during the oxidation of aniline with APS in water (synthesis of PANI) and in the mixture water-isopropanol (synthesis of PANI-IPA-1.5).

The oxidation of aniline with APS proceeds in two distinct exothermic phases in both syntheses of PANI and PANI-IPA-1.5 (Fig. 1). However, the addition of isopropanol as a co-solvent remarkably slowed the polymerization. In this case the athermal period between two exothermic phases becames significantly prolonged (Fig. 1). The introduction of isopropanol into the reaction mixture was accompanied by the decrease of conductivity of polymerization product, from 4.8×10^{-3} S cm^{-1} for PANI synthesized in water, to 2.1×10^{-6} S cm^{-1} and 1.5×10^{-6} S cm^{-1} for PANI-IPA-1.5 and PANI-IPA-24 samples synthesized in water-isopropanol mixture, respectively.

PANI synthesized in water contains nanorods, nanosheets and nanogranules (Fig. 2A). The introduction of isopropanol as a co-solvent into the reaction system leads to the changes in the polymeric product morphology. In the sample PANI-IPA-1.5, nanorods were frequently flattened having the form of nanoribbons, the content of nanosheets was reduced, and some submicrospheres were observed (Fig. 2B). After longer time of synthesis (PANI-IPA-24), majority of nanostructures have been covered with granular PANI (Fig. 2C).

In the FTIR spectra characteristic bands of PANI are observed at about 1579 cm^{-1}, 1493 cm^{-1}, 1300 cm^{-1}, 1242 cm^{-1}, 1146 cm^{-1} and 824 cm^{-1} in all three synthesized samples. Intensity of the band at about 1146 cm^{-1}, which characterizes the conductivity of a sample, decreases in the order: PANI > PANI-IPA-1.5 > PANI-IPA-24. This is in accordance with the results of conductivity measurements. The band at ~756 cm^{-1}, which is indicative for *ortho*-coupling between monomeric units, is relatively much stronger in the spectra of samples synthesized in the presence of isopropanol.

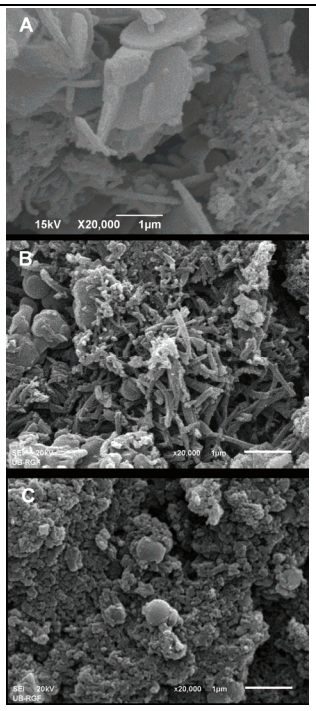

Figure 2. SEM images of: (A) PANI, (B) PANI-IPA-1.5, (C) PANI-IPA-24.

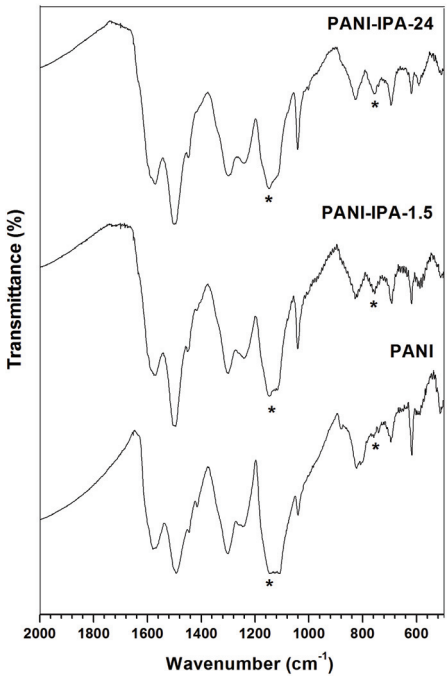

Figure 3. FTIR spectra of PANI and PANI-IPA samples.

Conclusion

Polyaniline synthesized by dopant-free template-free falling-pH method in water/isopropanol mixture had significantly changed physico-chemical properties compared to those of PANI synthesized by the same method in water. Isopropanol slowed down polymerization reaction, remarkably reduced conductivity of PANI and changed its molecular structure and morphology.

Acknowledgement

This work was supported by the Ministry of Education and Science of the Republic of Serbia (project OI 172043).

References

[1] G. Ćirić-Marjanović, Polyaniline Nanostructures, Chapter 2, in Nanostructured Conductive Polymers, A. Eftekhari (Ed.), London, John Wiley & Sons, 2010, 19–98.

[2] M.Trchová, E.N. Konyushenko, J. Stejskal, I. Šeděnková, P.Holler and G. Ćirić-Marjanović, J. Phys. Chem. B., 2006, 110, 9461–9468.

[3] A. Rakić, D. Bajuk-Bogdanović, M. Mojović, G. Ćirić-Marjanović and M. Milojević-Rakić, S. Mentus, B. Marjanović, M. Trchová, J. Stejskal, Mater. Chem. Phys., 2011, 127, 501–510.

J-03-P

POLYANILINE-DECAVANADATE HYBRID NANOMATERIAL: PREPARATION AND CHARACTERIZATION

N. Bošnjaković-Pavlović[1], I. Holclajtner-Antunović[1], A. Rakić[1], D. Manojlović[2], G. Ćirić-Marjanović[1]

[1]*Faculty of Physical Chemistry, University of Belgrade, Studentski Trg 12-16, 11158, Belgrade, Serbia*
[2]*Faculty of Chemistry, University of Belgrade, Studentski Trg 12-16, 11158, Belgrade, Serbia*

Abstract
Nanostructured polyaniline (PANI) sulfate/hydrogen sulfate was synthesized by the oxidative polymerization of aniline in water, using ammonium peroxydisulfate (APS) as an oxidant. PANI decavanadate (PANI-DV) organic-inorganic hybrid material was then prepared by the treatment of PANI sulfate/hydrogen sulfate with the excess of ammonium decavanadate solution. The incorporation of decavanadate anions into the PANI matrix was confirmed by inductively coupled plasma optical emission (ICP-OES) and FTIR spectroscopies. Scanning electron microscopy (SEM) revealed that the morphology of obtained PANI-DV consisted predominately from nanorods that formed a network. The electrical conductivity of PANI-DV was 4.4×10^{-7} S cm^{-1}.

Introduction
Polyaniline (PANI) is one of the most important conducting polymers, which has extensively been studied because of its simple and cost-effective synthesis by chemical/electrochemical oxidative polymerization of aniline, unique acid/base doping/dedoping chemistry, good electrical conductivity and environmental stability, electroactivity and other properties which enable its versatile applicability. The half-oxidized, protonated, electrically conductive form of PANI (emeraldine salt) contains, depending on synthetic route, various proportions of diamagnetic units $[(–B–NH^{+}=Q=NH^{+}–)_n(–B–NH–)_{2n}](A^{–})_{2n}$ and paramagnetic units $[(–B–NH^{+\bullet}–B–NH–)_n](A^{–})_n$, where B, Q and $A^{–}$ denote a benzenoid ring, quinonoid ring and dopant anion, respectively. The preparation of PANI nanostructures has been the subject of intense research during the recent years owing to their significantly enhanced dispersibility and processibility, and improved performance in comparison with ordinary granular and colloidal PANI in many applications such as sensors, catalysts, fuel cells, data storage, actuators, membranes, solar cell devices, rechargeable batteries, and electrochemical supercapacitors [1,2].

Polyoxometalates (POMs) are large class of inorganic metal (Mo,V,W)-oxygen macromolecular compounds. The applications of POMs are associated with

their interesting properties: high molecular weight, redox activity, polarity, surface charge distribution, electron and proton transfer/storage ability, and the formation of Brønsted acid centers [3]. They have many potential applications in catalysis, electrochromic devices, energy storage and conversion devices (batteries, supercapacitors, fuel cells), sensors, membranes, and biomedicine [3,4]. The decavanadate anion, $[V_{10}O_{28}]^{6-}$, belongs to the group of polyoxovanadates, which are especially interesting because of their biochemical activity. It is known that decavanadate (DV) affects lipid structures, protein function and several biochemical processes. It has been considered as the major protein-bounding vanadate species.

To improve the stability, conductivity and catalytic characteristics of POMs, and to make them less dependent on environmental conditions, as well as because many applications of POMs require their use in the form of solid materials or coatings, different procedures for the incorporation of POM into different substrates were developed. Since positive charge of conducting polymer chains may be counterbalanced with negative charge of polyoxoanions, conducting polymers such as PANI provide a suitable network for bulky polyoxoanions incorporation [5]. The purpose of the present work is to prepare and characterize novel nanostructured hybrid material PANI-DV.

Experimental

PANI sulfate/hydrogen sulfate was synthesized by the oxidative polymerization of aniline in water with APS as an oxidant, according to the previously reported procedure [5]. Ammonium decavanadate, $(NH_4)_6V_{10}O_{28}\times 5.14\ H_2O$ (ADV), was prepared according to the literature method [4]. PANI sulfate/hydrogen sulfate (1.0 g) was treated 40 min with 1.5×10^{-2} M ADV (80 ml) and then slowly filtered with continuous addition of 1.5×10^{-2} M ADV (320 ml) as an eluent during 3h. Obtained PANI-DV was dried in vacuum and characterized.

Results and Discussion

Nanorods (possibly nanotubes) predominate in the morphology of PANI-DV, as revealed by SEM (Fig. 1, left). Nanorods have a diameter of 60–90 nm and form a network. The morphology of PANI-DV is not significantly changed in comparison with the morphology of starting PANI sulfate/hydrogen sulfate [5]. The electrical conductivity of PANI-DV was significantly lower (4.4×10^{-7} S cm^{-1}) than the conductivity of starting PANI sulfate/hydrogen sulfate (2×10^{-3} S cm^{-1}), indicating that the process of ion exchange (replacement of sulfate/hydrogen sulfate anions with DV anions) was accompanied by partial deprotonation of PANI chains. The elemental composition of PANI-DV shows significantly decreased sulfur content (1.8 wt%) compared with the content of sulfur in PANI precursor (5.86 wt%). This means that sulfate and hydrogen sulfate ions were removed from the polymer matrix during the elution with ADV. ICP-OES analysis revealed that PANI-DV contains 5.2 wt% of vanadium, which corresponds to 9.8 wt% of DV.

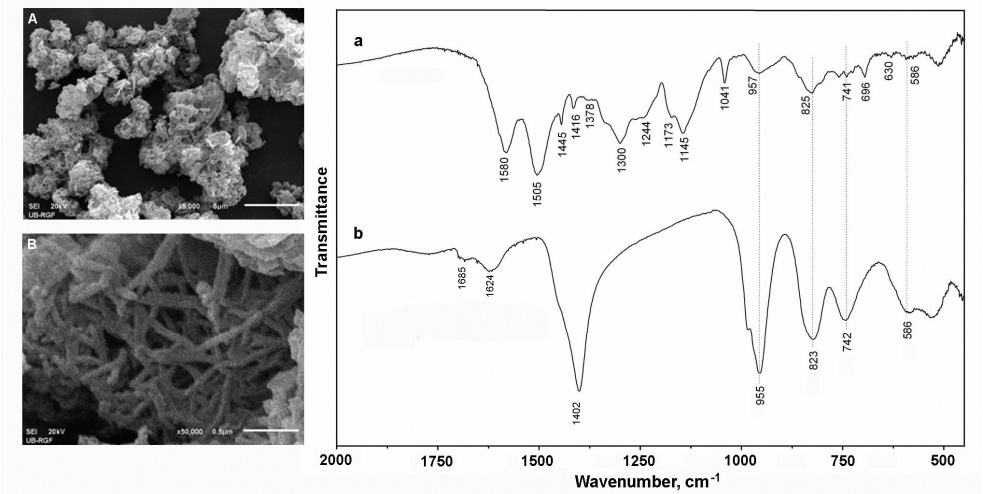

Figure 1. Left**:** SEM images of PANI-DV at two magnifications: (A) ×5000, (B) ×50 000. Right: FTIR spectra of PANI-DV (a) and ADV (b).

FTIR spectroscopy confirmed the incorporation of decavanadate ions into the PANI matrix by the characteristic bands of DV ion at 957, 825, 741, and 586 cm^{-1} (Figure 1, right), in the spectrum of PANI-DV. The analysis of bands in the region 2800–3300 cm^{-1} indicates hydrogen bonding interactions between PANI and DV.

Conclusion

Novel nanostructured hybrid material containing DV ions incorporated into the PANI supporting matrix was prepared and characterized by various techniques.

Acknowledgement

This work was supported by the Ministry of Education and Science of the Republic of Serbia (projects OI 172043).

References

[1] G. Ćirić-Marjanović, Polyaniline Nanostructures, Chapter 2, in Nanostructured Conductive Polymers, A. Eftekhari (Ed.), London, John Wiley & Sons, 2010, 19–98.

[2] M. Trchová, E.N. Konyushenko, J. Stejskal, I. Šeděnková, P. Holler, G. Ćirić-Marjanović, J. Phys. Chem. B., 2006, 110, 9461–9468.

[3] U. B. Mioč, M. R. Todorović, M. Davidović, Ph. Colomban, I. Holclajtner-Antunović, Solid State Ionics, 2005, 176, 3005–3017.

[4] M. R. Todorović, U. B. Mioč, I. Holclajtner-Antunović, D. Šegan, Mater. Sci. Forum, 2005, 494, 351–356.

[5] G. Ćirić-Marjanović, I. Holclajtner-Antunović, S. Mentus, D. Bajuk-Bogdanović, D. Ješić, D. Manojlović, S. Trifunović, J. Stejskal, Synth. Met. , 2010, 160, 1463–1473.

J-04-P

MICROSTRUCTURAL ORGANIZATION OF POLY(URETHANE-SILOXANE) COPOLYMERS

M. V. Pergal[1], D. Gođevac[1], V. V. Antić[2],
D. Vasiljević-Radović[1], J. Djonlagić[4]
[1]*ICTM-Center of Chemistry, University of Belgrade, Studentski trg 12-16, Belgrade, Serbia,* [2]*Faculty of Agriculture, University of Belgrade, Nemanjina 6, Belgrade, Serbia,* [3]*Faculty of Technology and Metallurgy, University of Belgrade, Karnegijeva 4, Belgrade, Serbia*

Abstract
The study reports the structure and properties of poly(urethane-siloxane) copolymers, intended to be used as potential biomedical implants. The structural elucidation of poly(urethane-siloxane)s was carried out by ^{1}H and quantitative ^{13}C NMR spectroscopy. The poly(urethane-siloxane) film surface was characterized by AFM and it was found that the surface smoothness increase with increasing soft poly(ε-caprolactone)-*b*-poly(dimethylsiloxane)-*b*-poly(ε-caprolactone) segment content. The synthesized poly(urethane-siloxane)s were double-crystalline multiblock polymers. Spherulite-like superstructures were observed in copolymers by AFM, which are believed to arise from crystallization of the hard and/or PCL segments, depending on the composition and the length of the hard segments.

Introduction
Thermoplastic polyurethane elastomers (TPUs) are the materials of choice in cardiovascular applications due to their desirable mechanical properties and good blood contacting properties. However, the biostability of TPUs in long–term medical applications remains a concern because many TPU compositions were reported to degrade significantly via hydrolytic and/or oxidative mechanisms. The use of poly(dimethylsiloxane) as the soft segment in biomedical TPUs provide a good alternative to polyester and polyether based TPUs, as these materials exhibit good biocompatibility, biostability, good thermal and oxidative stability, low surface energy, water repellency and physiological inertness. Biocompatibility of TPUs is strongly influenced by the chemical composition, surface hydrophilicity, degree of crystallinity and polymer surface topography [1].

In this work, the influence of the content of soft segments (40-95 wt.%) on the structure, degree of crystallinity and morphology of synthesized TPUs, which are essential for their biocompatibility evaluation, was investigated.

Experimental
Poly(urethane-siloxane) copolymers (TPUs), based on poly(ε-caprolactone)-*b*-poly(dimethylsiloxane)-*b*-poly(ε-caprolactone) (PCL-PDMS-PCL) as soft segment and 4,4′-methylenediphenyl diisocyanate (MDI) and 1,4-butanediol (BD) as hard segment, was synthesized by two-step solution polyaddition [2].

NMR experiments were performed on Bruker Avance 500 spectrometer. The AFM characterizations were conducted with an AutoProbe CP-Research SPM (TM Microscopes-Veeco) instrument (contact mode). Differential scanning calorimetry (DSC) was done using a DSC Q1000V9.0 Build 275 thermal analyzer.

Results and Discussion

NMR analysis showed that the syntheses of the polyurethanes were successful, resulting in TPUs with different lengths of the hard segments (HS). The synthesized TPUs showed that the average hard segment lengths increased from 1.2 to 14.4 MDI-BD units with increasing hard segment content.

Table 1. The composition of the poly(urethane-siloxane)s, the average length of the hard segments, RMS surface roughness (R_q) and results of DSC (second run).

Polymer	Hard segments, wt. %[a]	L_n (HS)[b]	R_q, nm	T_g, °C	T_{mHS}, °C	T_{mPCL}, °C	X_{cHS}, %	X_{cPCL}, %
TPU-5	4.5	1.2	84	-64	-	49	-	40
TPU-10	11.3	1.7	42	-58	-	47	-	37
TPU-15	13.4	1.9	22	-51	-	46	-	33
TPU-20	16.3	3.8	38	-56	209	45	3	30
TPU-30	26.9	4.0	48	-60	209	45	14	31
TPU-40	36.2	4.7	53	-53	208	44	13	29
TPU-50	47.2	10.2	59	-58	208	44	15	27
TPU-60	62.1	14.4	62	-49	213	36	14	14

[a] Determined by ^{1}H NMR spectroscopy; [b] Determined by quantitative ^{13}C NMR spectroscopy.

The TPUs were semicrystalline polymers in which both the hard and soft segments participated. Representative DSC curves corresponding to the second heating and cooling of the TPUs are presented in Fig. 1. The results indicated that the glass transition temperature of the PCL segments of the copolymers was in the range from -64 to -49 °C and for the prepolymer was -69 °C.

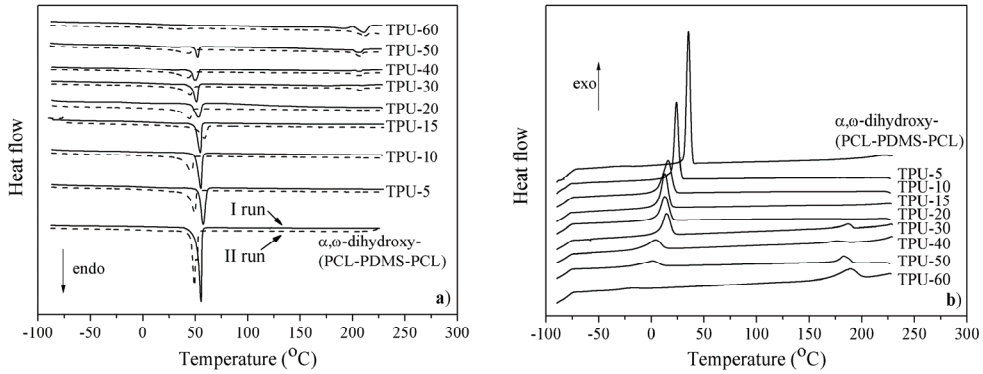

Figure 1. DSC thermograms of TPUs and the *α,ω*-dihydroxy-(PCL-PDMS-PCL) prepolymer obtained during: (a) heating and (b) cooling run.

The TPUs with HS higher than 20 wt.% showed melting temperature in the range from 208 to 213 °C corresponding to the melting of hard segments. In the thermograms of the TPU samples with a HS content below 20 wt.%, the absence of a melting peak indicates that the HS could not form a crystalline structure, probably because of their short chain length and the lack of their organization. The melting temperatures of PCL-segments in copolymers were decreased from 49 to 36 °C with increasing HS content. The degree of crystallinity of HS, X_{cHS}, tended to increase slightly with increasing content of MDI-BD segments, *i.e.*, HS length. The degree of crystallinity of PCL segments, X_{cPCL}, tended to decrease with increasing HS content, from which it can be concluded that the presence of the hard segments disturbed the crystal growth of the PCL segments.

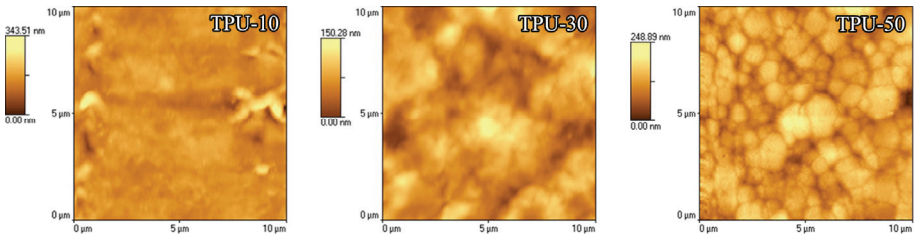

Figure 2. 2D AFM images of selected TPUs (scan area 10 µm × 10 µm).

The surface topography of the TPUs was observed by AFM. The distribution of hard and soft phases of the polymer surface was analyzed by 2D AMF images. It is known that the bright and darker regions represent the crystalline and the amorphous phases. AFM images clearly show that the formation of a spherulitic superstructure was increased on with increasing HS content. The average size of the spherulites was in the range from 1.2 to 1.5 µm. The obtained results showed that the samples with higher R_q values showed rougher copolymer surface.

Conclusions

The TPUs were double-crystalline polymers in which both the hard and soft segments participated. It can be concluded that average lengths from 3.8 to 14.4 MDI-BD units were effective segment lengths for a crystalline HS to be formed. The surface roughness was increased with increasing HS content. AFM images confirmed the presence of a spherulitic morphology, which arises from the crystallization of the PCL segments or/and hard segments depending on HS content.

Acknowledgments

This work was financially supported by the Ministry of Education and Science of the Republic of Serbia (No. 172062).

References

[1] S. Gogolewski, Colloid. Polym. Sci., 1989, 267, 757-85.
[2] M. V. Pergal, V. V. Antic, M. N. Govedarica, D. Godjevac, S. Ostojic, J. Djonlagic, J. Appl. Polym. Sci., 2011, 122, 2715-2730.

J-05-P

POLY(URETHANE-SILOXANE) NETWORKS BASED ON HYPERBRANCHED POLYESTER: MECHANICAL AND THERMAL PROPERTIES

M. V. Pergal[1], J. V. Džunuzović[1], R. Poręba[2], M. Špírková[2]
[1]*ICTM-Center of Chemistry, University of Belgrade, Studentski trg 12-16, 11000 Belgrade, Serbia,* [2]*Institute of Macromolecular Chemistry AS CR, v.v.i., Nanostructured Polymers and Composites Department, Heyrovskeho nam. 2, 16206 Praha 6, Czech Republic*

Abstract
Mechanical and thermal properties, hardness as well as degree of microphase separation of novel poly(urethane-siloxane) networks based on hyperbranched polyester of the forth pseudo generation were investigated using a variety of experimental methods. According to the combined results obtained from DSC and DMTA experiments, these networks exhibit two glass transition temperatures, of the soft and hard segments, and one secondary relaxation process. The results showed increase of crosslinking density and microphase separation and improvement of mechanical properties with decreasing content of soft ethylene oxide-poly(dimethylsiloxane)-ethylene oxide segment.

Introduction

Polyurethanes (PUs) are considered as one of the most useful class of polymers in coating applications. Contrary to other polymers, PUs have the advantage of using many available reactants as well as superior elastomeric properties. The careful design of PU structure is crucial to obtain good mechanical properties and adhesive strength of the coatings [1]. Macrodiol can play an important role to improve these properties. Poly(dimethylsiloxane) (PDMS) is attractive due to several advantages such as low surface tension, unique flexibility, low glass transition temperature, high thermal stability and good water resistivity. In the last few years, the PDMS has been used in PUs synthesis to improve the properties such as thermal stability, adhesive strength, shape memory properties and water resistance. Recently PU with PDMS has been proposed as a component of marine coating due to its smooth surface, to protect the coating from the fouler attachment. Due to the low surface energy of the PDMS, the PU coating is enriched by Si and makes the surface very smooth. The use of hyperbranched polyester (HBP) as crosslinker for the synthesis of PUs based on PDMS leads to the formation of networks with good chemical resistance and thermal properties [2].

In this work, mechanical and thermal properties, as well as hardness of PU networks based on aliphatic Boltorn® hyperbranched polyester of the forth pseudo generation were investigated using DSC, DMTA, and hardness measurements.

Experimental

The PU networks were synthesized by two-step polymerization in solution (NMP/THF) using α,ω-dihydroxy-(ethylene oxide-poly(dimethylsiloxane)-ethylene oxide) (EO-PDMS-EO, ABCR), 4,4′-methylenediphenyl diisocyanate (MDI, Aldrich) and hyperbranched aliphatic polyester of the forth pseudo generation with average hydroxyl functionality of 23 (BH-40, Perstorp Specialty Chemicals AB) [2]. The soft EO-PDMS-EO content was varied from 15 to 40 wt.%. In samples with digit numbers, the number shows the EO-PDMS-EO weight content.
Dynamic mechanical thermal analysis (DMTA) of samples was carried out on ARES G2 Rheometer (TA Instruments) in the temperature range from -135 to 180 °C, at strain 0.1 %. Differential scanning calorimetry (DSC) was performed on DSC Q1000V9.0 Build 275 thermal analyzer in the temperature range from -90 to 200 °C, at a heating rate of 10 °C/min. The hardness measurements of the PU films were performed on a Shore A apparatus (Hildebrand, Germany).

Results and Discussion

The influence of soft segment content on the viscoelastic properties of the polyurethane networks was investigated by dynamic mechanical thermal analysis of selected samples. Three peaks can be observed in the temperature dependence of *G*" (Fig. 1), indicating existence of microphase separation of PUs.

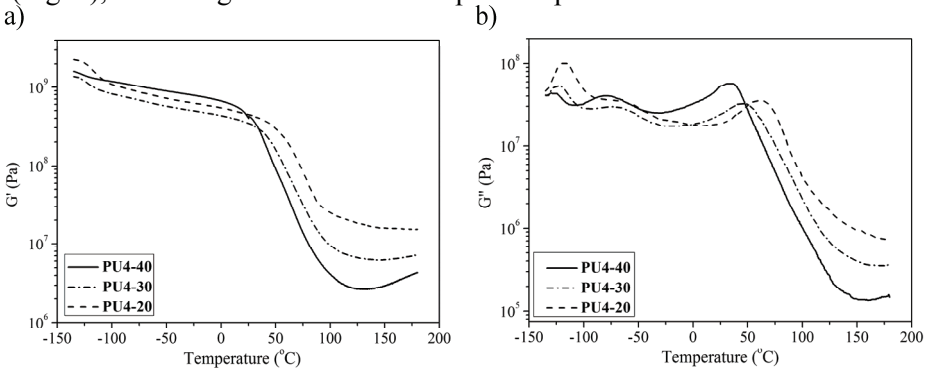

Figure 1. Storage (*G*') and loss (*G*") moduli of the PUs *vs*. temperature at 1 Hz and a heating rate of 3 °C/min.

From the Fig. 1 it can be observed that all investigated PUs show T_g of the soft EO-PDMS-EO segment, T_{gSS}, in the temperature range between -126 and -118 °C, due to the well phase separation of PDMS. Peak observed in the region between -80 and -67 °C is associated with the subglass relaxation process and is probably a consequence of the movement of the part of the chain which contains urethane groups connected to the Boltorn® HBP (BH-40). The third peak detected in the region between 35 and 61°C is ascribed to the glass transition temperature of the hard segments (MDI-HBP), T_{gHS}, (Table 1). From DMTA results, value of *G*' for PU samples is higher than values of the loss modulus in the whole investigated temperature region. This observation indicates that cohesion and stability of the PU network is not destroyed under investigated experimental conditions.

Table 1. Results of DSC, DMTA and hardness of PU networks

Sample	G''			$\nu\times10^4$ (mol/cm^3)	T_{gHS} (DSC) (°C)	Hardness (Shore A)
	T_{gSS} (°C)	T_2 (°C)	T_{gHS} (°C)			
PU4-40	-126	-80	35	9.08	49	94
PU4-30	-124	-72	47	18.48	54	96
PU4-20	-118	-67	61	44.40	56	98

Values of the crosslinking density, ν can be easily calculated from the rubbery plateau moduli and are summarized in Table 1. Crosslinking density of the synthesized PUs decreases with increasing soft EO-PDMS-EO content. The increase of the crosslinking density increased hardness of PUs from 94 to 98 Shore A (Table 1), which is in agreement with DMTA results.

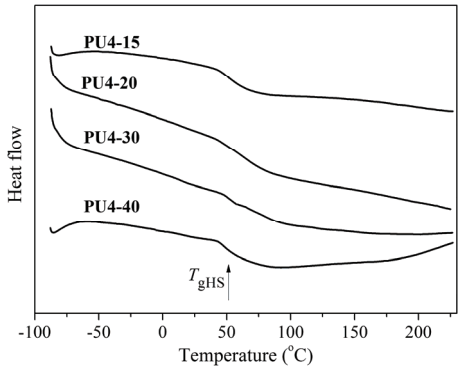

Figure 2. DSC thermograms (second run) of the selected synthesized PUs.

Thermal properties of the synthesized PUs were also examined by DSC (Fig. 2). A T_g of synthesized PUs decreases with increasing EO-PDMS-EO content from56 to 49 °C (Table 1). Higher T_g of PUs is attributed to increased hydrogen bonding and crosslinking density of samples.

Conclusions

DMTA results revealed existence of microphase separation of PUs due to presence of EO-PDMS-EO. Two thermal transitions were detected by DMTA and they depend on the soft segment content. The first one (at -126 to -118 °C), corresponds to the glass transition of soft segments. The second transition, located at 35 to 61°C, well detectable by DSC and DMTA, corresponds to the glass transition of hard segments. The second relaxation peak is located in the temperature region -80 to -67 °C. The results showed that the decrease of EO-PDMS-EO content enhanced microphase separation, improved mechanical properties and hardness of PUs.

Acknowledgments

This work was financially supported by the Ministry of Education and Science of the Republic of Serbia (No. 172062) and the Grant Agency of the Czech Republic (No. P108/10/0195).

References

[3] E. Žagar, M. Žigon, Prog. Polym. Sci, 2011, 39, 53-88.
[4] M. V. Pergal, J. V. Džunuzović, M. Kićanović, V. Vodnik, M. M. Pergal, S. Jovanović, Russ. J. Phys. Chem. A, 2011, 85, 2251-2256.

J-06-P

POLY(URETHANE-ESTER-SILOXANE) NETWORKS

J. V. Džunuzović[1], M. V. Pergal[1], V. V. Vodnik[2]
[1]*ICTM-Center of Chemistry, University of Belgrade, Studentski trg 12-16, 11000 Belgrade, Serbia*
[2]*Institute of Nuclear Science "Vinča", University of Belgrade, P. O. Box 522, 11001 Belgrade, Serbia*

Abstract
The waterproof performance and formation of hydrogen bonds in polyurethane (PU) networks based on Boltorn® hyperbranched polyester of the third pseudo generation (BH-30), α,ω-dihydroxy-(ethylene oxide-poly(dimethylsiloxane)-ethylene oxide) (EO-PDMS-EO) and 4,4'-methylenediphenyl diisocyanate (MDI) were studied in this work. Obtained results revealed that as the content of EO-PDMS-EO decreases, the degree of microphase separation increases, while the water resistance of the prepared PU networks decreases.

Introduction
The application of hyperbranched polyesters (HBP) or PDMS macrodiols for the preparation of polyurethanes has gained great attention over the last years, since these polymers have properties which can be applied to improve and modify performances of PUs for specific applications [1,2]. Besides, it has been shown that the combination of both, PDMS macrodiol and HBP, can also be used for the synthesis of PU networks [3]. Such networks are good candidates for coating applications, because numerous end functional groups in HBP provide fast curing and formation of highly crosslinked system with good mechanical properties, while the presence of PDMS improves thermal and surface properties and brings elasticity in such material, due to its low glass transition temperature. The aim of the present work is the investigation of the influence of EO-PDMS-EO content on the water resistance and the extent of hydrogen bonding in the polyurethane networks synthesized using Boltorn® hyperbranched polyester of the third pseudo generation, EO-PDMS-EO and MDI.

Experimental
PUs based on BH-30, EO-PDMS-EO and MDI were synthesized according to the procedure described elsewhere [3]. The last two numbers in the name of PUs represent EO-PDMS-EO content. FTIR spectra of the synthesized PUs were recorded using ATR NICOLET 380 FTIR spectrometer. Water absorption of the synthesized PUs was determined at room temperature by their immersion for 48 h in distilled water. The water contact angles of the synthesized PUs were determined on Krüss DSA100 instrument, using the sessile drop method, at 22 ^{o}C.

Results and Discussion
The chemical structure of PUs was examined by FTIR spectroscopy. In the FTIR spectra of PUs (Figure 1a) absorption bands characteristic for the amide II and

amide III vibrations (1258 cm^{-1} and 1537 cm^{-1}), overlapped bands of Si-O-Si and C-O-C groups (1015 and 1080 cm^{-1}), Si-CH_3 linkage (790 cm^{-1}), symmetric and asymmetric -CH_2- and -CH_3 (2961, 2903 and 2875 cm^{-1}), aromatic C=C (1596 and 1412 cm^{-1}) and H-bonded –NH stretching vibration (3306 cm^{-1}) are visible. The formation of urethane bonds was confirmed from the absence of isocyanate peak at 2260 cm^{-1}.

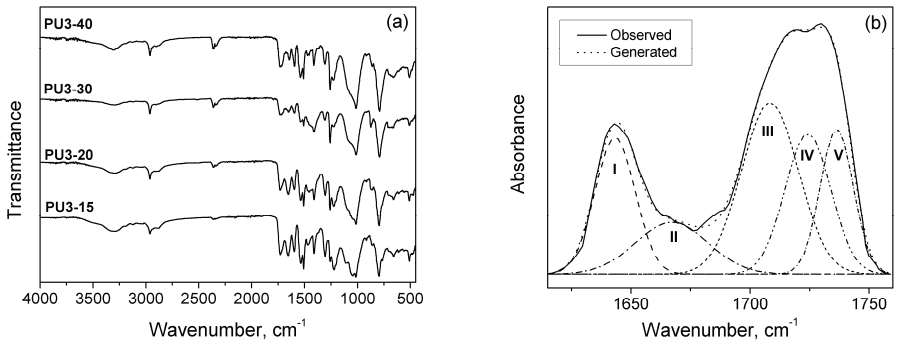

Figure 1. (a) FTIR spectra of PUs and (b) curve-fitting FTIR spectra of PU3-40.

Table 1. Curve fitting results of the C=O stretching regions from the PUs FTIR spectra.

Sample	Area I ($CO_{ester\text{-}H\ bonding}$), %	Area II ($CO_{order\ urethane\text{-}H\ bonding}$), %	Area III ($CO_{disorder\ urethane\text{-}H\ bonding}$), %	Area IV ($CO_{free\ ester}$), %	Area V ($CO_{free\ urethane}$), %
PU3-40	16.7	14.2	31.3	22.3	15.5
PU3-30	19.7	17.2	25.9	22.2	15.0
PU3-20	21.5	38.4	10.1	16.8	13.2

To investigate the extent of hydrogen bonding in the synthesized PUs and to obtain individual spectral bands and areas in the overlapping spectra of C=O region, the Gaussian deconvolution method (OriginPro 8) was applied. The absorbance region of the C=O groups of PU3-40 is given in Figure 1b, while curve fitting results for selected PUs are listed in Table 1. Five absorbance peaks were observed in the C=O region corresponding to the: H-bonded C=O groups from ester bonds (1645 cm^{-1}), H-bonded urethane C=O groups in ordered hard domains (1680 cm^{-1}), H-bonded urethane C=O groups in disordered domains (1710 cm^{-1}), free C=O groups from ester bonds (1725 cm^{-1}) and free urethane C=O groups (1735 cm^{-1}) [4]. As the content of EO-PDMS-EO decreases, the possibility for H-bonding between urethane groups and H-bonding between urethane and ester carbonyl groups generally increases, while the fraction of H-bonding between –NH urethane and ether oxygen from EO-PDMS-EO, free ester and free urethane C=O decreases. It can be concluded that ordering of the hard segment domains, i.e. the tendency of H-bonds formation between hard segments is more pronounced in samples with lower EO-PDMS-EO content, resulting in higher degree of microphase separation.

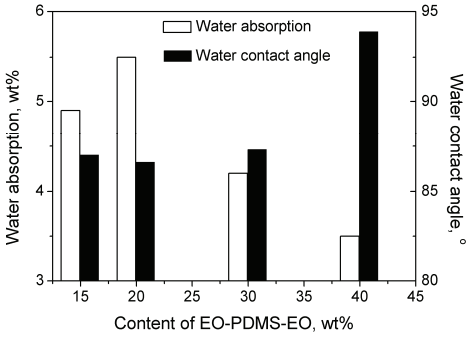

Figure 2. Values of the water absorption and water contact angles of the PU networks.

The waterproof performance of the PU networks was investigated by measuring their water absorption and water contact angle and obtained results are given in Figure 2. The weight percent of the water absorption decreases while the water contact angle increases as the EO-PDMS-EO content increases, due to the hydrophobic character of PDMS and possible migration of the EO-PDMS-EO to the surface of PUs.

Conclusions

The presented results revealed that the tendency of H-bonds formation between hard segments in prepared PU networks decreases with increasing EO-PDMS-EO content. The increase of EO-PDMS-EO content also induced better water resistance of PUs.

Acknowledgments

This work was financially supported by the Ministry of Education and Science of the Republic of Serbia (Project No. 172062).

References

[1] P. K. Maji, A. K. Bhowmick, J. Polym. Sci. Part A Polym. Chem., 2009, 47, 731-745.
[2] R. Hernandez, J. Weksler, A. Padsalgikar, J. Runt, Macromolecules, 2007, 40, 5441-5449.
[3] J. V. Džunuzović, M. V. Pergal, S. Jovanović, V. V. Vodnik, Hem. Ind., 2011, 65, 634-644.
[4] Z. S. Petrović, J. Ferguson, Prog. Polym. Sci., 1991, 16, 695-836.

J-07-P

MICROWAVE SYNTHESIS OF NEW STAR SHAPED POLYESTER POLYOLS BASED ON L-LACTIDE

I. S. Ristić1, M. Marinović-Cincović2, B. Pilić1, V. Simendić1, S. Cakić3

[1] *University of Novi Sad, Faculty of Technology, Bulevar cara Lazara 1, Serbia*
[2] *University of Belgrade, Vinča Institute of Nuclear Sciences, Serbia*
[3] *University of Nis, Faculty of Technology, Bulevar oslobodjenja 124, Serbia*

Abstract
The molecular architecture of biodegradable polymers can be adjusted by incorporating multifunctional polyols into the polyester backbone to obtain branched polymers. The aim of our work was to prepare biodegradable polyester polyols based on L-lactide and castor oil in presence of tin(II) 2-ethylhexanoate as catalyst in microwave field. The polyester polyol was synthesized by core-first method which involves a polymerization of L-lactide from OH groups on castor oil. FTIR and ^{1}H NMR spectroscopy measurements were used to confirm the molecular structure of the synthesized products. DSC measurements were used to evaluate the crystallinity of obtained polyols. Thermal stability was investigated by thermogravimetric analysis, and results have shown the dependence of thermal stability on the arm length of the star shaped polyesters.

Introduction
Biodegradable polymers are useful materials for medical and pharmaceutical applications. They have a hydrophobic backbone with hydrolysable anhydride and/or ester bonds that may hydrolyze to monomers in an appropriate medium. Fatty acids are considered as suitable candidates for the preparation of biodegradable polymers, because they are natural body components. Manipulation of mechanical and physical characteristics of these polymers can be achieved by variation of polymer architectures. Star-shaped polymers consist of at least three linear polymeric chains radiating from one single multifunctional branched point [1]. The main feature of star-shaped polymers, make them different from the linear analogues of identical molar masses, is their compact structure and the multiple functionality. Final properties of the resulting star-shaped polymers may be adjusted by choosing the respective chemical structure of an arm and core, depending on the required application [2]. The aim of this work was the synthesis of star-shaped polyester polyol based on L-lactide arms and castor oil as core.

Experimental
Materials
Monomer *(3S)-cis*-3,6-dimethyl-1,4-dioxane-2,5-dione (L-Lactide), 98% *(*purity) was purchased from Sigma-Aldrich, Wisconsin. Initiator castor oil (CO) having the hydroxy number ($OH_{\#}$) 170 mg KOH/g and acid value 1.27 mg KOH/g was

supplied from Merck Chemical Co. Catalyst tin(II) 2-ethylhexanoate (purity of 95%, density 1.251 g cm^{-3} at 25 °C) was supplied from Sigma-Aldrich.

Microwave synthesis of polyester polyol

Microwave polymerization of L-lactide initiated by castor oil was performed according to our previous work [3]. This involves the addition of the dry monomer and castor oil in the glass ampoule, followed by the addition of tin(II) 2-ethylhexanoate. Very short polymerization times were 10, 20 and 30 minutes and carried out in microwave reactor.

Characterisation of prepared samples

The characterization of molecular structure of obtained materials was carried out by FTIR Bomem Hartmann & Braun MB-series, in the band ranged from 400 to 4000 cm^{-1}. ^1H NMR spectra were recorded on Bruker DPX-300 NMR (300 MHz). Samples were dissolved in deutereted chloroform and chemical shifts are given in δ from Me_4Si as an internal standard. Thermal properties of the samples were investigated by differential scanning calorimetry (DSC) using Setaram 151R instrument (heating rate 10 °C min^{-1}) and thermogravimetric analysis (TGA) on Setaram Setsys Evolution-1750 instrument in nitrogen atmosphere (heating rate 20 °C min^{-1}).

Result and Discussion

In the FTIR spectrum of polyester asymmetrical valence vibrations of C-O-C of the aliphatic polylactide chains were shifted at 1187 cm^{-1}, and symmetrical valence vibrations of C-O-C of the aliphatic chain at 1090 cm^{-1}, compared with bands at 1276 and 1099 cm^{-1}, which appeared in monomer L-lactide. Bands at 1455 and 1383 cm^{-1} originated from asymmetric and symmetric bending vibration of C-H from CH_3, respectively. Band from valence vibration of C=O of aliphatic ester splits at two bands, at 1758 cm^{-1} (in poly(L-lactide) chains), and at 1745 cm^{-1} (in castor oil). In the ^1H NMR spectrum peak H1 originated from proton of terminal methyl group in ricinoleic acid (in castor oil), Figure 1.

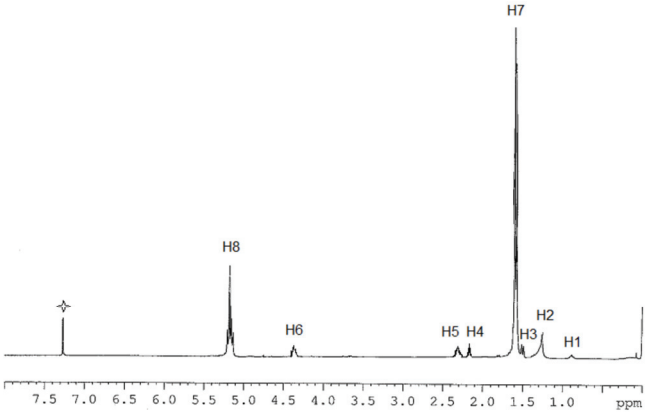

Figure 1. 1H NMR spectrum of obtained polyester polyol.

Peak H2 ascribed protons in methine groups from C4-C7 and C14-C17 in ricionoleic acid. When lactide polymerisation starts (from castor oil hydroxyl

groups) the peak related methylene proton attached to hydroxyl group (C***H***–OH) at 3.61 ppm [4] nearly disappeared, while a new peak at 4.32 ppm appeared, which represented the methylene protons connected to poly(L-lactide) chains. Peaks H3 and H5, due to chemical bonding between polylactide chains and castor oil, were shifted from 1.4 ppm and 2.21 ppm in crude castor oil [4] to 1.48 ppm and 2.42 ppm in polyester polyol. Peaks at 1.57 and 5.13 ppm (H7 and H8) were assignable to methyl and methine proton originated from lactic acid in main chain. Peak which noted with * originated from solvent.

The results of thermal property investigation were summarized in Table 1. For all synthesized samples was observed crystallization and melting from poly(L-lactide) arms. As expected melting temperature of samples increased as molecular masses of poly(L-lactide) arms increase. For star-shaped polyesters with the different arm length which was denoted by the molar mass of samples, the TGA curves show degradation temperature higher than 295 °C. Longer arms actually mean the higher molar mass of samples which can effectively enhance thermal stability.

Table 1. The DSC and TG data of different polyester polyol samples.

Sample name	T_g (°C)	T_c (°C)	T_m (°C)	T_{dec} (°C)
PE-ol-3000	45.5	86.4	130	295
PE-ol-4000	44.2	82.1	130.8	300
PE-ol-5000	43.8	91	133.2	324
PE-ol-6000	40.6	83.3	134.6	330

Conclusions

Star-shaped polyester polyol was obtained by polymerization of L-lactide, using, as an initiator, castor oil. Used polymerization method can be a fundamental technique for producing a low-melting polyol derived from renewable resources. FTIR and ^{1}H NMR spectroscopy confirmed presumed structures of obtained star shaped polymers. The polyester polyol has low crystallinity and a low melting point, so that its working properties is good when used in various medical and pharmaceutical applications. The investigation of thermal degradation by TGA method indicated that the novel star-shaped polyesters with higher molar masses have enhanced thermal stability.

Acknowledgment

This paper was supported by Ministry of Education and Science-Republic of Serbia, project number III 45022.

References

[1] S. Bywater, Adv. Polym. Sci., 1979, 30, 89–116.

[2] P. F. Rempp, P. J. Lutz, Polymeric materials encyclopedia, vol. 10. Boca Raton: CRC Press, 1996, 7880–7885.

[3] Lj. Nikolic, I. Ristic, B. Adnadjevic, V. Nikolic, J. Jovanovic, M. Stankovic, Sensors, 2010, 10, 5063-5073.

[4] E. Mistri, S. Routh, D. Ray, S. Sahoo, M. Misra, Ind. Crop. Prod., 2011, 34, 900–906.

J-08-P

THE EFFECT OF IONIC CONTENT ON THE THERMAL PROPERTIES OF ANIONIC POLYURETHANE DISPERSIONS

S. Cakić[1], I. S. Ristić[2], D. T. Stojiljković[2], J. Budinski-Simendić[2]

[1] *University of Niš, Faculty of Technology, Bulevar oslobodjenja 124, Serbia*
[2] *University of Novi Sad, Faculty of Technology, Bulevar cara Lazara 1, Serbia*

Abstract
The thermal stabilities of waterborne polyurethane dispersions have been correlated with content of ionic groups by changing the amount of dimethylol propionic acid (4.5, 7.5 and 10 wt% to the prepolymer weight). Three water-based polyurethane dispersions were synthesized by modified dispersing procedure using polycarbonate diol, isophorone diisocyanate, dimethylol propionic acid, triethylamine and ethylenediamine. The effect of the dimethylol propionic acid content on the thermal properties of polyurethane films was measured by TGA and DSC methods. The physico-mechanical properties, such as hardness, adhesion test and gloss of the dried films were also determined considering the effect of dimethylol propionic acid content on coating properties.

Introduction

Water-based polyurethane dispersion (PUD) show very good mechanical and chemical properties and match the regulatory pressures for low volatile organic compound (VOC) emission. Polycarbonate diols used as the soft segment component in polyurethane synthesis are usually produced from dimethylcarbonate or ethylene carbonate and a linear aliphatic diol [1]. The properties of polyurethane dispersions are related to their chemical structure and they are mainly determined by the interaction between the hard and soft segments and/or between the ionic groups.

In the present study, water-based polyurethane dispersions, with different molar ratio of polycarbonate diol (PCD) to dimethylol propionic acid (DMPA), were prepared by the modified dispersing process. The aim was the investigation of PUDs' structure-thermal properties relationships. The effect of molar ratio of polycarbonate diol to DMPA on the thermal properties of the polyurethane dispersions was investigated.

Experimental

Materials

Polycarbonate diol T5652 with a molecular weight of 2000 (hydroxyl value 56.3 mg KOH/g) was kindly provided by Asahi Kasei Corporation. Isophorone diisocyanate (IPDI) and DMPA were supplied by Aldrich. Ethylenediamine (EDA) was obtained from Zorka, Serbia; 1-methyl-2-pyrrolidone (NMP), dimethyl

formamide (DMF) and triethylamine (TEA) were received from Merk-Schuchardt. The dibutyltin dilaurate used as catalyst was supplied by Bayer AG.

Synthesis of the waterborne polyurethane dispersions

Three waterborne polyurethane dispersions were prepared using NCO/OH = 1.5 by method in which the dispersing procedure was modified. In the modified procedure only the dispersing stage was varied compared to the standard procedure. The prepolymer solution was mixed with a small amount of deionized water for dispersion of polymer in water. Solvent was added to reducing the viscosity, if necessary. The DMPA content was 4.5, 7.5 and 10 wt. % (with respect to the prepolymer weight), in order to change the ionic-group content in the polyurethane ionomers. The formulations used in the preparation of the polyurethane dispersions are summarized in Table 1.

Table 1. The compositions of synthesized polyurethane dispersions.

Sample	IPDI (g)	PCD (g)	DMPA (g)	TEA (g)	EDA (g)	Water (g)	DMPA/PCD (mol/mol)	TRS (%)
PUD 1	20	60	4 (4.5)[a]	3	0.9	204	1.0	30.1
PUD 2	32	60	8 (7.5)	6	1.8	251	2.0	30.0
PUD 3	40	60	12 (10)	9	1.8	280	3.0	30.3

[a] Percentage of DMPA content based on prepolymer weight

Characterization of obtained samples

Polyurethane films were prepared by casting the aqueous dispersions on leveled glass surfaces and dried at room temperature for 7 days, and then at 60 ^{o}C for 12h. Thermogravimetric analyses (TGA) were performed on the Setaram Setsys Evolution-1750 instrument. Samples were heated from 30 °C to 600 °C at the heating rate of 20 °C min^{-1} in nitrogen atmosphere with the gas flow rate of 20 cm^{3} min^{-1}. Differential scanning calorimetry (DSC) was performed on Setaram 151R instrument. The non-isothermal measurement was scanned from −60 to 150 °C with heating rate 5 °C min^{-1}.

Results and discussion

The thermal stability of the polyurethanes was determined by TGA, Figure 1a.

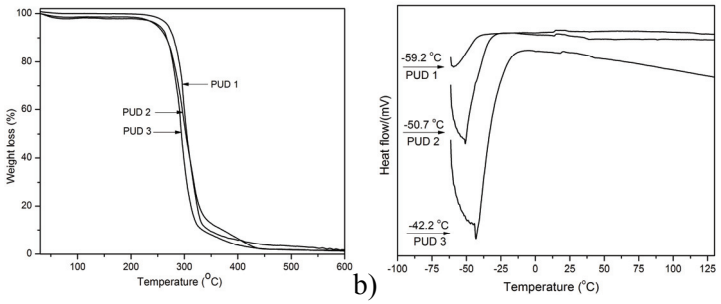

a) b)

Figure 1. Thermal properties of cured films of PUD 1, PUD 2 and PUD 3
a) TG curves and b) DSC curves.

According to TGA results the decreasing of DMPA content results in slight increase of the decomposition temperature.

The DSC thermograms (Figure 1b) showed only one glass transition temperature. The T_g value of the polyurethane ionomer increases by increasing DMPA content. As expected, increasing DMPA content i.e., hard segment, leads to an increase in the glass transition temperatures of the polyurethane ionomer due to restriction of the soft segment motions by the hard segments [2].

In Table 2 physical and mechanical properties of coating are given. It can be observed from presented results that sample with the highest ionic groups content, PUD 3 exhibits better hardness properties than samples PUD 1 and PUD 2.

Table 2. Physical and mechanical properties of polyurethane films.

Sample	Hardness (s)	Gloss (%)	Adhesion
PUD 1	32.2	147.6	5B
PUD 2	51.0	122.7	5B
PUD 3	67.9	121.7	5B

This is in agreement with previous conclusion that an increase in the ionic groups as hard segment content increased the extent of crosslinking of the polyurethanes. The gloss of the polyurethanes decreases by increasing the DMPA content.

Conclusions

The thermal stability of the polyurethane ionomer was increased by decreasing the DMPA content due to the lower hard segment content. The glass transition temperatures of the polyurethane ionomer was increased by increasing DMPA content, due to restriction of the soft segment motions caused by the hard segments. The increasing of the DMPA content i.e. hard segment caused the increasing of König hardness of the coatings, whereas the gloss of the coatings decreased.

Acknowledgment

This paper was supported by Ministry of Education and Science-Republic of Serbia, project number III 45022 and TR 33034.

References

[1] E. Foy, J.B. Farrell, C.L. Higginbotham, J. Appl. Polym. Sci., 2009, 111, 217–227.

[2] V. G-Pacios, V. Costa, M. Colera, J.M. M-Martinez, Int. J. Adhes. Adhes., 2010, 30, 456–465.

J-09-P

CHARACTERISATION OF EXOPOLYSACCHARIDE PRODUCED BY BACILLUS SP. NS032

J. Stefanović[1], D. Ilić[2], B. Kekez[2], G. Gojgić-Cvijović[1], D. Jakovljević[1] , M. Vrvić[1,2]

[1]IChTM - Department of Chemistry, University of Belgrade, Njegoševa 12, P.O. Box 473, 11000 Belgrade, Serbia (jovana_stefanovic@chem.bg.ac.rs)
[2]Faculty of Chemistry, University of Belgrade, Studentski trg 12-16, P.O. Box 51, 11158 Belgrade, Serbia

Abstract
In this study, the main structural monomer units and configuration of their glycosidic linkages of a exopolysaccharide obtained from a strain of *Bacillus licheniformis* was investigated. The chemical structure of this polymer, after purification of crude material, was analyzed by chemical methods, planar chromatography, elemental analysis and FTIR.

Introduction
Microbial exopolysaccharides are the group of biopolymers whose structural chemistry is very complex. Usually some types of microorganisms can be characterized by the presence of several carbohydrate polymers. The economic significance of these compounds is related to the fact that some of these polymers is nowadays widely accepted products of biotechnology, while others are in various stages of research. The use of microbial polymers varies widely due to good mechanical properties for application as fiber, films, adhesives, rheology modifiers, hydrogels, emulsifiers, and drug delivery agents. Biopolymers with industrial application are often bacterial and fungal products, like levan, dextran, β-glucan, pullulan. In this work we reported a route to produce of purified exopolysaccharide produced by strain of *Bacillus licheniformis,* and determination of main structural characteristics of this polymer.

Experimental
Exopolysaccharide was produced by strain of *Bacillus licheniformis* which was isolated from petroleum sludge sample taken from Oil Refinery Novi Sad. The strain was identified using 16S rRNA gene sequence analysis [1]. The organism was cultivated in sucrose broth for 10 days at 28 oC [2]. After removal of biomass the crude polysaccharide was isolated from fermentation culture by precipitation with two volumes of ethanol.
Polymer was analyzed for its carbon, hydrogen and nitrogen content using the Vario EL III device (GmbH Hanau Instruments, Germany). Nitrogen content usually was indication for the presence of protein as impurities. After treatments with Dnase, Rnase and Pronase and dialysis, purified polysaccharide was precipitated by acetone and lyophilized. In this way was obtained purified polysaccharide, without nitrogen, with content of C and H that corresponded to polysaccharide molecules (Table 1.). Monomer components was determined by planar chromatography of the acid hydrolizate of the glycan. The ATR-IR spectrum of pure polysaccharide was obtained

using Thermo Nicolet 6700 FT-IR Spectrophotometer with Smart Orbit Diamond ATR (attenuated total reflectance) accessory.

Results and Discussion

Planar chromatography of the hydrolyzed crude polysaccharide, comparing with standards of authentic monosaccharides, showed two main components, fructose and glucose, in about equal proportions. After further treatments, in hydrolysate of purified polymer was detected only one component, D-Fructose, which indicated that investigated polymer is fructan. Additional evidence that purification of polysaccharide was successful was found in the results of elemental analysis of crude and purified polymer (Table 1). The FT-IR spectrum of the purified polysaccharide showed the spectral pattern typical for polysaccharides. As shown in Fig.1, absorption bands between 1128 cm^{-1} and 1014 cm^{-1} corresponded to C-O-C and C-O-H stretching vibrations [3], the bands in the range of 1200-1500 cm^{-1} ascribed to C-H deformation vibration, the band at 1645 cm^{-1} was due to bound water. Strong, wide band at 3000–3500 cm^{-1} and band at 2936 cm^{-1} was assigned to the hydroxyl groups stretching vibration of polysaccharide and C-H stretching [4]. Absorption band in the anomeric region (950-700 cm^{-1}) at 891 cm^{-1} is specific for the β-configuration of the glycosidic linkages. Based on the FT-IR spectra it was concluded that investigated polymer had β-configuration of glycosidic linkages.

Table 1. Elemental chemical composition.

	% N	% C	% H
Crude sample	7.44	30.58	5.13
Purified sample	/	44.42	6.20

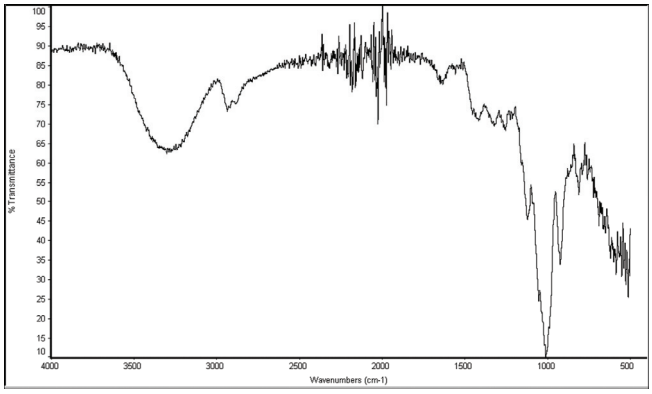

Figure 1. FTIR spectrum of purified exopolysaccharide produced by *B. licheniformis.*

Conclusion

The present study showed, on the basis of chemical methods, planar chromatography, elemental analysis and FTIR, that investigated exopolysaccharide is homopolymer,

composed of a D-fructose, as the O-specific monomer, with β-configuration of the glycosidic linkages.

Acknowledgement. This work was supported by the Ministry of Education and Science of the Republic of Serbia through Project III 43004.

References

[1] G. D. Gojgic-Cvijovic, J. S. Milic, T. M. Solevic, V. P. Beskoski, M. V. Ilic, L. S. Djokic, T. M. Narancic, M. M. Vrvic, Biodegradation, 2012, 23, 1-14.
[2]. J. Liu, J. Luo, Y. Sun, H.Ye, Z. Lu, X. Zeng, Biores. Technol., 2010, 101, 6077-6083.
[3] M. Wu, Y. Wu, J. Zhou, Y. Pan, Food Chemistry, 2009, 113,1020–1024.
[4] M. Mathlouthi, J. L. Koenig, Adv. Carbohydr. Chem. Biochem., 1987, 44, 7–89.

J-10-P

SYNTHESIS OF GUM ARABIC-NATAMYCIN CONJUGATE

J. R. Stefanović[1], D. M. Jakovljević[1], G. Đ. Gojgić-Cvijović[1], M. M. Vrvić[2]
[1]*IChTM - Department of Chemistry, University of Belgrade, Njegoševa 12, P.O. Box 473, 11000 Belgrade, Serbia (jovana_stefanovic@chem.bg.ac.rs)*
[2]*Faculty of Chemistry, University of Belgrade, Studentski trg 12-16, P.O. Box 51, 11158 Belgrade, Serbia*

Abstract
In this work, natamycin, a polyene antibiotic belonging to the family of macrolides, was coupled to the periodate oxidized polysaccharide gum Arabic. Resulting conjugate was characterized by UV-Vis and FT-IR data.

Introduction

Natamycin (pimaricin) is a polyene macrolide antibiotic produced during fermentation by *Streptomyces natalensis*. This antibiotic (Fig.1.) Has been used for many years in the food industry as well as in veterinary medicine, but insolubility in water limits its wider use. Gum Arabic is a water soluble, highly branched complex polysaccharide, comprised mostly of galactose, arabinose, rhamnose, and glucuronic acid. This polymer is used in many fields due to non-toxicity, water solubility, and biocompatibility. In order to increase solubility of natamycin, coupling of periodate oxidized polysaccharide gum Arabic and antibiotic was performed. Resulting conjugate was characterized by UV-Vis and FT-IR data. Obtained conjugate was soluble in water.

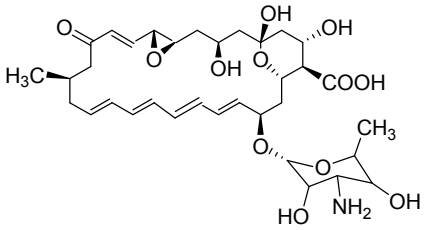

Figure 1. Structure of natamycin.

Experimental

Oxidation of gum Arabic to polyaldehyde derivative was done with sodium periodate in aqueous solution at 20 °C. Excess periodate was removed from reaction mixture by dialysis and oxidized polymer was lyophilized. Aldehydo groups in polysaccharide were determined by titration with standardized iodine solution [1]. In these conditions, sample of 50% oxidized gum Arabic was obtained. Coupling reaction between oxidized gum Arabic and natamycin was done in borate buffer (pH 9,1) in the dark, with continuos stirring, at 40 °C, during 48 h. Resulting conjugate was purified by dialysis and lyophilized.

Results and discussion

Synthesis of gum Arabic-natamycin conjugates was achieved by coupling reaction between aldehyde groups of oxidized polysaccharide and amine groups of antibiotic. Coupling reaction was monitored by UV-Vis (GBC Cintra 40 spectrophotometer) and IR (Nicolet 6700, in ATR mode) spectroscopy, by comparing spectra of oxidized polysaccharide and synthesized conjugate. UV spectra of native and oxidized gum Arabic do not have absorption in UV-Vis range (Fig.2a). After coupling reaction, spectrum of synthesized conjugate was significantly different (Fig.2b), with absorptions (λmax 294, 309, and 324 nm) slightly shifted in relation to natamycin [2]. Based on this, it can be concluded that aldehyde groups introduced in gum Arabic molecule are successfully coupled with antibiotic.

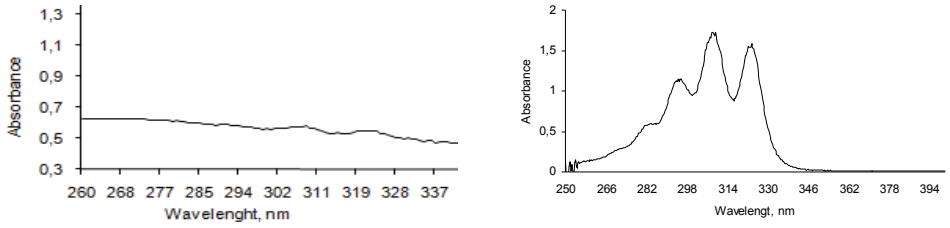

a) *b)*

Figure 2. UV spectra of oxidized gum Arabic (a) and gum-arabic-natamicyn conjugate (b).

FT-IR data suggest the chemical bonding between oxidized gum Arabic and natamycin, too. FT-IR spectrum of oxidized glycan (Fig. 3a) showed a strong band in the 3000-3500 cm−1 region from OH stretching, band at 2800–3000 cm–1 correlated to CH2 stretching, stronger band at 1642 cm–1 and the weak band at about 1400 cm–1 corresponded to COO-asymmetric and COO-symmetric stretching, respectively. The characteristic bands of dialdehyde glycan at 1730 cm-1 and 880 cm-1 correlated to the aldehyde symmetric (C=O), and the hemiacetal, respectively [3]. FT-IR spectrum of the pure natamycin showed bands at 3277 cm-1 (–NH2 deformation), 1715 cm-1 (-C=O vibration), 1695 cm-1 (ester function), 1577 cm-1 (CH=CH stretch), 1266 cm-1 (C-O-C epoxy), 1142 cm-1 (=C-O-C= vibration). FT-IR spectrum of conjugate (Fig.3b) showed absorption bands characteristic for both, gum Arabic and antibiotic.

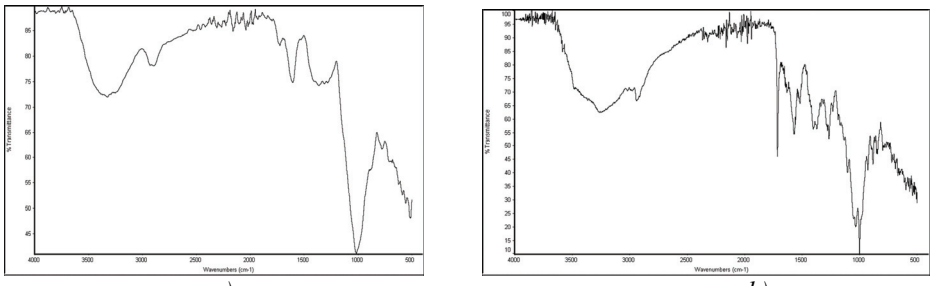

a) *b)*

Figure 3. FT-IR spectra of oxidized gum Arabic (a) and gum Arabic-natamycin conjugates (b).

Conclusion

The synthesis of gum Arabic-natamycin conjugate was achieved by covalent coupling between oxidized polysaccharide and antibiotic. Conjugate was characterized by UV-Vis and FT-IR data. Significantly increasing the solubility in water of obtained product can be indication for potential new uses in various pharmacological applications.

Acknowledgement. This work was supported by the Ministry of Education and Science of the Republic of Serbia through Project III 43004.

References

[1] G. Dryhurst, Periodate Oxidation of Diol and Other Functional Groups, Pergamon Press, London, 1966, 116.
[2] K.Dornberger, D. Voigt, W. Ihn, J. Vokoun, H. Thrum, Tetrahedron, 1976, 32, 3069-3073.
[3] U. J. Kim, S. Kuga, M. Wada, T. Okano, T. Kondo, Biomacromolecules 2000, 1, 488-492.

J-11-P

CELLULOSE ORIENTATION AND PURITY ASSESSMENT AFTER TWO DIFFERENT PROCEDURES OF CELL WALL ISOLATION FROM MAIZE STEMS. A COMBINED MICROSCOPIC FLUORESCENCE DETECTED LINEAR DICHROISM AND IMAGE ANALYSIS STUDY

D. Djikanovic Golubovic[1], A. Savic[1], J. Simonovic[1], G. Steinbach[2], M. Jeremic[3], G. Garab[2], K. Radotic[1]

1. *Institute for Multidisciplinary Research, University of Belgrade, Kneza Viseslava 1, Belgrade, Serbia*
2. *Institute of Plant Biology, Biological Research Center, Hungarian Academy of Sciences, H-6701 Szeged, Hungary*
3. *Faculty of Physical Chemistry, University of Belgrade, Studentski Trg 12, 11000 Belgrade, Serbia*

Abstract

The effects on cellulose orientation and purity of two different methods for cell wall isolation from maize stems were investigated by using fluorescence-detected linear dichroism (FDLD) microscopy technique. Image analysis has shown that treatment with sulfuric acid have provided better results than previously applied method for cell wall isolation including enzymatic treatment.

Introduction

One of the most promising new sources for biofuel is "cellulosic ethanol", made from the cellulose contained in fibrous plant material such as cornstalks, grasses and forest trimmings. Maize is nowadays very important plant source for bioethanol. The main problem in obtaining pure cellulose is impossibility to separate it completely from lignin, due to very strong connection between these two polymers in the cell wall.

Linear dichroism (LD) of cell walls carries important information on their molecular organization. We measured LD of of the maize stem cell walls by differential polarization fluorescence imaging [1]. The samples were isolated by two different procedures. The cell wall fragments were stained by Congo Red which predominantly binds to cellulose, a major cell wall component that determines its anisotropy. By monitoring FDLD of the cell walls after various treatments, we could trace the degree of cellulose purity in the intermediate steps during cell wall isolation. FDLD image analysis show different degrees of anisotropy and purity of cellulose contained in the cell

wall. The structural changes were in parallel followed by using FTIR spectroscopy.

Material and methods

Cell walls were isolated from maize stem and purified according to a procedure of Chen *et al.* [2]. Other way of isolation of cell wall is with sulphuric acid [3] and then we treated sample with high pressure and strong mechanical force in FastPrep-24.

The samples were stained with Congo Red, which has been shown to intercalate into the cellulose matrix [4]. Samples were incubated for 2 h in 1 % (w/v) solution of Congo Red (Fluka) at room temperature.

Cell wall samples were measured in the differential polarization laser scanning microscope (DP-LSM) (Carl Zeiss Jena, Jena, Germany).

Results and discussion

During the imaging process, FDLD image and fluorescence emission image were stored as two separate channels. Sample was imaged by changing the focal planes with fixed increment. Sets of images were stacked in order to examine 3D structure of samples. As the basis for the surface rendering, fluorescence emission channel was used, while FDLD channel was used for object extraction based on threshold level settings.

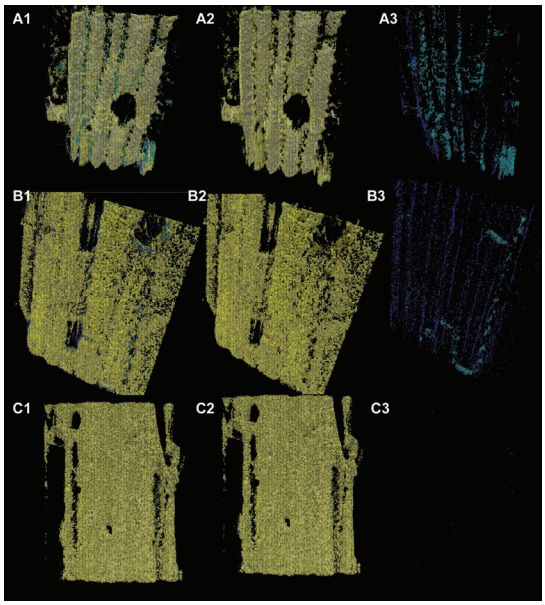

Figure 1. Rendered 3D images from the stacks of fluorescence emission images and FDLD images. Color scale: dark blue, 0^o polarization, gray, 45^o polarization, yellow 90^o polarization. 1, all objects presented, 2, extracted objects polarized from 45^o-90^o, 3, extracted objects polarized from 0^o-45^o A) untreated cell wall, B) plants treated with cellulaze pectinase, C) plants treated with sulphuric acid

The most important aim of the method was to examine if different structures have manifested the same or different FDLD values. The color bar scale of FDLD intensity was set from dark blue for the 0^o orientation, followed by gray for 45^o orientation, and finishing as yellow for 90^o orientation. For 3D image rendering software 3D Doctor was used.

Conclusion

Comparing the two cell wall isolation procedures, we obtained better results of cellulose purity for the maize stem treatment with acid. With this procedure horizontal elements in fiber structure were absent (Fig 1C3), which indicates that in

this case cellulose is more purified, i.e. more appropriate, for further procedure of ethanol production. In the process where the cell wall was treated with cellulase and pectinase, partially present horizontal structure remained.

These results are consistent with the changes in characteristic bands of cellulose and lignin in FTIR spectra of isolated cell walls in both procedures.

This procedure may be used for application in biofuels industry, in order to facilitate obtaining ethanol from cellulose fibers, which is the subject of our interest.

Acknowledgements

This work was supported by the grants No 45012 and No 173017 of the Ministry of education and science of the Republic of Serbia, as well as by the bilateral Hungary-Serbia project "Structural anisotropy of the plant cell walls of various origin and their constituent polymers, using DP-LSM", in 2010-2012.

References

[1] G. Steinbach, I. Pomozi, O. Zsiros, A. Pay, G. V. Horvath, G. Garab, Cytometry Part A , 2008 , 73A, 202-208.

[2] M. Chen, A. Sommer, J. W. McClure, J. Phytochem. Anal., 2000, 11, 153–159.

[3] S. V. Pingali et al, Biomacromolecules, 2010, 11, 2329–2335.

[4] J. P. Verbelen, S. J Kerstens Microsc 2000, 198, 101–107.

J-12-P

POLY(NiPAAm-co-IA) HYDROGELS SYNTHESIZED BY γ-IRRADIATION: SWELLING BEHAVIOR IN WATER

J. Spasojević [1], J. Krstić [1], A. Radosavljević [1],
M.a Kalagasidis-Krušić [2], Z. Kačarević-Popović [1]

[1]Vinča Institute of Nuclear Sciences, University of Belgrade, P.O. Box 522, 11001 Belgrade, Serbia (jelenas@vinca.rs), [2]Faculty of Technology and Metallurgy, University of Belgrade, P.O. Box 3503, 11120 Belgrade, Serbia

Abstract

In this study, N-isopropylacrylamide/itaconic acid copolymeric (poly(NiPAAm-co-IA)) hydrogels were synthesized by γ-irradiation induced simultaneous polymerization and crosslinking of monomers. The influence of comonomer concentration (IA) on the swelling behavior in water was investigated. The results showed that values of network parameters increase with an increase of IA, and that the swelling transport mechanism is a non-Fickian transport.

Introduction

Hydrogels are a class of polymeric materials which have been utilized in a wide range of application due to easily adjustable properties. Stimuli-sensitive, also called intelligent polymers, change their structure and physico-chemical properties in response to physical or chemical stimuli. These smart polymers have a vast potential for applications in pharmaceutical technology, biotechnology industry, and in solving environmental problems. Among them, temperature- and pH-sensitive polymers are the most frequently studied [1].

PolyNiPAAm is the best-known temperature-sensitive polymer that attracts huge interest in biomedical applications due to well-defined lower critical solution temperature (LCST) in water around 32 ^{o}C, which is close to the body temperature. The temperature-sensitive networks containing ionizable functional groups exhibit pH-sensitivity. With the increase of ionizable groups, the volume change at the transition increases because of increasing electrostatic interaction between the same charged groups and the transition temperature rises. In recent years, a series of papers has been published about hydrogels from the copolymers of acrylamide and diprotic itaconic acid (IA) and maleic acid (MA), and showed that the use of even very small quantities of diprotic acid proved to impart remarkable properties to the hydrogels of starting monomers and/or homopolymers [2].

γ-irradiation induced synthesis has been recognized as highly suitable tool for crosslinking of polymeric hydrogels. This method is relatively simple and do not require addition of any extra materials such as initiator and/or crosslinker. Moreover, the degree of crosslinking, which strongly determines the extent of swelling in hydrogels, can be controlled easily by varying the irradiation dose. Therefore, γ-irradiation is found to be very useful in preparing hydrogels for medical applications, where even a small contamination is undesirable [1-3].

The aim of this work was to synthesized polyNiPAAm and poly(NiPAAm-co-IA) hydrogels by γ-irradiation induced simultaneous polymerization and crosslinking, and to investigate the influence of IA concentration on network parameters and swelling behavior in water, as well as to determine diffusion properties of hydrogels.

Experimental

The NiPAAm monomer was used as a base monomer in the synthesis of hydrogels, while the IA was used as comonomer. Solution of NiPAAm (10 wt.%) was prepared in distilled water. Different amounts of IA were added to 5 ml of NiPAAm solution in order to obtain NiPAAm/IA mass ratios 100/0, 98.5/1.5, 97/3 and 95.5/4.5. Monomer solutions were bubbled with argon for 20 min, to remove oxygen, and exposed to γ-irradiation (^{60}Co source) up to absorbed dose of 50 kGy, at a dose rate of 0.6 kGy/h. The obtained hydrogels were immersed in an excess of deionized water, which is changed every day during one week, to remove uncrosslinked polymer and/or residual monomers, and dried at room temperature. Dynamic swelling measurement was performed in deionized water at 25 ± 1 ^{o}C, using dry gels (xerogels). The swelling process was monitored gravimetrically.

Results and Discussion

When a xerogel is brought into contact with a solution, the solution diffuses into the network and volume phase transition occurs, resulting in the expansion of the hydrogel. Diffusion involves the migration of fluid into pre-existing or dynamically formed spaces between the hydrogel chains. The capacity of swelling is one of the most important parameters for evaluation the properties of hydrogels. As can be seen from Table 1, the characteristic parameters obtained from swelling measurement in water of an ionic hydrogel strongly depend on the concentration of ionizable groups in network. The results showed that the equilibrium swelling degree (SD_{eq}) of poly(NiPAAm-co-IA) hydrogels increase as the comonomer concentration increases because of increasing the electrostatic interactions of the neighboring carboxylate groups in IA in the hydrogels [4]. Moreover, the values of network parameters, average molar mass between the network crosslinks (M_c) and distance between the macromolecular chains ie. pore size (ξ), also increase with increasing amount of IA, whereas the xerogel densities decrease.

Table 1. Characteristic parameters obtained from swelling measurement in water at 25 ^{o}C. (S0) - (S3) are symbols of the synthesized hydrogels.

poly (NiPAAm/IA)	SD_{eq}	M_c *(g/mol)*	ξ *(nm)*	ρ_{xg} *(g/cm^3)*	*k (1/min)*	*n*	$D\times10^5$ *(cm^2/min)*
100/0 (S0)	9.2	627	3.7	0.91	0.024	0.52	0.23
98.5/1.5 (S1)	29.1	2905	10.9	0.80	0.014	0.64	1.14
97/3 (S2)	37.1	4041	13.8	0.79	0.013	0.65	1.21
95.5/4.5 (S3)	52.6	7034	20.4	0.78	0.012	0.66	1.28

To obtain a more quantitative understanding of the nature of the sorption kinetic in poly(NiPAAm-co-IA) hydrogels, the initial swelling data were fitted to

equation $M_t/M_{eq} = k\ t^n$, were M_t is the amount of absorbed water in time t, M_{eq} is the maximum absorbed amount, k is a constant incorporating characteristics of macromolecular network system and the penetrant, n is the diffusion exponent, which is indicative of the transport mechanism. This equation is valid for initial stage of swelling ie. for the first 60 % of the normalized solvent uptake. The characteristic constants n and k were calculated from the slope and intercept, respectively, of the linear parts of logarithmic form of kinetic equation of swelling. The obtained results are presented in Table 1, and indicated that hydrogel systems show non-Fickian or anomalous diffusion ($0.5 < n < 1$) when the rates of diffusion and polymer chain relaxation are comparable [5].

The study of diffusion phenomena of water in hydrogels is important because that clarifies the polymers behavior. For hydrogel characterization, the diffusion coefficients (D) can be calculated by using the equation $D^n = (k/4)\ (\pi/r^2)$, were r is the radius of gel disc. The D values are also presented in Table 1. The diffusion coefficients increase with an increase in IA content in the hydrogels. This is due to the hydrophilicity for these copolymeric hydrogels in the order of (S0) < (S1) < (S2) < (S3), and the more hydrophilic groups in the gel, the easier the diffusion for water molecules [1,2].

Conclusion

The poly(NiPAAm-co-IA) hydrogels were successfully synthesized by γ-irradiation. The equilibrium swelling degree (SD_{eq}) of copolymeric hydrogels increase with an increase of IA content, due to incorporation of more specific acid groups into the network and consequent higher swelling capacity of gels. The network parameters M_c and ξ also increase with increasing amount of IA, whereas the xerogel densities decrease. In the diffusion transport mechanism study, the results indicate that the swelling transport mechanism is a non-Fickian transport. The diffusion coefficients (D) of poly(NiPAAm-co-IA) hydrogels increase with an increase of IA content, so the water molecule easily infiltrates into hydrogels for gels containing higher IA content.

Acknowledgements

This work is financed by the Ministry of Education and Science of Republic of Serbia, projects 45005 and 172062, and International Atomic Energy Agency (IAEA), project CRP: F23028, contract No. 15384.

References

[1] B. Taşdelen, et al, J. Appl. Polym. Sci., 2004, 91, 911-915.
[2] B. Taşdelen, et al, Rad. Phys. Chem., 2004, 69, 303-310.
[3] A. Krklješ et al, Polym. Bull., 2007, 58, 271-279.
[4] B. Taşdelen, et al, Int. J. Pharmaceut., 2004, 278, 343-351.
[5] J. Krstić, et al., 10th International Conference on Fundamental and Applied Aspects of Physical Chemistry, Proceedings, 2010, Vol. I, 110-112.

J-13-P

CALCULATION OF CROSSLINK DENSITY IN CURED FILMS OF ALKYD/MELAMINE RESINS

M. Jovičić, R. Radičević, J. Pavličević, O. Bera
University of Novi Sad, Faculty of Technology, Novi Sad, Serbia

Abstract
Baking enamels were prepared by mixing the synthesized alkyd resins and a commercial melamine resin (weight ratio of 70:30 based on dried mass). Curing of coating films was performed in an oven at 150 °C for 1 h. The viscoelastic properties of the cured film were evaluated by a dynamic mechanical analysis (DMA). The values of the storage modulus, loss modulus and loss factor tanδ were assessed in the temperature range from −30 to 120 °C. DMA were used to determine the crosslink density and the glass transition temperature of cured films.

Introduction

The dynamic mechanical analysis (DMA) is commonly used to characterize a material in response to vibration forces. In principle, DMA techniques detect the viscoelastic behavior of polymeric materials and yield quantitative results for the tensile storage module E' and the corresponding loss module E'', the loss factor tanδ as the quotient of loss and storage, tanδ=E''/E' [1]. E' and E'' characterize the elastic and viscous component of a viscoelastic material under deformation, respectively. The interpretations and application of dynamic data provide information on network structure which can be utilized to calculate the crosslink density (υ_e), elastically effective chain length between crosslinks (M_c) and the glass transition temperature of the crosslinked resin [2].

Alkyd resins are widely used in surface coating systems usually in combination with other resins, frequently with melamine resin. The melamine resin is a minor constituent and plays the role of a crosslinking agent. In this work, baking enamels were prepared by mixing the synthesized alkyds with a commercial melamine resin. The viscoelastic properties of the cured film were evaluated by a dynamic mechanical analysis (DMA). According to the height of the storage modulus rubbery plateau, it is possible to obtain the crosslink density of cured resin mixtures. DMA was also used to determine the glass transition temperature of cured films.

Experimental

Three alkyd resins were synthesized differing in values of acid number (AN) and hydroxyl number (HN): alkyd AG based on glycerine (AN_{AG}=2.1 mgKOH/g, HN_{AG}=218.9 mgKOH/g); alkyd ATMP based on trimethylolpropane (AN_{ATMP}=9.2 mgKOH/g, HN_{ATMP}=241.8 mgKOH/g) and alkyd AEP based on ethoxylated pentaerythritol (AN_{AEP}=4.5 mgKOH/g, HN_{AEP}=252.7 mgKOH/g). Detailed information about the synthesis and properties of these alkyd resins can be found in our previous work [3]. Imino type, isobutylated melamine-formaldehyde resin, produced by INEOS Melamines, commercial name Maprenal MF580/55IB, was used as 55 % solution in isobutanol. Baking enamels were prepared by mixing the

synthesized alkyds with a commercial melamine resin in weight ratio of 70:30 based on dried mass. Curing of coating films was performed in an oven at 150 °C for one hour. Dynamic mechanical properties of cured coating films (20×10×1 mm) were determined by DMA 2980 TA Instruments. The DMA spectra of films were recorded in tensile mode in the temperature range of -30 °C to 120 °C at a frequency of 1 Hz and with a heating rate of 5 °C/min.

Results and Discussion

The representative dynamic spectra of E', E'' and tanδ versus temperature of the alkyd AG/melamine coating films are shown in Fig. 1. The breadth and shape of the tanδ, detected for all samples, indicate the heterogeneity of the ingredients used in the coating formulation [4]. The glass transition temperatures, T_g, which were taken as the maxima of tanδ and maxima of E'' in DMA spectra of coating, are reported in Table 1.

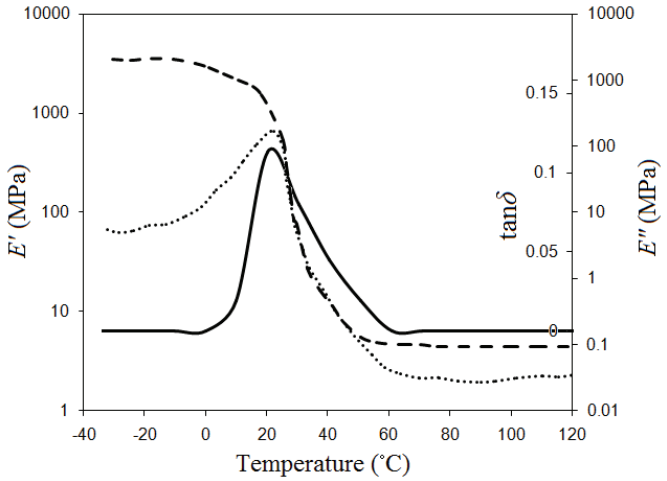

Figure 1. Storage modulus (E'), loss modulus (E'') and tanδ versus the temperature for the cured alkid AG/melamine coating.

The crosslink density (υ_e), the number of moles of elastically effective network chains per cubic centimeter of sample, can be determined from the DMA data using the kinetic theory of rubber elasticity [5]. The E' values in rubbery region at $T>T_g$ (E'_{min}) are taken to calculate υ_e using eq. 1 [4,5]:

$$\nu_e = \frac{E'_{\min}}{RT} \tag{1}$$

where R is the gas constant and T is the temperature at E'_{min}.

The weight of sample in grams which contains 1mol of elastically effective network chain (M_c), can be calculated using eq. 2:

$$M_c = \frac{\rho}{\nu_e} \tag{2}$$

where ρ is the density of coating films. The values of ρ were determined experimentally and found to be in the range of 1.01-1.11 g/cm^3 for the all coating films. The values of υ_e and M_c of the coatings are reported in Table 1.

Table 1. Values of T_g, E'_{min}, v_e, and M_c of coatings.

Film	T_g (°C)		E'_{min} (Pa)	v_e	M_c
	E''_{maks}	$\tan\delta_{maks}$	at 110 °C	(mol/m^3)	(g/mol)
Alkyd AG/melamine	16	28	$1{,}90\cdot10^6$	631,3	1740
Alkyd ATMP/melamine	17,5	31	$2{,}48\cdot10^6$	835,6	1290
Alkyd AEP/melamine	22	35	$4{,}36\cdot10^6$	1542,4	650

The data obtained for υ_e indicate that the coating alkyd AEP/melamine is having tighter network compared to films alkyd AG/melamine and ATMP/melamine. The above observation is reconfirmed with the observed value of M_c, which is the highest for the alkyd AG/melamine crosslinked film. The mixtures consisting of alkyd resin prepared from ethoxylated pentaerythritol show higher values of the crosslink density than those obtained from alkyd based resins with glycerin or trimethylolpropane due to high hydroxyl number of alkyd AEP.

Conclusions

Dynamic mechanical properties of cured alkyd/melamine coatings were determined by DMA instruments. The DMA data provide information on network structure which were used to calculate crosslink density (υ_e), elastically effective chain length between crosslinks (M_c) and the glass transition temperature (T_g) of the crosslinked alkyd/melamine films. Due to the highest hydroxyl number of alkyd based on ethoxylated pentaerythritol, the alkid AEP/melamine resins mixture have higher values of the crosslink density than those obtained from alkyd AG/melamine and alkyd ATMP/melamine.

Acknowledgements

The authors wish to express their gratitude to the Ministry of Education and Science of the Republic of Serbia for the financial support (Project III45022).

References

[1] T. Frey, K.H. Groβe-Brinkhaus, U. Röckrath, Progr. Org. Coat., 1996, 27, 59-66.
[2] R. Narayan, K.V.S.N. Raju, Progr. Org. Coat., 2002, 45, 59–67.
[3] R. Radičević, M. Jovičić, J. Budinski-Simendić, Prog. Org. Coat., 2011, 71, 256-264.
[4] L.W. Hill, J. Coat. Technol., 1992, 64, 29–41.
[5] L.W. Hill, Progr. Org. Coat., 1997, 31, 235-243.

ENVIRONMENTAL PROTECTION
FORENSIC SCIENCES
PHARMACEUTICAL
PHYSICAL CHEMISTRY

K-01-SL

REMOVAL OF URANIUM ANIONIC SPECIES FROM AQUEOUS SOLUTIONS BY POLYETHYLENIMINE – EPICHLOROHYDRIN RESINS

S. Sarri[1], P. Misaelides[1], D. Zamboulis[1], J. Warchol[2]
[1] *Department of Chemistry, Aristotle University, 54124 Thessaloniki, Greece*
[2] *Department of Water Purification and Protection, Rzeszow University of Technology, Rzeszow, Poland*

Introduction

The presence of uranium in the biosphere is not only due to natural sources but also to various human activities (e.g. mining, nuclear power production, military activities etc). Uranium is highly soluble in waters and can easily be transferred in the biosphere through aquatic pathways.
The uranyl-ion (UO_2^{2+}) is the most dominant species in low pH aqueous solutions (pH< 4.5), whereas in those of higher pH values (4.5>pH>7.5) different uranium hydrolysis products of the general type $(UO_2)_x(OH)_y^{(2x-y)+}$ are formed. The formation of phases such as $UO_2(OH)_2$, which can be precipitated, is also possible. In alkaline solutions uranium forms a number of pH-dependent complexes increasing its solubility, availability and mobility in the environment. Uranyl-carbonato-complexes (e.g. $UO_2(CO_3)_2^{2-}$ and $UO_2(CO_3)_3^{4-}$) can also frequently be found in natural waters in the presence of carbonates [1].
Various natural and synthetic sorbents were investigated and used for the removal of uranium cationic species from aqueous solutions. On the other hand, the number of works on the removal of uranium anionic species is rather limited.
This contribution presents the results of the investigation of the uranium anionic species removal from alkaline aqueous solutions by two recently prepared polyethylenimine – epichlorohydrin resins.

Experimental

Two polyethylenimine - epichlorohydrin resins were prepared using low- and high molecular weight polyethylenimine and characterized at the Chemistry Department of the Aristotle University. A modification of a previously described synthesis method was applied for the preparation of the resins [2].
For the sorption experiments 30 mg of the resins were contacted in polypropylene tubes for 24 hours with 10 mL of uranium solutions (C_{init}: 10 to 2000 mg U/L, pH_{init} 8, 9 and 10 adjusted using NaOH at room temperature). After separation of the solid and liquid phases by centrifugation, the equilibrium pH was measured and the uranium concentration determined spectrophotometrically by means of the Arsenazo III method at 660 nm [3]. The obtained data were used to calculate the uptake capacity in mg/g and construct the corresponding sorption isotherms. The experiments were performed under equilibrium conditions with atmospheric CO_2.

The uranium uptake data were modeled using a number of 2-, 3- and 4-parametric isotherm equations (Langmuir, Freundlich, Redlich-Peterson, Langmuir- Freundlich, Toth, Dubinin–Raduszkiewicz) [4].

The sorption kinetics was also investigated for and modeled using the pseudo-first and pseudo-second order equations [4].

The surface and the interior of the resin grains, prior and after the uranium sorption, were examined by SEM/EDS.

Results

The experimental results demonstrated that both resins can very efficiently remove anionic uranium species from aqueous solutions. Fig. 1 presents the isotherms for the sorption of uranium by the low- and high molecular weight (L.M.W. and H.M.W) polyethylenimine – epichorohydrin resins.

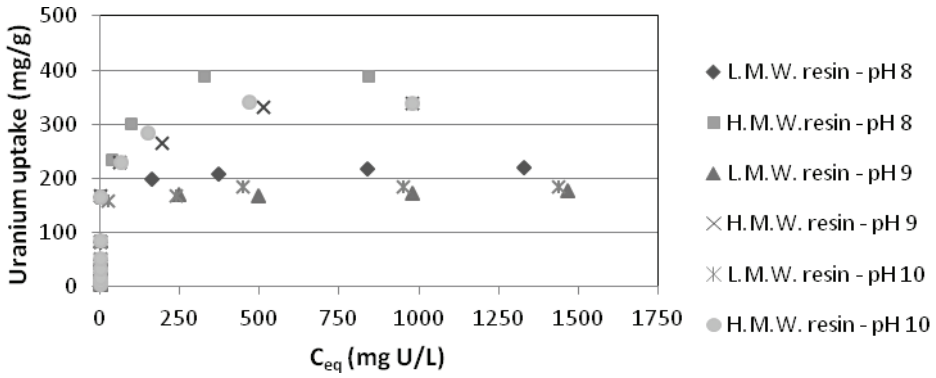

Figure 1. Uranium sorption isotherms for the low- and high molecular weight (L.M.W. and H.M.W) polyethylenimine – epichorohydrin resins.

The enhanced uranium uptake from solutions of pH_{init} 8 can be explained taking into account its speciation and the ratio charge of the complex to the number of uranium atoms. The increasing competition from the side of the hydroxyl-ions was also one of the reasons for the lower uptake from solutions of pH_{init} 9 and 10.

The two resins showed similar behavior. However, the H.M.W. showed higher uptake capacity than the L.M.W. one and was selected for the modeling using the 6 abovementioned isotherm equations (s. example for pH_{init} 8 in Table 1). This Table shows that the uranium uptake data could successfully be reproduced by more than one isotherm equations.

The uranium uptake by the investigated sorbents was very fast. In the first 2 min. ca. 75% of the uranium could be removed from the solutions. The equilibrium was established in less than 15 min. The kinetic data could be very well fitted by the pseudo-second order equation (L.M.W.: h =125 mg/(g min), k=0.008 g /(mg min), R^2=1; H.M.W.: h= 250 mg/(g min), k=0.004 g /(mg min), R^2=1).

Table 1. Modeling of the uranium uptake data for solutions of pH_{init} 8.

Isotherm equation	q_{max}	K	n	R^2
Langmuir	338.5	0.4989	-	0.916
Freundlich	-	3.5162	67.58	0.892
Redlich - Peterson	230.2	0.8172	0.9252	0.950
Langmuir – Freundlich	373.3	0.2114	0.7147	0.932
Toth	458.7	1.343	0.3836	0.949
Dubinin–Raduszkiewicz	362.5	0.00252	0.092	0.933

The examination of the resins grains by SEM/EDS revealed that the uranium was concentrated on their surface (s. Fig. 2) indicating that precipitation also contributed to the overall removal. No diffusion in the bulk of the grains was observed as in the case of other anionic species (e.g. chromates, iodides, perrhenates).

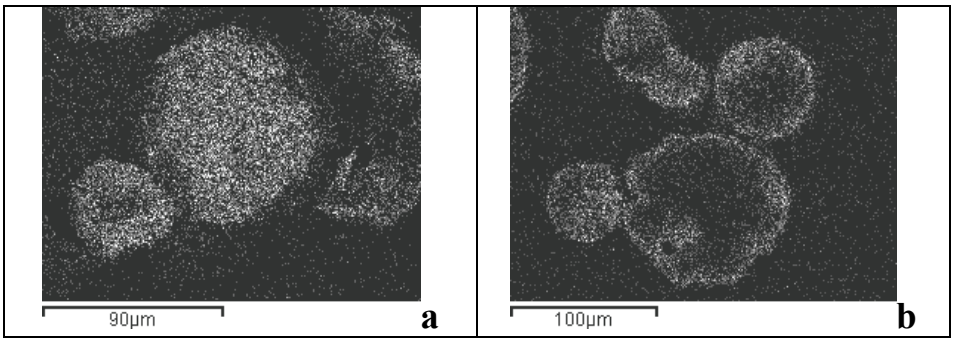

Figure 2. U-mapping (U Mα_1) of the surface (a) and of a section (b) of resin grains.

References

[1] C. Moulin et al, Appl. Spectrosc., 52(1998) 528-535.
[2] D. Ebner et al, Sep. Sci. Technol., 34 (1999) 1277-1300.
[3] S.B. Savvin, Talanta, 11 (1964) l–6.
[4] G. Gerente et al, Environ. Sci. Technol., 37 (2007) 41–127.

K-02-SL

APPLICATIONS OF BENTONITE IN THE ENVIRONMENTAL PROTECTION

P. Banković[1], Z. Mojović[1], N. Jović-Jovičić[1], M. Žunić[1], A. Milutinović-Nikolić[1],

[1] *University of Belgrade – Institute of Chemistry, Technology and Metallurgy, Center for Catalysis and Chemical Engineering, Njegoševa 12, Belgrade, Serbia*

Abstract

Smectite rich clay from Bogovina, Serbia, was submitted to pillaring and organomodification. Pillared and organomodified materials were characterized using XRD, ICP-OES and N_2 physisorption methods. The obtained pillared and organoclays were employed as adsorbents, catalysts and electrode materials in the processes of removal and detection of different organic and inorganic water pollutants.

Introduction

Smectites have large surface area, wide pore size distribution, moderate surface acidity, high cation exchange capacity, low anion exchange capacity and ability of water uptake through exchangeable cations hydration, also known as swelling [1, 2]. The ability of cation exchange and swelling make smectites prone to various types of modification enabling their different applications. For instance, pillaring and organomodification of bentonite clays rich in smectite have been widely applied for the obtainment of catalysts and adsorbents for the environmental protection [3, 4].

Pillared clays are hydrothermally stable materials that can be designed for specific catalytic purposes by designing their porosity and the chemical composition of pillars incorporated within their interlamellar region trough the control of synthesis conditions and the right choice of pillaring agents and/or impregnation [5–7].

Smectite can be rendered organophilic by organomodification when exchangeable cations are replaced with quaternary alkylammonium ions (QAACs) [8]. Organoclays are attractive materials due to their ability to adsorb both organic pollutants and toxic heavy metals from water [9].

In this work, smectite rich bentonite from local deposits in Bogovina, Serbia, was employed in the synthesis of nanomaterials for prevention and management of water pollution by pillaring and organomodification. Obtained pillared (PILCs) and organoclays (OBs) were also used as electrode materials for the detection of organic pollutants in water.

Materials and Methods

Smectite rich bentonite clay from Bogovina [10] was used in this work. After milling, sieving and hydroseparation, <74 μm and <2 μm fractions were used for

further modifications and denoted as B2 and B74 respectively. Both B2 and B74 were submitted to the Na-exchange procedure (samples Na-B2 and Na-B74).
The procedure according to Baskaralingam [11, 12] was adopted for the organobentonite preparation. Two series of synthesized organobentonites (OBs) were obtained by dropwise addition of surfactant–bromide solutions into a stirred Na-B74 dispersion. In the first series the starting material was modified with different amounts of hexadecyltrimethylammonium (HDTMA) ion with respect to the amount of exchangeable cations (Na^+). The samples were denoted as 0.2HDTMA-B, 0.5HDTMA-B, 1.0HDTMA-B corresponding to 0.2, 0.5, 1.0 and 2.0 times of CEC value, respectively. The second series was obtained using QAACs with different alkyl chain lengths: HDTMA, dodecyltrimethylammonium (DDTMA) and tetramethylammonium (TMA) ions. Here presented samples designated as 0.2HDTMA-B, 0.2DDTMA-B, 0.2TMA-B, 2.0HDTMA-B, 2.0DDTMA-B and 2.0TMA-B.

The process of pillaring was carried out according to a common procedure [13]. Pillaring solutions were adjusted to have the molar ratio $M^{n+}/(Al^{3+}+M^{n+})=0.10$ (where $M^{n+}=Cu^{2+}$, Co^{2+} or Fe^{3+}), OH $/(Al^{3+}+M^{n+})=2.0$ and the metal ion/Na-B2 ratio of 20 mmol M^{n+}/g. Obtained samples were denoted AlCu10 PILC, AlCo10 PILC and AlFe 10 PILC. Another series of PILCs with different Fe^{3+} content was also synthesized. In this case the pillaring solutions contained pillaring cations in the following $Fe^{3+}/(Al^{3+}+Fe^{3+})$ molar ratios: 0.00, 0.01, 0.05, 0.10, 0.15 and 0.20. The obtained PILCs were denoted as Al PILC, AlFe1 PILC, AlFe5 PILC, AlFe10 PILC, AlFe15 PILC and AlFe20 PILC, respectively. Pillaring was performed by dropwise addition of pillaring solutions into stirred Na-B2 dispersion. The pillaring procedure was described in details elsewhere [14].
X-ray diffraction (XRD) patterns for powders of investigated samples were obtained using a Philips PW 1710 X-ray powder diffractometer with a Cu anode (λ=0.154178 nm).

A Spectro Spectroflame M - inductively coupled plasma optical emission spectrometer, was used for the analysis of the chemical composition of all investigated samples.
Nitrogen adsorption-desorption isotherms were determined on a Sorptomatic 1990 Thermo Finnigan at -196 °C. Samples were outgassed at 160 °C, during 20h. Specific surface area of the samples, S_{BET}, was calculated according to Brunauer, Emmett, Teller method [15]. Dubinin-Radushkevich method was used for the calculation of micropore volume, V_{mic} [16].

Catalytic degradation of organic water pollutants (azo-dyes Tartrazine and Acid Yellow 99, phenol and toluene) was tested in Catalytic Wet Peroxide Oxidation (CWPO) process [3] using PILCs as catalysts. Catalytic tests were carried out in a thermostated Pyrex reactor, and equipped with a stirrer. Aqueous solutions (100 ml) of each organic pollutant were stirred with 0.5 g of solid catalyst and 35% hydrogen peroxide in excess. Aliquots were taken at predetermined time intervals. Supernatant solutions were separated from the solid phase by centrifugation and analyzed by UV-Vis spectrophotometry (Electron Nicolet

Evolution 500 UV-VIS spectrophotometer) or gas chromatography (Shimadzu GC-9A gas chromatograph).

OBs were tested as adsorbents of organic water pollutants (Acid Orange 10 – AO10) and toxic metals (Pb^{2+}). The adsorption experiments were carried out in a thermostated shaker (Memmert WNE 14 and SV 1422). The samples were withdrawn from the shaker at regular time intervals and solid phase was separated from the solutions by centrifugation. Supernatant solution was used for the measurements. AO10 concentration was determined by Thermo Electron Nicolet Evolution 500 UV-VIS spectrophotometer, while Pb^{2+} concentration was measured by ICP-OES (ICAP 6500 Duo ICP, Thermo SCIENTIFIC Spectrometer).

In order to use the PILCs and OBs as electrode materials, the samples were homogeneously dispersed in 5 mass % Nafion solution in mixture of isopropyl alcohol and water. The electronic conductivity of the samples was enhanced by adding 10 mass % of carbon black Vulcan XC72 (Cabot Corp.) into the initial suspension. Each of these suspensions was placed on the surface of a glassy carbon rotating disc electrode and solvent was removed by evaporation. The electrodes served as working electrodes for electrochemical investigations in a three-electrode glass cell. The reference electrode was Ag/AgCl in 1 M KCl, while a platinum foil served as a counter electrode. Phenol degradation was investigated for starting concentration of phenol of 10 mM in 0.1 M H_2SO_4 at room temperature using 757 VA Computrace Metrohm.

Characterization

The influence of applied modification on the smectite (001) basal spacing, d_{001}, and porous structure for selected representative pillared and organobentonite materials is presented in Tables 1 and 2, together with the results of the chemical analysis of the PILCs.

Table 1. Main physical and chemical properties of the starting and PILC materials.

Sample	d_{001} [nm]	S_{BET} [m^2/g]	V_{mic} [cm^3/g]	mmol/100g sample			
				Al	Fe	Cu	Co
B2	1.53	125	0.051	481,5	107,3	-	-
Na-B2	1.28	123	0.051	474,3	107,3	-	-
Al PILC	1.72	177	0.087	859,3	110,9	-	-
AlFe1 PILC	1.75	203	0.094	740,7	132,4	-	-
AlFe5 PILC	1.74	151	0.070	715,7	178,9	-	-
AlFe10 PILC	1.75	190	0.090	656,4	214,7	-	-
AlFe15 PILC	1.74	187	0.087	637,0	304,1	-	-
AlFe20 PILC	-	197	0.086	629,6	357,8	-	-
AlCu10 PILC	1.58	153	0.063	851,9	107,3	19,7	-
AlCo10 PILC	1.72	142	0.057	851,9	100,2	-	2,9

* S_{BET} – specific surface area, V_{mic} – micropore volume

Table 2. Main physical properties of the starting and OB materials.

Sample	d_{001} [nm]	S_{BET} [m^2/g]	V_{mic} [cm^3/g]
Na-B74	1.28	120	0.051
0.2TMA-B	1.28	148	0.101
2.0TMA-B	1.40	133	0.062
0.2DDTMA-B	1.30	35	0.034
2.0DDTMA-B	1.81	2	-
0.2HDTMA-B	1.44	20	0.010
0.5HDTMA-B	1.52	20	0.008
1.0HDTMA-B	2.00	3	-
2.0HDTMA-B	2.00	1	-

The Na-exchange process lowered d_{001} smectite basal spacing from 1.53 nm for the starting bentonite to 1.28 nm. Pillaring led to increase in the smectite basal spacing in all obtained PILCs, which is a proof of the successful incorporation of pillaring species in the interlamellar region of smectite. Intercalation of HDTMA ions increased the basal spacing from 1.28 nm for Na-rich bentonite to 2.00 nm for 1.0HDTMA and 2.0HDTMA-B (Fig. 1). Since the increase of (mol HDTMA)/(mol exchangeable Na^+) above 1 did not cause the increase of the basal spacing, it can be assumed that additional HDTMA ions, after replacing all Na^+ cations within interlayer region, were attached to the particle surface. The XRD results of the synthesized organobentonites indicated that monolayers of surfactants were predominantly formed within the interlayer space of 0.2-organobentonites, 0.5 HDTMA and 2.0TMA-B, while pseudo-trilayer were formed in 1.0- and 2.0HDTMA-B [17, 18]. However, the changes obtained in the d_{001} of 0.2-OBs were smaller than those theoretically predicted, which can be expected for lower surfactant loadings [19]. Comparing to Na-B2, S_{BET} values obtained for the PILCs showed increase. The most pronounced increase was in the case of Fe containing PILCs. Among them, the increase was slightly lower in the case of the AlFe5 PILC, possibly due to some inconsistence in the pillaring procedure that might have occurred. However the level of Fe^{3+} incorporation in the AlFe5 PILC was more than satisfying. The incorporation of Cu^{2+} and Co^{2+} was much lower, probably due to incompatibility in the valence and coordination between these ions and Al^{3+}. The specific surface area of the OB samples decreased in the order TMA> DDTMA-B>HDTMA-B. The presence of larger organic cations, such as HDTMA and DDTMA, in the interlamellar region resulted in pore blocking that inhibited the passage of nitrogen molecules. On the other hand, the increased S_{BET} value for TMA-B was mainly due to the presence of newly developed micropores in the interlamellar region. Iron to aluminium content in the PILCs corresponded to those in the pillaring solutions.

Adsorption, Catalytic and Electrocatalytic Tests

In figures 1–3 are presented results of adsorption of Acid orange 10 dye (50 ppm) and Pb^{2+} from single-component and their mixed two-component aqueous solutions on the series of HDTMA-B samples with different surfactant loading where curves 1, 2, 3, and 4 correspond to 2.0HDTMA-B, 1.0HDTMA-B, 0.5HDTMA-B and

0.2HDTMA-B, respectively [9]. The influence of alkyl chain length on the adsorption of organic pollutants is here described by the adsorption of AO10 on 2.0TMA-B (1), 2.0DDTMA-B (2) and 2.0HDTMA-B (3) (Fig. 4).

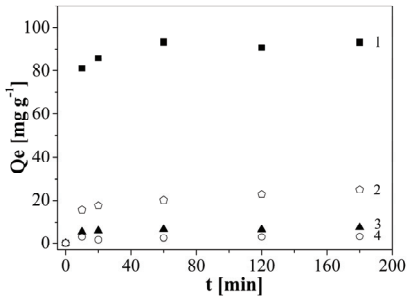

Figure 1. Adsorption of AO 10 from single-component solution.

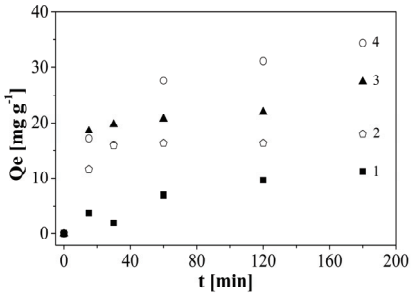

Figure 2. Adsorption of Pb^{2+} ions from single-component solution.

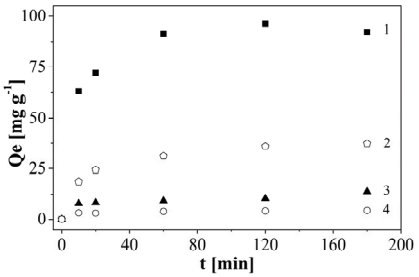

Figure 3. Adsorption of AO 10 from two-component solution.

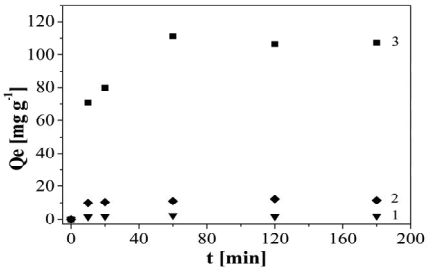

Figure 4. The influence of alkyl chain length on the adsorption of AO10.

Increasing surfactant loading and alkyl chain length led to increased organophilicity which resulted in increased azo dye and decreased Pb^{2+} adsorption. Simultaneous adsorption of AO10 and Pb^{2+} improved the adsorption of the dye by adsorbents with molar ratio QAAC/exchangeable cations up to 1. A possible explanation for this might be the attraction between SO_3- groups in AO 10 to Pb^{2+} previously adsorbed on surface area free of organic cations.

The influence of Fe content of PILCs and temperature on the CWPO degradation of azo dyes was studied on the example of Tartrazine ($93{,}6\times10^{-6}$ mol dm^{-3}) as presented in Figs. 5 and 6 [20]. The removal of toluene (2×10^{-3} mol dm^{-3}) and phenol (5×10^{-4} mol dm^{-3}) by CWPO were also tested (Figs. 7 and 8, respectively) [21, 22].

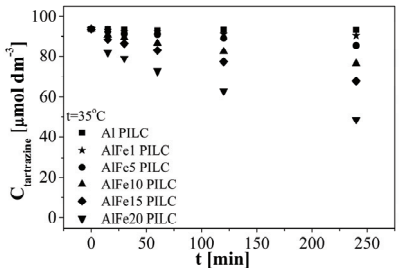

Figure 5. CWPO of tartrazine – the influence of Fe content in the PILCs.

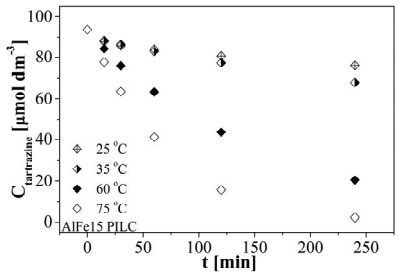

Figure 6. CWPO of tartrazine – the influence of temperature.

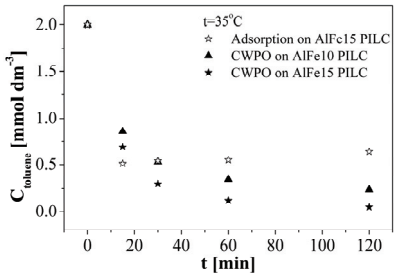

Figure 7. CWPO and adsorption of toluene – the influence of Fe content.

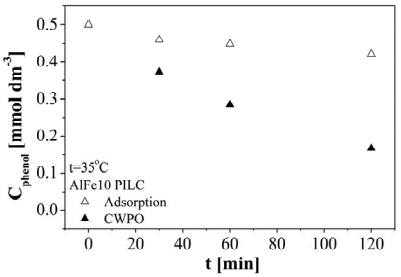

Figure 8. CWPO and adsorption of phenol.

Increasing efficiency of the CWPO removal of tartrazine with increased Fe content in the PILC catalysts confirmed catalytic role of iron. Results of the toluene removal by CWPO corroborated these findings. Higher temperatures promoted the degradation of tartrazine. Phenol removal was the least efficient however still significant with respect to its removal by adsorption.

Increased electrode surface area leads to increased electrochemical activity. Pillaring yields materials with developed micro/mesoporosity. Therefore Al PILC, AlCu10 PILC, AlCo10 PILC and AlFe10 PILC were tested as electrode materials in the electrocatalytic oxidation of phenol in acidic solution [23]. The modification of clay minerals by surfactants is a method to hydrophobize the mineral and therefore to increase the adsorption capacity for organic pollutants. Therefore electrocatalytic oxidation on the series 0.2TMA-B, 0.2DDTMA-B and 0.2HDTMA-B was also investigated [24]. Successive cyclic voltammograms obtained at the polarization rate of 10mVs at AlFe10 PILC and 0.2HDTMA-B electrode (here chosen as the representative ones) are shown in Figs. 9 and 10, respectively. Table 3 summarizes current densities and current density drops after 10 cycles (electrode deactivation) around the potential of 950 mV vs. Ag/AgCl corresponding to phenol oxidation.

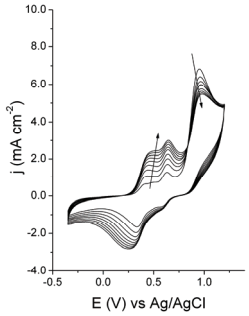

Figure 9. CV for phenol oxidation in H_2SO_4 on AlFe10 PILC electrode.

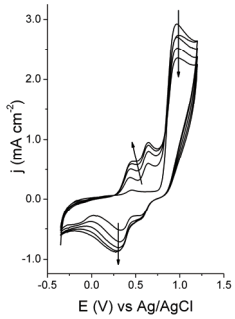

Figure 10. CV for phenol oxidation in H_2SO_4 on 0.2HDTMA-B electrode.

Table 3. Phenol oxidation current densities.

Sample	j_I [mAcm^{-2}]	$(j_I - j_X)/j_I$ [%]
Al PILC	5.42	35.43
AlCo10 PILC	8.71	30.89
AlCu10 PILC	5.95	20.84
AlFe10 PILC	7.45	26.44
0.2TMA-B	7.36	-
0.2DDTMA-B	1.98	-
0.2HDTMA-B	1.08	-

Prolonged cycling resulted in the decrease of current density related to phenol oxidation and simultaneous occurrence and increase in the current densities of cathodic peaks (600 and 300 mV) and anodic peaks (440 and 640 mV) related to phenol oxidation products – hydroquinone and catechol.

Among the PILCs, AlFe10 PILC showed the best performance, i.e. high activity and low deactivation rate, while the best organomodified electrode material was 0.2TMA-B.

Conclusion

Pillared and organomodified clays based on Bogovina bentonite were synthesized and characterized. XRD, chemical and N_2 physisorption analyses confirmed the incorporation of introduced species. Orgnomodified clays showed good performance as adsorbents for simultaneous removal of organic and inorganic water pollutants. Increasing organophilicity increased dye adsorption. CWPO degradation of organic water pollutants increased with increasing Fe content of the PILCs and temperature. Both PILCs and OBs showed significant activity as electrode materials in electrocatalytic oxidation of phenol.

Acknowledgment

Supported by the Ministry of Education and Science of the Republic of Serbia (Project III-45001).

References

[1] Vaccari, Catal. Today, 1998, 41, 53–71.
[2] F. Wypych, K.G. Satyanarayana, Clay Surfaces: Fundamentals and Applications, Elsevier, Amsterdam, 2004.

[3] M. N. Timofeeva, S. T. Khankhasaeva, Y. A. Chesalov, S. V. Tsybulya, V. N. Panchenko, E. T. Dashinamzhilova, Appl. Catal. B-Environ., 2009, 88, 127–134.
[4] J.J. Lee, J. Choi, J.W. Park, Chemosphere, 2002, 49, 1309–1315.
[5] P. Cool, E. F. Vansant, Molecular Sieves Vol. 1, Springer-Verlag, Berlin-Heidelberg (1998)
[6] Gil, L. M. Gandia, M. A. Vicente, Catal. Rev. – Sci. Eng., 2000, 42, 145–212.
[7] J. Kloprogge, J. Porous. Mat., 1998, 5, 5–41.
[8] Y. Chun, G. Sheng, S. Boyd, Clays Clay Miner., 2003, 51, 415–420.
[9] N. Jović-Jovičić, A. Milutinović-Nikolić, P. Banković, Z. Mojović, M. Žunić, I. Gržetić, D. Jovanović, Appl. Clay Sci., 2010, 47, 452–456.
[10] Z. Vuković, A. Milutinović-Nikolić, Lj. Rožić, A. Rosić, Z. Nedić, D. Jovanović, Clays Clay Miner., 2006, 54, 699-704.
[11] P. Baskaralingam, M. Pulikesi, D. Elango, V. Ramamurthi, S. Sivanesan, J. Hazard. Mater., 2006, 128, 138–144.
[12] N. Jović-Jovičić, A. Milutinović-Nikolić, I. Gržetić, D. Jovanović, Chem. Eng. Technol., 2008, 31, 567–574.
[13] V. Kaloidas, C. A. Koufopanos, N. H. Gangas, N. G. Papayannakos, Microporous Mater., 1995, 5, 97–106.
[14] P. Banković, A. Milutinović-Nikolić, Z. Mojović, N. Jović-Jovičić, M. Žunić, V. Dondur, D. Jovanović, Appl. Clay Sci., 2012, 58, 73–78.
[15] F. Rouquerol, J. Rouquerol, K. Sing, Adsorption by Powders and Porous Solids, Academic Press, London (1999).
[16] M. M. Dubinin, J. Colloid Interf. Sci., 1974, 46, 351–356.
[17] G. Lagaly, Solid State Ionics, 1986, 22, 43–51.
[18] G. Lagaly, M. Ogawa, I. Dékány, Clay mineral organic interactions. In: Bergaya, F., Theng, B.K.G., Lagaly, G. (Eds.), Handbook of Clay Science: Developments in Clay Science, vol. 1. Elsevier, Amsterdam, (2006).
[19] S. Y. Lee, S. J. Kim, S. Y. Chung, C. H. Jeong, Chemosphere, 2004, 55, 781–785.
[20] P. Banković, A. Milutinović-Nikolić, Z. Mojović, N. Jović-Jovičić,M. Žunić, V. Dondur, D. Jovanović, Appl. Clay Sci., 2012, 58, 73–78.
[21] P. Banković, A. Milutinović-Nikolić, Z. Mojović, A. Rosić, Ž. Čupić, D. Lončarević, D. Jovanović, Chinese J. of Catal., 2009, 30, 14–18.
[22] P. Banković, A. Milutinović-Nikolić, N. Jović-Jovičić, J. Dostanić, Ž. Čupić, D. Lončarević, D. Jovanović, Acta Physica Polonica A, 2009, 115, 811–815.
[23] P. Banković, Z. Mojović, A. Milutinović-Nikolić, N. Jović-Jovičić, S. Marinović, D. Jovanović, Appl. Clay Sci., 2010, 49, 84–89.
[24] Z. Mojović, N. Jović-Jovičić, P. Banković, M. Žunić, A. Abu Rabi-Stanković,A. Milutinović-Nikolić, D. Jovanović, Appl. Clay Sci., 2011, 53, 331–335.

K-03-O

FABRICATION OF MONODISPERSE POLY(DL-LACTIC ACID) MICROPARTICLES USING DROP MICROFLUIDICS

G. T. Vladisavljević, [1] W. J. Duncanson,[2] H. C. Shum,[3] D. A. Weitz[2]

[1]Department of Chemical Engineering, Loughborough University, Loughborough, LE11 3TU, UK, [2]Department of Physics, Harvard University, Cambridge, MA 02138, US, [3]Department of Mechanical Engineering, University of Hong Kong, Hong Kong

Abstract

Monodisperse poly(dl-lactic acid) particles with a diameter between 11 and 121 μm were fabricated by drop microfluidics/solvent evaporation method using flow focusing glass capillary device. In the dripping regime, the ratio of droplet diameter to orifice diameter was in the range of 0.37−1.34 and was inversely proportional to the 0.39 power of the ratio of the continuous phase flow rate to dispersed phase flow rate.

Introduction

Biodegradable particles have been used for the encapsulation and controlled release of pharmaceutical actives, ultrasound and molecular imaging, fabrication of scaffolds, cell cultivation, etc. The most commonly used biodegradable synthetic polymers are poly(lactic acid) (PLA) and poly(lactic-co-glycolic) acid (PLGA), since they both have good biocompatibility and mechanical strength [1]. Monodisperse particles are favourable in drug delivery and ultrasound imaging because they exhibit predictable biodegradation rate, controlled drug release profile and acoustic response [2]. The conventional methods of droplet generation such as atomization processes, rotor/stator mixing and high-pressure homogenization result in polydisperse particles whose mean size cannot be precisely controlled. As a departure from traditional 'top-down' emulsification approach where small droplets are formed by reducing the size of larger droplets, a number of 'bottom-up' methods have been recently developed, where small droplets are directly formed by injecting one liquid through a micro -channel or -nozzle into another immiscible liquid. The purpose of this study was to investigate a novel approach to the fabrication of PLA microparticles based on flow focusing microfluidic device [3]. We have chosen borosilicate glass as a construction material for the device fabrication, because glass is more chemically robust than poly(dimethylsiloxane), does not swell, and has more stable surface properties.

Material and Methods

The microfluidic device (Fig. 1 left), set on the stage of an inverted Leica DM-IRBE microscope, was connected to syringes containing the continuous and

dispersed phases via medical tubing. The dispersed phase consisted of a mixture of 5 % (w/w) poly(dl-lactic acid) (PLA) (15,000 g·mol^{-1}), 95 % (w/w) dichloromethane (DCM) and 0.1–2 mM Nile red dye. The continuous phase was 5 % (w/w) aqueous solution of polyvinyl alcohol (87-89% hydrolyzed). Each phase was pumped into the device by a separate Harvard Apparatus PHD 22/2000 syringe pump. The droplet formation was recorded using a Phantom V5.1 high-speed camera at the rate of 800–2000 frames per second and frames were analysed using ImageJ v.1.44 software to estimate droplet diameter. The device was fabricated by inserting a round capillary with a tapered tip into the centre of a square capillary. To minimize wetting with DCM, the tip was treated with *2*-[methoxy (polyethylenoxy) propyl] trimethoxysilane. Hypodermic needles were glued over both ends of the square tubing to act as tube connectors for the oil and water phase, while the exposed end of the round capillary served for sample collection.

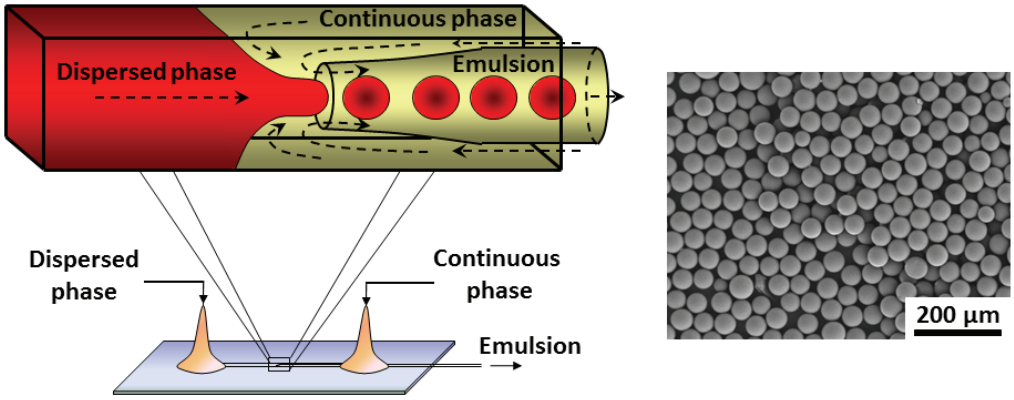

Figure 1. Schematic diagram of flow focusing glass capillary device (left) and Scanning Electron Micrograph of 23 µm poly(dl-lactic acid) microparticles (right).

Results and Discussion

Figs. 1 (right) is a Scanning Electron Micrographs of PLA particles showing a smooth surface with negligible porosity and spherical shape. After complete evaporation of DCM, the particle size was 2.7 times smaller than the size of the original droplets.

Fig. 2 is a log-log plot of drop diameters D_d scaled by the orifice diameter D_o versus ratio of volumetric flow rates of dispersed to continuous phase, Q_c/Q_d. Experimental data follows a linear trend with an equation of the best fit line: $D_d/Q_o = 0.23(Q_c/Q_d)^{-0.39}$.

Droplets formed in the dripping regime had diameters of $1.34D_o > D_d > 0.37D_o$. In dripping regime, the continuous phase flows through the orifice faster than the dispersed phase and the size of the droplets is determined by the balance between the drag of the continuous phase pulling the droplet downstream and interfacial tension force that resist the flow in the dispersed phase as pinch-off occurs. In jetting regime, the dispersed phase flows faster than the continuous phase and it is

the inertial force of the dispersed phase that must overcome the interfacial tension force. The uniform droplets were obtained only in the dripping regime.

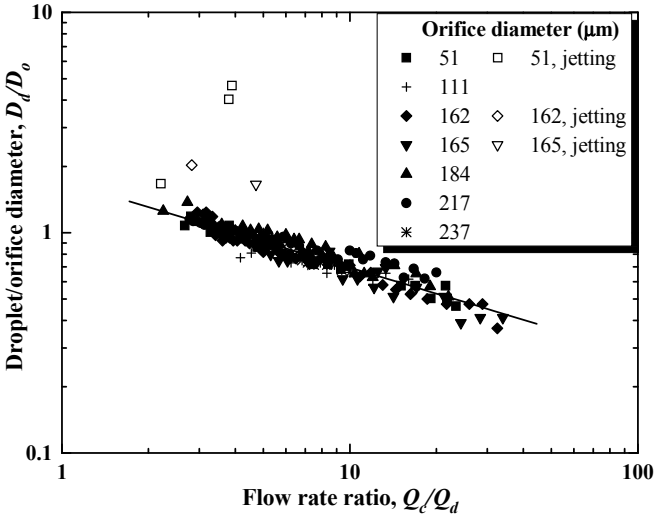

Figure 2. Droplet diameter/orifice diameter versus ratio of volumetric flow rates of dispersed to continuous phase. Open symbols are data points obtained under jetting.

Conclusion

We have developed a novel method for production of poly(lactic acid) particles based on drop microfluidics in glass capillary devices and solvent evaporation. The size of the droplets formed in the microfluidic device has been closely controlled by phase flow rates and orifice size of the collection capillary. Our method is not limited to PLA and can be used to fabricate particles from a wide range of biodegradable material.

Acknowledgment

This work was supported by the Engineering and Physical Sciences Research Council of the UK (grant ref. number EP/HO29923/1) and the Royal Academy of Engineering.

References

[1] J. M. Anderson, M. S. Shive, Adv. Drug. Del. Rev., 1997, 28, 5–24.
[2] C. Berkland , M. King , A. Cox , K. Kim, D. W. Packa, J. Controled Release, 2002, 82, 137–147.
[3] A. S. Utada, L. Y. Chu, A. Fernandez-Nieves, D. R. Link, C. Holtze, D. A. Weitz, MRS Bull., 2007, 32, 702–708.

K-04-P

COMPARISON OF CHROMATOGRAPHICALLY OBTAINED AND COMPUTED HYDROPHOBICITY PARAMETERS OF ACE INHIBITORS

J. V. Odović[1], B. D. Marković[2], J. B. Trbojević-Stanković[3], S. M. Vladimirov[2], K. D. Karljikovic – Rajić[1]

[1] *Department of Analytical Chemistry, University of Belgrade-Faculty of Pharmacy, Vojvode Stepe 450, 11221 Belgrade, Serbia*

[2] *Department of Pharmaceutical Chemistry, University of Belgrade-Faculty of Pharmacy, Vojvode Stepe 450, 11221 Belgrade, Serbia*

[3] *Clinical Center "Dr Dragiša Mišović", Heroja Milana Tepića 1,11000 Belgrade, Serbia.*

Abstract

The lipophilicity of seven angiotensin – converting enzyme (ACE) inhibitors (enalapril, quinapril, fosinopril, lisinopril, cilazapril, ramipril and benazapril) with significantly different structure was studied. The software packages were used to calculate different ACE inhibitors hydrophobicity parameters, log*P* values, while experimentally determined *n*-octanol/water partition coefficients, log$P_{O/W}$, were obtained from relevant literature. The correlations between all collected log*P* values and chromatographically obtained hydrophobicity parameters, R_M^0 and C_0 values were studied. The good correlations ($r > 0.90$) indicate that the log*P* calculations can be useful in ACE inhibitors lipophilicity evaluation, as high-throughput screening technique.

Introduction

Lipophilicity is one of the most significant properties of biologically active substances [1]. Lipophilicity is characterized by the *n*-octanol/water partition coefficient (log$P_{O/W}$) and traditional technique for determination molecules lipophilicity, it's log*P* value, is so-called *shake flask* method. The chromatographic techniques are known as well established methods that can yield a significant amount of reproducible retention data for structurally different compounds which can be correlated with their physicochemical and biological properties at the first place lipophilicity [1]. Alternatively, *in silico* hydrophobicity parameters, calculated log*P* values, are generally accepted as measure of drug's lipophilicity [2].

In our previous study [3] we reported the lipophilicity of several ACE inhibitors based on RP-TLC research. Continuing this research in the present study correlations between calculated hydrophobicity parameters (log*P* values) and chromatographically obtained R_M^0 and C_0 values, as reliable measures of lipophilicity were examined in the aim to establish possible application of *in silico* hydrophobicity parameters in ACE inhibitor's lipophilicity investigations.

Experimental

The seven selected ACE inhibitors were investigated: 1. enalapril maleate, 2. quinapril hydrochloride, 3. fosinopril sodium, 4. lisinopril dihydrate, 5. cilazapril monohydrate, 6. ramipril, and 7. benazepril hydrochloride.

The TLC study of ACE inhibitors lipophilicity, were performed by RP-TLC, as previously reported [3], with additional experiments carried out to include ramipril and benazepril in these correlations.

The Excel 2003 from Microsoft Office and Origin 7.0 PRO (Origin Lab Corporation, USA) were used to perform the statistical analysis of the regression. The software packages Molinspiration Depiction Software (Molinspiration Cheminfirmatics) [4], Virtual Computational Chemistry Laboratory [5] and CS Chem Office, version 7.0 [6] were used to calculate different ACE inhibitors hydrophobicity parameters, log*P* values.

Results and Discussion

The seven ACE inhibitors were studied to evaluate the correlation between their calculated and chromatographically obtained hydrophobicity data. On the base of obtained R_F values the hydrophobicity parameters R_M^0 and C_0 were calculated.

The hydrophobicity parameters, log*P* values of the seven investigated ACE inhibitors, were calculated using different software packages (Clog*P,* Alog*Ps,* AClog*P,* AB/log*P,* Milog*P,* Alog*P,* Mlog*P,* KOWWINlog*P*, XLOGP_2, XLOGP_3) and experimentally determined log$P_{O/W}$ were obtained from Clarke's Analysis of drugs and Poisons [7]. The differences between calculation methods used led to distinctions between absolute ACE inhibitor's logP values. The relationships between all collected log*P* values were studied. The best agreements were obtained between experimentally determined log$P_{O/W}$ and three calculated log*P* values: KOWWINlog*P* (r = 0.9997), AClog*P* (*r* = 0.9937) and Milog*P* values (r = 0.9742).

In the aim to examine the application and reliability of *in silico* hydrophobicity parameters in lipophilicity evaluation of ACE inhibitors, chromatographically established hydrophobicity parameters R_M^0 and C_0 were correlated with all collected log*P* values. The good correlations with $r > 0.90$ were obtained in majority of relationships (Table 1). One of the best relationship was established for KOWWINlog*P* and R_M^0 ($r = 0.9805$) or C_0 ($r = 0.9768$) parameters obtained by the usage of water-methanol mobile phase. The KOWWINlog*P* values previously showed the best relationship with experimentally determined log$P_{O/W}$. The Milog*P* values showed slightly lower correlation coefficients – corresponding values for water-methanol were 0.9585 for R_M^0 and 0.9575 for C_0. Although AClogP values showed good correlation with experimentally obtained log$P_{O/W}$ the lowest *r* values were obtained – 0.7556 (R_M^0) and 0.7351 (C_0).

Table 1. The correlation coefficients, *r*, between R_M^0 or C_0 values (for all used modifiers) and different log*P* values.

	Water-methanol		Water-acetone		Water-ethanol	
	R_M^0	C_0	R_M^0	C_0	R_M^0	C_0
log$P_{O/W}$	0,9813	0,9942	0,9929	0,9362	0,8842	0,9174
Clog*P*	0,9373	0,8485	0,8563	0,9606	0,826	0,9607
Alog*Ps*	0,8652	0,7714	0,7907	0,8846	0,7508	0,8959
AClog*P*	0,5709	0,5404	0,5592	0,5105	0,485	0,5445
AB/log*P*	0,9499	0,897	0,8911	0,9641	0,8483	0,9454
Milog*P*	0,9187	0,9211	0,9232	0,8175	0,8569	0,8606
Alog*P*	0,898	0,8316	0,8494	0,8784	0,8609	0,9251
Mlog*P*	0,9423	0,8651	0,8795	0,9423	0,9018	0,9812
KOWWIN	0,9613	0,9541	0,9605	0,9147	0,8468	0,9064
XLOGP_2	0,8639	0,7567	0,7747	0,8889	0,7693	0,9134
XLOGP_3	0,9707	0,902	0,9125	0,9641	0,8625	0,9757

Conclusion

Lipophilicity is one of the most important properties of biologically active substances and lipophilicity calculations have attracted considerable interest in drug research. The correlations between *in silico* hydrophobicity parameters, (calculated log*P*) and chromatographically obtained hydrophobicity parameters (R_M^0 and C_0) were established. The good correlations indicate that computed log*P*, with careful selection of method calculation could be used as high-throughput screening technique for ACE inhibitor's lipophilicity evaluation.

Acknowledgment

This work was partly supported by the Ministry of Education and Science, Belgrade, Serbia, as a part of Project TR34031.

References

[1] R. Kaliszan, Chem. Rev., 2007, 107(7), 3212-3246.
[2] R. Mannhold, G. I. Poda, I. V. Tetko, J. Pharm. Sci., 2009, 98, 861-893.
[3] J. Odovic, B. Stojimirovic, M. Aleksic, D. Milojkovic-Opsenica, Z. Tesic, J. Serb. Chem. Soc., 2006, 71(6), 621-628.
[4] Molinspiration software: www.molinspiration.com
[5] Virtual Computational Chemistry Laboratory: www.vcclab.org
[6] CS Chem Office, Version 7.0, Cambridge Soft Corporation, Cambridge, MA, U.S.A., 2001.
[7] A. C. Moffat, M. D. Osselton, B. Widdop (eds) Clarke's Analysis of Drugs and Poisons. 4th ed., Pharmaceutical Press, London, 2011.

K-05-P

MOLECULAR DOCKING STUDIES, SYNTHESIS AND STRUCTURAL CHARACTERIZATION OF TWO NOVEL SOFT CORTICOSTEROIDS

V. Dobricic,[1*], B. Markovic,[1] V. Savic, [2] N. Milenkovic,[1]
S. Vladimirov, [1] O. Cudina, [1]

[1]*Department of Pharmaceutical Chemistry*
[2]*Department of Organic Chemistry*
University of Belgrade-Faculty of Pharmacy, Vojvode Stepe 450, 11221 Belgrade, Serbia

Abstract
In this study molecular docking calculations were performed on dexamethasone (anti-inflammatory drug) and four derivatives of hydrocortisone and methylprednisolone, simulating the interactions of these structures with the receptor for dexamethasone. Based on these results, methyl ester glycine amides of cortienic acids obtained from hydrocortisone and methylprednisolone were selected as compounds with potential anti-inflammatory activity. These compounds were synthesized in two steps from hydrocortisone and methylprednisolone. The first step is periodic oxydation of hydrocortisone and methylprednisolone to corresponding cortienic acids. The second step is amidation of obtained cortienic acids with glycine methyl ester hydrochloride. These compounds were structurally characterized using spectroscopic methods.

Introduction
Traditional drugs often undergo complex, multiple metabolic conversions to analog metabolites and reactive intermediates. Soft drugs are active as such, and consequently will produce the desired pharmacological activity at the site of application, but a predicted facile enzymatic process will metabolically deactivate the soft drug in a one-step process to an inactive species.[1] Cortienic acid is a metabolite of corticosteroids and it lacks anti-inflammatory activity. Soft corticosteroids are derived from cortienic acid and undergo predictive metabolism that reduces their toxicity. [2] The aim of this study is to select potentially active derivatives of hydrocortisone and methylprednisolone using molecular docking calculations and to synthesize and characterize these compounds.
Results and discussion

Molecular docking experiments
Molecular docking calculations were performed using Autodock v4.2 into the 3D structure of receptor for dexamethasone (pdb code:1m2z). Binding energies of

cortienic acids obtained from hydrocortisone and methylprednisolone (compounds 1 and 2, Figure 1) and methyl ester glycine amides of these acids (compounds 2 and 4, Figure 1) were calculated. These values were compared with the binding energy of dexamethasone (Table 1).

Table 1. Binding energies of synthesized compounds and dexamethasone.

Compound	Binding energy (kcal/mol)
Dexamethasone	-12.40
Compound 1	-10.74
Compound 2	-12.59
Compound 3	-11.32
Compound 4	-11.59

Compounds with the highest binding energies (compounds 2 and 4) were selected, synthesized and structurally characterized.

Synthesis of methyl 2-(11β,17α-dihydroxy-3-oxo-androst-4-en-17β-carboxamido) acetate

Hydrocortisone was oxydized to compound 1 (Figure 1) according to the literature procedure[3]. Compound 1 (50 mg, 0.14 mmol) was dissolved in 1,4-dioxane (10 ml) at room temperature. Subsequently, glycine methyl ester hydrochloride (MGH, 21 mg, 0.17 mmol), dimethylaminopyridine (DMAP, 21 mg, 0.17 mmol) and dicyclohexylcarbodiimide (DCC, 45 mg, 0.22 mmol) were added. After four days, reaction mixture was filtered and evaporated to dryness. Dry residue was dissolved in methanol and purified by preparative thin-layer chromatography, eluting with 95:5:1 (v/v/v) chloroform/methanol/glacial acetic acid, to yield the product (compound 2, Figure 1) as pale-yellow crystalline solid (12 mg, 20%). Melting point: 224-227.8 ^{o}C; IR (ATR) ν_{max} (cm^{-1}): 3423.65, 2921.08, 1742.67, 1653.61, 1515.21, 1238.33; m/z = 418.3 (M^{+}-1), 386.23, 368.27, 300.85, 342.27, 350.39, 400.30.

Synthesis of methyl 2-(11β,17α-dihydroxy-6-methyl-3-oxo-androsta-3,4-dien-17β-carboxamido)acetate

This compound (compound 4, Figure 1) was prepared, starting from methylprednisolone, as described in the preparation of compound 2. White crystalline solid was obtained (yield: 22%). Melting point: 142.5-144.5 ^{o}C; IR (ATR) ν_{max} (cm^{-1}): 3343.26, 2936.29, 1747.05, 1651.57, 1600.25, 1523.47, 1210.84; ^{1}H NMR (500 MHz, CD_3OD) δ 7.49 (d, 1H, J=10.1 Hz), 6.25 (dd, 1H, J=10.0 and 1.7 Hz), 5.99 (s, 1H), 3.73 (s, 3H), 2.78-2.71 (m, 2H), 1.50 (s, 3H), 1.13 (d, 3H, J=6.3 Hz), 1.00 (s, 3H); ^{13}C NMR (500 MHz, CD_3OD) δ 178.07, 177.35, 172.41, 161.02, 127.53, 119.83, 86.59, 71.07, 58.38, 52.73, 52.64, 46.50, 44.86, 41.99, 39.81, 34.67, 34.31, 32.96, 25.12, 22.13, 18.22, 17.88; m/z = 430.1 (M^{+}-1), 380.18, 398.22, 354.22, 412.23, 313.13, 362.16.

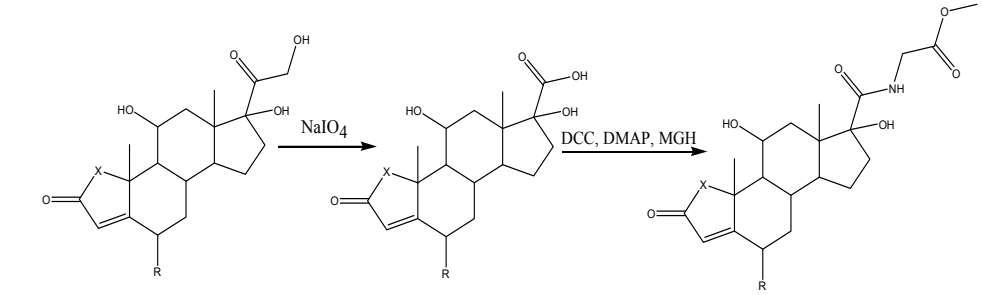

Figure 1. Synthesis of compounds 1-4.

Conclusion

Molecular docking calculations showed that compounds 2 and 4 have higher binding energies than compounds 1 and 3 (cortienic acids). This indicates that compounds 2 and 4 might have anti-inflammatory activity, which will be investigated *in vivo* by using the test of inhibition of croton oil-induced ear edema on rats. As potentially active soft corticosteroids, compounds 2 and 4 were synthesized in two steps and structurally characterized using spectroscopic methods.

Acknowledgement

This work was supported by the Ministry of education and science, Belgrade, Serbia, as part of project No. 172041.

References

[1] Membranes and Barriers: Targeted Drug Delivery, in S. Rao, Ph. D. Rapaka (Eds), NIDA Research Monograph, 1995, 154.

[2] N. Bodor, P. Buchwald, Soft drug design:general principles and recent applications, Center for Drug Discovery, University of Florida, Health Science Center, Florida.

[3] S. Nicholas, N. Bodor, Soft steroids having anti-inflammatory activity, US patent No 4996335, 1991.

K-06-P

COMPARISON OF STATIC AND CONTINUOUS HOLLOW FIBRE LIQUID-PHASE EXTRACTION OF LUTETIUM

K R. Kumrić[1], T M. Trtić-Petrović[1], G T. Vladisavljević[2]

[1]Laboratory of Physics, Vinča Institute of Nuclear Sciences, University of Belgrade, P.O. Box 522, Belgrade, Serbia, [2]Loughborough University, Department of Chemical Engineering, Leicestershire LE11 3TU UK

Abstract

This work is a comparative study of the efficiency of the lutetium (III) extraction in membrane-assisted liquid-phase extraction (LPE) carried out under static and continuous operation mode using di(2-ethylhexyl)phosphoric acid (DEHPA) as a carrier. The removal of Lu(III) from the donor solution and its recovery into the acceptor phase were compared for the two operation modes investigated. Additionally, the applicability of both systems for purification of ^{177}Lu-radiopharmaceutical was discussed.

Introduction

Radionuclide ^{177}Lu possesses favorable radiophysical characteristics for therapeutic application in nuclear medicine [1]. One of the main steps in the production process of ^{177}Lu-radiopharmaceutical is the separation of bound from unbound radionuclide. Membrane-assisted LPE offers the possibility of purification of the ^{177}Lu-radiopharmaceuticals, after the labeling procedure [2, 3].

Membrane-assisted LPE operates in a three-phase system and involves simultaneous extraction and re-extraction. The pores of a microporous hydrophobic membrane are filled with the organic phase (extractant) held by the action of capillary forces, while the feed (donor) and the stripping (acceptor) solutions are placed on each side of the membrane. Membrane-assisted LPE can be performed in a miniaturized system under static or continuous mode of operation.

The aim of the present study was to compare the removal efficiency and re-extraction of Lu(III) achieved in a static and continuous flow membrane-assisted LPE system. The systems were investigated with regard to the potential application in purification of ^{177}Lu-radiopharmaceutical.

Results and Discussion

Lutetium was extracted using two different membrane-assisted LPE systems: (i) static, hollow fibre LPE system (HF-LPE) in the absence of flow of any phase, and (ii) dynamic, HF-LPE system with recirculation of the aqueous donor and acceptor phases. Microporous polypropylene hollow fibre membrane, ACCUREL 50/280 (Membrana GmbH, Wuppertal, Germany) was used in the experiments. The extraction was performed under predetermined optimum experimental conditions [3]: the donor phase of 2 mg dm^{-3} Lu(III) in 0.2 M sodium acetate buffer at pH 3.5, the organic phase composed of 5% DEHPA in di-hexyl ether and the acceptor

phase of 2 M HCl. The membrane wall was impregnated with the organic phase, the acceptor phase was in the lumen of HF, and the donor phase was outside the HF. The efficiency of mass transfer of Lu(III) through the liquid membrane was evaluated using the following parameters: the removal efficiency (*R*) that represents the fraction of Lu(III) removed from the donor phase, the extraction efficiency (*E*) that represents a fraction of Lu(III) initially present in the donor phase that was found in the acceptor after extraction and the memory effect (*M)* that is the fraction of Lu(III) captured in the organic phase.

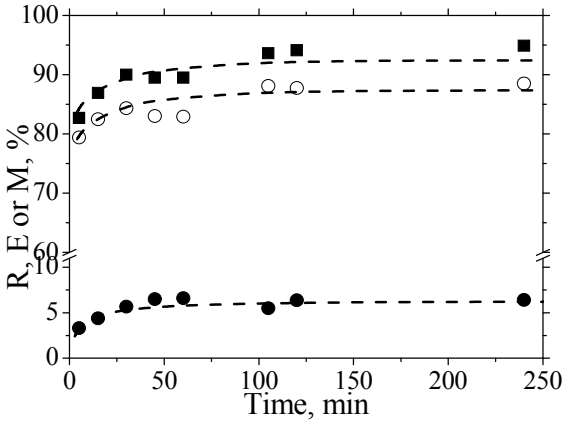

Figure 1. Time dependence of the efficiency parameters *R* (■), *E* (●) and *M* (○) in the static three phase HF-LPE system.

Fig. 1 shows the time-dependent parameters of Lu(III) transfer in HF-LPE under stagnant mode of operation with a volume of acceptor of 0.01 cm^3. As can be seen, the stagnant system was efficient in terms of the removal of Lu(III) from the donor phase, but poorly efficient in terms of Lu(III) recovery from the organic into the acceptor phase. As the acceptor volume increased from 0.01 to 0.06 cm^3 as a result of increased HF length, the extraction efficiency improved from 5 to 15 % but even at the highest acceptor volume, 85% of the extracted amount of Lu(III) remained in the membrane. A further increase of the acceptor volume beyond 0.06 cm^3 was impractical.

Continuous HF-LPE of Lu(III) was carried out in the self-designed membrane contactor containing a single HF membrane. This configuration enables recirculation of both aqueous phases. Fig. 2 shows the time-dependent efficiency parameters in HF-LPE under recirculation of the acceptor phase (3 cm^3) through the lumen of the fibre and donor phase (20 cm^3) outside the fibre. As can be seen from Fig. 2, continuous HF-LPE system enables not only efficient removal of Lu(III) from the donor to the organic phase, but also its recovery from the organic to the acceptor phase. The accumulation of Lu(III) in the membrane was less than 5%, meaning that re-extraction of Lu(III) was almost complete.

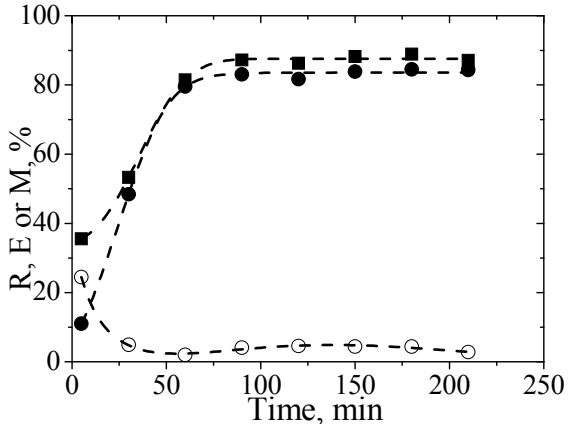

Figure 2. Time dependence of the efficiency parameters *R* (■), *E* (●) and *M* (○) in the HF-LPE system with the recirculation of aqueous phases (donor flow rate: 5.3 cm^3 min^{-1}, acceptor flow rate: 0.4 cm^3 min^{-1}).

Conclusion

The removal efficiency of Lu(III) from the aqueous donor solution was very high when both static and continuous HF-LPE were applied, which is of prime importance with regard to the potential application in purification of ^{177}Lu-based radiopharmaceuticals. The main advantage of continuous over static system is almost complete re-extraction of Lu(III) into the acceptor phase.

Considering practical aspects, static HF-LPE is easier to operate, which is very important when working with radioactive material, and more suitable for low volume production, as is often the case in radiopharmaceutical production. Continuous HF-LPE requires higher volumes of donor phase for the operation and there are more potential leakage points that can cause accidental release of radioactive material.

Acknowledgment

We acknowledge the support to this work provided by the Ministry of Education and Science of Serbia through project *Physics and Chemistry with Ion Beams*, No. III 45006.

References

[1] S. Banerjee et al., Nucl. Med. Biol., 2004, 31, 753-759.
[2] K. Kumrić et al., Sep. Purif. Techn., 2006, 51, 310-317.
[3] T. Trtić-Petrović et al., J. Sep. Sci., 2010, 33, 2002-2009.

K-07-P

LIQUID-PHASE MICROEXTRACTION IN A SINGLE HOLLOW FIBRE - DETERMINATION OF MASS TRANSFER COEFFICIENT

T. M. Trtić-Petrović[1], K. R. Kumrić[1],T. Vladisavljević[2],
J. S. Đorđević[1], J. Åke Jönsson[3]

[1]Laboratory of Physics, Vinča Institute of Nuclear Sciences, University of Belgrade, Belgrade, Serbia, [2]Loughborough University, Department of Chemical Engineering, Leicestershire UK, [3]Center for Analysis and Synthesis, Department of Chemistry, Lund University, Sweden

Abstract

In this study, the mass transfer coefficient of two local anesthetics in liquid-phase microextraction (LPME), which is performed in a single hollow fibre, was investigated. Previously developed mathematical model has been applied for the determination of the overall mass transfer coefficient based on the acceptor phase, K_A, in an unsteady-state LPME [1].

Introduction

Miniaturized LPME has been developed using flat or hollow fibre membrane and applied to concentrate analytes prior to chromatographic analysis [2]. Recently, an alternative concept of unsteady-state LPME in a single hollow fibre (HF-LPME) has been introduced [3] and focused mainly on sample preparation and equilibrium sampling.

The quantification of mass transport coefficients in LPME is important for a proper design and operation of the process and for the purpose of identification of rate limiting steps during mass transfer of solute(s) through the membrane. The overall mass transfer coefficient based on the acceptor phase, K_A, in HF-LPME has been estimated from time-dependent concentration of extracted analyte in the acceptor phase while maintaining a constant analyte concentration in the donor phase:

$$K_A = -\frac{V_A}{A}\frac{\partial}{\partial t}\left[\ln\left(\frac{C_A^* - C_A}{C_A^*}\right)\right] \quad (1)$$

where V_A is the volume of the acceptor phase, A is the area of the hollow fibre wall, and C_A^* and C_A is the equilibrium and actual concentration of the analyte in the acceptor phase in time t. The proposed conditions can be achieved either using a relatively large volume of the donor phase or tuning the extraction conditions in order to get a very low enrichment factor, so that the analyte concentration in the bulk of the donor phase can be regarded as a constant. The purpose of this work was to determinate the overall mass transfer coefficient of the selected drugs in an unsteady-state HF-LPME.

Results and Discussion

The investigated local anesthetics bupivacaine (Bup) and lidocaine (Lid) are amines with the values of the dissociation constants (pK_a) of 8.9 and 8.5, respectively. The equilibrium extraction could be reached by adjusting the pH of the acceptor solution. The stripping of the investigated compounds was complete at the acceptor pH at least 3 pH units below the pK_a value of the analyte. With increasing acceptor pH, the amount of nonextractable form of the amines in the acceptor decreased, the back extraction of the amine decreased and the resistance to the mass transfer in the acceptor phase increased.

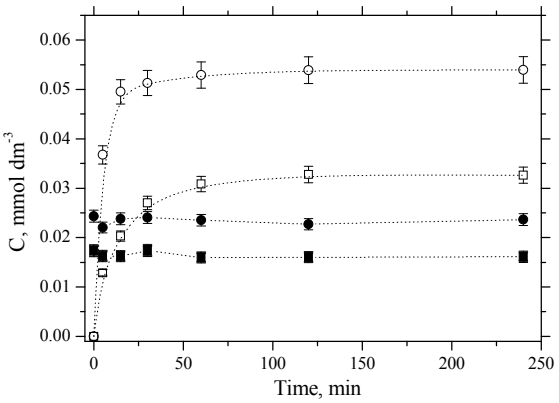

Figure 1. Time dependence of Lid and Bup in the acceptor (C_A) and donor (C_D) phases. Legend: Lid C_D - ●, C_A - ○; Bup C_D - ■, and C_A - □.

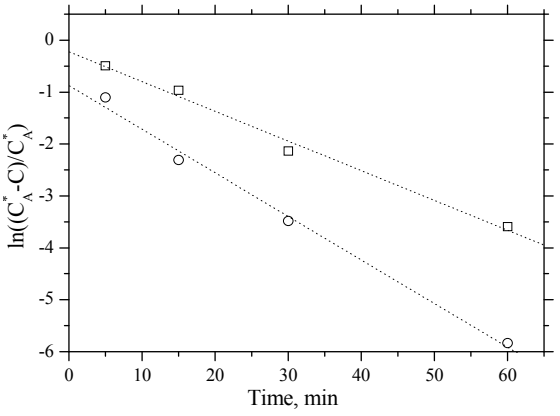

Figure 2. Semi-log plot of the local anesthetics concentration driving force versus time. Legend: ○ - Lid and □ - Bup.

The investigated drugs were extracted in the three phase extraction system [4], from the donor phase (0.067 mol dm^{-3} phosphate buffer at pH 7.5 or blood plasma), through the organic phase placed in the hydrophobic membrane pores (5% TOPO in di-hexyl ether), and finally reextracted into the acceptor phase. The experimental conditions of the acceptor pH can be found in Ref. [3]. Fig. 1 shows the time dependence of the concentration of the investigated drugs in the donor and acceptor phase. Comparing the initial concentration of the drug in the donor phase (0.025 and 0.018 mmol dm^{-3} for Lid and Bup, respectively) and the concentration at certain extraction time, it can be seen that the depletion of the drug from the donor phase was less than 5%, and Eq. (1) can be applied for determination of K_A.

Fig. 2 is a plot of the ratio of concentration driving force (the difference between the equilibrium and actual concentration of the analyte in the acceptor phase) and equilibrium concentration in the acceptor phase versus time for the studied local anaesthetics. The similar dependence was obtained for the extraction

of the local anesthetics from plasma sample. The slope of $\ln[(C_A^* - C_A)/C_A^*]$ vs. t line is equal to $-K_A A/V_A$ and enables K_A to be determined in a batch system under unsteady-state conditions. The calculated values of K_A of the investigated drugs are given in Table 1. The mass transfer coefficient of the drug with higher protein binding (Bup) was higher for extraction from buffer solution than that from plasma solution i.e. K_A was higher for the higher initial drug concentration.

Table 1. The overall mass transfer coefficient of studied local anesthetics.

Compound	Donor	C_D^{in}, mmol dm^{-3}	pH_A	$K_A \times 10^4$, cm min^{-1}
Lidocaine	buffer	0.024	7.2	5.0
Lidocaine	plasma	0.024 ([a]PB 11%)	7.2	5.1
Bupivacaine	buffer	0.017	7.4	3.4
Bupivacaine	plasma	0.017 ([a]PB 69%)	7.4	3.0

[a]PB is protein binding defined and estimated in Ref. [4]

Conclusion

The determination of the overall mass transfer coefficient in HF-LPME under non steady-state conditions was demonstrated in this paper. The results show that the developed mathematical model was successfully applied for determination of K_A.

Acknowledgment

We acknowledge the support to this work provided by the Ministry of Education and Science of Serbia through project No. III 45006.

References

[1] K.Kumrić, et al, J. Sep. Sci., 2012, in press.
[2] J.Å. Jönsson, et al, J. Sep. Sci., 2001, 24, 495-507.
[3] S. Pedersen-Bjergaard, et al, J. Chromatogr. A, 2008, 1184, 132-142.
[4] Trtić-Petrović, et al, J. Chromatogr. B, 2005, 826, 169-176.

K-08-P

^{99m}Tc-COMPLEX OF NOVEL DIAMINE-DIOXIME LIGAND

M. Mirković[1], S. Vranješ-Đurić[1], D. Stanković[1], Đ. Petrović[1], D. Mijin[2], N. Nikolić[1]

[1]*Laboratory for Radioisotopes, Vinča Institute of Nuclear Sciences, University of Belgrade, P.O.Box 522, 11001 Belgrade, Serbia*
[2]*Faculty of Technology and Metallurgy, University of Belgrade, Karnegijeva 4, P.O. Box 3503, 11120 Belgrade, Serbia*

Abstract
Novel diamine-dioxime ligand, 4,7-diaza-3,8-diethyldecane-2,9-dione bis oxime (LH_2), derivative of hexamethyl-propylene amine oxime (HMPAO), was synthesized in order to develop new brain perfusion imaging agent, based on ^{99m}Tc(V) complexes. The ^{99m}Tc(V)-d,l-HMPAO complex is well-known radiopharmaceutical for brain imaging. The structures of the synthesized compound were characterized by UV-Vis, IR, ^{1}H NMR and ^{13}C NMR. The procedure for radiolabeling of diamine-dioxime with ^{99m}Tc was developed and radiolabeling yield of the ^{99m}Tc-complex was followed by paper and thin-layer chromatography. The maximum radiolabeling yield was obtained when the reactions were carried out at pH~9 within 10 min at room temperature (RT). Biodistribution studies on rats has shown significant uptake of ^{99m}Tc-complex (2.1% ID), 2 min after injection.

Introduction
The clinical usefulness of ^{99m}Tc-labeled complexes depends on their ability to rapidly cross cell membranes, high stability and rapid clearance from vital organs and tissues [1]. Among radiopharmaceuticals for imaging cerebral blood flow (CBF) by single-photon emission computed tomography (SPECT) in nuclear medicine, ^{99m}Tc-*d,l*-HMPAO (hexamethyl-propylene amine oxime) and ^{99m}Tc-*l,l*-ECD (ethyl cysteinate dimer), combine the best overall features of high brain uptake, fixed regional distribution within the brain and their distribution in the brain is proportional to CBF in a wide range [2]. Both the ligands form neutral and lipophilic complexes with ^{99m}Tc possessing an oxotechnetium core. The HMPAO belongs to the class of diamine-dioxime compounds, which are good chelating agents due to the presence four nitrogen atoms that coordinate with ^{99m}Tc(V) in aqueous media. The goal of this work was to examine the use of a new ligand, derivative of HMPAO, as a potential candidate for the brain-perfusion imaging in SPECT. Although the ligand shows stereoisomerism, the presented work is based on research of isomeric mixtures of the meso- and d,l- diastereoisomers without the diastereo-enantio separation.

Experimental

^{99m}Tc ($T_{1/2}$=6 h, E_γ=140 keV) was eluted from a ^{99}Mo-^{99m}Tc generator (The Vinča Institute of Nuclear Sciences, Belgrade, Serbia). All reagents obtained from commercial sources were of analytical grade and used without further purification. IR spectra were recorded on a Bomem MB 100 IR spectrophotometer using prepared KBr pellets. The ^{1}H and ^{13}C NMR spectral measurements were performed on a Varian Gemini 2000 (200 MHz) at RT with deuterated DMSO (d^6-DMSO) as solvents. The melting points were determined by Mel-Temp melting point apparatus (Laboratory Devices Inc., USA). Radioactivity measurements were done in a NaI(TI) well-type gamma counter (LKB Wallac Compu Gamma Counter, Finland). Spectrophotometric measurements were carried out using an Uvicon 810/820 spectrophotometer (Kontron Instruments, Austria) with 10 mm quartz cells.

Preparation of ligand. 4,7-diaza-3,8-diethyldecane-2,9-dione bis oxime (LH_2) was prepared using the method described in the literature [3]. Yield: 80%, mp: 133-134 °C. λ_{max}= 205 nm. Selected IR data (KBr, pallets, cm^{-1}): ν_{OH} 3264, $\nu_{(OH, NH)}$ 3212. ^{1}H NMR (200 MHz, DMSO-d_6, δ ppm): 0.76 (CH_3(C5), 3H, t, *J*=7.5 Hz), 1.35-1.50 (CH_2(C4), 2H, m), 1.62 (CH_3(C1), 3H, s), 2.34 (CH_2(C6), 2H, s), 2.90 (CH(C3), 1H, t, *J*=7.3 Hz), 10.32 (-OH, 1H, s). ^{13}C NMR (200 MHz, DMSO-d_6, δ ppm): 10.89 C(1), 157.56 C(2), 63.12 C(3), 25.83 C(4), 8.37 C(5), 46.50 C(6).

Results and Discussion

Radiolabeling procedure. Radiolabeling conditions were optimized to give the maximum yield of ^{99m}Tc-complex. Complexation studies of ligand with ^{99m}Tc(V) were carried out using $SnCl_2$ as a reducing agent. Dissolution of desire amount of LH_2 in oxygen-free double-distilled H_2O was achieved by acidification with HCl_{conc} to pH 1.5-2. The solution was bubbled with N_2 gas and cooled in an ice bath. Then, appropriate volume of $SnCl_2$ stock solution (5 mg of anhydrous $SnCl_2$ in 0.05 ml of HCl_{conc} diluted up to 10 mL of H_2O) was added and the pH adjusted to 9. After the addition of sodium pertechnetate ($^{99m}TcO_4^-$, 18.5-37 MBq/mL), the solution was gently shaken and allowed to stand 10 min at RT. The total reaction volume in vial was maintained at 4 mL. Sn(II):LH_2 mole ratio was 1:55.

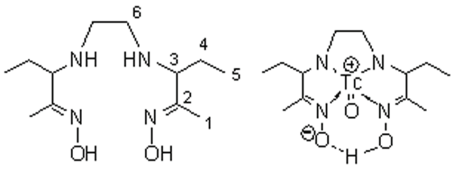

Figure 1. Structure of LH_2 and proposed structure of ^{99m}Tc-complex.

According to the literature data for similar diamino-dioxime ligands and their ^{99m}Tc(V)-labeled complexes [4], proposed structures of LH_2 and ^{99m}Tc-complex are shown in Fig.1. Numbering of C-atoms in Fig.1 was used for ^{1}H NMR and ^{13}C NMR spectra interpretation.

Radiolabeling yield. The labeling yield as well as the stability of the ^{99m}Tc-complex were determined using a combination of two chromatographic systems: paper chromatography on Whatman No.1 with acetonitrile:water (1:1) as the mobile phase and TLC on silica gel 60 strips with saline as the mobile phase. Stability of the ^{99m}Tc-complex was determined by investigation of radiochemical purity of the complex at different time intervals after labeling (Fig.2A). The content of free $^{99m}TcO_4^-$ and ^{99m}Tc-reduced-hydrolyzed in the form of $^{99m}TcO_2$ were considered as radiochemical impurities.

Biodistribution of ^{99m}Tc-complex. Healthy male 8-weeks old Wistar rats, 200-250 g body weight (n=3 per each time point) were intravenously (i.v.) injected through the tail vein with 0.1 mL of ^{99m}Tc-complex (approx. 0.5–1.0 MBq per animal). The animals were sacrificed *via* spinal cord dislocation at 2, 5, 15, 30 and 60 min after injection and the radioactivity in brain was measured. ^{99m}Tc-complex exhibits good uptake in the brain (2.10% of injected dose (%ID)) at 2 min after injection (Fig.2B.)

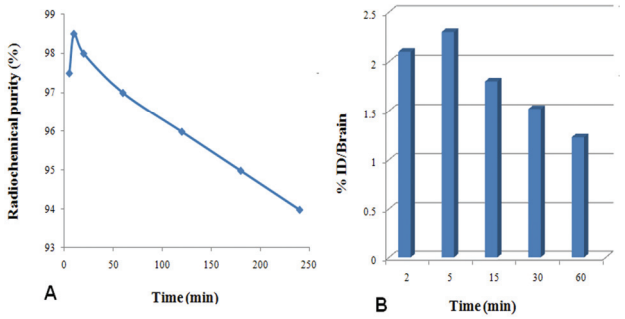

Figure 2. Radiochemical purity(A); Brain uptake(B) of the ^{99m}Tc-complex.

Conclusion

A new diamine-dioxime ligand, 4,7-diaza-3,8-diethyldecane-2,9-dione bis oxime (LH_2) were synthesized in high yields, characterized by UV-Vis, IR, ^{1}H, and ^{13}C NMR and successfully labeled with ^{99m}Tc(V). From the obtained results, it can be concluded that ^{99m}Tc(V) complex could be made easy with a ligand such as LH_2. This complex showed good stability, higher than 94% up to 4h during storage at RT. The present study suggests that complex exhibited favorable properties as promising candidates for cerebral perfusion imaging.

References

[1] M. Mallia, S. Subramanian, et al, Bioorg. Med.Chem. 2006, 14, 7666-7670.
[2] F. Shishido, K. Uemura, et al, J. Cereb. Blood. Flow Metab. 1994, 14, 66-75.
[3] S. Banerjee, G. Samuel, et al, Nucl. Med. Biol., 1999, 26, 327-338.
[4] L. Canning, et al, United States Patent, Patent number 4.789.736, 1988,

K-09-P

^{99m}Tc(I)-TRICARBONYL LABELING OF ETHYLENE DIAMINE-N,N´-DI-3-PROPANOATE DIETHYL ESTER AS POTENTIAL RADIOPHARMACEUTICAL AGENT

M. Lakić[1], D. Janković[1], A. Savić[2], Lj. Sabo[3], T. Sabo[2]
[1]*Vinča Institute of Nuclear Sciences, University of Belgrade, Serbia*
[2]*Faculty of Chemistry, University of Belgrade, Serbia*
[3]*Clinical Center of Serbia, Belgrade, Serbia*

Abstract
There is an increasing interest for the ^{99m}Tc labeling of biomolecules by using bifunctional chelating agents like ethylenediamine-N,N´-di-3-propanoate diethyl ester (deeddp). To find new ligand, which can be linked to the small biomolecules and coordinated with $[^{99m}Tc(CO)_3(H_2O)_3]^+$ precursor, is a challenging task. Radiolabeling of deeddp with $[^{99m}Tc(CO)_3(H_2O)_3]^+$ precursor, stability studies and biodistribution of formed complexes were carried out, including challenge with histidine. Radiochemical yield of ^{99m}Tc(I)-tricarbonyl-deeddp complexes was higher than 95%. These complexes were stable *in vitro* and showed a very good biological behavior. The radiochemical and biological features of the novel ^{99m}Tc(I)-complexes, as well as, the nature of the ligands, make them very promising candidates for labeling of tumor specific biomolecules.

Introduction
Technetium radiopharmaceuticals, as complexes of the ^{99m}Tc radionuclide, are of great importance in diagnostic nuclear medicine. Over the last few years, the chemistry of a novel organometallic species, $M(CO)_3^+$ (M=Tc, Re), has been intensively developed and the water soluble technetium tricarbonyl complex $[^{99m}Tc(CO)_3(H_2O)_3]^+$ was seen to be very versatile and effective precursor for labeling biomolecules [1]. The three coordinated molecules of water are labile and could be readily exchanged with various mono-, bi- and tridentate ligands. New chelating agents have been synthesized with the aim toward the design and development of site-specific radiopharmaceuticals [2-4].The aim of this study is to label ligand deeddp with ^{99m}Tc(I)-tricarbonyl precursor. The stability of the formed complexes and theirs *in vitro* and *in vivo* properties were investigated too.

Experimental
The sample of ligand was prepared by dissolving in water appropriate amount of substance for obtaining 10^{-3} mol/dm^3 solutions. pH was adjusted to 9.0. ^{99m}Tc-carbonyl precursor was prepared according to the manufacturer instruction (IsoLinkTM, Mallinckrodt Medical B.V., The Netherlands). ^{99m}Tc(I)-tricarbonyl-ligand complexes were prepared by addition of 0.9 ml of ligand solutions to 0.1 ml of $[^{99m}Tc(CO)_3(H_2O)_3]^+$ precursor with appropriate pH values. The vial was heated for 30 min in boiling water bath. The labeling efficiency of ^{99m}Tc(I)-tricarbonyl targeted ligand was determined using gradient HLPC equipped with UV and radioactive γ-detector on Nucleosil 100-5 C-18 column. The 0.1% solution of TFA

(trifluoroacetic acid) in H_2O and 0.1% of TFA in acetonitrile were used as mobile phases. Aliquot of 100 µl of the ^{99m}Tc complexes (final concentration of ligands 10^{-6} M) was added to 900 µl of a 10^{-2} M histidine solution in PBS (phosphate buffered saline), pH 7.4. The samples were incubated at 37^0 C and periodically aliquots were removed and analyzed by HPLC. TCA (trichloroacetic acid) precipitation method for determining the percentage of ^{99m}Tc(I)-tricarbonyl-deeddp bound to proteins (12% human albumin, incubation at 37ºC for different time intervals) was very useful. All lipophilicity measurements were done by solvent extraction method with n-octanol equilibrated with 0.15M phosphate buffers (pH=6.0-7.5). Organ biodistribution studies were carried out on white health Wistar rats (four weeks old). The animals were sacrificed 5, 30, 60 and 120 minutes after application of 0.1ml of ^{99m}Tc(I)-tricarbonyl-deeddp. The radioactivity per organ of interest was measured in a NaI(Tl) detector.

Results and Discussion

The bifunctional chelating agent approach is currently among the cutting edge technologies used in the design of new radiopharmaceuticals. The choice of a chelator agent may be crucial in the biological behavior of a radiopharmaceutical.

A novel bifunctional chelating agent deeddp has been synthesized and characterized. Radiolabeling of deeddp with the $[^{99m}Tc(CO)_3(H_2O)_3]^+$ precursor with heating at 95ºC and at pH 8-9 led to the formation of ^{99m}Tc(I)-tricarbonyl-coordinated complexes of deeddp with a radiochemical yield higher than 95% as determined by HPLC analysis. The three peaks in the radio-HPLC profile indicated the presence of isomers (Fig.1). Radiochemical stability was monitored during 24 h. ^{99m}Tc(I)-tricarbonyl-deeddp complexes showed a good stability and less than 5% of radiochemical impurities were observed even for the later time point studied. Challenge experiments with up to 1000-fold molar excess of histidine showed no degree of transchelation for radiocomplex during 24 h at 37°C.

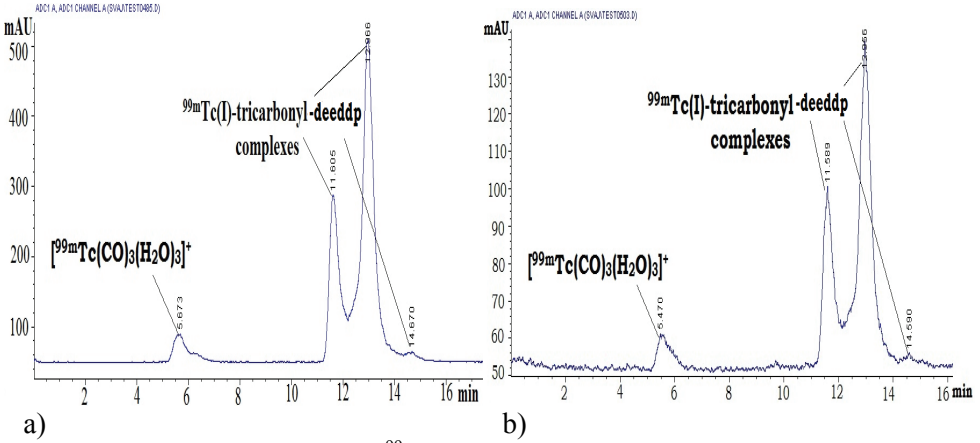

Figure 1. Radiochromatograms of ^{99m}Tc(I)-deeddp complexes a) 30 minutes after labeling b) 24h after labeling.

We assessed the interaction of ^{99m}Tc(I)-tricarbonyl-deeddp complexes with human serum albumin as an important constituent of human blood which could affect on their biological behavior. At 1h, the binding was 10.49±1.23%. The lipo-hydrophilic character of ^{99m}Tc(I)-tricarbonyl-deeddp complexes was evaluated based on the octanol/water partition coefficient (K_d). K_d value was 0.63±0.05 (mean±S.D.) arguing for a higher lypophilic character of the complexes.

Figure 2 shows the biodistribution results for ^{99m}Tc(I)-tricarbonyl-deeddp complexes. The first set of biodistribution data, 5 min post injection (pi), showed a very high uptake in liver, kidneys and intestine. The radioactivity was quickly cleared from liver and kidneys, thereby reaching very low levels within 120 min pi. Moreover, a remarkable intestinal uptake was observed for ^{99m}Tc(I)-tricarbonyl-deeddp complexes even at the later time points studied.

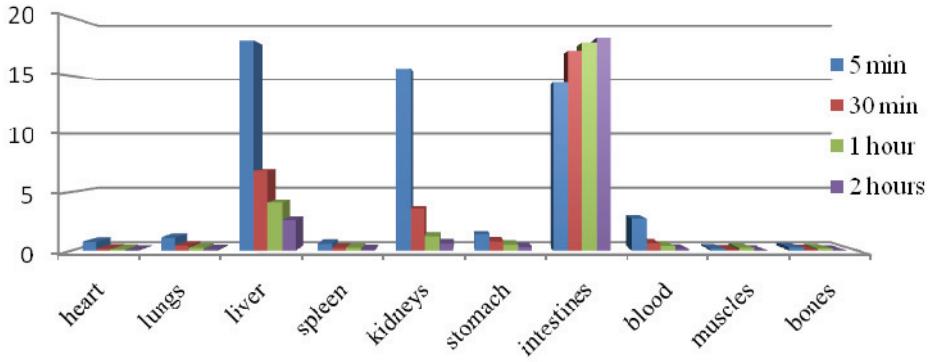

Figure 2. Organ distribution data of ^{99m}Tc(I)- tricarbonyl-deeddp in Health Wistar rats (% ID/g)

Conclusion

The studied ligand, having a bifunctional NN donor atom set, was easily coordinated with ^{99m}Tc(I)-tricarbonyl core in aqueous solution forming neutral complexes. Radiochemical purity and yield of labeling were very high. The complexes were very stable for at least 24 hours. The labeled deeddp ligand has been shown to be very stable against ligand exchange, and due to its relative lipophilicity has a very good biodistribution profile. With these points in mind this chelating agent provides a promising architecture for use in labeling tumor specific biomolecules.

References

[1] R. Alberto, R. Schibli, A. Egli, P. A. Schubiger, J. Am. Chem. Soc., 1998, 120, 7987-7988.

[2] R. Schibli, R. La Bella, R. Alberto, et al, Bioconj. Chem., 2000, 11, 345-351.

[3] M. Santimaria, U. Mazzi, S. Gatto, et al, J. Chem. Soc. Dalton Trans., 1997, 42, 1765-1771.

[4] G. N. Kaluđerović, T. J. Sabo, Polyhedron, 2002, 21, 2277-2282.

PHYSICOCHEMICAL EVALUATION OF TECHNETIUM-99m COMPLEXES WITH BACLOFEN

D. Stanković, D. Janković, M. Mirković, M. Lakić,
S. Vranješ-Djurić, N.Nikolić
Laboratory for Radioisotopes,Vinča Institute of Nuclear Sciences,
University of Belgrade, P.O.Box 522, 11001 Belgrade, Serbia

Abstract
The ^{99m}Tc-labeling of baclofen (Bac), a muscle relaxant, as well as physicochemical properties of the labeled compounds are investigated. Two different approaches for the labeling with ^{99m}Tc have been studied: direct reduction with tin(II)chloride and the 'organometallic approach' using $[^{99m}Tc(CO)_3(H_2O)_3]^+$ precursor. The direct labeling approach was not successful and the yield was poor. The use of $[^{99m}Tc(CO)_3(H2O)_3]^+$ precursor pointed at the formation of ^{99m}Tc(I) coordinated complexes with high yield. In this approach, pH didn't influence the yields. Promising results of *in vitro* experiments suggest that ^{99m}Tc(I)-baclofen may be of potential use for diagnosis of some central nervous system disorders.

Introduction

Baclofen is a structural analogue of gamma-aminobutyric acid (GABA). It is a selective agonist of $GABA_B$ receptors in central nervous system and it's primarily used to treat spasticity. Also, it is in the early stages of use for the treatment of alcoholism. Baclofen is a muscle relaxant medicine commonly used to decrease spasticity related to multiple sclerosis, spinal cord injuries, or other neurological diseases. It could be used in oral use or intrathecal way. Its ways in organism are not well known nowadays [1].

^{99m}Tc has ideal physical properties for many applications in nuclear medicine therefore it is still the radionuclide of choice. A large number of techniques for radiolabeling with ^{99m}Tc have been developed. They are classified as: direct labeling, the preformed chelate approach and the bifunctional chelating or indirect labeling approach. The study of technetium radiopharmaceuticals has been stimulated by the availability of radioactive ^{99m}Tc(I) precursor $[Tc(CO)_3(H_2O)_3]^+$ [2]. As the three water ligands are labile, they can be readily exchanged with different mono-, bi- and tridentate donor ligands, like phosphines, thioethers and aromatic amines. Hydrophilic organometallic $[^{99m}Tc(H2O)_3(CO)_3]^+$ precursor allows the formation of Tc (I) radiopharmaceuticals based on the fac-$[^{99m}Tc(CO)_3]^+$ (I) core. This way is known as 'organometallic labeling approach'[3]. In this paper the possibility for the formation of ^{99m}Tc complexes with baclofen was studied.

Experimental

All chemicals used in our experiments were of analytical purity grade (Sigma Aldrich and Merck).The direct labeling method was investigated performing different experiments by varying the reducing agent amount, the labeling mixture pH (3.0-8.0) and the reaction temperature. An aqueous solution of baclofen (10^{-3}M) was prepared.

To a 10 ml vial, 0.3 ml of baclofen solution in H_2O was added and followed by $SnCl_2x2H_2O$ solution (10^{-4}M) in 0.1 M HCl, thus molar ratios Sn(II):baclofen were 1:1, 1:10, 1:25 and 1:50. The stock solution of $SnCl_2x2H_2O$ was prepared by dissolving of the measure amount of the pure salt in concentrated HCl and then diluting it with doubly distilled water under the define volume. pH of these mixtures was adjusted at 3.0, 5.0 and 8.0, to the total volume of 3.0 ml. 18.5 MBq $^{99m}TcO_4^-$ eluate in 0.9% NaCl, from ^{99m}Tc-generator (Vinča) was added. The reaction mixtures were allowed to stand at room temperature (RT) or heated at boiling temperatures for 30min.

$[^{99m}Tc(CO)_3(H2O)_3]^+$ion was prepared by addition of 1ml of ^{99m}Tc-pertechnetate (740-1110 MBq$^{99m}TcO_4^-$) to a penicillin vial with lyophilized form of 7.15 mg sodium carbonate, 4.5 mg sodium boranocarbonate, 2.85 mg sodium tetraborate and 8.5 mg sodium tartarate (IsoLink^{TM}, Mallinckrodt Medical B.V., The Netherlands). After heating for 30 minutes in a boiling water bath and cooling, pH of solution was adjusted to desired value with 1M HCl. ^{99m}Tc-carbonyl-baclofen was prepared by addition of 0.1 ml of investigated muscle relaxant solutions to 0.9 ml of $[^{99m}Tc(CO)_3(H_2O)_3]^+$ precursor. The samples were labeled with ^{99m}Tc (I), without and with heating (30 min in boiling water bath). The complex stability after 24 hour time was investigated, too.

HPLC analysis was performed by isocratic HPLC. All measurements were made on liquid Chromatograph, Hewllet Packard 1050 (C18column (250x4,6mm)) with UV and Raytest gamma flow detector. The different methanol/water mixtures prepared from HPLC grade water, were used as mobile phases.

Results and Discusion

The direct labeling method was not successful and the labeling yield was poor. Varying of the reducing agent amount, the labeling mixture pH (3.0-8.0) and the reaction temperature did not improve the yield substantially. However the use of $[^{99m}Tc(CO)_3(H2O)_3]^+$ precursor, at pH 3.0, 5.0 and 8.0 with and without heating resulted in the formation of ^{99m}Tc(I) coordinated complexes of baclofen in high yields that was shown by radiochromatograms. The best results are obtained at pH 3.0 (Fig.1) and 8.0 at RT. The retention times together with the labeling yield are summarized in Table 1.

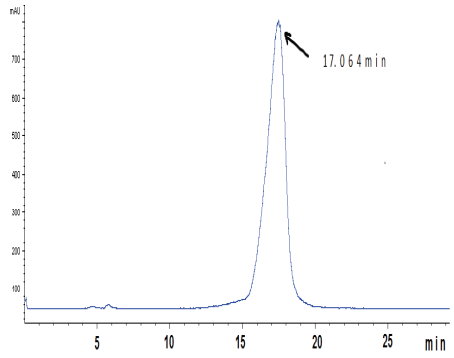

Figure1. HPLC radiochromatogram of ^{99m}Tc(I)-Bac labeled at RT, pH=3.0

Table 1. The influence of pH and heating on retention times (R_t) and labeling yield (Y) of baclofen coordinated to $[^{99m}Tc(CO)_3(H_2O)_3]^+$ precursor.

Samples	pH	3.0		5.0		8.0	
	^{99m}Tc-species	R_t (min)	Y (%)	R_t (min)	Y (%)	R_t (min)	Y (%)
$[^{99m}Tc(CO)_3(H_2O)_3]^+$ +Bac, at RT	$^{99m}Tc(CO)_3$ ^{99m}Tc(I)-Bac	5.238 17.064	0.3 99.7	5.215 16.238	11.2 88.8	5.082 16.354	1.2 98.8
$[^{99m}Tc(CO)_3(H_2O)_3]^+$ +Bac, with heating at 95^0C	$^{99m}Tc(CO)_3$ ^{99m}Tc(I)-Bac	5.296 16.770	4.9 95.1	5.262 14.386	14.9 85.1	4.940 16.659	6.8 93.2
$[^{99m}Tc(CO)_3(H2O)_3]^+$ +Bac, at RT after 24h	$^{99m}Tc(CO)_3$ ^{99m}Tc(I)-Bac	5.257 17.076	1.6 98.4	5.317 15.277	14.8 85.2	5.267 14.417	7.1 92.8
$[^{99m}Tc(CO)_3(H2O)_3]^+$ +Bac, with heating at 95^0Cafter 24h	$^{99m}Tc(CO)_3$ ^{99m}Tc(I)-Bac	5.325 15.327	15.2 84.8	5.346 15.513	15.9 84.1	5.248 14.151	8.2 91.8

HPLC results revealed that radiolabeling yields were not significantly affected by pH values within the range pH 3.0–8.0 at RT. We assume that the different retention times of formed complexes are a consequence of the influence of pH and temperature on the structure and composition of these complexes. Bac contains both a carboxyl and an amino group and by a change in pH these groups are in their protonated or deprotonated forms. Depending on the forms, Bac can be mono- or bidentate ligand and easily forms different complexes with the *fac*-$[^{99m}Tc(CO)_3]^+$ (I) core. The following experiments on animals should show the impact of different structures of the complexes on their biological behavior. All complexes showed excellent stability in 24 hour time (>80%).

Conclusion

The results presented in this paper reveal that complexation of the baclofen are highly dependent on the labeling approach and the oxidation state of ^{99m}Tc. Direct ^{99m}Tc-labeling of baclofen, known to be weak-chelating agent, gave high concentrations of $^{99m}TcO_2^-$ and free $^{99m}TcO_4^-$. The best labeling yield was obtained with $[^{99m}Tc(CO)_3(H_2O)_3]^+$ precursor when labeling was done at RT.

References

[1] A. C. Miracle, M. A.Fox at al., Am. J. Neuroradiol., 2011, 32, 1158-1164.
[2] R. Alberto, R. Schibli, A. Egli, P. A. Schubiger, J. Am. Chem. Soc., 1998, 120, 7987-7988.
[3] A. Egli, R. Alberto, L. Tannatoli, R. Schibli at al, J. Nucl. Med., 1999, 40, 1913-1917.

K-11-P

PREPARATION OF ^{90}Y-LABELED TIN FLUORIDE COLLOID FOR RADIOSYNOVECTOMY

D. Janković, S. Vranješ-Djurić, M. Marković, M.Mirković, D.Stanković, M. Lakić, N. Nikolić

Laboratory for radioisotopes, Vinča Institute of Nuclear Sciences, University of Belgrade, P.O.Box 522, Belgrade 11001, Serbia

Abstract

In this study, tin fluoride colloid (SnF-c) was prepared, labeled with ^{90}Y and characterized with respect to its physicochemical properties.

Particle size of SnF-c, at constant concentration of SnF_2, was dependent on pH, concentration of NaF, temperature and time. The particle size of SnF-c decreased with an increase in NaF concentration and a decrease in reaction mixture pH. Radiolabeling yield of ^{90}Y-SnF-c at higher temperature increased and it was greater than 98% for the preparation at 95 ^{o}C. Due to high labeling yield and stability, ^{90}Y-SnF-c might be a promising agent for radiosynovectomy.

Introduction

Radiosynovectomy (RS) was introduced as a modality for the treatment of rheumathoid arthritis as early as 1950's and the number of studies has been growing each year [1, 2]. Due to its convenience, long-term effects, repeatability and surgery avoidance, RS has been used for the treatment of resistant synovitis of individual joints after failure of long-term systemic pharmacotherapy and intra-articular steroid injections. The method is based on local intra-articular injection of β-emitting radionuclides in colloidal form to counteract and control synovial inflammation. Particle size, shape, charge and stability of a radiocolloid suspension are significant parameters that determine its organ distribution in vivo. The selection of proper radiopharmaceutical for the treatment of large, medium or small joints depends on the penetration range of β-emitting radionuclide and colloid particle size [3]. Yttrium-90 (^{90}Y) is a clinically acceptable β-emitting radionuclide and due to a half-life of 64.4 hours, $E_{max\beta-}$ of 2.27 MeV and a mean/maximum penetration depth of 3.6/11 mm it is ideal for therapy purpose. Our experiments included investigation of the factors influencing preparation of SnF-c and ^{90}Y-labeling, as well as the stability of the prepared radiocolloid.

Experimental

$^{90}YCl_3$ was purchased from Polatom, Poland, in a no-carrier-added form. All other reagents and solvents purchased from commercial sources were used without further purification.

To prepare ^{90}Y-SnF-c, 1 ml aliquots of nitrogen purged water for injection, containing 0.125 mg SnF_2 and different amounts of NaF with pH maintained at 5.1 and 5.9, were filtered (0.22 μm, Millipore Co.), dispensed into vials under nitrogen atmosphere and lyophilized for 24 h. The level of NaF was varied: 0.2, 0.5, 1, 2.5 and 5 mg/mL designated as SnF-c1, SnF-c2, SnF-c3, SnF-c4 and SnF-c5

formulation, respectively. The final pH of suspensions was kept at 5.1 and 5.9. Freeze-dried formulations (in triplicate) kept in shielded vials were reconstituted with 5 ml of water for injection. Then 5-15 μl of $^{90}YCl_3$ stock solution (about 185 MBq) was added to each vial. The reaction vials were shaken at room temperature (RT) or at 50 and 95 ^{o}C for 15, 30 or 60 min and cooled to room temperature. Then, the suspensions were additionally shaken at low speed up to 3 h.

The radiolabeling yield (RY) of radiolabeled colloid was determined by instant thin layer chromatography (ITLC). Particle size distribution, polydispersity index and zeta potential (ZP) were measured by Dynamic Light Scattering (DLS) technique using a Zetasizer Nano ZS (Malvern, UK) with 633 nm He-Ne laser and 173^{o} detection optics (backscatter detection). The radioactive particle size distribution (RPSD**)** of ^{90}Y-SnF-c was performed by successive membrane filtration steps of a single sample through 1.0, 0.4 and 0.2 μm pore size membrane filters. The stability of ^{90}Y-SnF-c was evaluated for a period up to 7 days by determining its radiochemical purity (RCP) with ITLC at different times after preparation.

Results and Discussion

The main goal of this study, the preparation of ^{90}Y-SnF-c, which can be successfully used for RS was achieved. The SnF-c used in this study as colloid template appears to be very suitable for labeling with beta emitting radionuclides. The SnF-c was prepared in lyophilized form and the particle size of the colloid was adjustable by varying the ratio of SnF_2 to NaF (w/w ratio SnF_2: NaF up to 1:200).

Radiolabeling of SnF-c with ^{90}Y is a simple procedure, which provides a very high yield of labeled particles. ITLC-SG/saline method enables quantitative determination of ^{90}Y-labeled colloid remained at the origin and unbound ^{90}Y in the form of $^{90}YCl_3$, which migrates with the solvent front. Although the radiolabeling of SnF-c with ^{99m}Tc occurs nearly instantaneously, the radiolabeling with ^{90}Y required an extended period of boiling. The RY of ^{90}Y-SnF-c increases as a function of temperature and time, reaching the highest value of >98% at 95 ^{o}C, after reaction mixture boiling for 30 min. Obviously, the heating step during SnF-c labeling was essential to get a product with high radiolabeling yield and improved stability. The stability and size-range of all batches of ^{90}Y-SnF-c, prepared by heating and agitation for different times were analyzed. As observed in our set of experiments, temperature, agitation and time affect both the radioactivity tagged to particles and the size of particles. The particles come in contact with each other and the probability of their sticking together depends on repulsive as well as attractive forces, due to increasing temperature and agitation time.

To better understand the formation of ^{90}Y-SnF-c as well as their radiolabeling and to define primary particles (templates), the particle size of lyophilized formulations (for SnF-cT1 to SnF-cT5) reconstituted with water (no YCl_3 added) was measured. Our results of PSD measurement confirmed the existence of primary colloidal particles (templates) with diameter of 123-138 nm in SnF_2-NaF suspensions at room temperature before radiolabeling. These primary particles in all formulations first aggregate, and finally agglomerate as a function of temperature, agitation and aging (schematic presented in Fig. 1).

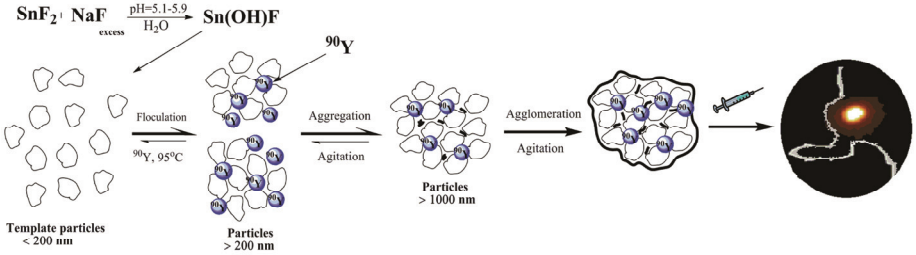

Figure 1. Formation of ^{90}Y-Labeled tin fluoride agglomerates from template particles.

The factors affecting the formation of stable, cemented SnF agglomerates were not well understood. Generally, if an aggregate survives long enough, sufficient cementation will occur to form stable agglomerate that can no longer be ruptured along the lines of contact of the original flocculating particles. To test the formation of stable agglomerate, the sample was withdrawn from the light scattering cell into syringe, re-syringed, put back into the cell and then particle sizes were measured again. The average particle diameter value remained unchanged. According to the results obtained, we conclude that the agglomeration rate increases with increasing temperature during radiolabeling and prolonged time of shaking, and that the large particles are agglomerates of the small ones.

The rate of Sn(II) hydrolysis depends on the concentration of NaF in the reaction mixture. We assumed that SnF_2 in formulations (Y-SnF-c1 - Y-SnF-c3) was partially hydrolyzed because the present NaF concentrations were not sufficient to completely suppress Sn(II) hydrolysis. Higher concentrations of NaF (>1 mg/mL) in the reaction mixture prevented formation of Sn(II) hydroxo complexes in the suspension.

The ^{90}Y-SnF-c demonstrated high *in vitro* stability in either human serum or human synovial fluid at 37 ^{o}C up to 7 days.

Conclusion

The present study has shown that ^{90}Y-SnF-c particles can be prepared with high labeling yield and *in vitro* and *in vivo* stability. The particle size of ^{90}Y-SnF-c was controllable by manipulating the conditions under which the colloids form. The optimum size of colloid particles can be easily designed for different therapeutic applications. Promising results suggest that ^{90}Y-SnF-c depending on particle size, may be of potential use for RS.

References

[1] P. Schneider, J. Farahati, C. Reiners, J.Nucl. Med., 2005, 46, 48-54.
[2] W. U. Kampen, M. Voth, J. Pinkert, A. Krause, Rheumatology, 2007, 46, 16-24.
[3] C. Turkmen, J. Coag. Dis., 2009, 1, 29-36.

K-12-P

THE INFLUENCE OF VARIOUS INORGANIC CHLORIDE SALTS ON THE SYNERGIC EFFECT IN THE EXTRACTION OF PARACETAMOL FROM AQUEOUS SOLUTIONS BY THE DIETHYL ETHER/1-BUTANOL MIXTURES

G. M. Nikolić[1], J. V. Živković[1], D. Vlajin[1], D. Atanasković[1], M. G. Nikolić[2]

[1]*University of Niš, Faculty of Medicine, Department of Chemistry, 18000 Niš, Serbia; e-mail:* goranhem@yahoo.com
[2]*University of Niš, Faculty of Natural Sciences, Department of Chemistry*

Abstract
We investigated the influence of ammonium-, sodium-, and potassium chloride on the synergic effect in the extraction of paracetamol from aqueous solutions by the diethyl ether/1-butanol solvent mixture. All the salts used in this study improved extraction efficacy of paracetamol and synergic effect was observed in the whole composition range of binary solvent mixtures. Highest distribution rate value was obtained by the use of KCl for the solvent mixture rich in 1-butanol.

Introuction
Determination of paracetamol in various samples is of great importance because its misuse may lead to serious toxic effects (eg. hepatic necrosis) [1]. Diethyl ether alone or in combination with some other organic solvents is often used for liquid-liquid extraction step during the sample preparation for analysis [2]. However, as in the case of some other phenolic compounds [3], paracetamol is poorly extracted with diethyl ether and this problem could be surmounted by the use of salting-out or/and extraction with binary mixtures of organic solvents (synergism) [3, 4]. We already reported the synergic effect in the extraction of paracetamol from aqueous NaCl solution [4] and in this paper we present the results concerning the influence of various inorganic chloride salts on the synergic effect in the extraction of paracetamol from aqueous solutions with the diethyl ether/1-butanol mixtures.

Materials and Methods
All the chemicals used in this study were of analytical grade quality and have been used without further purification. Stock solution of paracetamol (0.01 mol dm^{-3}) was prepared by dissolving exactly weighted mass of pure substance in doubly distilled water and 0.01 mol dm^{-3} solution of HCl was added to adjust the pH value to ~2. For each series of extractions stock solution was diluted 100 times with water or 2 mol dm^{-3} solution of appropriate salt. Extraction was performed by the shake-flask method for each binary solvent mixture composition in triplicate.

The absorbances of aqueous phases were measured by the Evolution 60 UV/Vis scanning spectrophotometer (Thermo Scientific, USA) at 243 nm and the distribution ratio (D) of paracetamol was calculated by using the equation

$$D = \frac{A_0 - A}{A} \times \frac{V_{aq}}{V_{org}}$$

where A_0 and A were absorbances of the aqueous phases before and after extraction, and V_{aq} and V_{org} were the volumes of aqueous and organic phase, respectively.

Synergic effect in the extraction of paracetamol was quantified by calculating the synergic coefficient, K_c, according to the equation

$$K_c = log\ (D_{mix}/D_{add})$$

where D_{mix} represented experimental and D_{add} theoretically predicted distribution ratio values, respectively [5].

Theoretically predicted distribution ratio was calculated as

$$D_{add} = D_1 \times x_1 + D_2 \times (1\text{-}x_1)$$

where D_1 and D_2 represented distribution ratios of paracetamol for pure solvents, and x_1 was mole fraction of one pure solvent in binary mixture.

Results and Discussion

The dependence of paracetamol distribution ratio on the composition of diethyl ether/1-butanol binary mixture is shown in Fig.1.

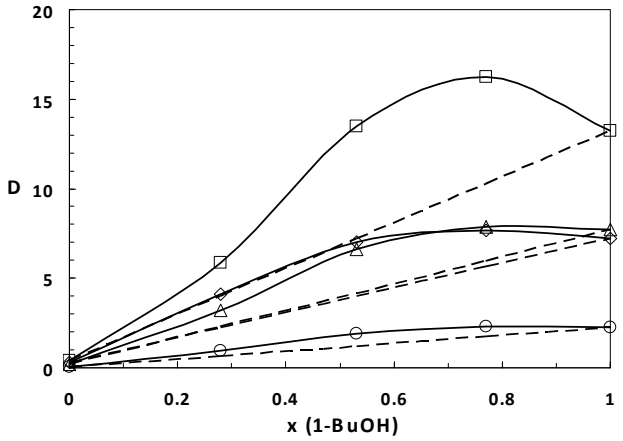

Figure 1. Dependence of paracetamol distribution ratio on the composition of diethyl ether/1-butanol binary mixture from the aqueous solutions with no salt added (circles), NH_4Cl (triangles), NaCl (rhombs), and KCl (squares), respectively. Dashed lines present dependence of respective values for D_{add} on the composition of diethyl ether/1-butanol mixture.

Distribution ratios of paracetamol were higher than theoretically predicted values for all the systems investigated in this work in the whole composition range of the diethyl ether/1-butanol binary mixture. Highest distribution rate value was obtained by the use of KCl for the solvent mixture rich in 1-butanol. It is noteworthy that although D values for pure 1-butanol are much higher than D values for pure diethyl

ether in all cases the highest D values were obtained with the mixtures containing small amounts of diethyl ether. Similar results indicating that solvent mixtures are more efficient than individual solvents have been reported in the literature for the extraction of ascorbic and nicotinic acids by the ethyl acetate/1-butanol and butyl acetate/1-butanol binary solvent mixtures with the explanation that some kind of complexes were formed in the extraction mixture [5].

Values of synergic coefficient, K_c, obtained for systems investigated in this study are shown in Table 1.

Table 1. Values of synergic coefficient, K_c, for the extraction of paracetamol from aqueous solutions by the diethyl ether/1-butanol binary mixtures.

x	K_c			
(1-BuOH)	No salt	NH_4Cl	NaCl	KCl
0.28	0.202	0.153	0.264	0.175
0.53	0.219	0.199	0.244	0.270
0.77	0.130	0.117	0.131	0.197

Highest K_c value was obtained again in the system containing KCl but this time at the approximately equimolar composition of solvent mixture. Also it can be noted that presence of NH_4Cl, in contrast to NaCl and KCl, resulted in lower K_c values in comparison to the extraction of paracetamol from pure aqueous solution.

Conclusion

All the salts used in this study improved extraction efficacy of paracetamol and synergic effect was observed in the whole composition range of binary solvent mixtures. Highest distribution rate value was obtained by the use of KCl for the solvent mixture rich in 1-butanol.

Acknowledgements

This work was supported by the Ministry of Education and Science of the Republic of Serbia under the Project TR 31060.

References

[1.] M. Espinosa Bosch, A. J. Ruiz Sánchez, F. Sánchez Rojas, C. Bosch Ojeda, J. Pharm. Biomed. Anal., 2006, 42, 291-321.
[2.] H. Li, C. Zhang, J. Wang, Y. Jiang, J. Paul Fawcett, J. Gu, J. Pharm. Biomed. Anal., 2010, 51, 716-722.
[3.] G. M. Nikolić, J. M. Perović, R. S. Nikolić, M. M. Cakić, Facta Universitatis Ser. Pys. Chem. Techn., 2003, 2, 293-299.
[4.] G. M. Nikolić, J. V. Živković, M. G. Nikolić, F. Miljković, Eur. J. Pharm. Sci., 2011, 44 (Suppl.1), 183-184.
[5.] N. Ya. Mokshina, O.V. Erina, O.A. Pakhomova, R.V. Savushkin, Russ. J. Phys. Chem. A, 2007, 81, 1964-1967.

K-13-P

SOME RESULTS OF THE IDENTIFICATION OF CERTAIN PRINTINGS

G. Perović[1], D. Mitraković[2]

[1]*BIA, Kraljice Ane bb, Belgrade , Serbia*
[2]*Technology and metallurgy faculty,University of Belgrade, Belgrade, Serbia*

Abstract
The results obtained enable determining of specific characteristics of the reproduction proofs, especially those obtained with digital printers. Characteristics of the proofs which can be presented numerically, in the form of diagrams and histograms, as well as photographs of enlarged, characteristic details, make the profile of the given printer. Based on the profile it is possible to determine which of the examination printers made the proof in question.

Introduction
Because of its importance for the functioning of modern society, and their ability to obtain possession of legal or material benefit, of the document (personal documents, notes, banc paper etc) are constantly subject to falsification, or unauthorized reproduction. Although some have elements of protection against forgery, the materials from which they were made (protected paper) and the graphic design and printing techniques which are printed, the documents were produced graphically, that is, using the usual graphics manufacture can be relatively successfully reproduced. The development of computer technology causes rapid and constant increase in performance and quality of personal computers and its peripherals (scanners, digital cameras as input devices and output devices like printers) thus increasing the print quality of reproduced prints, with constantly falling prices of such equipment. Availability of equipment to play, with its high quality, has led to a flood of forgeries done on different types of digital color printer. In this regard, the expert witnesses involved in examination of forged documents, there is a new problem, detection of type and brand (manufacturer) device which was a forgery made, or even detect whether it is done in precise printer.

The aim of this paper was to presents some results obtained by methods for determing certain parameters of the quality of printed impressions, using common PC configuration (computer, scanner, printer) and relatively cheap software, Adobe's Photoshop and Media Cybernets's Image-Pro Plus and the availability of laboratory equipment (microscope and digital cameras).

Results and Discussion
The properties of some fragments of the prints were subject of our investigation, see Figure 1.

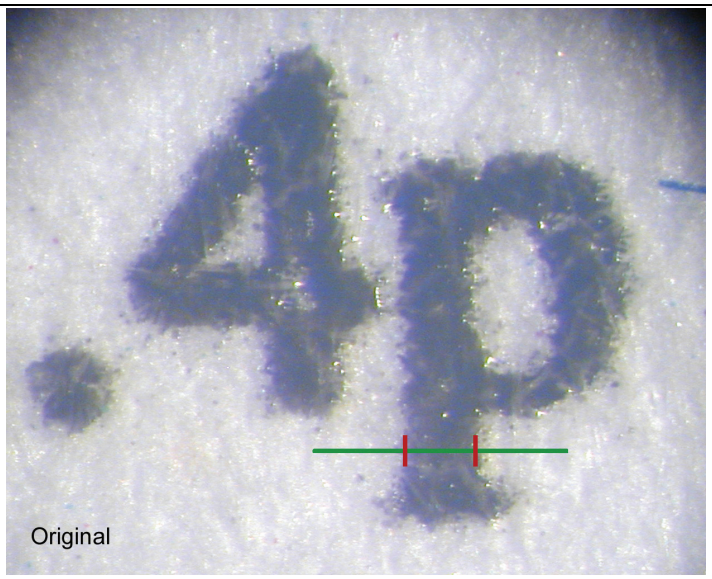

Figure 1. Fragment of the prints.

The sharpness of image was measured by measuring the change in intensity, the angle of inclination of the boundary curve of intensity image (Fig. 1.), and the transition between the printed and not-printed, clean paper. The results of field measurements examined the prints are presented in the Table 1.

Table 3. The angle of inclination of the boundary curve (degrees).

mage	Red_1	$Green_1$	$Blue_1$	Red_2	$Gree\ n_2$	$Blue_2$
Original	17.28	19.09	21.90	31.02	25.86	32.47
HP 2000	29.85	25.68	67.04	63.43	81.64	69.34
Deskjet 990	46.00	56.30	51.91	45.80	31.67	44.14
Tektronix Phaser 780	15.94	34.57	47.65	12.35	23.74	49.61
Tektronix Phaser 860	28.14	26.88	35.35	21.81	35.38	52.03
Ofset B2	13.08	15.60	17.97	31.01	12.93	26.99
Ofset Speedmaster	11.02	17.80	22.34	12.49	17.90	17.10

A small angle means a sharper image, and index 1 and 2 refer to the left and right edge of prints. Due to the fact that all measurements performed on enlarged prints to digital photos, recorded through a microscope, and to sharpenes done manually by observing the desired detail on the camera LCD display, in interpreting the results should be taken, because the sharpnes of the obtained image directly affects the measurement result. As with the measurement accuracy and here is a raster structure hindered the determination of contour images.

Conclusion

Development of computer equipment and software for computer preparation for printing and digital printing processes influenced the increase in production of forged documents. In order to develop methods to recognize fraudulent documents, based on research conducted in this study, it was concluded the following:

- Defined procedure for determining the thickness of protective threads. It was found that neither printed flat offset printing technique and drawn thread with average thicknesses of 156 and 67 micron thickness exceeds several times the original thread of 22 micrometers. Varying the thickness of the original thread is only 5 μm, while the difference of maximum and minimum measured values in print or 69 μm or 67 μm in cartoons.
- Some of the precision and sharpness of reproduction prints, prints measuring segments of known dimensions and measuring the change in intensity at the border between the prints and non-printed paper. Compared to the original, measured 205 micrometers, the most accurate image reproduced with the DeskJet 990 printer with 278μm. The following Phaser 860 (294 mil), Phaser 780 (305 mil), HP2000 (311μm), Speedmaster Offset (319 mil) and offset SORMZ B2 (352 mil). The sharpest prints are offset, then prints laser printer and the end of reproduction obtained by using ink-jet printer.

Acknowledgement

This research has been done thanks to the resources of the project 172015 Ministry of Science and Technology, R. Serbia.

References

[1] H. Andersson, M. Wigilius, 8th Europpean Conference for Police and Government Document Exeperts, Bratislava, Slovak Republic, September 2002.

[2] G. Perović, Master thesis, Faculty of Technology an Metallurgy, Belgrade, 2004.

K-14-P

PRINTER IDENTIFICATION BASED ON DOT RADIUS

G. Perović[1], T. Grozdić[2] , D. Mitraković[3]

[1]*BIA, Kraljice Ane bb, Belgrade , Serbia*
[2]*Insitute or multidisciplinary research, University of Belgrade Kneza Višeslava 1a,11000 Belgrade, Serbia, (gtomisi@imsi.bg.ac.rs)*
[3]*Technology and metallurgy faculty,University of Belgrade, Belgrade, Serbia*

Abstract
Forensic document examiners more and more often have to answer questions related to printing technology, type and model of printer by which the document was produced. In this paper, the microscopically enlarged details of the prints, obtained by different printing technologies (electrophotography, ink-jet, offset lithography), were examined using image analysis software.

Introduction
In today's digital world, the document, as a form of information, have been created on different printers, that are available on the market, and they are increa-singly subject to fraud and counterfeiting. Answering the fundamental question – whether the questioned document is original or not? – forensic document examiners more and more often have to respond to requests related to printing techno-logy, type and model of printer by which the document was produced.

These various technologies will make prints of different characteristics, due to differences in the process of reproduction, printer mechanism, image reso-lution, rasterization method, dot size and shape, type of colorants, bonding to the printing substrate, deformation of print image elements, geometric or dimensional distortion of microscopic details of prints, etc. In recent years many authors have dealt with printer forensics, based on print quality analysis.

Oliver et al. [1] have suggested the application of ImageXpert, machine-vision based, portable device, which is usually used to analyze the print quality, printed circuit board, etc. Mikkilineni at al. [2] have developed strategy for printer identification, that involves a printer characterization based on the unique properties of the printed image called "intrinsic signature", that are characteristic of speci-fic printer or model. As an intrinsic signature these authors reported banding. Another method for bending investigation, in order to identify the printer, has been given by Tchan [3], using digital image analysis system, consisting of a high-resolution CCD camera connected to the computer.

Dasari and Bhagvati [4] have dealt with the identification of a color ink-jet and laser printers and photocopiers using HSV color space (Hue, Saturation, Value or brightness). Gupta et al. [5] have analyzed the reproductions of original docu-ments by microscopic examination of the pattern of the image, using the Video Spectral Comparator and a microscope with a camera. Lampert et al. [6] have pro-posed a technique that is based on the fact that the texts printed on different printers have a different appearance, especially in the edge area of the prints.

Huber-Mörk et al. [7] have examined relative displacement between prints generated by the different printing processes, which are successively, one after the other applied to the paper, in security documents production.

Kee and Farid [8] have dealt with technique for modeling geometric degradation caused by printer. They determined the deviation in the shape of the selected letters in relation to the ideal geometric shape of this letter. The set of all these deviations makes the printer profile. Otherwise, the methods of Bulan et al. [9] and Wu et al. [10] are not based on analysis of individual print details, but on analysis of whole page document's geometric distortion, that is caused by the imperfection and differences of the paper feeding mechanism of different printers. Akao at al. [11] have dealt with identification of the ink-jet printers by estimation of spur gear teeth number, actually spur marks from these spur teeth, while Ryu et al. [12] have studied identification of the color laser printers, by halftone texture analysis.

Experimental

In our paper two laser printers (Phaser 780 and Phaser 860), two ink-jet printers (HP 2000 and HP DeskJet 990cxi) and two offset lithography printing presses (Heidelberg Offset SORMZ B2 and Heidelberg Speedmaster B1) were examined. Examination of prints, obtained by different printing technologies, based on the Image Pro Plus software. This software analyzes the image detail obtained using a microscope and digital camera.

Results and Discussion

Dot radius was measured from the original crest motif on Serbian (blue) passport data page (offset lithography printing) and scanned reproductions of this motif, obtained by different technologies of printing. The average shape and size of the dots are shown by radial graph (Fig. 1).

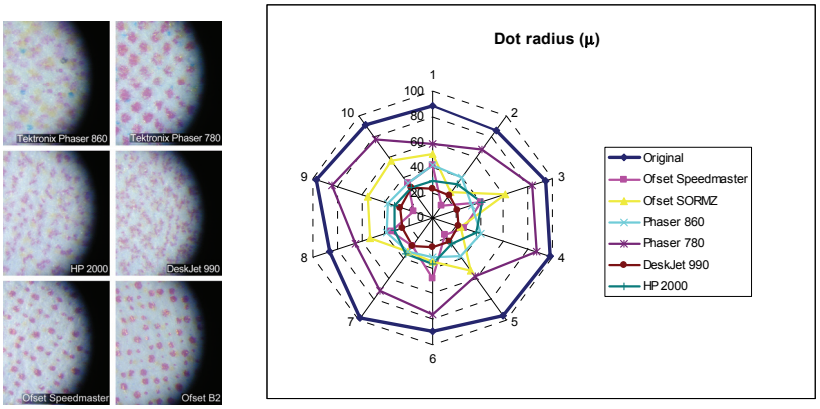

Figure 1. Enlarged print details and results of dot radius measurement.

Compared to the original print, on which the dots are in the range of 85 to 100μ, all examined reproductions have noticeably smaller dots. Closest to the original print is Phaser 780 printer, whose dot size is between 58 and 86μ. With this printer we can see the regular halftone texture at an angle of approximately 45 °, similar to the original print. Knowing resolution of tested printers, it can be concluded that the size of the dots on the print regularly depends on the resolution and raster frequency. The smallest dot was measured on the print from highest resolution printer (DeskJet 990, 2400x1200 dpi). Same dependence on the resolution occurred when the printers of the same printing technology were compared. Dots printed on offset printing presses vary in size, although the printing plates for both presses were built with the same film. Dots on the print from SORMZ press are larger than those on the print from Speedmaster, because the first one is old, low quality machine, without ink control system, with manually developed plates, resulting in a significant dot gain.

Conclusion

This paper presents the method for determining certain features of prints, by which it is possible to identify corresponding printing devices. The method is based on the fact that different printing technologies and different printer models bring a distinctive noise in the process of reproduction of text and images, which can be identified. The advantage of this method is that they are non-destructive, as opposed to the conventional examinations of documents, which are based on analytical methods of testing the composition of printing ink and paper. Also, these methods do not require complicated and expensive laboratory equipment.

References

[1] J. Oliver, J. Chen, IS&T's NIP18 Conf., 2002, 218-222.
[2] A. K. Mikkilineni, P.-J. Chiang, G. N. Ali, G. T.-C. Chiu, J. P. Allebach, E. J. Delp, IS&T's NIP20 Conf., 2004. 20, 306-311.
[3] J.S. Tchan, Journal of Imaging Science and Technology, 2007, 51(4), 299.
[4] H. Dasari, C. Bhagvati, Lect. Notes on Comp. Sci., 2006, 3852, 692-701.
[5] G. Gupta, C. Mazumdar, M.S. Rao, R.B. Bhosale, Digital Investigation, 2006, 3, 43-55.
[6] C. H. Lampert, L. Mei, T. M. Breuel, CIS, 2006, 1, 639-644.
[7] R. Huber-Mrök, H. Ramoser, H. Penz, K. Mayer, D. Heiss-Czedik, A. Vrabl, Pattern Recognition Letters, 2007, 28, 2037-2045.
[8] E. Kee, H. Farid, Proc. ACM MM&SEC'08, 2008, 3-10.
[9] O. Bulan, J. Mao, G. Sharma, IEEE (ICASSP), 2009, 1401-1404.
[10] Y. Wu, X. Kong, X. You, Y. Guo, IEEE (ICIP), 20090, 2909-2912.
[11] Y. Akao, A. Yamamoto, Y. Higashikawa, IWCF, 2009, 25-32.
[12] S.-J. Ryu, H.-Y. Lee, D.-H. Im, J.-H. Choi, H.-K. Lee, IEEE (ICASSP), 2010, 1846-1849.

K-15-P

ABSORPTION CHARACTERISTICS OF CYAN DYES

J. S. Kiurski[1], D. Ž. Obadović[2], M. Cvetinov[2], J. Krstić[1], I. Oros[1]

[1]*Faculty of Technical Sciences, Department of Graphic Engineering and Design, Trg Dositeja Obradovica 6, Novi Sad, Serbia*
[2]*Faculty of Sciences, Department of Physics, Trg Dositeja Obradovica 4, Novi Sad, Serbia*
e-mail: kiurski@uns.ac.rs

Abstract
In this paper, absorption characteristics of cyan dyes with application of UV-VIS spectroscopy, was presented. Samples of printing cyan dyes were taken from the dyes unit on printing machine. The obtained spectral data showed the typical absorption profile of phthalocyanines. All spectra show a strong UV absorption in the 200-300 nm region that can be attributed to the π - π* and n - π* of the amino, carboxylic and aromatic moieties. Also, obtained spectra could be a good indicator of dye aging process.

Introduction
The phthalocyanines are widely used in textile, paint, printing ink and plastic industries (Fig.1). Although the shade range of the phthalocyanines is rather limited and covers only the bluegreen regions of the spectrum, their excellent fastness to light, and high absorptivity render them adapt for many applications. The insolubility of phthalocyanines necessitates preparation of soluble derivatives for application as dyes for textile fibbers. Phthalocyanine pigments in the form of aqueous dispersions are used in pad-dyeing with resin emulsions. Because of their excellent stability to acids, alkalis and solvents phthalocyanines are particularly useful in spin dying [1].

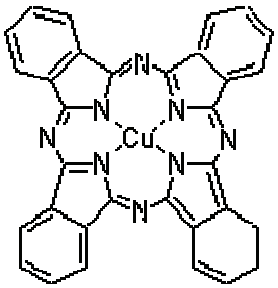

Figure1 Structure of cyan (copper phthalocyanine, CuPc) β-form.

Experimental
The cyan samples were taken from dye unit on offset printing machine before and after 20,000 printed sheets.

Ultraviolet-visible (UV-VIS) absorption spectra were recorded using spectrophotometer UV-VIS SPECORD 205, Analytik Jena. Dye samples were prepared by dilution in appropriate organic solvent (DMSO).

Results and Discussion

The absorption maximum of phthalocyanines is calculated by assuming the Π-electrons to be one dimensional free electron gas, resonating between two equivalent limiting structures of the phthalocyanine ring with constant potential energy along its length. In the normal state, the most stable energy states of the electron gas, each contains two electrons in accordance with Pauli's exclusion principle. The remaining states are empty. The existence of the first absorption band is a consequence of the jump of a Π - electron from the highest energy level. The spectrum of the phthalocyanine in the visible region is composed of at least seven bands, the main absorption occurring between 600 and 700 nm.

The CuPc molecule (copper phthalocyanine) is planar and has fourfold symmetry, and consists of a central copper atom surrounded by four ligands which have pyrrole and benzene rings. It containes an odd number of electrons and the obtained spectrum has two orbitals whose relative position depends rather sensitively on the computional details, as discussed in the literature [2]. One of them is of π symmetry, delocalized over the pyrrole and benzene rings, while the other one is a singly-occupied state of in-plane symmetry, with a large amplitude on the Cu and neighboring N atoms [2]. The current understanding is that the correct ordering of these states has the (doubly-occupated) π orbital as the HOMO, with the (singly-occupated) Cu-related orbital lower in energy. Moreover, it has been shown that errors arising from self-interaction, which are present in standard DFT functionals, artificially shift the position of all molecular orbitals (especially the strongly Cu-localized orbital close to the vacuum level) in some cases giving rise to a spurious crossing with the HOMO level.

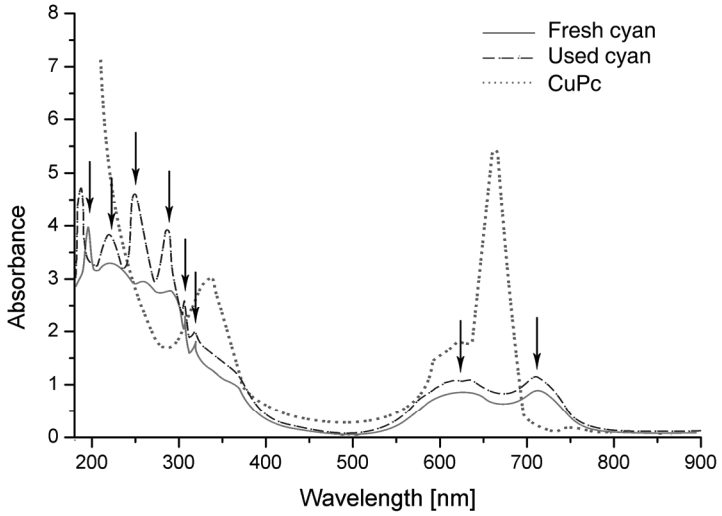

Figure 2 UV-VIS spectra of the cyan dyes before and after printing.

Cu-phthalocyanine shows absorption bands in two regions: the band in the range 600-700 nm is found in the visible region of spectra and it is responsible for the blue color feature of the colorant. Another band between 200 and 400 nm overlaps a wide range of the emission Cu-band. The spectral characteristics for cyan printing dye samples are: 207, 226, 263, 294, 312, 320, 624 and 713 nm, Fig.2. UV-VIS spectrum shows that the bands in region of 624-713 nm split and shift to red, which means successive protonation happened and caused the loss of symmetry. The spectra of the fresh dye were similar to the spectrum of color after 20,000 printed sheets with the difference intensity in the region of 200 - 290 nm. The UV-VIS spectrum obtained showed the typical absorption profile of phthalocyanines. It was detected a strong UV absorption band in the 200-300 nm region in all investigated cyan dyes samples, that can be attributed to the π - π^* and n - π^* of the amino, carboxylic and aromatic moieties [3].

The changes in the absorption intensities are due to the color changes in printing processes during the photochemical aging. The color changes are influenced with products of degradation. In Cu-Pc the blue color is produced by the colorant that has high absorption coefficient, covering the color of polycarbonate matrix which is evaluated with aging process.

Conclusion

Cu-phtalocyanine as cyan dye was investigated using UV-VIS spectroscopy in order to determine the start of aging process. The obtained UV-VIS spectra showed the typical absorption profile of phthalocyanines as a main structure of cyan dye. The spectra of the fresh and used dyes were similar but with different intensity. All spectra showed a strong UV absorption in the region of 200-300 nm which could be attributed to the π - π^* and n - π^* of the amino, carboxylic and aromatic moieties. UV-VIS spectrum shows that the bands in region of 624-713 nm split and shift to red, which means successive protonation happened and caused the loss of symmetry. It was concluded that after 20,000 printed sheets these days can almost used in printed process.

Acknowledgment

The authors acknowledge the financial support of the Ministry of Education and Science of the Republic of Serbia (Projects No. TR 34014 and ON 171015).

References

[1] P. S. Harikumar, Electrochemical studies on metal phthalocyanines, PhD Thesis, Cochin University of Science and Technology, India, 1990.

[2] H. Vazquez, P. Jelinek, M. Brandbyge, A. P. Jauho, Corrections to the density-functional theory electronic spectrum: copper phtalocyanine, App. Phys. A., 2009, **95**, 257-263.

[3] J. Lindon, G. Tranton, J. Holmes. Biomacromolecular application of UV-VIS absorption spectroscopy, Elsevier, 2000, 131-136.

K-16-P

VANADIUM TOXICITY IN *Phycomyces blakesleeanus*

M. Stanić[1], M. Žižic[1], M. Živić[2], J. Zakrzewska[3]

[1]*Institute for Multidisciplinary Research, University of Belgrade, Kneza Višeslava 1, 11030 Belgrade, Serbia.*
[2]*Faculty of Biology, University of Belgrade, Studentski trg 16, 11000 Belgrade, Serbia.*
[3]*Institute of General and Physical Chemistry, Studentski trg 12-16, 11000 Belgrade, Serbia.*

Abstract
We investigated the interactions of vanadium in two physiologically-relevant redox states: vanadate (+5) and vanadyl (+4), with 24h old mycelium of fungus *Phycomyces blakesleeanus*. Vanadate at first caused increased biomass production and synthesis of polyphosphates, and then showed its toxic effects at higher V^{5+} concentration. Vanadyl exhibited toxic effects even at low concentrations. Our results suggest that the main pathway of vanadium introduction into the cells of this fungus under natural conditions involves three steps: extracellular V^{5+}/V^{4+} reduction, V^{4+} influx and vacuolar storage, and V^{5+} import at higher concentrations.

Introduction
The interest in biological investigations for vanadium has increased considerably during the past three decades, in line with its role as an essential ultra-trace element for most, if not all living organisms [1]. Vanadium has been reported to have a therapeutic effect in treatment of diabetes [2] and some types of cancer [3]. The release of vanadium to water and soil occurs primarily as a result of weathering of rocks and soil erosion and involves the conversion of the less-soluble V^{3+} form to the more soluble V^{4+} and V^{5+} [4]. Taking into account its toxicity, vanadium may pose an environmental threat due to anthropogenic activity-related increase of its level in the environment [5]. Fungi are of major interest regarding both, environmental and medical implications of vanadium, because they take up and accumulate trace metals [6], and represent the main route of vanadium entrance into the ecosystem [7]. Having this in mind, it is perplexing that data on vanadium metabolism in fungi are very scarce, being almost exclusively obtained on two ascomycetous yeast species: *S. cereviese* and *H. polymorpha* [8].

Materials and Methods
The wild-type strain of the fungus *P. blakesleeanus* (Burgeff) (NRRL 1555(-)) was used. To determine the influence of both oxidation forms of vanadium on its growth, *P. blakesleeanus* was cultivated on medium [9] without or with sodium orthovanadate (1; 5; 7; 10 and 20mM) or vanadyl sulphate (0.5; 1 and 5mM). For the purpose of NMR measurements, 24 h old mycelium was prepared according to [10]. The ^{31}P NMR measurements were performed using Apollo upgrade, Bruker MSL 400

spectrometer operating at 161.978 MHz for ^{31}P. The assignment of NMR spectra and all other experimental details were performed as described previously [10].

Results and Discussion

The growth and development of *P. blakesleeanus* in the presence of vanadate and vanadyl was monitored by ^{31}P NMR spectroscopy, and it was observed that V^{5+} caused increase in PPc (core polyphosphates) and the decrease in Pi (orthophosphates) signal intensity, while V^{4+} had inverse effect on PPc and practically no effect on Pi (Fig. 1).

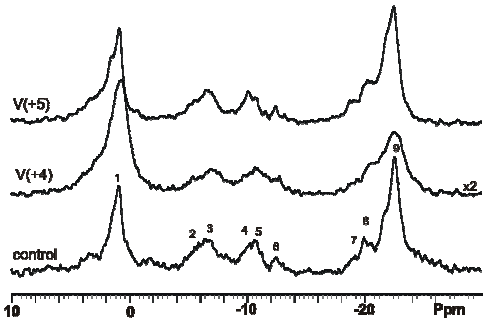

Figure 1. ^{31}P NMR spectra of *P. blakesleeanus* cultivated on V(+4) and V(+5) containing medium.
The signals assignments: (1) Pi -inorganic phosphates, (2) γATP, (3) PPt - terminal residues of PolyP and pyrophosphate, (4) αATP, (5) NAD(H) and UDPG, (6) UDPG - second resonance, (7) βATP, (8) PPp - penultimate PolyP residues, (9) PPc - central PolyP residues

Also, lower V^{5+} concentrations (1mM, 5mM) had statistically significant stimulating effect ($P<0.05$, $n=3$) on biomass yield (Fig. 2), while higher V^{5+} concentrations reduced growth. Vanadyl sulfate added into growth medium above concentration of 0.5 mM slows growth. *P. blakesleeanus* could grow and complete its life cycle with used vanadyl (up to 5mM), and vanadate concentrations (up to 20 mM). In case of vanadate, increase in biomass yield is followed by almost unchanged ratio of PPc/Pi signal intensity (Fig. 2), already proposed indicator of fungus growth and development, but only up to concentration of 5mM. At higher concentrations, PPc/Pi signal intensity ratio in ^{31}P NMR spectra decreases. When mycelium was cultivated with V^{4+} it resulted in an immediate decrease of PPc/Pi ratio.

Proposed mechanisms for vanadium detoxification imply reduction of more toxic V^{5+} to V^{4+}, either in the cytoplasm [11] or in the cell wall [12, 13]. Apparently greater toxicity of V^{4+} compared to V^{5+} in *P. blakesleeanus* could suggest different and/or additional mechanism of vanadium detoxification, involving vacuolization. Vacuolar polyphosphates are believed to be the molecules chelating toxic metal ions [14], so vacuolization of V^{5+} leads to increased PolyP synthesis and concomitant reduction in Pi signal intensity. Paramagnetic V^{4+} makes the part of PolyP signal NMR invisible due to broadening, which results in the decrease of PPc signal intensity (Fig. 1). Also, Wilsky et al. have noticed that conversion of V^{5+} to V^{4+} is only possible at low V^{5+} concentrations, while in V^{5+} excess this process cannot keep pace with the rate of V^{5+} influx and it accumulates intracellularly, leading to growth reduction, as shown for V^{5+} concentrations higher than 5mM. Entrance of V^{5+} into the cell only at high concentrations could explain its apparent lesser toxicity compared to V^{4+}.

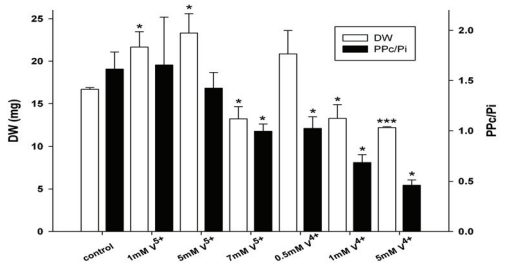

Figure 2. Influence of different concentrations of V^{5+} and V^{4+} on growth and development of *P. blakesleeanus.* White bars – dry weight (mg), black bars – PPc/Pi Significance is expressed in relation to control
*** - $p<0.001$, * - $p<0.05$

Acknowledgement
Supported by Serbian Ministry of Education and Science grant No. 173040

References

[1] D. Rehder, Bioinorganic vanadium chemistry, 2008, John Wiley & Sons Ltd.
[2] K. Thompson, C. Orvig, J. Inorg. Biochem. 2006, 100, 1925–1935.
[3] A. Bishayee, A. Waghray, M.A. Patel, M. Chatterjee. Cancer Lett., 2010, 294, 1–12.
[4] T. N. K. Kumar, H.D. Revanasiddappa, J. Iranian Chem. Soc. 2005, 2, 161.
[5] B. K. Hope, Sci. Total Environ., 1994, 141, 1-10.
[6] P. Kalac, L. Svoboda, Food Chem. 2000, 69, 273–28.
[7] N. W. Lepp, S.C.S. Harrison, B.G. Morrell. Environ. Geochem. Health, 1987, 9, 61-64.
[8] I. Mannazzu, Ann. Microbiol., 2001, 51, 1-9.
[9] R. P. Sutter, Proc. Natl. Acad. Sci. USA, 1975, 72, 127-130
[10] M. Živić, J. Zakrzewska, M. Žižić, G. Bačić, Antonie van Leeuwenhoek , 2007, 91, 169-177.
[11] G. R. Willsky, D. A. White, B.C. McCabe, J. Biol. Chem., 1984, 21, 13273-13281.
[12] L. Bisconti, M. Pepi, S. Mangani, F. Baldi, BioMetals, 1997, 10, 239-246.
[13] H.P. Bode, C. Friebel, G.F. Fuhrmann, Biochim. Biophys. Acta, 1990, 1022, 163-170.
[14] I. Kulaev and T. Kulakovskaya, Annu. Rev. Microbiol., 2000, 54, 709-734.

K-17-P

SEM-EDS ANALYSIS OF THE SYSTEM *BIOMINERAL TISSUE – NATURAL MEDIUMS* IN THE FORENSIC EXAMINATION

N. V. Radosavljević-Stevanović[1], R. S. Nikolić[2], N. S. Krstić[2], B. M. Kaličanin[3]
[1]*The National Crime-Technical Centre, Ministry of Interior of the Republic of Serbia, Kneza Miloša Str. 103, 11000 Belgrade*
[2]*Department of Chemistry, Faculty of Sciences and Mathematics, University of Niš, Višegradska Str. 33, 18000 Niš, Serbia*
[3]*Department of Pharmacy, Faculty of Medicine, University of Niš, Bulevar dr Zorana Djindjića 81, 18000 Niš, Serbia*

Abstract
In this study the changes of the teeth mineral tissues which were exposed to the influence of the different natural soil and water mediums were analysed by Scanning Electron Microscopy - Energy Dispersive Spectroscopy. Results show alterations of elemental content in mineral tissue and significant changes on the surfaces of teeth samples that were exposed to the soils and waters mediums. Thus, such study can be utilised to direct to the kind of medium in which biomineral teeth tissue was put off.

Introduction
Hard mineral tissues, bones and teeth, are readily available biopsy material which is relatively easily analysed and applied in the forensic examination, especially bones. It is potentially interesting and convenient in the cases when it was exposed to the influence of different outer mediums. The basic structure unit of bones and teeth is hydroxyapatite $Ca_{10}(PO_4)_6(OH)_2$ (HAp) [1]. By the influence of the outer mediums agents, the mineral tissue of teeth is altered, what is recognized, among all, according to changes in elemental content of the Hap [2, 3].
According to the qualitative and quantitative alterations that occurred in the mineral teeth tissue after it had been exposed to different types of mediums, the aim of examination was to obtain the information potentially useful for forensic expertises using Scanning Electron Microscopy - Energy Dispersive Spectroscopy (SEM-EDS).

Experimental
The model systems for examination of the interactions natural environment mediums-anthropogenic material were human teeth exposed to the influence of different types of soils: urban city soils from the park (medium I), soils of mostly clay content (medium II) and soils of mostly limestone content (medium III) from the city of Niš and surrounding area, and different types of water: commercial water "aqua viva" (medium IV) and a solution of the "rainwater model system" (medium V).The teeth were exposed to the mention mediums in the mass ratio 100:1 and left for three months at room temperature (t = 22–25 °C).
The structural characterization of the mineral teeth matrix, of both – control sample and the group of samples exposed to outer environment mediums influences, was done by the techniques of SEM-EDS analysis. SEM-EDS examination of *in situ* teeth tissue

(covered by the vapour of colloidal gold) was performed by the „FEI QUANTA 200“ in the National Crime-Technical Centre of the Ministry of Interior in Belgrade.

Results and discussion

Results of SEM-EDS analyses of the untreated and the samples of teeth that were exposed to the soils mediums influence are shown in the Figure 1.

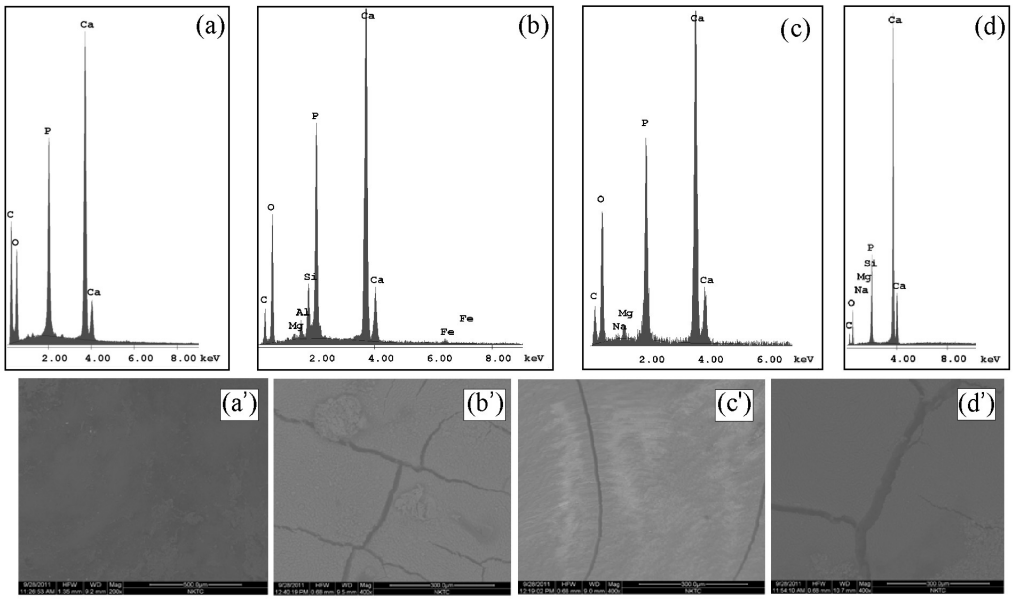

Figure 1. EDS spectra and SEM micrographs for untreated teeth (a), teeth exposed to the medium I (b), medium II (c) and medium III (d)

On the basis of comparison of SEM-EDS analyses results of untreated and treated samples that were exposed to the soils mediums, the alterations in content and the surface appearance of the hard mineral teeth tissue were observed. EDS spectra directs to the local change of metals in the researched mineral tissue that occurs due to the adsorption. Al, Mg, Si and the traces of Fe can be noticed in the teeth tissue that was exposed to the urban city soils (Fig. 1b); the adsorption of Mg and Na is performed from the clay enriched medium (Fig. 1c); the increase of Ca, Si, Mg, Na and significant change of Ca/P ratio are noticed for the teeth samples that were exposed to limestone enriched soils (Fig.1d). The cracks on the teeth surface were noticed, originated from the teeth interaction with the all surrounding soils environments (Fig. 1b′/c′/d′). The ratio of Ca/P content is altered probably as the result of adsorption of Ca^{2+} ions from the surrounding environment or adsorption of the excessive content of phosphates on the crystal surface or substitution of Ca^{2+} ions by the ions from the surrounding environment [4, 5]. The small diameters of Na^{+}, Mg^{2+} and Al^{3+} ions enable them to migrate easily into the internal teeth tissues [3]. According to comparison of SEM-EDS analyses results of untreated and treated samples that were exposed to the water mediums, slightly alterations in content and no significant change of surface appearance of the hard mineral teeth tissue were observed (Fig. 2). EDS spectra directs to the local change of elements in the researched mineral tissue that occurs due to the

adsorption. Mg can be noticed in the teeth tissue that was exposed to the "aqua viva" water system (Fig. 2b) while the adsorption of Na and Cl is performed from the "rain-water model system", together with the altered ratio of Ca/P (Fig. 2c) for the reasons already described [4, 5].

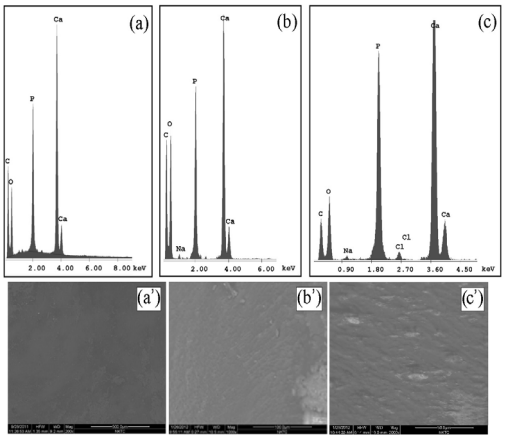

Figure 3. EDS spectra and SEM micrographs for untreated teeth (a), teeth exposed to the medium IV (b), medium V (c).

Conclusions

SEM-EDS analysis shows alterations of metal content in mineral tissue and changes on the teeth surfaces for the teeth samples exposed to the soils environment. Less intensive changes in mineral content and no significant changes on the teeth surface were noticed for the teeth exposed to water systems. According to the mentioned differences, the directions related to the kind of environment can be performed.

Acknowledgements

This work was supported by the Ministry of Education and Science of the Republic of Serbia under the Projects No. III45017 and TR34008.

References

[1] J. Andjić, Osnovi oralne fiziologije i biohemije, Naučna knjiga, Beograd, 1990.
[2] B. Nowak, Analyst, 1995, 120, 747-750.
[3] R. Nikolić, B. Kaličanin, N. Krstić, Connect. Tissue Res., 2012, 53(3), 229-235.
[4] W.H. Arnold, P. Gaengler, Ann. Anat., 2007, 189(2), 183-190.
[5] S. Kannan, F. Goetz-Neunhoeffer, J. Neubauer, J.M.F. Ferreira, J. Am. Ceram. Soc., 2008, 91(1), 1-12.

K-18-P

THE SEDIMENT IN LAKE PALIĆ

T. Grozdić, A. Hegediš , M. Nikčević, G. Mesaroš

Institute or multidisciplinary research, University of Belgrade, Kneza Višeslava 1a,11000 Belgrade, Serbia, (gtomisi@imsi.bg.ac.rs)

Abstract

The lake serves as the recipient of treated wastewater of the city of Subotica and Palić. Effluent quality is of great importance for lake Palić.Treatment plant inadequately purified waste water and in it have high concentrations of organic matter and phosphorus and nitrogen. To improve the water quality of lakes, it is necessary to reduced nutrients to a minimum. New treatment plant facilities for urban wastewater of Subotica and Palić, ought to ensure that the purified water contains minimal amounts of organic matter and compounds of nitrogen and phosphorus.

Introduction

Palić lake area 576 ha, the width between 360 and 920m, 8250m maximum length, maximum depth 2.0 m, and a total coastline of 20 km [1]. During the first half of the nineteenth century, changes were observed in the lake which indicated that the lake eutrophication progressed. Since 1969th-1971. the concept of rehabilitation is established in the lake Palić. [1] From 1972 to 1975. was partially implemented plan of rehabilitation. Plant for treatment of municipal wastewater, anticipated program of rehabilitation of Palić Lake, was built and put into operation 1975th year. But so purified wastewater continue to be burdened with organic substances, nitrogen and phosphorus compounds. It is not done either aging or processing of bioactive silt.

Construction of new plants for urban waste water treatment began in 2006. year and was completed in 2010. year. The capacity of the cleaner 36 000 m^3 for a day without rain and 72 000 m^3 for a rainy day. Paper [2] has been analyzed the water quality of Lake Palić. Nutrient concentrations, as indicators of water quality, are also increasing. The concentration of total nitrogen increased at all sites, while high concentrations of orthophosphate and uniform throughout the year. High concentrations of nitrogen and phosphorus as a result of intensive organic production, with negative consequences for eutrophication of the lake. The values of saprobic index, water quality and sectors, corresponding class II-III water quality. The water quality of the lake sector IV belongs to the class IV in the summer. On the basis of results of tests of water quality [2], finds the trend of increasing saprobic lakes and increasing amounts of suspended matter and silt in the lake Palić. Within the phytoplankton community during the year, observed qualitative and quantitative dominance of Bacillariophyta species partition.

The paper discussed the physic-chemical parameters of the chemical analysis of lake sediments sampled in July 2010, a month after the beginning of a new plant for wastewater treatment.

Results and Discussion

Table 1. Results of physic-chemical tests of sediment-mud from Palić Lake in July 2010. year.

Physic-chemical parameters	sector II thickness of sediment 20 cm	sector II thickness of sediment 50 cm	sector III thickness of sediment 20 cm	Sector IV thickness of sediment 20 cm	sector IV thickness of sediment 60 cm
Susp. Solids %	**48,39**	**35,52**	**52,78**	**40,12**	**51,41**
Organic sludge %	**20,12**	**22,66**	**22,82**	**26,52**	**20.87**
inorganic sludge% on 800º C	**79,88**	**77,34**	**77,18**	**73,48**	**79,13**
Total phosphorus mg/L	**7010**	**24300**	**12900**	**2880**	**2890**
Total organic carbon TOC mg/L	**44000**	**65900**	**36590**	**50000**	**28000**
Total nitrogen mg/L	**11000**	**6800**	**3000**	**5000**	**3600**
Carbonates and bicarbonates mg/L	**37540**	**31650**	**47320**	**53270**	**39900**
Chlorides mg/L	**75**	**158**	**85**	**108**	**586**
Cadmium mg/L	**1,4**	**1,1**	**0,5**	**0,4**	**0,4**
Iron mg/L	**21100**	**18100**	**16000**	**16100**	**14500**
Manganese mg/L	**597,0**	**711**	**500**	**440**	**411**
Chromium mg/L	**216**	**189**	**52,7**	**23,1**	**26,8**

In July 2010.year the recorded value of the suspended solids in lakes water is 2 mg/L in the first sector and 46 mg/L in the fourth sector. The recorded value of suspended solids is less than the recorded value for the same sector. Suspended solids for sector I is 37.1 mg/L and for sector IV is 137.4 mg/L in April 2005. year. The thickness of sludge in the lake Palić, especially in the fourth sector, which ranges from 50 - 60 cm and more. Inorganic matter in the sludge has an average of about 79% of these sites, and is dominated by salts of calcium, iron and sodium in the form of carbonates, sulfates and chlorides, see Table 1. The concentrations of sulfates, arsenic, lead, copper, zinc and nickel are within the normal range for lake sediment, and for this reason are not presented in Table 1. By examining the composition and number of inhabitants of lake bottom was confirmed that the living conditions are very unfavorable in the mud. In the third sector of the lake in 2005. The reduced number of registered individuals Chironomidae and Oligochaeta, while in the tourist part of the lake found only a few representatives of Chironomidae [2, 3].

Conclusion

The lake serves as the recipient of treated wastewater and the city of Subotica and Palić. Effluent quality is of great importance for the lake. In order to improve the water quality of lakes, it is essential that the intake of nutrients is reduced to a minimum. New treatment plant for urban wastewater of Subotica and Palić, ought to ensure that the purified water contains minimal amounts of organic matter and compounds of nitrogen and phosphorus. Palić lake water quality could be improved by introducing water from the Tisa River, but large quantities of silt into the lake creating unfavorable conditions for the whole eco system. Eutrophication of the lake is in an advanced stage. Eutrophication of the lake could be deacreased by removal of lakes sludge and/or mixing water from lake Palić with water from Tisa river, which is of satisfactory quality.

Acknowledgement

This research has been done thanks to the resources of the project TR 37 009 Ministry of Science and Technology, R. Serbia.

References

[1] Dj. Seleši,Voda Palićkog jezera od 1781. do 1999. godine, JVP Palić-Ludaš, Subotica, 2000.
[2] T. Grozdic, Ecologica, 2011,64, 657-663.
[3] R. Pantle, H. Buck,Gas und Wasserfach, 1955, 96(18), 604.

K-19-P

^{137}Cs DESORPTION FROM MOSS *HOMALOTHECIUM SERICEUM* (HEDW.) SCHIM. USING ACID SOLUTIONS

A. Čučulović[1], D. Veselinović[2]

[1]*INEP-Institute for the Application of Nuclear Energy, University of Belgrade, Banatska 31b, 11080 Zemun, Serbia, anas@inep.co.rs*
[2]*Faculty of Physical Chemistry, University of Belgrade, P.O. Box 137, 11000 Belgrade, Serbia*

Abstract
Desorption of ^{137}Cs in samples of *Homalothecium sericeum* (Hedw.) Schimp. using: H_2SO_4 (**A**), HNO_3 (**B**), H_2SO_4-HNO_3 (**C**) acid solutions with pH values 4.60, 5.15 and 5.75 and distilled water (**D**) pH values 6.50 was investigated. After five consecutive desorptions lasting 24 hours it was shown that between 22.8% (solution (**C**) pH 5.75) and 33.2% (solution (**C**) pH 4.60) of ^{137}Cs was desorbed from the moss. Desorptions performed with solutions (**A**), (**B**) and (**C**) pH 5.75 are the weakest and approximately the same (about 23%).

Introduction
Moss has a slow growth rate and relatively large surface area to biomass ratio; the lack of the waxy cuticles and associated stomata means that many contaminants can be absorbed over the whole external surface; they do not have a rooting system; and they obtain nutrients from dry and wet precipitation by absorption through their leaves which lack cuticles. Mosses may be considered as the most commonly applied organisms for biomonitoring studies of radioactive contamination [1]. Cesium-137 (^{137}Cs) is one of the most frequent artificial radionuclides found in the environment because of different anthropogenic discharges such as atmospheric nuclear weapons testing, accidental releases from nuclear power plants, chronic emissions from nuclear power plants, and chronic emissions from nuclear reactors and fuel-reprocessing plants. Cesium-137 is an emitter of gamma and beta radiation, with a long radioactive half-life (30.17 years). The first nuclear weapons were detonated in New Mexico and Japan in 1945. The partial meltdown of the reactor at Chernobyl in April 1986 released high amounts of radionuclides into the environment, especially ^{137}Cs. Following the Chernobyl reactor accident, numerous studies involving monitoring of the long-lived fission product ^{137}Cs were undertaken using mosses as biological indicators to update the inventory of this long-lived radionuclide [2].

In our previous work we followed ^{137}Cs and metal desorption in *Cetraria islandica* lichen, while in this one we follow ^{137}Cs desorption in *Homalothecium sericeum* (Hedw.) Schimp. moss [3,4]. In this work we attempted to investigate

whether ^{137}Cs could be isolated with acid solutions as simulated acid rain without destruction of the moss cellular structure, which would imply that the whole amount of ^{137}Cs in the plant is ion-exchangeable.

Matherial and Methods

Homalothecium sericeum (Hedw.) Schimp. moss, originating from Montenegro was collected in 2002, (10 g dry mass) and covered with 200 mL of distilled water (D) and acid solutions: (A) H_2SO_4, (B) HNO_3 and (C) H_2SO_4-HNO_3. Solutions (A) and (B) were made by adding concentrated H_2SO_4, HNO_3, respectively to 200 mL of distilled water (pH 6.50) to the required pH value: 4.60; 5.15 and 5.75. Solution (C) was obtained by mixing 100 mL of solution (A) and 100 mL of solution (B) with identical pH values. Samples were consecutively desorbed with solution five times and desorption series were repeated twice. Desorptions were performed at room temperature and lasted 24 hours. After each desorption, after filtration, moss samples were dried at room temperature to a constant mass. Activity levels of ^{137}Cs were measured in samples before and after each desorption on an ORTEC-AMETEK gammaspectrometer with 8192 channels, resolution of 1.65 keV and efficiency of 34% at 1.33 MeV ^{60}Co, with a measurement error below 5%. Specific activities were calculated based on measurements (Bq/kg). The pH value of a solution was measured on a pH meter (MA 5730 Iskra).

Results and Discussion

Activity levels of ^{137}Cs (Bq/kg) in *H. sericeum* (Hedw.) Schimp. moss before desorption and the percentage of non-adsorbed ^{137}Cs in moss after each of the five consecutive desorptions with solutions (**A**), (**B**) and (**C**), and also distilled water (**D**), and the total amount (%) of desorbed ^{137}Cs are given in Table 1. Activity levels of ^{137}Cs in samples of moss before desorption were from 476 Bq/kg to 552 Bq/kg. Five successive steps with distilled water desorbed 31.3% of the initial $^{137}Cs^+$ in *H. sericeum*. With the acid solution (**A**), (**B**), (**C**) the amount of total desorbed $^{137}Cs^+$ (Table 1) ranged from 22.8% (pH 5.75, solution (**C**)) of the initial radiocesium in moss to 33.2% (pH 4.60, solution (**C**)). ^{137}Cs is significantly, but not completely desorbed from moss. Changes of the desorbed amount of ^{137}Cs with the number of consecutive desorptions have an exponential form. The percentage of the total absorbed amount of ^{137}Cs from moss is almost twice times lower than for lichen [2-4].

The final mass of the moss was only slightly decreased after this procedure (approximately 5%), indicating that desorption was achieved without significant destruction of the plant structure.

Moss desorbed using the solutions described above did not undergo any visible structural changes.

Table 1. Activity of ^{137}Cs in moss before desorption (Bq/kg), percentage of remaining ^{137}Cs in moss after each desorption and total desorbed ^{137}Cs from moss (%)

pH	**4.60**			**5.15**			**5.75**			**6.50**
Solution	**A**	**B**	**C**	**A**	**B**	**C**	**A**	**B**	**C**	**D**
Activity of ^{137}Cs in moss before desorption (Bq/kg)										
	552	513	498	538	476	493	550	505	490	523
Percentage of remaining ^{137}Cs in moss after each desorption (%)										
I	83.2	85.1	82.3	82.1	84.1	83.2	91.0	87.5	89.1	87.9
II	78.5	81.1	77.2	76.9	80.3	80.0	85.6	81.1	86.4	82.0
III	74.8	78.6	73.5	72.9	77.2	77.1	83.1	78.5	81.8	76.9
IV	71.8	76.7	68.7	70.2	75.1	73.5	77.5	77.1	78.8	71.1
V	68.2	75.2	66.8	69.3	71.1	70.3	76.1	76.6	77.2	68.7
Total desorbed ^{137}Cs from moss (%)										
	31.8	24.8	33.2	30.7	28.9	29.7	23.9	23.4	22.8	31.3

Conclusion

These results indicate that NO_3^- and SO_4^{2-} anions do not have a significant influence on ^{137}Cs desorption. Reduction of the percentage of desorbed Reduction of ^{137}Cs with increase in the pH value, i.e. reduction of the concentration of H^+ ions, indicated that they have a significant, but not dominant influence on ^{137}Cs desorption from moss.

References

[1] C. Papastefanou, M. Manolopoulou, T. Sawidis, J. Environ. Radioact. 1989, 9, 199-207.

[2] A. Čučulović, R. Čučulović, T. Cvetić Antić, D. Veselinović, Arch. Biol. Sci., Belgrade, 2011, 63 (4), 1117-1125.

[3] A. Čučulović, D. Veselinović, Š. S. Miljanić, J. Serb. Chem. Soc., 2006, 71 (5), 565-571.

[4] A. Čučulović, D. Veselinović, Š. S. Miljanić, J. Serb. Chem. Soc., 2009, 74(6), 663-668.

K-20-P

SPATIAL VARIABILITY OF ^{137}Cs ACTIVITIES IN THE SOIL OF BELGRADE REGION (SERBIA)

Lj. Janković-Mandić[1], R. Dragović[2], M. Đorđević[2], M. Đolić[1], A. Onjia[1], S. Dragović[3]

[1]*University of Belgrade, Vinča Institute of Nuclear Sciences, P.O. Box 522, Belgrade*
[2]*University of Niš, Faculty of Science and Mathematics, Višegradska 33, Niš*
[3]*University of Belgrade, Institute for the Application of Nuclear Energy, Banatska 31b, Belgrade*

Abstract

In this study, the specific activities of ^{137}Cs in surface soils from the territory of Belgrade in the period 2006-2010 were determined by gamma-ray spectrometry. Mean specific activity of ^{137}Cs was 23 Bq/kg and the corresponding absorbed dose was 1.5 nSv/h.The specific activities of ^{137}Cs in soil were geographically mapped. The significant spatial variability of ^{137}Cs specific activities of was observed.

Introduction

As the consequence of the nuclear tests carried out since 1945, large amounts of various radioactive materials were emitted into the atmosphere and subsequently distributed all over the world. Radionuclide ^{137}Cs was introduced into the atmosphere through nuclear weapon tests notably in the northern hemisphere in 1945 and then produced as the result of the accidents especially in Chernobyl in 1986 and routine processes of nuclear reactors. Among radionuclides in the soil deposited after Chernobyl accident, ^{137}Cs poses considerable environmental and radiological problems because of its relatively long half-life (30.17 y), its abundance in the fallout, high mobility and similarity to potassium as the major plant nutrient [1].

The aim of this work was to investigate the spatial variability of the specific activity of ^{137}Cs in soil samples collected across the territory of Belgrade, the capital of Serbia, using gamma-ray spectrometry. The absorbed gamma dose rate in air due to this radionuclide is also assessed.

Materials and Methods

The samples of undisturbed surface soil (n=250) were taken from 70 regions in Belgrade, during 2006-2010. Samples were dried at 105 °C to constant weight, homogenized and passed through a 2 mm mesh sieve. The specific activities of ^{137}Cs were measured by HPGe gamma-ray spectrometer (ORTEC-AMETEK, 34% relative efficiency and 1.65 keV FWHM for ^{60}Co at 1.33 MeV, 8129 channels) for 60 ks. The activity of ^{137}Cs was determined using its 661.66 keV gamma-ray line. The software package Gamma Vision 32 was used to process the spectra obtained [2]. From these results external effective dose rates were calculated according to the internationally accepted activity to dose rate conversion equations [3-6]. The specific activities of ^{137}Cs were geographically mapped using ArcGIS from ESRI [7].

Results and Discussion

Descriptive statistics for the specific activities of ^{137}Cs in soil samples collected from the territory of Belgrade and the corresponding external effective dose rates are presented in Table 1.

Table 1. Descriptive statistics for the specific activity of ^{137}Cs in soil samples collected from the territory of Belgrade during 2006-2010 and the corresponding external effective dose rates.

Parametar	^{137}Cs (Bq/kg)	D_{Cs} (nSv/h)
Mean	23	1.5
St. deviation	20	1.2
Median	15	1.0
Range	84	56
Mode	11	0.6
Minimum	3	0.2
Maximum	87	5.8

The mean of ^{137}Cs specific activity obtained in this study is comparable to those reported for Republic of Srpska (26 Bq/kg), Italy (40 Bq/kg) and FYR Macedonia (71 Bq/kg) [8-10].

The significant variability of the specific activities of ^{137}Cs in analyzed samples of soil was observed (Fig. 1).

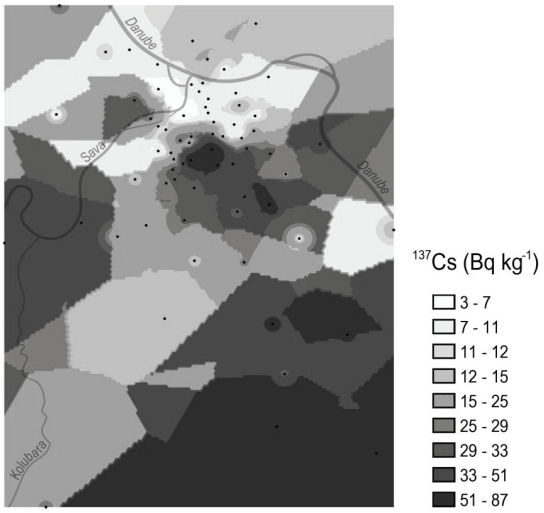

Figure 1. Spatial distribution of the ^{137}Cs specific activity in Belgrade soil.

Conclusion

The presence of ^{137}Cs has been detected in all soil samples, with high variability of its specific activity, ranging from 3 Bq/kg to 87 Bq/kg. The observed range reflects

the inhomogeneity of the deposition process following the Chernobyl accident. The results of the present study will be valuable database for future estimations of the impact of radioactive pollution.

Acknowledgement

This work was supported by the Ministry of Education and Science of the Republic of Serbia (Project No. III 43009).

References

[1] UNSCEAR, 2000, United Nations, New York.
[2] ORTEC, Gamma Vision 32, 2001, Oak S.N. Ridge, USA.
[3] A.Tahir et al., *Radiat. Prot. Dosim.* 2006,118, 345-351.
[4] K. Jamil, J. Environ. Radioact. 1998, 41, 207-216.
[5] S. Ali et al., Sci. Total. Environ. 1996, 187, 247-252.
[6] J.R. Lamarsh, Introduction to Nuclear Engineering, 1983, New York.
[7] ESRI, 2009. Environmental Systems Research Institute Inc., Redlands, CA.
[8] M. Janković et al., Radiat. Meas. 2008, 43, 1448-1452.
[9] E. Bellotti et al., Appl. Radiat. Isot. 2007, 65, 858-865.
[10] S. Dimovska et al., *Radiat. Prot. Dosim.* 2010, 138, 144-157.

K-21-P

BIOSORPTION OF Cu(II) ON XANTHATED LAGENARIA VULGARIS SHELL

M. M. Kostić[1], M.D. Radović[1], J. Z. Mitrović[1], D. V. Bojić[1], D. Milenković[2], T. D. Anđelković[1], A. Lj. Bojić[1]

[1]*Department of Chemistry, Faculty of Science and Mathematics, University of Niš, 33 Višegradska Str., 18000 Niš, Serbia*
[2]*High Chemical Technological School, Department of Chemical Technology, Kosančićeva 36, 37000 Kruševac, Serbia*

Abstract
This study investigated the feasibility of chemically modified *Lagenaria vulgaris* shell as a novel sorbent for copper removal from water. *Lagenaria vulgaris* has been functionalized by introducing xanthate groups by carbon disulphide treatment in alkaline medium. By investigating effects of contact time and sorption isotherms on the adsorbed amount of Cu(II) ions by xanthated *Lagenaria vulgaris* (xLVB), it was established that sorption equilibrium was reached after 50 minutes of contact time and that there is the best agreement with Langmuir isotherm model.

Introduction
Nowadays, increased presence of heavy metals (cadmium, copper, chromium, lead, mercury, nickel, zinc) in industrial waste waters is major problem for humanity and science. Because of their negative effects to humans, animals and overall environment, it is very important to remove heavy metals from wastewaters [1, 2]. Conventional methods for removing heavy metals from aqueous solutions include chemical precipitation, oxidation/reduction, electrochemical treatment, evaporative recovery, filtration, ion exchange and membrane technologies. These processes may be ineffective or cost-expensive, especially when the metals in solution are in range of 1-100 mg dm^{-3} [3, 4]. In recent years, sorption technology and using biomaterials for wastewaters treatment are developed and used, as high efficient but low-cost method. One of such biomaterials is *Lagenaria vulgaris*.
Lagenaria vulgaris belongs to *Cucurbitaceae* family. It is appropriate adsorbent of heavy metals because of its lignocellulosic composition with a capacity for binding metal cations due to hydroxyl, carboxylic, lactonic and phenolic groups present in their structure. Adsorption capabilities of chemically modified, xanthated *Lagenaria vulgaris* biosorbent (xLVB) were tested for Cu(II) metal ions, through effects of contact time and initial metal concentration.

Experimental
<u>*Reagents.*</u> All chemicals were of analytical reagent grade and used without further refinement. HNO_3, NaOH, CS_2, $CuSO_4$ were purchased from Merck (Germany). All solutions were prepared with deionized water.

Preparation of biosorbent. *Lagenaria vulgaris* shell was roughly crushed, washed with deionized water and grounded by laboratory blender. Biomass was soaked in 0.3 M HNO_3 for 24 hours and after that, washed with deionized water and treated with 0.1 M NaOH for 30 min. Excess alkali was removed by thoroughly washing and sorbent was dried in the oven at 55±5°C to constant weight. Dried biomass was fractionized using standard sieves (Endecotts, England).

Xanthation procedure: 5 g of prepared adsorbent (granulation from 0.8 to 1.25 mm) was soaked in 5 M NaOH, stirred for 90 minutes and washed with deionised water; then it was esterified with 0.5 cm^3 of CS_2 and 50 ml 2.5 M NaOH for another 90 minutes. After that, biomass was washed with deionized water and dried at 40°C. As a result, xanthated *Lagenaria vulgaris* biosorbent (xLVB) was prepared for removing heavy metals from aqueous solutions.

Batch biosorption experiments. The stock solution of Cu(II) was prepared in 1.00 g dm^{-3} concentration using $CuSO_4$. Working standard solutions were prepared just before use by the appropriate dilution of the stock solutions. The pH of the solutions was adjusted pH-metrically to the pH 5 with nitric acid or sodium hydroxide (0.01 M) that turned out to be optimal value. Experiment on the adsorption of metal ions by xLVB was carried out in batch conditions, by agitating 125 cm^3 of 50.0 mg dm^{-3} metal ion solutions of Cu(II), contacted with 0.5 g biosorbent. At required time intervals: 0, 1, 2, 5, 10, 20, 40, 60, 90, 120 and 180 min, 4.0 cm^3 of samples were withdrawn and analyzed using a flame atomic adsorption spectrometer (Analyst A300, Perkin Elmer, USA).

Results and discussion

Contact time effect. In this study the effects of contact time on the sorbtion of Cu(II) ions on xLVB was studied. As it is shown in Figure 1. sorption process has 2 phases; in the first phase, after 20-30 minutes of sorbent-sorbate contact time it was removed most of Cu(II) ions (10.238 mg g^{-1}). The sorption equilibrium was reached after 50 minutes of contact time (12.364 mg g^{-1}). Initial concentration of investigated ions decreases from 50 mg dm^{-3} to level of 0.54 mg dm^{-3}. The effects of contact time on the adsorption of Cu(II) ions by *xLVB.* are shown in Figure 1.

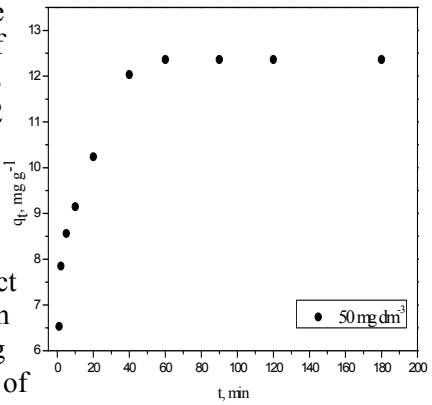

Figure 1. Effect of contact time on adsorption capacity of Cu^{2+}.

Sorption isotherms. The sorption data were tested against Langmuir, Freundlich and Temkin adsorption isotherm models. In Table 1 are presented equilibrium model parameters for adsorption Cu(II) onto xLVB and their values, for each model. r^2 (the correlation coefficient) in respect to sorption of Cu(II) ions has values 0.9984, 0.9643 and 0.8310 for Langmuir, Temkin and Freundlich model,

respectively. Accordingly, the adsorption characteristics of xLVB for Cu(II) ions are the best fitted by Langmuir isotherm model, with regard to the Temkin and Freundlich isotherm model. The enhancement in metal adsorption capacity can be explained using Pearson rule [5]; according to this rule, soft bases will form stable complexes with metals such as copper [6]. Xanthate group can be classified as soft base, thus xLVB will certainly show high adsorption capacity.

Freundlich constant n is a measure of the deviation of the adsorption from linearity. The adsorption is linear if the *n* has value about 1; if the value of *n* is higher, adosrption is favorable. Vice versa, if below 1, adsorption is unfavorable. In this study, Freundlich constant n has value 4.06, which implies to favorable adsorption.

Table 1. Equilibrium model parameters for adsorption of Cu(II) onto xLVB.

Langmuir isotherm			Freundlich isotherm			Temkin isotherm		
K_L (dm^3 mg^{-1})	q_{max} (mg g^{-1})	r^2	K_F (dm^3 g^{-1})	n	r^2	Kt	b_T (kJ/mol)	r^2
0.2886	23.17	0.998	6.839	4.06	0.831	1.003	0.959	0.964

Conclusions

This study show that the xanthated *Lagenaria vulgaris* shell can be used as efficient and inexpensive material for removal Cu(II) from polluted water. Biosorption process is fast and in the first phase (20 min) achieved very high sorption capacity (10.238 mg g^{-1}). Sorption equilibrium was reached after about 50 minutes of contact time with q_e 12.36 mg g^{-1}. Sorption process can be the best fitted by Langmuir isotherm model, which indicates monolayer adsorption at specific energetically homogeneous sites, without interaction between molecules adsorbed on neighboring sites.

Acknowledgement

Authors would like to acknowledge for financial support to the Ministry of Education and Science of the Republic of Serbia (Grant No TR34008).

References

[1] W. S. Wan Ngah, M.A.K.M. Hanafiah, Bioresour. Technol. 99 (2008) 3935.
[2] S. Liang, X. Guo, N. Feng, Q. Tian, J. Hazard. Mater. 170 (2009) 425.
[3] L. Sha, G. Xue-yi, F. Ning-chuan, T.Qing-hua, Trans. Nonferrous Met. Soc. Chna., 2010, 20, 187.
[4] D. L. Mitić-Stojanović, A. Zarubica, M. Purenovic, D. Bojic, T. Andjelkovic, A. Bojic, Water SA, 37(3) (2011) 303-312.
[5] R. G. Pearson, Inorg. Chem. 27 (1988) 734
[6] M. J. Winter, Complexes, d-block Chemistry, Oxford University Press, New York, 1994.

K-22-P

REMOVAL OF Cu(II) FROM WATER USING METHYL-SULFONATED *LAGENARIA VULGARIS* SHELL

M. N. Stanković, N. S. Krstić, R. S. Nikolić, D. V. Bojić,
J. Z. Mitrović, M. D. Radović, A. Lj. Bojić

Department of Chemistry, Faculty of Science and Mathematics, University of Niš, Višegradska Str. 33, 18000 Niš, Serbia

Abstract
Chemical modified *Lagenaria vulgaris* was used as biosorbent for removal Cu(II) from water. The adsorbent removal efficiency was determined as a function of contact time and initial pH. Kinetics models showed that metal adsorption follow a pseudo-second-order kinetic model. Results showed that the Cu^{2+} removal by msLVB increased with increasing pH from 2.0-5.0, and than slightly decrease at pH 6.0.

Introduction
Pollution of natural waters by metal ions is a serious problem nowadays. There are several methods to remove toxic metal ions from waste-waters: chemical precipitation, electrochemical technologies, ion exchange, reverse osmosis and sorption onto activated carbon [1]. But, these methods have high operational costs or leave secondary sludge so are no acceptable in the developing countries.
The shell of Lagenaria vulgaris can be used as a low-cost sorbent for heavy metals, largely due to its lignocellulosic composition with a capacity for binding metal cations due to hydroxyl, carboxylic, lactonic and phenolic groups present in their structure. The presented funcional groups indicate that the predominant biosorption mechanisms are ion-exchange, complexation and chelation [2]. *Lagenaria vulgaris* is common name in older literature for *Lagenaria siceraria* (Molina) Standley, a species of *Cucurbitaceae* family [3,4].
The effect of contact time and initial pH has been investigated. The sorption process nature has been evaluated with respect to its kinetic aspects.

Experimental
<u>*Preparation of biosorbent.*</u> Methyl-sulfonated *Lagenaria vulgaris* biomaterial (msLVB) was prepared by adding 200 mL of 1.5% solution of formaldehyde to 10 g of grounded and sieve fractionized raw material. After heating in flask under reflux at 80^0C for 2 h, 25 g $NaHSO_3$ (Merck) was added to and reaction mixture was heated for 3 h at 100 ^{0}C again under reflux. After cooling, the material was washed thoroughly with de-ionized water until sulfate reaction was over and oven-dried at 55°C. Obtained material was used for metal sorption studies.
<u>*Metal solution.*</u> Standard stock solution of Cu^{2+} (1000 mg Cu(II) L^{-1}, $CuSO_4 \cdot 5H_2O$, Merck) was used to prepare appropriate concentrations for the sorption studies. The pH of the solutions was adjusted pH-metrically to the required value with nitric

acid or sodium hydroxide (0.01 M), without buffering. pH of solutions was determined pH metrically (SensION3, HACH, USA).

The absorption equilibrium experiments. The batch adsorption experiments were conducted with constant amount of msLVB (4.0 g L^{-1}) added to 125 mL Cu(II) ion solutions of known concentrations (10, 20, 50, 100, 200, 400 mg L^{-1}) in 250 mL flasks shaken for 240 min at room temperature. Rate of metal sorption by msLVB was determined by analyzing residual Cu(II) ions in the filtered solutions after contact periods of 0, 1, 5, 10, 20, 40, 90, 120, and 240 min.

Cu(II) ions concentrations measurement. The concentrations of unadsorbed Cu(II) ions in the solution before and after adsorption were determined by using an atomic absorption spectrophotometer (AAS Analyst 300, Perkin Elmer, USA) at the wavelength 324.8 nm.

Results and Discussion

Biosorption kinetics. Experiments were performed with model wastewaters containing Cu(II) ions at initial concentrations 50.0 mg dm^{-3} and initial solution pH 5.0, at room temperature. The effect of contact time on the removal efficiency of msLVB for Cu(II) ions is shown at Fig. 1. The adsorption increased sharply with contact time in the first 20 min and reached equilibrium within about 40 min. Further increase in contact time did not show a significant increasing in biosorption.

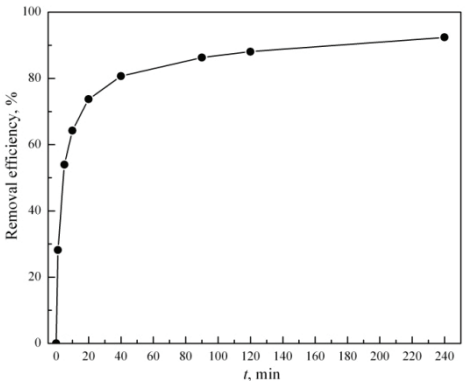

Figure 1. Removal efficiency of Cu(II) ions by msLVB (50.0 mg dm^{-3} Cu(II), pH 5.0, 22±2ºC).

In this study, the biosorption kinetic data were analyzed using following theoretical–models: pseudo-first-order, pseudo-second-order and Elowich model. The experimental data fit well to the pseudo-second order kinetic model, where the r^2 values were observed to be close to 1 (Table 1).

Table 1. Constants of pseudo-first order, pseudo-second-order and Elovich model kinetics based on the sorption of Cu(II) from 50 mgL^{-1} solutions, pH 5.0, by 4.0 gL^{-1} msLVB.

	Pseudo-first-order			Pseudo-second-order			Elovich model		
($mg\ g^{-1}$)	Q ($mg\ g^{-1}$)	K (min^{-1})	r^2	Q_{eq} ($mg\ g^{-1}$)	k_2 ($mg^{-1}min^{-1}$)	r^2	α	β	r^2
11.40	5.70	0.0221	0.828	11.52	0.018	0.999	27.027	0.698	0.958

Effect of initial pH. The influence of pH in the initial solution of Cu^{2+} was examined at different pH ranging from 2.0 to 6.0. Fig. 2 shows the effect of pH on the removal efficiencies of Cu^{2+} ions by msLVB. The Cu^{2+} removal by msLVB increased with increasing pH and attained values of 93.62 % at an initial pH of 5.0. The Cu^{2+} uptake increased significantly from 29.20% to 92.40% at pH ranging 2.0–5.0, and then slightly decrease on 91.68% at pH 6.0. The pH of the solution is one of the most significant parameters in the adsorption of metal ions from aqueous

solutions. This parameter is straightforward
ions with metal ions to actives sites on th
shows its minimum values at pH 2.0. At th
on the active sites became positive and r
surface active sites, which results in lower
increased, the ability of Cu^{2+} ions for comp
Removal eficiancy at pH 6.0 is quite lower
partial precipitation of Cu(II) ions in form
through blank experiment (treatment in
biosorbent).

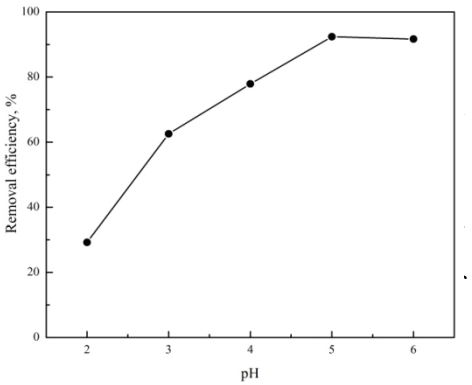

Figure 2. Effect of pH on the sorption of Cu^{2+} from 50 mg dm^{-3} solutions.

Conclusions

This study shows that the methyl-sulfonated *Lagenaria vulgaris* shell can be used for the removal of Cu(II) ions from wastewaters as a efficient low-cost biosorbent. Removal efficiency increased significantly with pH from 2.0 to 5.0, and then slightly decreases at pH 6.0. Biosorption kinetics follows a pseudo-second-order model.

Acknowledgements

This work was supported by the Ministry of Education and Science of the Republic of Serbia, Grant No. TR34008.

References

[1] R. Han, W. Zou, H. Li, Y. Li, J. Shi, J. Hazard. Mater., 2006, B137, 934–942.
[2] B. Volesky, Z.R. Holan, Biotechnol. Prog., 1995, 11, 235–250.
[3] H. M. Burkill, The useful plants of west tropical Africa, Royal Botanic Gardens, Kew,1985, 1,
[4] B. N. Shah, A. K. Seth, B. S. Nayak, Der. Pharmacia Lett., 2010, 2, 202-205.

K-23-P

DETERMINATION OF PESTICIDE RESIDUES IN WORKING CLOTHES

N. Andrić[1], D. Marković[2]

[1]Galenika Fitofarmacija AD, Batajnički drum bb, Zemun, [2]Fakultet za primenjenu ekologiju FUTURA,Lazarevački drum 13, Beograd

Abstract

The aim of the experiment was to determine possible presence of pesticide residues of active substances in the working clothes which is used in the laboratory for testing of pesticides. For better comparison, the experiment was performed on a sample of clean and work laundry (work clothes from the laboratory). Analysis was done on the gas-mass chromatograph. The results obtained for pure water from washing machine are expected and there is no trace of contamination in them. In the samples of water from washing machine of work clothes one pesticide was found - terbuthylazine, which was the purpose of this experiment. High resistance to hydrolysis of terbuthylazine explains its presence in water samples of work clothes.

Introduction

Pesticides are chemical substances which are used in farming, fruit growing and forestry as well as in communal hygiene. These chemicals are used for plant protection. They are used to control insect pests and plant diseases, for the destruction of weeds and to preserve the quality of agricultural products and increase yields, control of parasites and diseases dangerous to humans and animals.[1]

Because of their stability and durability (particularly organochlorine compounds), they can migrate, redistribute and finally accumulate in plants, animals and other living organisms for years. As a result of this behavior they can act far away from the point of use, which is characterized by global overdue effects. They can move in the form of aerosols, suspensions or solutions by air streaming, by ground and underground water, by migration of birds, animals and people, by transport of raw materials and food. Because of this, pesticides can often cause undesirable secondary effects on the environment. [2,3]

After use, pesticides undergo different physical, chemical and biochemical processes. While in some cases ends up as no hazardous materials, in the majority of cases pesticides occurs as toxic substances in agricultural products, soil and water (in original or modified form). The chemical structure of pesticides is essential. The absence of harmful residues in the environment is best achieved if pesticides are disintegrated to products that are found in abundance in the environment. In other words, pesticide molecules needs to be composed of fragments of biogenic type - amino acids, sugar, lipids, carboxylic acids and

inorganic residues, as in the case of organophosphorus pesticides where in the final stage of decomposition phosphorous acid occurs. [2]

Experimental

This kind of experiment is rare in Serbia because very little attention is given to the contaminated working clothes. Workers who are constantly wearing those clothes can be endangered, because even the small doses of contamination can be harmful considering bioaccumulation effect. Long-term exposition to the pesticides can cause serious health problems. Purpose of this experiment is to draw attention on this type of pollution and to prevent it.

The aim of the experiment was to determine possible pesticide residues of active substances in the working clothes. Working clothes is one that is used in the laboratory for testing of pesticides and involves working coats, shirts, pants, etc. For better comparison, the experiment was performed on a sample of clean and dirty laundry (work clothes from the laboratory). Clean laundry was washed in a washing machine with water only, without addition of detergent. The same was done with work clothes. Samples were stored in PET bottles.

Liter of water from the clean laundry was extracted with dichloromethane in a separating funnel. 400 ml of sample was transferred from PET bottle to the separation funnel and then added 100 ml of dichloromethane. The sample was stirred and extracted in a glass. The same procedure was repeated with next 400 ml. A further 200 ml of water from clean laundry was transferred into the funnel and added 50 ml of dichloromethane. The extract was also transferred into the cup. After these three extractions, in the glass is now 250 ml of dichloromethane and the analytes from the sample. The entire extraction procedure was repeated, only this time three times of 300 ml of sample was extracted with 250 ml of dichloromethane (containing analytes) from the cup. Again, we get 250 ml of dichloromethane containing unknown analytes. This sample was evaporated in the water bath to a volume of 10 ml. In this way the sample was concentrated. Extraction was performed in the same manner with the next liter of water from the clean laundry. The same procedure was applied on water samples of work clothes, ie., contaminated laundry. Analysis of these four samples was performed on the gas-mass chromatograph. [4]

Results and Discussion

The results obtained for pure water are expected and there is no trace of contamination in them. Identified compounds originate from nicotine, alcohol, fat, milk, butter, cosmetics and detergent. The same compounds were found in water samples of work clothes. However, in water samples from the work clothes was found one pesticide - terbuthylazine, which was the purpose of this experiment. Terbuthylazine is herbicide which is used to spray sunflower and maize. It belongs to the triazine group and to the third category of toxins. It is not known whether is carcinogenic, but it has low acute toxicity. Terbuthylazine is irritating to skin, eyes and respiratory tract. If it is found in water, it can affect the growth, physiology and

plant populations. This herbicide accumulates in fish, phytoplanktons and zooplanktons. For a fish is moderately toxic and highly toxic to zooplankton. Terbuthylazine is persistent in aquatic systems, because it is poorly hydrolysed and it is resistant to photolysis. If the pH of water is between 5 and 9 this pesticide is stable from 86 to over 200 days. There is no evidence that in small doses terbuthylazine is harmful to humans and animals. [6,7]

Conclusion

Although only one pesticide was found, we can consider that the experiment succeeded. High resistance to hydrolysis explains presence of terbuthylazine in water samples of work clothes. Work clothes were in contact with other active substances, but their presence was not detected probably due to their instability in aqueous systems. This experiment went only to the qualitative determination of pesticide residues in working clothes, which is a good start for their quantitative determination in the future. The next step is to attempt quantitative determination of pesticides in work clothes.

References

[1] D. Minić, Hemija pesticida, dobijanje i primena, Panda Graf, Beograd, 1994.
[2] D. Veselinović, I. Grzetić, Š. Đarmati, D. Marković, Stanja i procesi u životnoj sredini, FFH, Beograd, 1995.
[3] N. Mitić, Pesticidi u poljoprivredi i šumarstvu u Srbiji i Crnoj Gori, Društvo za zaštitu bilja Srbije, Beograd, 2004.
[4] V. Jovanović, M. Kopečni, S. Milonjić, A. Ruvarac, A. Spirić, V. Višacki-Hromatografija, teorijski i praktični aspekti, Institut za nuklearne nauke - Vinča, Beograd, 1988.
[5] http://www.pesticideinfo.org/Detail_Chemical.jsp
[6] http://www.who.int/water_sanitation_health/dwq/chemicals/terbuthylazine.pdf
[7] http://www.alanwood.net/pesticides/terbuthylazine.html

K-24-P

REMOVAL OF IODINE FROM AQUEOUS SOLUTIONS BY POLYETHYLENIMINE – EPICHLOROHYDRIN RESINS

S. Sarri[1], P. Misaelides[1], F. Noli[1], L. Papadopoulou[2], D. Zamboulis[1]

[1] *Department of Chemistry, Aristotle University, 54124 Thessaloniki, Greece*
[2]*Department of Physics, Aristotle University, 54124 Thessaloniki, Greece*

Introduction

The presence of iodine in the biosphere is not only due to natural sources but also to number of human activities (e.g. medical, industrial, nuclear energy production). Iodine isotopes (e.g. ^{131}I ($t_{1/2}$ = 8 days), ^{129}I ($t_{1/2} = 1.6\times10^7$ yr)) are also among the most abundant fission products and are released to the environment in cases of nuclear reactor accidents and nuclear explosions [1].

In the present study the ability of two recently prepared epichlorhydrin - polyethylenimine resins to remove iodine from aqueous media was investigated under various conditions.

Experimental

Two polyethylenimine - epichlorohydrin resins were prepared using low- (L.M.W.) and high molecular weight polyethylenimine (H.M.W.) and characterized at the Chemistry Department of the Aristotle University. A modification of a previously described synthesis method was applied for the preparation of the resins [2].

For the sorption experiments 30 mg of the resins were contacted in polypropylene tubes for 24 hours with 10 mL of ^{131}I-labeled NaI solutions (C_{init}: 300 to 5000 mg I^- /L) at room temperature. After separation of the solid and liquid phases by centrifugation, the iodine concentration in the liquid phase was determined by gamma-ray spectroscopy using HPGe detector (CANBERRA ReGe, resolution 2.1 keV) connected with a computer based gamma-spectroscopy set-up. The obtained data were used to calculate the uptake capacity in mg/g and construct the corresponding sorption isotherms.

Experiments both in absence and presence of background electrolytes (0.1 M NaCl and 0.033 M Na_2SO_4 – constant ionic strength 0.1 M) were performed using iodides solutions of pH_{init} 3 and 7 in the first case and pH_{init} 3 in the second one adjusted by HCl and NaOH.

The surface and the interior of the resin grains, prior and after the sorption, were examined by SEM/EDS (JEOL 840A SEM equipped with an OXFORD ISIS 300 SEM-EDS analyzer).

The experimental results were modeled using the Langmuir and Freundlich isotherm equations [3] and compared with literature data for other sorbents.

Results an Duscassion

Both investigated resins could effectively remove iodides from aqueous solutions. The H.M.W. resin showed higher sorption capacity than the L.M.W. one. This effect could be attributed to the structural differences between the two sorbents. The results also indicated that for both sorbents a higher iodine uptake was obtained at pH_{init} 3. The uptake capacity decreased with increasing pH_{init}. The last can be attributed to the stronger competition from the side of hydroxyl-ions for the same number of sorption sites.

Fig. 1 presents the experimental data obtained for the I^- - sorption by the two resins from solutions of pH_{init} 3 absence of background electrolyte. In the same figure the curves obtained by fitting the experimental data by the Langmuir isotherm equation and the 95% confidence limits of the fit are also given. All maximum sorption capacity - (Q_{max}), K - and the correlation coefficient (R^2) values are presented in Table 1 along the corresponding parameters obtained from the fitting by the Freundlich equation. The correlation coefficient values showed that the Langmuir isotherm equation could better reproduce the experimental results compared to the Freundlich one.

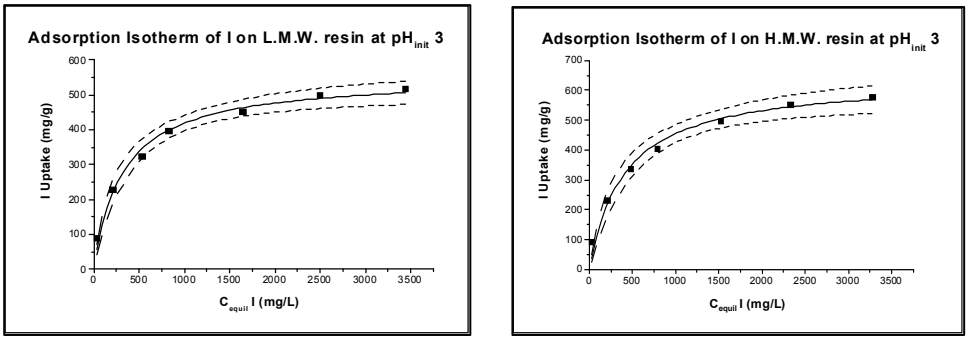

Figure 1. Adsorption isotherms for the I^- - sorption onto the two resins along the corresponding Langmuir isotherm fit. The dashed lines represent the 95% confidence limits of the fit.

Experiments performed in the presence of background electrolyte indicated that the presence of SO_4^{2-} ions in the solutions reduced the I-uptake to a higher extent than the presence of Cl^- ions, probably due to their larger size and charge. The maximum sorption capacity (Q_{max}) was, in the case of presence of Cl-ions, almost 1/3 of the value determined in absence of background electrolyte whereas the presence of sulfates reduced the I-sorption capacity by ca. 90%.

The examination of intersections of the I-loaded resins grains by SEM/EDS revealed that iodine was evenly distributed throughout the bulk of the resins and not bound only to their surface (Fig. 2).

Table 1. Langmuir- and Freundlich parameter values and corresponding correlation coefficients.

			Q_{max} (mg/g)	K (L/g)	n	R^2
L.M.W. resin	pH 3	Langmuir	552.4	0.00313	-	0.986
		Freundlich	-	45.91063	3.284	0.965
	pH 7	Langmuir	507.5	0.00377	-	0.986
		Freundlich	-	54.39033	3.652	0.932
H.M.W. resin	pH 3	Langmuir	638.8	0.00247	-	0.982
		Freundlich	-	42.2304	3.030	0.981
	pH 7	Langmuir	603.3	0.0027	-	0.983
		Freundlich	-	43.1532	3.112	0.967

pH= 3

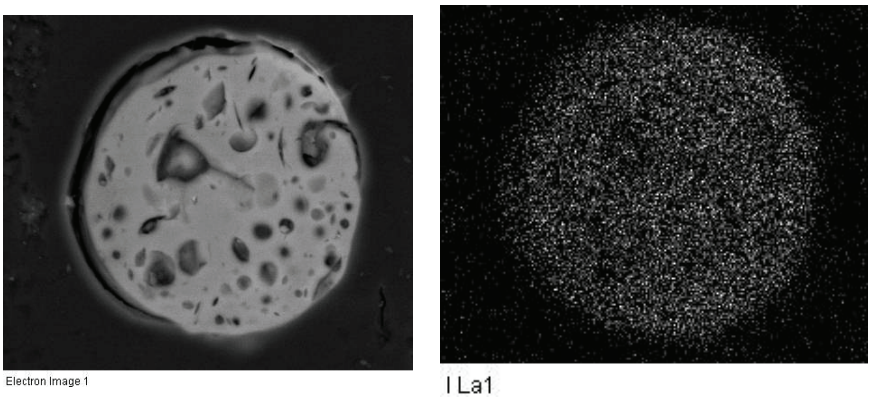

Figure 2. SEM image of a cross-section of a H.M.W. resin grain after I uptake (left) and the corresponding I-mapping (right).

The comparison of the experimental results with literature data indicated that the two resins showed higher I-sorption capacity than a number of natural raw and modified sorbents (e.g. Mg–Al (NO_3) layered double hydroxide, Mg–Al hydrotalcite-like compounds) but lower than a series of activated carbons of different origin).

References

[1] http://www.atsdr.cdc.gov/toxfaqs (last visited 7.5.2012)
[2] Ebner A.D., Ritter J.A., Pioehn H.J., Kochen R.L., Navratil J.D., Sep. Sci. Technol. 34 (1999) 1277-1300.
[3] Gerente G. et al., Environ. Sci. Technol. 37 (2007) 41–127.

K-25-P

REMOVAL OF NI(II) IONS BY TEMPERATURE TREATED RED MUD FROM ALUMINUM INDUSTRY

A. Milenković[1], S. Smiljanić[2], I. Smičiklas[1], M. Šljivić-Ivanović[1]

[1] *University of Belgrade, Vin a Institute of Nuclear Sciences, P.O. Box 522, Belgrade Serbia*

[2] *University of East Sarajevo, Faculty of Technology, Karakaj bb, 75400 Zvornik, Republic of Srpska, Bosnia and Herzegovina*

Abstract

Red mud is a waste produced in excessive amounts by the aluminum industry. Due to heterogenic mineral composition it represents a promising sorbent material. In this study, Ni(II) removal from aqueous solutions was studied. As-received red mud was subjected to temperature treatment, in the range 200-900^{o}C. The influence of annealing temperature and initial solution pH on Ni(II) removal efficiency was analyzed and discussed.

Introduction

Red mud, a waste sludge obtained after alkaline digestion of bauxite ore, is composed mainly of Fe, Al and Si oxides, as well as titania, sodalite, gypsum, calcite, etc [1]. It was intensively studied as an immobilization agent for various toxic substances [1, 2]. The previous experiments on Ni(II) removal from aqueous solutions by thoroughly rinsed red mud from the "Bira " Alumina Factory confirmed the applicability of this industrial waste to remove Ni(II), dominantly by specific sorption and precipitation mechanisms [3]. Ni(II) sorption capacity could be enhanced by annealing rinsed sample at 600^{o}C [3]. The original red mud is highly alkaline, which can benefit the removal of hydrolysable cations such as Ni(II). In this study, the influence of temperature treatment on removal efficiency of as-received red mud was studied, as well as the influence of initial solution pH.

Experimental

As-received red mud (without prior washing or neutralization) was dried at 105^{o}C and milled in the mortar. The 15 g portions of obtained powder were annealed at 200, 400, 600, 800 and 900^{o}C, in the electrical furnace, for 3 h (samples denoted as BRM200-BRM900). Ni(II) ions removal was tested in batch conditions, by agitating 0.1 g of solid phases with 20 mL of $2\cdot10^{-3}$ mol/L $Ni(NO_3)_2$ solution, at room temperature, for 24 h. The initial pH values were adjusted in the range 2-6, by adding minimum volumes of HCl and NaOH solutions. Clear supernatants were separated from the solid phase by centrifugation and filtration. Final pH values were measured. Initial and the residual concentrations of nickel in the supernatants

were determined by flame Atomic Absorption Spectrometer (Philips Pye Unicam SP9, at 232.0 nm).

Results and discussion

Starting material showed the weight losses of 4.13 %, 5.93%, 6.66% 7.93% and 8.13% after annealing at 200°C, 400°C, 600°C, 800°C and 900°C, respectively. The effects of temperature treatment and initial solution pH on Ni(II) removal and final pH values are presented in Fig. 1.

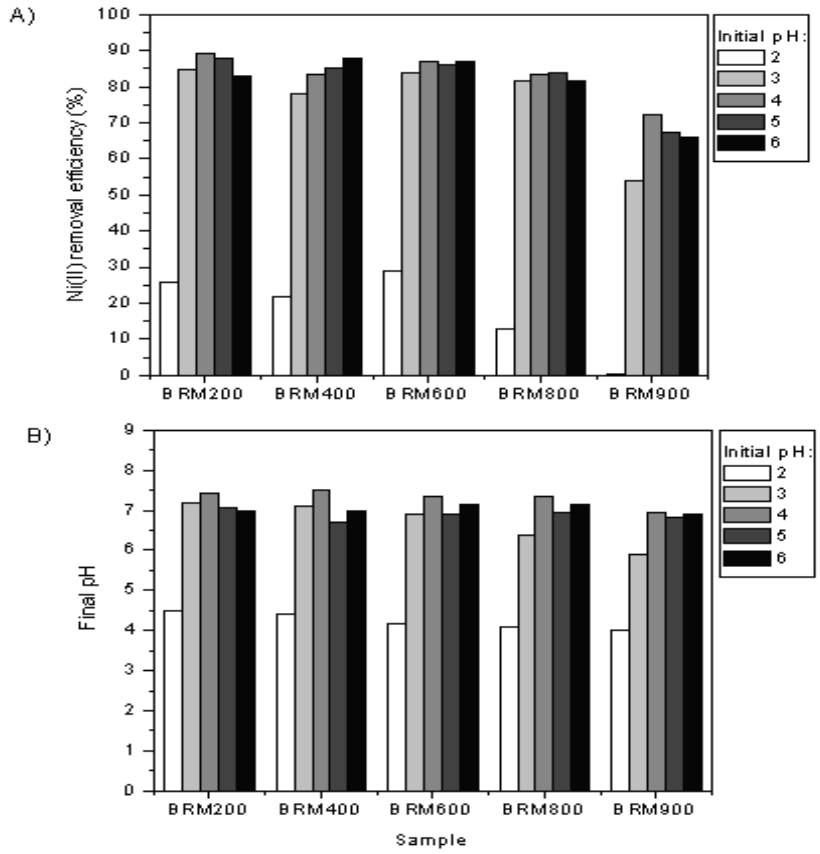

Figure 1. The influence of temperature treatment and initial pH on (A) Ni(II) removal efficiency and (B) final pH values.

Depending on applied sorbent sample, the process efficiency increased rapidly from 0.5%-28.9 % to 53.8%-84.7 % with the increase of initial pH from 2 to 3 (Fig. 1, a), whereas further pH rise up to 6 produced less significant changes. Such behavior can be associated with the buffering capacity of red mud [3]. pH values measured after equilibration (Fig. 1, b) were lowest for initial pH 2, while higher and rather comparable in the initial pH range 3-5.

Heat treatments induce physical and chemical changes in red mud, consequently, thoroughly washed sample showed the maximum sorption after annealing at 600^{o}C [3]. In this study, the excess amounts of NaOH added during ore digestion partially covered the differences between physico-chemical properties of sorbents. The most obvious effect of temperature treatment was decrease of process efficiency using sorbent BRM900 at all investigated initial pH (Fig. 1, a). Furthermore, BRM800 exhibited lower Ni(II) removal at initial pH 2. This can be connected with the increased mineral phase crystallinity of these samples, the effect of particles sintering and somewhat lower final pH values especially in the initial pH range 2-3 (Fig.1, b).

The overall performance of annealed samples was enhanced using as-received red mud than rinsed powder [3]. The additional amounts of Ni(II) removed from the aqueous solutions in this study, can be attributed to the higher equilibrium pH values and the greater contribution of the $Ni(OH)_2$ precipitation.

Conclusions

Ni(II) removal by annealed red mud increased most rapidly in the initial pH range 2-3. The influence of temperature treatment in the range 200-800^{o}C, on process efficiency was less pronounced using as-received red mud, than in previous experiments with rinsed sample, due to higher and comparable final pH values. Heating at 900^{o}C resulted in lower Ni(II) removal rates in the entire investigated pH range.

Acknowledgments

This work was supported by the Ministry of Education and Science of the Republic of Serbia (Project No. III 43009).

References

[1] S. Wang, H. M. Ang, M. O. Tad, Chemosphere, 2008, 72, 1621–1635.
[2]Y. Liu, R. Naidu, H. Ming, Geoderma, 2011, 163, 1–12.
[3] S. Smiljanić, I. Smičiklas, A. Perić-Grujić, B. Lončar, M. Mitrić, Chem. Eng. J., 2010, 162, 75-83.

K-26-P

BERYLLIUM-7 CONCENTRATION ANALYSIS IN GROUND LEVEL AIR IN SERBIA

M. M. Janković[1], D. J. Todorović[1], B. Ž. Janković[2],
J. D. Nikolić[1], G. K. Pantelić[1], M. M. Rajačić[1]
[1]*University of Belgrade, Institute Vinča, Radiation and Environmental Protection Department, P.O. Box 522, 11001 Belgrade, Serbia*
[2]*Faculty of Physical Chemistry, University of Belgrade, Studentski trg 12–16, P.O. Box 137, 11001 Belgrade, Serbia*

Abstract
^{7}Be concentration in ground level air at five monitoring stations: Vinča, Zeleno Brdo, Zaječar, Vranje and Zlatibor was determined during the period from May 2011. to March 2012. Concentrations of ^{7}Be ranged from 1.5 to 7.9 mBq m^{-3} and exhibit maxima in the spring/summer period. It was found that the value of the symmetrical index *n* is the highest for Vranje.

Introduction

^{7}Be is a radioactive element (half-life 53.3 days) produced by cosmic rays in spallation processes with light elements (N, O, C), in the lower stratosphere (~70%) and the upper troposphere (~30%). Following production, ^{7}Be is promptly attached to aerosols with a diameter of 0.3-0.6 mm whose residence time in the atmosphere is around 20 days [1]. In the troposphere, apart from its decay, ^{7}Be is removed by wet deposition (the major mechanism for removal) and dry deposition. In ground level air, the residence time of ^{7}Be is around 10 days [2]. Ground level ^{7}Be has been measured in Belgrade, Serbia, since 1991, as a part of the air radioactivity monitoring programme in the Radiation and Environmental Protection Department Vinča Institute of Nuclear Sciences. The measured values of ^{7}Be in Belgrade air are in good agreement with the data for other regions, and showed that the ^{7}Be activity reaches its maximum in summer [3]. In this paper, concentrations of ^{7}Be measured at different locations in Serbia are presented. Symmetrical index, *n*, was used as mathematical parameter to describe changes of the concentrations of ^{7}Be in ground level air.

Experimental

Aerosol samples were collected on filter papers (Whatman 41, relative efficiency for deposited dust 80 %) by constant flow rate samplers (average air flow 35 m^{3} h^{-1}). The filter papers were then ashed at temperatures below 400 ^{o}C and a monthly composite sample containing 30–31 daily filters was formed (average volume 35×10^{3} m^{3}). The samples were measured in small metallic containers. The activity of the ^{7}Be was determined on an HPGe detector (Canberra relative efficiency 23 %) by standard gamma spectrometry. For calibration of detectors for measuring samples of aerosols, secondary radioactive material in the reference geometry of the plastic container vials was used which received from the primary reference of radioactive material, Czech Metrological Institute, Praha, 9031-OL-116/8, type

ERX, total activity 114.9 kBq on the day 03.03.2008. (^{241}Am, ^{109}Cd, ^{139}Ce, ^{57}Co, ^{60}Co, ^{88}Y, ^{113}Sn, ^{85}Sr ^{137}Cs, ^{210}Pb). The threshold of detection of the ^{7}Be in air was 10^{-6} Bq m^{-3} for ^{7}Be. Counting time intervals were 60000 s.

Results and Discussion

The activities of ^{7}Be in ground level air at different locations during the period May 2011.- March 2012.are presented in Fig. 1. Concentrations of ^{7}Be in air were in the range of 1.5–7.9 mBq m^{-3} and exhibited a maximum in summer and a minimum in winter.

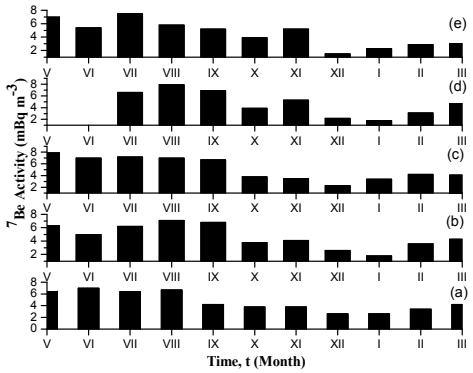

Figure 1. ^{7}Be activity in the ground level air, at: (a) Vinča, (b) Zeleno Brdo, (c) Zaječar, (d) Vranje and (e) Zlatibor.

The symmetrical index, n, which defines the magnitude of ^{7}Be content changes with time (in months), can be obtained directly from a derivative of dc(^{7}Be)/dt peak curve, based on the following equation:

$$n = 1.88 \frac{\left| \left[\frac{d^2 c(^7Be)}{dt^2} \right]_L \right|}{\left| \left[\frac{d^2 c(^7Be)}{dt^2} \right]_R \right|} \quad (1)$$

where 1.88 is the constant, indices L and R correspond to the left and right peak d^2c(^{7}Be)/dt^2 values (extrema) on the second derivative c(^{7}Be) *vs*. t curves. Equation (1) is similar to the equation, which is present in the second Kissinger technique (Kissinger, 1957). Fig. 2 shows the second (d^2c(^{7}Be)/dt^2) derivative curve of the normalized beryllium-7 concentrations (c(^{7}Be)), in function of time, at different considered locations. The changes of the first and the second derivatives of curves follow the monthly changes of concentrations of ^{7}Be in time. As can be seen from Fig. 2, course of the second derivate curve for all locations has one expressed minimum which corresponds to the maximum value of ^{7}Be concentration in summer months. The second minimum occurs for the month November, corresponding to increased concentrations of ^{7}Be in this month at all locations except Zaječar. Using this graphical method and Eq. (1), the estimation results of the symmetrical index (n) values are as follows: Zlatibor (n = 1.74), Vinca (n = 1.82), Zeleno Brdo (n = 2.50), Vranje (n =

2.98) and Zajecar (n = 1.94). Values of symmetrical index increase with increasing mean annual concentrations of ^{7}Be except for Zaječar where the highest mean annual concentration was obtained but symmetrical index was 1.94. It should be emphasized that these are preliminary results for the concentration of ^{7}Be at locations Zaječar, Vranje and Zlatibor. For better monitoring of changes of of symmetrical index, it is necessary to have data for many years.

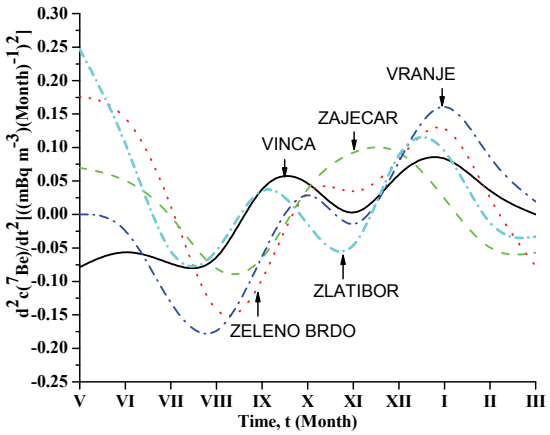

Figure 2. The second ($d^2c(^7Be)/dt^2$) derivative curves of the normalized ^{7}Be concentrations ($c(^7Be)$) in function of time (in Months), at different locations.

Conclusion

The obtained values of ^{7}Be concentrations in ground level air at five different locations in Serbia show a fluctuation which has oscillatory characteristics with enhanced activity in summer months. Application of symmetrical index as a mathematical parameter is shown that with increase of the annual mean concentration of ^{7}Be, values of symmetrical index increases. The results presented in this paper are preliminary, so it is necessary to monitor changes in concentration of ^{7}Be in ground level air at various locations in Serbia for many years.

Acknowledgment

The investigation was partially supported by the Ministry of Education and Science of the Republic of Serbia under the following Projects III43009.

References

[1] J. S. Gaffney, N. A. Marley, M. M. Cunningham, Natural radionuclides in fine aerosols in the Pittsburgh Area, Atmos. Environ., 2004, 38, 3191-3200.

[2] A. Baeza, L. M. Del Río, A. Jiménez, C. Miró, J. M. Paniagua, M. Rufo, Analysis of the temporal evolution of atmospheric ^{7}Be as a vector of the behavior of other radionuclides in the atmosphere, J. Radioanal. Nucl. Chem., 1996, 207, 331-344.

[3] D.Todorovic, D. Popovic, G. Djuric, M. Radenkovic, ^{7}Be to ^{210}Pb concentration ratio in ground level air in Belgrade aea, J. Eniviron. Radioact., 2005, 79, 297-307.

[4] H. E. Kissinger, Reaction kinetics in differential thermal analysis, Anal. Chem., 1957, 29, 1702–1706.

K-27-P

THE INFLUENCE OF MILLING TIME OF NATURAL CLAY ON ITS HEAVY METAL ADSORPTION BEHAVIOR

K. R. Kumrić[1], T.a M. Trtić-Petrović[1], A. B. Đukić[2], J. D. Grbović Novaković[2], A. S. Radosavljević Mihajlović[2], Lj. Matović[2]

[1]Laboratory of Physics, Vinča Institute of Nuclear Sciences,University of Belgrade, P.O. Box 522, 11001 Belgrade, Serbia, [2]Laboratory of Materials Sciences, Vinča Institute of Nuclear Sciences, University of Belgrade, P.O. Box 522, 11001 Belgrade, Serbia

Abstract

The influence of different milling times of natural Serbian clay on simultaneous removal of heavy metals (Pb(II), Cd(II), Cu(II), Zn(II)) from an aqueous medium was investigated. Changes in sorption behavior were correlated with changes in microstructure of the clay induced by milling. The highest removal efficiency, more than 95% for all heavy metals, revealed the sample milled for 19h, although the significant improvement was achieved after 2h of milling.

Introduction

Wastewaters with heavy metals originate from a large number of industries. In order to avoid water pollution, the removal of heavy metal ions from the industrial wastewaters is needed before disposal. Adsorption appears to be an attractive process in view of its efficiency and the easiness with which it can be applied [1].

Clay minerals are good adsorbents for metal ions from aqueous solutions due to their high cation exchange capacity and high specific surface area. Also, clay minerals have the advantage of being abundant and inexpensive [2]. To improve sorption properties of clay minerals different techniques of modification were used [3].

The aim of the present study was to investigate the simultaneous adsorption of Pb(II), Cd(II), Cu(II), Zn(II) ions onto the natural clay from Serbian mine Bogovina by measuring the effect of milling time of clay on the adsorption process.

Results and Discussion

A sample of the natural clay was obtained from the mine Bogovina (Serbia). Mechanical milling was performed in Turbula Type 2TC Mixer, in the air, and ball-to-powder ratio 4:1. Samples of natural clay were milled at different times: 1, 2, 10 and 19 h. After the milling, the samples were characterized in terms of microstructure and chemical composition, and the heavy metal sorption from the aqueous solutions was studied using a batch technique.

The XRD pattern of the unmilled clay is presented in Fig. 1. The diffracted X-rays were collected over 2θ range 4-70° using a step width of 0.05° and measuring time 1 s per step. The most prominent phase is montmorillonite (M)

with concomitant minerals quartz (Q) and calcite (C). The diffractogram after 19 h of milling is shown in the insert of Fig. 1. The changes of the montmorillonite microstructure after milling are revealed in: increase of basal spacing (derives from the shift of the (100) reflection towards lower 2θ angles), line broadening and the reduction of the diffraction intensities, suggesting the increase of structural disorder, fragmentation and exfoliation of the clay mineral particles.

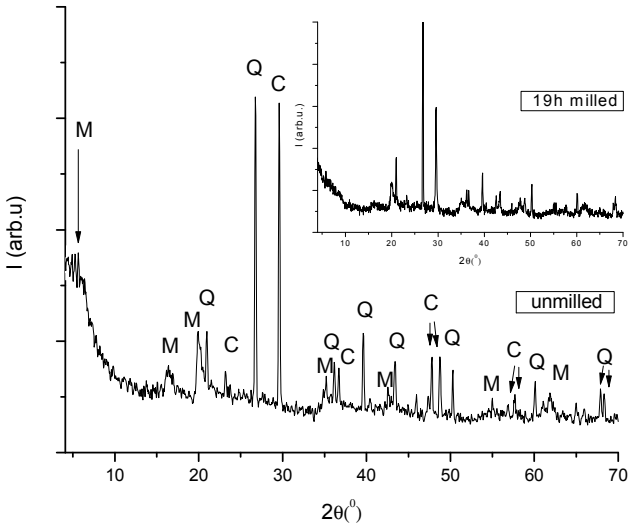

Figure 1. XRD diffractograms of the unmilled clay. In the insert is presented diffractogram of the 19 h milled clay.

Heavy metal sorption experiments were carried out by mixing 0.05 g clay and 25 cm^3 aqueous solution of metal ions (total concentration 50 mg dm^{-3}, pH 5.5) in closed polypropylene bottles at room temperature. Metal ions solution was prepared in milli-Q water using the analytical reagent grade $Pb(NO_3)_2$, $Cd(NO_3)_2$, $Cu(NO_3)_2$ and $ZnCl_2$. The samples were shaken for 60 min at stirring speed of 200 rpm. The liquid phases were separated from the solid phases by filtration. The heavy metal ion concentration in each sample was determined with a Metrohm's polarography system 797 VA Computrace analyser by using Metrohm's procedure No. 231/2 e. Adsorption behavior of Pb(II), Cd(II), Cu(II) and Zn(II) on natural clay was determined on non-milled and milled clay samples, in terms of removal efficiency for each metal ion in solution.

The effect of milling time of clay on the removal efficiency of heavy metals is presented in Fig. 2. Removal efficiencies of Pb(II), Cd(II), Cu(II) and Zn(II) using the untreated clay sample are 91.0, 36.5, 79.8 and 34.3%, respectively. On the other hand, heavy metal uptake is significantly improved by milling. It can be seen that removal efficiencies are increased with increasing the milling time of clay. Removal efficiencies of Zn(II) and Cd(II) ions are increased to 95%, while for Pb(II) and Cu(II) ions are greater than 99%. This behavior is related to the increasing of the surface area due to decrease of the mineral particle size, that

causes a larger number of edges sites, as well as exfoliation of the clay mineral particles.

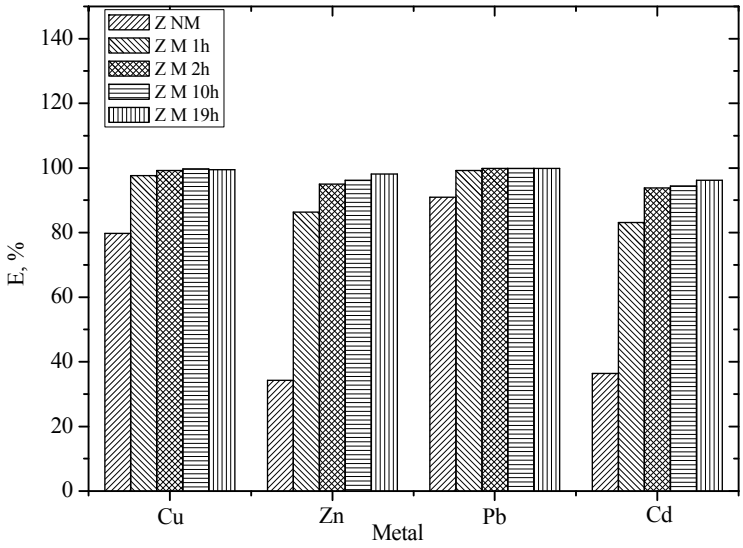

Figure. 2. The effect of milling time on the removal efficiency of heavy metal ions from the aqueous solutions (Z NM - non-milled clay, Z M 1h, Z M 2h, Z M 10h, Z M 19h - 1 h, 2 h, 10 h and 19 h milled clay, respectively)

Conclusion

Highly efficient (>95%) simultaneous removal of heavy metal ions (Pb(II), Cd(II), Cu(II) and Zn(II)) from aqueous solution was achieved by applying different milling times for modification of natural row clay mineral. Thus, one can conclude that the milling represents good alternative to the other techniques of clays modifications for the application in the industrial wastewater treatment.

Acknowledgment

We acknowledge the support to this work provided by the Ministry of Education and Science of Serbia through projects No. III 45006 and 45012.

References

[1] U. K. Garg et al., Biores. Technol., 2008, 99, 1325-1331.
[2] M. Malandrino et al., J. Colloid Interface Sci., 2006, 299, 537-546.
[3] Bhattacharyya, K.G., Gupta, S.S., Adv. Colloid Interface Sci., 2008, 140, 114-131.

K-28-P

COMPARATIVE RADIOLOGICAL IMPACT ASSESSMENT IN AREAS OF ELEVATED NATURAL RADIOACTIVITY IN GREECE AND SERBIA

H. Florou1, S. Dragović2, G. Trabidou1, M. Ćujić2, P. Kritidis1, J. Petrović2, M. Sotiropoulou1, J. Kovačević3

[1]National Centre for Scientific Research "Demokritos", Institute of Nuclear and Radiological Sciences and Technology, Energy and Safety, Aghia Paraskevi 15310, POB 60228, Athens, Greece, e-mail: eflorou@ipta.demokritos.gr
[2]University of Belgrade, Institute for the Application of Nuclear Energy, Banatska 31b, Belgrade, Serbia, e-mail: sdragovic@inep.co.rs
[3]Geological Institute of Serbia, Rovinjska 12, Belgrade, Serbia

Abstract

The activity concentrationsof natural radionuclides ^{238}U, ^{232}Th and^{40}K in selected areas of elevated natural background radioactivity in Greece, Milos - an island of volcanic origin in Cyclades Archipelago, Aegean Sea and Serbia - Stara Planina mountain rich in uranium deposits are presented. External dose rates to humans were derived as an indicative parameter for the radiological impact assessment.

Introduction

The island of Milos (36^0 42´N, 24^0 27´E) in Cyclades Archipelagos is part of the Hellenic volcanic arc, which is located in the southern Aegean Sea, in Greece. This is located parallel to the subduction zone of the lithospheric plates of the Eastern Mediterranean Sea [1]. Besides, the Island is characterized by the presence of geothermal vents, which are used for energy production by the Public Power Corporation. As it has been reported, there is direct and indirect influence on the abiotic materials and organisms inhabited especially the coastal areas of Milos by the underground hydrothermal fluids emitted by the vents [2-3]. The lithospheric environment of the island is characterized by alumino silicate and iron sulfate ores and volcanic ash, whereas soils are mainly texturally calcareous and clay. In terms of Stara Planina (44^0 21´N, 19^0 14´E), the pre-Tertiary terrigenous sandstones represent the most significant bearers of mineralizations in Serbia. The significant deposit and a number of occurrences are identified in Perm-Triassic sediments of Stara Planina[4-6]. The Stara Planina massif on the western border of the Carpatho-Balkanides is the result of complex tectonic processes that folded and faulted the region during the Baykalian orogeny, Caledonian and Variscan orogenies, and the Alpine orogeny.The activity concentrations of ^{238}U, ^{232}Th and ^{40}K in different geological materials, soil and sediment are presented in this paper. In terms of the radiological impact assessment, the outdoor gamma ray exposure at 1 m above ground level was calculated from the soil activity concentrations using

the dose rate conversion factors of 0.462, 0.604 and 0.0417 nGy h^{-1} per Bq kg^{-1} for ^{238}U, ^{232}Th and ^{40}K, respectively [7].

Results and Conclusions

Table 1. Activity concentrations of the natural radionuclides in abiotic materials from the island of Milos (Greece) and Stara Planina (Serbia) (Bq kg^{-1}) and the total external dose rate range (nGy h^{-1}).

Sample	^{238}U	^{232}Th	^{40}K	External dose rate (nGy h^{-1})
Milos island				
Soil	≤ 1- 1420	26 - 94	458 - 1796	35-848
Caoline	129 ± 66	74 ± 39	298 ± 390	
Perlite	111± 44	84 ± 23	1242 ± 264	
Bentonite	142 ± 78	74 ± 25	456 ± 215	
Alumino silicate	95 ± 45	53 ± 27	838 ± 509	
Volcanic ash	88 ± 7	70 ± 6	758 ± 19	1sample
Iron pyrite	75 ± 5	33 ± 5	991 ± 20	1sample
Baryte	37 ± 6	72 ± 24	246 ± 229	
Volcanic material	295 ± 335	74 ± 35	451 ± 269	
Rock	104 ± 8	63 ± 6	3893 ± 25	1sample
Sediment (coastal-sandy)	85 - 127	26 - 86	429 - 1352	
StaraPlanina				
Soil	19-160	12-130	270-1010	27-195
Greenish to redish sandstones	37 ±4	53 ±5	960 ±10	
Red fine grained sandstones	170 ± 10	65 ± 5	1190 ± 20	
Gray and reddish gray sandstones	760 ± 10	53 ± 5	1190 ± 20	
Gray sandstones and siltstones with organic matter	5560 ± 10	61 ± 3	940 ± 10	
Red sandstones with siltstones	37 ± 5	49 ± 5	880 ± 10	
Arkosic metasandstone	120 ± 10	89 ± 8	690 ± 10	
Schist	45 ± 5	47 ± 5	780 ± 20	
Meta conglomerate	54 ± 5	63 ± 4	560 ± 10	
Metasiltstone	25 ± 5	32 ± 8	530 ± 10	
Albitized microdiorite	150 ± 10	73 ± 5	1940 ± 80	
Diabase	37 ± 5	28 ± 5	410 ± 20	

The range of the calculated total external dose rate from soil in the island of Milos was broad (35-848 nGy h^{-1}). It is noteworthy, that the reported range in the Greek territory varies from 100 to 1000 nGy h^{-1} (mean value approximately 80 nGy h^{-1} [8-9]). Therefore, the observed maxima in Milos lay at the upper limit of the reported values for the natural radiation background of Greece. The total external gamma dose rate at the investigated areas on Stara Planina is about 1.5-fold higher of value reported for the whole territory of Serbia [10]. The total external gamma dose rate in the area affected by uranium mining activities was reported to be 91 nGy h^{-1} [11]. The conclusions can be summarized as:

- The highest value of ^{238}U (5560 Bqkg^{-1}) in Stara Planina and wider value-range in Milos
- Comparable values of ^{232}Th for the various geological settings in between the two national sets
- The highest value of ^{40}K in Milos and comparable values in between the two national sets
- Wider range and higher maxima of the dose rates from soil in Milos
- Higher values of the external dose rates in Stara Planina and Milos island if compared to the mean natural background respectively

References

[1] M. D. Fytikas, Geophys. Res. I. G. M. R. XVIII(1), 1975.
[2] P. Kritidis, H. Florou, Proc. Nat. Conference Environmental Science and Technology, Aegean University, Mytilini September, 1989, B, 24-34.
[3] H. Florou, P. Kritidis, Rad. Prot. Dos., 1992, 45(1/4), 277-279.
[4] Z. Nikić, J. Kovačević, P. Papić, Water Air Soil Poll.,2008, 192, 47-58.
[5] J. Kovačević, Bull. Geoinst., 1999, 36, 119-134.
[6] J. Kovačević, Z. Nikić, P. Papić, Sed. Geol., 2009, 219, 252-261.
[7] UNSCEAR, Sources and Effects of Ionizing Radiation, UNSCEAR 2008 Report. New York: United Nations, 2010.
[8] H. Florou, G. Trabidou, P. Kritidis, Proc. Nat. Conference HNPS2012, Athens, 25-26 May, 2012, 1, 50.
[9] G. Trabidou, H. Florou, A. Angelopoulos, L. Sakelliou, Rad. Prot. Dos., 1996, 63(1), 63-67.
[10] S. Dragović, Lj. Janković-Mandić, M. Momčilović, A.Onjia, Arch. Oncol. 2007,15, 78–80.
[11] M. Momčilović, J. Kovačević, M. Tanić, M. Đorđević, G. Bačić, S. Dragović, Environ. Monit. Assess., 2012, doi 10.1007/s10661-012-2634-9.

K-29-P

RADIOACTIVITY IN DRINKING WATER FROM SMEDEREVSKA PALANKA

M. M. Janković[a, *], N. B. Sarap, D. J. Todorović
University of Belgrade, Institute Vinča, Radiation and Environmental Protection Department, P.O. Box 522, 11001 Belgrade, Serbia

Abstract
In this work, a study of the radioactive content of 1 tap and 1 spring water "Kiseljak" from Smederevska Palanka was carried out. The natural activity concentration of alpha emitting radionuclides are within the range recommended by Serbian current regulations. Gross beta activity for Kiseljak water exceeds limit of 1 Bq l^{-1} given by Serbian current regulations. For this reason gamma spectrometry analysis was performed and it was found that the content of ^{40}K in water Kiseljak is 0.9 Bq l^{-1}.

Introduction
The determination of radionuclides in environmental samples is a crucial task in relation to the protection of human health. Natural waters contain both alpha and beta emitters in widely varying concentrations which are responsible for a generally small fraction of the total dose received from natural and artificial radioactivity [1]. The most radiotoxic and of concern to human health among the radionuclides present in ground water is radium, especially ^{226}Ra. ^{228}Ra has short half-life and will decay before being transported over long distances. The consumption of water-containing radium can cause its accumulation in bone tissues, leading to accumulation of significant dose, which in turn produces bone and head-sinus cancer. Therefore, the systematic control of water quality has become an important parameter of environmental studies. In Serbia, according to current regulations [2], radioactivity concentrations in drinking water for gross alpha and gross beta should be 0.5 and 1.0 Bq l^{-1}, respectively. If one of the guideline values is exceeded, radionuclides have to be identified by alpha and/or gamma spectroscopy, and their individual activity concentrations need to be measured. These guidelines ensure an exposure lower than 0.1 mSv y^{-1} assuming a water consumption rate of 2 l d^{-1}. If the estimated dose is higher than 0.1 mSv y^{-1} the reduction in consumption or radionuclide concentration is necessary. *G*iven the fact that the bottled water Kiseljak was already tested before and the analysis has shown higher gross beta activity, we believe that periodic monitoring of this water is substantially.

Experimental
In order to determine gross alpha and beta activity, volumes of 3 l of water were evaporated to a small volume, under infrared lamp. The remaining was heated to

* Corresponding author. University of Belgrade, Institute Vinča, Radiation and Environmental Protection Department, P.O. Box 522, 11001 Belgrade, Serbia. Tel/Fax: +381 11 806 64 37. E-mail address: marijam@vinca.rs (M. Janković)

dryness at 450 ºC [3]. The residues were transferred quantitatively to a stainless-steel planchet. Gross alpha and beta activity in water samples were determined by α / β low level proportional counter Thermo Eberline FHT 770 T. Calibration was performed by using standard source of ^{90}Sr (EM145, Prague) with an activity of 189.4 Bq on the day 1. 8. 2011. for beta activity and standard source of ^{241}Am (EM445, Prague) with an activity of 224 Bq on the day 1. 8. 2011. for alpha activity. The counting gas was a mixture of 90 % argon and 10 % methane. The counting efficiencies for the system are 23 % for alpha and 33 % for beta. The counting time was 3600 s for gross alpha and beta activities. In order to performed gamma spectrometric measurements, water samples were boiled to reduce their volume from approximately 8000 ml to 200 ml and then poured into 250 ml cylindrical polyethylene vials. The samples were stored for 1 month to reach the radioactive equilibrium. Measurements were performed using a HPGe Canberra detector with a counting efficiency of 23 %. Geometric efficiency for water matrices in the plastic bottle of 200 ml was determined by a reference water material (Czech Metrological Institute, Praha, 9031-OL-116/8, type ERX) spiked with a series of radionuclides (^{241}Am, ^{109}Cd, ^{139}Ce, ^{57}Co, ^{60}Co, ^{88}Y, ^{113}Sn, ^{85}Sr, ^{137}Cs, ^{210}Pb) with total activity of 114.9 kBq on the day 03.03.2008. The activity of ^{226}Ra and ^{232}Th was determined by their decay products: ^{214}Bi (609 keV, 1120 keV and also 1764 keV), ^{214}Pb (295 keV and 352 keV) and ^{228}Ac (338 keV and 911 keV), respectively. The activities of ^{40}K were determined from its 1460 keV γ-line. ^{235}U was determined on 185.7 keV corrected for ^{226}Ra (186 keV). ^{238}U was determined by ^{234}Th (63 keV) or by ^{234}Pa (1000 keV) *($T_{1/2}$ =1.17 min)*. The activity of ^{137}Cs was determined from its 661 keV line.Counting time interval was 60000 s.

Results and Discussion

Table 1 shows the results for gross alpha and beta activity concentrations for 1 tap and 1 spring water collected in Smederevska Palanka. Gross alpha activity for both samples is within recommended level of 0.5 Bq l^{-1}. Gross beta activity for tap water is below than recommended level of 1 Bq l^{-1}. For spring water, Kiseljak, gross beta activity was 2.25 ± 0.27 Bq l^{-1} which exceeds the permitted limit. Beacuse of that, it is necessary to performed gamma spectroscopy. The specific activities of natural radionuclides ^{226}Ra, ^{232}Th, ^{238}U, ^{235}U and produced ^{137}Cs in investigated waters measured by gamma spectrometry were below the detection limits of our measuring system. MDC for ^{226}Ra, ^{232}Th, ^{238}U, ^{235}U and ^{137}Cs was <0.04, <0.03, <0.02, <0.009 and <0.006 Bq l^{-1}, respectively. Serbian law recommends that activity concentration in drinking water should not exceed 490 mBq l^{-1} for ^{226}Ra, 590 mBq l^{-1} for ^{232}Th, 2900 mBq l^{-1} for ^{235}U and 3000 mBq l^{-1} for ^{238}U [2]. Content of ^{40}K in spring water was (0.9 ± 0.2) Bq l^{-1}. Contribution of ^{40}K in gross beta activity was 0.73 Bq l^{-1}, so we can conclude that in addition to ^{40}K, there are other beta emitters, such as ^{90}Sr, which included in the gross beta activity. Determination of ^{90}Sr in this water is the aim of our next study. Because, gross beta activity in natural water originate from natural long-lived isotopes ^{40}K, ^{210}Pb, ^{228}Ra and artificial isotopes such as ^{90}Sr and ^{137}Cs [4] and the total beta activities should be obviously equal to the sum of activities of beta isotopes. On the other hand, content

of ^{40}K in tap water was below MDC (0.14 Bq l^{-1}). Our results for tap water are comparable with those obtained for tap waters in Vojvodina [5], Turkey [6] as well as Italy [7]. Kiseljak water was analyzed as bottled water by Joksic et al. 2007 [8], and results was showed high beta activity because of presence of ^{40}K in quantity of 2.8 Bq l^{-1}.

Table 1. Gross alpha and beta activity concentrations in tap water and spring water Kiseljak.

Sample	Gross alpha activity concentration / Bq l^{-1}	Gross beta activity concentration / Bq l^{-1}
Tap water	0.046 ± 0.015	0.35 ± 0.05
Spring water Kiseljak	0.078 ± 0.026	2.25 ± 0.27

Conclusion

The data generated in this study provide the radiological characterisation of drinking water from Smederevska Palanka. The results show that although both water can be considered potable from a radiological point of view, it is advisable to regulate their radioactive content periodically and give to the consumer more detailed information about the activity concentration of these waters.

Acknowledgment

The investigation was partially supported by the Ministry of Education and Science of the Republic of Serbia under the following Projects III43009.

References

[1] UNSCEAR. Ionizing radiation: sources and effects of ionizing radiation, United Nation Scientific Committee on the Effects of Atomic Radiation, Report the General Assembly with Scientific Annexes, United Nations Sales Publication, United Nations, New York, 1993.

[2] Official Journal, Regulation on limits of radionuclide content in drinking water, foodstuffs, feeding stuffs, drugs, items of general use, building materials and other goods to be placed on the market, 86, 2011.

[3] EPA, Prescribed Procedures for Measuremen of Radioactivity in Drinking Water. EPA-600/4-80-032. Method 900.0., 1980.

[3] C. R. Cothern, W. L. Lappenbusch, J. Michel, Drinking water contribution to natural background radiation, Health Physics, 1986, 50, 33–47.

[5] N. Todorovic, J. Nikolov, I. Bikit, Gross alpha and beta activity measurements in drinking water using liquid scintillation analysis. The XXVI Symposium of Society for Radiation Protection of Serbia and Montenegro, Proceedings, 12-14. October, Tara, Belgrade, Serbia, 2011, 83-87.

[6] N. Damla, U. Cevik, G. Karahan, A. I. Kobya, Gross α and β activities in tap waters in Eastern Black Sea region of Turkey, Chemosphere, 2006, 62, 957-960.

[7] M. Forte, R. Rusconi, M. T. Cazzaniga, G. Sgorbati, The measurement of radioactivity in Italian drinking water, Microchemical Journal, 2007, 85, 98-102.

][8] J. Joksic, M. Radenkovic, Š. Miljanic, Natural radioactivity of some spring and bottled mineral waters from several central Balkan sites, as a way of their characterization, J. Serb. Chem. Soc., 2007, 72 (6), 621-628.

K-30-P

PLANE (*Platanus acerifolia* Ait.) BARK AND TREE-RINGS AS BIO-INDICATORS

D. M. Marković [1], I. R. Milošević [2*], G. Roglić [3], D. Manojlović [3], Lj. Ignjatović[4] and D. Vilotić [4]

[1]*The Faculty of Applied Ecology, Singidunum University, Lazarevački drum 13;*
[2]*Institute of Physics, University of Belgrade, Pregrevica 118;*
[3]*Faculty of Chemistry, University of Belgrade, Studentski trg 12-16;*
[4]*Faculty of Physical Chemistry, University of Belgrade, Studentski trg 1;*
[5]*Faculty of Forestry, University of Belgrade, Kneza Višeslava 1, Serbia,*
*(*novovic@ipb.ac.rs)*

Abstract

By analyzing metal content in bioindicators such as lichen, moss, fern, leaves etc., we can see an integral response to the pollution level in the region. Tree-ring analysis in contrast enables us to return to previous periods accurately and to understand trends of metal accumulation. Tree-rings and bark of plane (*Platanus acerifolia* Ait.) from Belgrade, Serbia was used as an indicator of environmental pollution. The Pb, Cd and Mn content in bark and tree-rings was determined by inductively coupled plasma atomic emission spectrometry (ICP-OES). A slight Pb concentration increasing trend in the plane tree-rings is observed in the entire period of investigation. A similar Cd and Mn concentration trand was noticed for plane tree-rings. Rough barks (linden) accumulate higher contents of the investigated elements than smooth barks (plane).

Introduction

The environment is under great influence from different sources. The use of vegetation provides the cheapest and simplest indicator for monitoring trace metal levels in the environment. Trees of temperate regions usually form visible annual growth rings, which can be dated accurately. It is therefore possible to collect wood samples of different age and analyze their heavy metals content in order to get a chronological record of trace elements pollution in the tree's environment [1, 2, 3].

The plane is a large deciduous tree growing to 20–35 m (exceptionally over 40 m) tall, with a trunk up to 3 m or more in circumference and it is a popular urban roadside tree. The bark is usually pale grey-green and smooth.

Experimental

We collected tree-rings and bark of plane (*Platanus acerifolia* Ait.) from the King Aleksandar Boulevard in 2010. In 2010 the reconstruction of the boulevard begins in about 2.5 km and the plane trees were cut. Two trees of similar size were selected (Latitude: 44º47′47″ N; longitude: 20º29′47″ E and latitude: 44º47′51″ N; longitude: 20º29′38″ E) for our purposes. Stem disks were taken from felled trees at breast height (1.3 m). For further analysis the disks were cut into segments with a stainless steel knife. Each plane core was divided into 3 year segments starting from 1935 to 2009.

Bark was taken as a separate sample from the stem disk. The content of elements in solution samples was determined by inductively coupled plasma atomic emission spectrometry (ICP-OES). ICP-OES measurement was performed using Thermo Scientific iCAP 6500 Duo ICP (Thermo Fisher Scientific, Cambridge, United Kingdom) spectrometer equipped with CID86 Charge Injector Device (CID) detector, standard glass concentric type nebulizer, quartz torch, and alumina injector. The optical system purged with argon and the Echelle polychromator thermostated at 38 ºC. The digestion was performed on an Advanced Microwave Digestion System (ETHOS 1, Milestone, Italy) using HPR-1000/10S high pressure segmented rotor. In the digestion, about 0.5 g of powdered tree-ring sample precisely weighed was mixed in each clean vessel with a mixture of 3 ml H_2SO_4 and 5 ml HNO_3 and then heated with microwave energy for 30 min. The temperature was controlled with a predetermined power program. After cooling and without filtration, the solution was diluted to a fixed volume of 25 ml for tree-rings and 50 ml for soils

Results and Discussion

Figure 1 shows the mean Pb, Cd and Mn concentrations in the plane tree-rings sampled from the King Aleksandar Boulevard.

From Figure 1(a) it can be noticed a slight increasing Pb concentrations trend in the plane tree-rings in almost the entire study period. Also we can observe two periods of low Pb concentrations dating from 1950 to 1964 and from 1989 to 2003. The highest Pb concentration in the plane tree-rings was measured in the period 1980/82.

The Cd concentration in the plane tree-rings (Figure 1(b)) indicates different changes of the concentration trends. From 1938 to 1961 it can be seen decreasing trend of Cd concentrations. The period from 1965 to 1994 can be roughly characterized as a period of small Cd fluctuations in the plane tree-rings. From 1994 to 2009 intense increase in the Cd concentration can be noticed. The maximum Cd concentration was measured in the period 1962/64.

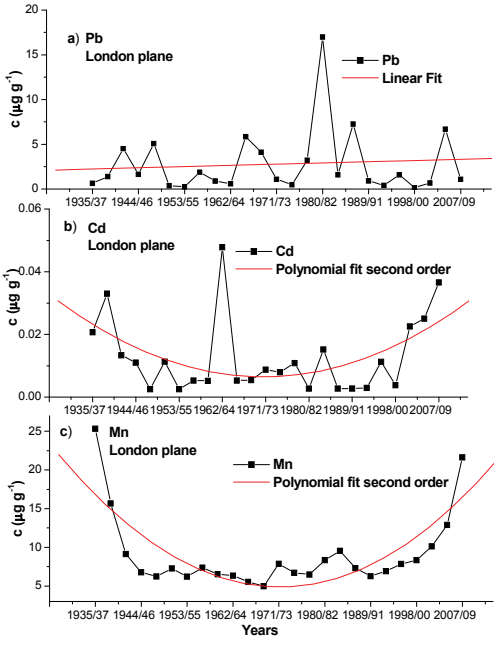

Figure 1. Mean Pb (a), Cd (b) and Mn (c) concentrations (µg g-1 dry weight) in plane (Platanus acerifolia Ait.) tree-rings at King Aleksandar Boulevard from 1935 to 2009.

Three characteristic periods, as in the case of Cd, we can observe for Mn (Figure 1(c)). The first period is the period of decreasing Mn concentrations in the

plane tree-rings dating from 1935 to 1949. The second period of nearly constant Mn concentrations is observed from 1949 to 1991, while the third dating from 1991 to 2009 is the period of constant Mn increase.

Table 1 shows average Pb, Cd and Mn concentrations in the bark and tree-rings of plane (our study) and Linden [4] as well as bark/wood ratio. Both species are deciduous trees. Bark can be used as an indicator of air pollution for different pollutants [5, 6]. Rough barks are known to accumulate metals more than smooth barks [7]. Linden bark is rough and for the plane it is smooth. From Table 1 it is noticeable that Pb and Mn concentrations in the linden bark where the higher than

Table 1. Average Pb, Cd and Mn concentrations (μg g^{-1}) in bark and tree-rings (wood) of plane [our study] and Linden [4] as well as bark/wood ratio.

Elements	London plane (Belgrade)		Bark/wood ratio	Linden (Obrenovac)		Bark/wood ratio
	bark	wood		bark	wood	
Pb	2.84	2.77	1.03	23.9	3.0	7.97
Cd	0.013	0.013	1.00	-	-	-
Mn	8.77	9.14	0.96	11.1	2.1	5.29

in the plane bark. By comparing the average concentrations of analyzed elements (Table 1) in the bark and tree-rings of plane and linden it can be seen that in the case of linden considerably higher concentrations were in their bark while in the case of plane approximately the same concentration are in the bark and tree-rings.

Conclusion

Slightly increased Pb concentration trend in the plane tree-rings has been seen in almost the entire period of investigation. The characteristic minimum concentration of Pb was obtained in the period from 1989 to 2003 and can be connected with the crisis of the nineties in our region. There was a similarity in the trend of change in concentration from 1935 to 2009 for Cd and Mn. In the linden bark (rough type bark) were found higher concentrations of analyzed elements than in the plane bark (smooth type bark).

References

[1] D. M. Marković, I. Novović, D. Vilotić, Lj. Ignjatović, Russ J Phys Chem, 2007, 81, 1493-1496.
[2] D. M. Marković, I. Novović, D. Vilotić, Lj. Ignjatović, Environ Monit Assess, 2009, 151, 377-382.
[3] S. A. Watmough, T. C. Hutchinson TC, Environ Pollut, 1996, 93, 93-102.
[4] D. M. Marković, I. R. Milošević, D. Vilotić, Environ Sci Poll Res, DOI 10.1007/s11356-012-1024-82012, 2012.
[5] T. El-Hasan, H. Al-Omari, A. Jiries, F. Al-Nasir, Environ Int, 2002, 28, 513-19.
[6] O. O. Odukoya,T.A. Arowolo, O. Bamgbose, Environ Int, 2000, 26, 11-16.
[7] D. Barnes, M. A. Hammadah, J. M. Ottaway, Sci Total Environ, 1976, 5, 63-67.

K-31-P

LARCH (*Larix europaea* Lam.) AND DOUGLAS-FIR (*Pseudotsuga menziesii* Mirb.) BARK AND TREE-RINGS AS BIO-INDICATORS

I. R. Milošević[1*], D. M. Marković[2], G. Roglić[3], D. Manojlović[3], R. Balić[3], Lj. Ignjatović[4] and M. Veselinović[5]

[1]*Institute of Physics, University of Belgrade, Pregrevica 118;*
[2]*The Faculty of Applied Ecology, Singidunum University, Lazarevački drum 13;*
[3]*Faculty of Chemistry, University of Belgrade, Studentski trg 12-16;*
[4]*Faculty of Physical Chemistry, University of Belgrade, Studentski trg 1,*
[5]*Institute of Forestry, Kneza Višeslava 3,Belgrade, Serbia, (*novovic@ipb.ac.rs)*

Abstract
Tree-rings and bark of larch (*Larix europaea* Lam.) and Douglas-fir (*Pseudotsuga menziesii* Mirb.) from two locations in Serbia were used as indicators of environmental pollution. The Cd, Mn and Pb content in bark and tree-rings of larch and Douglas-fir were determined by inductively coupled plasma atomic emission spectrometry (ICP-OES). Average Cd, Mn and Pb concentrations were higher in the tree-rings of larch from the Avala location, while they were higher in Douglas-fir tree-rings for the REIK-Kolubara location. In almost all larch and Douglas-fir bark samples at both sites were measured higher concentrations of examined elements than in tree-rings.

Introduction
Dendrochemistry has emerged in recent years as a valuable tool enabling reconstruction of past pollution episodes. A basic assumption of dendrochemical studies is that the chemical make-up of the annual woody increment at least partly reflects the chemistry of the environment in which it was formed. Increased metal concentrations have been recorded in tree rings formed during periods of high industrial activity, increased urbanization and high traffic loads [1-4]. Douglas-fir is highly recommended species for dendrochemical studies [5].

Experimental
We collected tree-rings and bark of larch (*Larix europaea* Lam.) and Douglas-fir (*Pseudotsuga menziesii* Mirb.) from two locations in Serbia in March 2010. The first one is Avala and it is the mountain located 16 km south-east of Belgrade. Avala is a traditional picnic resort for Belgraders. The second location is REIK Kolubara. Douglas-fir and larch at the Kolubara location have been applied in our country for the rehabilitation by a forestation of the mechanically damaged land. Three larch and Douglas-fir trees of similar size were selected at each location. Stem disks were taken from felled trees at breast height (1.3 m). For further analysis the disks were cut into segments with a stainless steel knife. Each core was divided into 3 year segments starting from 1980 to 2009. Bark was taken as a separate sample from the stem disk. The content of elements in solution samples was determined by inductively coupled

plasma atomic emission spectrometry (ICP-OES). ICP-OES measurement was performed using Thermo Scientific iCAP 6500 Duo ICP (Thermo Fisher Scientific, Cambridge, United Kingdom) spectrometer equipped with CID86 Charge Injector Device (CID) detector, standard glass concentric type nebulizer, quartz torch, and alumina injector. The optical system purged with argon and the Echelle polychromator thermostated at 38 ºC. The digestion was performed on an Advanced Microwave Digestion System (ETHOS 1, Milestone, Italy) using HPR-1000/10S high pressure segmented rotor. In the digestion, about 0.5 g of powdered tree-ring sample precisely weighed was mixed in each clean vessel with a mixture of 3 ml H2SO4 and 5 ml HNO3 for tree-ring sample and then heated with microwave energy for 30 min. The temperature was controlled with a predetermined power program. After cooling and without filtration, the solution was diluted to a fixed volume of 25 ml.

Results and Discussion

Figure 1 shows the mean concentrations of Cd (a and b) and Mn (c and d) in larch and Douglas-fir tree-rings from 1980 to 2009 at the Avala and REIK-Kolubara locations. At Avala location (Figure 1(a)) it can be seen a similar Cd concentration trend change for the both examined tree species (larch and Douglas-fir). In the entire study period, mean Cd concentrations in tree-rings of larch and Douglas-fir have an increasing trend. Higher mean Cd concentrations were measured in the larch tree-rings than in tree-rings of Douglas fir in almost the entire study period at Avala location. Also at Avala location, as well as in the case of Cd, it can be seen similar behavior of Mn concentration trends in tree-rings of larch and Douglas-fir (Figure 1(c)).

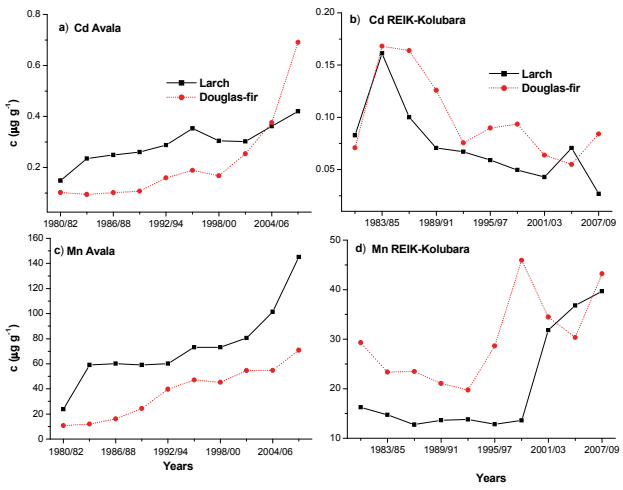

Figure 1. Mean Cd (a and b) and Mn (c and d) concentrations in larch and Douglas-fir tree-rings on Avala and REIK-Kolubara locations from 1980 to 2009.

Mean Cd concentrations measured in larch and Douglas-fir tree-rings from REIK-Kolubara location are shown on Figure 1(b). In this case also it can be noticed a good correlation between time trend changes of mean Cd tree-rings concentrations in larch and Douglas-fir. However, in this case after the maximum (1983/85) in almost all remain period mean Cd concentrations have a decreasing trend. In contrast to the Avala location at this location were measured higher mean

Cd concentrations in samples of Douglas fir. A similar trend of changes in mean Mn concentrations in larch and Douglas-fir tree-rings can be seen on a REIK-Kolubara location (Figure 1(d)). As in the case of Cd on REIK Kolubara location mean Mn concentrations are higher in Douglas fir tree-rings.

Average Cd, Mn and Pb concentrations in larch and Douglas-fir bark and tree-rings (wood) are shown in Table 1. For both locations in almost all samples higher concentrations of the examined elements are measured in the bark than in tree-rings. Bark accumulates pollutants straight from the atmosphere and they are deposited mainly on the surface. Bark can be roughly divided into living inner bark and dead outer bark [6]. The inner bark reflects the metal ion flow within a tree. Airborne pollutants are mainly accumulated in the outer bark. Element concentrations in the barks reflect concentrations both within the phloem and absorbed to bark predominately via wet and dry atmospheric deposition [7].

Table 1. Average Cd, Mn and Pb concentrations (μg g^{-1}) in bark and tree-rings (wood) of Larch and Douglas-fir from Avala and REIK-Kolubara locations.

Tree	Larch				Douglas-fir			
Locations	Avala		REIK-Kolubara		Avala		REIK-Kolubara	
Elements	bark	wood	bark	wood	bark	wood	bark	wood
Cd	0.75	0.29	0.16	0.07	1.12	0.22	0.60	0.10
Mn	176.2	73.6	154.2	20.6	144.8	37.5	208.9	30.0
Pb	2.46	2.71	1.80	0.37	1.72	1.20	0.91	0.88

Conclusion

Larch and Douglas fir tree-rings showed a similar Mn and Cd concentrations trends in both studied sites. Mean Cd and Mn concentrations in larch tree-rings were higher at the Avala location, while on-site REIK-Kolubara they are higher in Douglas-fir tree-rings. Higher Cd, Mn and Pb average concentrations in larch and Douglas-fir tree-rings were measured at the Avala location for both tree species.

References

[1] S. A. Watmough, T. C. Hutchinson, Environ Pollut, 1996, 93, 93-102.
[2] D. M. Marković, I. Novović, D. Vilotić, Lj. Ignjatović, Russ. J. Phys. Chem., 2007, 81, 1493-1496.
[3] D. M. Marković, I. Novović, D. Vilotić, Lj. Ignjatović, Environ Monit Assess, 2009, 151, 377-382.
[4] R. P. Guyette, B. E. Cutter, G. S. Henderson, J Environ Qual, 1991, 20, 146-50.
[5] B. E. Cutter, R. P. Guyette, J Environ Qual, 1993, 22, 611-619.
[6] L. Harju, K. E. Saarela, J. Rajander, J. O. Lill, A. Lindroos, S. J. Heselius, Nucl Instrumn Meth B, 2002, 189, 163-167.
[7] N. W. Lepp, Environ Pollut, 1975, 9, 49-61.

K-32-P

REMOVAL OF POLLUTANTS BY SURFACTANT MODIFIED ZEOLITES

M. Marković[1]*, M. Kragović[1], M. Petrović[1], A. Daković[1], D. Krajišnik[2], J. Milić[2]

[1]*Institute for Technology of Nuclear and Other Mineral Raw Materials, P.O. Box 390, 11000 Belgrade, Serbia, *e-mail:marija_markovic84@yahoo.com*
[2]*Department of Pharmaceutical Technology and Cosmetology, Faculty of Pharmacy, University of Belgrade, P.O. Box 146, 11 221 Belgrade, Serbia*

Abstract
In this paper results on adsorption of chromate and lead by the natural zeolite and three organo-zeolites obtained by treatment of zeolite with three different levels (10, 20, 30 mmol/100g) of cetylpyridinium chloride (CPC) are presented. It was determined that adsorption of chromate increased with increasing the amount of CPC at the surface and also with increasing the initial chromate concentration. Presence of surfactant at the zeolite surface had no influence on lead adsorption.

Introduction
Wastewaters from mining operations, electroplanting plants, power-generating plants, etc. contain several toxic heavy metals. These discharges have important levels of cadmium, chromium, copper, lead and mercury. Among the different techniques proposed for heavy metals removal (reduction, precipitation, biosorption, nano and ultrafiltration) adsorption on natural sorbents as low-cost sorbents seems to be quite attractive [1].

Natural zeolites are microporous minerals formed from hydrated crystalline aluminosilicates with three-dimensional structures consisting of the tetrahedral SiO_4 and AlO_4. The partial substitution of Si^{4+} by Al^{3+} results in a negative charge that is compensated by exchangeable cations (Na^+, K^+, Ca^{2+} or Mg^{2+}). The cation exchange properties has been used to modify the surface of the zeolites by adsorbing a cationic surfactants. At a low surfactant concentration (below external cation exchange capacity) the surfactant cations are exchanged with the exchangeable cations of the natural zeolite until a monolayer of surfactant cations is formed at the external surface. At higher concentrations (above external cation exchange capacity) a bilayer and/or admicelle of surfactant molecules are attached to the external surface, where the outer layer of surfactant molecules is bound by hydrophobic interactions. The bilayer formation results in charge reversal on the external surface, providing sites where anions will be retained and cations repelled, while neutral low polar species can partition into the hydrophobic core. Organo-zeolites with amounts of cetylpyridinium chloride (CPC) equal to ECEC of zeolite (10 mmol/100g – sample ZCPC-10) and above ECEC (20 mmol/100g and 30 mmol/100g – samples ZCPC-20 and ZCPC-30) were tested as carriers for drugs (e.g. diclofenac sodium) [2].

Since chromium preferably exist in the nature in anionic form, in this paper preliminary investigations of chromate adsorption on the same organo-modified

zeolites were conducted. Because of known affinity of the natural zeolite for adsorpion of heavy metals [3], it was also determined if the presence of CPC at the zeolitic surface has influence on lead adsorption.

Experimental

A sample of natural zeolitic tuff from Zlatokop deposit (Vranjska Banja) was used as starting material. The cation exchange capacity (CEC) was 148 meq/100 g and the external cation exchange capacity (ECEC) was 10 meq/100 g. The zeolite was modified with three levels of cetylpyridinium chloride (CPC). Details on the preparation of organo-zeolites are given elsewhere [2].

Chromate adsorption was performed using 0.5 g of each organo-modified zeolites and 50 ml K_2CrO_4 (concentrations of 6.3 to 27.4 mg/l). For lead adsorption 1.0 g of either the natural zeolite or ZCPC-20 was mixed with 50 ml of aqueous solution of $Pb(NO_3)_2$ (10567 mg/l). In all experiments, after the reaction time (24 h), suspensions were centrifuged at 10000 rpm for 10 min to separate the solution and solid. The initial and non sorbed concentrations of Cr or Pb in supernatants were determined by atomic absorption spectrophotometry using an "Analytic Jena Spekol 300". Percentage of adsorbed chromium or lead was calculated from the difference between the initial and final concentration of each pollutant in the aqueous supernatant.

Results and discussion

Since the natural zeolite, has no affinity for anionic species, in the preliminary experiment it was confirmed that it was ineffective in chromate adsorption. Results on chromate adsorption on the three organo-zeolites are presented at Fig 1. As can be seen from the Fig.1, for the organo-zeolite with the lowest amount of CPC (ZCPC-10), low adsorption of chromate (0.075 mg/g), was observed only for the lowest initial chromate concentration. These results indicated that organo-zeolite with monolayer conformation does not readily adsorb chromate as expected for hydrophobic surface. When the surfactant loading is greater than 100% ECEC (ZCPC-20 and ZCPC-30), the adsorption of anionic chromate species took place progressively with increasing in surfactant loading. At concentration of CPC above ECEC, adsorbed surfactant molecules form bilayer or patchy bilayer and in this condition, anion exchange took place and chromate has a stronger affinity for the positively charged surfactant head group than for the counterions already adsorbed. From Fig. 1 it can be also seen for ZCPC-20 and ZCPC-30 that amount of adsorbed chromate increased with increasing the initial chromate concentration.

For the lowest chromate concentration (6.3 mg/l) amount of adsorbed chromate was 0.56 mg/g for ZCPC-20 and 0.62 mg/g for ZCPZ-30. For the highest chromate concentration (27.4 mg/l) adsorption of chromate was 1.28 and 1.96 mg/g for ZCPC-20 and ZCPC-30 respectively. Additionally, results of adsorption of lead by the natural zeolite and ZCPC-20 showed that presence of bilayer of surfactants at the zeolite surface had no influence on adsorption of lead (adsorbed amount of lead 69.9 mg/g for the natural and 72.0 mg/g for ZCPC-20).

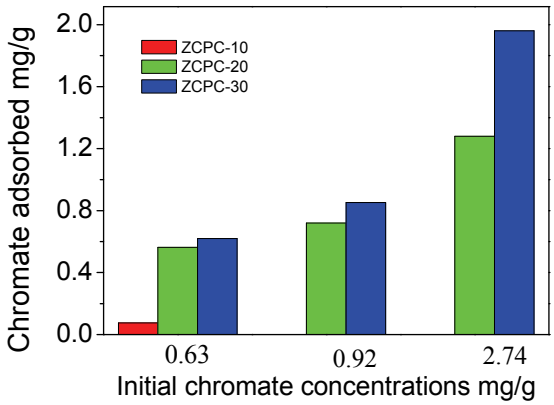

Figure 1. Chromate adsorption by organo-zeolites – ZCPC-10, ZCPC-20 and ZCPC-30.

Conclusion

The results reported in this paper indicated that organo-zeolites were effective in heavy metals removal. The availability of the natural zeolite, its low cost and simple modification with surfactants makes this material suitable for potential practical application for wastewater treatments.

References

[1] V. M. Boddu, K. Abburi, J. L. Talbott, E. D. Smith, Environ. Sci. Technol., 2003, 37, 4449-4456.
[2] D. Krajišnik, A. Daković, M. Milojević, A. Malenović, M. Kragović, D. Bogdanovic, V. Dondur, J. Milić, Colloids Surf. B, 2011, 83, 165-172.
[3] M. Kragović, A. Daković, Ž. Sekulić, M. Trgo, M. Ugrina, J. Perić, G. Diego Gatta, Appl. Surf. Sci., 2012, 258, 3667-3673.

K-33-P

XRF ANALYSIS OF HEAVY METAL CONTENT IN SOIL SAMPLES USING MINIPAL 4 SPECTROMETER

M. Kuzmanoski, M. Todorović, M. Aničić Urošević, S. Rajšić, M. Tasić

Institute of Physics, University of Belgrade, Serbia

Abstract

Monitoring of heavy metal content in urban park soil is important, as their elevated concentrations can have detrimental effect on human health. We present preliminary results of test of performance of MiniPal 4 XRF spectrometer for analysis of heavy metal content in soil and the results of analysis of soil from a city park in Belgrade center. The obtained results are generally in agreement with heavy metal content in soil in Belgrade central area, including parks, reported in some other studies.

Introduction

Heavy metals are naturally present in soil. Their elevated concentrations in urban soil can affect human health. Children are at higher risk of exposure to toxic heavy metals in park soil, and more sensitive to their effects. Thus, it is important to monitor level of heavy metals in urban park soil. For this purpose, X-ray fluorescence (XRF) spectrometry is a convenient method, as it is nondestructive, requires little sample preparation and allows multielemental analysis. PANalytical MiniPal 4 is a compact benchtop energy dispersive XRF spectrometer, used primarily in mining and cement industries, but also for research purposes [1]. Here we test the performance of this spectrometer in analysis of heavy metal content in soil samples, and present our preliminary results of the analysis of soil samples collected at different depths from a city park in the center of Belgrade, in Spring of 2011.

Experimental

The soil samples were taken from several locations in the park, from three layers at depths of 0-10 cm, 10-20 cm and 20-30 cm, using steel corer. For each of the layers a composite sample was made. After drying, sieving and milling, 5g of each of the soil samples was pressed into a pellet at the pressure of 30 tons for 60 s. In this study a MiniPal 4 XRF spectrometer was used for elemental analysis. It is equipped with 9W Rh tube and silicon drift detector, with resolution FWHM = 145eV for 5.9keV 55Fe. The calibration of the instrument was performed using six reference materials (soil and lake sediment), pressed into pellets. The following elements have been measured: Ba, Ca, Cr, Cu, Fe, K, Mn, Ni, Pb, Rb, Ti, V, Zn and Zr. Optimal measurement parameters (tube voltage, current and filter) were found for different sets of elements. The analysis of the spectral data was performed using MiniPal/MiniMate software.

Results and Discussion

In this study we focus primarily on Cr, Cu, Fe, Mn, Ni and Zn, as common heavy metal pollutants for urban soil. Lead and V are excluded from the analysis because

the calibration results for these elements were not satisfactory. The values of the calibration parameters are shown in Table 1.

Table 1. Calibration results for analyzed elements.

Element	Correlation	Relative RMS (%)	Concentration range (ppm)
Cr	0.9982	6.2	75.0 - 4310.0
Cu	0.9999	1.4	16.9 - 390.0
Fe	0.9832	6.1	32733.0 - 67400.0
Mn	0.9984	3.7	390.0 - 3460.0
Ni	0.9863	12.9	27.8 - 291.0
Zn	0.9981	4.0	44.0 - 345.0

Prior to analysis of soil samples, we analyzed two soil reference materials (SARM42 and GBW07406) as unknown samples, in order to test our calibration method. The average values of element concentrations obtained from three repeated measurements are in agreement with the corresponding certified values, as shown in Table 2.

Our analysis showed very low concentration of Cr, close to the limit of detection, both in the top (0-10 cm) and the deeper layers of soil samples from the park. The concentrations of other elements in the top layer are the following: 27 ppm for Cu, 35431 ppm for Fe, 795 ppm for Mn, 54 ppm for Ni and 100 ppm for Zn. These values are in agreement with those reported in some earlier studies on elemental analysis of soil in the Belgrade central area [2, 3]. Copper and Zn concentrations showed increase with depth, which could indicate washing out of these elements from the top layer of soil. Manganese and Fe concentrations are higher in the top layer than in deeper layers. Variability of Ni concentration with depth was not significant.

More details related to the performance of MiniPal 4 spectrometer in analyzing heavy metals in soil samples from the Belgrade park will be presented.

Table 2. Measured and certified values of concentrations of analyzed elements for SARM 42 and GBW07406 soil reference materials

Element	SARM42		GBW07406	
	Certified (ppm)	Measured (ppm)	Certified (ppm)	Measured (ppm)
Cr	4310	4032	75	62
Cu	17	19	390	390
Fe	32733	33394	56584	57121
Mn	774	785	1450	1489
Ni	125	153	53	51
Zn	44	50	97	95

Conclusion

Test of the applicability of PANalytical MiniPal 4 energy dispersive XRF spectrometer for the analysis of heavy metal content in soil samples showed that it can be successfully used for this purpose. The obtained values for concentrations of

Cr, Cu, Fe, Mn, Ni and Zn are in agreement with those reported for soil in the Belgrade central area in some other studies [2,3].

Acknowledgement

This paper was realized as a part of the project No III43007 financed by the Ministry of Education and Science of the Republic of Serbia within the framework of integrated and interdisciplinary research for the period 2011-2014.

References

[1] V. Oreščanin, I. Lovrenčić Mikelić, L. Mikelić and S. Lulić, X-Ray Spectrom., 2008, 37, 508-511.

[2] M. Marjanović, M. Vukčević, D. Antonović, S. Dimitrijević, Đ. Jovanović, M. Matavulj and M. Ristić, J. Serb. Chem. Soc., 2009, 74 (6), 697-706.

[3] I. Gržetić and R. A. Ghariani, J. Serb. Chem. Soc., 2008, 73 (8-9), 923-934.

K-34-P

EFFECTS OF BIODEPOSIT PRODUCTION IN AMAGASAKI PORT, JAPAN

V. Jovanović[1], Y. Kozuki[2], R. Yamanaka[2],M. Miyoshi[3]
[1]*IHTM, University of Belgrade, Belgrade, Serbia;*
[2]*Department of Ecosystem Engineering, Graduate School of Engineering, University of Tokushima, Japan*
[3]*Ecosystem Design, Institute of Technology and Science, University of Tokushima*

Abstract
Effects of biodeposition by mussels *Mytilus galloprovincialis*, was investigated *in situ* during two consecutive summer periods, using sediment traps. Experiment took place in the vicinity of vertical coastal structures, inside of Amagasaki port. The sedimentation rate was found to be doubled due to deposition of faecal material under the quaywall colonized by mussels, comparing to mussel-free referent station. The effect of mussels through the biodeposition was even more significant on the organic carbon and nitrogen fluxes that were three times higher near the wall causing local organic enrichment.

Introduction
Material suspended in the water column precipitates by so called natural sedimentation. On the other hand, mussels filter water column and feed on suspended particles, mainly phytoplankton and detritus. Particles they capture but cannot ingest mussels pack and excrete as faeces and pseudofaeces [1]. Because they are too large and cohesive to be transported further, they rapidly settle to the bottom. Thus, this process, known as biodeposition adds new material to the sediment changing in that way settling rates, composition and quantity of the deposited material. Environmental effects of these processes have yet to be assessed.
In this report we present the results concerning the investigation of natural sedimentation and biodeposition by mussel *Mytilus galloprovincialis.* Their importance arises from the fact that these invasive species have the ability to bind to the vertical concrete surfaces, such as seawalls and quays, which dominate the landscape of Osaka Bay. Here, in the nutrient rich waters, they reach high biomass even when most other species vanish due to the harsh living conditions in mid-summer. Amgasaki port was selected as a case study of Osaka Bay. The experiment was conducted in July 2007 and August 2008 when major deposition events occur due to concentration of phytoplankton and activity of mussels at that time.

Experimental
Particles from natural sedimentation and biodeposition were collected in replicate traps placed at 2.5 m below the water surface and at 7 m below the surface (*i.e.* 2 m from the bottom) on three sampling stations. Two stations were next to quaywall with attached mussels while third, referent station was at 50 m distance from the wall. Traps from this station collected only naturally sedimented material. Construction details of the

traps and their moorings are given schematically elsewhere [2]. Multiple samples of the bottom sediments have been taken on each sampling station.

All pretreament and analytical procedures were performed in laboratory. The amount of particulate matter (PM) accumulated in sediment traps were determined after freeze dying. Determination of particulate organic carbon (POC) and particulate nitrogen (PN) was performed using *Termo Finnigan CN Soil Analyser* (FLASH EA 1112) after the residue had been treated with HCl solution to remove carbonates. Content of particulate organic matter (POM) in deposited material and sediments was estimated according to Martin and Knauer [3].

Results and Discussion

Figure 1 represents the mass fluxes of particulate matter expressed as dry grams per m^2 per day, collected in sediment traps in two analyzed periods.

Results show that the quantity of accumulated matter in stations near the wall (stations 1A, 2A, 2B) is significantly higher than control trap values (3A and 3B) for both periods (Mann Whitney U-test; $p<0.001$).

Amounts of particles that settle in traps at stations 1A and 2B are tripled and doubled respectively, in relation to those in referent traps from the same depth (3A and 3B), mainly as a consequence of mussels activity.

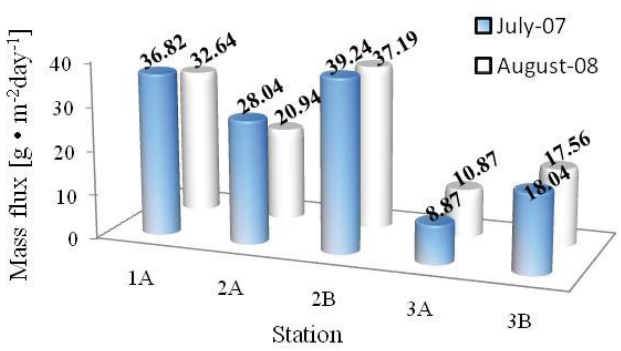

Figure 1. Mass fluxes from different stations at the time of experiments. Letters A and B denote depths of 2.5 m and 7 m below the water surface. Numbers 1 and 2 denote stations near the wall. Referent stations are marked by number 3

Distribution of collected particulate matter among the stations in two years follow the same pattern indicating similarity of the processes affecting downward flux of PM in Amagasaki port.

Composition of settling material and sediments accumulated at different sampling stations is given in Table 1.

On the basis of obtained results, we can say that both POC and PN behave in the same manner: amount of POC and PN are higher in traps and sediments near quaywall (positions 1A, 2A, 2B, 1S and 2S) than those at referent site (3A, 3B and 3S).

The POC/PN ratios, or shorter C/N, varied between 6 and 7 for collected deposits, and between 6 and 10 for the bottom sediments. Such values are characteristic for productive coastal areas indicating phytoplankton, fecal pellets and other easily degraded material [4].

Stations	POC[mg/g] 2007	2008	PN[mg/g] 2007	2008	C/N[ratio] 2007	2008	POM[%] 2007	2008
1A	111.1	149.5	16.6	25.8	6.7	5.8	25.6	34.4
2A	118.5	153.3	18.1	26.6	6.6	5.8	27.3	35.3
2B	86.6	114.0	12.9	18.7	6.7	6.1	19.9	26.2
3A	102.5	115.6	15.5	18.7	6.6	6.2	23.6	26.6
3B	59.3	85.9	8.3	13.2	7.2	6.5	13.6	19.7
1S*	129.4	108.6	18.6	17.7	7.0	6.1	29.8	25.0
2S	68.9	64.0	10.1	9.2	6.8	7.0	15.8	14.7
3S	24.6	26.0	2.5	2.8	9.8	9.4	5.7	6.0

Table 1. POC, PN, C/N and POM in sediment traps and sediments at different sampling stations during two analy-sed periods.
*1S, 2S and 3S are sediments below stations 1-3.

Content of particulate organic matter (POM) ranges between 13.6% (3B) and 35.3 % (2A) implying that both naturally sedimented and biodeposited particles contained mostly inorganic constituents, whose amount tend to increase with depth. Dilution with mineral fractions can explain the drop of organic content in lower traps as well as in sediments**.**

Sediment samples collected at the referent site (3S) contain lower organic matter comparing to those collected at stations near the wall (1S and 2S), idicating that organic matter, accumulated under the walls, causes local organic enrichment. Due to low current velocities in Amagasaki port, slow tidal flushing (less than 1 m at the time of experiments) and waves directed landwards, organic material couldn't be dispersed. Also, it couldn't be utilized by benthic organisms because most of them escaped or died due to anoxic conditions at the bottom [5]. In collected sediment samples redox potential (Eh) values ranged from -200 to -315 $mV^{(KCl\ Ag/AgCl)}$. Because of this, the fate of organic matter depends mainly on microbial degradation, which is tardy in anoxic conditions existing at bottom.

Concludion

Our results indicate that biodeposit production by mussels *Mytilus galloprovincialis* significantly affect downward flux of particulate matter in the vicinity of coastal structures they inhabit. Sedimentation rates are doubled, and the deposition of POC and PN tripled compared to the control values. In the low oxygen ambient decomposition of organic matter is slow leading to local organic enrichment.

References

[1] C. B. Jørgensen,. Mar. Ecol. Prog. Ser., 1996, 142, 287-302.
[2] V. Jovanović et al., J.Coastal Zone Strudies, 2009, 24, 97-111.
[3] J. Martin, G. Knauer, Geochimica at Cosmochimica Acta, 1973, 37, 1639-1653.
[4] T. R. Parsons, Biological oceanographic Processes, Oxford, Pergamon Press, 1977.
[5] Y. Mishima, A. Hoshika, T. Tanimoto, Journal of Oceanography, 1999, 55, 1-11.

PHASE BOUNDARIES

MULTICOMPONENT MONOLAYER GAS ADSORPTION: THE EFFECT OF MOLECULAR SIZE AND THE NUMBER OF BINDING SITES ON SORPTION RATES

O. Jakšić[1], Z. Jakšić[1], I. Jokić[1], D. Ranđelović[1], Lj. Kolar-Anić[2]
[1] *Institute of Chemistry, Technology and Metallurgy, University of Belgrade – Njegoševa 12, 11000 Belgrade, Serbia, olga@nanosys.ihtm.bg.ac.rs*
[2] *Faculty of Physical Chemistry, University of Belgrade, Studentski trg 12-16, 11000 Belgrade, Serbia, lkolar@ffh.bg.ac.rs*

Abstract
Multicomponent monolayer gas adsorption on solid surfaces is studied. Master equations for multicomponent gas adsorption are formulated. Sorption rates and the number of free binding sites for each gas species are modeled using physical parameters of the system. The procedure for estimation of surface density of adsorbed molecules is explained and demonstrated on some industrial and semiconductor gases. These results may be used for adsorption based sensor design/technology or related fundamental research.

Introduction
The development in micro and nano technologies leads to the fabrication of new micro and nano structures whose functioning depends highly on adsorption-desorption processes. That dependence can be crucially favorable like for instance in adsorption-based (bio)chemical plasmonic sensors [1], or very undesirable like in microresonators where adsorption-induced mass fluctuations provoke frequency instabilities [2].

In this work we focus on modeling adsorption-desorption process, its constants and parameters, in order to set-up a model suitable for analyzing multicomponent gas adsorption on solids in time span from the beginning till the equilibrium is reached and afterwards. This model could be used in many analytical applications where adsorption-desorption processes play important role in both detection and measurement.

Theory
Starting premises are similar to that of Langmuir's: the surface is homogenous, all molecules of the same gas species are alike. Molecules in gas phase behave as ideal gas, adsorbed molecules do not collide or interact and do not form multilayer islands. Average residential time of adsorbed particles is the same for all particles of the same gas. The flux of arrivals of gas molecules of the species i, $R_{a,i}$, onto the solid surface is proportional to its partial pressure, p_i, and free surface [3]

$$R_{a,i} = \frac{1}{\sqrt{2\pi m_i k_B T}} p_i \left(1 - \sum_{j=1}^{r} \theta_j \right) \quad (1)$$

Here, θ_j are fractions of occupied surfaces for each of r surrounding gases, m_i is mass of a single molecule of i_{th} gass, k_B is Boltzmann constant, T is temperature.

The rate of desorption of the species i onto the solid surface is proportional to its number of adsorbed molecules, $N_{a,i}$, and inversely proportional to their mean residential time $\overline{\tau_i}$. According to the ideal gas law, the final expression for rate equation of the number of adsorbed molecules for each gas is then

$$\frac{\mathrm{d}N_{a,i}}{\mathrm{d}t} = \frac{A\alpha_{s,i}}{\sqrt{2\pi m_i k_B T}} p_i \left(1 - \sum_{j=1}^{r} \theta_j\right) - \frac{N_{a,i}}{\overline{\tau_i}} = \frac{A\alpha_{s,i}}{V}\sqrt{\frac{k_B T}{2\pi m_i}} N_{g,i}\left(1 - \sum_{j=1}^{r} \theta_j\right) - \frac{N_{a,i}}{\overline{\tau_i}} \quad (2)$$

where $\alpha_{s,i}$ is sticking probability of adsorption for i_{th} gass, $N_{g,i}$ is the number of free gas molecules, A is surface area and V is gas chamber volume. In order to be able to find the solution for the number of adsorbed molecules for each gas or to conduct the stochastic analysis of this process, one must transform equation (2) into a more suitable form.

Results

Adsorption-desorption process is usually studied as a second order reaction, according to the following stoichiometric equation

$$A_g + A_f \underset{k_d}{\overset{k_a}{\rightleftarrows}} A_a \quad (3)$$

and the corresponding differential equation:

$$\frac{dN_{a,i}}{dt} = k_{a,i} N_{g,i} N_{f,i} - k_{d,i} N_{a,i} \quad (4)$$

where a free gas molecule A_g and a free adsorption center A_f reversibly transform into an adsorbed molecule A_a, with an adsorption rate k_a and a desorption rate k_d and the number of free adsorption centers for the species i is $N_{f,i}$.

Equations (2) and (4) were analyzed with respect to surface densities of adsorbed molecules for different gases. In case of multi-component environment with r gases, one has r parallel reactions, each of which obeys differential equation

$$\frac{\mathrm{d}N_{a,i}}{\mathrm{d}t} = \frac{\alpha_{s,i}}{n_{s,i}V}\sqrt{\frac{k_B T}{2\pi m_i}}\left(N_{0,i} - N_{a,i}\right)\left(N_{a,i}^{\max} - \sum_{j=1}^{r}\frac{n_{s,i}}{n_{s,j}} N_{a,j}\right) - \frac{N_{a,i}}{\overline{\tau_i}}$$

$$k_{a,i} = \frac{\alpha_{s,i}}{n_{s,i}V}\sqrt{\frac{k_B T}{2\pi m_i}} \qquad k_{d,i} = \frac{1}{\overline{\tau_i}} \qquad N_{0,i} = \frac{p_i V}{k_B T} \qquad N_{a,i}^{\max} = n_{s,i} A \quad (5)$$

$N_{0,i}$ is the overall number of molecules of the species i in the system, $N_{a,i}^{\max}$ is the number of places that molecules of the species i would take to fully populate surface A in monolayer and $n_{s,i}$ is the maximal surface density of adsorbed molecules. As we can see from eq. (4) the adsorption rate constant and the maximum number of binding sites for the species i depend on its molecular size through the surface density.

The constants and parameters in eq. (5) are necessary for further analysis (deriving time evolutions of the number of adsorbed molecules or its mean, determining equilibrium coverages...). In order to provide the surface density of adsorbed molecules the following procedure is used:

The molecule structure is obtained using the chemical structure information available in the PubChem Substance and Compound database through the unique chemical structure identifier CID. Then, molecular projected surface area was obtained using Marvin 5.9.3, 2012, ChemAxon (http://www.chemaxon.com), fig.1.

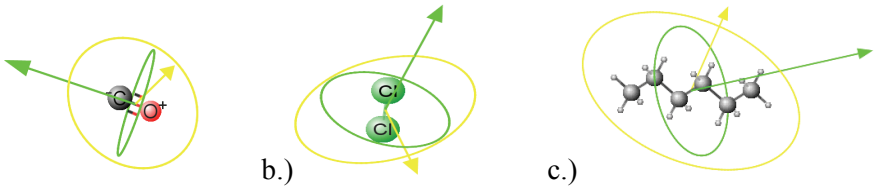

a.) b.) c.)

Figure 1. Maximal and minimal projection areas of a.) carbon monoxide b.) chlorine and c.) hexane in A^2 (8.13 – 11.01, 9.62 – 16.70, 21.59 – 40.59), respectively.

Since spheres cannot cover rectangular areas completely, molecular projected surface areas were corrected by a factor of $4/\pi$, before being inversed in order to give the number of adsorption centers per unit area for that species. The obtained data were compared with the experimental results from [4], as shown in table 1.

Table 1. The maximum number of binding sites in 10^{18} molecules/m^2.

gas	CH_4	CO	N_2	Ar	O_2	CO_2
ref [4]	6.3	6.6	6.6	7.7	7.7	6.1
our data	6.52	7.15	7.5	7.08	7.34	6.52

Hence, molecules of different gas species occupy different number of free adsorption centers when adsorbing onto the same surface. Moreover, molecules of the same gas, that have strongly unisotropical geometry, like chain carbohydrates, can also have different estimates of potentially free places for themselves. In that case, we may assume that there are some preferable orientations for adsorption [4].

Conclusion

Procedure has been proposed for the estimation of the number of binding sites, parameter needed for the stochastic and deterministic analysis of multicomponent adsorption. Obtained data were approved by experimental values from literature.

Acknowledgement

This work was funded by Serbian Ministry of Education and Science through the projects TR 32008 and ON 172015.

References

[1] I. Abdulhalim, M. Zourob and A. Lakhtakia, 2008, Electromagn., 28, 214-242.
[2] Z. Djurić, I. Jokić, M. Djukić and M. Frantlović, 2010, Microelec. Eng., 87, 1181-1184.
[3] D. Do, 1998, Adsorption Analysis: Equilibria and Kinetics, Imperial College Press, London.
[4] I. Langmuir, 1918, J. American Chem. Soc., 40, 1361-1403.

L-02-P

ADSORPTION OF CONGO RED ON NATURAL AND ORGANO-ZEOLITES

M. Kragović*, A. Daković, M. Marković and Ž. Sekulić
Institute for Technology of Nuclear and Other Mineral Raw Materials, Franchet d'Esperey 86, P.O.Box 390, 11000 Belgrade Serbia; e-mail: m.kragovic@itnms.ac.rs*

Abstract
Results of Congo Red (CR) adsorption by the natural (NZ) and organo-zeolites obtained by treatment of NZ with three different levels (10, 20, 30 mmol/100g) of cetylpyridinium chloride (NZCP10, NZCP20 and NZCP30) are presented. It was determined that NZCP10 has the best adsorption capacity for CR. Adsorption of CR by NZ and NZCP10 was followed by determination of adsorption isotherms. Much higher adsorption of CR was achieved with NZCP10. The results were fitted to the Langmuir and Freudlich adsorption model. For NZ, adsorption of CR was well described with both models, while for NZCP10 the best fit of experimental data was achieved with the Langmuir model (r^2=0.98). From the Langmuir isotherm, calculated maximum adsorbed amount of CR was 21 and 56 mg/g for NZ and NZCP10, respectively.

Introduction

Dyes are important pollutants, causing environmental and health problems to humans and aquatic animals. Several techniques (precipitation, flocculation, adsorption, etc.) are used for removal of dyes from wastewater. It is believed that adsorption is the simplest and the most cost-effective technique [1]. Congo Red (CR) [1-naphthalenesulfonic acid, 3,3´ -(4,4´ -biphenylenebis (azo)) bis (4-amino-) disodium salt] is a benzidine based anionic diazo dye. It is well known that CR can be metabolized to benzidine, a known human carcinogen. The treatment of CR contaminated wastewater can be complicated due to its complex aromatic structure providing the dye physicochemical, thermal and optical stability, and resistance to biodegradation [2]. Natural zeolite (NZ) is an abundant natural aluminosilicate available all over the word. The most common NZ is clinoptilolite. In the past years, the NZ has been explored as effective adsorbent for removal of CR [3]. In order to improve efficacy of NZ for removal of organic molecules, i.e., dyes, surface of NZ is often modified with long chain organic cations (surfactants). The objective of this research was to investigate adsorption of CR by NZ and organo-zeolites obtained by modification of NZ with surfactant - cetylpyridinium chloride (CP) .

Experimental

The starting material was the natural zeolite from the Zlatokop deposit, Vranjska Banja with the particle size <0.043 mm. Cetylpyridinium chloride (CP) was used for the preparation of organo-zeolites. In order to obtain organo-zeolites with

different CP loadings, 10 wt % aqueous suspension of the NZ was treated with CP amounts equivalent to 100%, 200% or 300% of external cation exchange capacity (ECEC) of NZ. The samples were denoted as NZCPC10, NZCP20 and NZCP30.

In the initial dye adsorption study, 25 mL of CR solution (C=300 mg/L) was mixed with 0.5 g of either NZ or each organo-zeolite. To study the effect of the initial CR concentrations, 0.5 g of NZ or NZCP10 was mixed with 25 ml of aqueous solutions, containing various initial CR concentrations (100 - 2000 mg/L). In all experiments, after the reaction time (24h), suspensions were centrifuged at 10,000 rpm for 10 min to separate the solution and solid. The initial and non-adsorbed concentrations of the CR in supernatants were determined by using UV/VIS spectrometer Analytic Jena Spekol 1300, at λ=496 nm.

Results and Discussion

Preliminary results on adsorption of CR by NZ and organo-zeolites NZCP10, NZCP20 and NZCP30 are given at Fig. 1a. As can be seen, adsorption of CR was 11.9 mg/g (78%) for NZ, 15.2 mg/g (100%) for NZCP10, 14.2 mg/g (93.42%) NZCP20 and 13.5 mg/g (88.81%) for NZCP30. Results showed that NZ as well as organo- zeolites were efficient in adsorption of CR. For organo-zeolites, it was observed that adsorption of CR slightly decreased with increasing the amount of CP at the zeolite surface. Thus, the highest adsorption of CR was achieved when the amount of CP was equal to 100% of ECEC.

The isotherms for CR adsorption on NZ and NZCP10 are given at Fig. 1b. From Fig. 1b, it is observed that adsorption of CR by both adsorbents followed a non linear type of isotherm and much higher adsorption of CR was achieved with the NZCP10. For fitting the data, the Langmuir and Freudlich adsorption equations were selected:

Langmuir equation: $q_e=(q_m K_L C_e)/(1+K_L C_e)$

where, q_e is the amount of dye adsorbed per unit of adsorbent at equilibrium (mg/g), C_e is equilibrium concentration of CR (mg/L), q_m is the maximum amount of CR that can be adsorbed by the solids (mg/g), K_L is the Langmuir constant related to the energy of adsorption (L/mg).

Freundlich equation: $q_e=K_F C_e^{1/n}$,

where K_F (mg $^{1-1/n}$ $L^{1/n}$ g^{-1}) and n are the Freundlich adsorption isotherm constants. Table 1 presents the fitted isotherm parameters for the Langmuir and Freudlich isotherms. Both models well described adsorption of CR by NZ (for Langmuir model r^2=0.94 and for Freudlich model r^2=0.96). For adsorption of CR by NZCP-10, the best fit of the experimental data was achieved with the Langmuir model. From Langmuir isotherm, calculated maximum amount of CR adsorbed by NZCP10 was significantly higher (54.2 mg/g) than for NZ (21 mg/g) . These results indicated that presence of CP at the zeolitic surface increased the adsorption of CR. Also, the value of the Freundlich parameter n >1 for both adsorbents

indicated that CR adsorption is favorable physical process under applied experimental conditions [3].

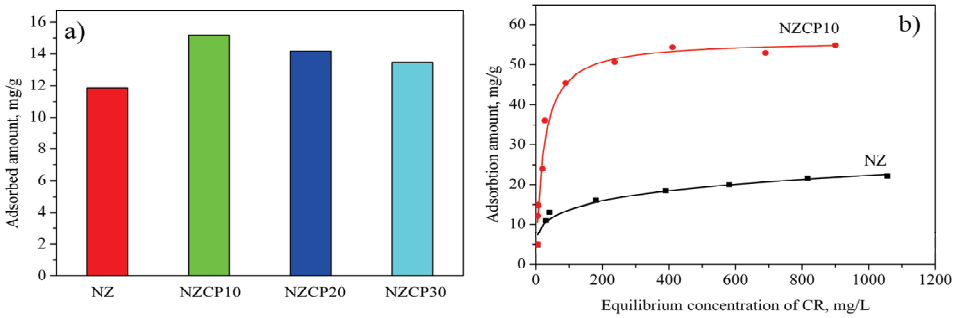

Figure 1. a) Adsorption of the CR by NZ and organo-zeolites; **b)** Isotherms for adsorption of CR by NZ and NZCP10.

Table 1. Adsorption parameters of isotherms for adsorption CR on NZ and NZCP10.

Materials	Freundlich			Langmuir		
	K_F	n	r^2	K_L	q_m	r^2
NZ	5.11	4.66	0.96	0.0375	21.00	0.94
NZCP10	11.99	4.17	0.84	0.0456	56.24	0.98

Conclusion

Results of adsorption of CR by NZ and its organo-modified form (NZCP10) showed that significantly higher CR adsorption has been achieved on organo-modified zeolite. Both Freundlich and Langmuir isotherms well described adsorption of CR by NZ. Langmuir model best described adsorption of dye by NZCP10. The results suggested that surfactant molecules at the zeolitic surface have positive influence on adsorption of CR.

References

[1] Sh. Wang, E. Ariyanto J. Colloid Interface Sci., 2007, 314, 25–31.
[2] M. K. Purkait, A. Maiti, S. DasGupta, S. De, J. Hazard. Mater., 2007,145, 287-295.
[3] V. Vimonses, Sh. Lei, B. Jin, Ch. W.K. Chow, Ch. Saint, Chem. Eng. J., 2009, 148, 354-364.

L-03-P

DETERMINATION OF THE POINT OF ZERO CHARGE OF Cu(II), Zn(II) AND Ag(I) DOPED HYDROXYAPATITE

M. Šljivić Ivanović, V. Stanić, A. Milenković, I. Smičiklas

University of Belgrade, Vin a Institute of Nuclear Sciences, P.O. Box 522, Belgrade, Serbia

Abstract

In order to additionally characterize Cu(II), Zn(II) and Ag(I) doped hydroxyapatite (HAP) powders, their points of zero charge (pH_{PZC}) were determined. pH_{PZC} values were similar for all investigated samples (6.51±0.09 for CuHAP, 6.46±0.16 for ZnHAP and 6.65±0.14 for AgHAP). The obtained values were also comparable to pHpzc reported for synthetic calcium hydroxyapatite, indicating that dopant cations were incorporated in crystal lattice during the synthesis.

Introduction

Synthetic hydroxyapatite (HAP, $Ca_{10}(PO_4)_6(OH)_2$) exhibit chemical similarity to the mineral component of bones and teeth in mammals, and due to nontoxic and biocompatible properties it has been widely used in the fields of the reconstruction of damaged bone and teeth [1]. Based on the flexibility of HAP structure, Ca^{2+}, PO_4^{3-}, and/or OH^- ions can be substituted by variety of ionic species, which may alter the crystallinity, lattice parameters, morphology, solubility and other characteristics. Cu(II), Zn(II) and Ag(I) doped hydroxyapatite samples (CuHAP, ZnHAP and AgHAP) have shown a promising antimicrobial activity [2, 3]. Surface properties of these materials are important for potential application in purification of microbiologically polluted water and bone tissue engineering. In this study, the points of zero charge (pH_{pzc}) of CuHAP, ZnHAP and AgHAP samples were determined.

Experimental

Doped HAP samples were synthesized by neutralization method, at 95ºC, using CaO, as well as CuO, ZnO or Ag_2O dissolved in H_3PO_4. The details about powders preparation and characterization are reported elsewhere [2, 3]. Samples with M/Ca = 0.4 mol % (M = Cu, Zn or Ag) were used in this study. All powders were nonstoichiometric, with (M+Ca)/P<1.67. The pH_{PZC} values were determined by batch equilibration technique [4]. 20 mL of 0.1, 0.01 and 0.001 mol/L KNO_3 solutions were equilibrated with 0.1g of doped HAP samples for 24 h, on a horizontal shaker, at ambient temperature (20 ± 1ºC). The initial pHs were adjusted

in the range 3-12, by adding minimum amounts of NaOH or HNO_3 solutions. The pH_{PZC} were defined from the plateau parts of the plots pH_{final} vs. $pH_{initial}$.

Results and Discussion

The dependencies pH_{final} vs. $pH_{initial}$ are given in Fig. 1. Large variations of electrolyte concentration caused small drifts of final pH values, confirming that KNO_3 was an inert electrolyte in respect to all doped HAP surfaces.

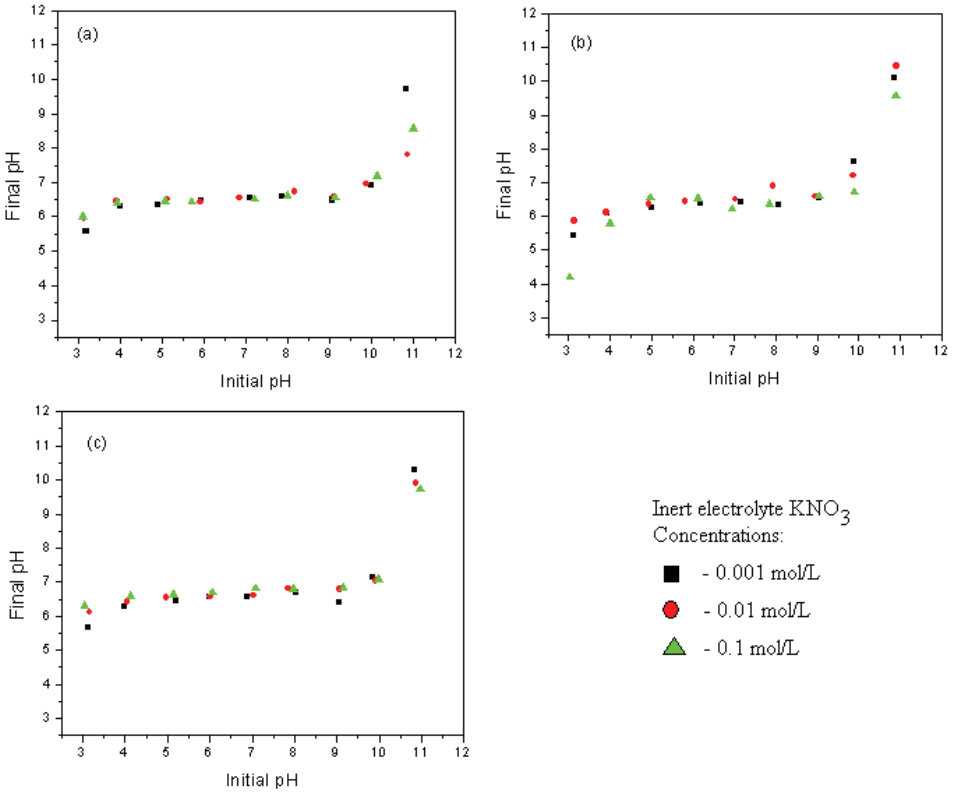

Figure 1. Determination of the point of zero charge (pH_{PZC}) of hydroxyapatite powders doped with (a) Cu(II), (b) Zn(II) and (c) Ag(I) ions.

The obtained curves were of similar shape. Final pH values increased with the increase of initial pH to ~ 4, where the plateaus began. In the pH range from ~4 to ~10 final pHs were independent of the initial ones, indicating buffering properties of the samples. Further increase of initial pH above 10 caused increase of final pH values.

The calculated pH_{PZC} were: 6.51±0.09 for CuHAP, 6.46±0.16 for ZnHAP and 6.65 ±0.14 for AgHAP. Dependences between initial and final pH values, as well as the lengths of the buffering pH region, corresponded to the behavior of synthetic HAP [5, 6]. As a consequence of different stoichiometry, crystallinity, degree of CO_3^{2-}

incorporation, etc., pH_{PZC} of HAP powders obtained by different synthetic routes may fluctuate as well. The points of zero charge obtained for doped samples were in the range of values determined for synthetic calcium hydroxyapatite samples [5, 6, 7]. These results indicated incorporation of Cu(II), Zn(II) and Ag(I) into the apatite crystal lattice during the precipitation, and thus support the results of previous chemical and instrumental analysis [2, 3].

Conclusion

The points of zero charge of Cu(II), Zn (II) and Ag(I) doped hydroxyapatite were determined by batch equilibration technique. KNO_3 was found to be an inert electrolyte in respect to analyzed powders. The pHpzc for doped HAP samples were comparable with the values obtained for various synthetic calcium hydroxyapatite powders. It can be concluded that dopant cations at applied level were incorporated in HAP crystal lattice by substitution of Ca(II). Electrical charge disbalance which occurred due to incorporation of monovalent Ag, might be compensated by creation of cationic vacancies or simultaneous substitution of PO_4^{3-} by CO_3^{2-}.

Ackonwledgments

This work was supported by the Ministry of Education and Science of the Republic of Serbia (Project No.III 43009).

References

[1] L. L. Hench, J. Wilson, Science, 1984, 226, 630-636.
[2] V. Stanić, Dj. Janaćković, S. Dimitrijević, S. B. Tanasković, M. Mitrić, M. S. Pavlović, A. Krstić, D. Jovanović, S. Raičević, Appl. Surf. Sci., 2011, 257, 4510–451.
[3] V. Stanić, S. Dimitrijević, J. Antić-Stanković, M. Mitrić, B. Jokić, I. Plećaš, S. Raičević, Appl. Surf. Sci., 2010, 256, 6083–6089.
[4] S. K. Milonjić, A. Lj. Ruvarac, M. V. Šušić, Thermochim. Acta 1975, 11, 261–266.
[5] I. Smičiklas, S. Milonjić, P. Pfendt, S. Raičević, Sep. Purif. Technol., 2000, 18, 185-194.
[6] Đ. Janaćković, I. Janković, R. Petrović, Lj. Kostić Gvozdenović, S. Milonjić, D. Uskoković, Key Eng. Mater. 2003, 240-242, 437-440.
[7] I. Smičiklas, A. Onjia, S. Raičević, Sep. Puri. Technol., 2005, 44, 97–102.

L-04-P

DETERMINATION OF CRITICAL MICELLAR CONCENTRATION OF TENSIDE MIXTURES

S. N. Blagojević[1], N. I. Potkonjak[2], B. R. Simonović[1]

[1]*Institute of General and Physical Chemistry, University of Belgrade, Studentski trg 12-16, 11000 Belgrade, Republic of Serbia*
[2] *Chemical Dynamics Laboratory, Vinča Institute of Nuclear Sciences,University of Belgrade, Mike Petrovića Alasa 12-14, 11001 Belgrade, Serbia*

Abstract
The critical micellar concentration (CMC) of tenside mixtures were determined by conductometric titration method in aquerious solution. It was found that mixtures with nonionic tensides have a much smaller CMC.

Introduction
Surfactants constitute the most important group of detergent components, and they are present in all types of detergents. Increasing surfactant concentration leads to a decrease in both surface tension and interfacial tension until the point is reached at which surfactant clusters begin to form. Above this concentration (the critical micelle concentration CMC) changes in surface and interfacial activity are only minimal. There is a big difference in CMC for anionic and nonionic tensides. Determination of CMC in tenside mixture was done by conductometric method.
Washing and cleaning in aqueous wash liquor is a complex process involving the cooperative interaction of numerous physical and chemical influences. In the broadest sense, washing can be defined as both the removal by water or aqueous surfactant solution of poorly soluble matter and the dissolution of water-soluble impurities from textile surfaces.
Surfactants are amphiphilic molecules that possess both hydrophobic and hydrophilicproperties. A typical surfactant molecule consists of a long hydrocarbon 'tail' that dissolves in hydrocarbon and other non-polar solvents, and a hydrophilic 'headgroup' that dissolves in polar solvents (typically water)[1]. One example of a dual character molecule having a head-group and a non-polar tail is sodium dodecyl sulphate (SDS), $NaOSO_3C_{12}H_{25}$.When a sufficient amount of SDS is dissolved in water, several bulk solution properties are significantly changed, particularly the surface tension (which decreases) and the ability of the solution to solubilize hydrocarbons, (which increases). These changes do not occur until a minimum bulk SDS concentration is reached. This concentration is called the *critical micelle concentration* (*CMC*)**.** Several experiments, including light scattering and NMR[2], show that below the *CMC*, the surfactant exists mainly as solvated monomeric species, whereas above the *CMC* these monomers undergo self-assembly to form roughly spherical structures (having an overall diameter of ~5 nm) known as micelles. Micelles are the simplest of all self-assembly structures.[3]

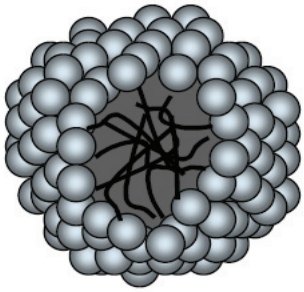

Figure 1. Schematic representation of a spherical micelle.

Modern detergent formulation, always have a mixture of few surfactants and for estimating detergency power and concentration of is it very important to determine critical micelle concentration.
Below the *CMC*, the addition of surfactant to an aqueous solution causes an increase in the number of charge carriers for example (Na (aq)+ and $OSO_3C_{12}H_{25}$ (aq)-) and consequently, an increase in the conductivity. Above the *CMC*, further addition of surfactant increases the micelle concentration while the monomer concentration remains approximately constant (at the *CMC* level). Since a micelle is much larger than a tenside monomer it diffuses more slowly through solution and so is a less efficient charge carrier. A plot of conductivity against surfactant concentration is, thus expected to show a break at the *CMC* (Fig 2).

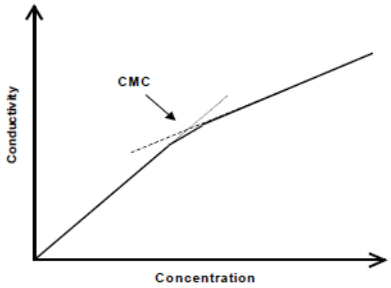

Figure 2. Determination of CMC.

Experimental
All experiments were done in thermostated 50 ml conductometric cell at 25C and in 18MΩ demi water with Hach Sension 5 conductivity meter. The solution of tenside mixture used for conductometric titration was 10g/L, and a titration step from pipette was 0.5ml. The conductivity vs concentration graph was plotted and the CMC was calculated as cross point of two linear parts of graph using ORIGIN software.

Results and discussion

We study CMC for tenside mixture of anionic and nonionic tenside in different ratio. For this study we use SLES and ά-olefin sulfonates (anionic) and different amfoteric and nonionic tensides (coco betaine, coco amide, and various etoxylated alcohols) in various ratios.

Table 1. CMC of various tenside mixtures.

	CMC (g/L) /25C
SLES/AOS	0,33
SLES/AOS/coco betaine	0,31
SLES/AOS/coco amide	0,31
SLES/AOS/C12-C15-7EO	0,15
SLES/AOS/C10-7EO	0,12
SLES/AOS/ C9-C11-7EO	0,13

The ratio of SLES/AOS (80/20) and in the other experiment SLES/AOS/tenside (75/15/10)

Conclusion

Nonionic tenside have a great influence for CMC of mixture. Mixture of anionic with nonionic tenside can be used in a lower concentration.

Favorable detergency properties of nonionic surfactants derive largely from the following factors:

- Low critical micelle concentration (CMC)
- Very good detergency performance
- Excellent soil antiredeposition characteristics with synthetic fibers

The low CMC values of nonionic surfactants indicate that they display high detergency performance even at relatively low concentrations.

Acknowledgment

The support of this research by the Ministry of Education and Science of Republic of Serbia through projects No.172015 is gratefully acknowledges.

References

[1] J. Falbe, Surfactants in consumer product, Springer-Verlag, Berlin, 1987
[2] G. Zhisheng, et al, J.Colloid and interface science, 1990, 137, issue 1, 137-146.
[3] P. Latellier, A. Mayaffre, J .Colloid and Interface Science, 2008, 327, 186-190.

COMPLEX COMPOUNDS

M-01-P

CONDUCTOMETRIC STUDY OF COMPLEX FORMATION BETWEEN OCTAAZAMACROCYCLIC LIGAND AND Co^{2+}, Ni^{2+}, Zn^{2+}, Cu^{2+}, Ag^{+} AND Cd^{2+} METAL CATIONS

B. B. Petković[1], D. Stanković[2], S. Samaržija Jovanović[1], S. P. Sovilj[2]

[1]*Department of Chemistry, Faculty of Natural Sciences and Mathematics, University of Priština, 38220 Kosovska Mitrovica, Serbia (bedpet@sezampro.rs)*
[2]*Faculty of Chemistry, University of Belgrade, P.O. Box 118, 11158 Belgrade, Serbia*

Abstract
The complexation reactions between octaazamacrocyclic ligand N,N',N'',N'''-tetrakis(2-pyridylmethyl)-1,4,8,11-tetraazacyclotetradecane (*tpmc*) and Co^{2+}, Ni^{2+}, Zn^{2+}, Cu^{2+}, Ag^{+} and Cd^{2+} metal cations have been studied conductometrically in acetonitrile and aqueous solution. The conductance data show different stoichiometry of the complexes in two studied solutions. Mostly, complexes were formed in molar ratio of 1:1 (ML) in both solutions, but in some cases 2:1 (M_2L) complexes are evident. The stability constants of the resulting 1:1 complexes were determined from computer fitting of the conductance/mole ratio data. The conductometric data and formation constants were compared with sensor behavior and selectivity of recently reported *tpmc* based ISE [1]. The study also should contribute to better explanation of very good selectivity of this ISE.

Introduction

The octaazamacrocyclic ligand *tpmc* with four 2-pyridylmethyl pendant groups (N,N',N'',N'''-tetrakis(2-pyridylmethyl)-1,4,8,11-tetraazacyclotetradecane) as a macrocyclic flexible ring through coordination provides interesting structural and chemical properties [2]. In that respect the ligand should be capable to accommodate a wider variety of cations and form relatively stable complexes. Still, the most of synthesized complexes are dinuclear Cu(II)/*tpmc* complexes, which in addition to *tpmc*, also contain different bridged ligands and small number of some dinuclear cobalt(II) complexes [3a,b].

Therefore, the conductometric study of formation complexes between *tpmc* ligand and different metal ions can contribute to gain new information's concerning the transport phenomena of the ligand–electrolyte complex in the solution, stoichiometry of the reactants and solvent nature impact on complexation process. The selectivity phenomena of binding ligand toward different ions were crucial fact for functioning of ion-selective electrodes. The goal of this work is also to try to find which of copper(II) complexes is responsible for sensor activity of *tpmc* based ion selective membrane and more clarify its sensor properties.

Experimental

The conductometric procedure. acetonitrile or aqueous solution of 1.0×10^{-4} M nitrate salt of examined ions was placed in a titration cell and the conductance of the solution was measured. Then the *tpmc* concentration was increased by adding the ligand solution (5×10^{-3} M) in aliquots of 0.05 cm^3 to the titration cell and the conductance of the resulted solution was measured after each step at the desired temperature. All measurements were done in the solutions adjusted thermostatically to 23 ^{0}C with constant stirring. A conductometric cell with a cell constant of 0.60 cm^{-1} was used throughout the studies. The complex formation constant and the molar conductance of complex were obtained by computer fitting of the molar conductance-mole ratio data to the appropriate equations [4] using a nonlinear fitting with Matlab.

Results and Discussion

The molar conductances versus ligand/cation mole ratio plots for *tpmc* complexes with examined cations are shown in Figs. 1. and 2. As is seen, addition of *tpmc* to Co^{2+}, Ni^{2+}, Zn^{2+}, Cu^{2+} and Cd^{2+} cations in AN at constant temperature results in an increase in molar conductivity because of more mobility of these *tpmc* caton complexes toward free solvated cations in question, while in aqueous solution opposite situation is observed. When the donor properties of the solvent are low, as in case of acetonitrile, cations are poorly solvated and can easily be complexed by the *tpmc* and formation constants of complexes are higher. The most of cations formed relatively stable mononuclear complexes in both media, while dinuclear complexes are evidenced for Zn^{2+} always, and Cu^{2+} and Ag^{+} only in aqueous solution.

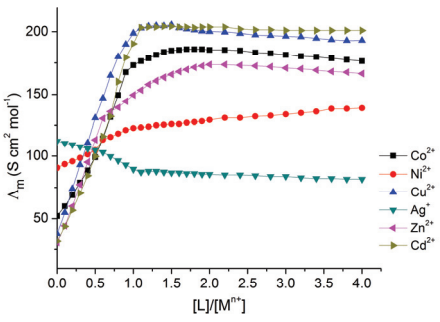

Figure 1. Plot of molar conductance, Λ, vs. V (cm^3 of added ligand) for the binding of Co^{2+}, Ni^{2+}, Zn^{2+}, Cu^{2+}, Ag^{+} and Cd^{2+} by *tpmc* in acetonitrile at 23 ^{0}C.

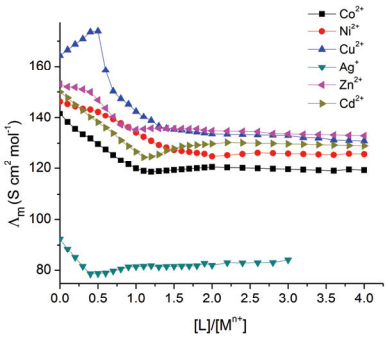

Figure 2. Plot of molar conductance, Λ, vs. V ($cm^3$of added ligand) for the binding of Co^{2+}, Ni^{2+}, Zn^{2+}, Cu^{2+}, Ag^{+} and Cd^{2+} by *tpmc* in aqueous solution at 23 ^{0}C.

Recently developed *tpmc* based copper-selective electrode exhibits very good selectivity toward many studied cations. The rate of selectivity coefficients

for these cations was 10^{-3}-10^{-4} except for silver ion which strong interferes due to its interaction with polymer matrix itself [5]. From conductometric results and formation constants for assumed stoichiometry of 1:1 (Table 1), it is obvious that such selectivity is not based on stability of mononuclear copper/*tpmc* complex. The most likely, the good selectivity of electrode was derived from formation of dinuclear copper/*tpmc* complex, the most conductive of all of examined complexes.

Table 1. Formation constants (K_{ML}) and molar conductance (Λ_{ML}) of different M^{n+}/tpmc complexes in acetonitrile and aqueous solutions.

Cations	Acetonitrile		Aqueous solution	
	$\log K_{ML}^{(SD<0.1)}$	Λ_{ML}	$\log K_{ML}^{(SD<0.1)}$	Λ_{ML}
Co^{2+}	>7	176.4	6.4	119.2
Ni^{2+}	4.1[a]	188	b	b
Cu^{2+}	>7	193.1	4.9[c]	130.5
Zn^{2+}	b	b	b	b
Ag^{+}	5.6[c]	88.4	b	b
Cd^{2+}	>7	201	>7	125.5

a – value is less certian, assumed stoichiometry taken into calculations did not give a good fit
b – data can not be fitted to equations
c – first data points conditioned by forming dinuclear complexes are not considered in fitting

Conclusion

Solvent properties were considered as the major factors influencing the formation constants of *tpmc*–cation complexes. The nature of the solvent also favoured type of stoichiometry of complexes. Conductometric results suggests that dinuclear complex is main carrier of ISE potentiometric response and provides faster ion exchange at the membrane/aqueous solution interface.

Acknowledgement

Financial support for this study was granted by the Ministry of Science and Technological Development of the Republic of Serbia, Project Number 45022.

References

[1] B. B. Petković, S. P. Sovilj, M. V. Budimir, R. M. Simonović, V. M. Jovanović, Electroanalysis, 2010, 22, 1894.

[2] J. Costamagna, G. Ferraudi, B. Matsuhiro, M. Campos-Vallete, J. Canales, M. Villagran, J. Vargas, M. J. Aguirre, Coord. Chem. Rew., 2000, 196, 125.

[3] a) E. Asato, H. Toftlund, S. Kida, M. Mikurya, K. Murray, Inorg. Chim. Acta, 1989, 165, 207; b) S. P. Sovilj, N. Avramović, N. Katsaros, Trans. Metal. Chem., 2004, 29, 737.

[4] Gh. H. Rounaghi, A. Soleamani, K. R. Sanavi, J. Incl. Phenom. Macro, 2007, 58, 43.

[5] D. M. Sejmanović, B. B. Petković, M. V. Budimir, S. P. Sovilj, V. M. Jovanović, Electroanalysis, 2011, 23, 1849.

M-02-P

CYTOTOXIC ACTIVITY OF AZAMACROCYCLIC Cu(II) DICARBOXYLATE COMPLEXES

M. Antonijević-Nikolić[1], G. Vučković[2], S. B.Tanasković[3], J. Antić-Stanković[3], V. Živković-Radovanović[2]

[1]*Higher Technological School of Professional Studies, 15000 Šabac, Serbia*
[2]*Faculty of Chemistry, University of Belgrade, P.O.Box 118, 11158, Serbia*
[3]*Faculty of Pharmacy, Vojvode Stepe 450, 11000 Belgrade, Serbia*

Abstract
Cu(II) complexes with *N,N′,N″,N‴*-tetrakis (2-pyridylmethyl) -1,4,8,11–tetraazacyclotetradecane (tpmc) and dianion of one the aliphatic dicarboxylic acids: butanedioic (succinic acid = $succH_2$), pentanedioic (glutaric acid = $glutH_2$), hexanedioic acid (adipic acid = $adipH_2$) and decanedioic acid (sebacic acid = $sebH_2$) having general formula $[Cu_4(L)(tpmc)_2](ClO_4)_6 \cdot xH_2O$, L=succ (**1**) or glut (**2**), x=2; L=adip, x=7 (**3**); L=seb, x=6 (**4**) were isolated and screened for cytotoxic activity along with free ligands and simple Cu(II) salt as control. They were tested on four human cancer cell lines *in vitro*. In some cases detected activities for the complexes were enhanced compared with the corresponding controls.

Introduction
In literature many reports highlighted the application of transition metal complexes as anticancer agents [1]. Copper is crucial for human life as a component of enzymes and proteins. Furthermore, some of copper(II) complexes were found with anti-inflammatory, antiulcer, anticonvulsant, antiamoebic, antidiabetic, antimicrobial and antitumor activities [2]. A number of *in vivo* studies have indicated that biologically active compounds become more bacteriostatic and carcinostatic upon chelatation [3]. In addition, Cu(II) complexes with *N,N′,N″,N‴*-tetrakis(2-pirydilmethyl)-1,4,8,11-tetraazacyclotetradecane (tpmc) and some of the secondary ligands (aliphatic/aromatic mono- and dicarboxylates or aminocarboxylates) exhibited antibacterial activity *in vitro.*

Previously we described tetranuclear Cu(II)tpmc complex with succinato dianion as bridged ligand which structure is determined by X-ray analysis [4a]. By using somewhat modified procedures, we prepared related complexes containing glutarato, adipato and sebacinato ligands [4b]. In this work, cytotoxic activity of all 4 complexes is tested and considered.

Results and discussion
Based on solved X-ray analysis of succinato complex **1** [4a] and analogy of the analytical and spectral properties of the complexes **2**-**4** it is proposed the same structure of the complex cation presented in figure 1.

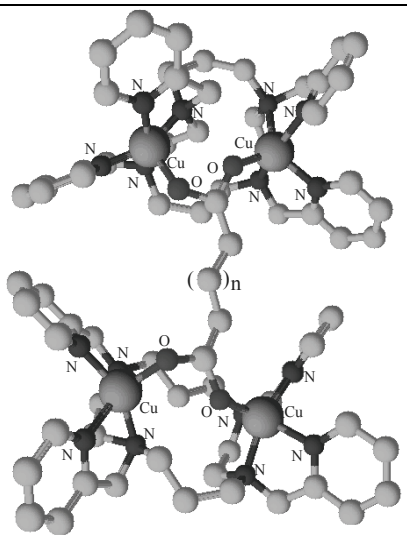

Figure 1. The presentation of the complex cation $[Cu_4(L)(tpmc)_2]^{6+}$ (L= succ, glut, adip, seb ligands) within complexes **1-4;** n=0-2, or 6.

The cytotoxic effects of the complexes were examined on 4 human tumor cell lines: estrogen-receptor-positive human breast cancer (MCF-7), human cervix adenocarcinoma (HeLa), human malignant melanoma (Fem-x) and human acute monocytic leukemia (THP1) cells. Stock solutions of the test complexes **1-4** and controls were made in DMSO and diluted for use in the nutrient medium (RPMI 1640 without phenol red, supplemented with L-glutamine, streptomycin, penicillin, fetal bovine serum and HEPES, adjusted to pH 7.2) The cells were treated with the appropriate amounts of compounds of interest or corresponding vehicle (control cells), then seeded in duplicate in 96 well plates. MTS test was used to assess the metabolic activity. Significantly different values from control (vehicle-treated cells) are denoted: *P≤0.05, **P≤0.01, ***P≤0.0001. The obtained cytotoxic properties of the complexes are presented in Figure 2. Ligands and $Cu(ClO_4)_2 \cdot 6H_2O$ used as controls were inactive under the studied conditions, while all complexes have promoted significant decreases in the viability of the tested cells, which occurred in a dose-dependent fashion. It is obvious that in general going from complex **1** containing μ-succ to complex **4** with μ-seb ligand with increasing the number of $–CH_2-$ groups in dicarboxylate the cytotoxic activity also increase. This is in accordance with the fact that cell membranes are liposolubile, so the complex with higher degree of hydrophobic properties more easily penetrates inside the cell.

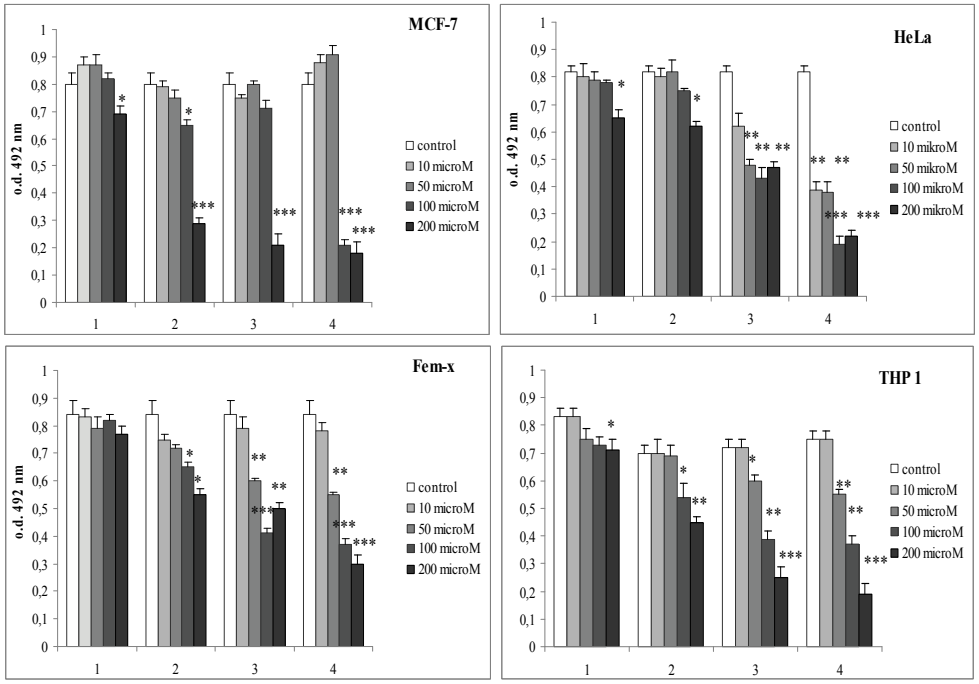

Figure 2. Results of MTS test.

Conclusion

Tetranuclear cationic octaazamacrocyclic Cu(II) complexes with α,ω-dicarboxylates were screened to cytotoxic activity on four human cancer cell lines *in vitro*. The obtained results indicate that the tested complexes have a considerable activity upon the evaluated cell lines in a concentration-dependent matter. These are the first examples of the numerous up to now described metal tpmc complexes which citotoxicity is considered.

References

[1] A. C. Barve, S. Ghosh, A. A. Kumbhar, A. S. Kumbhar, V. G. Puranik, Transition Met. Chem. 2005, 30, 312–316.

[2] M. Buczkowska, A. Bodtke, U. Lindequist, M. Gdaniec, P. J. Bednarski, Arch. Pharm. Chem. Life Sci. 2011, 344, 605–616.

[3] Z. H. Chohan, M. Arif, M. A. Akhtar, C. T. Supuran, Bioinorg. Chem. Appl., 2006, 2006, 1-13.

[4] a) G. Vučković, M. Antonijević-Nikolić, T. Lis, J. Mroziński, M. Korabik, D. D. Radanović, J. Mol. Struct., 2008, 872, 135-144; b) S. B. Tanasković, M. D. Antonijević-Nikolić, G. N. Vučković, 44th Meeting of the Serbian Chemical Society, Belgrade, 2006, Book of Abstracts 55, NH-P03, Proceedings 117-120, in extenso; M. D. Antonijević-Nikolić, S. B. Tanasković G. N. Vučković, 45th Meeting of the Serbian Chemical Society, Novi Sad, 2007, Book of Abstracts 73, NH1, Proceedings 194-197, in extenso; S. B. Tanasković, M. D. Antonijević Nikolić, G. N. Vučković, 46th Meeting of the Serbian Chemical Society, Belgrade 2008, Book of Abstracts 65, NH-01.

M-03-P

COMPLEX OF IRON(II) WITH POTASSIUM 3-DITHIOCARBOXY-3-AZA-5-AMINOPENTANOATE DIHYDRATE

S. R.Trifunović[1], D. Bulatović[2], M.Kosović[2], Z. Leka[2]

[1]*Department of Chemistry, Faculty of Science, Universtity of Kragujevac,R.Domanovica, P.O. Box60, Kragujevac, Serbia (e-mail: srecko@kg.ac.rs),* [2]*Faculty of Metallurgy and Technology, University of Montenegro, Cetinjski put bb, 81 000 Podgorica, , Montenegro (e-mail:* zorica@ac.me)

Abstract

The complex of iron(II) with dithiocarbamato ligand, potassium-3-dithiocarboxy-3-aza-5-aminopentanoate dihydrate, Kdaap·$2H_2O$,was synthesized and characterized by elemental analysis, infrared and electronic absorption spectroscopy and by measuring the magnetic moment. The spectral data suggest tridentate coordination of $daap^-$ ligand with Fe(II) ion *via* two nitrogen atoms (amino and imino group) and oxygen atom from carboxylic group.

Introduction

A large number of transition metal complexes with dithiocarbamates are known where metal ions are in different oxidation states. The neutral complexes of the type $M(dtc)_x$, where x is the number of dithio related ligands, found wide application in agriculture, medicine and vulcanization [1]. Dithiocarbamates contain sulfur, nitrogen and oxygen donor atoms as ligators atoms forming complex compounds with transition metals. Coordination of transition metal with dithio-ligands is done the most frequently *via* two sulfur atoms the so-called bidentate coordination, forming four-membered chelate ring. Some dithiocarbamato-ligand is possible bind *via* the nitrogen and oxygen atoms. For heavy metal complexes with dithio-ligands four geometric structures can be assumed: a square-planar, tetrahedral, trigonal or octahedral, depending on the coordination number of the central metal ion.

The previously synthesized and described potassium-3-dithiocarboxy-3-aza-5-amino-pentanoate dihydrate (Kdaap·$2H_2O$), as uncoordinated ligand contains deprotonated carboxyl group while is dithio group protonated [2]. The $daap^-$ ligand can coordinate as bidentate *via* two sulfur atoms, forming four-membered chelate ring or as a tridentate *via* nitrogen atoms from amine and imine group and oxygen atoms from carboxylic group, building two five-membered rings. In the previously synthesized and described complexes of Cu (II), Ni (II), Zn (II), Cd (II), Pt (II) and Pd (II), the $daap^-$ ligand was coordinated through the sulfur atoms [3,4].

The aim of this work is the synthesis and physico-chemical characterization of Fe(II)-daap complex by elemental analysis, IR and UV spectroscopy and magnetic moment measurements.

Experimental

The ligand, K-daap·$2H_2O$, was synthesized as it described earlier [2].

Preparation of bis (3-dithiocarboxy-3-aza-5-aminopentnoato)-iron (II), Fe(daap)$_2$

Iron(II) bis-dithiocarbamate was obtained by direct reaction of Fe(II) and K-daap ligand in 1:2 molar ration.. Aqueous solution of 1 mmol (0.278 g) $FeSO_4 \cdot 7H_2O$ was slowly added to aqueous solution of 2 mmol (0.536 g) K-daap with stirring at room temperature for half an hour. During mixing the brown solid was precipitated and separated by filtration, washed with H_2O and acetone and finally dried in air.

Analytical Methods

Elemental analisys C, H, N and S are performed using the standard method, with the Vario III CHNOS Elemental Analyzer, Elemental Analysensysteme GmbH. Fe analysis was performed by atomic absorption spectrometry using the Perkin-Elmer spectrophotometer, Model 1100-B.

IR spectrum in the 4000-400 cm^{-1} region was recorded on FTIR 8700 (Shimadzu) spectrophotometer using the KBr disc.

UV-VIS spectrum in the 200-440 nm region was recorded using the buck scientifik 105 UV-VIS spectrophotometer.

The magnetic moment was determined at room temperature using a MSB-MKI magnetic susceptibility balance, Sherwood Scientific Ltd., Cambridge.

Results and discussion

The complex Fe(II)dtc was synthesized from Fe(II) salt and polydentate dithiocarbamate, K-daap·$2H_2O$, in the molar ratio 1:2 at room temperature. This complex is air-stable and obtained in high yield. The assumed formula of the obtained complex is $[Fe(OOCCH_2N(CSSH)CH_2CH_2NH_2)_2]\cdot 3H_2O$. The results of elemental analysis (Table 1) confirm the composition of the complex in the stoichiometric ratio of metal: ligand = 1:2, while the IR spectrum can confirm the structure of complex. The obtained complex was dark brown, stable at room temperature, slightly soluble in water. In the IR spectrum of Fe(daap)$_2$·$3H_2O$ dithiocomplex all major bands characteristic for the dithiocarbamate complexes are observed (Table 2). Pronounced singlet at 948 cm^{-1} induced by vibration of C-S bond, confirms the equivalence of sulphur atoms in the dithio group (CSS^-) [5]. The presence of band at 2634 cm^{-1} represents the characteristic for protonated S-H group, which indicates that the metal is not tied to the ligand *via* sulphur atoms [5]. On this basis it can be assumed that the metal coordinated with ligand *via* oxygen atoms from carboxyl groups and two nitrogen atoms of amino and imino groups. The band in the area of 524 cm^{-1} can be attributed to vibration of Fe-N bond, and band at 470 cm^{-1} to vibration of Fe-O bond [6]. The absence of the band in the region 1700-1750 cm^{-1} indicates the deprotonated carboxyl group of the resulting complex, which also can be confirmed by the bands at 1589 cm^{-1} and 1411 cm^{-1} of asymmetric and symmetric vibration of carboxyl groups [5]. The broad band at 1589 cm^{-1} suggests overlapping COO^- and N-C bands. In the IR spectrum of the complex the wider band spears at 3408 cm^{-1} which can be attributed to vibrations of OH-group [5].

Two absorption bands which lie in the range of 200-400 nm of ectronic absorption spectrum can be attributed to d-d transition and the charge transition (with Fe^{2+} in nitrogen) M → L [7].

By measuring the magnetic moment at room temperature a diamagnetic d^6 low-spin complex Fe^{2+} was determined and according that the octahedral structure can be assumed.

In the complex with the central metal ion of small electronegativity (as Fe^{2+}) the stability of the complex increases in the series of ligand donor atoms O<N>S> P. Thus, Fe^{2+} as the transition acid (between hard and soft) will be coordinated via N rather than via S atoms.

Table 1. Elemental analysis data of the complex.

Epirical formula	Formula weight [g/mol]	Yields [%]	Found (Calcd.) [%]				
			C	H	N	S	Fe
$Fe(daap)_2 \cdot 3H_2O$ $FeC_{10}H_{24}N_4S_4O_7$	496	81,59	25,00 (24,20)	4,72 (4,84)	11,15 (11,29)	26,01 (25,80)	10,60 (11,29)

Table 2. Important IR bands (cm^{-1}) for the free ligand and its iron (II)complex.

Compound	COO^-		CSS^-		S-H	N⋯C	OH^-	Fe-O	Fe-N
	ν_{as}	ν_s	ν_{as}	ν_s					
K-daap$\cdot 2H_2O$	1597	1414	963	635	2631	1453			
$Fe(daap)_2 \cdot 3H_2O$	1589	1411	948	644	2634	1589	3408	470	524

Conclusion

In obtained Fe(II) complex, dithiocarbamato ligand, $daap^-$, acts as tridentate ligand and coordination takes places via O atom of the –COO group, N atom from NH_2 group and imino N atom, resulting in octahedral diamagnetic $Fe(daap)_2$ complex.

References

[1] G. Pandey, K. K. Narang, Bioinorganic Chem.istry and Applications, 2005, 3, 3-4.

[2] B. Prelesnik, K. Andjelković, Z. Marković, T. Sabo, S. R. Trifunović, Acta Cryst. 1997, C53, 719.

[3] S R. Trifunović, Z. Marković, D. Sladić, K. Andjelković, T. Sabo, D. Minić, J. Serb. Chem. Soc., 2002, 67, 115.

[4] Z. Leka, S. A. Grujić, S. Lukić, S. Skuban, S. Trifunović, J.Serb.Chem.Soc. 2004, 69(2),137– 143.

[5] K. Nakamoto, Infrared Spectra of Inorganic and Coordination Compounds,Wiley, New York, 1970.

[6] S. A. Shaker,Y. Farina, A. A. Salleh, European Journal of Scientific Research 2009, 33(4), 702-709.

[7] A. B. P. Lever, Inorganic Electronic Spectroscopy, Mir, 1987.

M-04-P

MALDI TOF OF ALUMINIUM FLUOROQUINOLONE COMPLEXES

M. Cvijovic[1], P. Djurdjevic[1], P. Traldi [2], B. Nastasijevic[3], J. Zvezdanovic [4]
[1]*University of Kragujevac, Faculty of Science, Chemistry Department, 34000 Kragujevac, Serbia*
[2]*CNR –ISTM,35127 Padova, Italy,*
,[3]*Department of Physical Chemistry,Vinca Institute of Nuclear Sciences, University of Belgrade, P.O.Box 522,11001Belgrade,Serbia,*
[4]*University of Nis, Faculty of Technology, 16000 Leskovac, Serbia*

Abstract
Mass spectral studies of aluminium fluoroquinolone complexes provided information about species formed in these systems, especially polinuclear species. Metal complexation as means of ionization has been undertaken by ion-molecule reaction involving laser-desorbed metal ions. The formation of FQLs –aluminium ion is effected when the antibiotic loses the acidic proton from carboxylic acid moiety and proceeds to form a covalent bond with metal ion. The most favour binding site is negatively charged oxygen. The administration of drugs which may contain aluminium (III) ion (antacids, phosphate binders, vaccines, etc) may form metal – FQLs complexes. This reaction leads to altered bioactivity of the drug and/or developing aluminum toxic effects.

Introduction
Fluoroquinolones (FQLs) are synthetic antibacterial agents that inhibit the bacterial DNA gyrase and DNA regulation activity [1] . These broad –spectrum antibiotics have been clinically used for several types of infections which include urinary tract infections, skin and soft tissue infections and respiratory tract infections
The complexation has been investigated for fleroxacin, moxifloxacin and ciprofloxacin with aluminium in solutions by equilibrium technique and ESI. Polymerization was not observed by these techniques and owing to importance of such reactions it has been studied by LDI Mass Spectrometry.

FQLs are small molecules and to avoid saturation by matrix ions signals it has been used LDI-MS measurements instead MALDI.

Experimental
LDI-MS measurements were performed using a MALDI-TOF TOF UltrafleXtreme time-of-flight mass spectrometer (Bruker Daltonics, Bremen, Germany), equipped with 1 kHz smart-beam II laser Nd Yag (l=355 nm) and operating in the positive reflectron ion modes.

The instrumental conditions employed to analyze molecular species in the m/z range 50-3000 in positive ion mode were: ion source 1 voltage: 25.00 kV; ion source 2 voltage: 22.30kV, lens voltage: 7.70kV, pulsed ion extraction time: 80 ns, reflector voltage: 26.45 kV, and reflector 2 voltage: 13.45 kV.The data aquisited by Flex Analysis Bruker Daltonics Software.

Results and Discussion

In the interest of maximizing the abundance of the signal generated by the metal complexes, the effect of the pH of the solution on the formation of the metal complexes was investigated. The most representative spectra are for metal to ligand concentration ratio 2:1 to 1:3 (C_{Al} =2.5x 10^{-5} mol/L) in the pH range 3.0 to 6.0. [2] The MALDI spectra for aluminium and ciprofloxacine system are shown in Fig.1 and Fig. 2. Identified dimer species [AL_2L_5] by MALDI are: for fleroxacin *m/z* 1894.7, moxifloxacin *m/z* 2054.3 and for ciprofloxacin *m/z* 1703.8. These species have not been identified in solutions so probably these species are consequences of cluster formation. From coordination chemistry point of view the coordination of two metal ions with 5 ligands is not probable. The clusters with more deprotonated ligands can form in gas phase, *i.e.* in the plume generated by laser irradiation.

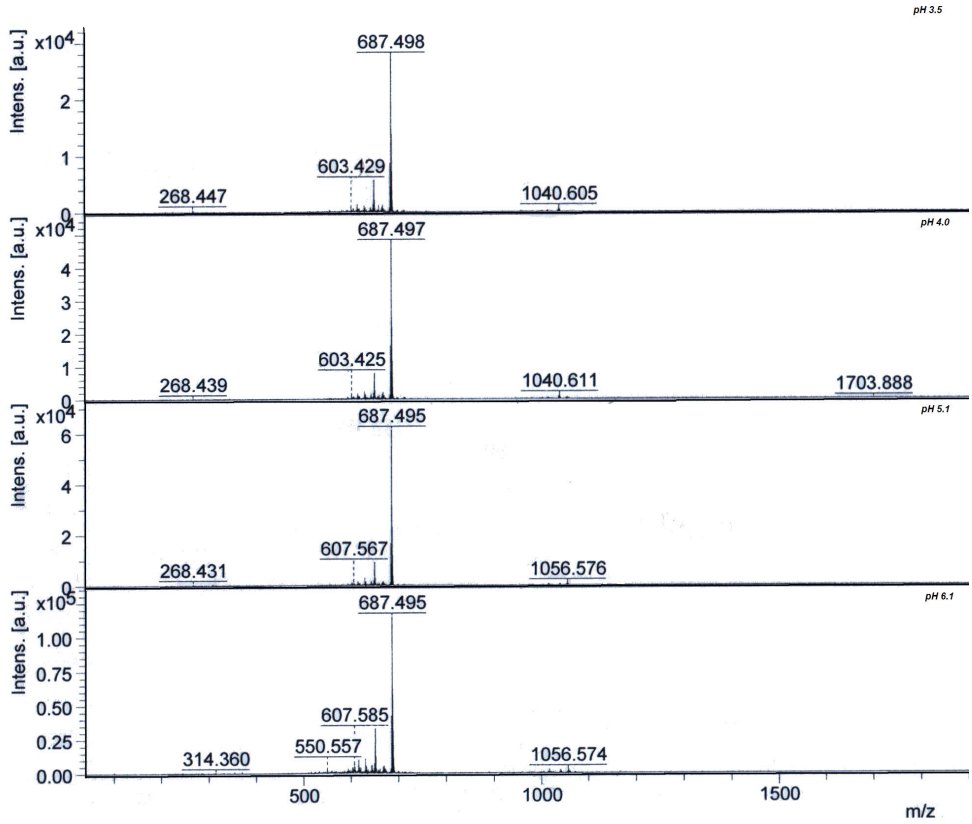

Figure. 1. LDI spectra of aluminium and ciprofloxacine systems for different pH values.

In this figure it is seen complex AlL, AlL_2 and AlL_3 species , but also polimer Al_2L_5 H values.

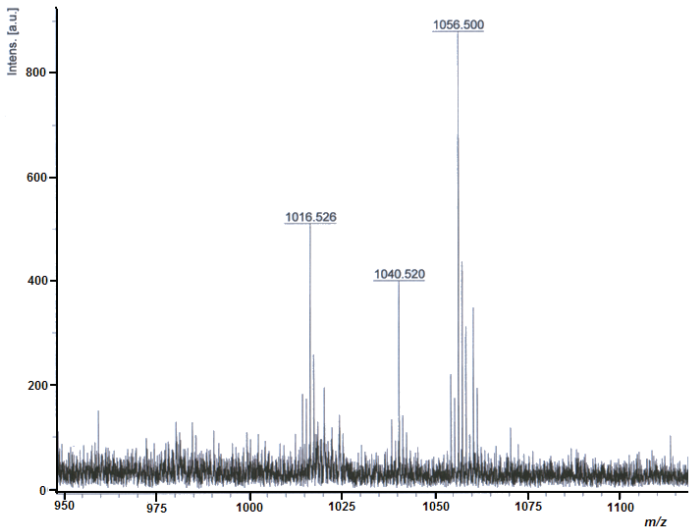

Figure 2. LDI spectrum of aluminium and ciprofloxacine system, zoom area for adduct ions with Na for *m/z* 1040 and adduct with K for *m/z* 1056.

Conclusions

The identified dominating species, characteristic for solutions of Al^{3+} and each of the three examined antibiotics (fleroxacin, moxifloxacin and ciprofloxacin), were the binary complexes AlL, AlL_2 and AlL_3 whose abundance was pH dependent. At pH range pH 4−6,the signal for the (L + H)+ ions decreases as some percentage of the quinolones deprotonate and the metal complexation begins to dominate. This is in agreement with previous ESI MS investigation of these systems. Polymerization of Aluminium – Fluorquinolone complexes may proceed in the gas phase accompanied by further clustering with deprotonated ligands. LDI indicated the formation Al_2L_2 core. The interaction between FQLs and Al^{3+} in the gastrointestinal tract should be considered with attention by biomedical point of view. Neutral complexes may permeate the membrane [3] and lead to Al toxicity.

References

[1] P. G. Higgins, A. C. Fluit, F. J. Schmiz, Curr. Drug Targets, 2003, 4, 181-191.

[2] Y. Kawai, K. Matsubayashi, H. Hakusui, Chem. Pharm. Bull.,1996, 44, 1425-1430.

[3] S. Mazzaferro, I. Perruzza, S. Constantini, M. Pasquali, L. Onorato, D. Sardella, R.Giordano, L. Ciaralli, P. Ballanti, E.Gonucci, A. G. Cinotti, G. Coen, Nephrol. Dial. Transplant., 1997, 12(12), 2679-2682.

M-05-P

COBALT(II)-REDUCED DEXTRAN COMPLEXES CHARACTERIZATION BY ELECTRONIC SPECTROSCOPY

Ž. Mitić[1], M. Cakić[2], G. M. Nikolić[1], A. Veselinović[1], Lj. Ilić[3]
[1]*Faculty of Medicine, University of Niš, RS-18000 Niš, Serbia*
e-mail: zak_chem2001@yahoo.com
[2]*Faculty of Technology, University of Niš, RS-16000 Leskovac, Serbia*
[3]*PCI "Zdravlje", RS-16000 Leskovac, Serbia*

Abstract
The cobalt(II) ion complex formation with reduced low-molecular dextran (RLMD) was investigated by electronic (UV–Vis) spectroscopy, and formation of Co(II)–RLMD complexes was observed at pH 7.0–13.5. With increase in solution pH the light absorbance maxima of complex solutions show red shift compared with $[Co(H_2O)_6]^{2+}$ ion. Increase and appearances of the preponderance of absorbance maxima (510, 581 and 628 nm) at pH higher than 13.5 have been connected with the decomposition of Co(II)–RLMD complex next to $[Co(OH)_6]^{4-}$ ion. Thus, these spectrophotometric criteria can be applied for the confirmation of the success of complex synthesis. The spectrophotometric parameters of the synthesized Co(II)–RLMD complexes are characteristic for Co(II) ion in octahedral (O_h) coordination.

Introduction

Dextran is exopolysaccharide described as a α-(1→6) linked polymer of α-D-glucopyranose units. The numerous investigations have indicated that the polysaccharide dextran and its derivatives have the extraordinary power to forming the water-soluble complexes with various biometals [1–3]. Reduced low-molecular dextran, was chosen as a new material for complexing, and the subsequent interactions with Co(II) ions by electronic spectroscopy were investigated in this study. Electronic spectroscopy can get the relatively reliable information about the ligand arrangement in transitional metal complexes. Co(II) ion builds numerous complex compounds with the different geometric structure, such as tetrahedral (T_d), square-planar (D_{4h}), and octahedral (O_h). The major goal of this work is to use electronic (UV–Vis) spectroscopy to verify the coordination of this type of Co(II) ion complexes.

Experimental

Co(II) ion complex synthesis with RLMD has been described in detail by Mitić et al. [4]. Vis spectra of the water solutions of the complexes were recorded on a VARIAN Cary-300 UV–Vis spectrophotometer, in the wavelength range of 400–900 nm with wavelength accuracy ± 0.2 nm, in quartz cells (1×1 cm) at room temperature with redistilled water as a reference.

Results and Discussion

Depending on pH, Co(II)–RLMD complexes behave differently considering the wavelength at which they show absorbance maxima. This range of wavelengths in the Vis spectra is 583–624 nm (Fig. 1). Bathochromic shifts of the absorbance maxima of the complexes with increasing pH, confirm the presence of different types of complexes. The reddish $[Co(H_2O)_6]^{2+}$ ion absorbs at 512 nm, while the synthesized complexes absorb within the range 583–624 nm. With increase in solution pH, the absorbance maxima shift to longer wavelengths compared with the $[Co(H_2O)_6]^{2+}$ ion.

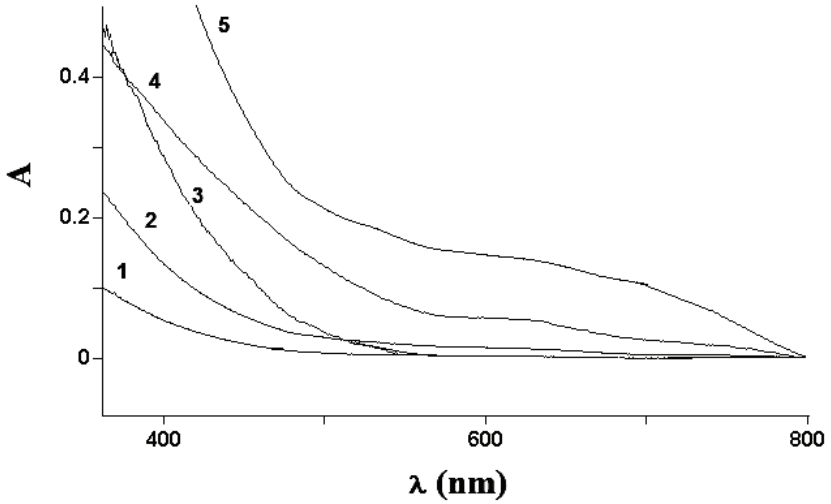

Figure 1. Vis spectra of Co(II)–RLMD complexes were synthesized at pH 7.5(1), pH 11.0 (2), pH 12.0 (3), pH 13.0 (4) and pH 13.5 (5)

In octahedral surroundings of the ligands Co(II) ion builds complex compounds with the coordination number six which can have one from two possible d^7 configurations: high-spin $t_{2g}^5 e_g^2$ with weak-field ligands, or low-spin $t_{2g}^6 e_g^1$ with strong-field ligands. High-spin Co(II) complexes with weak-field ligands; weak Jahn-Teller effect is expected according to the Jahn-Teller theorem [5], complexes are octahedral with tetragonal distortion. Wide absorption bands in the Vis spectra of synthesized Co(II)–RLMD complexes, are the result of preponderance of allowed transitions close by the energy, which manifests like the unique asymmetric absorption band. In the area of wavelength around 500 nm, absorption spectra of the high-spin Co(II) ion complexes in weak-field ligands, with configuration $t_{2g}^5 e_g^2$ and coordination number six were registered. Absorbance maxima, because of the synergistic effect, shift to the red region of Vis spectrum (bathochromic effect). Strengthening of the metal-ligand bond (Co–O) diminishes the splitting energy of d-levels, absorbance maxima shift to larger wavelengths (curve 1–5, Fig. 1). Increase and appearances of the preponderance of absorbance maxima (510, 581 and 628 nm) at pH higher than 13.5 have been connected with the decomposition of Co(II)–RLMD complex next to $[Co(OH)_6]^{4-}$ ion. Thus, these

spectrophotometric criteria can be applied for the confirmation of the success of complex synthesis.

From the Vis spectra of Co(II)–RLMD complexes, which are synthesized under different reaction conditions, it was possible to see that the wavenumbers interval of the absorbance maxima is found to be from 16,026 to 17,153 cm^{-1}. The ligand crystal field splitting energies (Δ) are from 2.07 to 2.22 eV. According to literature data these energy values, have been found in the area of the energy which is characteristic of the octahedral ligand field (Δ_o) [6]. Co(II) complexes of organic molecules, such as carbohydrates, are known to adopt alternative coordination arrangements, particularly tetragonal and these exhibit distinct spectral properties in the Vis range resulting from Jahn-Teller distortion [5]. This points to the possibility that in the structure of the synthesized Co(II)–RLMD complexes, analogical with copper(II)-dextran complexes [3], Co(II) ions are probably in the octahedral or tetragonally distorted O_h surroundings (square-bipyramidal) with O atoms, which can originate from a ligand or solvent.

Conclusion

$[Co(H_2O)_6]^{2+}$ ion absorbs at wavelength 512 nm, while synthesized Co(II)–RLMD complexes absorb within the range 583–624 nm. With increase in solution pH, the absorbance maxima shift to longer wavelengths compared with the $[Co(H_2O)_6]^{2+}$ ion. The complex which is decomposed at pH over 13.5 shows the preponderance of absorbance maxima (510, 581 and 628 nm). The spectrophotometric parameters of the investigated complexes are characteristic of a Co(II) ion in the octahedral or tetragonally distorted octahedral coordination with O ligand atoms.

Acknowledgment

This work was realized within OI 172044 project, funded by the Ministry of Education and Science of the Republic of Serbia.

References

[1] Ž. Mitić, G. Nikolić, M. Cakić, R. Nikolić, Lj. Ilić, Russ. J. Phys. Chem., 2007, 81, 1433–1437.
[2] M. Cakić, Ž. Mitić, G. S. Nikolić, Lj. Ilić, G. M. Nikolić, Spectrosc. Int. J., 2008, 22, 177–185.
[3] Ž. Mitić, M. Cakić, G. M. Nikolić, R. Nikolić, G. S. Nikolić, R. Pavlović, E. Santaniello, Carbohydr. Res., 2011, 346, 434–441.
[4] Ž. Mitić, M. Cakić, G. Nikolić, Spectrosc. Int. J., 2010, 24, 269–275.
[5] H. Jahn, E. Teller, Proc. R. Soc. London, Ser. A, 1937, 161, 220–225.
[6] A. B. Lever, Inorganic Electronic Spectroscopy, 3rd Ed., Elsevier, 1986.

M-06-P

ANALYSIS OF COPPER-SALICYLIC ACID COMPLEXES BY ESI-MS

I.Kostić[1]*, T. Anđelković[1], D. Milojković[1], T. Cvetković[2], D. Pavlović[2], D. Anđelković[1]

[1]*Faculty of Sciences and Mathematics, University of Niš,Višegradska 33, 18000 Niš, Serbia*

[2]*Faculty of Medicine, University of Niš, Bulevar dr Zorana Đinđića 81, 18000 Niš, Serbia*

Abstract

Interaction of copper(II) with salicylic acid was investigated by electrospray-ionization mass spectrometry (ESI-MS). Quantification was performed by calculating the area of ESI-MS total ion current chromatograms of loop injection obtained by analyzing series of salicylic acid solutions and series of mixed copper-salicylic acid solutions. Compared series of studied systems of salicylic acid and copper(II), showed that with the increase of copper(II) concentration, peak area of salicylate ion in loop chromatogram decreases.

Introduction

Metal complexes play fundamental role in synthetic, biological, and catalytic processes in water and soil, even when they are present at very low concentrations. Determining the coordination structure of complexes at trace levels or in complex mixtures is a very difficult task.

Understanding environmental behavior of some heavy metals, such as Cu(II) in systems containing natural organic matter (NOM) requires knowledge of metal-NOM complexes. Salicylic acid is a commonly used model for NOM and has an aromatic nucleus and phenolic and carboxylic functional groups like humic acid.[1]

All investigated solutions were made in pre-washed polyethylene eppendorf tubes by dilution of concentrated stock solutions with the solvent methanol/water (50/50 v/v). All the obtained solutions were stored at +4°C and in dark place. The presence of 50% deionized water in the solvent is intended to facilitate protonation ESI processes and provide better ion yields.

Solutions of salicylic acid were analyzed by ESI-MS immediately after preparation. Mixed solutions of salicylic acid and copper(II) ion were analyzed after 30 minutes. ICIS© modul of *Xcalibur™ 1.3* software is used for calculating the areas of each ESI-MS total ion current chromatogram of 20 μL loop injection for the defined mass range of pure solutions of salicylic acid and mixed solutions of salicylic acid and copper(II). The areas are presented in absolute nondimensional units of *Xcalibur*™ software (*count–second units*) that have no physical meaning. [2, 3]

Results and Discussion

Semiquantification was performed by calculating the area of ESI-MS total ion current chromatograms of loop injection obtained by analyzing series of ligand solution and series of solutions of salicylic acid with copper(II) (Table 1 and Fig. 1).

Table 1. Values of peak area of salicylic acid without and with presence of copper(II) ion.

Concentration of salicylic acid (μM)	Peak area in mass range of salicylate ion (abs. units $\times 10^6$)					
	Cu (μM) 0	Cu (μM) 1	Cu (μM) 3	Cu (μM) 5	Cu (μM) 7	Cu (μM) 9
3	4.12	3.67	2.86	2.17	1.80	1.53
5	8.51	5.39	4.86	4.41	3.28	3.03
7	9.53	7.57	6.47	6.13	4.83	4.48
9	12.2	9.61	7.64	6.55	5.33	4.88

The quantification is based on the fact that all areas of chromatograms are in direct function of the peak intensities. In systems where there is interaction between salicylic acid and copper (II), the intensity of the observed characteristic ion is reduced. [4]

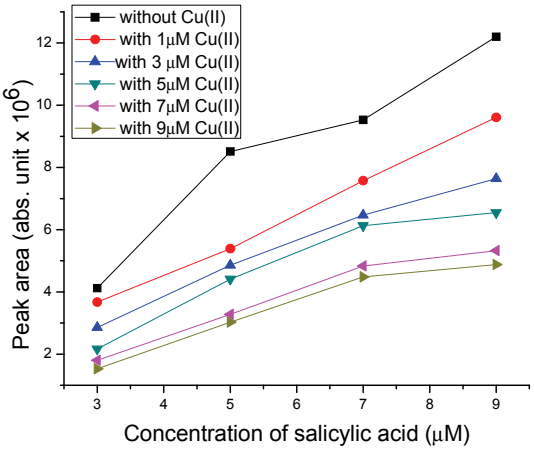

Figure 1. Concentration of salicylic acid *versus* peak area, for different concentrations of Cu(II).

This decrease is caused by coordination bonding or other interactions between copper(II) and salicylic acid and due to change the molecular and ionic composition of the sample. This leads to reduction of number of ions generated in the unit of time. In systems of salicylic acid with copper(II), for identical salicylic acid concentration, proportionally smaller area of chromatographic peak is

obtained, and the relative decrease in area can be related to the strength of the interaction of copper.

Conclusion

ESI-MS technique can be used for semiquantitative analysis of the system Cu(II)-salicylic acid. ESI-MS total ion current chromatograms of 20 μL loop injections of systems Cu(II)-salicylic acid, indicate a stabile peak and signal integrity. Comparing a series of studied systems of copper(II) with salicylic acid, the values of peak area shown that with increase concentration of copper(II) peak area of salicylate ion in loop chromatogram decreases.

Acknowledgements

This study was supported by the Ministry of Science and Technological Develoment of the Republic Serbia and was performed as a part of Project III 41018.

References

[1] I. Kostić, T. Anđelković, R. Nikolić, A. Bojić, M. Purenović, S. Blagojević, D. Anđelković, J. Serb. Chem. Soc., 2011, 76, 1325–1336.
[2] D. Anđelković, PhD Thesis, Faculty of Sciences and Mathematics, University of Niš, Niš, 2012.
[3] Y. Bai, F. R. Song, M. L. Chen, J. P. Xing, Z. Q. Liu, S. Y. Liu, Anal. Sci., 2004, 20, 1147-1151.
[4] Z. L. Cheng, K. W. M. Siu, R. Guevremont, S. S. Berman, J. Am. Soc. Mass Spectrom., 1992, 3, 281-288.

M-07-P

ESI-MS AND UV/VIS CHARACTERIZATION OF CHROMIUM(III)-2,2´-BIPYRIDINE INTERACTION

D. Milojkovic[1*], T. Andjelkovic[1], R. Nikolic[1], I. Kostic[1],
T. Cvetkovic[2], D. Pavlović[2], D. Andjelkovic[1]

[1]*Faculty of Sciences and Mathematics, University of Niš,Višegradska 33, Niš, Serbia*
[2]*Faculty of Medicine, University of Niš, Bulevar dr Zorana Đinđića 81, Niš, Serbia*
**Corresponding author: e-mail: dannica.milojkovic@gmail.com*

Abstract
Interaction of chromium(III) and 2,2-bipiridine was determinated by electrospray ionization mass spectrometry (ESI) and UV/VIS spectrophotometry. Obtained data show significant coordination interaction of chromium(III) and 2,2´-bipiridine, which is in accordance with ligand structure complexity. A new approach in semiquantitative determination of ligand in free form is applied, by obtaining Loop-chromatogram of Full Scan mode. ESI-MS characterization provides acquisition of mass spectra directly from solution, analyzing species in their native environment.

Introduction
2,2'-bipyridine (bipy) is characterized as a bidentate chelating ligand, which forms complexes with many transition metals, *i.e.* chromium. Bipy is widely used and has industrial applications and in agriculture as a pesticide in terms.
Complexes of Cr(III) with cordination number 6 and octahedral structure, are the most common and the most stable coordination compounds of chromium, thus their synthesis, crystal structure, stability, electronic spectra and photochemical and other characteristics are extensively studied.
Generally, the coordination properties and reaction pathways of chromium ion and bipy are complex, due to different electrohemical equilibrium states as Cr(II)/Cr(III), the coordination saturation of chromium with anions and molecules of matrix, redox conditions, *etc* [1].

ESI-MS has found application in coordination chemistry, therefore the study of the equilibrium interactions of metals and ligands in solutions. For a complete understanding of species equilibria in solution, it is necessary to know the number, the stereochemistry and stability constants of complex species that occur in a given system, that is usually obtained from spectrophotometry (UV/VIS) measurements.

All reagents used were *pro analysis* or HPLC grade purity. ESI-MS investigation was performed on LCQ Deca Ion Trap Mass Spectrometer (Thermo Finnigan, USA) with auxiliary equipment. UV/VIS characterisation was performed on SHIMADZU UV-1650PC with double beam.

Results and Discussion

Results of UV/VIS spectrophotometric determination of interaction of Cr(III) with bipy are shown in Fig. 1.

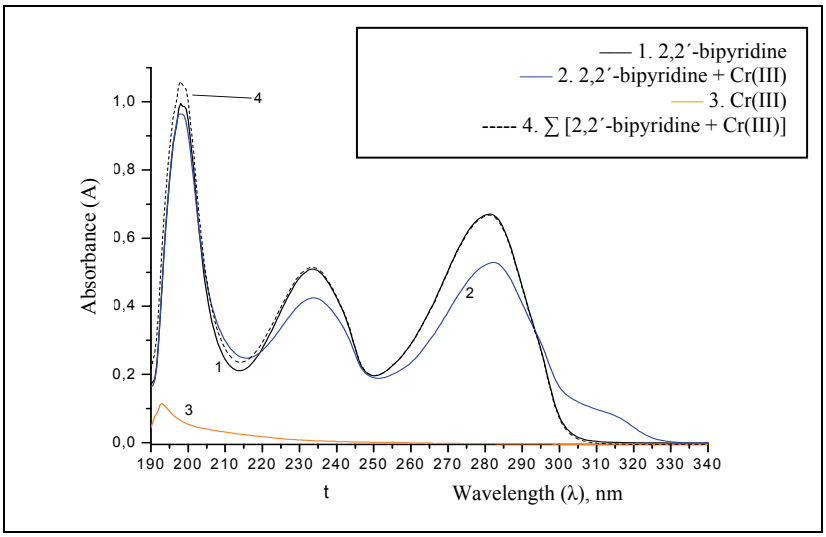

Figure 1. UV/VIS spectra of: (1) bipy, c = 11.43 μmol/L, (2) bipy, c = 11.43 μmol/L + Cr(III), c = 15.00 μmol/L, (3) Cr(III), c = 15.00 μmol/L and (4) the mathematical representation of the sum of independent spectra of bipy and Cr(III), solvent CH_3OH/H_2O = 50/50.

For the obtained spectral curves corresponding sub-integral area were calculated showing that the interaction exist in the system.

Molecular structure of nucleophilic bipy in the condition of ESI source allows the formation of protonated molecular ion, $[M+H]^+$ *m/z* 157, so the positive polarity mode was chosen (Fig. 2). The main ion *m/z* 157 (rel. int. 100%) is basic ion, and other ionic species have small signal intensity (rel. int. <13%). Isotopic patern corresponds roughly to the theoretically calculated. Optimization of operating conditions of the instrument – ESI sources and ion optics – was carried out according to ion *m/z* 157 of bipy [2]. Quantitative analysis of monocomponent system of bipy was performed by injecting precise volumes of solutions (20 μL) using a Loop device. ESI-MS Loop-chromatograms showed good form and integrity of the signal (Fig. 2), in the total ion current (TIC) for the observed range of *m/z* 156-158 [3].

Surface of the ESI-MS Loop-chromatograms peaks in the mass range *m/z* 156-158 for different concentrations of bipy was calculated using the algorithm ICIS (EXCALIBUR® program). Analogous experimental procedure and calculation of the surface of ESI-MS Loop-chromatograms peaks for different concentrations of solution of bipy and Cr(III) was done [4]. Difference of areas under peak chromatograms is a result of coordination interaction of bipy and Cr(III). Area obtained from the chromatogram of bipy in the presence of Cr(III) is

67.44% lower than the analogous chromatogram of bipy in the absence of Cr(III), which shows considerable coordination interaction of bipy and Cr(III).

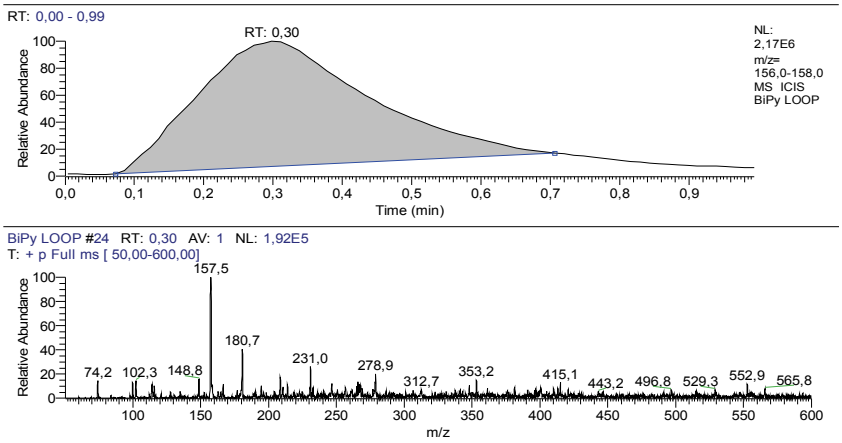

Figure 2. ESI-MS Loop-chromatogram of bipy; c = 1.057 μmol/L, solvent CH_3OH/H_2O = 50/50, positive ionisation mode, flow rate = 100 μL/min.

Conclusion

Loop-chromatogram technique can be used as a fast technique for obtaining data of type and extent of interaction between chromium(III) and bipy. Analysis of species in their native environment by soft ionization technique - ESI, provides conditions that allow acquisition of mass spectra directly from solution.

Acknowledgements

This work was supported by the Ministry of Science and Technological Develoment of the Republic Serbia and was performed as a part of Project III 41018.

References:

[1] J. Wang, K. Ashley, E. R. Kennedy et al., Analyst, 1997, 122, 1307-1312.
[2] F. Sahureka, R. C. Burns, E. I. Von Nagy Felsobuki, Inorg. Chim. Acta, 2002, 332, 7–17.
[3] A. R. S. Ross, M. G. Ikonomou, J. A. J. Thompson., K. J. Orians, Anal. Chem., 1998, 70, 2225–2235.
[4] D. Andjelković, PhD Thesis, Faculty of Sciences and Mathematics, University of Niš, Niš, 2012.

M-08-P

SPECTROPHOTOMETRIC DETERMINATION OF BORON IN COMPLEX WITH CURCUMIN – EFFECT OF $Ca(OH)_2$

O. A. Kovačević, S. Zlatanović,
B. T. Kovačević, S. Stanojlović

University of Belgrade, Institute of General and Physical Chemistry, Studentski trg 12/, P.O. Box 551, 11000 Belgrade, Serbia

Abstract
Analytical procedure that includes drying step in the preparation of the sample, after or within some acid treatment, boron has a pronounced tendency to adhere to vessel walls. The consequence is a great decrease of boron concentration in analyzed solution. Accordingly, the absorbance of the boron-curcumin complex formed in the corresponding solution is reduced. The addition of $Ca(OH)_2$ in the preparation process before the drying step, in an amount less than 0.05 g/mL of test boron solution (C_B=0.46 mg/L), allows retention of boron in the solution and/or its recovery to the aqueous solution. In this case, spectrophotometric determination provides real value of the boron content.

Introduction
Two boron-curcumin complexes, rubocurcumin and rosocyanin, were used for spectrophotometric determination of boron in the range from 0.1 to 1 mg/L [1-2]. In our experience, during drying step in the preparation of the sample, after or within some acid treatment, boron has a pronounced tendency to adhere to vessel walls. Then, the recovery of boron in solution is uncertain. In several analytical methods, a similar effect causes interference, known as the "memory effect" [2]. We found that the addition of $Ca(OH)_2$ in the systems allows the retention of boron in the solution and/or its recovery to the aqueous solution. Surface charge at solid/aqueous interface is pH dependent. At low pH they tend to be positively charged and negatively charged at high pH. Depending on the sign and magnitude of the surface charge an uptake of ionic species from solution occurs. At surface charge equals to zero, which is pH dependent, adsorbed ionic species was released [3]. According to the Pourbaix diagrams [4] boron species in aqueous solution are anionic, mainly $B(OH)_4$[-], $B_2O(OH)_5$[-] and $B_3O_3(OH)_4$[-]. By addition of $Ca(OH)_2$ isoelectric point was reached and boron ions was released into solution. The aim of this work was to establish how the addition of $Ca(OH)_2$ in a boron solution contributes to the determination of boron through boron-curcumin complex.

Experimental
Samples were prepared in accordance with preparation procedure T1 or T2. Procedure T-1: Solution consisting of 2.00 mL of boron solution R_C (C_B=0.46

mg/L) and 8.0 mL of curcumin solution (0.04 % curcumin , 3.57 % oxalic acid, and 4 % hydrochloric acid in isopropanol) in PTFE vessel was dried in a water bath at 56 ^{0}C. Before the spectrophotometric determination of boron it is necessary to remove turbidity in isopropanol solution. Procedure T-2: Mixture of $Ca(OH)_2$, up to 0225 g, and 2 mL of boron solution R_C (C_B=0.46 mg/L) was placed in PTFE vessel and dried. At the end of this process, 2.0 mL of deionized water was added, and proceed according to T-1.

The spectra were recorded on a Thermo Electron Corporation, Evolution 600, UV-Visible Spectrophotometer, with bandwidth of 2.0 nm, scan speed of 60 nm/min, data interval of 1.0 nm, using a tungsten lamp. Linear regression analysis shows: ABS_{540} nm = -0.00574 + 0.68556C_B (mg B/L), R = 0.99882.

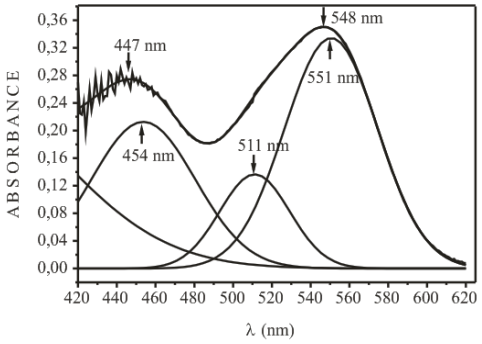

Figure 1. Absorption spectra of boron-curcumine complex; boron solution R_C (C_B=0.46 mg/L).

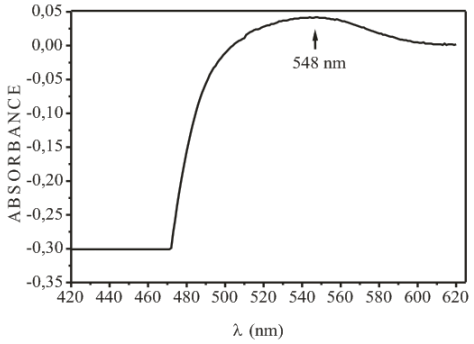

Figure 2. Absorption spectra of boron-curcumine complex; boron solution R_C; drying treatment without $Ca(OH)_2$.

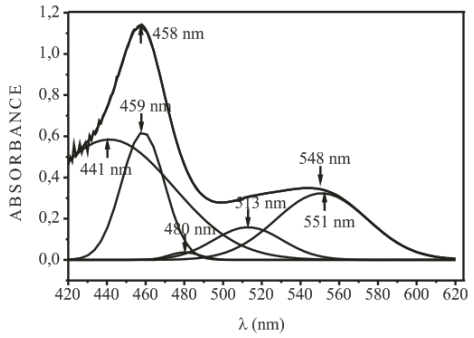

Figure 3. Absorption spectra of boron-curcumine complex; boron solution Rc with 0.0278 g $Ca(OH)_2$/mL of R_C.

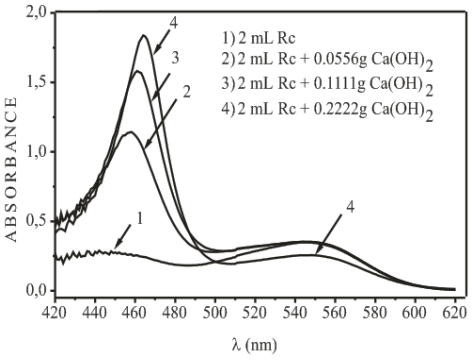

Figure 4. Absorption spectra of boron-curcumine complex; boron solution Rc with $Ca(OH)_2$ up to 0.11 g/mL of R_C.

Results and Discussion

Recorded spectrum of boron-curcumin complex, and deconvoluted spectrum, corresponding to the control solution Rc, which contains 0.46 mg B/L, were given in Fig. 1. Sample was prepared according to procedure T1. Absorption in the region 500-620 nm is relevant for boron determination. Region below 500 nm usually were not considered, beceause it is not function of boron content. Figures 1,

2 and 3 give evidence that the peaks in the area below 500 nm are primarily a function of Ca content, present in the system. Fig. 2 shows the resulting spectra of the control solution Rc, prepared by procedure T2, without addition of $Ca(OH)_2$. The decrease in absorbance in the area from 500 nm to 620 nm, that corresponds to boron content in the system, and particularly a large decrease in absorbance in the region below 500 nm, indicate that the problem with formation of curcumin complex is not only caused by the loss of boron in solution. As it is seen on Fig. 3 and Fig. 4, the addition of $Ca(OH)_2$ in the system prevents the problem of this kind. On Fig. 3, the spectrum of control solution Rc, and its deconvoluted spectrum, for sample with 0.0278 g $Ca(OH)_2$/mL of R_C, prepared in accordance with procedure T2, gave evidence that the addition of $Ca(OH)_2$ does not affect the absorption spectra in the region 500-620 nm. Spectra of control solution R_C, where sample was treated in accordance with procedure T2, and where different amounts of $Ca(OH)_2$ were added, is shown on Fig. 4. The addition of Ca $(OH)_2$ in an amount exceeding 0.05 g $Ca(OH)_2$/mL of R_C, provokes a decrease in the absorption spectrum, and therefore the measured value of the boron content is incorrect.

Conclusions

The addition of $Ca(OH)_2$ in the preparation process before the drying step, in an amount less than 0.05 g per 1 ml of test boron solution, allows retention of boron in the solution and/or its recovery to the aqueous solution, as can been seen in absorption spectra of boron-curcumin complex.

Acknowledgment

This work was supported by the Ministry of Education and Science of the Republic of Serbia, under the Project No TR-31055 and TR-31093.

References

[1] W. T. Dible, E. Truog, and K. C. Berger, Anal. Chem., 1954, vol. 26, No. 2, 418-421.
[2] R. N. Sah and P. H. Brown, Microchem. J., 1997, 56, 285–304.
[3] M. Kosmulski, Adv. Coll.Interface Sci.,2012, 171-172, 77-86.
[4] Atlas of Eh-pH diagrams, Geological Survey of japan Open File Report No. 419, National Institute of Advanced Industrial Science and Technology, May 2005.

GENERAL
PHYSICAL CHEMISTRY

N-01-P

SALTING-OUT THIN-LAYER CHROMATOGRAPHY OF AMINO ACIDS ON SILICA GEL USING AMMONIUM SULPHATE SOLUTIONS

V. M. Živković-Radovanović[1], J.Bratić[2], G. N. Vučković[1],
M. D. Antonijević-Nikolić[3] , S. B. Tanasković[4]
[1]*Faculty of Chemistry, University of Belgrade, P.O.Box 118, 11158Belgrade;*
[2]*Faculty of Agriculture, University of East Sarajevo, Vuka Karadžića 30, 71123 Eastern Sarajevo, Bosnia-Herzegovina;*
[3]*Higher Technological School of Professional Studies, 15000 Šabac; Serbia*
[4]*Faculty of Pharmacy, Vojvode Stepe 450, 11000 Belgrade;*

Abstract
14 amino acids of different structure were separated by salting-out thin-layer chromatography (SOTLC) using ammonium sulphate solutions on silica gel. The obtained results were discussed in aspect of amino acids composition and structure. They were consistent with separation mechanisms of non-polar hydrophobic interactions.

Introduction
Some of the mixed aminocarboxylato Co(III) complexes were successfully separated with ammonium-sulphate or other salts solutions on different sorbents [1]. The proposed mechanism was based on non-specific hydrophobic interactions connected with the coordinated aminocarboxylates. The aim of this work was consideration of the effect of some free amino acids on chromatographing parameters during SOTLC on silica gel using $(NH_4)_2SO_4$ solutions.

Experimental
The studied amino acids (Table I) and other chemicals used were of analytical grade. Aqueous solutions of amino acids (50 mg/cm^3) were spotted on Polygram SIL G/UV_{254} sheets for TLC. Aqueous $(NH_4)_2SO_4$ solutions of different concentration (1.9-9.2 mol %) were used for ascending chromatographic technique at 20 ± 2°C. Detection as violet spots was achieved by spraying with 0.1 % ethanol solution of ninhydrin and heating at 110 °C. Average R_F-values (from at least 3 repeated experiments) were taken for further considerations. Program Origin 61 was used for drawing and calculations.

Results and Discussion Studied amino acids (Table I) could be divided in groups due to their composition and structure: Nos.1-5 are α-amino acids with normal hydrocarbon side chain; Nos. 6-8 are stuctural isomers of aminoacids 3-5; Nos.1, 9,10. have elongated hydrocarbon chain between –COOH and $–NH_2$ group; pairs of α-amino acids: 2 and 11, 12 and 13 and 3 and 14, respectively, insted of -H atom contain –OH group in hydrocarbon part of the molecule. R_M-values ($\log[(1-R_F)/R_F]$) are given in the same Table 1.

Table 1. R_M -values of investigated amino acids.

No.	Amino acid	Ammonium sulphate mol%				*m**
		1.9	4.0	6.4	9.2	
1	glycine	-0.954	-0.954	-0.954	-0.908	0.006
2	S-alanine	-0.688	-0.659	-0.602	-0.501	0.026
3	S-α-amino-*n*- butiric acid	-0.477	-0.347	-0.176	-0.052	0.059
4	S-*n*-valine	-0.308	-0.105	0.052	0.288	0.080
5	S-*n*-leucine	-0.087	0.140	0.501	0.788	0.123
6	α-amino-*i*- butiric acid	-0.501	-0.389	-0.213	-0.087	0.058
7	S-valine	-0.347	-0.158	0	0.250	0.080
8	S-leucine	-0.158	0.105	0.432	0.753	0.126
9	β-alanine	-0.659	-0.602	-0.545	-0.477	0.025
10	γ-amino butiric acid	-0.525	-0.410	-0.269	-0.087	0.060
11	S-serine	-1.123	-1.123	-1.061	-0.954	0.024
12	S-phenyl alanine	-0.288	-0.105	0.140	0.432	0.099
13	S-tyrosine	-0.908	-0.720	-0.501	-0.288	0.085
14	S-threonine	-0.826	-0.689	-0.545	-0.432	0.054

***** *m* is the slope of the line: $R_M = R_M^0 + m \cdot mol\ \%\ of\ (NH_4)_2SO_4$

It is seen that increase of salt concentration causes enhanced retention. The Linear dependence rule [2] was found and the obtained salting-out efficiencies (*m*-values in Table I) were dependent of hydrocarbon size of the molecule. There is reversed-phase order of the investigated compounds 1-5; 6-8; 1,9,10. However, amino acids with the normal side hydrocarbon chains have slightly stronger retention then their corresponding isomers with branched chain. Differences in chromatographic parameters of amino acids 2 and 3 compared with isomeric one, 9 and 10 are also small. It could be concluded that the size of hydrocarbon part of the molecule is the most important factor of the retention. Significant decrease in retention occurred when one of H- atom is replaced with polar –OH group, which is seen from the Figure 1. All results are consistent with the mechanisms of non-specific hydrophobic interactions.

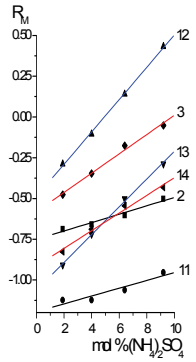

Figure 1. Dependence of RM-values on mol % of (NH4)2SO4. Numbers near lines denote amino acid No. in Table I.Conclusion.

The size of hydrophobic hydrocarbon part in the studied amino acid molecule was the most important factor affecting their retention and separation during SOTLC on silica gel, whereas the effect of its structure was smaller.

Introduction of the polar –OH group in the hydrocarbon part causes decrease of the retention. All results were consistent with separation mechanisms of non-specific hydrophobic interactions.

References

[1] a) G. Vučković, D. Miljević, T. J. Janjić, M. B. Ćelap, J.Chromatogr., 1992, 609, 427-431; b) T. J. Janjić, V. Živković, G.Vučković, M.B.Ćelap, J.Chromatogr., 1992, 626, 305-309; c) J.Janjić, V. Živković, G.Vučković, M.B.Ćelap, Chromatographia, 1993, 37, 534-538; d) V.Živković-Radovanović, G.Vučković, Chromatographia, 2008, 67, 259-267.

[2] J. Janjić, V. Živković, M. B.Ćelap, Chromatographia, 1993, 38, 355-358.

N-02-P

Cu(II) EFFECT ON FLOATABILITY AND ZETA POTENTIAL OF SPHALERITE

D. R. Vučinić, S. Đ.Deušić, A. Đ. Tomašević,
Faculty of Mining and Geology, University of Belgrade, Belgrade, Serbia

Abstract
Sphalerite ((Zn, Fe)S; 13% Fe) has very good natural floatability (hydrophobicity) in a acidic medium (86%) and very poor in an alkaline medium (21%). The negative zeta potential in alkaline medium confirms the chemisorption of hydroxyl ions in the electrical double layer of the mineral. The positive zeta potential is at pH below 6.5 due to the surface oxidation and the formation of hydrophobic zinc, iron-deficient sites (Zn_{1-x} , Fe_{1-y})S and H^+ adsorption. Cu(II) from the solution induces the rise of the flotation recovery up to 95% only in acidic medium. The ion exchange $Zn^{2+} \rightleftarrows Cu^{2+}$, the Cu^{2+} adsorption on the metal-deficient surface sites and $Cu^{2+} + e \rightarrow Cu^{+}_{surf}$, $½\ S^{2-}_{surf} \rightarrow ½\ S^{o} + e$ surface reactions contribute to the negative sphalerite zeta potential, similar to the zeta potential of chalcocite, Cu_2S and elemental sulfur which increases the mineral surface hydrophobicity.

Introduction
The surface oxidation of sulphide minerals causes the formation of different surface species, promoting or not the natural floatability. The hydrophobic species which made sulphide minerals floatable are metal-deficient sulphide oxidation products and elemental sulfur [1]. The interaction between zinc sulphide and hydrophobic xanthate-type surfactants (RCS_2M) is weak. Successful flotation using xanthates can be accomplished only after activation by heavy-metal ions [2-3]. Adsorption of modifying reagents is controlled by the electrical double layer at the mineral-water interface, because of that zeta potential can be used to delineate the interfacial phenomena [4]. The present paper is an attempt to determine the influence of dissolved copper on the floatability and zeta potential of sphalerite.

Experimental
A sphalerite from the Trepča deposit (Zn 53.12 wt%, Fe 13.01%, Pb 250 ppm, Cu 85 ppm, Cd 1520 ppm, Mn 4670 ppm) was used. The pH modifiers were HCl and NaOH. $CuSO_4$ was added in order to introduce Cu(II) into the mineral suspensions. $NaNO_3$ was used to adjust ionic strength ($I=1x10^{-2}$ mol dm^{-3}). All the reagents were of p.a. Flotation tests were conducted in a modified Hallimond tube (the partical size of -208+104 μm). Zeta potential measurements (SSA of sample: 2.25 $m^2\ g^{-1}$) were taken on a Riddick Zeta-meter using microelectrophoresis. The mineral suspension was stirred for three minutes after each reagent addition.

Results and Discussion
In the presence of pH regulators the tested sphalerite has very good natural floatability (collectorless floatability) in a weakly acidic medium at pH 5.3-5.8 (about 86%) and very poor in an alkaline medium (about 21% at pH 8.5), (Fig.1).

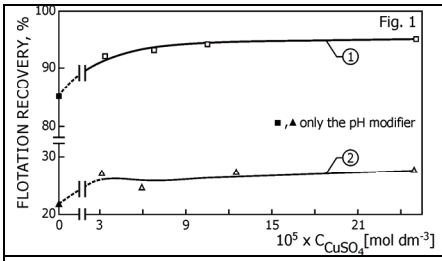

Figure 1. Flotation recovery of sphalerite: 1) pH=5.3-5.8; 2) pH=8.5.

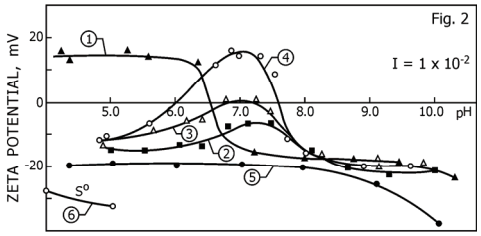

Figure 2. Sphalerite zeta potential in the presence of pH modifiers (1) and pH modifiers and Cu(II): 2) $2.5x10^{-4}$ mol dm^{-3}; 3) $5.0x10^{-4}$ mol dm^{-3}; 4) $8.0x10^{-4}$ mol dm^{-3}; [5) chalcocite, Cu_2S; 6) elemental sulfur].

The zeta potential-pH curve of mineral (Fig.2, curve 1) shows a positive zeta potential in acidic media and a negative one in alkaline media, with the IEP at pH 6.5. Many investigators have noted that oxidation at the sphalerite surface is a slow process in air or in alkaline solution, which can be the explanation for a poor floatability of examined sphalerite at pH above 7. Also, the hydrolysis of the surface metal ions from the mineral lattice and adsorption of OH^- may result in the surface sites ≡Zn–OH, ≡Fe–OH or other ≡Me–OH (≡ the surface). The negative values of the sphalerite zeta potential in alkaline medium confirm the chemisorption of hydroxyl ions in the electrical double layer of the mineral . On the other hand, the positive zeta potential is at pH below 6.5 due to the prevalence of positive charged species in the Stern layer of the electrical double layer of sphalerite. As the sphalerite used in this study contained about 13% Fe(II) in the crystal lattice we presumed that the first stage of surface oxidation for our sample (Zn,Fe)S in the air-saturated acid solution, coupled with cathodic reduction of atmospheric oxygen, was the formation of hydrophobic zinc, iron-deficient sites:

$$(Zn,Fe)S \rightarrow (Zn_{1-x}, Fe_{1-y})S + xZn^{2+} + yFe^{2+} + 2(x+y)e \quad \text{.....(1)}$$

$$\tfrac{1}{2}(x+y)O_2 + 2(x+y)H^+ + 2(x+y)e \rightarrow (x+y)\,H_2O \quad \text{.....(2)}$$

promoting good collectorless floatability and domination of cations in Stern layer. The potential-determining ions are Zn^{2+} and Fe^{2+} passed in the liquid phase by anodic oxidation. Also, the adsorption of H^+ ions at sites ≡S- well as diffusion metal cations from the bulk mineral on the metal-deficient surface sites can effect on positive zeta potential. A small value of zeta potential of about +16 mV confirms a small degree of the electrochemical oxidation, but apparently sufficient for a successful flotation of mineral. Observed weak increase in pH value of suspension for 10 min of acidic conditioning also supports the presumed mechanism. Cu(II) from the solution induces the rise of the flotation recovery up to 95% in acidic medium ((pH=5.3-5.8) (Fig.1, curve 1). However, in alkaline conditions the mineral floats weakly independent of Cu(II) concentration (Fig.1, curve 2). This effect at pH=8.5 can be explained by the formation of surface $Cu(OH)_2$, which together with the hydrolyzed surface species of

zinc and iron depresses the mineral. The unchanged values of zeta potential in the presence of Cu(II) at pH above 8 favor this explanation (Fig.2, curves 1-4). On the other hand, Cu(II)-modified sphalerite has a negative zeta potential at pH below 6 (curves 2-4). Literature data indicate that the dominant reaction in acidic medium in the system sphalerite-Cu(II) is the ion exchange $Zn^{2+} \rightleftarrows Cu^{2+}$. The thermodynamic equilibrium constant, $K=6.5x10^{9}$, calculated as a ratio of the ZnS ($2.6x10^{-26}$) and CuS ($4.0x10^{-36}$) solubility products, indicates the high affinity of sphalerite for Cu^{2+} ions from the solution. Also, the Cu^{2+} adsorption on the metal-deficient surface sites of $(Zn_{1-x}, Fe_{1-y})S$ is possible process. Cu^{2+} present on the mineral surface can cause the following reactions: $Cu^{2+}+e \rightarrow Cu^{+}_{surf}$ ...(3); $\frac{1}{2} S^{2-}_{surf} \rightarrow \frac{1}{2} S^{o}+e$ ...(4).

Because of that the zeta potential of Cu(II)-modified sphalerite in acidic medium is similar to the zeta potential of chalcocite, Cu_2S (Fig.2, curve 5) and elemental sulfur (Fig.2, curve 6), which increases the hydrophobicity of mineral surface, i.e. collectorless floatability (Fig.1, curve 2). Cu(II) from the solution induces less negative (Fig.2, curves 2-4) or positive (curve 4) zeta potential of sphalerite above pH 5. In the pH range from 6 to 8 the dominant copper species present in the solution are Cu^{2+},$Cu(OH)^{+}$, $Cu_2(OH)_2^{2+}$ [3]. The adsorption of Cu(II)-hydroxy cations in the Stern layer of the electrical double layer of mineral is evidenced by the electrokinetic behavior of sphalerite and by the decrease of the floatability in this pH region. The centers on sphalerite surface for chemical adsorption of copper-cation species are $\equiv S^{-}$ and metal-deficient $(Zn_{1-x}, Fe_{1-y})S$ sites. The physical adsorption of Cu(II)-hydroxy cations by hydrogen bonds is also possible on some ≡M-OH and ≡SH centers.

Conclusion

The examined sphalerite with 13%Fe has a good natural floatability and the positive zeta potential in an acidic medium due to the surface oxidation and the formation of hydrophobic zinc, iron-deficient sites $(Zn_{1-x},Fe_{1-y})S$ and H^{+} adsorption. Cu(II) in acidic solution induces the rise of the flotation recovery up to 95% and a negative zeta potential. The ion exchange $Zn^{2+} \rightleftarrows Cu^{2+}$, the Cu^{2+} adsorption on the metal-deficient surface sites as well as $Cu^{2+}+e \rightarrow Cu^{+}_{surf}$, $\frac{1}{2} S^{2-}_{surf} \rightarrow \frac{1}{2} S^{o}+e$ surface reactions contribute to the mineral surface hydrophobicity. Also, the adsorbed Cu-hydroxy species on sphalerite at higher pH present the surface sites for interaction with hydrophobic xanthate-type surfactants.

Acknowledgement

The authors are indebted to the Research Fund of the Republic of Serbia for the financial support (projects no. 33007; no.176010).

References

[1] A. N. Buckley, R. Woods, Appl. Surf. Sci., 1984, 17, 401-414.
[2] S. Jain, D.W. Fuerstenau, in K. S. E. Forssberg (Ed.), Flotation of Sulphide Minerals, Elsevier, Amsterdam, 1985, 159-174.
[3] J. Ralston, T. W. Healy, Int. J. Miner. Process., 1980, 7, 203-217.
[4] D. W. Fuerstenau, Pradip, Adv. Colloid Interface Sci., 2005, 114, 9-26.

ZETA POTENTIAL OF MAGNETITE/AQUEOUS SOLUTION INTERFACE AT ELEVATED TEMPERATURES

S. Vidojkovic[a†], V. Rodriguez-Santiago[a, b, †], M. V. Fedkin[a], D. J. Wesolowski[d], S. N. Lvov[a, b, c,*]

[a]*The EMS Energy Institute;* [b]*Department of Energy and Mineral Engineering; and* [c]*Department of Materials Science and Engineering, The Pennsylvania State University, University Park, PA 16802, U.S.A.*
[d]*Chemical Sciences Division, Oak Ridge National Laboratory, Oak Ridge, TN 37831-6110, U.S.A.*
[†]*Present address: Vinca Institute of Nuclear Science, P.O.Box 522, Belgrade, Serbia*

Abstract
The effect of temperature on zeta potential at the magnetite/water interface was studied applying high temperature electrophoresis technique. The first reliable experimental data were obtained on the zeta potential of magnetite at the elevated temperature up to 200°C in pressurized aqueous solution. The isoelectric points of magnetite were determined at pH 6.35, 6.00, 5.25, and 5.05 for temperatures 25, 100, 150, and 200 °C, respectively which were found to be consistent with published surface titration and mass titration data. The obtained dependence of the zeta potential of magnetite on pH and temperature can be utilized for development of methods for controlling and reduction oxide deposition in high temperature water cycles.

Introduction

The deposit in industrial systems using high temperature aqueous medium is typically composed of steel oxidation products, uppermost magnetite (Fe_3O_4) [1, 2], which are normally present in the colloidal form and tend to precipitate on the inner surfaces of process lines [1, 2]. The electrokinetic behavior of colloidal particles, involving colloidal stability and potential for aggregation onto a substrate, is determined by zeta potential [3], which influences the extent of the electrostatic interaction between the colloids and other surfaces and strongly depends on pH and ionic strength. In this study, we used an originally developed high temperature microelectrophoresis cell [4] to measure the electrophoretic mobility of magnetite particles and to obtain the zeta potential at the magnetite/aqueous solution interface at temperatures up to 250 °C.

Results and Discussion

Measurements of the electrophoretic mobility of magnetite particles were conducted using the high-temperature zetameter system designed and constructed in our laboratory. The details of the experimental design have been published elsewhere [4, 5]. Electrophoretic experiments were carried out at the following sets of parameters: t = 25 °C and P = 1 bar; t = 100 °C and P = 20 bar; t = 150 °C and P

= 20 bar; and t = 200 °C and P = 40 bar, 250oC and P =40bar.The experimental data obtained from the electrophoresis tests are listed in Table 1.

Table 1. Zeta potential for magnetite at different temperatures and pH.

t (°C)	pH (±0.05)	ZP, mV
25°C	3.90	32.6
	4.45	26.3
	7.20	-46.5
	8.60	-135.7
	9.50	-140.9
100°C	4.00	68.0
	4.50	105.2
	5.85	50.2
	6.15	-45.9
	7.01	-64.8
150°C	3.70	49.1
	4.90	43.8
	5.70	-61.2
	6.00	-111.8
	7.30	- 66.8
200°C	4.00	88.7
	4.85	64.8
	5.60	-115.0
	6.10	-105.1
	7.30	-76.6
250°C	5.53	111.94
	6.31	-155.7
	6.5	-162.4
	6.83	-185.9

Figures 3(a-d) show that at temperatures 25, 100, 150, and 200 °C, the isoelectric points (pH_{IEP} at ZP=0) were determined at pH 6.35, 6.00, 5.25, and 5.05, respectively. For the measured temperatures, the zeta potential curves have inverted "s" shape, which is typical of many amphoteric oxides. It was noticed that for all measured temperatures except 25 °C, the zeta potential curves exhibit a very sharp decline at the pH region close to pH_{IEP}. It can be inferred that at elevated temperatures, a small shift in pH causes considerable change in the zeta potential close to the IEP. This may lead to an abrupt overturn of a colloidal system that contains magnetite particles and hence indicates the importance of thorough pH control in high temperature industrial processes. The obtained pH_{IEP} decreases with increasing temperature, which is similar to the trend observed in other surface charge and zeta potential studies at elevated temperatures [5, 6].

Performed experiments provided evidences on sign and magnitude of zeta potential in typical high temperature power plant and pressurized water reactors. Obtained results proved that magnetite surface would maintain a negative charge in neutral and slightly basic environments. It means that high electrostatic repulsion of magnetite particles will ensure its colloidal stability and less probability to deposit under condition of fossil plant water cycles. Aggregation of magnetite particles may be educed by decrease in solution pH, which would result in more abundant porous deposits that can cause underdeposit corrosion. At the same time, it was demonstrated that probability for precipitation of magnetite in nuclear plants reactors condition will be high. Besides that, it was shown that microelectrophoresis technique can be successfully used for measurements of zeta potential of magnetite at temperatures up to 250oC. On the basis of the acquired zeta potential values it is possible to predict behavior of magnetite particles and their deposition in many other industrial processes and to develop methods for prevention deposition of iron oxides by shifting of sign of charged colloidal particles of iron oxides. Taking in consideration scarcity of zeta potential data of magnetite at high temperatures, results obtained in this study are of great significance for elucidation the nature and extent of interactions between the colloidal particles at the heat exchange surfaces of industrial plants and their further control.

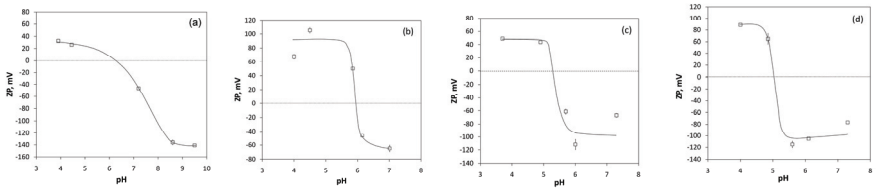

Figure 1. Zeta potential of magnetite versus pH at different temperatures: (a) 25 ^{o}C, (b) 100 ^{o}C, (c) 150 ^{o}C, and (d) 200 ^{o}C.

Acknowledgements

We thank Dr. Jorgen Rosenqvist for useful discussions during his visit at Penn State University. This research was supported in part by the National Science Foundation (EAR 07-32559), the Division of Chemical Sciences, Geosciences, and Biosciences, Office of Basic Energy Sciences, U.S. Department (DJW and SNL) through contract with Oak Ridge National Laboratory (DE-AC05-00OR22725), and by the United States Department of State through a Fulbright Grant provided to the first author of the paper (SV).

References

[1] H. M. Shalaby, Corrosion, 2006, 62, 930-941.
[2] R. L. Tapping, C. W. Turner, R. H. Thompson,, Corrosion, 1991, 47, 489-495.
[3] R. J. Hunter, Foundations of Colloid Science, Oxford University Press, 2001.
[4] X. Y. Zhou, X. J. Wei, M. V. Fedkin, K. H. Strass, S. N. Lvov, Rev. Sci. Instrum., 2003, 74, 2501-2506.
[5] M. V. Fedkin, X. Y. Zhou, J. D. Kubicki, A. V. Bandura, S. N. Lvov, M. L. Machesky, D. J. Wesolowski, Langmuir, 2003, 19, 3797-3804.
[6] D. Wesolowski, M. Machesky, D. Palmer, L. Anovitz, Chem. Geol., 2000, 167, 193-229.

GEOPHYSICAL CHEMISTRY

O-01-P

ASTRONOMICAL RADIATION SOURCES AND ORIGIN OF ATMOSPHERIC OXYGEN OF PRE-OXYGENATED EARTH: SOLAR PHOTON RADIATION

Pavle I. Premović
Laboratory for Geochemistry, Cosmochemistry and Astrochemistry, University of Niš, P.O. Box 224, 18000 Niš, Serbia

Abstract
This preliminary report explores a possibility that the solar photon radiation source is related to the origin of free O_2 derived from oceanic and/or atmospheric water on pre-oxygenated Earth (POE) which has been overlooked in the previous studies. POE was probably subject to intense solar photon radiation (ultraviolet light, X- and γ-rays), greatly increasing during short times of solar flares and superflares. I tentatively suggest that the solar photon radiation and subsequent geochemical processes may have contributed to the origin of O_2 in the atmosphere on POE.

Introduction
Currently, there are two (major) scientific hypotheses about the origin of free O_2 on POE. The first hypothesis, free O_2 was generated through photosynthetic activity of anoxic microorganisms; second hypothesis, free O_2 was produced by the direct solar photodissociation of atmospheric water H_2O. This process is considered to be only capable of yielding small amounts of free O_2. Recently, Premović [1] proposed a third a hypothetical alternative, that a high shock (pressure/temperature) decomposition of H_2O vapor derived mainly from the impacting icy comet in the ocean (or on land) could have been an alternative source of free O_2 in the pre-oxygenated atmosphere. These hypotheses still remain (more or less) speculative and warrant further research.
The purpose of the present review is to explore a possibility that dissociation of oceanic H_2O and/or atmospheric H_2O vapor by the solar photon radiation can generate O_2 in the atmosphere on POE.
Solar ionizing radiation. The Sun has been probably the single greatest source of astronomical radiation to POE on a continuing basis. The ancient Earth was probably subject to intense solar ionizing radiation greatly increasing during short times of solar winds, flares and superflares. There are two types of solar ionizing radiation. The first one is electromagnetic radiation mainly composed of the energetic UV, X- and γ-ray photons; the other main type, so-called solar cosmic rays (SCR), consists predominantly of high energy protons and electrons (95 %). X- and γ-rays and cosmic rays may also originate from non-solar sources often as galactic cosmic radiation coming from outside the solar system.
Overall effect of the above two types of solar ionizing radiation on oceanic or atmospheric H_2O on POE is shown in the following direct dissociation reaction

$$2H_2O \text{ (oceanic or atmospheric)} \rightarrow H_2 \text{ (g)} + O_2 \text{ (g) or } 2H + 2OH$$

where g stays for gas phase. This dissociation is followed by escape of H and H_2 in space. In general, the loss of hydrogen to space should be approximately equal

the total O_2 content in the pre-oxygenated atmosphere. Probably, similar reaction can be written for the atmospheric CO_2 [$2CO_2 \rightarrow 2CO\ (g) + O_2\ (g)$]. In this report my attention will be focused only on the decomposition of oceanic and atmospheric H_2O on POE by solar photon radiation.

The amount of H_2O decomposed by the above reaction depends strongly on the timescale of radiation emission and the fraction of the incident radiation that can reach a given level of atmosphere. Under the conditions of the current atmosphere, the photolysis rate of atmospheric H_2O vapor corresponds to about 5×10^5 g s^{-1}. *Some rough calculations*. Before any further discussion, let us do some informative rough calculations. The present atmosphere has mass of 1.2×10^{21} g. A simple calculation shows that 2.5×10^{14} g of H_2O is necessary to convert by any solar ionizing radiation **(**or any of their combination) to generate the pre-oxygenated atmosphere with 5×10^{-8} atm of O_2. Assuming that the mass in the global ocean on POE was about the same as today (1.4×10^{24} g), it requires to decompose about 3×10^{18} H_2O molecules per cm^{-2} of the global ocean.

*Solar photon radiation***.** As stated above, I will consider only dissociation of oceanic H_2O by solar photon radiation, leaving consideration of solar winds, SCR and galactic cosmic radiation for future work. The direct photodissociation of H_2O molecules requires solar photons of wavelengths less than about 200 nm. These are photons of the following radiations: the vacuum ultraviolet light (VUV), X-rays and γ-rays. The present-day (upper) atmosphere absorbs almost all photons of solar VUV, X-rays and γ-rays. The quantity of solar VUV-X radiation received at Earth's surface or at any atmospheric level depends on two main variables: the emission of radiation by the Sun and its extinction through absorption and scattering by the constituents of atmosphere (mainly O_3, N_2 and O_2).

*Model atmosphere 1***.** Models of the pre-oxygenated atmosphere are diverse, and often contradictory, as the evidence on which they are based. In the study of atmospheric composition it is often convenient to use simplified photochemical atmospheric models. Such models have proved very useful in studies of certain aspects of the atmospheric chemistry. I assume for simplicity with a model of the pre-oxygenated atmosphere which is thick enough to prevent complete evaporation of global ocean and with enough ambient heating to prevent complete freezing of this ocean. I will begin with the simplest possible model of this atmosphere which is saturated with H_2O vapor at about 25 °C. I assume that an atmospheric column density is about 30 g cm^{-2} for H_2O vapor or about 10^{24} molecules cm^{-2}. Of note, the column densities of H_2O vapor in the existing atmosphere are about 2.5 g cm^{-2}. I will name this atmosphere model as MA1 (a short notation for model atmosphere 1). In fact, MA1 is the excellent starting point for my future investigation since it is so thin that the all incident ionizing radiation reach the ocean surface. My model represents a simplification of the real pre-oxygenated atmosphere and, of course, the validity of my conclusions will therefore depend upon the assumptions I made.

VUV-X and γ-ray photons. Astronomical consideration indicates that the overall luminosity of the Sun during the pre-oxygenated period was approximately 70-75 % of the present day luminosity. In contrast, the VUV, X- and γ-ray luminosity

during this time was likely much higher than today. Therefore, much higher fluxes of solar photons of VUV-X radiation and γ-rays were reached POE than at present. However, the present-day solar photon flux of γ-rays compared to that of VUV-X radiation is lesser by at least for five orders of magnitude and thus they were probably far less important in the direct solar photodissociation of pre-oxygenated oceanic and atmospheric H_2O. For this reason, I here limit my discussion to dissociation of oceanic and atmospheric H_2O by solar VUV-X photons.

A mean total photon flux of solar VUV-X reaching this surface is probably about 1.5×10^{11} photons cm^{-2} s^{-1} with a mean total energy flux of roughly about 7 ergs cm^{-2} s^{-1} (or 4.5 TeV cm^{-2} s^{-1}). A given photochemical process is generally characterized by the quantum efficiency (QE) which is determined as a ratio between the number of reacted molecules or the molecules of the reaction product and the number of the absorbed photons. The QE (H_2O) for liquid H_2O dissociation under the VUV-X radiation is higher than 1. This gives a minimum photodissociation rate of ca. 1.5×10^{7} g s^{-1} of H_2O in the global ocean.

If we make the reasonable assumption that a mean total H_2O photodissociation rate for MA1 is about 2×10^{11} molecules cm^{-2} s^{-1}, as estimated for the pre-oxygenated atmosphere, then this process would decompose 3×10^{7} g s^{-1} of H_2O in MA1.

A major O_2 sink on POE was volcanic gases (primarily H_2). These gases currently consumed ca. 5×10^{5} g s^{-1} and suggested that during photosynthetic Earth this consumption was somewhat higher. The photolysis of oceanic and atmospheric H_2O probably generate roughly this amount of O_2 in MA1. If this is correct than QE (O_2) for this photolysis is about 1.7×10^{-2} and it is probably an upper limit.

Solar flares and superflares. Solar flares have energy of 10^{32} erg which is about 10^3 times more than that of the quiet Sun but they only last for about 10^3 s. In the POE's time the Sun would have had on average 5 such flares per day. These flares would photochemically generated at least 3×10^{7} g s^{-1} of O_2 (averaged over a year) in MA1. Recently, it is discovered stellar flares with 10^2 to 10^7 times more energy than the largest solar flare. These superflares have durations of hours to days. Let us assume that the superflare did occur with 10^{36} erg once during the pre-oxygenated era and lasted for about a week. This gives 6×10^{7} g s^{-1} of O_2 (averaged over a year). However, the superflares appear to take place every few million years so their generation rate of O_2 in MA1 could be much higher. Thus, volcanic gases of pre-oxygenated atmosphere could possibly be overwhelmed (at least for a short time) by the photochemically generated O_2.

Conclusion

I tentatively conjecture that dissociation of oceanic and/or atmospheric H_2O by solar photon radiation could generate the important levels O_2 (at least for a short time) on POE.

References

[1] P. I. Premović, Int. J. Impact. Eng., 2003, 29, 575-587.

O-02-P

CRETACEOUS-PALEOGENE BOUNDARY CLAY AT CARAVACA (SPAIN): ARSENIC ANOMALY

Pavle I. Premović
Laboratory for Geochemistry, Cosmochemistry and Astrochemistry, University of Niš, P.O. Box 224, 18000 Niš, Serbia

Abstract
A high As content has been reported in Cretaceous-Paleogene boundary (KPB) clay at Caravaca. One of the interpretations suggests this chalcophile element comes from combustion of fossil fuels such as crude oil, coal or oil shales near the Chicxulub impact KPB site. Combustion was triggered by the KPB asteroid impactor. This report shows that the calculated global As surface density 27 millions times less than the experimental As surface density at Caravaca, contradicting the fossil fuels hypothesis. This calculation is based on proven crude oil reserves (ca. 10^{16} g) of the giant supercharged Pimienta-Tamabra petroleum system close to the Chicxulub impact site.

Introduction
Apart from well-known anomalous Ir, the prominent KPB clays worldwide show the high concentrations of (so-called) non-chondritic trace elements such as chalcophiles As, Sb, Cu, Zn, Mo, Ga, Hg, Re, and Se. According to Hildebrand and Boynton [1], these elements represent a primary geochemical signal of the KPB impact at Chicxulub (Mexico). The source of the chalcophile element anomalies at KPB is still problematic.
Gilmour and Anders [2, 3] examined the distribution of chalcophiles in bulk boundary clays at eight prominent marine sites at Caravaca, Gubbio (Italy), Højerup (Denmark), Woodside Creek, Flaxbourne River (New Zealand), Zumaya (Portugal) and Deep Sea Drilling Project 465A (Central Pacific). These researchers concluded that, in contrast to Ir which is mainly meteoritic, As (like other chalcophiles) is non-meteoritic and non-oceanic in origin. I readily anticipate their conclusion throughout this report. Previously, Gilmour and Anders [2, 3] also proposed that combustion (ignited by the Chicxulub impactor) of fossil fuels (such as crude oil, coal or oil shales) was a possible source of relatively highly volatile As (as well other chalcophiles) in these prominent boundary clays worldwide. This brief report re-examines each of these possibilitities mathematically for the case anomalous As in the boundary clays at Caravaca. For this purpose, comprehensive geochemical data for anomalous As in the boundary clay at Caravaca will be used which are published by Schmitz [4].

Results and Discussion
The boundary section Caravaca is among the most continuous and complete marine sections for the KPB transition. The Caravaca section is located in the Betis Cordilleras (southerneast Spain). The KPB section at Caravaca consists of a ca. 1

cm-thick Ir-rich dark marl (BC) overlain by a grey-to-brown marl, Fig. 1 . A basal 2-3 mm thick red sublayer (RSC) of BC enriched with Ir is marking the KPB.
Schmitz [4] carried out the analyses of the decarbonated boundary samples from Caravaca using instrumental neutron activation analysis (INAA). Relative error in the precision of the analyses ranges from 5 % to 10 %. Total uncertainties (including accuracy errors) were up to 20 %. Throughout this paper we make a reasonable postulates that As are wholly located in the non-carbonate fraction of the boundary clays studied, i. e. the carbonate fraction of this section is essentially their diluents.

Distribution of As

The abundance distribution of As across the decarbonated BC is given in Fig. 1. This element shows a prominent peak at the RSC (ca. 900 ppm). The duration of the peak in As at Caravaca is similar to that of the Ir anomaly, which is geologically instantenous. In addition, simultaneous presence of anomalous Ir and As in RSC is rather surprising in view of their separate origins: Ir from the carbonaceous chondrite bolide and As from terrestrial source(s).

According to Fig. 1 the As contents in the decarbonated RSC shows 180-fold increases in its concentration compared with the decarbonated latest Maastrichtian layer. This manifold increase of As strongly argues against a possibility that pulse of calcite dissolution in the shallow water of Caravaca played a major role in the formation of the RSC and its enrichment with As.

As in ejecta fallout may be derived from and the chondrite CI impactor and/or target rocks at Chicxulub. The target rocks probably were mainly derived from the Earth's total (continental + oceanic) crust. Table 1 shows the average concentrations of As in this terrestrial material and CI chondrites. Obviously, none of these sources is adequate for anomalous As in the decarbonated RSC. It is also not possible to explain the As enrichment of the decarbonated RSC by any sedimentary enrichment process (e. g. diagenetic condensation, secondary remobilization and/or redistribution etc.) of As derived from these sources without some dubious argumentation.

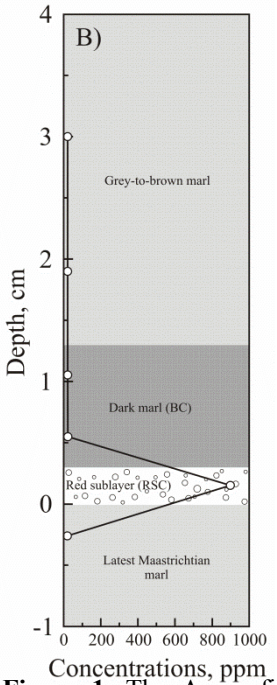

Figure 1. The As profile across BC

Table 1. Average As contents (ppm) of geological materials and CI chondrites

Material / Chalcophile	Decarbonated RSC[a]	Continental crust[b]	CI chondrites[b]
As	900	1.80	1.90

[a][4]; [b] [5].

As and the mass of crude oil burned

In this note, I will consider a possibility that As in the RSC from combustion of crude oil near the Chicxulub impact site.

The global surface density of As (d_{As}) is given by

$$d_{As} = M_C C_{As} f_B f_S / A_E$$

where M_C is the mass of crude oil burned, C_{As} the average concentration of As in crude oil is about 0.134 ppm [6], f_B is the smoke fraction for crude oil burned, f_S is the fraction of the crude oil As released into into the stratosphere and globally dispersed more or less evenly over the Earth surface area A_E (ca. 5×10^{18} cm^2).

The Chicxulub impact crater is located adjacent to the Cantarell very large oil reservoir in the southern Gulf of Mexico, suggesting that abundance of fossil hydrocarbonas in the Chicxulub target rocks was likely to have been above global mean crustal abundance. The formation of the Cantarell oil field is a direct consequence of the KPB impact and it belongs to the giant supercharged Pimienta-Tamabra petroleum system. This system is the most important in the southern Gulf of Mexico and has a cumulative production and remaining reserves of about 10^{16} g of known petroleum.

Let us assume that the amount of crude oil burned during the Chicxulub impact was equal to the crude oil reserves of (ca. 10^{16} g) of the gigantic Pimienta-Tamabra petroleum system.. The average smoke yield for crude oil, determined from laboratory experiments by Ransohoff *et al*. [7], was about 75 g kg^{-1} of oil burned , i.e., $f_B \sim 0.075$). In general, the smoke emission factor for crude oil is about up to 10 % [8]. Let us then make a peculiar assumption that all As of crude oil burned is emitted into the stratosphere and deposited globally on the Earth surface, i. e. $f_S \sim 1$. Using these values, one can calculate that d_{As} ~20 pg cm^{-2}. I estimate from the experimental data of Schmitz (1988) that the surface density of As of the decarbonated RSC is about 540 μg cm^{-2} (assuming an average density of 2 g cm^{-3}), which are about more than 27 millions times higher than d_{As}.

Proved recoverable coal reserves of the world are about 9×10^{17} g and a mean As concentration in coal is ca. 13 ppm [6]. Assuming that all world coal burns and then its As is uniformly dispersed over the Earth's surface, I estimate this burning would generate a global density of As equals around 2 μg cm^{-2}, which is about 270 times smaller than d_{As}.

Conclusion

Fossil fuels (crude oil, coal or carbonaceous shales) close to Chicxulub are probably not responsible for As enrichments in worldwide distributed prominent marine KPB clays.

References

[1] R. Hildebrand, W. V. Boynton, Meteoritics, 1989, 24, 277–278.
[2] I. Gilmour, E. Anders, Lunar and Planetary Science Conference, 1988, 19, 389.
[3] I. Gilmour, E. Anders. Geochim. Cosmochim. Ac., 1989, 53, 503-511.
[4] B. Schmitz, Geology, 1988, 16, 1068-1072.
[5] Geochemical Earth Reference Model: Reservoir Data 2012.
[6] J. Matschullat, Sci. Total Environ., 2000, 249, 297-312.
[7] L. M. Ransohoff, K. Knudson, B. W. Bush, R. D. Small, Pacific-Sierra Research Corporation, Los Angeles, 1989.
[8] R. P. Turco, O. B. Toon, T. P. Ackerman, J. B. Pollack, C. Sagan C., Science, 1990, 247, 166-176.

O-03-P

MEGACRYOMETEOR FROM SVRLJIG (SERBIA): PRELIMINARY PHYSICOCHEMICAL STUDY

P. I. Premović[1], M. G. Đorđević[1], M. S. Pavlović[2],
D. S. Petrović[3], M. D. Petrović[3], Đ. D. Petrović[3]
[1]*Laboratory for Geochemistry, Cosmochemistry and Astrochemistry, University of Niš, P.O. Box 224, 18000 Niš, Serbia*
[2]*Institute of Nuclear Sciences Vinča, P.O. Box 522, 11001 Belgrade, Serbia*
[3]*Mrgudova 13, Svrljig, Serbia*

Abstract
Megacryometeor from Svrljig is probably derived from a tropospheric water at a maximum attitude of about 6 km under anomalous atmospheric conditions.

Introduction
The fall of large ice blocks (weighing about one to hundreds of kilograms) from the clear sky is one of the most interesting and controversial issues in atmospheric sciences. They are recently named megacryometeors by Martinez-Frias and Travis [1] and represent large atmospheric ice chunk conglomerations In general, the megacryometeors are formed under clear-sky conditions which differ from those of the cumulonimbus cloud conditions of common hailstones. They are neither classical hailstones nor ice products of atmospheric processes at high attitudes; they are often confused even with meteors because they can leave small impact craters. Scientific research shows that that the composition of the megacryometeors is similar to the tropospheric rainwater in the areas of their fall [1]. They are not ice junks from aircraft either. Indeed, a detailed historical review of the megacryometeors imply that there many documented cases of their fall which go back to the first half of the 19th centrury before invention of the airplanes.
At present, no model is able to satisfactory explain how the megacryometeors can be formed and maintained in the atmosphere [1]. It is interesting to mention here that there is a hypothesis that the megacryometeors could be a new type of geoindicators of global climate changes [2].
In our opinion, by use of a detailed physicochemical analysis of megacryometeors it will be possible to learn more about their nature and origin. In this brief paper, we report some observations and preliminary experimental, computer modeling and ballistic estimation results related to megacryometeor from Svrljig.

Observations
On August 9th 2010, at around 1 pm, an ice chunk weighing roughly 6 kg fell from clear sky and crashed through the roof of the old (about 100 years) house of the family Petrović from Svrljig. Mr. Dragan S. Petrović, the owner of the house, was outside in the garden sitting on the grass about six meters from the impact site. He was witness of strong but strange “whistling noise” caused by the ice impactor

followed by a strong bang. Due to the arrangement of the tiles (so-called ćeramida) of the roof, an irregular hole 0.75 m × 1 m, were produced.

Figure 1. Megacryometeor from.

A small part of the ice chunk was found situated under the roof in the attic, whereas three relatively large ice fragments (about 2 kg) fell in the garden area. The attic plaster was severely cracked. These pieces were collected and transferred into the freezer. We picked up one of these megacryometeor fragments (Fig. 1) to perform the physicochemical analyses in Laboratory for Geochemistry, Cosmochemistry and Astrochemistry (University of Niš). This piece of the ice chunk was preserved under frozen conditions for later studies.

Results and Discussion

The Svrljig megacryometeor has a rather high pH of 9.8 and relatively low conductivity 28 μS cm^{-1}. For comparison, megamicrometeor water usually has a pH in the range of from 7.0 - 7.9 and conductivity values from 56 - 69 μS cm^{-1}. Qualitative analysis tests for chloride, carbonate and ammonium ions have not shown traces of these chemical species. Table 1 displays a summary of the concentrations of main trace elements in the ice chunk obtained by the inductively coupled plasma optical emission spectrometry (ICP-OES). These values are comparable with those measured in atmospheric (unequivocally tropospheric) waters.

Table 1. The trace elements concentrations (ppm) of the Svrljig megacryometeor.

Mg	Si	Al	Zn	B	Sr	Mn	Ba	Ag
1.5	1.5	0.1	0.05	0.2	0.05	0.03	<0.005	<0.03

Cu	Cr	Co	Ni	Mn	V	Zn	Fe
0.03	<0.05	<0.3	0.10	0.05	<0.05	<0.10	<0.20

Recent computer modelling shows that the mass of the Svrljig megacryometeor was up to 8 kg and its maximum impact speed was 1235 km h^{-1}; the kinetic energy of this meteor was up to 0.5 MJ. Such an energetic megacryometeor is capable of breaking tiles (ćeramida) arrangement with the total

thickness of about 10 cm and to make a roof hole of 40 cm or less. These calculated values roughly correspond to the observed ones. A ballistic trajectory calculation implies that the Svrljig megacryometeor fell from a maximum height about 6 km (troposphere) less than 2 km far from Svrljig. Of note, at this attitude temperature is about -30 °C. It has been suggested that the formation of the megacryometeors occur within a range of temperature from -10 to -20°C [3]. Further study is in progress.

References

[1] J. Martinez-Frias J and D. Travis D. in S. Leroy, I. S. Stewart(Eds.), Environmental catastrophes and recovery in the Holocene, Abstracts Volume, London, Brunel University, 2002.

[2] IUGS Geoindicators, htpp://www.lgt.lt/geoin/.

[3] F. Rull, A. Delgado, J. Martinez-Frias, Philosophycal Transactions of the Royal Society A; Mathematical, Physical and Ingeneering Sciences, 2010, 268, 3145-3152.

EDUCATION, HISTORY

P-01-P

METHODOLOGY AND METHODS OF PHYSICO-CHEMICAL ANALYSIS OF KURNAKOV

T. J. Halasi, S. S. Kalamkovic*

Faculty of Sciences, Departman of Chemistry, Biochemistry and Enviromental Protection, Trg Dositeja Obradovica 3, Novi Sad,

**Primary School "Prva vojvodjanska brigada", Seljackih buna 51a, Novi Sad*

Abstract

Kurnakov was a Russian physicalchemist who was internationally recognized as the originator of physicochemical analysis and he was one of the principal founders of the platinum industry in the USSR. During the first decade of the 20th century, Kurnakov was concerned with the solution of industrial problems such as platinum refining, metallic alloys, metallography and salt manufacturing and he played a vital role in the planning and construction of new laboratories.

Kurnakov's biography

Nikolai Semenovich Kurnakov (*Никола́й Семёнович Курнако́в*, December 6, 1860–March 19, 1941) was born in Nolinsk (*Нолинск*, 57° 33′ 27″ N, 49° 56′ 18.96″ E) and he died in Barvikha (*Барви́ха*, 55° 44′ 30″ N, 37° 16′ 43″ E). He attended a high school at Nizhny Novgorod (*Нижний Новгород* 56° 20′ 0″ N, 44° 0′ 0″ E) and he studied at the Mining Institute, in Sanct Peterburg (*Санкт-Петербург*, 59° 57′ 0″ N, 30° 19′ 0″ E) were he graduated at Institute of Mines in 1882. He was a professor of inorganic chemistry (1893), professor of Physical Chemistry and General Chemistry (1902), together with Dmitri Ivanovich Mendeleev (*Дми́трий Ива́нович Менделе́ев*, 1834-1907) and Nikolai Aleksandrovich Menshutkin (*Никола́й Алекса́ндрович Меншу́ткин*, 1842-1907), at the St. Peterburg Polytechnic Institute (1899-1908), director of the General Chemistry Laboratory of the Academy (1922) and upon the death of Chugaev (*Лев Алекса́ндрович Чуга́ев*, 1873-1922), director of the initially-small Institute of Physicochemical Analysis, and the following year he became editor of its Journal *Известия Института физико-химического анализа* (*Известия Сектора физико-химич. Анализа*).[1][2] Kurnakov created the Institute of Physical and Chemical Analysis. A mineral was named kurnakovite in his honor. The Kurnakovs had two children, son Nikolai Nikolaevich Kurnakov (1889-?), a chemist who worked at the Baikov Metallurgical Institute of the Academy of Sciences of the USSR., daughter Vera Nikolaevna Kurnakov (1898-1921). After the death of his wife (1940), Kurnakov's health deteriorated and he died in a sanatorium.[1]

Kurnakov's work

Kurnakov's first scientific interest was in salts. He completed a series of experiment on the chemistry of coordination complexes that were generalized in

his dissertation *On Complex Metallic Bases* (*Сложных Металлических Основаниях*, 1893), summarized the results of his study of the chemistry of complex compounds, and described the reaction of Pt(I1) and Pd(I1) isomers with thiourea, now known as Kurnakov's reaction [3][4]. He published his first paper on alum crystallization and sodium thioantimoniate in 1882.[5] His invention of an automatic pyrometer (1903) proved to be a major advance in the technique of thermal analysis, for recording heating and cooling curves-with the aid of which he significantly improved the methodology of thermal analysis.

Physicochemical analysis is based on the phase rule and on the principles of continuity and correspondence, which were introduced by Kurnakov. Kurnakov carried on a systematic study of heterogeneous systems (1898) and he used physicochemical analysis like important method of studying systems made up of two, three, or more components, (alloys, minerals, solutions, carbides, oxides, semiconductors, superconductors, systems formed by organic compounds). Together with Zhemchuzhnyi (*Сергéй Фёдорович Жемчужный*, 1873-1929), Kurnakov established the relationships between composition and properties in binary systems, including electric conductivity (measure of how well a material accommodates the transport of electric charge σ = lG/S) (1906), solidity (1908), escape pressure (1908-1913) and basic composition electroconductivity diagrams for systems of two metals which form continuous solid solutions.[6] Kurnakov and his associates discovered a number of berthollides in metallic systems, as well as the theoretically important case of the formation of daltonides in the transitions of solid solutions of gold and copper. These results permitted Kurnakov to formulate the general conclusion that "a chemical individuum belonging to a specific chemical compound represents a phase, which possess singular or Dalton points on the lines of its characteristics" (1914) [4]. "In equilibrium systems," he said, "discreteness and continuity are intercombined and coexist." Physicochemical analysis involves the measurement of various physical properties of systems, most often phase transition temperatures and other thermal properties (thermal conductivity, heat capacity, thermal expansion), electrical properties (conductivity, dielectric permittivity), and optical properties (refractive index, rotation of the plane of polarization of light), measured the density, viscosity and hardness, as well as the dependence of the rate of the transformations occurring in a system on the system's composition. X-ray diffraction analysis and techniques of microscopic metallography are extensively used in physicochemical analysis. [7] The continuity principle holds that during continuous changes in the parameters of a state the properties of a system also undergo continuous change (provided that the number of phases in the system remains constant), when the number of phases changes, certain properties change abruptly (continuity being broken). According to the correspondence principle, each phase or group of phases of a system corresponds to a certain geometric shape (point, line, surface, volume) on the composition-properties diagram. The onset of phase crystallization corresponds to the liquidus curves (or surfaces), above which is located the region of existence of one liquid phase (solution or melt), the end of crystallization corresponds to the solidus lines

(or surfaces), below which only solid phases exist. During a continuous change in the composition of a system, the components of the system may form a chemical compound. If the compound does not undergo dissociation and has an unvarying composition (daltonide), a singular point is observed on the composition-properties diagrams.

Conslusion

Kurnakov, one of Russia's most distinguished and versatile chemists, was an active force in the development of science and technology both in his homeland and abroad. He is regarded as the founder of a new chemical discipline, physicochemical analysis, probably the largest contemporary school of Soviet chemistry with applications in numerous branches of technology.

References

[1] G. B. Kauffman, The Life and Work of Nikolai Semenovich Kurnakov, Platinum Metals Review, 1982, 26 (3), 129-133.
[2] G. B. Kauffman, Nikolaĭ Semenovich Kurnakov, the reaction (1893) and the man (1860–1941) a ninety-year retrospective view, Polyhedron, 1983, 2 (9), 855-863.
[3] N. T. Kuznetsov, N. S. Kurnakov's Contribution to Coordination Chemistry, Russian Journal of Inorganic Chemistry, 2010, 55 (11), 1777-1783.
[4] Н. С. Курнаков, Сборник избранных произведений, 1938-1939, томах 2, Ленинград.
[5] Н. С. Курнаков, Введение в физико-химического анализа, 1940, 4-е изд, Москва.
[6] Г. Г. Уразов, Академик Н. С. Курнаков - основатель физико - химического анализа. - ИСФХА, 1941, 14, 9-35.
[7] А. Т. Григорьев, Воспоминания о жизни и деятельности академика Н. С. Курнакова. - В кн.: Николай Семенович Курнаков в воспоминаниях современников и учеников, Москва, 1961, 28-30.

P-02-P

OTTO HAHN'S WORK IN PHYSICAL CHEMISTRY

Tibor Halasi, S. Kalamkovic[*], M. Mark[**]

Faculty of Science, Department of Chemistry, Biochemistry and Environmental Protection, Trg Dositeja Obradovica 3, 21000 Novi Sad, Serbia, tibor.halasi@dh.uns.ac.rs, [*]Primary School "Prva vojvodjanska brigada", Novi Sad, Serbia, [**]Faculty of Sciences, Department of Physics, Novi Sad, Serbia

Abstract

Otto Hahn was a German physical chemist who discovered the fission of heavy atomic nuclei, and for that work he was awarded with Nobel Prize . He has worked with Meitner, Zincke, Strasman, Born, Flügge and Seelman-Eggebert. With Meitner he measured the absorption of α-radiation. Hahn was discovered: Radioactinium (RdAc), Thorium C (ThC), Mesothorium I (MsTh1) Mesothorium II (MsTh2), Uranium Z (1921) and nuclear isomers Proactinium.

Hahn's biography

Otto Hahn (March 8th, 1879, Frankfurt-on-Main-July 28, 1968, Göttingen) was a German physical chemist and Nobel-laureate, a pioneer in the fields of radioactivity and radiochemistry. He is regarded as "the father of nuclear chemistry". On November 15th 1945 the Royal Swedish Academy of Sciences announced that Hahn had been awarded the 1944 Nobel Prize in Chemistry "For his discovery of the fission of heavy atomic nuclei". Some historians have documented the history of the discovery of nuclear fission and believe Meitner should have been awarded the Nobel Prize with Hahn. Hahn Otto colleagues considered the "father of the atomic age".

Otto Han's father wanted his son to become an architect, but his dream did not realize. Otto did not show enough skills in engineering, is a bad draw and had no sense of space. [1, 2] At the summer of 1901. Otto oral exams and defending a doctoral thesis "On Bromine Derivates of Isoeugenol" in organic chemistry. Professor Theodor Zincke (1843-1928) offers him the position of assistant. Otto Hahn sees its future in the chemical industry.

Hahn's work

September 1904. Otto went to London to investigate radiochemistry, she knew only through newspaper articles. For 100g white barium salt Hahn should have extracted 10 mg of Radium, Marie Curie method (*Marie Sklodowska Curie*, 1867-1934), the method of fractional distillation. Moreover, in addition to radium discovered a substance that releases the active short-lived isotope of thorium, radiotorijum. On one of the classes Plank (*Max Karl Ernst Ludwig Planck*, 1858-

1947), 1907. Otto meets a physicist Lise Meitner (1878-1968), with which he measured the absorption of α-radiation. First they measured the β-radiation Mesothorium I and II by the method used for the Rutherford-α-particles, magnetic removal, (Figure 1). [3]

Figure 1. Otto Hahn and Lise Meitner. [3]

Hahn was discovered: Radioactinium (RdAc), Thorium C (ThC), Mesothorium I (MsTh1) Mesothorium II (MsTh2), Uranium Z (1921) and nuclear isomers Proactinium.[1] Physicists have until 1938. thought that the neutron bombardment of uranium occur such elements whose molecular weights greater than uranium. Physicists haven't presumed that the bombardment of uranium occurring two elements with a lower molecular weight. Born (*Max Born*, 1882-1970), Flügge (*Siegfried Flügge*, 1912-1997), Seelman-Eggebert (*Walter Seelmann-Eggebert*, 1915-1988), Strasman (*Friedrich Wilhelm "Fritz" Strassmann*, 1902-1980), Han and reveal another 25 new elements and 100 new isotopes. Strasman worked with Hahn and he was very helpful when using the method of Fermi **(***Enrico Fermi*, 1901-1954**)** and the discovery of nuclear fission. (Figure 2)[4][5] In Canada, presented the hypothesis that the thorium and radiotorium there must be some other radioactive substance. The supstance is a direct product of thorium, which accumulates in the mineral. If you remove thorium from the

mineral remains of its products. So they discovered two immediate thorium products Mesothorium I and Mesothorium II. [1]

Figure 2. Otto Hahn and Fritz Strassman, München, 1938.[5]

Hahn is the January 1915. began to work in groups to produce toxic gases controlled Habera Institute of Chemistry. Max Plank in 1923. Hahn proposed for the Nobel Prize. Kaiser Wilhelm Institute's November 15th 1945. announced that the Nobel Prize "for their discovery of nuclear fission of heavy atomic nuclei" earned Otto Han, and Hahn was then in captivity. "Mainau Declaration", which is supported by 52 scientists, Hahn published in cooperation with Bor 1955. and was open to appeal against the use of nuclear weapons. "In Berlin I learned of all that had happened since Hitler had come to power. Although Geheimrat Haber, Director of the Insitute of Physical Chemistry, was not himself under pressure to resign, he was powerless to prevent 'non-Aryan' members of his staff from being removed from their jobs. He therefore wrote to Minister Rust, offering his ownresignation. Geheimrat Planck, President of the Kaiser Wilhelm Society, and Haber now asked me to take over the director-ship of the Institute of Physical Chemistry, provisionally, alongside my directorship of the Chemical Institute. I agreed to this, but only a few days later I was informed that a new director had been appointed, This was Professor Jander, an active member of the Nazi party. I had refused to join the party."[6]

Conslusion

”The discovery of nuclear fission by Otto Hahn and Fritz Strassmann opened up a new era in human history. It seems to me that what makes the science behind this discovery so remarkable is that it was achieved by purely chemical means.”[7][8]

Acknowledgements
The autors wish to thank the Ministry of Education and Science, Goverment of Republic of Serbia for supporting the scientific project ”The quality of the education system in Serbia's European perspective” (KOSSEP), Code 179010.

References

[1] M. Mladenović, Velikani fizike (dvadeseti vek), Faculty of Science, Prirodno-matematički fakultet, Novi Sad, 2008, 377- 400.
[2] K. Fajans, Otto Hahn, The Journal of Nuclear Medicine, 1966, 397-401.
[3] P. Rife, "Lise Meitner" Jewish Women: A Comprehensive Historical Encyclopedia, Jewish Women's Archive, March 1st 2009; http://jwa.org/encyclopedia/article/meitner-lise, April 30, 2012.
[4] G. Walton, N., Nuclear fission, Q. Rev. Chem. Soc., 1961, 15, 71-78.
[5] E. H. Berninger, Otto Hahn, Rowohlt Taschenbuch Verlag GmbH, Hamburg, 1974, 123.
[6] O. Hahn,, My life, (The Autobiography of a Scientist), Herder and Herder, New York, 1970, 144-145.
[7] http://profpaulcutter.com/PDF/Hi-tech%20Studies/Nazi_Atomic_Bomb.pdf, May 15, 2012.
[8] L. Meitner, Recollections of Otto Hahn, Stuttgart, 2005.

P-03-P

GERMAIN HENRI HESS AND LAW OF HEAT SUMMATION

Tibor Halasi, S. Kalamkovic*, R. Halasi**

*Faculty of Science, Department of Chemistry, Biochemistry and Environmental Protection, Trg Dositeja Obradovica 3, 21000 Novi Sad, Serbia, tibor.halasi@dh.uns.ac.rs, *Primary School "Prva vojvodjanska brigada", Novi Sad, Serbia, **DPNNS, Novi Sad, Serbia*

Abstract

This paper presents an overview of the work and creativity of scientists Hess and its significance for the development of physical chemistry. Hess's law made it seem highly likely that the law of conservation of energy applied to chemical changes as well as to physical changes. Indeed, to generalize further, the laws of thermodynamics very likely held in chemistry as in physics. This line of experiment and reasoning made it seem that chemical reactions, like physical processes, had an inherent spontaneous direction in which entropy was increased.

Hess's biography

Germain Henri Hess (*Герман Иванович Гесс, Жермен Анри, Герман Генрих*, August 7, 1802-November 30, 1850) was born in Geneva, Switzerland and he died in St. Petersburg. He was a Swiss-born Russian chemist and doctor, whose studies of heat in chemical reactions formed the foundation of thermochemistry, Hess's Law. He moved with his family to Russia when his father, an artist, became a tutor to a rich family. Hess studied medicine, on the advice of the mother at the University of Tartu, from 1822 to 1826, and became a Doctor of Medicine.[1] Hess turned to chemistry after a meeting with Berzelius (*Jöns Jakob Berzelius*, 1779-1848), the famous Swedish chemist, and went to Stockholm University to study under him and he spent barely a month in Berzelius's laboratories. On his return to Russia, Hess joined an expedition to study the geology of the Urals before setting up a medical practice in Irkutsk. After practicing medicine in Irkutsk for two years, Hess returned to St. Petersburg, where he remained a member of the academic establishment.

Hess's Law of Constant Heat Summation

Hess proposed a law regarding the heats or enthalpies of reaction in 1840 called the Hess's law, the first law of thermodynamics, law on thermochemistry. This law states that "the heat change in a particular reaction is the same whether it takes place in one step or several steps", "in a series of chemical reactions, the total energy gained or lost depends only on the initial and final states, regardless of the

number or path of the steps." Hess was able to demonstrate that the quantity of heat produced (or absorbed) in going from one substance to another was the same no matter by what chemical route the change occurred, or in how many stages. [2]

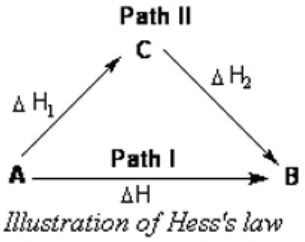

Figure 1. Illustration of Hess's law. [3]

Applications of Hess's law:

- Determination of Heat of Formation
- Determination of Heat of Transition
- Determination of Enthalpy of Transition
- Determination of Heats of Various Reactions
- Determination of Enthalpy of Hydration
- Determination of Standard Enthalpy of Reaction
- Calculation of Bond Energies ($\Delta_{bond}H^{\Theta}$)
- Bond energy of C – H bond = (1664) / 4 = 416 kJ mol^{-1}
- Enthalpy of atomization ($\Delta_{a}H^{\Theta}$)[4]

Hess's work

Hess's other work concerned the investigation of minerals and analysis of silver-telluride (Ag_2Te, Hessite). He discovered that the oxidation of sugars yielded saccharic acid.

Hess wrote the most successful domestic textbook on chemistry and a truly modern textbook "Foundations of pure chemistry", which went seven editions from 1831 to 1849. and was the standard Russian work for several decades. Hess's textbook has learned a whole generation of local chemists, including Mendeleev (*Дми́трий Ива́нович Менделе́ев*, 1834-1907), Butlerov (*Алекса́ндр Миха́йлович Бу́тлеров,* 1828-1886), Zinin (*Николай Николаевич Зинин*, 1812-1880) and Voskresensky (*Александр Абрамович Воскресенский*, 1809-1880).[5][6]

Conslusion

Unfortunately, Hess thermochemical work was truly appreciated until much later, when Ostwald (*Friedrich Wilhelm Ostwald*, 1853-1932) reprinted them in his monograph series "Classics of Science".[7]

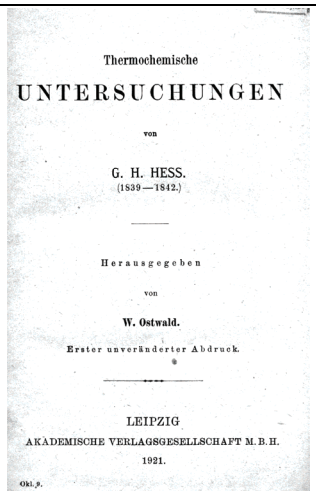
Thermochemische

UNTERSUCHUNGEN

von

G. H. HESS.
(1839—1842.)

Herausgegeben

von

W. Ostwald.

Erster unveränderter Abdruck.

LEIPZIG
AKADEMISCHE VERLAGSGESELLSCHAFT M. B. H.
1921.

Figure 2. Front Page of The Ostwald's book. [7]

Hess's law is useful in calculating the enthalpies of many reactions whose direct measurement is difficult or impossible ($\Delta H = \Delta H_1 + \Delta H_2$).

Acknowledgements:
The autors wish to thank the Ministry of Education and Science, Goverment of Republic of Serbia for supporting the scientific project "The quality of the education system in Serbia's European perspective" (KOSSEP), Code 179010.

References

[1] H. M. Leicester, Germain Henri Hess and the Foundations of Thermochemistry, The Journal of Chemical Education, 1951, 28 (11), 581-583.
[2] E. von. Meyer, A History of Chemistry from the Earliest Times to the Present Day, The Macmillan Company, 1898, 507. (cites that Ostwald refers to G. H. Hess, and his 1840 work, Constanz der Warmesummen, as being the founder of thermo-chemistry).
[3] http:chemmaster.co.in/showchapter.php?id=7&id2=95&title=Thermodynamics, May 25th 2012.
[4] I. Muller, A History of Thermodynamics - the Doctrine of Energy and Entropy, New York: Springer, 2007, 154-155.
[5] В. А. Волков, Е.В. Вонский, Г. И. Кузнецова, Выдающиеся химики мира, М. ВШ, 1991, 656.
[6] А. М. Корзухина, Русское физико-химическое общество и его роль в русской физике (1870—1917) ИИЕТ РАН. Годичная научная конференция 2003 г., М. Диполь-Т, 2003, 172-173.
[7] G. H. Hess, Thermochemische Untersuchungen, edited Ostwald, Akademische Verlagsgesellschaft M. B. H., Leipzig, 1921.

FOOD PHYSICAL CHEMISTRY

Q-01-P

APPLICATION OF DIFFERENTIAL PULSE POLAROGRAPHY IN ANALYSIS OF PECTIN

S. Milić[1], J. Bogdanović Pristov[1], S. Veljović Jovanović[1], S. Gorjanović[2], D. Sužnjević[2*]

[1]*Institute for Multidisciplinary Research, University of Belgrade, Kneza Viseslava 1, 11000 Belgrade, Serbia*

[2]*Institute of General and Physical Chemistry, P. O. Box 45, 11158 Belgrade 118, Serbia*

Abstract

Differential pulse polarography (DPP) with dropping mercury electrode (DME) was used to determine quantitatively galacturonic acid (GA), methylated polygalacturonic acid (met PGA), pectin (PC) and pectinase (PE) in 0.1 M $NaClO_4$ as supporting electrolyte. Current peaks of GA, met PGA, PC and PE, at -1.55, -1.50, -1.40 and -1.60 V *vs* SCE respectively, were found suitable for quantitative determination in the concentration range considered. Enzymatic reaction between PE and PC was followed and possibility to determine simultaneously of PC and PE was proved.

Introduction

Pectin is an acidic polysaccharide consisting of D-galacturonic acid units with very small quantity of neutral sugars. The monomers are linked together by 1-4 glycosidic linkage. Part of the acid is present as methyl ester. The textures of fruits and vegetables are largely influenced by the pectin content. Many food processors and pectin ingredient suppliers need to determine pectin content to control the quality of their products. Various chemical and instrumental methods, including HPLC, GLC, infrared spectroscopy, HPAEC using pulsed-amperometric detection (PAD), were applied for determination of pectin content in food products. Some of the methods, measuring pectin as galacturonic acid content, are quite accurate, and well-correlated to pectin content. In most cases pectin extraction and hydrolysis are required prior to analysis [1-2]. Until now, electrochemical methods have not been often used in pectin determination. The aim of the presented work was to explore possibility to apply differential pulse polarography (DPP), with dropping mercury electrode (DME) in detection and quantification of pectin and polygalacturonic acid.

Materials and methods

Chemicals Pectin (PC) from citrus fruits, methylated polygalacturonic acid (met PGA) from orange, pectinase (PE) from *Aspergillus niger*, sodium perchlorate (Sigma) and D-(+) galacturonic acid (GA) (Fluka) were used. Analytical grade (99.999) gaseous nitrogen was purchased from Messer-Tehnogas (Belgrade). Deionized water was used for preparing all experimental solutions.

Instrumentation. The current-potential (*i-E*) curves were recorded by polarographic analyzer PAR (Princeton Applied Research) model 174A, equipped with X-Y recorder (Houston Omnigraphic 2000). Dropping mercury electrode (DME) with a programmed dropping time of 1 s as working electrode, saturated calomel electrode (SCE) as a reference and a Pt-foil as auxiliary electrode were used. The *i-E* curves were obtained at different direct current intensity with alternative current modulating pulse of $25mV_{pp.}$ Scan rate of potential changes was 10 mVs^{-1}.

Procedure. Supporting electrolyte (0.1 M $NaClO_4$) in the electrolytic cell was deairated by passing nitrogen, than he inert atmosphere was kept constant during *i-E* curve recording. Dry met PGA, GA, as well as dry PC, or PC solution, with or without PE, dissolved in acetate buffer (pH 5.0), were added in defined amount into the cell solution (20 ml). Then, after bubbling of experimental solution 30 s with nitrogen, the corresponding i-E curves were recorded at room temperature.

Results and discussion

Until now, DPP was not applied for quantitative determination of PC as important ingredient of various natural products. Polarographic behavior of monomer of PGA (GA) at DME, in O.1 M $NaClO_4$ as supporting electrolyte, was firstly investigated. A well defined and symmetrical current peak of GA was recorded at potential about -1.55 V *vs* SCE (not shown). Obtained data gave the opportunity to quantify GA from applied solution.

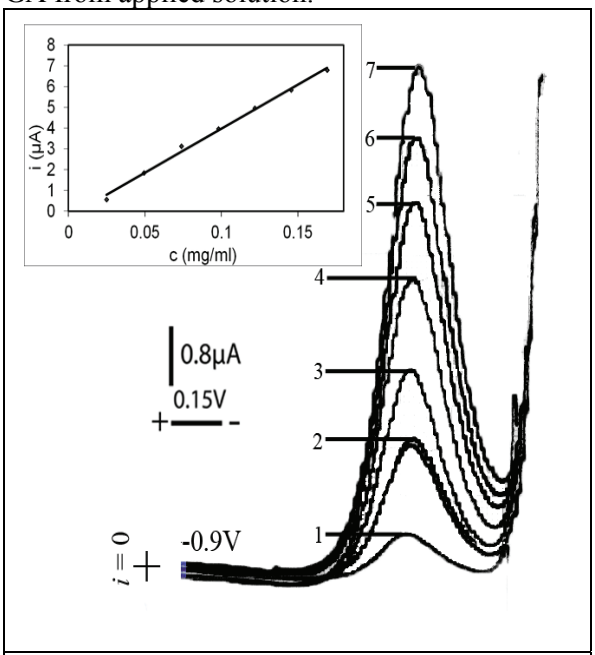

Figure 1. DPP curves of **1**. 0.02 **2**. 0.05 **3.**0.07 **4**.0.10 **5**.0.12 **6**.0.14 **7**. 0.17 mg/ml met PGA in 0.1 M $NaClO_4$.

Also, a well defined DPP peak of met PGA was recorded at somewhat less cathodic potential in respect to GA, i.e. at about -1.5 V *vs* SCE (**Fig. 1).** In concentration range from 0.02 to 0.17 mg/ml, the current linearly depended on PGA concentration (**Fig. 1**., insert).

Possibility for simultaneous determination of PC and PE, an enzyme that breaks PC into simple sugars and GA, was investigated

A well defined peak of PE at potential about -1.6 V *vs* SCE, shown in **Fig. 2.**, was found suitable for quantitative determination. Peak current showed linear dependence in considered concentration range

(**Fig. 2.**, insert). The measurable current of PE was not detected at concentrations bellow 0.05 *mg/ml*, probably due to protein adsorption at the electrode surface.

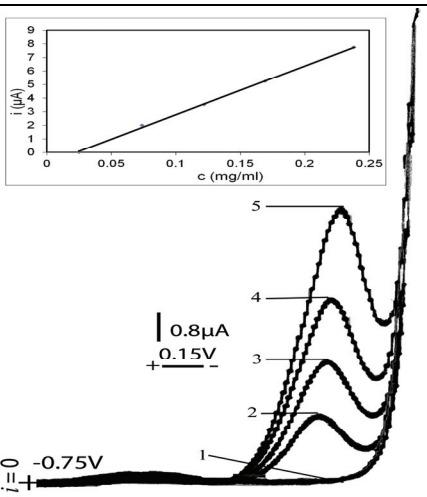

Figure. 2. DPP curves of **1**.0.02 **2**. 0.07 **3.** 0.12 **4**. 0.17 **5**. 0.23 mg/ml PE in 0.1 M $NaClO_4$.

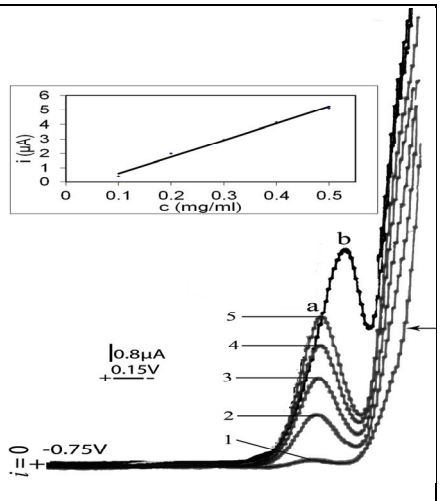

Figure 3. a) DPP curves of 1. 2 2. 4 3. 6 4. 8 5. 10 mg PC in 20 ml of 0.1 M $NaClO_4$; b) solution 5 after addition of PE (0.125 mg/ml).

The solution containing different amount of PC was initially studied (**Fig. 3., curves a, 1-5).** Current peaks recorded at about -1.4 V *vs* SCE depended linearly on applied PC concentrations **(Fig. 3.,** insert). Subsequently, PE was added into solution 5 (**Fig. 3.**, **curve a 5**) and possibility to measure PC and PE simultaneously was proved (**curve b).**

Conclusion

An easy-to-handle, rapid and reproducible method for detection and quantification of galacturonic acid, polygalacturonic acid, pectin and pectinase, based on differential pulse polarography, was developed. Simultaneous determination of pectine and pectinase was shown; it could be widely used to assess contamination of various complex samples after hydrolysis.

Acknowledgements

This research was supported by Ministry of Education and Science of Republic Serbia, grant No. III43010.

References

[1] M. Monsoor, et al, Food Chem, 2001, 74, 233-2382.
[2] H. Garna, et al, J. Agric. Food Chem. 2004, 52, 4652-4659

Q-02-P

MASS TRANSFER KINETICS DURING OSMOTIC DEHYDRATION OF SOUR CHERRY IN SUGAR BEET MOLASSES

M. Petrovic[1], T. Brdarić[1], K. Rajkovic[2] and V. Pavelkić[1]
[1]*Institute "Kirilo Savić", Vojvode Stepe 51, Belgrade, Serbia;*
[2]*High Chemical and Technological School for Professional Studies, Kruševac, Serbia*

Abstract
The present work aimed to study kinetics of osmotic dehydration (OD) of sour cherry in terms of solid gain and water loss. Sugar beet molasses (solid content 80, 60 and 40%) with NaCl (5%) was used as an osmotic medium. One temperature level of osmotic solution (room temperature) for 300 min was evaluated. Experimental results were fitted in the Peleg's empirical model of osmotic drying kinetics which expresses the influence of analyzed experiment factors on water loss (WL) and solid gains (SG). Mass transfer coefficients of water, Peleg rate constant (k_1) and Peleg capacity constant (k_2), were also estimated.

Introduction
Osmotic dehydration is a process of partial removal of water by submersing fruits in hypertonic solution [1]. This gives rise to two major simultaneously countercurrent mass transfer fluxes, namely water flow from the product to the surrounding solution and solute infusion into the product. Leakage of the product natural solutes quantitatively could be neglected, but may be important for the nutritional value of the product. The kind of osmotic agent used and hence its molecular weight or ionic behaviors strongly affects the kinetics of water removal and the solid gain. The most commonly used osmotic agents are sucrose and sodium chloride [2]. Besides these osmotic agents, sugar beet molasses emerges as a suitable raw-material for the preparation of hypertonic solutions [3]. The purpose of the present work was to study mass transfer parameters during the osmotic dehydration of sour cherry in sugar beet molasses (80%, 60%, 40% with 5% NaCl at room temperature) and examine the predictive capacity of Peleg's equation to the experimental data.

Materials and Methods
Sour chery, used for the experiment, were purchased on the local market in Belgrade, Serbia. Sugar beet molasses was obtained from sugar factory in Pećinci, Serbia. Prior to the treatment, the fruits are thoroughly washed and cut. After cutting, the initial mass of the samples was measured. As osmotic agent pure sugar beet molasses (around 80% solid content) and sugar beet molasses solutions (with 40% and 60% solid content) with the addition of 5% NaCl were used. Solutions were made prior to use. All analytical measurements were carried out in accordance to AOAC methods [4].
The water loss (WL) and the solid gain (SG) of fruit after time "t" of osmotic treatment are defined as [5]:

$$WL(\%)=\frac{(M_0-m_0)-(M-m)}{M_0}\times 100 \qquad SG(\%)=\frac{(m-m_0)}{M_0}\times 100$$

Where M_0 is the initial mass of fresh fruit before the osmotic treatment, M is the mass of sour cherry after time "t" of osmotic treatment, m is the dry mass of sour cherry after time "t" of osmotic treatment and m_0 is the dry mass of fresh fruit. Peleg's model [6] is widely used to describe the osmotic dehydration curves and is calculated according to equation:

$$M = M_0 \pm \frac{t}{k_1 + k_2 t}$$

where M is moisture content at time t (g), M_0 is initial moisture content (g), k_1 is the Peleg rate constant (g^{-1}), and k_2 is the Peleg capacity constant (g^{-1}).

Result and discussion

The OD process was studied in a terms of WL and SG as shown in Figure 1 and Figure 2. The increase of WL with the immersion times were observed. The clear trend of higher initial rate of WL, and subsequent slower rate of SG were obtained. The highest value of WL (62.75%) was observed in the samples immersed in the molasses with 80% solid content and with 5% NaCl at room temperature for 300 minutes. Figure 2 presents the degree of penetration of solids from the osmotic solution into the samples (SG value). The increase of concentration of hypertonic solution (molasses) caused a decrease of SG of treated samples at room temperature.

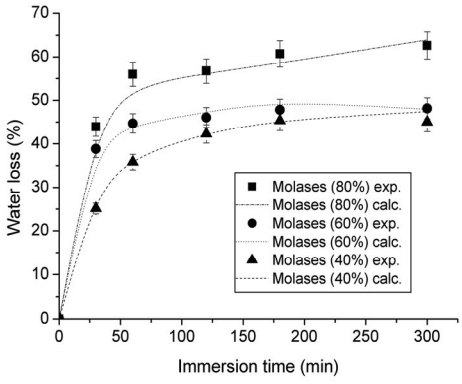

Figure 1. Dependence of water loss on dehydration time of sour cherry treated with beat molasses (solid content of 40, 60 and 80%) - Comparison of experimental and calculated data.

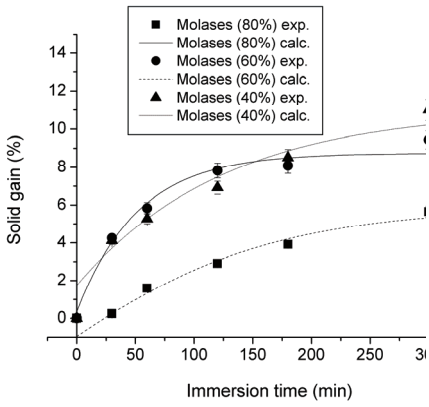

Figure 2. Dependence of solid gain on dehydration time for the different solid content of sugar beet molasses (40, 60 and 80%) - Comparison of experimental and calculated data.

The Peleg's rate (k_1) and capacity (k_2) constants were evaluated from experimental data (Table 1). High values of R^2 suggest that the Peleg equation in appropriate way describes the mass transfer kinetics during the OD of sour cherry in sugar beet molasses and indicate a good fit to the experimental data.

Table 1. Peleg's equation parameters.

Solid content (%)	Water loss			Solid gains		
	k_1	k_2	R^2	k_1	k_2	R^2
80	0.06±0.01	0.29±0.02	0.997	11.0±0.4	1.80±0.1	0.974
60	0.10±0.02	0.30±0.05	0.979	2.30±0.3	1.50±0.2	0.995
40	0.15±0.05	0.40±0.03	0.989	1.70±0.2	1.30±0.2	0.981

Conclusion

Peleg's equation parameters (k_1 and k_2) for the solid gain and water loss presented a good fitting to the experimental data. The equation parameters exhibit a trend of decreasing with the increase of the solid content in sugar beet molasses for water loss and are inversely proportional for solid gain. The presence of NaCl in osmotic media has some influences on mass transfer kinetics: it increases viscosity of the osmotic media and hence improves solid gain and decreases water loss.

Acknowledgement

This study was supported by Ministry of Education and Science of Republic of Serbia, Project TR 31055.

References

[1] P. M. Azoubel, F. Elizabeth, X. Murr, , Journal of Food Engineering, 2004, 61,291–295.
[2] S. Mizrahi, S. Eichler, O. Ramon, Journal of Food Engineering, 2001, 49, 87–96.
[3] Lj. Lević, V. Filipović, T. Kuljanin, PTEP, 2007, 11, 132-134.
[4] AOAC, Official method 963. 22, Washington, 2000.
[5] B. Singh, A. Kumar, A. K. Gupta, Journal of Food Engineering, 2007, 79, 471–480.
[6] M. Peleg, Journal of Food Science, 1988, 53, 1216–1219.

Q-03-P

THERMAL ANALYSIS OF RASPBERRY AND BLACKBERRY SEED FLOUR

D. Micić, S. Ostojić, M. Simonović, M. Dojčinović,
S. Hranisavljević, B. R. Simonović
University of Belgrade, Institute of General and Physical Chemistry, Studentski trg 12, 11000 Belgrade, Serbia

Abstract
Thermal characteristic of red raspberry (*Rubus ideaus*) and blackberry *(Rubus fruticosus)* seed flours have been followed by Modulated Differential Calorimetry (MDSC) and Thermogravimetric analysis (TGA). MDSC allows the separation of the (total) heat flow signal into the heat capacity (reversible heat flow) and the kinetics components (non-reversible heat flow). Thermal events in the low temperature region of seed flour have been approximately separated suggesting that there are two independent thermal processes.

Introduction
Fruit seeds are byproducts from fruit processing, and seed flour is the primary byproduct from seed oil production. Recent study showed that red raspberry seed flour obtained from the cold-pressing procedure may contain a significant level of antioxidants [1]. These data suggest the potential of developing novel uses of fruit seed flours as food ingredients rich in beneficial food factors for improving human diets, while enhancing the profitability of fruit production and processing industries. Additional research is required to investigate fruit seed flours for their contents of health beneficial factors to promote their value-added utilization as beneficial food ingredients. MDSC nonreversing signal may contain important information on irreversible processes, such as slow chemical reactions (oxidation, curing, evaporation, etc.) and nonequilibrium phase transitions (crystallization and reorganization); it may even enable to separate the complicated simultaneous fusions, glass transitions and annealings, common in many macromolecules and complex mixtures [2,3].
The present study was conducted to investigate the seed flours of red raspberry (*Rubus ideaus*) and blackberry *(Rubus fruticosus)* for their thermal characteristics by mean of Modulated Differential Calorimetry (MDSC) and Thermogravimetric analysis (TGA).

Experimental
Fruit seed flour preparation. Fruit seed were the solid residues from the cold-pressing fruit pulp. Seeds were drayed at room temperature, to the constant moisture of 6-7% and grinded immediately before thermal analysis.
Thermal analysis. MDSC and TGA of blackberry and raspberry seed flours have been performed on TA Instruments DSC Q 1000, Differential Scanning

Calorimeter and TGA measurements on TA Instruments TGA Q 500 Thermogravimetric Analyzer under N_2 purge flow of 50ml/min and 60ml/min respectively. MDSC scans were conducted in temperature range from -90 ^{0}C to150 ^{0}C, with heating rate Hr = 5 ^{0}C/min with modulation of ±0.50 ºC amplitude and 40s period of modulation. and TGA scans were performed in temperature range of 25 ^{0}C to 700 ^{0}C with heating rate Hr = 5 ^{0}C/min.

Results and Discussion

In Fig. 1. and 2. are presented MDSC curves of blackberry and raspberry seed flours.

Total DSC curve is characterized with overlapping effect in low-temperature region caused by the freezing and unfreezing of large-amplitude motion [4]. It was shown that thermal transitions, observed in the range of −80 to −10 ^{0}C were independent on water content, and they were mainly attributed to lipid melting transitions [5]. Broad endothermic peak with T_m at about 93 ^{0}C corresponds to protein denaturation [5].

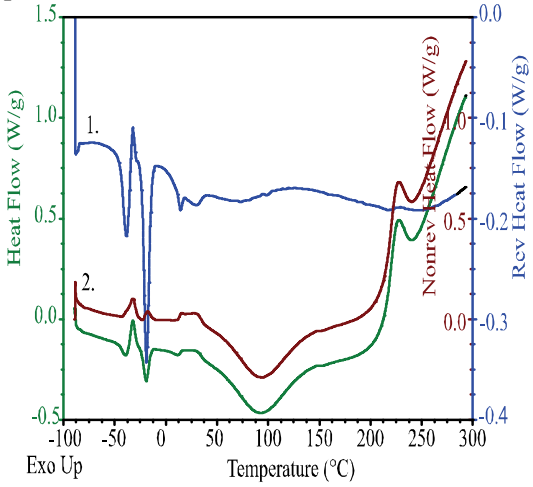

Figure 1. MDSC curves of blackberry seed flour.

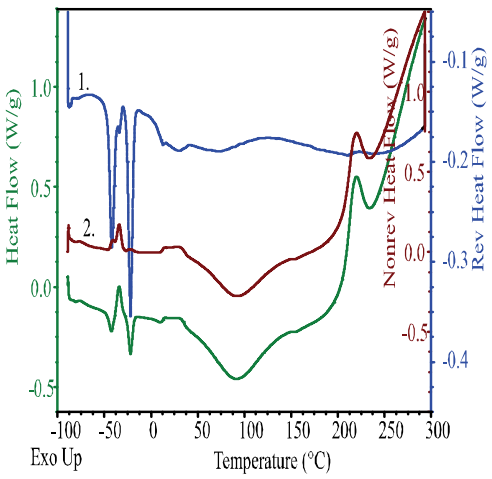

Figure 2. MDSC curves of raspebrry seed flour.

Using MDSC, the reversing (curve 1.) and nonreversing (curve 2.), thermal events in the low temperature region of seed flour have been approximately separated [4], reversing (curve 1), suggesting that there are two independent thermal processes.

In Fig. 3. TGA curves of blackberry and raspberry seed flour are presented . Results from TGA analysis are shown in Table 1.

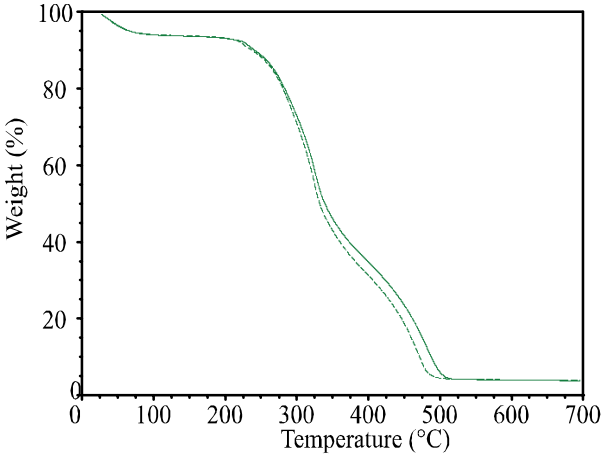

Figure 3. TGA curves of blackberry (dashed curve) and raspberry (solid curve) seed flour.

Table 1. Results obtained from TGA curves of blackberry and raspberry seed flour

seed flour	I weight loss (moisture) (%)	II weight loss (%)	III weight loss (%)	Residue (700^0C) (ash) (%)
raspberry	6.09	60.92	31.70	1.29
blackberry	6.22	57.33	35.28	1.16

Results obtained from TGA and DSC curves indicated similarity in thermal behavior of raspberry and blackberry seed flour.

Conclusion

Using MDSC, thermal events in low temperature region (MDSC curve) of seed flour have been approximately separated (reversing curve 1), suggesting that there are two independent thermal processes. Similarity of thermal behavior of blackberry and raspberry seed flours suggesting on composition resemblance of these seeds.

Acknowledgements

This work was supported by the Ministry of Education and Science of the Republic of Serbia, under the Projects No TR-31093 and TR-31055.

References

[1] J. Parry, L. Su, J. Moore, Z. Cheng, M. Luther J.N. Rao, J-Y Wang, L. L. Yu , J. Agric. Food Chem., 2006,. 54, 3773-3778.
[2] B. Wunderlich, Y. Jin, A. Boller, Thermochimica Acta, 1994, 283, 277-293.
[3] Lai & Lii, TA Instruments, 1996.
[4] M. Pyda, B. Wunderlich, Macromolecules,2005, 38, 10472-10479.
[5] S. B. Matiacevich, M. L. Castellion, S. B. Maldonado, M. P. Buera Thermochimica Acta, 2006, 448, 117–122.

Q-04-P

DRYING KINETICS OF RASPBERRY

L. Pezo, S. Ostojić, S. Zlatanović,
A. Jovanović, S. Stanojlović, O. Kovačević, B. Kovačević
Institute of General and Physical Chemistry, University of Beograd,
Studentski Trg 12, 11000 Belgrade, Serbia, latopezo@yahoo.co.uk

Abstract
The drying kinetics of raspberry in a laboratory dryer was studied. The changes of color on raspberry's surface were determined by digital camera. *R* (red) color index frequency was calculated during the experiment. A mathematical model to predict the shrinking of geometrical bodies was proposed, assuming unidirectional drying and two-dimensional shrinkage. Thermal analysis, by means of differential scanning calorimetry (DSC) and thermogravimetry (TGA) of fresh and dried raspberries have been studied.

Introduction
Mathematical modeling is widely used in developing kinetics models to predict the mass transfer of drying process at atmospheric pressure [1]. The main objective of this study was to determine the effects of process parameters: drying air temperature, air velocity and sample surface on the diffusion model coefficients and the values of moisture diffusivity and heat transfer coefficients by using multiple regression analysis, and to test the most appropriate drying model for understanding the drying behavior of raspberry.

Materials and Methods
The raspberries (aver. diameter 11.4 mm, and aver. weight 2.9 g for single fruit), were carefully placed on the trays. The initial and final moisture contents of the products were determined at 105 ^{o}C. Raspberries of average initial moisture content 85.7% (wb), were dried, at temperatures of 50^{o}C, relative air humidity 50-55%, at the velocities of drying air of 1.2 m/s. The kinetics models were selected with the correlation coefficient (r^2), the reduced chi-square (χ^2), mean bias error (*MBE*), root mean square error (*RMSE*) and relative standard deviation (*RSD*), to determine the quality of that fitting function [2]. Color images of raspberries during drying process were captured in triplicate, by a common home camera. All the acquired images were 24 bit RGB (16.8 millions of colors). The macro function of the digital camera has been used, to cover a scene area of approximately Ø10 cm. The dimensions of raspberries were measured by a digital micrometer. Differential scanning calorimetry (DSC) and thermogravimetry (TGA) of fresh and dried raspberries have been performed under N_2 purge flow of 50ml/min and 60ml/min respectively. DSC scans were conducted in temperature range from -90ºC to 400ºC, with heating rate Hr=5Cº/min, and TGA scans were performed in temperature range of 25ºC to 900ºC with heating rate Hr=5Cº/min.

Results and Discussion

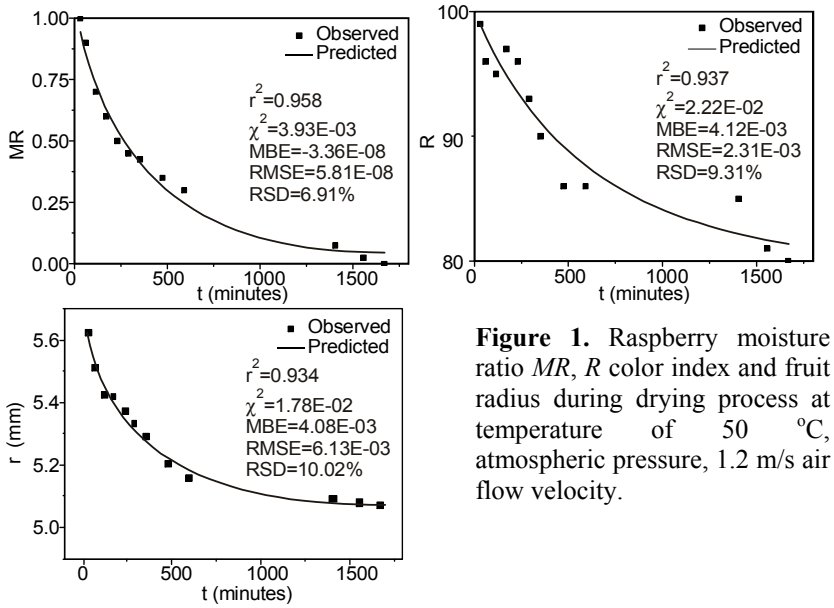

Figure 1. Raspberry moisture ratio *MR*, *R* color index and fruit radius during drying process at temperature of 50 °C, atmospheric pressure, 1.2 m/s air flow velocity.

The moisture content data at the given drying conditions fitting computations with the drying time were carried on the several drying models. The moisture ratio (*MR*), as well as the *R* color index and overall fruit diameter changes during the drying experiment are presented on Fig. 1. The best model describing the thin layer-drying characteristic was chosen as the one with the highest r^2 and the lowest χ^2, *MBE* and *RMSE*. *RSD* should be below 15%. It was determined that the best fitting results were obtained with logarithmic model, $MR = 0.989 \cdot \exp(-0.003 \cdot t) + 0.034$. Fick's second law was used for effective diffusion calculus, using Arrehnius type relationship, in the temperature range of (45-55°C, triplicate measurement of *MR* was performed for each time step). Calculated effective diffusion coefficient was 3.2E-10m^2/s, and activation energy of 20 to 40 kJ/mol, were in accordance to literature values [3]. The best model describing the color changes characteristic was logarithmic model, $R = 19.402 \cdot \exp(-0.002 \cdot t) + 80.494$. The obtained prediction results of fruit radius correspond very well to those achieved by experimental measurement. Obtained DSC and TGA curves of fresh and dried raspberries, (Fig 2.) show differences of thermal stability between fresh and dried fruits caused by water loss during drying process [4]. It can be seen, from DSC curve that phase transition of ice melting and water evaporation are dominant thermal events, as the sample water content is high. High water content (85.7%) is also observed from corresponding TGA curve of fresh raspberries. DSC curve is characterized by three endothermal peaks with maximums at T_{m1}=-40.7ºC, T_{m2}= -20.23 ºC and T_{m3}=114.0ºC respectively and one glass transition T_g= 42.3 ºC. Results are in agreement with [4], which showed that glass transition temperatures of raspberries are influenced by water content, [5,6], as it was found that dried food material has similar thermal properties of semi-

crystalline polymers. Water content of dried sample obtained from TGA curve, dashed curve was 19.3%.

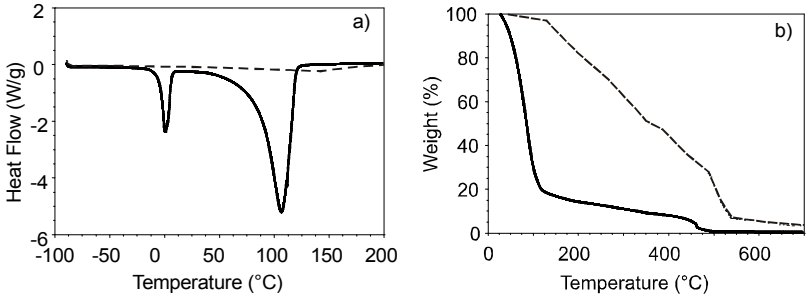

Figure 2. a) DSC curves of dried (dashed curve) and fresh (solid curve) raspberries and b) TGA curves of dried (dashed curve) and fresh (solid curve) raspberries.

Conclusion

The best model adequately describe the drying behavior of raspberry fruit, with gained r^2 of 0.937. Statistical analysis, including comparison tests, showed that the model adequately represent the browning process, showing r^2=0.958. Finally, a mathematical model to predict the shrinking of geometrical spherical bodies was proposed, assuming unidirectional drying and two-dimensional shrinkage with accuracy of r^2=0.934. Thermal analysis shows differences of thermal stability between fresh and dried fruits caused by water loss during process of drying.

Acknowledgement

The authors acknowledge for the financial support the Ministry of Science of the Republic of Serbia, TR – 31055, TR – 31093, 2011-2014.

References

[1] A. Kaya, O. Aydın, C. Demirtas, Biosyst Eng, 2007, 96 (4), 517–524.
[2] E. K. Akpinar, J. Food Eng., 2006, 73, 75–84.
[3] P. P. Lewicki, E. Jakubczyk, J. Food Eng., 2004, 64, 307–314.
[4] R. M., Syamaladevi, S. S., Sablani, J. Tang, J. Powers, B. G. Swanson, J. Food Eng., 2009, 91, 460–467.
[5] S. Shyam, S.Roopesh, R. M. Syamaladevi, B. G. Swanson, Food Eng. Rev., 2010, 2, 168–203.
[6] G. Uretir, M. Ozilgen, S. Katnas, J. Food Eng., 1996, 30, 339–350.

Q-05-P

THERMAL ANALYSIS OF OSMOTICALLY DEHYDRATED MEAT

S. Ostojić[1], S. Zlatanović[1], D. Micić[1], D.a Šuput[2], B. R. Simonović[1], Ljubinko Lević[2]

[1] *University of Belgrade, Institute of General and Physical Chemistry, Studentski trg 12, 11000 Belgrade, Serbia*

[2] *Faculty of Technology, University of Novi Sad, Bulevar Cara Lazara 1, 21000 Novi Sad, Serbia*[1]

Abstract

Besides the water, proteins are the most important component of meat and this approves the relevance of studying their denaturation, particularly that of myofibrillar proteins. Water loss, obtained from thertmogravimetric analysis (TGA) and protein stability, obtained from differential scanning calorimetry (DSC), expressed as temperature (T_m) and enthalpy (ΔH) of protein denaturation, during the storage was followed. Results have been compared to fresh pork meat thermal characteristics. Water activity (a_w) of fresh and dehydrated pork meat have been obtained from DSC and TGA results.

Introduction

Knowledge of thermal transitions occurring in foods during processing is essential in evaluating the parameters required for producing the highest quality [1-4]. The advantage of the DSC method is that it can be used in complex mixtures and at high concentrations of proteins, which is the situation occurring in meat. A typical curve from thermal transitions found in a muscle is composed of three major transition zones. The first transition displays its maximum between 54ºC and 58ºC and has been attributed to myosin [4,5] the second transition, which occurs between 65ºC and 67ºC, was assigned to collagen [5,6] and to sarcoplasmic proteins [2]. The third transition has been assigned to actin and is found between 80ºC and 83ºC [6]. For the second transition it has also been shown that both isolated actomyosin and myosin and its sub-units undergo transitions in the same temperature range [2]. The aim of this study was to follow thermal stability and water content in osmotically dehydrated meat samples during two months storage.

Experimental

*Osmotic dehydration***.** Pork meat was osmotically dehydrated (OD) in the solution of sugar beet molasses [7], packed in modified atmosphere (30% CO2 - 70% N2) and stored for 2 months under the refrigerator temperature (4ºC).

*Thermal anaysis***.** DSC and TGA of fresh and osmotically dried pork meat have been performed on TA Instruments DSC Q 1000, and TGA measurements on TA Instruments TGA Q 500, under N2 purge flow of 50ml/min and 60ml/min respectively. DSC scans were conducted in temperature range 3ºC -150 ºC, and -80 ºC - 180ºC heating rate, Hr=5Cº/min, and TGA scans in temperature range 25ºC-900ºC, Hr=5Cº/min.

Results and Discussion

Thermal behavior of pork meat samples is shown in Figures 1.2. 3. and 4. Fig. 1 is a DSC curve of fresh pork meat with peaks at about -0.3ºC, 69ºC and 93°C, and total denaturation enthalpy of 970J/g.

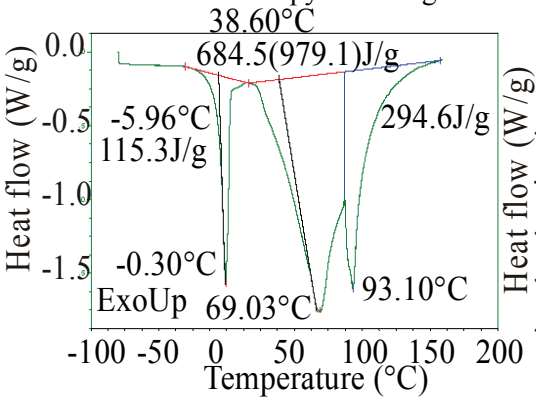

Figure 1. DSC curve fresh pork. meat.

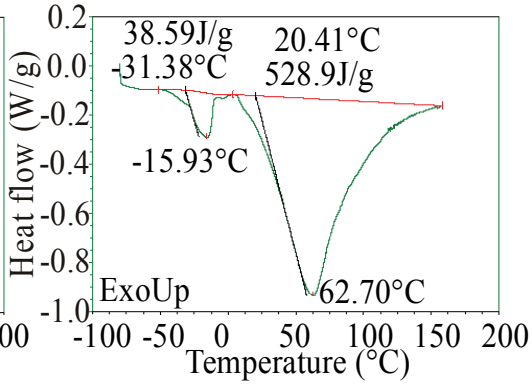

Figure 2. DSC curve of OD pork meat.

.

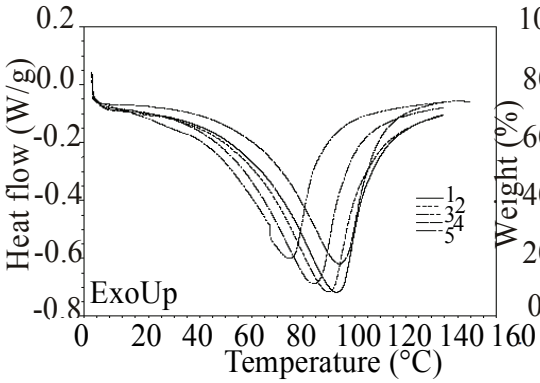

Figure 3. DSC curves of OD pork meat: **1**) 7 days, **2**) 15 days, **3)** 30 days ,**4)** 45 days **5)** 60 days of storage.

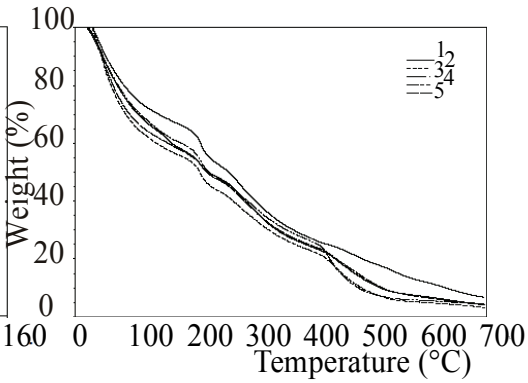

Figure 4. TGA curves of OD pork meat: **1**) 7 days, **2**) 15 days, **3)** 30 days ,**4)** 45 days **5)** 60 days of storage.

First transition corresponds to water melting, second transition, which occurs at 69ºC, was assigned to collagen [6] and the third transition has been assigned to actin [5]. On Fig. 2. is DSC curve of osmotically dehydrated pork meat, where process of protein denturation is presented as one broad endothermal peak with temperature maximum T_m=57ºC and total denaturation enthalpy (ΔH) of 430J/g. Decreased denaturation enthalpy and temperature maximum of protein denaturation suggesting that destabilization of meat proteins and conformational changes have been induced by process of osmotic dehydratation. Thermal stability of osmotically dehydrated pork meat has been followed by DSC and TGA in the storage time period of 60 days. Results are presented on Fig. 3. and 4. and Table 1

Table 1. Thermodynamic parameters of protein transitions for OD and fresh pork meat.

…Time (days)	Onset temp. T_o(°C)	Peak temp. T_m (°C)	Enth ΔH (J/g)	Moisture (%)	Residue at 700 °C (%)	Water activity a_w
0	53.26	89.30	652.3	37.70	5.65	0.745
15	59. 65	95.06	668.1	43.78	4.91	0.729
30	35.36	66.81	678.5	41.66	4.76	0.722
45	59.74	79.68	716.7	34.26	4.67	0.735
60	67.16	99.05	694.3	42.27	3.93	0.742
Fresh meat	27.56	81.92	979.1	70.90	1.45	0.938

From results obtained it can be assumed that there were no changes of protein stability during storage period of 60 days, considering enthalpy of (ΔH) and temperature of denturation (Tm). Slight variations of moisture affected the water activity (a_w) (results obtained by DSC and TGA) of osmotically dehydrated pork meat.

Conclusion

It was shown that sugar beet molasses solution affects thermal stability (DSC results), and water loss (TGA results) of dehydrated pork meat compared to fresh pork meat. No significant changes, during two months storage time have been induced concerning protein thermal stability, but there were slight changes of water content during storage (TGA) what influenced a_w.

Acknowledgements

This work is part of projects No. TR-31055 and TR-31093, suported by the Ministry of Education and Science Republic of Serbia.

References

[1] F. Jimenez-Colmenero, S. Cofrades, J. Carballo, P. Fernandez, F. J. Fernandez-Martın, Agric. Food Chem.,1998, 46, 4706-4711.
[2] E. Tornberg, Meat Science, 2005, 70, 493–508.
[3] C. Tortoe, African Journal of Food Science ,2010, 4, 303 – 324.
[4] S. A. Anglea, V. Karathanos, M. Karel, Biotechnol. Prog., 1993, 9, 204-208.
[5] M. H., Stabursvik, E. M. Martens, Journal of Texture Studies, 1982, 13, 291–309.
[6] E. Stabursvik, H. Martens, J. Sci. Food Agric., 1980, 31,1034–1042.
[7] N. M. Misljenovic, G. B. Koprivica, L.L. Pezo, L. B. Levic, B.L. Curcic, V.S.Filipovic, M.R. Nicetin, Thermal Science, 2012, 16, 43-52 .

Q-06-P

EFFICIENSY OF OSMOTIC DEHYDRATION OF PORK MEAT USING DIFFERENT OSMOTIC SOLUTIONS

L. L. Pezo[1], V. S. Filipović[2], M. R. Nićetin[2], B. Lj. Ćurčić[2], N. M. Mišljenović[2], G.Koprivica[2], Lj. B. Lević[2]

[1]University of Beograd, Institute of General and Physical Chemistry, Studentski trg 12-16, 11000 Belgrade, Serbia, [2]University of Novi Sad, Faculty of Technology, 21000 Novi Sad, Bulevar cara Lazara 1, Serbia

Abstract

In order to analyze the efficiency of mass transfer kinetics during osmotic dehydration (OD), pork meat was dehydrated in three different osmotic solutions (sugar beet molasses, ternary solution and combination of these solutions in a 1:1 ratio) under atmospheric pressure, at room temperature *T* (20°C), with manual stirring on every 15 minutes. The most significant kinetic parameters of the process: water loss (*WL*) and solid gain (*SG*), were determined after 1, 3 or 5 hours of dehydration.

Introduction

OD process as an important method for preserving solid food, which involves partial water removal from food stuff immersed in hypertonic aqueous solutions. Due to low energy consumption and mild temperatures, which is considered minimal processing, OD is suitable as a pretreatment for many processes, to improve nutritional, sensorial and functional properties of food without changing its integrity. The difference in the chemical potential of water between the raw material and the osmotic medium is the driving force for dehydration. Osmotic temperature, concentration of osmotic solution and immersing time are the most important variables in osmotic process. Increasing the osmotic solution concentration induces an increase in the mass transfer [1].

Materials and methods

Initial moisture content of the fresh meat was 74.64±0.48%. Three different solutions were used as hypertonic mediums. Solution 1, ternary osmotic solution, was made from sucrose in the quantity of 1.200g/kg water, NaCl in the quantity of 350g/kg water and distilled water. Solution 2 was combination of the first and third in ratio 1:1. Solution 3, sugar beet molasses, with inital dry matter content of 80.00%, was obtained from the sugar factory Pećinci. The material to solution ratio was 1:5 (w/w). Samples from all three solutions after 1, 3 and 5h were taken out to be lightly washed and gently blotted, to remove excess water. Dry matter content of the fresh and treated samples was determined by drynig at 105°C for 24h in a heat chamber until constant weight. Three key process variables were measured: moisture content, change in weight and change in the soluble solids. Using these values, *WL* and *SG* were calculated, [2,3].

Results and discussion

The Response surface method was performed to determine the optimum osmotic dehydration conditions for pork meat cubes OD process. Table 1 shows the ANOVA calculation regarding the response models developed when the experimental data fitted (second order polynomial – SOP model), for all the dependent variables.

Table 1. Analysis of variance for the responses, for all solutions.

Term	Source	Sum of squares					
		Solution 1		Solution 2		Solution 3	
		WL	*SG*	*WL*	*SG*	*WL*	*SG*
Linear	Time	0.160*	0.011*	0.089*	0.008*	0.037*	0.006*
	Temp	0.056*	0.008*	0.033*	0.001*	0.009*	0.001*
	Conc	0.006*	0.000	0.042*	0.000	0.001*	0.000
Quad.	Time	0.016*	0.001*	0.008*	0.000	0.011*	0.001*
	Temp	0.001*	0.000	0.000	0.000	0.001*	0.000
	Conc	0.000	0.001*	0.000	0.000	0.000	0.000
Cross product	Time Temp	0.001*	0.000	0.000	0.000	0.001*	0.000
	Time Conc	0.003*	0.000	0.002*	0.000	0.002*	0.000
	Temp Conc	0.003*	0.001*	0.001*	0.000	0.003*	0.000
Error	Error	0.002	0.001	0.001	0.001	0.002	0.001
r^2		99.1	95.7	99.2	88.3	98.8	94.4

*Significant at 95% confidence level

ANOVA revealed that the linear terms contributed substantially in most of the cases to generate a significant SOP model. The linear terms of SOP model were found significant, at 95% confidence level, and their influence were found most important in all model calculation. *WL* was significantly affected by all process variables, treatment time, temperature, and concentration, at 95% confidence level, for all osmotic solutions. The main influential variable seems to be the treatment time, while temperature and concentration terms are also very statistically significant at 95% confidence level. *SG* is most affected by treatment time, and temperature terms are also significant at 95% confidence level. All SOP models had insignificant lack of fit tests, and r^2 values for all solutions *WL* (98.8-99.2) and *SG* (88.3-95.7) were found very satisfactory and showed the good fitting of the model to experimental results. The contour plots of *WL* and *SG*, were superimposed to ascertain the optimum osmotic dehydration conditions for pork meat cubes, for all solutions used in the experiment (Fig. 1). An optimum operating area was derived and crosshatched and point A was deduced by approximating the optimum position in obtained area on graph. The optimum OD conditions for solution 1 are as follows: soaking time 4 h, concentration and temperature of 72% and 45°C. The optimum OD conditions for solution 2 should be: treatment time 3 h, concentration 57% w/w, and temperature of 40°C. Coordinates of optimized point for temperature, time concentration graph, for

solution 3 were: 40°C, 3.7 h and 63% w/w. Contour plots (shown on Fig. 1) of both *WL* and *SG* tend to grow with temperature and processing time. The desired responses for the optimum drying conditions in solution 1 were: *WL*=0.53, *SG*=0.15. *WL* was much lesser for OD process in solution 2 and solution 3: 0.41 and 0.45. *SG* was very similar to OD in solution 1.

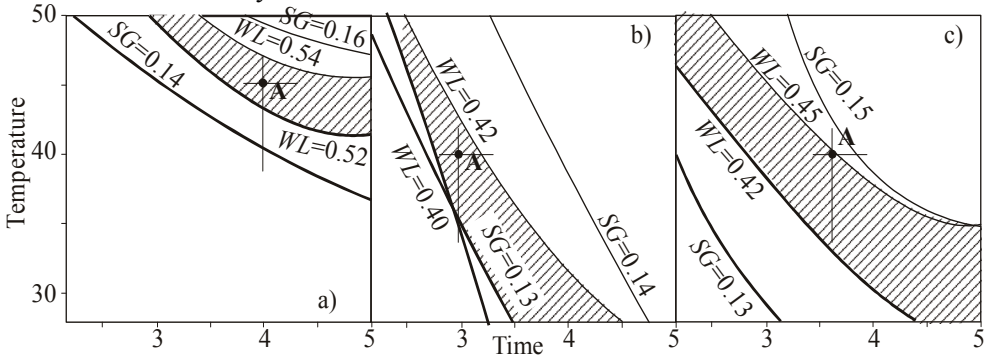

Figure 1. Optimum contour plots of the system responses for a) solution 1, b) solution 2, c) solution 3.

Conclusion

According to presented results it can be concluded that all three solutions are satisfying osmotic mediums. At the end of treatment *SG* were the lowest in samples immersed in solutions 1 and 2. While, the best results considering *WL* were achieved using solution 1. During OD of pork meat, in all three osmotic solutions, water removing process was most intensive at the beginning and after 3 hours had tendency of slowing down, and can be limited to 3 hours.

Acknowledgement

These results are part of project supported by the Ministry of Education and Science of the Republic of Serbia, TR-31055, 2011-2014.

References

[1] M.A.C. Silva, Z.E.Silva, V.C. Mariani, S. Darche, Food Sci. Technol. Int., 2012, 45, 246-252.

[2] G. Koprivca, N. Mišljenović, Lj. Lević, L. Jevrić, Journal on Processing and Energy in Agriculture, 2010, 14, 27-31.

[3] N. Mišljenović, G. Koprivca, L. Pezo, T. Kuljanin, M. Bodroža Solarov, B. Filipčev, APTEFF, 2011, 42, 91-100.

Q-07-P

APPLICATION OF RESPONSE SURFACE METHOD ON PORK MEAT OSMOTIC DEHYDRATATION

L. L. Pezo[1], B. Lj. Ćurčić[2], M. R. Nićetin[2], V. S. Filipović[2], G. B. Koprivica[2] , N. M. Mišljenović[2], Lj. B. Lević[2]

[1]University of Beograd, Institute of General and Physical Chemistry, Studentski trg 12-16, 11000 Belgrade, Serbia, [2]University of Novi Sad, Faculty of Technology, 21000 Novi Sad, Bulevar cara Lazara 1, Serbia

Abstract

The main objective of here presented article was to examine the influence of different osmotic parameters on the mass transfer kinetics during osmotic treatment of pork meat cubes (*M. triceps brachii*), shaped 1x1x1cm, under atmospheric pressure. The observed parameters included: osmotic solution temperature (20, 35 and 50^{o}C), immersion time (1, 3 and 5 hours) and sugar beet molasses concentration (60, 70 and 80% w/w). The system's response parameters observed were: water loss (WL), solid gain (SG), final dry matter content (DM) and water activity (a_w). The optimization of process parameters was obtained, using response surface methodology (RSM).

Key words: Osmotic dehydration, pork meat, sugar beet molasses, Response surface method

Introduction

Meat represents a cellular system with great biochemical and structural complexity, created by a network of muscular fibers surrounded by connective tissue. One of the most important constituent of meat is water [1, 2]. Physicochemical, sensory and technological properties of fresh meat are related with water content. Water is held in myofibrils, functional proteins of meat, but also it may exist in the intracellular space between myofibrils and sarcoplasm [3]. One of the potential preservation techniques for producing products with low water content and improved nutritional, sensorial and functional properties is osmotic dehydration (OD). In OD process, mass transfer is caused by a difference in osmotic pressure: water outflow from product to solution, solute transfer from solution into the product, and leaching out of the products own solutes [4]. Sugar beet molasses is known as an excellent medium for OD, primarily due to the high dry matter (80%) and specific nutrient content. [4].

Materials and methods

Pork meat was purchased at the butcher shop "Mesara Štrand" in Novi Sad, just before use. Initial moisture content of the fresh meat was 72.83%. Sugar beet molasses solution, with inital dry matter content of 85.04%, was obtained from the sugar factory Pećinci. Distilled water was used for dilution of solutions. The sample to solution ratio was 1:5 (w/w). The process was performed in laboratory jars at solution different temperature with manual agitation on every 15 minutes. After OD, the samples were taken out from

osmotic solutions to be lightly washed with water and gently blotted to remove excessive water. Dry matter content was determined by drying the material at 105 ºC in a heat chamber until constant mass was achived (Instrumentaria Sutjeska). Water activity (a_w) of the OD samples was measured using TESTO 650, with an accuracy of ±0.001 at 25ºC. Soluble solids content of the molasses solutions was measured using Abbe refractometer, at 20 ºC. In order to describe the mass transfer kinetics of the OD, experimental data from three key process variables are usually obtained: moisture content, change in weight and change in the soluble solids. Using these, WL, SG, were calculated for different solutions and processing times [4]. Process variables were coded, according to central composite full factorial design (3 level-3 parameter) with 27 runs (1 block) [5]. RSM was selected to estimate the main effect of the process variables on mass transfer variables, during the OD.

Results and Discussion

The most intensive increase in dry matter content was observed as the increase from initial 27.17 to 71.11 % in sugar beet molasses solution, concentrated to 80% w/w, after 5 hours of experiment. The huge difference in osmotic pressure between hypertonic solution and the meat tissue, causes the vast initial loss of the water at the beginning of the dehydration process, and the WL increased with immersion time. The maximum WL was 0.58, after 5 hours, at maximum concentrations. SG increases with immersion time. The aim of OD is the achievement of as low as possible solid uptake, and the most acceptable results were achieved by using sugar beet molasses concentrated to 80% w/w (0.17 g/g i.s.w.), after 3 hours of osmotic process. During the OD process, total mass of the meat samples was evidently reduced. It was shown that weight reduction (WR=WL-SG) is most intensive in the first hour of the process, while at the end of the process, weight reduction value decreased. To determine optimal condition for the WL/SG ratio must be considered. High value of WL/SG ratio is the most important indicator of the effectiveness of OD treatment. The highest value of WL/SG ratio was 3.64, achieved by immersion of meat for 3 hours in sugar beet molasses 70% concentration, at 20^{o}C. The second order polynomials (SOP) were used to predict the system responces. ANOVA calculation regarding the response models developed was used to evaluate the fitting with experimental data. The analysis revealed that the linear terms contributed substantially in all of the cases to generate a significant SOP model, at 95% confidence level, and their influence were found most important in all model calculation. The SOP models for all variables were found to be statistically significant and the response surfaces were fitted to these models. The r^2 values for WL (99.1), SG (95.7), a_w (93.0) and DM (99.3), were found very satisfactory and showed the good fitting of the model to experimental results. Fig. 1 shows the superimposed graph of the dehydration conditions of pork meat in sugar beet molasses solution. An optimum operating area was derived and crosshatched and point A was deduced by approximating the optimum position in obtained area on graph.

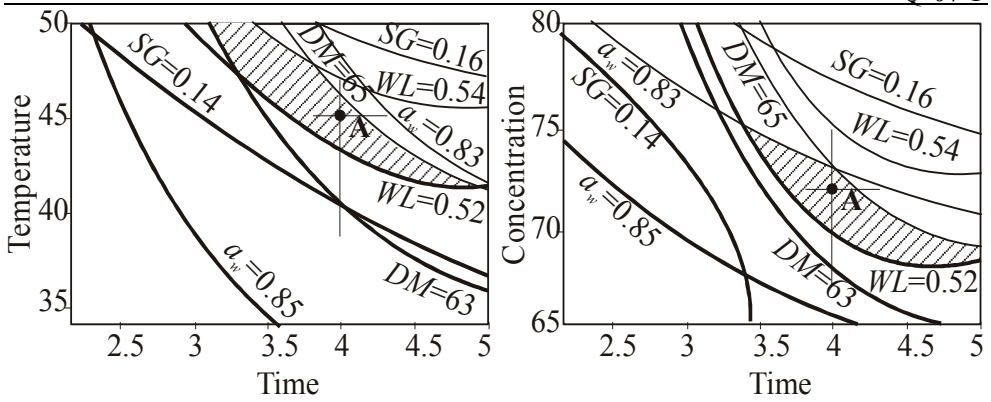

Figure 1. Optimum contour plots of the system responses.

Conclusion

The optimum dehydration process parameters were found by superimposition of the contour plots of all responses. Optimum process parameters, for OD in sugar beet molasses solution were: osmotic time of 4 h, molasses solution concentration of 72% and temperature of 45°C. The predicted responses for the optimum drying conditions in sugar beet molasses solution were: DM of 64.5%, WL in the close vicinity of 0.53, SG about 0.15 and a_w in the range of 0.83 to 0.84. During OD of meat, water removing process was most intensive at the beginning and after 3h had tendency of stabilization. The use of sugar beet molasses as osmotic agent is economy and environmentally reasonable considering that molasses is a side product of sugar industry.

Acknowledgement

These results are part of project supported by the Ministry of Science and Technological Development of the Republic of Serbia, TR-31055, 2011-2014.

References

[1] M. Castro-Giraldez, P. Fito, J. Food Eng., 2010, 99, 24-30.
[2] E. Puolanne, M. Halonen, Meat Sci., 2010, 86, 151-165.
[3] J. Barat, M. Alino, A. Fuentes, R. Grau, J. B. Romero, J .Food Eng., 2009, 93, 108-113.
[4] G. Koprivca, N. Mišljenović, Lj. Lević, L. Jevrić, Journal on Processing and Energy in Agriculture, 2010, 14, 27-31.
[5] G .E. P. Box, D. W. Behnken Technometrics, 1960, 2, 455–475.

Q-08-P

MACRO ELEMENTS COMPOSITION OF THE OSMOTICALLY DEHYDRATED PORK MEAT IN SUGAR BEET MOLASSES SOLUTION

S. Zlatanović[1], O. A. Kovačević[1], S. Ostojić[1],
B. P. Dojčinović[2], M. Pavlović[1] and D. Šuput[3]

[1] *University of Belgrade, Institute of General and Physical Chemistry, Studentski Trg 12, 11000 Belgrade, Serbia,*
[2]*University of Belgrade, Institute of Chemistry , Technology and Metallurgy, Studentski trg 12-16, 11000 Belgrade , Serbia,*
[3] *University of Novi Sad, Faculty of Technology, Bulevar Cara Lazara 1, 21000 Novi Sad, Serbia*

Abstract
An important advantage of sugar beet molasses, which is medium for osmotic dehydration, is enrichment of the food material in minerals and vitamins, which penetrate from molasses into the meat tissue. Macro elements composition of the raw pork meat and osmotic dehydrated pork meat in the solution of sugar beet molasses were investigated. The combination of thermal treatment at 350 ºC, and wet acid treatment at 160 ºC was used for samples preparation. Detection of elements present in the corresponding solutions was performed by ICP-OES. Results suggests that sugar beet molasses solution affects treated pork meat samples concerning concentration of macro elements. Content of macro elements in the osmotic dehydrated pork meat, compared to the content obtained for the raw pork meat, shows a significant increase of the content of Na, K and Ca cations for 5.5, 4 and 13 times, respectively. Comparing the values of Mg content in the dehydrated and raw pork, significant changes were not found.

Introduction

Sugar beet molasses (SBM) is medium for osmotic dehydration (OD), primarily due to the high dry matter (80%) and specific nutrient content.[1] Minerals and vitamins from sugar beet molasses, as hypertonic solution, penetrate from SBM into the meat tissue and enrichments the food material. Pork meat has a high content of Na, K, Ca and Mg, and variation in macro elements content is mainly determinated by food processing. [1-4] In this work, following changes in the content of macro elements, we examined the influence of sugar beet molasses on pork meat in the process of osmotic dehydration.

Experimental

Dry matter content of the samples was determined at 105 ^{o}C in a laboratory oven until constant mass was achived. The combination of thermal treatment at 350 ºC, and wet acidic treatment at 160 ºC was used for samples preparation. The dry samples were processed for minerals determination by wet digestion, where ca. 5 g

each, were weighed exactly to four decimal places, and transferred to vessels, into which 4.5 ml 65% HNO_3 and 10.5 ml 35% HCl were added. The treatments were repeated to obtain the white sediments that were dissolved in 0.07 M HNO_3. The content of metals present in the corresponding solutions was determined by inductively coupled plasma optic emission spectrometry (ICP-OES). ICP-OES measurement was performed using Thermo Scientific ICAP 6500 Duo ICP (Thermo Fisher Scientific, Cambridge, United Kingdom) spectrometer equipped with RACID86 Charge Injector Device (CID) detector, standard glass concentric nebulizer, quartz torch, and alumina injector. Samples were analyzed in triplicate.

Results

Result of processing the pork meat with the SBM in osmotic dehydration is enriched meat with amended nutritional characteristics. Contents of macro elements, Na, K, Ca and Mg, in SBM before and after osmotic dehydration, raw pork meat, and OD pork meat, were presented in Tab. 1.

Table 1. The content of macro elements in SBM, pork meat and osmotically dehydrated (OD) pork meat, determined by ICP-OES.

Sample	W 105 ºC (%)	Na (mg/100 g)	K (mg/100 g)	Ca (mg/100 g)	Mg (mg/100 g)
Sugar beet molasses, before OD	20.73±0.64	749±21	1939±9	289±3	37.9±0.7
Sugar beet molasses, after OD	26.79±0.78	689±7	1731±12	268±6	35.9±0.7
Pork meat.	72.71±0.54	62±1	250±9	6.3±0.3	29.1±0.6
OD pork meat	43.69±0.15	342±10	988±6	89±1	37.8±0.8

From the standpoint of materials analysis, SBM is a very specific material. Selection of appropriate mineral extraction procedure is not an easy task. During the preparation of material, selection and implementation of procedure, and inhomogeneity of the samples, are the main reasons for results dissipation. The results obtained, with relative standard deviations below 5%, enable reliable observation of changes in the macro elements composition in all materials during OD. Comparison of macro elements content between SBM and fresh meat shows significantly higher levels of Na, K and Ca in SBM, which was not the case with Mg content. OD pork meat has a significant increase in the content of Na, K and Ca cations with respect to the content obtained for the raw pork meat for 5.5, 4 and 13 times, respectively. The content of Mg cation in the OD pork meat is slightly raised and reaches a value as in the SBM.

Conclusion

Accurate values for the mineral content of raw and OD meat are thus of special importance as relatively small errors may affect results of dietary surveys and intake estimates to a great extent. Influence of molasses on pork meat in the process of osmotic dehydration was investigated. For this purpose, the contents of macro elements in sugar beet molasses, pork meat and osmotic dehydrated pork meat were determined in the prepared solution by ICP-OES. The results show that sugar beet molasses significantly influence the content of macro elements in pork meat treated in osmotic dehydration process. At the same time, the content of Mg cation is only slightly increased reaching a value of molasses. This work is part of the optimising of the technological process of osmotic dehydration of meat in sugar beat molasses. Findings in this work provide fundamental data for improvement, control and optimising of the technological process (osmotic dehydration) in order to produce nutritionally valuable products.

Acknowledgements

This work was supported by the Ministry of Education and Science of the Republic of Serbia, under the Project No TR-31055 and TR-31093.

References

[1] B. Filipčev, Lj. Lević, M. Bodroža-Solarov, N. Mišljenović, G.Koprivica, Int. J. Food Prop., 2010,13, 1035-1053.
[2] M. Della Rosa, F. Giroux, J. Food Eng. , 2001, 49, 223-236.
[3] M A. C. Silva, Z. E. Silva , V. C. Mariani, S. Darche, Food Sci. Technol. Int., 2012, 45, 246-252.
[4] N. M. Mišljenović, G. B. Koprivica, L. L. Pezo, L. B. Lević, B. L. Ćurčić, V. S. Filipović, M. R. Nićetin, Thermal Science, 2012, 16, 43-52.

Q-09-P

THE POTENTIAL ANTIMICROBIAL EFFECT OF *Lactobacillus plantarum* IN OSMOTICALLY DEHYDRATED PORK MEAT

M. D. Pavlović[1], M. M. Mandić[2], D. S. Mitić-Culafić[2]

[1]*Institute of General and Physical Chemistry, University of Belgrade Studentski Trg 12, Serbia*
[2]*University of Belgrade – Faculty of Biology, Chair for microbiology, Studentski Trg 16, Belgrade, Serbia*

Abstract
The potential antimicrobial activity of *Lactobacillus plantarum* against nonpathogenic strain *Listeria innocua*, closely related to foodborne pathogen *Listeria monocytogenes*, as well as its antifungal capacity was investigated. 28-day study of osmotically dehydrated meat inoculated with both strains showed that *L. plantarum* and its products possess antimicrobial and antifungal effects.

Introduction
Listeria monocytogenes is one of the most virulent foodborne pathogens, dangerous and persistent bacteria, considered to be one of the most important agents of foodborne disease [1]. Nonpathogenic strain *Listeria innocua* is often used in microbiological studies as a replacement of *L. monocytogenes*, because of its similarity to pathogenic form. The empirical use of microorganisms and/or their natural products for preservation of foods (biopreservation) has been a common practice in the history of mankind. The lactic acid bacteria produce an array of antimicrobial substances [2] and several *Lactobacillus* strains are used as starter cultures for the manufacture of fermented foods [3]. In meat, osmotically dehydrated in sugar beet molasses, *L. innocua* and *Lactobacillus plantarum* were inoculated with aim to investigate the potential antimicrobial activity of *L. plantarum* and its products on *L. innocua*, used as nonpathogenic surrogate of foodborne pathogen *L. monocytogenes*.

Experimental
The sample of osmotically dehydrated meat was split into four portions: control, portion inoculated with *L. plantarum*, portion inoculated with *L. innocua* overnight culture and portion inoculated with both cultures in 1:1 ratio. The working cultures were prepared from frozen permanents by overnight incubation (37°C) in brain heart infusion (BHI) broth. Portions of inoculated meat were stored at 4oC. The number of bacteria in each portion was determined on the first, 7th, 14th and 28th day of inoculation, for *L. innocua* on BHI agar and de Man, Rogosa and Sharpe (MRS) medium for *L. plantarum*.

Antimicrobial activity of *L. plantarum* was assessed by the agar-well diffusion method. Briefly, 7 ml of heated top agar was inoculated with 70 µl of an overnight culture of *L. innocua* and poured into a Petri dish. Wells in agar were filled with 50 µl of an overnight culture of *L. plantarum* and its concentrated culture filtrate, respectively. The plates were incubated at 37°C for 24h. After 24h, the diameter of the inhibition zone was observed. For determination of yeasts and moulds, on the 28th day of inoculation, 10-6 dilutions of each sample were plated onto Sabouraud agar plates supplemented with streptomycin (0.5 mg/ml)

Results and discussion

The number of bacteria in samples increased regularly during observed period of 28 days after inoculation. The number of *L. innocua* was increasing until the 14^{th} day. After 14 days the number of *L. innocua* the decreased. In the mixed cultures (*L. plantarum* and *L. innocua*) number of *L. plantarum* colonies increased regularly, but the number of *L. innocua* colonies was significantly lower (Table 1.). Based on the results of the experiment, we presume that *L. plantarum* is better adjusted in competition for nutrients in medium than *L. innocua*.

Table 1. The growth of L. plantarum and L. innocua on osmotically dehydrated meat.

Day	Control	*L. innocua*	*L. plantarum*	*L. innocua* + *L. plantarum*	
1	0	$2.6x10^4$	$8.7x10^3$	$1.4x10^4$	$9.3x10^3$
7	yeasts	$1.5x10^4$	$1.5x10^4$	$5.7x10^3$	$2.2x10^3$
14	yeasts	$1.1x10^4$	$5x10^5$	$1.0x10^3$	$1.2x10^5$
28	yeasts	n.d.	$5.5x10^6$	n.d.	n.d.

n.d. not detected

Agar-well diffusion method was used to show that products of *L. plantarum* have certain antimicrobial effect. The largest zone of inhibition was found around well with pure overnight culture of *L. plantarum* (Fig. 1.). Antimicrobial products of *L. plantarum* obtained after filtration of overnight culture (0.45 µm), exhibited lower antimicrobial effect compared to overnight culture. The results of this study showed that *L. plantarum* and its products have antimicrobial effect on nonpathogenic species *L. innocua* and potential antimicrobial effect on closely related foodborne pathogens such as *L. monocytogenes*.

The highest number of yeasts and moulds was identified in control samples. Conversely, the lowest number of yeasts and moulds was found on the plates with mixed cultures of *L. plantarum* and *L. innocua* (data not shown). The decreased growth of yeasts and moulds in the presence of individual and mixed cultures of *L. plantarum* and *L. innocua* pointed the antifungal capacity of these strains.

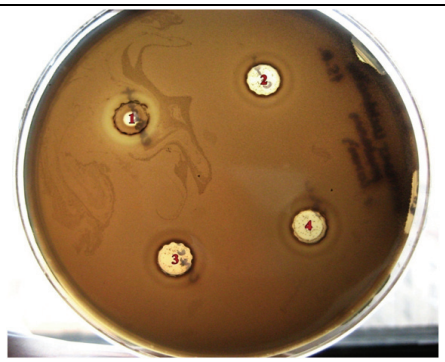

Fig. 2. Results of agar-well diffusion method (1 – pure overnight culture of *L. plantarum*; 2,3,4 – *L. plantarum* culture filtrates).

Antimicrobial substances certainly do have potential in food applications when used under the proper conditions. Since lactic acid bacteria are commonly found in meat, bacteriocins produced by the tested bacteria have been isolated and explored for the potential use in meat dehydration process.

Conclusion

The potential of using bacteriocins of lactic acid bacteria, primarily used as biopreservatives, represents a perspective, alternative antimicrobial strategy against the continuously increasing problem of antibiotic resistance. The further investigation is needed to isolate and characterize the substances with antimicrobial and antifungal capacity.

Acknowledgement

This work was suppuort by the Ministry of Education and Science TR 31055.

References

[1] V. Křepelková, R. Sovják, Agricultura Tropica et Subtropica, 2011, 44, 4.
[2] A. Gálvez, H. Abriouel, R. L. López, N. B. Omar, International Journal of Food Microbiology, 2007, 120, 51-70.
[3] A. Mami, J. E. Henni, M. Kihal, World Journal of Dairy & Food Sciences, 2008, 3, 39-49.

Q-10-P

EVALUATION OF TBA METHODS FOR ASSESSING LIPID OXIDATION IN MEAT DEHYDRATED IN MOLASSES

M. D. Pavlović[1], D. Z. Šuput[2], M. M. Mandić[3],
A. P. Jovanović[1], D. S. Mitić-Ćulafić[3]

[1]*University of Belgrade, Institute of General and Physical Chemistry, Studentski Trg 12, Belgrade, Serbia*
[2]*University of Novi Sad, Faculty of Technology, Bulevar Cara Lazara 1, Novi Sad, Serbia*
[3]*University of Belgrade, Faculty of Biology, Studentski Trg 16, Belgrade, Serbia*

Abstract
The effectiveness of different thiobarbituric acid (TBA) methods for measurement of secondary lipid oxidation products was evaluated on pork meat, dehydrated in sugar beet molasses and stored for 105 days at 4°C, under modified atmosphere conditions. Aqueous-acid-extraction TBA method (EM). under different conditions of incubation, and steam distillation TBA method (DM) were tested and low TBA values were obtained in all procedures. Primary lipid oxidation products were also low, except for microbiologically contaminated sample with increased water activity value. TBA-EM may be the inadequate method for the analysis of oxidative stability of meat dehydrated in molasses, due to interferences from molasses which cause erroneously high absorbance at 532 nm.

Introduction

Free fatty acids (FFA), peroxide values (PV) and thiobarbituric acid-reactive substances (TBA-RS) have been most commonly used determinants of the degree of lipid oxidation in meat. Malondialdehyde (MDA), a secondary oxidation product of polyunsaturated fatty acids with three or more double bonds, reacts with TBA to form a stable chromophore with maximal absorbance at 532 nm. High level of sucrose (44-54%), other sugars and their degradation products in molasses [1], used for osmotic dehydration of meat, could generate interfering yellow chromagen overlapping the pink peak of TBA-MDA aduct [2]. The interferences from sucrose can be reduced by incubating TBA and MDA at temperatures lower than 50°C, while the reaction time can be reduced by increasing the concentration of TBA [3]. Modified aqueous-acid-extraction method was used to measure MDA in the presence of sucrose in meat [3]. The effectiveness of different TBA methods [3][4], was evaluated and compared with other lipid oxidation determinants (PV, FFA).

Experimental

Osmotically dehydrated (OD) pork meat (with approximately 10% sucrose), packed under modified atmosphere (MAP) (30% CO_2 : 70% N_2) was stored at 4 ± 0.5 ^{0}C for 105 days. Water content of the samples was determined according to [5]. Water activity (a_w) was measured using TESTO 650 (Germany) at 25ºC. pH was determined according to [6]. Acid value (FFA) was measured after cold lipid

extraction of samples, according to [7]. Peroxide value (PV) was measured after cold lipid extraction of samples, according to [8]. Secondary lipid oxidation products were determined using EM-TBA [3], and DM-TBA [4] and expressed in TBA-RS. The incubation conditions in EM-TBA were: A) 100°C/25 min with 20 mM TBA, B) 40°C/70 min, with 80 mM TBA and C) 20 °C/20 h with 20 mM TBA. D) DM-TBA. MicroSoft Excel software (MicroSoft Office 2003) was used for statistical analyses. All measurements were performed in triplicate.

Results and Discussion

Dehydration in sugar beet molasses solution caused a significant moisture loss in meat samples, from 75.957±0.045%, before OD, to 40.433±0.244%, after OD, during 105 days of observation. The a_w values decreased with the osmotic treatment from 0.938±0.002 to 0.872±0.002. During storage a_w values raised to 0.894±0.001. pH values of OD meat decreased from 6.693±0.11 to 6.387±0.006 and than increased to pH to 6.98±0.004. The concentration of free fatty acids remained low, in the range of 17.64±0.5 to 22.3±0.54 mg KOH/g of sample (0.049-0.63 % FFA). Peroxide values were also low (PV=0), except for microbiologically contaminated sample with PV=12.98 mg O_2/kg. It is well established that microbial metabolism could influence, both negatively and positively the production of lipid peroxides and carbonyl compounds in infected meat [9].

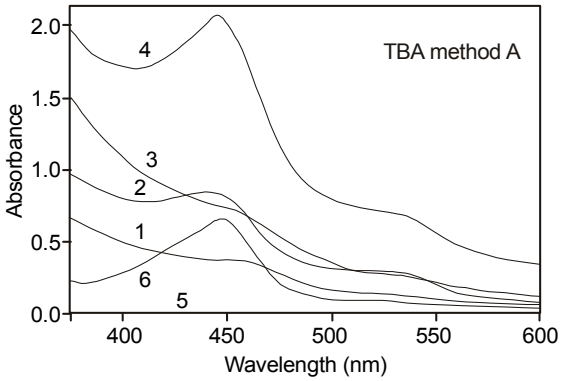

Figure 1. Scans of molasses and sucrose absorbance in TBA method A (TBA-EM, 100°C/25 min, 20 mM TBA). Scans: 1) 10% molasses, before TBA test; 2) 10% molasses, after TBA test; 3) 20% molasses, before TBA test; 4) 20% molasses after TBA test; 5) 10% sucrose before TBA test; 6) 10% sucrose after TBA test.

The effectiveness of different TBA tests in minimizing the interferences of sugar molasses, used as osmotic solution, was measured by EM-TBA under different conditions of incubation (A, B and C). Interferences, which cause erroneously high value of TBA-RS in meat samples dehydrated in molasses, were detected as absorption at 350 nm, 450-460 nm, and 532 nm. The reaction of molasses (Fig. 1, scan 2 and 4) and sucrose (Fig. 1, scan 6) with TBA was dependent on concentration and maximal at 100°C, and diminished when the incubation temperature was decreased to 40°C, (data not shown). The oscillations in TBA-RS, obtained in DM-TBA, (Fig. 2. D.) and EM-TBA-A (Fig. 2. B.) compared to EM-TBA-B (Fig. 2. B.), are also suggestive of interferences from molasses (i.e. difference in molasses content in meat samples). The low TBA values, obtained in

all TBA procedures may be due to the low level of lipid oxidation. It is also possible that MDA, produced in dehydrated meat, is in volatile chelated form, because of the absence of water, and, therefore, not being held in meat [2].

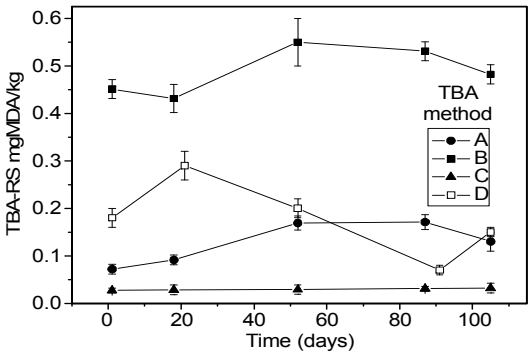

Figure 2. TBA-RS kinetics at 4°C, during storage of pork meat dehydrated in molasses and packed in MAP. TBA method: A) TBA-EM, 100°C/25 min, 20 mM TBA, B) TBA-EM, 40°C/70 min, 80 mM TBA, C) TBA-EM, 20°C/20 h, 20 mM TBA, D) TBA-DM, steam distillation

Conclusion

The effectiveness of different conditions of incubation in minimizing the interferences of molasses ingredients was measured by aqueous acid extraction method and distillation TBA method. Low TBA values were obtained in all TBA procedures. Primary lipid oxidation products were, also, low, except in microbiologically contaminated sample with increased water activity value, where elevated peroxide values was obtained. Low PV and TBA values in all analyzed methods are indicative of low lipid oxidation in OD pork meat under storage in modified atmosphere and 4°C or loss of MDA from dehydrated meat.

Acknowledgement

This work was suported by the Ministry of Education and Science, Republic of Serbia, project No. TR-31055.

References

[1] M. R. El-Gewely, Biotechnology Annual Review, Elsevier, 2007, 13, 315-316.
[2] J. Fernandez, J. A. Perez-Alvarez & , J. A. Fernandez-Lopez, Food Chemistry, 1997, 59, 345-353.
[3] B. Wang, R. D. Pace, A. P. Dessai, A. Bovell-Benjamin, B. Phillips, Journal of Food Science, 2002, 67, 2833-2836.
[4] B. C. Tarladgis, A. M Pearson & L. R. Dugan, Journal of the Science of Food and Agriculture, 1964, 15, 602-607.
[5] ISO 1442:1997: Meat and meat products - Determination of moisture content.
[6] ISO 11289:1993: Heat-processed foods in hermetically sealed containers - Determination of pH.
[7] ISO 660:1996: Animal and vegetable fats and oils - Determination of acid value and acidity.
[8] ISO 3960:1998. Animal and vegetable fats and oils – Determination of peroxide value.
[9] K. E. Moerckl, H. R. Ball, J. Agric. Food Chem., 1979, 27, 854-859.

Q-11-P

COMPARISON STUDY OF HISTAMINE ANALYSIS IN FISH PRODUCTS USING HPLC AND ELISA METHODS

D. Spiric, S Stefanovic, V. Jankovic, R. Petronijevic,
D. Nikolic, S. Jankovic, B. Borovic

Institute of Meat Hygiene and Technology, Kacanskog 13, Belgrade

Abstract

Histamine is natural neurotransmitter and vital signal molecule in every organism, but it also poses significant issue in food safety, since it is involved in scombroid poisoning and histamine intolerance in humans as well as the disease known as gizzard erosion in chicken consuming fish meal. Regulatory limits are set for histamine in fish and fish products, as well as reference analytical method for its determination. The aim of this study was to compare results of histamine analysis obtained using ELISA and HPLC methods. Twenty three sample units from 71 screen positive samples obtained by ELISA method were confirmed by HPLC method, to contain elevated content of histamine. Results obtained with ELISA method and HPLC method for the same analysed samples generally showed weak linearity in comparison of results obtained ($p<0.05$; r =0.86), since ELISA results for histamine content higher than 200 mg/kg didn't show linear response.

Introduction

Histamine is a potent biogenic amine with multiple activities in the acute inflammatory and allergic responses [5]. It has many vital functions as neurotransimtter in healthy individuals in control of gastric acid secretion, mediation of vascular permeability, immunomodulation, hematopoiesis and balancing day-night rhythm [9]. Mast cells, basophiles and other cells after synthesis of histidine decarboxylase are major source of histamine in normal tissues [12]. Histamine is also well known as cause of scombroid poisoning and histamine intolerance. Fish with high levels of free histidine (e.g. *Scombroidae*), which is converted to histamine by bacterial histidine decarboxylase, are those most often implicated in scombroid poisoning [2]. Quality loss and histamine accumulation often occur after frozen fish are thawed and kept for long periods of time at room temperature before further processing. Since histamine is heat resistant, it can remain intact in canned products [7]. Action levels have been established for histamine in regulations targeting scombroid poisoning: of the nine samples, two cannot be higher than 100 mg/kg (and 200 mg/kg) levels but none can be higher than 200 mg/kg (or 400 mg/kg for enzyme matured products) [1]. This regulation also prescribes HPLC as reference method for histamine analysis in fish product. The aim of this study was to compare results of histamine analysis using commercial ELISA test kit with results obtained by HPLC method for same samples [4].

Materials and Methods

Fish samples were prepared according to the test protocol, using 0.1 M HCl and derivatization reaction. A histamine conjugate is bound on the surface of a microtiter plate. Samples and standards containing derivatized histamine and an

antibody directed against histamine are given into the wells of the microtiter plate. Immobilized and free histamine compete for the antibody binding sites. After 30 minutes incubation period, the wells are washed with diluted washing solution to remove unbound material. A peroxidase conjugate directed against the histamine antibody is given into the wells and after another 30 minutes incubation, the plate is washed again. Then a substrate solution is added and incubated for 20 minutes, resulting in the development of a blue colour. The colour development is inhibited by the addition of a stop solution, and the colour turns yellow. The yellow colour is measured photometrically at 450 nm. The concentration of histamine is indirectly proportional to the colour intensity of the test sample.

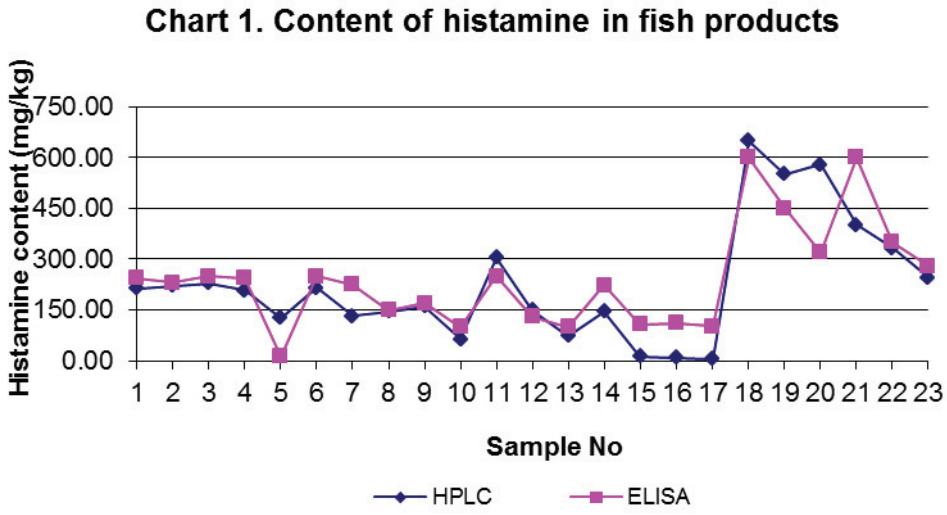

Confirmatory analysis of screen positive samples obtained by ELISA method, were performed by HPLC method [10]. After extraction with 6% trichloracetic acid, aliquot portion was treated with 2M NaOH and histamine was derivatized by benzoyl-chloride for 30 minutes at 37°C. Derivatization reaction was terminated with saturated NaCl solution. Histamine was extracted from the aqueous phase using diethyl ether which was evaporated to dryness under nitrogen stream and dry residue was reconstituted in methanol. Extract was filtered through 0.22 µm nylon syringe filters and injected into HPLC system.

Separation was performed on Phenomenex Gemini C18 column on Waters 2695 separation module coupled with Waters 2487 UV detector at 254nm. Data acquisition and processing was performed using Empower software.

Results and Discussion

Seventy one units of fifteen samples (ten tuna cans, two samples of frozen scomber, two samples of frozen tuna and one sample of frozen herrings) were screen positive. All these samples were analysed by confirmatory HPLC method, resulting in 23 units of seven samples with high content of histamine (Chart 1).

Other samples were designed as false positive. Correlation between data was good for histamine content lower than 200 mg/kg but weaker for high histamine contamination ($p<0.05$; $r=0.86$).

One of the first studies on good correlation between monoclonal antibody-based immunoassays and HPLC methods for histamine analysis in food revealed good correlations between these two methods [11]. According to other authors [6] among the quantitative kits, "Histamine Food EIA" showed the best correlation with HPLC method for fish products ($R^2 = 0.9132$). Poor correlation was found between Veratox kit and HPLC method, obtained by same authors. Regarding results from wine as matrix analysed, Veratox commercial kit was compared with HPLC method and revealed a good correlation ($r = 0.91$) [8], regarding histamine content. Variations in histamine content obtained by different commercial kits are also studied [3], and it was observed that there was a strong correlation between "Veratox" and "MaxSignal" commercial kit methods, with $R^2=0.98$ for the data set overall.

Conclusion

Twenty three units of seven samples were confirmed by HPLC to contain high level of histamine, but seventy one units of fifteen samples (ten tuna cans, two samples of frozen scomber, two samples of frozen tuna and one sample of frozen herrings) were screen positive using ELISA commercial test kit. False positive results are due to the matrix effect, since most of the samles were canned tuna products in brine, oil and vegetable sauce, either because crossreaction with some other biogenic amine with similar antigen structure. Correlation between obtained data set was good for 23 samples, positive by both methods. Since most of the positive samples were canned fish products it is important to prevent use of spoiled fish for conserving, because unlike histamine producing bacteria, histamine is thermoresistant, and also it is very important to use sensitive enough methods for histamine analysis, that can provide results in good correlation with reference method.

Acknowledgment

Study was supported by the Ministry of Education and Science of Serbia within the Project III-46009.

Literature

[1] COMMISSION REGULATION (EC) No 2073/2005.
[2] J. M. Hungerford, Toxicon, 2010, 56, 231–243.
[3] J. Hungerford, W.-H. Wu, Food Control, 2012, 25, 448-457.
[4] Immunolab Histamine Senitive GmbH, Germany.
[5] M. Jutel, T. Watanabe, M. Akdis, K. Blaser, C.A. Akdis, Current Opinion in Immunology, 2002, 14:735–740.
[6] S. Kose et al, 2011, 125, 1490–1497.

H.-F. Kung et al, Food Control, 2009, 20, 1013–1017.
[7] A. Marcobal C Food Research Internationa,l 2005, 38, 387–394.
[8] L. Maintz, N. Novak , American Journal of Clinical Nutrition, 2007, 85,1185–1196.
[9] F. Ozogul et al, Ozogul Y., International Journal of Food and Technology, 2002, 37, 515-522.
[10] D. Serrar et al, Food Chemistry, 199554, 85-91.
[11] E.Schneider et al, Trends in Immunology, 23, 255-263.

Q-12-P

COMPARATIVE ANALYSIS OF THE PRESENCE OF SOYBEAN AND GLUTEN IN MEAT PRODUCTS

V. Janković, V. Matekalo Sverak, S. Lilić, B. Velebit, B. Lakićević, R. Petronijević
Institute for Meat Hygiene and Technology, Kaćanskog 13, Belgrade, Serbia

Abstract
Use of soybean and gluten in production of meat products is topical and attractive both for the producers and consumers. However, soybean and gluten belong to the group of basic allergens and thus they are potentially hazardous for consumers. Therefore, it is necessary to conduct adequate and continuous control of meat products for the presence of the above-mentioned allergens. This work gives an overview of the analysis of meat products from retail shops for the presence of soybean and gluten, using an ELISA method.

Introduction
Use of ingredients of plant origin in production of meat products is topical and attractive both for the producers and consumers. Soybean protein products are widely used in the meat industry because of their high nutritive value, favourable technological and organoleptic characteristics and low price as well [1]. Use of soybean has a favourable effect on the product quality: it increases stability of the filling, enriches the product with proteins and improves its other desirable characteristics. Wheat gluten is used in preparation of various meat and fish products because of its unique adhesive, cohesive and film forming characteristics. Gluten is very effective and it is used for binding meat chunks or trimmings together (to form steaks or chops), and it may be also applied simply by dusting meat pieces with dry gluten. It is also used as an emulsifier in producing sausages and other meat products [1].

The aim of this work was to analyse the presence of soybean and gluten in meat products using reference analytical methods – ELISA, not only because of the product quality and authenticity but also in order to protect the health of consumers.

Materials and Methods
Altogether, 100 samples of meat products from retail shops were tested. Samples were prepared according to the appropriate procedure for the specific kit, and were tested in two repeats.

To analyze meat products for the presence of soybean, the following commercial ELISA kits were used: Tepnel and Romer Lab. To detect the presence of soybean, the Tepnel Biokits Soya protein Assay kit was used, with the limit of detection of 0.5% and the quantification range of 0.7 to 14%, while the Romer Lab assay kit, AgraQuant Soy, was used for detection of allergens, with a quantification range of 40-1000 ppb.

For analysis of gluten, the internationally acknowledged and recommended method ELISA-R5 according to Mendez [2,3,6] was used. For these analyses, the

Biokits-Tepnel ELISA kit has been recommended by the AOAC (The Association of Analytical Communities). In addition, the Immunolab ELISA kit was also used.

For gluten, the limit of detection by the Tepnel kit is 1 ppm, with the quantification range of 3-50 ppm (with the possibility to extend the range by additional dilution), while the limit of detection for the Immunolab Gliadin/Gluten kit is 0.3 ppm with the limit of quantification is 2 ppm.

Results and Discussion

Table 1. Presence of soybean protein and gluten in samples of retail meat products.

Type of sample	Number of samples	Number of samples with detected presence of soybean proteins	Number of samples with detected presence of gluten	Number of samples without indicated presence of allergens but with detected presence
Boiled sausage (coarse ground boiled sausages)	20	7	2	3 (soybean-2, gluten-1)
Boiled sausage (boiled sausages with meat pieces)	20	4	1	1 (gluten)
Meat tins (chunk meat tins)	20	6	ND	1 (soybean)
Boiled sausages (liver sausages and pâté)	20	11	1	3 (soybean-2, gluten-1)
Fermented sausages	20	1	ND	0

ND – presence not detected

Table 2. Comparative analysis of soybean protein in meat product samples using the Tepnel and Agra Quant test kits.

Type of sample	Tepnel (%)	Agra Quant (ppb)
Boiled sausage (coarse ground boiled sausages)	4.7-5.6	>1000
Boiled sausage (boiled sausages with meat pieces)	8.4-9.6	>1000
Meat tins (chunk meat tins)	1.2-2	>1000
Boiled sausages (liver sausages and pâté)	6-5.9	>1000
Fermented sausages	1.2	>1000

Table 3. Comparative analysis of gluten in meat product samples using the Tepnel and Immunolab test kits.

Type of sample	Tepnel (ppm)	Immunolab (ppm)
Boiled sausage (coarse ground boiled sausages)	8-12	8-12
Boiled sausage (boiled sausages with meat pieces)	7.2	6
Meat tins (chunk meat tins)	ND	ND
Boiled sausages (liver sausages and pâté)	9.1	12
Fermented sausages	ND	ND

Out of the total of 100 samples of meat products, the presence of soybean was detected in 29% of samples, gluten in 4% of samples, while in 67% of samples, the presence of the mentioned allergens was not detected (Table 1). The detected concentration of soybean for the Tepnel kit ranged from 1.2%, to 9.6%, while the values detected by the Agra Quant kit were greater than the quantification range of 1000 ppb (Table 2). As regards gluten, both kits detected almost equal concentrations (Table 3). Out of the total of 27 samples of meat products, the declarations of which did not indicate that they contained soybean or gluten, 8 of them (29.6%) showed the presence of one or both of these allergens. These results were in accordance with previously published research [4,7].

Conclusion

- Both ELISA kits, Tepnel (determination of percentage of soybean protein in the tested samples) and Agra Quant (determination of significantly lower concentrations of soybean allergen), have shown excellent results within their performances, and thus they can be safely used in control of quality and health suitability of foodstuffs,
- Both ELISA kits used, Tepnel and Immunolab, meet all requirements of Codex Alimentarius according to their performances in view of concentration readings (gluten free and very low gluten), and no differences were found by their comparative analysis, and
- Our research has shown that the control of soybean protein and gluten presence in meat products is necessary, because the presence of these allergens was identified in 29.6% of retail meat products, but their presence was not indicated in the meat product declarations, which poses a high risk for consumers.

Acknowledgment

This study was supported by the Ministry of Education and Science of Serbia within Project III-46009.

Literature

[1] M. Barać, S. Stanojević, S. Jovanović, M. Pešić, Soy Protein Modification - A Review, Acta periodica technologica, 2004, 35, 3-16.

[2] Codex Alimentarius Commission, Report of the 25th session of the Codex Committee on nutrition and foods for special dietary uses, Alinorm 04/27/26, Bonn, Germany, 3-7 November, 2003.

[3] Codex Alimentarius Commission: Draft revised standard for gluten-free foods, Step 8. http://www.codexalimentarius.net/web/archives.jsp?year=08 webcite ALINORM 08/31/26 2008.

[4] V. Janković Vesna, V. Matekalo Sverak, D. Vranić, B. Lakićević Brankica, R. Petronijević, Determination of gluten content in meat products. XIV International Symposium Feed technology-XII International Symposium NODA 2010, Novi Sad, Proceedings, 2010, 53-60.

[5] K. Kulp, G. Joesph, in Ponte Handbook of cereal science and technology, Marcel Dekker, Technology and Engineering, 2000, 118-123.

[6] J. Pokorná, Comparison of the Results of the ELISA, Czech J. Food Sci. 2011, 29(5), 471–479.

[7] E. Renčová, B. Tremlová, ELISA for Detection of Soya Proteins in Meat Products ACTA VET. BRNO, 2009, 78, 667-671.

FREE TOPIC

R-01-P

STABLE ISOTOPE ANALYSIS USING CIRCULAR STATISTICAL METHODS: APPLICATIONS IN TEMPORAL ANALYSIS FOR DOUBLE WEIGHTED DATA

D. Golobočanin[1], N. Miljević[2]

[1]*University of Belgrade, Vinca Institute for Nuclear Sciences, POB 522, 11001, Belgrade, Serbia*
[2]*Jaroslav Černi Institute for Development of Water Resources, 80 Jaroslav Černi, 11223 Belgrade, Serbia*

Abstract
Circular data arise in a number of different areas such as geological, meteorological, and hydrological sciences. The new method was developed for analyzing double weighted time series. We have applied the new circular statistical method to 54 years monthly data assembled in Otava meteorological station The obtained results have been compared with data computed with standard statistical methods. They were statistically significantly different on conventional p-level of 95%.

Introduction
Standard statistical techniques cannot be applied to analyze circular data. This is due to the circular geometry nature of the data space [1]. The sample mean of a data set on the circle is not the usual sample mean. Let α_1, α_2... α_n be independent observations on the unit circle, such that $0 \leq \alpha_j < 2\pi$, j=1,2,.. ,n. The mean direction $\overline{\alpha}$ is not given by the simple arithmetic mean. For example if we imagine a circle divided on 360 parts then $(345^o+15^o)/2=180^o$ but the line on 0^o represents the true mean obtained by vector addition.

One of the more statistically tractable variable combinations, and one routinely found in the literature, is a case of linear dependent variable and circular independent variable [2]. Circular statistics are appropriate for analysis of data that are circular or directional in nature. For example, January (month 1) follows December (month 12). Arithmetic averaging of a group of numerical months or dates is not appropriate with conventional sample statistics because the counting system is circular not linear. In conducting the analysis of the seasonality of annual maxima or extreme storms, the Julian day of the year was used for describing the date of occurrence. The average day of occurrence is analogous to the arithmetic mean and the seasonality index is analogous to a standardized measure of variation. Specifically, values of the seasonality index range from zero to unity with values near zero indicating wide variation in the dates of occurrence. A seasonality index near unity indicates low variation in the dates of occurrence and strong clustering of dates [3]. Circular statistics for dates of occurrence using Julian day-of-year d_i are computed as follows: Conversion of Julian day-of-year to compass direction (ϕ_i):

$$\phi_i = 360 \cdot \frac{d_i}{d_{tot}} \tag{1}$$

There d_{tot} is a number of days in current year (365 or 366). Compute then vectors for compass direction:

$$S = \sum_{i=1}^{n} P_i \cdot \sin(\phi_i); \qquad C = \sum_{i=1}^{n} P_i \cdot \cos(\phi_i) \qquad \varphi_2 = arctg\left(\frac{S}{C}\right) \tag{2}$$

In our case P_i is amount of precipitation for d_i but can be any other dependent variable.

$$\bar{\phi} = \begin{cases} \phi_2 & if \quad S > 0 \quad and \quad C > 0 \\ \phi_2 + 180 & if \quad C < 0 \\ \phi_2 + 360 & if \quad S < 0 \quad and \quad C > 0 \end{cases} \tag{3}$$

$$\bar{J} = \frac{d_{tot} \cdot \bar{\phi}}{360} \qquad SI = \frac{\sqrt{S^2 + C^2}}{\sum_{i=1}^{n} P_i} \tag{4}$$

$\bar{J}$ is a seasonal direction for weighted data and SI is a seasonality index. J_i is a day-of-year for given date of interest; d_{tot} is the total number of days in the current year; P_i is the data value for a given date (J_i), and n is the total number of data and date pairs.
In observed case, we have two more obstacles. First, our P_i input data set is already weighted on oxygen-18 content [4]. Second, experimental isotope oxygen-18 content ($\delta^{18}O$) data set can be often negative. To avoid this we scaled isotopic data to percent scale.

$$P_i = \frac{P_i^{obs} \cdot \delta_i^{18}O}{\sum_{i=1}^{n} P_i^{obs}}; \qquad \delta_i^{18}O = \frac{\delta_i^{18}O^{obs} - \delta^{18}O_{\min}^{obs}}{\delta^{18}O_{\max}^{obs} - \delta^{18}O_{\min}^{obs}} \cdot 100 \tag{5}$$

Indeed we have weighted our data two times. Equations (5) are our improvement to estimation of $\bar{J}$ and SI of weighted data.

Results and Discussion

We have applied described method to analyze 54 year data assembled from meteorological station Ottawa (1953-2007) [5]. We have calculated simple average for each month for precipitation and for $\delta^{18}O$ values during observed period. Then, we have calculated percent scaled isotopic data and weighted amount of precipitation following equations (5). The values for SI and $\bar{J}$ were obtained following equation (4). These results are showed on Table 1. The angles and intensities were showed as vectors on Figure 1.

Table 1. Angles and intensities.

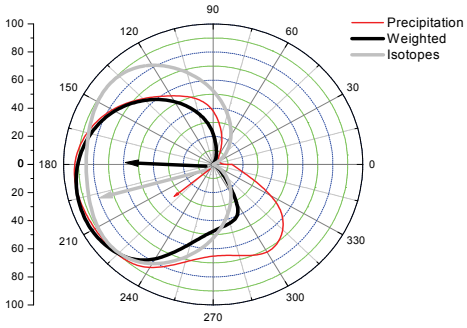

	$\bar{J}$	SI
Precipitation	229	0.14
Isotope content	180	0.21
Weighted	201	0.33

Figure 1. Circular percent diagram for precipitation, average weighted mean isotopic composition of the precipitation and isotopic content.

Conclusion

We have improved a Fisher algorithm for analyzing weighted time series. Circular statistics are appropriate for analysis of hydrological data that have circular nature. We calculate seasonal direction and seasonal index. Standard statistical approach is sensitive to numerate style. In our case results for seasonal direction obtained with both statistics (circular and standard) were statistically significantly different on conventional p-level of 95%. We will apply described method to monthly precipitation data and its $\delta^{18}O$ content for meteorological Station Zeleno Brdo (Belgrade).

References

1. N. I. Fisher, Statistical Analysis of Circular Data. Cambridge, University Press, 1995.
2. N. Fisher, A. Lee, Journal of the Royal Statistical Society, Series B, 1994, 56, 327-339.
3. S. Rao Jammalamadaka, A. SenGupta., Topics in circular statistics, World Scientific Publishing Co. Pte. Ltd., 2001.
4. N. Miljević, D. Golobočanin, N. Ogrinc, A. Bondžić**,** Isotopes in Environmental and Health Studies, 2008, 44, 137–148.
5. GNIP data base, http:isohis.iaea.org, Ottawa 1953–2007.

R-02-P

ENZYME-ASSISTED WATER EXTRACTION OF STINGING NETTLE LEAVES

V Rafajlovska[1*], S Sinadinović-Fišer[2], J Simonovska[1], O. Borota[2], M Janković[2]
[1]*Faculty of Technology and Metallurgy, Ss. Cyril and Methodius University in Skopje, Macedonia*
[2]*Faculty of Technology, University of Novi Sad, Serbia*

Abstract
Stinging nettle leaves were subjected to an enzyme-assisted water extraction (EAWE) under following conditions: leaves-to-water ratio of 1:18, pH of 8.1, enzyme concentration of 0.9% and an extraction time of 3 hours at 50°C with constant stirring speed of 200 rpm. The yields of obtained pressed residue and extract were determined, as well as the contents of proteins, fats and mineral materials in both fractions. The amount of each measured constituent in extract (around 71% of each) was found to be higher than in the pressed residue. The results were compared with those of conventional extraction with water when, however, higher amounts of proteins (58.29%) and fats (52.87%) related to the total content in leaves remained in the pressed residue.

Introduction

Stinging nettle (*Urtica dioica* L., *Uticaceae*) is a native perennial plant widely used as herb in folk and contemporary medicine, as well as a traditional food. The flavonoids, chlorophylls and carotenoids, vitamins, proteins, mineral materials, organic acids, oil, sitosterols, tannins and other components determined in this plant leaves are the main contributors to the observed medicinal effect.

The limitations of the conventional water extraction regarding yield and stability of extracted components, may be exceeded by the application of an enzyme for the hydrolysis of the cell wall constituents. Therefore, developing of an enzyme assisted extraction is in expansion [1,2].

In order to impose the necessity of using an enzyme in the extraction of stinging nettle leaves with water, in this study the yields of pressed residue and extract, as well as the contents of proteins, fats and mineral materials in both fractions were determined when the enzyme *Alcalase* 2.4 L was used during the extraction with water and the results were compared with those obtained for conventional water extraction (WE).

Experimental

Materials. Leaves of stinging nettle, picked in Jun 2011 from the locality Andon Dukov (350 m altitude), Ohrid region, Macedonia, were dried for 15 days on mats in the shade and at room temperature, spread into thin layers. Before the extraction, leaves were dried in oven at 30°C for 8 h, then milled and sieved to a powder with particle size of 0.2 mm. Enzyme *Alcalase* 2.4 L Food Grade, with specific activity,

optimal pH and temperature values of the activity, of 2.4AU/g, 6.5-8.5 and 50-70^{o}C, respectively, was provided by Novozymes A/S (Bagsvaerd, Denmark).

*Chemical analysis***.** *Content of dry matter* and *content of mineral materials* were determined by AOAC methods 925.10 and 923.03, respectively. *Content of proteins* was calculated from the nitrogen content determined by Kjedahl method using factor 6.25 (AOAC, 978.04). *Content of fats* was obtained by extraction using Grossfeld method [3]. *Content of proteins in solution* was determined using Lowry method [4] with Folin-Ciocalteu reagent by measuring the transmission at λ = 750 nm by Varian Cary Scan 50 spectrophotometer (Switzerland) in 1 cm quartz cells, at 25^{o}C. The values of the soluble proteins content were estimated using the calibration curve log(%T)=1.9838-0.5694C (r^2=-0.9622) plotted for Bovine serum albumin (22% solution in distilled water) used as standard, where T is the transmission and C is the concentration of proteins expressed in g/L extract.

*Extraction of stinging nettle leaves***.** Extractions were performed with modified procedures given by Dalev *et al*. [5]. The contents of dry matter, proteins, fats and mineral materials were determined in dry leaves and in obtained fractions.

Extraction with water. 50 g of grinded dried leaves was disintegrated in mixer with 300 mL distilled water for 3 min. The homogenous mass was transferred to the flask and 600 mL distilled water was added. After 3 h extraction at 50^{o}C and with a stirring speed of 200 rpm the mixture was filtered through the Buchner funnel using water jet vacuum pump. Pressed residue and extract were separated.

Enzyme-assisted extraction. 50 g of grinded dried leaves was disintegrated in mixer with 300 mL distilled water for 3 min. After addition of 600 mL of distilled water (leaves-to-water ratio 1:18 w/v), the homogenous mass was transferred into the three neck flask and its pH was adjusted from 7.7 to 8.1 using 0.1 mol/L NaOH. Then, 8.4 mL of enzyme *Alcalase* 2.4 L (0.9% v/w) was added and the mixture was incubated at 50^{o}C for 3 h with constant stirring speed of 200 rpm. After 3 h, pressed residue and extract were separated by filtering through the Buchner funnel using water jet vacuum pump.

Results and Discussion

The yields of pressed residue and extract and contents of proteins, fats and mineral materials in dry leaves and in fractions obtained with both water and enzyme-assisted water extraction of stinging nettle leaves are shown in Table 1.

In the stinging nettle leaves the content of dry matter of 91.24% was determined. The contents of proteins, fats and mineral materials related to the dry matter were 27.09%, 7.70% and 18.18%, respectively.

By employing the *Alcalase,* the content of dry matter that remained in the pressed residue was reduced about 1.8 times compared to water extraction, while the rest was transferred to the extract due to the enzymatic hydrolysis of the cell wall constituents. After enzyme-assisted extraction, also 1.9 times smaller amount of proteins, 1.8 times smaller amount of fats and 1.3 times smaller amount of mineral materials remained in the pressed residue than after conventional water

extraction. Hence, by extraction of stinging nettle leaves with enzymatic treatment the extract enriched in proteins, fats and mineral materials was yielded.

Table 1. Content of proteins, fats and mineral materials in dry stinging nettle leaves and in fractions obtained by water extraction of leaves without and with an enzyme treatment[a].

		Dry stinging nettle leaves	WE		EAWE	
			Pressed residue	Extract	Pressed residue	Extract
Yield	**(%*1)**	100.0	58.78	41.47	32.00	67.58
Proteins	**(%*1)**	27.09	26.86	94.27	25.27	28.38
	(%*2)	100.0	58.29	40.72	29.85	70.80
Fats	**(%*1)**	7.70	7.02	23.08	17.00	8.07
	(%*3)	100.0	52.87	47.10	29.15	70.77
Mineral materials	**(%*1)**	18.18	10.76	66.19	15.47	19.32
	(%*4)	100.0	34.78	66.21	27.23	71.86

[a]The values are expressed as percentage of: *1 - dry matter of fraction; *2 – total proteins; *3 - total fats; *4 - total mineral materials

Conclusions

The extractions of the stinging nettle leaves with both water and water in the presence of an enzyme, investigated in this study, are comparable in respect of the contents of proteins, fats and mineral materials distributed in-between the yielded fractions. Results of the enzyme-assisted extraction showed that the yield of the pressed residue was reduced in regard to those remained after the conventional extraction with water. Moreover, the extract obtained from stinging nettle leaves when the enzyme *Alcalase* 2.4 L was used during the extraction with water was enriched with all measured constituents i.e. with proteins, fats and mineral materials. Thus, the application of the enzyme-assisted extraction is beneficial from the aspect of production the extract with the high content of nutrients.

Acknowledgement

This work is part of the Project #III 45022 supported by the Ministry of Education and Science of the R. Serbia.

References

[1] M. Pinelo, B. Zornoza, A.S. Meyer, Sep. Purif. Technol., 2008, **63**, 620-627.
[2] E. Demirhan, D.K. Apar, B. Özbek, Korean J. Chem. Eng., 2011, **28**, 1 195-202.
[3] J. Trajković, J. Baras, M. Mirić, S. Šiler, Analize Životnih Namirinica, Tehnološko-metalurški fakultet, Beograd (1983), 95.
[4] K. Wilson, J. Walker, Practical Biochemistry: Principles and Techniques Cambridge University Press, Cambridge, 2000, 320-321.
[5] P. Dalev, A. Ljubomirova, I. Ivanov, Biotechnol. Lett., 1996, 18, 1 107-110.

INDEX

CIP Volume I

CIP - Каталогизација у публикацији
Народна библиотека Србије, Београд

544(082)
621.35(082)
66.017/.018(082)

MEĐUNARODNA konferencija iz fundamentalne i primenjene fizičke hemije (11 ; 2012 ; Beograd)
Physical Chemistry 2012 : proceedings. #Vol. #1 / 11th International Conference on Fundamental and Applied Aspects of Physical Chemistry, September 24-28, 2012, Belgrade ; [editors S.[Slobodan] Anić and Ž.[Željko] Čupić ; organized by Society of Physical Chemists of Serbia ... et al.]. - Belgrade : Society of Physical Chemists of Serbia, 2012 (Belgrade : Jovan). - VI, 498 str. : ilustr. ; 24 cm

"The Conference is dedicated to Professor Ivan Draganić" --> nasl. str. - Tiraž 200. - Bibliografija uz svaki rad.

ISBN 978-86-82475-27-9
1. Društvo fizikohemičara Srbije (Beograd)
a) Физичка хемија - Зборници b) Електрохемијско инжењерство - Зборници c) Наука о материјалима - Зборници
COBISS.SR-ID 193432332

CIP Volime II

CIP - Каталогизација у публикацији
Народна библиотека Србије, Београд

544(082)
621.35(082)
66.017/.018(082)

MEĐUNARODNA konferencija iz fundamentalne i primenjene fizičke hemije (11 ; 2012 ; Beograd)
Physical Chemistry 2012 : proceedings. #Vol. #2 / 11th International Conference on Fundamental and Applied Aspects of Physical Chemistry, September 24-28, 2012, Belgrade ; [editors S.[Slobodan] Anić and Ž.[Željko] Čupić ; organized by Society of Physical Chemists of Serbia ... et al.]. - Belgrade : Society of Physical Chemists of Serbia, 2012 (Belgrade : Jovan). - VI str., 499-782 str. : ilustr. ; 24 cm

"The Conference is dedicated to Professor Ivan Draganić" --> nasl. str. - Tiraž 200. - Bibliografija uz svaki rad. - Registar.

ISBN 978-86-82475-28-6
1. Društvo fizikohemičara Srbije (Beograd)
a) Физичка хемија - Зборници b) Електрохемијско инжењерство - Зборници c) Наука о материјалима - Зборници
COBISS.SR-ID 193433356